

COMPUTATIONAL CONTROL OF
LASER SYSTEMS FOR MICRO-MACHINING

by

AHMED ABDULRAOUF ABDULRAHMAN ISSA

B.ENG.

A thesis submitted for the degree of
Doctor of Philosophy

School of Mechanical and Manufacturing Engineering
Faculty of Engineering and Computing
Dublin City University


September 2007

Supervisors

Dr. Dermot Brabazon
Prof. Saleem Hashmi

Declaration

I hereby certify that this material, which I submit now for assessment on the programme of study leading the award of Doctor of Philosophy is entirely my own work and has not been taken from the work of others and to the extent of that such work has been cited and acknowledged within the text of my work.


24 sep. 2007

AHMED ISSA

ID No.:
52141128
September 2007

بِسْمِ اللَّهِ الرَّحْمَنِ الرَّحِيمِ

اللَّهُ نُورُ السَّمَوَاتِ وَالْأَرْضِ مَثَلُ نُورِهِ كَمِشْكَاةٍ فِيهَا مِصْبَاحٌ
الْمِصْبَاحُ فِي زُجَاجَةٍ الزُّجَاجَةُ كَأَنَّهَا كَوْكَبٌ دُرِّيٌّ يُوقَدُ مِنْ شَجَرَةٍ
مُبَارَكَةٍ زَيْتُونَةٍ لَا شَرْقِيَّةٍ وَلَا غَرْبِيَّةٍ يَكَادُ زَيْتُهَا يُضِيءُ وَلَوْ
لَمْ تَمْسَسْهُ نَارٌ نُّورٌ عَلَى نُورٍ يَهْدِي اللَّهُ لِنُورِهِ مَنْ يَشَاءُ وَيَضْرِبُ
اللَّهُ الْأَمْثَالَ لِلنَّاسِ وَاللَّهُ بِكُلِّ شَيْءٍ عَلِيمٌ ﴿٣٥﴾

صدق الله العظيم

In the name of God, Most Gracious, Most Merciful

☞ GOD is the light of the heavens and the earth. The allegory of His light is that of a concave mirror behind a lamp that is placed inside a glass container. The glass container is like a bright, pearl-like star. The fuel thereof is supplied from a blessed oil-producing tree that is neither eastern, nor western. Its oil is almost self-radiating; needs no fire to ignite it. Light upon light. GOD guides to His light whoever wills (to be guided). GOD thus cites the parables for the people. GOD is fully aware of all things. [35]

Holy Quran, Chapter – 24, Light (Al-Nur), Verse 35.

Publications

This work has been disseminated through the following publications.

Journal Papers:

- Issa, A., Brabazon, D., and Hashmi, S., 3D transient thermal modelling of laser micro-channel fabrication in lime soda glass, *Journal of Materials Processing Technology*, Accepted March 2007.

Conference Papers:

- Issa, A., Brabazon, D., and Hashmi, S., 3D transient thermal modelling of laser micro-channel fabrication in lime soda glass, *International Conference on Advances in Materials Processing and Characterization*, Anna University, Chennai, India, Eds. L. Karunamoorthy, D. Viswanathan, K. Padmanabhan, pp. 824 - 832, ISBN: 81-88237-75-2, 28th - 30th August 2006.
- Issa, A., Brabazon, D., and Hashmi, S., Process modelling of micro channel production using CO₂ laser in silica glass using RSM, *International Conference on Advances in Materials Processing and Technologies*, Ohio University, Las Vegas, NII6, 103, pp. 1 - 5, 30th July - 3rd August 2006.
- Issa, A., Brabazon, D., and Hashmi, S., Improvement of lime soda glass laser microfabrication processing parameters using design of experiments, *7th Conference on Rapid Design, Prototyping, and Manufacture*, Edited by D.M. Jacobson, A.E. Rennie, C.E. Bocking, MJA Print, pp. 9-20, ISBN 0-948314-494, 16th June 2006.
- Issa, A., Brabazon, D., and Hashmi, S., Laser-induced plasma effects on the process of microchannel fabrication in glass using CO₂ laser, *17th Annual Conference of the Irish Plasma and beam processing group in conjunction with the 15th Symposium on Fusion research in Ireland*, NCPST, Dublin City University, Glasnevin, Dublin 9, 13th and 14th June 2006.
- Issa, A., Brabazon, D., and Hashmi, M.S., Computer control of Nd:YVO₄ laser system for 3 dimensional microfabrication in polymers, *6th Conference on Rapid Design, Prototyping, and Manufacture*, Edited by D.M. Jacobson, A.E. Rennie, C.E. Bocking, X-CD Technologies, pp. 35 - 44, ISBN 0-9737783-1-8, 10th June 2005.
- Issa, A., Brabazon, D., and Hashmi, M.S., Three Dimensional microfabrication in polycarbonate using nano-second laser pulses, *8th Annual Sir Bernard Crossland Symposium*, Queens University Belfast, pp. 11-28, ISBN 1898012733, 6th and 7th April 2005.

Seminars and Posters:

- Issa, A., Brabazon, D., and Hashmi, M.S., Exploration of principles and applications of internal microfabrication in dielectrics, Plasma Processes for Biomedical Applications One-Day Workshop, Poster presentation, Seminar at the National Centre for Plasma Science and Technology, DCU – Ireland, 24th May, 2007.
- Issa, A., Brabazon, D., and Hashmi, M.S., Microfabrication in polycarbonate with a Nd:YVO₄ laser system, Poster presentation, Plasma Processes for Biomedical Applications One-Day Workshop, Seminar at the National Centre for Plasma Science and Technology, DCU – Ireland, 24th May, 2007.
- Issa, A., Brabazon, D., and Hashmi, M.S., Direct writing of microchannels in glass with a CO₂ laser system, Poster presentation, Plasma Processes for Biomedical Applications One-Day Workshop, Seminar at the National Centre for Plasma Science and Technology, DCU – Ireland, 24th May, 2007.
- Issa, A., Brabazon, D., Overview of Laser 3D Microfabrication in Polymers, Rapid Manufacturing Technologies Seminar, Mechanical and Manufacturing Engineering School, DCU – Ireland, 3rd April 2007.
- Issa, A., Brabazon, D., and Hashmi, M.S., Laser Microfabrication in Soda-Lime Glass: Theory and Experimental Results, Seminar at the National Centre for Plasma Science and Technology, DCU – Ireland, 28th July 2006.
- Issa, A., Brabazon, D., and Hashmi, M.S., 3 Dimensional Microfabrication in Polycarbonate Using Nanosecond Laser Pulses, Science and Technology Society, Seminar Series, DCU – Ireland, 25th February 2005.
- Issa, A., Brabazon, D., and Hashmi, M.S., 3 Dimensional Micromachining of Polymer Materials, IMechE Speak out for Engineering Competition, University College Dublin, UCD – Ireland, 4th February 2005.

Dedication

TO MY BELOVED MOTHER & FATHER

The source of all the good in me

Acknowledgments

First and above all, thanks to almighty Allah for His everlasting blessing and guidance in conceptualising, developing and completing my study. Indeed, without His help and will, nothing is accomplished.

I am to the highest degree thankful to my supervisor Dr. Dermot Brabazon, who has always helped me in countless ways. He has always initiated challenging research ideas, dedicated time, sourced out work opportunities that helped me financially and broadened my aspects and expertise. On top of all, his humbleness and hands on personality has always inspired me personally. Without his assistance and continuous reassurance I would not have had the confidence to become the engineer that I am now.

I am immensely indebted to my co-supervisor Prof. Saleem Hashmi for his kind, wise and generous supervision and financial assistance which ensured my wellbeing and comfort during my course of study.

I am greatly beholden to my brother and idol Dr. Sharif Issa, whose generous unconditional support was not only financial. His continuous encouragement gave me the strength to conquer this important stage of my career.

I very much thank Mr. Michael Tyrrell, Mr. Martin Johnson, Mr. Jim Barry, Mr. Michael May and the remaining department's technical staff whose expertise in various engineering fields facilitated the smooth running of this project.

I am ever owing favour to my little family in Ireland, Batoul, Zakarya and their wonderful kids for making me feel loved and cherished all the time. I am grateful to my family back home for always being concerned and encouraging me to do my best.

I genuinely show gratitude to my so many friends inside and outside DCU, namely, Nassir, Saiful, Helen, Karolina, Uday, Wissam, Soha, Chiara, Ram, Justyna, Dabnoun, Khaled, Lotfi, Sami, Assad, Fateh, Omar, and especially my best friend Mahmoud. I thank you all for being always concerned about my study, standing by my side without being asked to and most importantly your dazzling sense of humour, it made my life much easier. I cannot forget to be grateful to my office mates Tanya, Patrick, Tuty, Sharon and Mamun for creating a perfectly pleasant study environment.

I apologise for the so many names not included here, this only means that you are closer to my heart than you are to my mind.

Abstract

Depending on the size and geometry, laser-microfabricated structures in transparent materials have applications in telecommunications, microfluidics, micro-sensors, data storage, glass cutting and decorative marking applications. The relations of Nd:YVO₄ and CO₂ laser system parameter settings to the dimensions and morphology of microfabricated structures were examined in this work. Laser system parameters investigated included power, P , pulse repetition frequency, PRF , number of pulses, N , and scanning speed, U . Output dimensions measured included equivalent voxel diameter as well as microchannel width, depth and surface roughness.

A 3D microfabrication system was developed using the Nd:YVO₄ laser (2.5 W, 1.064 μm , 80 ns) to fabricate microstructures inside polycarbonate samples. Microstructure voxels ranged from 48 to 181 μm in diameter. Tight focusing was also achieved with this system using a microscope objective lens to produce smaller voxels ranging from 5 to 10 μm in soda-lime glass, fused silica and sapphire samples.

The CO₂ laser (1.5 kW, 10.6 μm , minimum pulse width of 26 μs) was used to fabricate microchannels in soda-lime glass samples. The cross-sectional shapes of the microchannels varied between v-shape grooves, u-shaped groves and superficial ablated regions. Microchannels dimensions also varied with widths ranging from 81 to 365 μm , depths ranging from 3 to 379 μm and surface roughness between 2 to 13 μm being produced depending on the process settings. The microchannel dimensions were studied in terms of the laser processing parameters using the response surface methodology (RSM) with the design of experiments technique (DoE). The collected results were used to study the effect of the process parameters on the volumetric and mass ablation rates. Moreover, a thermal mathematical model of the process was also developed in order to aid understanding of the process and to allow channel topology prediction a priori to actual fabrication.

Contents

Declaration.....	ii
Publications.....	iii
Dedication.....	v
Acknowledgments.....	vi
Abstract.....	vii
List of Tables.....	xiii
List of Figures.....	xv

Chapter 1 Literature Review

1.1 INTRODUCTION.....	1
1.2 EFFICIENCY OF LASERS FOR MICROFABRICATION.....	2
1.3 BREAKDOWN MECHANISMS FOR INTERNAL MICROFABRICATION.....	4
1.3.1 Avalanche ionisation.....	5
1.3.2 Multiphoton ionisation.....	6
1.3.3 Damage mechanisms – nanosecond to picosecond pulses.....	8
1.3.4 Damage mechanisms – sub-picosecond pulses.....	9
1.4 SURFACE BREAKDOWN MECHANISMS.....	10
1.4.1 Laser-induced plasma and shockwave.....	12
1.5 PARAMETERS AFFECTING THE MICROFABRICATION PROCESS.....	13
1.5.1 Direct process parameters.....	14
1.5.2 Calculated process parameters.....	16
1.5.3 Measured responses.....	18
1.5.4 Self-focusing effects.....	20
1.6 INTERNAL MICROFABRICATION.....	20
1.6.1 Range of microfabrication lasers.....	20

1.6.2	Applications	23
1.6.3	Inspection methods	24
1.6.4	Use of short-wavelength lasers in industry	27
1.6.5	Alternative focusing method in commercial systems	29
1.7	SURFACE MICROFABRICATION	31
1.7.1	Using short wavelength lasers.....	31
1.7.2	Surface microfabrication using CO ₂ lasers	32
1.7.3	Use of CO ₂ laser in research	34
1.7.4	Use of CO ₂ lasers in industry	35
1.8	TRANSPARENT MATERIALS FOR THIS STUDY	38
1.8.1	Polycarbonate.....	38
1.8.2	Soda-lime glass	40
1.9	STUDY FOCUS AND OBJECTIVES.....	43
1.9.1	Literature summary	43
1.9.2	Hypothesis.....	44
1.9.3	Aims of the study	45
1.9.4	Thesis outline	46

Chapter 2 Hardware and Software Setup

PART I: HARDWARE SETUP	47
2.1 INTRODUCTION.....	47
2.2 Nd:YVO ₄ LASER SYSTEM	47
2.2.1 Process layout	48
2.2.2 The laser system specifications.....	49
2.2.3 Controlling PC interface	52
2.2.4 The laser external optics.....	54
2.2.5 Focusing methods	56
2.2.6 Achromat lens focusing	57
2.2.7 Practical spot size calculations.....	58
2.2.8 Spherical aberration calculations	60
2.2.9 Microscope objective lens focusing.....	61
2.2.10 3D positioning stage.....	64
2.3 CO ₂ LASER SYSTEM HARDWARE AND SPECIFICATIONS.....	69
2.3.1 Controlling the CO ₂ laser system.....	71

2.3.2 The motion control system.....	72
PART II: SOFTWARE SETUP.....	73
2.4 INTRODUCTION.....	73
2.5 CAD MANIPULATION CODES	74
2.5.1 STL file format.....	74
2.5.2 STL ASCII format	76
2.5.3 STL binary format.....	77
2.5.4 Read STL code.....	78
2.5.5 Slice settings code.....	81
2.5.6 Planes code.....	82
2.5.7 Slicing code.....	83
2.6 POSITION CONTROL CODE	87
2.7 LASER CONTROL CODES	89
2.7.1 RS232 communication codes.....	89
2.7.2 Initial settings code	92
2.7.3 Settings before operation code.....	93
2.7.4 Laser control code.....	95
2.7.5 Laser switch code.....	95
SUMMARY	97

Chapter 3 Nd:YVO₄ Laser Experiments

3.1 INTRODUCTION.....	98
3.2 MICROFABRICATION EXPERIMENTS.....	98
3.2.1 The equipment used	98
3.2.2 Pulse energy and fluence calculations	98
3.2.3 Experiment design.....	99
3.2.4 Fabrication of samples	100
3.2.5 Experimental procedure	100
3.2.6 Inspection of the samples	101
3.2.7 Microfabricated voxel morphology analysis.....	105
3.2.8 Microfabricated voxel size analysis	106
3.2.9 Side view microscopic inspection.....	110
3.2.10 General discussions on the microfabrication experiment	112

3.3	DIMENSIONAL ANALYSIS EXPERIMENTS	113
3.4	THREE DIMENSIONAL CAD MICROFABRICATION	118
3.5	MICROFABRICATION WITH MICROSCOPE OBJECTIVE LENS	119
3.6	OVERALL DISCUSSIONS	124
	SUMMARY	125

Chapter 4 CO₂ Laser Experiments

4.1	INTRODUCTION.....	126
4.2	EQUIPMENT AND MATERIALS USED	126
4.3	SCREENING EXPERIMENT	126
4.4	DESIGN OF EXPERIMENTS.....	128
4.5	EXPERIMENTAL PROCEDURE	129
4.6	OPTICAL MICROSCOPE INSPECTION	131
4.7	SCANNING ELECTRON MICROSCOPE	131
4.8	LASER PROFILEOMETER INSPECTION	132
4.8.1	Length measured from each channel.....	132
4.8.2	Profile scanning procedure and software	133
4.8.3	Measurements and calculations of the channel parameters	137
4.8.4	Channel width measurement	138
4.8.5	Channel depth measurement	141
4.8.6	Surface roughness measurement	144
4.8.7	Other measurements.....	146
4.9	STATISTICAL ANALYSIS OF RESULTS	147
4.9.1	Design-Expert software and regression method	147
4.9.2	Width model results	148
4.9.3	Depth model results	157
4.9.4	Ra model results.....	165
	SUMMARY	175

Chapter 5 Thermal Mathematical Model

5.1	INTRODUCTION.....	177
5.2	EXPLANATION OF THE MATHEMATICAL MODEL.....	177

5.3 PROCESS CONSIDERATIONS.....	183
5.3.1 Material under experiments.....	183
5.3.2 Laser-material interaction	183
5.4 PROCESS SIMULATION	185
5.4.1 Planar isotherms.....	186
5.4.2 Channel 3D geometry	194
5.4.3 Thermal history	197
SUMMARY	198

Chapter 6 Discussions and Conclusions

6.1 INTRODUCTION.....	199
6.2 INDIRECT PROCESS RESPONSE PARAMETERS	199
6.2.1 Indirect parameters' equations	199
6.2.2 Parameters effects on channel width and depth.....	202
6.2.3 Parameters effects on the ablation rates	208
6.3 SIMULATED VERSUS EXPERIMENTAL MORPHOLOGY	215
6.4 COMPARATIVE PROCESS PARAMETERS' EFFECTS.....	220
6.4.1 Width and depth trends	220
6.4.2 Ra trend based on simulation results.....	224
6.5 GENERAL DISCUSSION	227
6.6 CONCLUSIONS AND FUTURE RECOMMENDATIONS.....	228
References.....	230

Appendices

APPENDIX A – BAND THEORY OF SOLIDS.....	A - 1
APPENDIX B – EXTRA PARTS OF CHAPTER 2.....	B - 1
APPENDIX C – EXTRA PARTS OF CHAPTER 3.....	C - 1
APPENDIX D – EXTRA RESULTS FROM CHAPTER 4.....	D - 1
APPENDIX E – EXTRA RESULTS FROM CHAPTER 5	E - 1
APPENDIX F – EXTRA RESULTS FROM CHAPTER 6.....	F - 1

Table 3.9: Breakdown thresholds summary for tested materials	124
Table 4.1: Control parameters ranges	128
Table 4.2: Control parameters levels and their corresponding DoE coding	128
Table 4.3: Design of experiments	130
Table 4.4: Microchannel experiments results	146
Table 4.5: General result notes.....	148
Table 4.6: ANOVA results of the width model	149
Table 4.7: Actual vs predicted and the residual from the width model	150
Table 4.8: Relative effects of the process model parameters on width.....	153
Table 4.9: ANOVA analysis of depth model.....	158
Table 4.10: Actual versus predicted of the design points	159
Table 4.11: Relative effects of the process model parameters on depth.....	162
Table 4.12: ANOVA analysis of Ra model	169
Table 4.13: Relative effects of the process model parameters on <i>Ra</i>	172
Table 4.14: Actual versus predicted of the design points	174
Table 5.1: Thermal properties of soda-lime glass.....	183
Table 5.2: Energy percentages needed for breakdown	184
Table 6.1: Indirect process parameters and ablation rates	202

List of Figures

Figures of Chapter 1

Figure 1.1: Schematic of breakdown mechanisms, (a) multiphoton absorption, (b) free carrier absorption and (c) impact ionisation.....	7
Figure 1.2: Schematic of the laser-induced plasma and shockwave.....	13
Figure 1.3: Spot size of a focused Gaussian laser beam - TEM_{00} mode.....	17
Figure 1.4: A basic microfabrication experimental set up.....	21
Figure 1.5: Oscillator-only micromachining in action.....	22
Figure 1.6: Dark-field scattering setup for determining the energy threshold for bulk damage using a low-NA objective for focusing fs laser pulses.....	22
Figure 1.7: Data recording-and-readout system.....	23
Figure 1.8: Waveguides fabricated using a Ti:Sapphire laser (810 nm) at 120 fs, 200 kHz mode locked pulses, and an average power of 975 mW.....	24
Figure 1.9: Optical microscope image of microfabricated structures in Corning 0211 glass.....	25
Figure 1.10: Void arrays: near surface (a) and (c) transmission microscopy; 15 μm deeper (b) and (d) confocal reflection microscopy.....	25
Figure 1.11: Binary data pattern stored in fused silica, (a) an optical microscope image and (b) a higher magnification SEM image.....	26
Figure 1.12: A 3D novelty shape marked inside BK7.....	27
Figure 1.13: Y-branch holes produced by femtosecond laser and chemical etching.....	28
Figure 1.14: Schematic of femtosecond laser etching.....	29
Figure 1.15: Helical waveguide.....	29
Figure 1.16: Schematic of Crystalix laser marking system configuration.....	30

Figure 1.17: SEM micrographs of TEA CO ₂ laser-irradiated soda-lime glass at: (a) 15 J/cm ² and (b) 10 J/cm ² . Scale = 200 μm	32
Figure 1.18: A 0.8 μm microcrack induced in glass by CO ₂ irradiation.....	33
Figure 1.19: Structures ablated in the surface of glass using CO ₂ laser	36
Figure 1.20: Glass cut edge with a CO ₂ laser, water aerosol and cooling technique.....	36
Figure 1.21: Glass marking with CO ₂ laser (a) a close-up of a 2.26 cm ² 2D code marked on CRT monitor glass with 25 W in 2.6 seconds, and (b) a design marked on glass using 20 W, a 125 mm focal length lens and a scanning speed of 114 cm/min	37
Figure 1.22: Surface marking of glass using a 10 W CO ₂ laser at a speed of 76 cm/s, (a) general image and (b) an close-up of text marking shows that the line width of the mark is 252 μm, with a crack depth penetration of 51 μm	38
Figure 1.23: The bonding structure of polycarbonate.....	39
Figure 1.24: Random network of pure silica glass.....	41
Figure 1.25: Two-dimensional analogue of soda-lime glass	41

Figures of Chapter 2

Figure 2.1: The complete laser system components	47
Figure 2.2: Process flow chart for the developed microfabrication system.....	48
Figure 2.3: Spectra Physics laser power supply used in this work	50
Figure 2.4: Monochromaticity of the emission spectra using a laser diode compared with krypton arc lamp and a black body source.....	51
Figure 2.5: Q-Switch pulses generation diagram.....	54
Figure 2.6: Optics plate top and side view.....	55
Figure 2.7: Rayleigh range of the laser beam propagation	57
Figure 2.8: Optical components setup for the achromat lens focusing.....	58
Figure 2.9: Beam size on photographic paper at 115 mm from the expander.	59
Figure 2.10: Spherical aberration in a basic lens	61
Figure 2.11: Laser beam focusing using an objective lens	61

Figure 2.12: Optical components parameters of the new setup	63
Figure 2.13: The 3D positioning stage built for this work.....	65
Figure 2.14: Stepper motor control block diagram	65
Figure 2.15: A basic set up of a stepper motor system	66
Figure 2.16: Schematic connection of a stepper motor to the control PC.....	67
Figure 2.17: Stepper motor driver, (a) Pins configuration and (b) motor's connection.	68
Figure 2.18: The CO ₂ laser resonator configuration	70
Figure 2.19: The CO ₂ laser system used in this study	72
Figure 2.20: Flow chart of the system's production process	73
Figure 2.21: A sample tessellated solid model	75
Figure 2.22: Right-hand rule, (a) an exterior surface and (b) an interior surface	75
Figure 2.23: The vertex-to-vertex rule. The left figure shows a violation of the rule and a correct configuration is shown on the right.....	75
Figure 2.24: CAD file manipulation code flow chart	79
Figure 2.25: Read STL code front panel.....	80
Figure 2.26: STL file filtering: (a) Original 4 facets vertex information, and (b) Reduced text file showing the same facet vertex information	81
Figure 2.27: Slice Settings code front panel	82
Figure 2.28: Planes code front panel.....	82
Figure 2.29: Slicing concept using Z planes	83
Figure 2.30: Single plane slice (planar contour)	83
Figure 2.31: Significance of segmentation, (a) slicing without segmentation and (b) slicing with segmentation.....	84
Figure 2.32: Filtering the repeated intersection points is necessary	85
Figure 2.33: Sample planar contour of a sphere	85
Figure 5.34: Part of the sphere build file.....	86
Figure 2.35: Full plot of the sphere.....	86
Figure 2.36: Flow chart of the Slicing Code.....	87

Figure 2.37: Position control code front panel.....	88
Figure 2.38: Flow chart of the positioning code	89
Figure 2.39: Serial port configuration in LabVIEW	90
Figure 2.40: Received data overflow in the serial port buffer	91
Figure 2.41: Initial settings code front panel displayed on stand up.....	92
Figure 2.42: Sample initial settings file	93
Figure 2.43: Laser Control code front panel	93
Figure 2.44: Front panel of the Settings Before Operation code	94
Figure 2.45: The front panel of the Diode Switch code displayed on stand up	96
Figure 2.46: The front panel of the Laser Control code while laser diode is ON.....	96

Figures of Chapter 3

Figure 3.1: Front panel of the fluence calculations code	99
Figure 3.2: Illustration of a sample's subsets and microfabricated voxels' settings..	101
Figure 3.3: Voxel diameter definition, (a) star-shaped, and (b) circular voxel.....	102
Figure 3.4: Microfabricated voxel morphology, (a) star-like voxel at low <i>PRF</i> effect, (b)spherical shape voxel at higher <i>PRF</i>	106
Figure 3.5: <i>PRF</i> effect on voxel size at $P = 0.2 W$	107
Figure 3.6: <i>PRF</i> effect on voxel size at $P = 0.3 W$	108
Figure 3.7: <i>PRF</i> effect on voxel size at $P = 0.4 W$	108
Figure 3.8: <i>PRF</i> effect on voxel size at $P = 0.5 W$	109
Figure 3.9: Number of pulses effect on voxel diameter at different power values....	110
Figure 3.10: Side images of microfabricated voxels, laser beam propagation was from the bottom of the image.....	111
Figure 3.11: Front panel of the intensity profile calculations code.....	112
Figure 3.12: Spatial resolution of microfabricated voxels.....	113
Figure 3.12: Spatial resolution of microfabricated voxels.....	113
Figure 3.13: Contents of the error checking sample	115

Figure 3.14: Steps leading to the final 3D sliced object (a) CAD design, (b) one planar contour and (c) fully sliced design	118
Figure 3.15: DCU logo fabricated inside polycarbonate	119
Figure 3.16: Voxels produced inside a 2 mm thick soda-lime glass sheet.	120
Figure 3.17: One voxels produced using 200 pulses inside a 2 mm thick soda-lime glass sheet.....	120
Figure 3.18: DCU logo microfabricated inside a 2 mm thick soda-lime glass sheet...	121
Figure 3.19: Two waveguides fabricated in a 2 mm thick fused silica sheet.....	122
Figure 3.20: Side view of the upper waveguide in figure 3.19	122
Figure 3.21: Microscopic image of the two waveguides from figure 3.19	123
Figure 3.21: Voxels in sapphire, (a) on the surface and (b) inside the sample	123

Figures of Chapter 4

Figure 4.1: Process control parameters, laser beam power, P , pulse repetition frequency, PRF , translation speed, U , and focus depth, Df	127
Figure 4.2: Microchannel schematic indicating response parameters measured: the channel's width, depth and roughness	127
Figure 4.3: Microscopic image of microchannel 10	131
Figure 4.4: SEM image of microchannel 19	132
Figure 4.5: The 3D laser profileometer.....	132
Figure 4.6: Schematic of the length covered by a laser pulse; effect of PRF and U .	133
Figure 4.7: 3D profile scanner controller code front panel.....	134
Figure 4.8: Schematic of top view of sample channel with data points illustrated....	135
Figure 4.9: A sample channel before aspect ratio correction.....	136
Figure 4.10: Sample channel with corrected aspect ratio	137
Figure 4.11: Microchannel parameters measurements, scan of CH 14.....	138
Figure 4.12: Front panel of the width and depth measurement code	139
Figure 4.13: Sample channel width measurement procedure	140

Figure 4.14: Top view of a sample channel width measurement procedure.....	140
Figure 4.15: Front view of a sample channel's width measurement.....	141
Figure 4.16: Sample channel depth measurement procedure	142
Figure 4.17: Auxiliary view of a sample channel's depth measurement procedure	143
Figure 4.18: Side view of a sample channel's depth measurement procedure	143
Figure 4.19: Roughness measurement code showing a profile line.....	144
Figure 4.20: Roughness measurement code showing the roughness profile	145
Figure 4.21: Actual versus predicted width values	151
Figure 4.22: Cubic representation of the design points and the experimental and width model results	151
Figure 4.23: Perturbation plot of the process control variables' effects on the width .	153
Figure 4.24: P and PRF contour showing the interactive effect on the width.....	154
Figure 4.25: 3D view of the interactive effect of P and PRF on width	155
Figure 4.26: P and U contour showing the interactive effect on the width	156
Figure 4.27: 3D view of the interactive effect of P and U on width.....	156
Figure 4.28: PRF and U contour showing the interactive effect on the width	157
Figure 4.29: 3D view of the interactive effect of PRF and U on width.....	157
Figure 4.30: Actual versus predicted scattering of the data points	160
Figure 4.31: Cubic representation of the design points and the experimental and depth model results	161
Figure 4.32: Perturbation plot of the process control variables' effects on the depth. .	161
Figure 4.33: P and PRF contour showing the interactive effect on the depth	163
Figure 4.34: 3D view of the interactive effect of P and PRF on depth.....	163
Figure 4.35: P and U contour showing the interactive effect on the depth.....	164
Figure 4.36: 3D view of the interactive effect of P and U on depth.....	164
Figure 4.37: PRF and U contour showing the interactive effect on the depth.....	165
Figure 4.38: 3D view of the interactive effect of PRF and U on depth	165
Figure 4.39: Idealised model of surface roughness.....	168

Figure 4.40: Actual versus predicted scattering of the data points	170
Figure 4.41: Perturbation plot of the process control variables' effects on Ra	171
Figure 4.42: Perturbation plot of the process control variables' effects on Ra at high P values.....	171
Figure 4.43: 3D view of the interactive effect of PRF and U on Ra	172
Figure 4.44: 3D view of the interactive effect of PRF and U on Ra at low P	173
Figure 4.45: 3D view of the interactive effect of PRF and U on Ra at high P	173

Figures of Chapter 5

Figure 5.1: Heat point source in the surface of the workpiece.....	178
Figure 5.2: The pulsed power input given by equation 5.4.....	180
Figure 5.3: SEM image of (a) minimum fluence channel 25, and (b) maximum fluence channel 21	185
Figure 5.4: Mesh elements generated for the Y-axis	187
Figure 5.5: Mesh elements generated for the X-axis	187
Figure 5.6: Schematic of the mesh generated for simulating planar isotherms	188
Figure 5.7: Front panel of the material selection code.....	189
Figure 5.8: Front panel of the planar isotherm simulation code	190
Figure 5.9: Channel 14: 3D isotherm of one pulse at $z = 0$	191
Figure 5.10: Channel 14: Top view of isotherm of one pulse at $z = 0$	192
Figure 5.11: 3D isotherms of three pulses of channel 14.....	192
Figure 5.12: Top view of three pulses isotherms of channel 14	193
Figure 5.13: Channel 14 isotherms of (a) 10 pulses and (b) 20 pulses	193
Figure 5.14: Mesh elements generated for the Z-axis.....	194
Figure 5.15: Front panel of 3D simulation code	195
Figure 5.16: Front panel of the 3D channel viewing code.....	196
Figure 5.17: Thermal histories of four points on the surface of glass sheet	198

Figures of Chapter 6

Figure 6.1: Channel cross-sectional area shape	200
Figure 6.2: I and F_M effect on width at $U = 100$ mm/min and different PRF values .	203
Figure 6.3: I and F_M effect on width at $U = 300$ mm/min and different PRF values .	204
Figure 6.4: I and F_M effect on width at $U = 500$ mm/min and different PRF values .	204
Figure 6.5: I and F_M effect on depth at $U = 100$ mm/min and different PRF values..	205
Figure 6.6: I and F_M effect on depth at $U = 300$ mm/min and different PRF values..	205
Figure 6.7: I and F_M effect on depth at $U = 500$ mm/min and different PRF values..	206
Figure 6.8: E_P and F effect on channel width for different U values.....	207
Figure 6.9: E_P and F effect on channel depth for different U values	207
Figure 6.10: E_P and F effect on total ablated volume at different U values	208
Figure 6.11: E_P and F effect on total ablated mass at different U values	209
Figure 6.12: Ranges of total energy deposited for different P settings.....	209
Figure 6.13: E_P and F effect on ablated volume per pulse at different U values	211
Figure 6.14: E_P and F effect on ablated volume per second at different U values	211
Figure 6.15: E_P and F effect on ablated volume per Joule at different U values	212
Figure 6.16: E_P and F effect on ablated mass per pulse at different U values	212
Figure 6.17: E_P and F effect on ablated mass per second at different U values	213
Figure 6.18: E_P and F effect on ablated mass per Joule at different U values	213
Figure 6.19: Effect of I and F_M on the total ablated volume at $U = 100$ mm/min	214
Figure 6.20: Effect of I and F_M on the ablated volume per pulse at $U = 100$ mm/min.	214
Figure 6.21: Effect of I and F_M on the ablated volume per (s) at $U = 100$ mm/min	215
Figure 6.22: Effect of I and F_M on the ablated volume per Joule at $U = 100$ mm/min.	215
Figure 6.23: Comparison of channel 21, (a) SEM and (b) simulated isotherms.....	216
Figure 6.24: Side view of three pulses from channel 19.....	217
Figure 6.25: Side view of three pulses from channel 20.....	218
Figure 6.26: Side view of three pulses from channel 21	218

Figure 6.27: Channel 5 comparison (a) microscopic and (b) simulated image	219
Figure 6.28: Channel 14 comparison (a) microscopic and (b) simulated image	219
Figure 6.29: Channel 23 comparison (a) microscopic and (b) simulated image	220
Figure 6.30: <i>PRF</i> and <i>P</i> effects on channel width at $U = 500$ mm/min.....	221
Figure 6.31: <i>PRF</i> and <i>P</i> effects on channel depth at $U = 500$ mm/min.....	222
Figure 6.32: Pulse energy effect on simulated channel width	223
Figure 6.33: Pulse energy effect on simulated channel depth.....	223
Figure 6.34: <i>PRF</i> and <i>P</i> effects on <i>Ra</i> at $U = 100$ mm/min.....	225
Figure 6.35: <i>PRF</i> and <i>P</i> effects on <i>Ra</i> at $U = 300$ mm/min.....	225
Figure 6.36: <i>PRF</i> and <i>P</i> effects on <i>Ra</i> at $U = 500$ mm/min.....	226
Figure 6.37: Pulse energy effect on simulated channel <i>Ra</i>	227

Chapter 1

Literature Review

1.1 Introduction

LASER stands for *Light Amplification by Stimulated Emission of Radiation* [1]. Since their invention, lasers have gained a wide range of application in the engineering, biomedical, telecommunication and industrial fields [2, 3, 4]. The first laser, a ruby laser, was reported in 1960 by T.H. Maiman [5]. Four years after that, some publications appeared reporting laser-induced damage in transparent materials using ruby lasers. Some of the first publications were those of Guiliano and Chiao et. al. [6, 7]. However, Chiao et. al. reported that this phenomenon was first reported by M. Hercher*. These initial workers reported the generation of thin, long streaks of ionisations and damages due to focusing intense laser beams inside optical materials. Whereas, low intensity laser beams pass through transparent materials without causing any observable effects, at sufficiently high laser intensities absorption, refractive index changes, removal of the material from the surface, production of internal voids, melting, vaporisation and even violent shattering may be induced [8].

Micromachining or microfabrication can be most easily defined as a machining process which forms structures that can be measured on a micrometer scale. Microfabrication can be applied to metals and other materials as well as transparent materials. However, throughout this thesis, the use of the microfabrication term refers to transparent material unless otherwise is stated. The terms microfabrication and micromachining will be used interchangeably in this thesis as they imply the same effect. In recent years, the structural alterations produced in transparent materials by ultrashort laser pulses have been used for micromachining [9, 10]. The availability of laser pulses with femtosecond duration allows materials to be subjected to higher laser intensities than ever before, opening the door to the study of laser/material interactions in a new regime [11]. Despite this long history, much still remains to be learned about the interaction of high-intensity laser pulses with transparent materials.

Microfabrication is achieved by tightly focusing a laser beam on the surface or underneath the surface of a target material causing localised heating, melting and the subsequent ablation of the material in the focal region [12-15]. Due to the tight focusability of lasers, the scale of the induced damage is generally in the micrometer range. Internal focusing allows the fabrication (void forming) of micro-scale volume elements (voxels) inside the bulk of the transparent material [15] which may be used in applications such as novelty markings [16] and optical data storage [17, 18]. The internal fabricated structures may also be continuous such as the fabrication of internal

* M. Hercher, Journal of Optical Society of America, Vol. 54, pp. 563, 1964.

microchannels or waveguides [10]. Since the microfabricated zone is either re-solidified material or void, it will have a refractive index different from the surrounding material. This refractive index change is induced by the deposition of energy at that specific point. The fabricated structures are permanent due to the photo modification of the optical, mechanical and chemical properties at the focal point [15]. On the other hand, when the laser is focused on the surface, the micro-structurally altered zones are usually ablated zones. The ablated shapes may be controlled by scanning the laser beam or the sample to produce either continuous or isolated structures such as microchannels or pixellated coded images respectively [19, 20].

1.2 Efficiency of lasers for microfabrication

The unique properties of lasers are directivity, monochromaticity coherence and high power irradiances or intensities [21, 22]. Moreover, Q-switched laser pulses are produced which have high power, energy or fluence peaks [1]. Q-switching is achieved by storing the energy during the population inversion (pumping) of the lasing material's atoms until it reaches a certain level and then releasing it very quickly. The generation of these pulses using different methods was illustrated by a number of workers [1, 23]. Q-switched or pulsed laser beam is more efficient for ablation due to the high energies that can be delivered in the short pulse durations [24]. This leads to precise and confined energy deposition in the focal region. Furthermore, transparent materials can only be efficiently ablated using pulsed laser beams because they produce high peak intensities within short time durations [24]. Many microfabrication or micromachining applications in scientific research and industry have been developed around lasers in the last few decades. Laser systems used for machining include CO₂, Nd:YVO₄, Nd:YAG, (ArF) excimer lasers and Ti:sapphire [19, 25-28].

The name and objective of microfabrication implies the necessity of using a machining tool that is smaller or at least comparable to the desired structures' scale. To accomplish that, two of the most significant laser beam attributes are the wavelength and pulse duration are controlled as they both contribute to ablation scale and precision [15, 29]. Focusability is a direct function of the laser emission wavelength [26]. In this field, the lasers used have wavelengths that range between few hundreds of nanometres such as (ArF) excimer laser 193 nm or the third (355 nm) and fourth (266 nm) harmonics of Nd:YVO₄ or Nd:YAG lasers (1064 nm) [25, 30, 31]. Lasers with wavelengths of a few micrometers such as CO₂ lasers 10.6 μm are also used for microfabrication [19, 32]. Proper focusing of laser beams can lead to an effective focal spot size that is

comparable to the emission wavelength [15]. If tight focusing is employed via high NA objectives lenses, then the focal spot can be downsized to fractions of the emission wavelength [15, 33]. The latter fact means that spot sizes of submicron or micron sizes can be achieved, which contributes to precision machining. Another important factor is the laser pulse duration.

The development of ultra-short pulse duration lasers has also contributed to the enhanced machining precision [29]. In this case, the absorption or diffusion timescales over which the thermal energy is deposited or transferred to the target materials are very small, resulting in confined and localised ablation with minimal or no heat affected zones [34, 35]. The short pulse duration advantage may be enhanced by having a laser system that can deliver the pulses at a high repetition rate, which can ensure a uniform heat deposition and reduce the amount of microcracking [29]. There are other properties of laser beams that make them very efficient for microfabrication. These are discussed below:

- **Absorption properties of transparent materials:** Transparent or dielectric materials absorb laser emission in nonlinear processes [11]. These nonlinear absorption mechanisms rely on the promotion or growth of free electrons in the focal region [36]. A high intensity pulsed laser beam can provide a high intensity of photons that can be non-linearly absorbed by the transparent material leading to its breakdown and consequent ablation [37].
- **Internal focusing:** The breakdown threshold intensity or fluence is distributed within a small confined volume from the focal spot [18]. This means that if the laser beam is focused inside a material that is transparent to the emission wavelength then the breakdown can take place in the bulk of the material without affecting the surface [38].
- **Universal machining:** Virtually any transparent material can be processed by laser irradiation and requires less sophisticated equipment compared to other techniques such as photolithography, ion-implantation or chemical etching techniques [9, 39-41]. Photolithographic processes are sophisticated and require photosensitive materials that are sensitive to certain wavelengths and usually require extra steps to obtain the required structure [9, 42]. In UV photosensitive micromachining, for example, the transparent material has to be sensitive to UV radiation [9, 40, 42, 43]. In this manner, lasers offer a cheaper and faster alternative for microfabrication applications [2].

- **Direct writing:** Laser microfabrication of transparent materials does not usually require further steps to produce the structures. This makes the process faster and cheaper compared to other techniques that require chemical etching for instance [2, 5, 44, 45].
- **Absence of physical contact:** Laser microfabrication does not involve physical contact between the tool and the material. This leads to more precise and cleaner machining without mechanical forces between the sample and tool that can cause residual stresses, related post machining defects and eliminates tool wear as in traditional machining [26, 29, 46, 47].
- **Dimensional accuracy:** Using computers or microprocessors to control lasers has led to a high accuracy of heat deposition into the target material [29, 45, 48].
- **Intricate structures:** Scanning the laser beam in the material enables the fabrication of intricate structures in 2D or 3D. These structures can be fabricated on the surface or in bulk samples [3, 29].

Microfabrication takes place when the laser irradiation causes the material to heat up, melt and vaporise or break down. There are several mechanisms which are likely to play a role in this process. These include the processing parameters, focusing, material properties and doping [39]. The study of laser-induced breakdown phenomenon in transparent materials is of particular importance to understanding the mechanisms taking place when transparent materials are to be micromachined. It is also important to know the scales of the laser beam intensities or parameters that will induce breakdown. Interestingly, high power lasers can be self destructive because crystals, mirrors, and other optical components show degradation when exposed to high laser irradiances over time [37, 49]. This fact is of practical design and economic importance to both laser manufacturers and users. The following discussion tackles the mechanisms leading to breakdown inside section 1.3 or on the surface section 1.4 of transparent materials.

1.3 Breakdown mechanisms for internal microfabrication

Laser-induced breakdown can be defined as the generation of a practically totally ionised gas and excited electrons (plasma). This plasma can be observed as a glow or a flash or a bright spark in the focal region [6, 8, 36]. The laser energy absorbed by the excited electrons can be released in radiative and nonradiative fashions [36, 50]. For that emitted in a nonradiative fashion, the energy can be stored in the bulk material as thermal energy, which gives rise to a sharp temperature increase within the breakdown

region. Previous research has shown average measured plasma temperatures in the range 5,000 to 20,000 °C, which is enough to cause damage in most dielectric materials [26, 49, 51]. The extent of the damage varied from tiny pits and bubbles to large fractures [6, 52].

There are various explanations of the laser-induced breakdown mechanisms in transparent materials [49]. A number of the breakdown mechanisms illustrated by Ready were hypersonic waves, intraband absorption, absorption at defects, high temperatures-microplasmas, superposition of stress waves, avalanche and multiphoton absorption [37, 49]. However, the most commonly quoted dielectric materials breakdown mechanisms in the literature are avalanche ionisation, multiphoton ionisation, or the combination of both [11, 26, 37, 53]. These absorption mechanisms are based on the generation and growth of free electrons. Dielectric materials absorb energy via mechanisms that are different from those for metals or conductors [51]. This is because, in dielectrics, there are no mobile electrons in the conduction band and it is separated from the valence band by a band gap, see appendix A for a brief summary of the band theory of solids [54]. The energy deposited by these mechanisms promotes electrons from the valence band to the conduction band and consequently induces breakdown and material damage in the dielectric material [26]. The following subsections summarise the principles of avalanche and multiphoton ionisation.

1.3.1 Avalanche ionisation

This mechanism is also called cascade or impact ionisation [51, 55]. Avalanche ionisation involves absorption of laser radiation by electrons when they collide with neutrons [36]. An electron already in the conduction band of the material linearly absorbs several laser photons sequentially, moving to higher energy states in the conduction band. In order to conserve both energy and momentum, the electron must transfer momentum by absorbing or emitting a phonon when it absorbs a laser photon. To cause ionisation, the minimum required electron energy is expressed by $nhf \geq E_g$, where n is the smallest number of photons which satisfies the relation, h is Planck's constant, f is the frequency corresponding to the laser emission wavelength and E_g is the band gap energy [22, 36] After the sequential absorption of n photons, if the electron's energy exceeds the conduction band minimum by more than the band gap energy, then the electron can collisionally ionise another electron from the valence band [11]. The impact or cascade ionisation can be expressed through the following reaction



where, e^- is the electron and M is a neutral molecule or atom. The reaction expressed in equation 1.1 will lead to cascade breakdown and the electron concentration will increase exponentially with time [36]. Avalanche ionisation therefore requires two necessary conditions, namely

- (1) That there exists an initial conduction band electron in the focal volume, and
- (2) That the electrons acquire energy greater than the band gap of the dielectric solid.

As mentioned earlier, avalanche ionisation requires some “seed” electrons in the conduction band of the material [8, 37, 49]. These initial electrons are provided either by thermally excited carriers or easily ionised impurity or defect states [11, 38]. These impurities or defect states have electrons in the conduction band or smaller band gap energies than the dielectric material itself [36]. These impurities may become ionised at low laser intensities. For example glasses, as dielectric transparent materials, contain Al, Ca, Mg and Na molecules, which will provide seed electrons upon partial ionisation [36].

1.3.2 Multiphoton ionisation

Photoionisation (PI) refers to direct excitation of an electron by the laser field. A single photon of visible light does not have enough energy to excite an electron in a transparent material from the valence to the conduction band. Hence, multiple photons are required to excite the electron [37]. Depending on the laser frequency and intensity, there are two different regimes of photoionisation, namely, multiphoton ionisation (MPI) regime and tunnelling ionisation regime [11]. Multiphoton ionisation takes place at high laser frequencies but still below that required for single photon absorption [11]. MPI involves a nonlinear ionisation that occurs due to the simultaneous absorption of several photons by an atom or molecule [11, 36]. This simultaneous absorption is different from the sequential absorption in avalanche ionisation. MPI is described by the following reaction



For the electron in equation 1.2 to be promoted from the valence to the conduction band by this simultaneous multiphoton absorption, it must absorb enough photons so that the number of photons absorbed, n , times the photon energy, hf , is equal to or greater than the band gap E_g of the material as is necessary for avalanche ionisation [11, 36].

Multiphoton ionisation can directly photoexcite carriers that can provide seed electrons for avalanche ionisation [11].

To summarise, breakdown occurs when the mechanisms described above deposit sufficient energy into transparent materials. High temperatures and pressures result and hence the material is ejected from the focal volume leaving permanent damage or a void surrounded by denser material [52]. The absorption can take place via avalanche, multiphoton ionisation or the mixture or both. Avalanche ionisation takes place when an electron already in the conduction band, as shown in figure 1.1 (b), absorbs photons linearly. Linear absorption is possible in this case since the electron is no longer hindered by the band gap [38]. When such an electron absorbs sufficient energy $n hf \geq E_g$, where n is the number of photons absorbed sequentially, it can then use the excess energy to ionise another electron via direct collision, also known as impact ionisation, see figure 1.1 (c) [11, 56]. The resulting two electrons in the conduction band can then continue the process of linear absorption and impact ionisation to achieve an exponential growth of free electrons. The seed electrons for avalanche ionisation can also be provided by multiphoton ionisation at sufficiently high laser intensities. The electron in figure 1.1 (a) simultaneously absorbs the energy from five photons to overcome the band gap. Once an electron is promoted to the conduction band, it serves as a seed electron to the avalanche ionisation [38, 56].

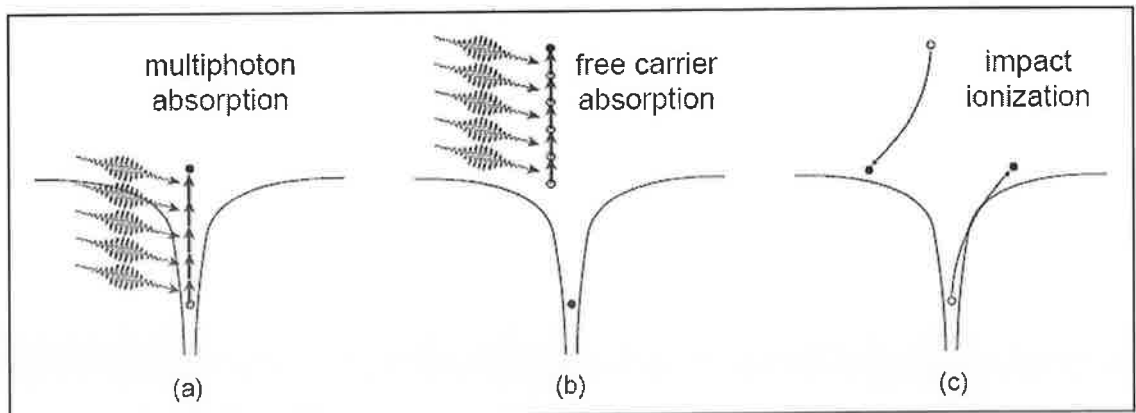


Figure 1.1: Schematic of breakdown mechanisms, (a) multiphoton absorption, (b) free carrier absorption and (c) impact ionization, adapted from [56].

So far, the processes were explained in terms of the laser emission frequency (corresponding to laser wavelength and photon energy), the material band gap, and the impurities in the material. These parameters will decide which process is most likely to

take place. The laser pulse width has a significant effect on the dominant breakdown mechanism as well, which is explained in the following sections.

1.3.3 Damage mechanisms – nanosecond to picosecond pulses

For pulse durations longer than a few tens of picoseconds, energy is transferred from the laser-excited electrons to the lattice within the time scale of the pulse duration. This energy is carried out of the focal volume by thermal diffusion. Damage occurs when the temperature of the material in the irradiated region becomes high enough for the material to melt or fracture [28, 57]. Energy is deposited into the material by the laser pulse and is transported out of the irradiated region by thermal diffusion, thus it is the relative rate of energy deposition and thermal diffusion that determines the damage threshold [11, 40].

For damage caused by pulses longer than a few tens of picoseconds, the source of the initial conduction-band electrons that seed the avalanche ionisation is very important [8, 53, 57]. Avalanche ionisation is very efficient for such pulses because the long pulse duration allows more time for exponential growth of the electron density. As avalanche ionisation is so efficient, the laser intensity required to produce damage is not high enough to directly photoionise electrons [40], so either thermally excited electrons or impurity and defect states provide the initial seed electrons for the avalanche [8, 57]. A high concentration of easily ionised impurity electrons lowers the threshold for optical damage compared to that of the pure material, making determination of the intrinsic breakdown threshold difficult [36, 37, 57]. The dependence of the breakdown threshold on the presence of impurity electrons in the conduction band also makes the threshold for optical breakdown and damage more probabilistic or non-deterministic [8, 40, 53].

Typical impurity generated concentrations of free electrons in the conduction band of a transparent solid are about 10^8 cm^{-3} [11]. A laser beam that has a wavelength of $1.064 \mu\text{m}$ and focused to a $10 \mu\text{m}$ diameter spot inside the material has a Rayleigh range, effective depth of focus, of about $\pm 74 \mu\text{m}$. Further details on the Rayleigh range calculations are presented in section 2.2.5. A typical cylindrical focal volume may be assumed and calculated as about 10^{-8} cm^3 . On average there is therefore about one impurity electron in the conduction band of the focal volume [11]. As the seed electrons are so critical for the breakdown process with long pulses, small fluctuations in the number of seed electrons in the focal volume strongly affects the breakdown process. For a constant laser energy that is near the threshold, some laser shots produce damage while others do not, depending on how many seed electrons are in the focal volume of

each laser shot [11]. Bass et. al. suggested that breakdown of transparent materials due to avalanche ionisation is a probabilistic nature and modelled the process statistically [58].

1.3.4 Damage mechanisms – sub-picosecond pulses

For pulses shorter than a few picoseconds, the mechanism for optical damage is simpler than for longer laser pulses. Absorption occurs on a time scale that is short compared to the time scale for energy transfer to the lattice, decoupling the absorption and lattice heating processes [57]. Electrons in the conduction band are heated by the laser pulse much faster than they can cool by phonon emission. The electron density grows through avalanche ionisation until the plasma frequency approaches the frequency of the incident laser radiation (the critical plasma density) [57]. This high density plasma strongly absorbs laser energy by free-carrier absorption. Only after the laser pulse is gone is energy transferred from the electrons to the lattice. This shock-like deposition of energy, on a time scale much shorter than the thermal diffusion time, leads to ablation of material on the surface or permanent structural change in the bulk.

For sub-picosecond laser pulses, PI or MPI plays an important role in the generation of conduction band electrons. PI or MPI by the leading edge of the laser pulse provides the seed electrons for avalanche ionisation during the rest of the pulse [40, 57]. This self-seeded avalanche makes short-pulse breakdown less dependent on defects in the material than long-pulse breakdown and therefore the threshold for short-pulse damage is deterministic [28]. For very short laser pulses, PI or MPI can dominate avalanche ionisation and produce a sufficient plasma density to cause damage by itself [11, 57]. Damage produced by pulses in the femtosecond range is far more regular from shot to shot and more confined than with longer pulses [39]. As short pulses require less energy than longer pulses to reach the intensity necessary to produce optical breakdown, they deposit less energy in the material. Less energy deposition leads to more precise ablation or bulk material modification. The deterministic breakdown, damage near threshold and controllable material alteration make femtosecond lasers an ideal tool for micromachining [28, 40].

Both avalanche ionisation and MPI require high laser irradiances, usually in excess of 10^8 W/cm² [8, 59]. However, breakdown of solids has been observed at irradiances as low as 10^6 W/cm² [36]. If the solid is transparent to the laser radiation, an apparently low breakdown irradiance may be due to a nonlinear phenomenon called self-focusing that causes the beam, above a given threshold laser power, to come to a tighter focus

than one would expect from the laws of optics using the index of refraction of the medium [8, 36, 49]. Self focusing is a reduction of the laser beam diameter below the value predicted from the optical properties of the unirradiated material. It can result from any process that leads to an increase in the refractive index with increasing the laser intensity and/or material temperature. As a result, the damage will take place at lower laser intensities due to the substantial concentration of light. Moreover, the damage threshold intensities will vary with the thickness of the material in the propagation direction [8].

1.4 Surface breakdown mechanisms

Surface breakdown mechanisms' nature and thresholds differ slightly from those described earlier for internal breakdown. When a high power laser pulse is focused on the surface of a target material, the laser intensity in the focal spot can lead to rapid local heating, intense evaporation and degradation of the material. If the laser intensity is high enough to cause ablation, then the ablated material compresses the surrounding gas and leads to the formation of a shock wave [36, 50]. For long pulses, the incident laser then interacts with the partially ionised material vapour and the condensed material clusters embedded therein, which both affect the efficiency and quality of the ablation [50]. Similarly as for the case of internal microfabrication, the interaction between a laser beam and the target is a complicated process and is dependant on many characteristics of both the laser beam and the material [37, 49]. Numerous factors affect ablation, including the laser pulse properties, such as pulse width, spatial and temporal fluctuations of the pulse, and power fluctuations [50, 60]. The mechanical, physical and chemical properties of the sample also influence the ablation process [47, 49, 50]. As in the case of internal breakdown, there is also in this case, a debate on the responsible breakdown mechanisms and they have been addressed by many researchers in the field [37, 49, 50]. When the laser pulse duration is in the order of microseconds or longer and the intensity is less than approximately 10^6 W/cm², vaporisation is likely the dominant process influencing the material removal from the target [50]. As surface processing of glass is presented in this thesis using a CO₂ laser, the following discussion will concentrate on the reported interaction between glasses and the emission wavelength of CO₂ laser (10.6 μm).

Kozhukharov et. al. [61] reported that in the IR spectral region, the light absorption by glasses is increased due to the oscillating modes of the glass network [61]. The laser

beam is first absorbed by the glass network then the light is transformed into heat energy. The surface of the glass is heated by thermal conduction until it reaches the softening point, melts and then evaporates. The authors add that this phenomenon happens in a short duration of time (150 – 180 ns) and because the thermal conductivity of glasses is low, the ablated zones are confined and localised [61]. Buerhop et. al. also stated that the Si-O bonds in glasses have a potential ionisation energy of 4.6 eV which cannot be broken by the photon energy of a CO₂ laser (approximately 0.1 eV) [47]. However, glasses absorb strongly at this wavelength due to the vibrational modes of the Si-O bonds [47, 62]. These vibrational mode according to Buerhop et. al. are converted to thermal energy by excitation of the lattice vibrations [47]. Siiman et. al. reported that soda-lime glass for, example, which serves as a base matrix for more complex glasses, has a high concentration of impurities, e.g. Fe³⁺ [63]. These impurities shift the ionisation potential of glasses to lower photon energies (i.e. higher wavelengths) [63]. Other authors that worked on glasses found that laser-glass interactions were often enhanced by the presence of defects that absorb strongly at the laser wavelength [18, 58]. To the last statement, they recommended that the deliberate introduction of defects by mechanical treatments, energetic particles or radiation to obtain stronger or more reproducible laser interactions [18, 58]. Evidently, the effects of defects, impurities or the constituents of glasses other than Si₂O cannot be avoided as will be explained in the following theory.

Radziemski et. al. stated that in the case of transparent material breakdown, MPI is only important at short wavelengths ($\lambda < 1\mu\text{m}$) due to the photon energies associated with these wavelengths [36]. This result of Radziemski et. al. agrees with these from other workers [18, 63]. Furthermore, MPI is a more dominant mechanism of the laser-induced damage only for photon energies greater than one-half of the bandgap energy [53]. The simultaneous absorption of 100 photons from a CO₂ laser ($h\nu = 0.1\text{ eV}$) would be required to ionise most gases and this is highly improbable [36]. Similarly, ionisation and breakdown of most dielectric materials would require about half of that amount of photons. The problem with initial electrons becomes more significant at longer wavelengths as MPI can not provide any electrons for the avalanche ionisation to take place. Experiments conducted in air using 10.6 μm CO₂ lasers revealed that air breakdown was probably initiated by aerosols. At such long wavelengths, if the target material is a transparent solid that is absorbing or has microscopic absorption sites in the surface, a mechanism other than MPI and avalanche ionisation is likely to take place [36].

Absorption of laser radiation at impurity sites causes its vaporisation thus driving a shock into the surrounding air. Absorption of laser radiation by electrons in the vapour or behind the shock leads to heating of the vapour or shocked air. This leads to a thermal generation of more electrons and concurrently to a higher absorption rate. This process is called thermal runaway. As mentioned earlier, the partial ionisation of Na, Ca, Mg and Al that are constituents of many glasses creates enough electrons in the vapour that a thermal runaway may occur [36].

The combination of the heat absorption and conduction due to the lattice vibrational modes and this latter mechanism of thermal runaway are considered in this study as they describe the process in depth and from physical perspectives that are comparable to the photoionisation theories explained earlier for bulk damage. Furthermore, this explanation involves the laser-induced plasma effects which could not be neglected in this study.

In summary, laser-induced breakdown thresholds on the surface of glass are substantially lower than those for the bulk breakdown [8, 49, 50]. This is mainly due to multiple reflections of the laser beam at absorptive defects, inclusions, imperfection, scratches, cracks or pores in the surface [8, 59]. MPI is very unlikely to take place at large wavelengths such as that of CO₂ lasers. Breakdown in this range rather depends on partial ionisation of alkaline oxides and vibrational modes in the glass network that create enough electrons to induce a thermal runaway [36, 61].

1.4.1 Laser-induced plasma and shockwave

Plasma is initiated at the target's surface, whose temperature can exceed 10^4 K, during the ablative interaction [50]. The breakdown temperatures in the case of CO₂ laser have been found to be lower than their low wavelength counterpart lasers [50]. Wood et. al. reported that the plasma generated on the surface of optical materials in air or the surrounding gas protects the sample by absorbing the incident laser power [8]. Based on the incident laser intensity, three different schemes of laser absorption waves are induced on the surface of the target material [36, 50]. The three schemes are:

- 1- Laser supported combustion waves (LSC)
- 2- Laser supported detonation waves (LSD)
- 3- Laser supported radiation waves (LSR)

The differences between these schemes originate from the different mechanisms that lead to the propagation of the waves' absorbing fronts into the cool transparent

atmosphere [36]. The general configuration of the absorption wave is shown in figure 1.2. The shock and absorption region waves are shown propagating away from the target surface, whereas the plasma behind the wave is expanding radially [36, 50]. Based on the intensity range used in the experimental work presented later in this thesis, the induced laser absorption wave is of the first type, namely LSC. The characteristic details of the LSC wave are explained in section 5.3.2 where a thermal mathematical model is developed for the process.

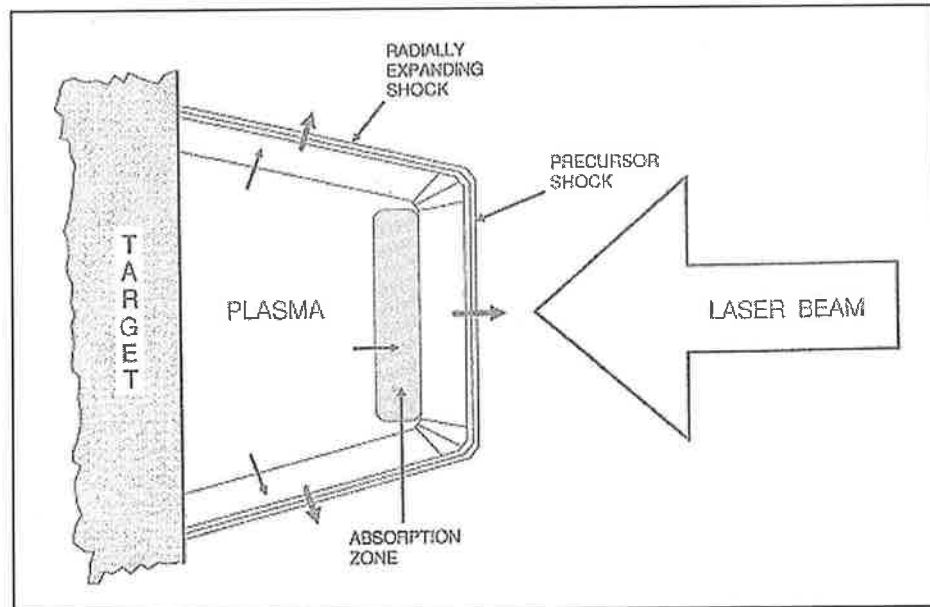


Figure 1.2: Schematic of the laser-induced plasma and shockwave [36].

1.5 Parameters affecting the microfabrication process

The microfabrication process, whether it takes place internally or on the surface, is highly dependant on various process parameters. Changes in the experimental parameters or conditions result in significant differences in the induced process and microfabricated structures. The previous discussion considered the effects of the fundamental parameters such as the emission wavelength, pulse width, material and the process purpose (internal or surface processing) on the atomic or electronic scale of the phenomena.

The work presented later in this thesis examines the effects of the laser processing parameters on the ablated region dimensions. This section focuses on the macroscopic scale of the microfabrication process. The reported process parameters in the literature are introduced, defined and their general effect trends are presented. It should be noted that the definitions and the values of the coming parameters may differ slightly from one research group to the other depending on the technique used. For example the focal

spot diameter for a certain laser beam may be measured using techniques such as the knife-edge scans [64] or calculated from the equations of laser beam propagation [65]. With both methods, the measurements are acceptable and yet potentially different, which affects other parameters such as the laser intensity and fluence. The units given to each parameter in this discussion are the most commonly used in the research field.

The laser processing parameters can be divided into two main categories, based on which parameters can be directly controlled by the laser system's operator. The first category includes direct process parameters such as laser power, pulse repetition frequency and number of pulses. The direct parameters are interrelated in a manner that determines the values of the parameters in the second category. The second category includes the indirect or calculated parameters such as laser intensity, pulse energy and fluence. The following discussion will illustrate the effect of the process control parameters, as depicted from the literature, on the measured process responses, such as the damage nature, scale and accuracy.

1.5.1 Direct process parameters

Laser power (P - W): The average power of the laser beam whether it is operating in the continuous mode CW or the pulsed mode affects the nature and scale of the resultant structures [66]. Miura et. al. investigated the effect of changing the average laser power on the cross-sectional area of waveguides fabricated inside various glass samples [67]. The authors found that the increase in power was directly proportional to the increase the cross-sectional area of the waveguides.

Pulse repetition frequency (PRF - Hz): The rate at which the laser pulses (usually Q-switched) are delivered to the sample greatly affects the morphology and the scale of the ablated zone [11, 35]. The pulse energy is inversely proportional to PRF . Low PRF settings tend to produce high pulse energies and hence incubate stresses due to thermal cycling and thermal shocks [35]. The result is that the material cracks and flakes on a microscopic scale [35]. If the pulses arrive at the focal volume at rates faster than the diffusion timescales of the material then accumulation of heat occurs within the focal region [11, 39]. Accordingly, the use of high PRF Q-switched pulses may ensure a more uniform deposition and accumulation of heat [11, 39]. These faster pulses are usually of lower energy and may not induce breakdown in the material. Due to its relation to the pulse energy, the PRF is usually inversely proportional to the size of the induced structural change. However, attention must be paid to the number of pulse delivered

with a certain *PRF*. The effect of Q-switched pulses' *PRF* should not be confused with train-pulse bursts. Some advanced setups employ high frequency bursts of low energy pulses [68, 69]. This technique ensures the accumulation of heat in the irradiated regions and therefore controls the size of the ablated structures and eliminates the cracking problem.

Number of pulses (*N*): The number of incident laser pulses on the target material affects the scale of depth and width of the ablated regions [70]. The number of pulses is usually linked with the *PRF* effect discussed earlier. Controlling the number of pulses at a given *PRF* value can determine whether heat accumulation or diffusion will take place. Furthermore, by adjusting the number of laser pulses, the amount of thermal energy deposited per unit area or volume can be controlled with great precision [12, 13, 39, 71-82].

Pulse width (τ - s): The time within which the laser pulse is active affects the precision and shape of the ablated zones [83, 84]. As the pulse width decreases, the heat affected zone becomes smaller or does not form. In the femtosecond range, the minimum induced features are not limited by the focal spot size, they become smaller than that [26]. This is due to the infinitely small time scale for heat diffusion [70]. A critical advantage of using ultrashort pulses relative to longer pulses is based on the fact that the electrons can acquire significant energy from the pulse before transferring the energy to the surrounding lattice, which can result in highly localised laser-induced breakdown [9].

Emission wavelength (λ - μm): The laser wavelength is directly proportional to the smallest achievable focal spot size. In order to achieve higher ablation precision, smaller wavelengths must be used [26, 70]. The wavelength was considered as a process parameter in the works of McGinty et. al. [25]. The authors recommended using shorter wavelengths for better quality of the induced structure. This was a direct result of smaller focal spot size and hence smaller heat affected zones. However this latter advantage would compromise the efficiency of material removal rate [25].

Focusing method: The tighter the beam is focused the lower the energy required for inducing the damage [85]. Optical microscope objectives are used for focusing the laser pulses inside the bulk of the transparent materials. The advantage of using microscope

objectives is that they tightly focus the laser beam to a spot size that is comparable to the laser's wavelength [15]. A wide range of numerical aperture values (NA from 0.45 to 1.4) of microscope objectives were used by various authors [11, 71-82, 85-99].

Scanning speed (U – mm/s): The scanning speed is usually a process parameter if the process involves the motion of the sample or laser beam. This is the case in applications such as surface texturing [64], waveguide fabrication [97] or microchannel / microtrenches fabrication [19, 25, 32, 100]. The speed, from these previous studies was found to be inversely proportional to the size of the induced structures (i.e. bump heights, width and depth of the microchannels). This a direct result of the lower time allowed for the material to absorb more laser energy at relatively high speed. The concept of feed rate relevant to the microchannel fabrication process will be discussed in section 4.9.4.

Number of passes: Some workers examined passing the laser beam along the same path to ablate the material from the focal region based on a layer-ablative manner [19, 25, 100]. This technique is proposed to reduce the induced defects associated with excessive heat, since less heat is delivered to the material per pass [19].

Material type: The nature of the ablation process is strongly dependant on the type of material [25, 70]. Some of the important material properties that affect the process are the band gap (ionisation potential), absorptivity, reflectivity, transmittance, percentage of impurities and thermal properties. The microfabrication experiments have usually been carried out on sheets of transparent materials. Among the materials reported in the literature are high silica, soda-lime glass, fused silica, silica glasses, aluminosilicate glasses, germanosilicate glasses, borosilicate glasses, polystyrene (PS), polycarbonate (PC), polymethylmethacrylate (PMMA), fluorozirconate, borate, sapphire, diamond, and many other transparent materials from the literature search.

1.5.2 Calculated process parameters

Pulse energy (E_P - J): The pulse, E_P , energy is defined as the value of the average laser power, P , divided by the pulse repetition frequency, PRF :

$$E_P = \frac{P}{PRF} \quad (1.3)$$

The pulse energy can also be measured using some detectors such as calorimeters and it can be related to the size of the resultant features as a process control parameter [42, 64, 101]. Some researchers identified the breakdown thresholds in terms of the pulse energy [75, 80, 81, 93].

Focal spot size ($D - \mu\text{m}$): Matsuoka et. al. studied the effect of spot size on the depth of ablation in borosilicate glass [30]. They found that the focal spot size was directly proportional to the depth of ablation. The focal spot size of the laser beam after exiting the focusing lens can be calculated. When a laser beam is focused by a lens, the focused spot size can be calculated accurately if the output mode is single mode such as the Gaussian TEM_{00} mode [21]. The focused spot size, D , for a Gaussian beam [65], shown in figure 1.3, can be calculated to a good approximation by

$$\frac{D}{2} = w_o = \frac{\lambda \cdot f}{\pi \cdot w} \quad (1.4)$$

where w is the beam radius at the lens inlet, f is the focal length of the lens, and $2w_o$ is the spot diameter at the focus see figure 1.3. Further Gaussian laser beam propagation equations are presented and used in sections 2.2.5 to 2.2.9.

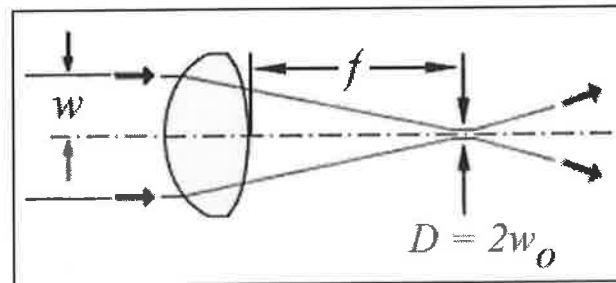


Figure 1.3: Spot size of a focused Gaussian laser beam - TEM_{00} mode, redrawn after [65].

Laser intensity ($I - \text{W}/\text{cm}^2$): The laser intensity strongly affects the scale, breakdown threshold and nature of the breakdown mechanism [70]. The laser intensity is given by

$$I = \frac{P}{\pi w_o^2} \quad (1.5)$$

where w_o is the focal spot radius. The breakdown thresholds were expressed in terms of the laser beam intensity in some works [47]. Generally, the intensity along with the

material properties gives an indication on the expected rise in temperature in the focal region and consequently indicates the machineability of the material [102].

Pulse and accumulated fluence ($F_P / F_{ACC} - \text{J/cm}^2$): The energy intensity/flux delivered by a single laser pulse at the focal spot is defined as the fluence and is measured in J/cm^2 [13, 83]. The fluence is calculated from

$$F_P = \frac{E_p}{\pi w_o^2} \quad (1.6)$$

where E_p is the pulse energy and w_o is the focal spot radius. Some researchers based their studies on the peak/maximum fluence, which is given by $F_{MAX} = 2 F_P$ [83, 103, 104]. The accumulated fluence is the total energy deposited by a number of pulses, N , and can consequently be calculated from

$$F_{ACC} = N \frac{E_p}{\pi w_o^2} \quad (1.7)$$

Herman et. al. studied the effect of the fluence on the micromachining etch rates of fused silica [35]. The same group reported in other publications that accumulated fluence of the laser energy inside the transparent material seems to control the magnitude of refractive index change [12, 13]. They reported that lower fluences produced better surface morphologies (i.e. less microcracks or swelling) [35]. Generally, the fluence is taken as the measure for breakdown threshold and is directly proportional to the size growth of the induced structures [48, 83, 97, 103]. Its relationship to the ablation size growth is sometimes linear [97] or non-linear [30, 103].

1.5.3 Measured responses

Voxel size (internal microfabrication - μm): The induced volume elements (ablated or affected region) are usually called voxels [15]. Some researchers have studied the sizes and the shapes of the resultant voxels in terms of the direct and calculated laser processing parameters [11, 71-81].

Channel dimensions (surface microfabrication - μm): The fabrication of microchannels is a typical application in this research field. Some studies were concerned with the dimensions (width and depth) of these microchannels as functions of

the laser processing parameters. Matsuoka et. al. studied the ablation depth as a function of pulse fluence and spot size [30]. McGinty et. al. studied the depth, width and volume of the ablated channels in terms of the number and energy of pulses, *PRF*, speed and number of laser passes [100].

Structural morphology: The geometry and morphology of the induced structures can be studied from different perspectives. These studies usually lead to judgements on the quality of the structures based on certain criteria. For example spherically shaped voxels may be desired for optical data storage. On the other hand uneven or star-like shapes of the voxels are better for novelty applications due to the enhanced scattering of light [105]. Other morphological observations may involve surface roughness, amount of microcracks and shapes of the structures [48]. The surface roughness and sidewall angles of microchannels cross-sections were studied by McGinty et. al. as a function of the control process parameters [100]. Morphology studies can provide useful information on the physical principles underlying the process.

Ablated volume ($V - \mu\text{m}^3$): Depending on the scale and geometry, the ablated zone volume could be measured or calculated. Using this measured quantity, the volumetric ablation rate can be measured per laser pulse, energy or length units. It can be beneficial in some studies such as the process efficiency and cost [35]. McGinty et. al. investigated the ablated volume of microchannels fabricated in polymers short wavelength laser under different conditions [25].

Ablated mass ($M - \text{kg}$): The mass of the material ablated from the irradiated zones can be measured based on the calculation or the measurement of the ablated volume and the material's density. This quantity can also lead to the calculation of mass ablation rates in a similar manner to the volume ablation rates [35].

Heat affected zone (HAZ - μm): This can be defined by the regions of altered microstructure due to the heat diffusion in the material during or after heat deposition by laser pulses. It is strongly affected by the laser emission parameters and the material properties. A rough estimate can be obtained from the diffusion length scale $L_D = \sqrt{\alpha \cdot \tau}$, where α (m^2/s) is the thermal diffusivity of the material and τ (s) is the pulse width [36, 102]. It can be seen from this scale that when the pulse width is very small (e.g. femtosecond) the heat affected zone will be very small or negligible [83].

Moreover, $\alpha = k / \rho.C_p$, where k (W/m.°C) is the thermal conductivity, ρ (kg/m³) is the density and C_p (J/kg.°C) is the heat capacity of the material [102]. Therefore, metals will have relatively larger heat affected zones because they have larger thermal conductivities.

1.5.4 Self-focusing effects

Self-focusing is discussed here as it may affect the results of microfabrication. A laser beam propagating through a transparent material induces an increase in the refractive index by an amount proportional to the laser intensity [106]. The refractive index change becomes non-linear at a critical power value which causes a catastrophic beam collapse [55]. Gaeta et. al. studied and modelled the self-focusing phenomena in fused silica [107]. The authors found that the dynamics of the process depended on the focusing method. For the case of a beam loosely focused, the pulse underwent catastrophic collapse which was halted by multiphoton absorption and plasma formation. As a result, the plasma density did not reach the critical density at any point in the material, indicating that material damage would not occur. When the beam was tightly focused into the medium, the self-focusing dynamics were governed by multiphoton absorption and plasma formation. In this case, they found that the peak intensity remained high for relatively long propagation distances and that at various points in the material the plasma density exceeded the critical density which resulted in damage.

The following two sections focus on internal and surface laser microfabrication systems and applications for transparent materials.

1.6 Internal microfabrication

1.6.1 Range of microfabrication lasers

Various types of lasers have been used for microfabrication in transparent materials. In the literature, it can be seen that lasers with different emission capabilities or characteristics were used. The laser emission wavelengths range from ultraviolet to infrared, the pulse widths range from nanosecond to femtosecond and the pulse repetition frequencies range from a few Hz to MHz. One of the simplest laser systems reported in the literature for use in microfabrication was an ArF (Argon Fluoride) excimer laser which had a 0.8 cm beam diameter, a pulse repetition frequency of 100 Hz, and a pulse width of 23 ns [99]. On the other hand, advanced lasers compared to the latter one, such as an ultrafast and a short wavelength F₂ (Fluoride) laser, were also

used [12, 13]. The following is a brief list of some laser types that have been used by some research groups:

- 1- ArF Excimer laser [108]
- 2- Nd:YAG laser [105]
- 3- Nd:YVO₄ laser [25, 45, 109]
- 4- Ti:Sapphire laser [18]
- 5- Fluoride F₂ laser [12]
- 6- CO₂ laser [19, 32, 61, 84]

The systems can vary in sophistication from one configuration to another. The most basic experimental set up for internal microfabrication was cited by Schaffer et. al. and is shown in figure 1.4 [86]. The laser pulses are focused inside the transparent material using a microscope or an objective lens. The focused laser beam serves as a point source of heat that can be moved through the bulk of a material to produce voxels or structural changes by the mechanisms explained earlier. Moreover, the direct laser parameters discussed earlier can be controlled in such a way that different processing settings can be delivered to the material.

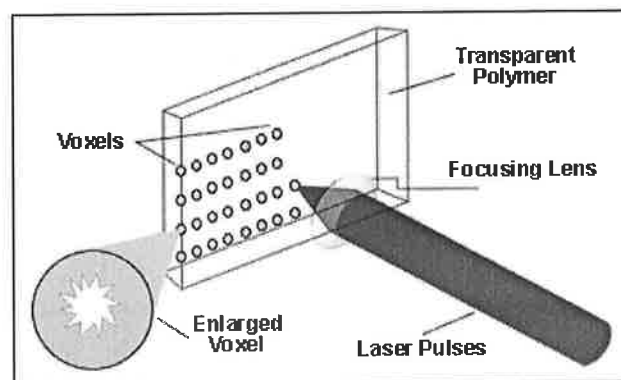


Figure 1.4: A basic microfabrication experimental set up, after [87].

Figure 1.5 shows another simple microfabrication system [85]. In this case, a train of femtosecond pulses from a laser oscillator was focused by a microscope objective into a thin glass sample. The bright blue spark was due to recombination of the electrons that were nonlinearly ionised by the pulses. Permanent structural changes were produced in the material at the laser focus.

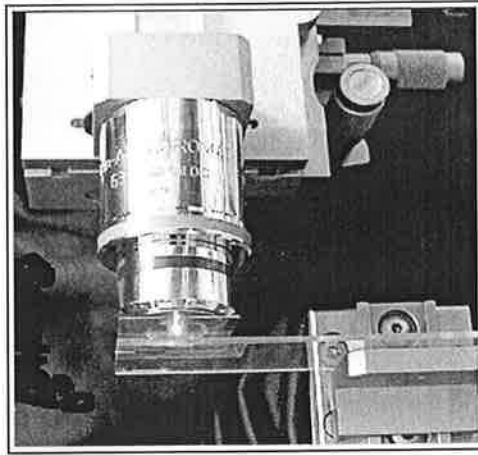


Figure 1.5: Oscillator-only micromachining in action [85].

More sophisticated microfabrication systems have been constructed by the same research group [11, 39, 52, 71-82, 86, 87]. The system shown in figure 1.6 includes a dark-field scattering setup to determine the energy breakdown thresholds [11].

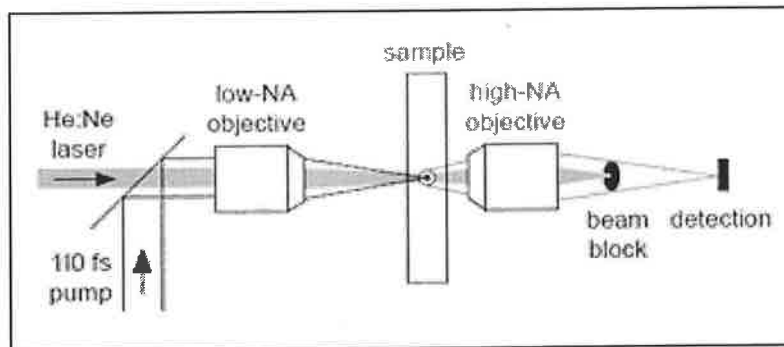


Figure 1.6: Dark-field scattering setup for determining the energy threshold for bulk damage using a low-NA objective for focusing femtosecond laser pulses [11].

Another configuration is the (in situ) CCD observation system [14, 17, 88, 89, 98]. As shown in figure 1.7, a Ti:sapphire laser was used for data storage application, and a phase contrast microscope configuration was used for data readout. The laser was focused at a point in a non-doped lithium niobate (LiNbO_3) crystal. A computer controlled 3 axis stage was used to control the position of the crystal. 3D binary data was recorded in the sample at a wavelength of 762 nm and a pulse width of 130 fs using an objective lens with a numerical aperture of 0.85. A Zernike phase-contrast configuration was used for reading. This detected the refractive index change caused by laser emission using an objective lens having a numerical aperture of 0.75. A CCD camera was used to capture the read out images [88].

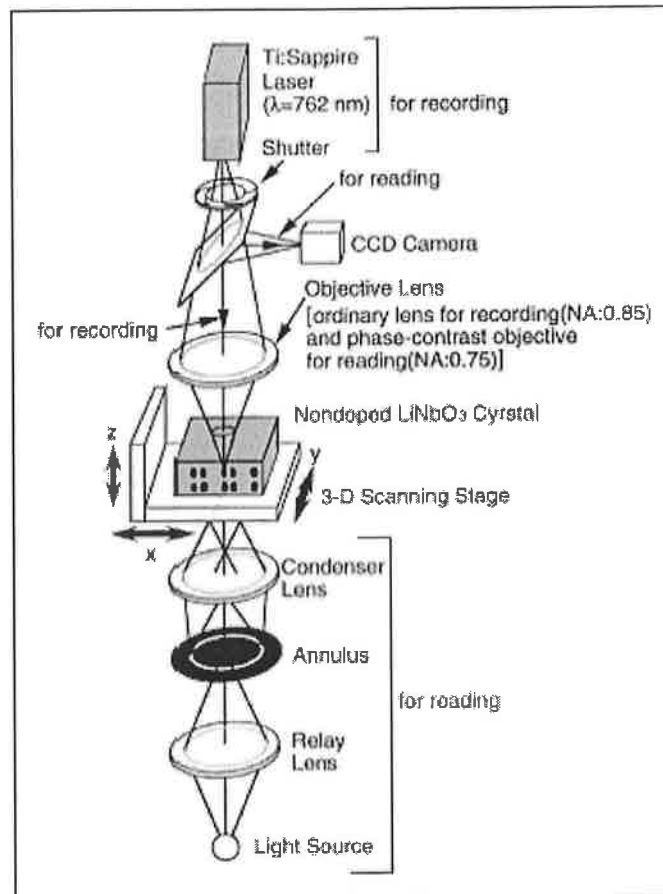


Figure 1.7: Data recording-and-readout system [88].

1.6.2 Applications

The technique of locally altering the structure of bulk transparent materials can be utilised for various applications. In the literature, the production of waveguides and other optical devices fabricated in three dimensions using the refractive index changes produced by microfabrication were reported [9, 14, 71, 85, 86, 110, 111]. Figure 1.8 shows sample waveguides produced by Hirao et. al. using a femtosecond Ti:sapphire laser [111]. The direct writing of single and multi-mode optical waveguides [97, 110, 112, 113], waveguide splitters [9, 85] and waveguide amplifiers [39] have also been performed. According to researchers in the field, the most interesting feature of laser microfabrication is the ability to produce three-dimensional structures in transparent materials [9, 110]. Three-dimensional binary data storage using the same technique was reported by previous workers [17, 18, 52, 72, 77, 78, 82, 85, 88-90, 94-96]. Three-dimensional waveguide splitters have been fabricated by drawing three intersecting waveguides inside a transparent material [85, 113]. As the three waveguides did not all lie in the same plane, it would be very difficult to fabricate such a splitter using conventional, photolithographic or ion-implantation techniques [39,113]. Microchannels and microelectromechanical systems (MEMS) were successfully fabricated using the

laser microfabrication technique in various transparent materials [14, 19]. Qin et. al. reported the fabrication of 3D microchannels in quartz samples using a two step process, firstly irradiating the sample to create internal defect sites in the form of microcracks and later the sample was irradiated along the same pattern to create smooth microchannels [48]. Kamata et. al. reported the design and fabrication of an optical vibration sensor using a Ti:sapphire femtosecond laser by fabricating internal waveguides in three soda-lime glass pieces [114]. The glass pieces were aligned together so that the three waveguides formed a single through-waveguide. The middle piece was positioned on a suspended beam; hence the losses in light transmission were related to mechanical vibrations of the middle piece[114].

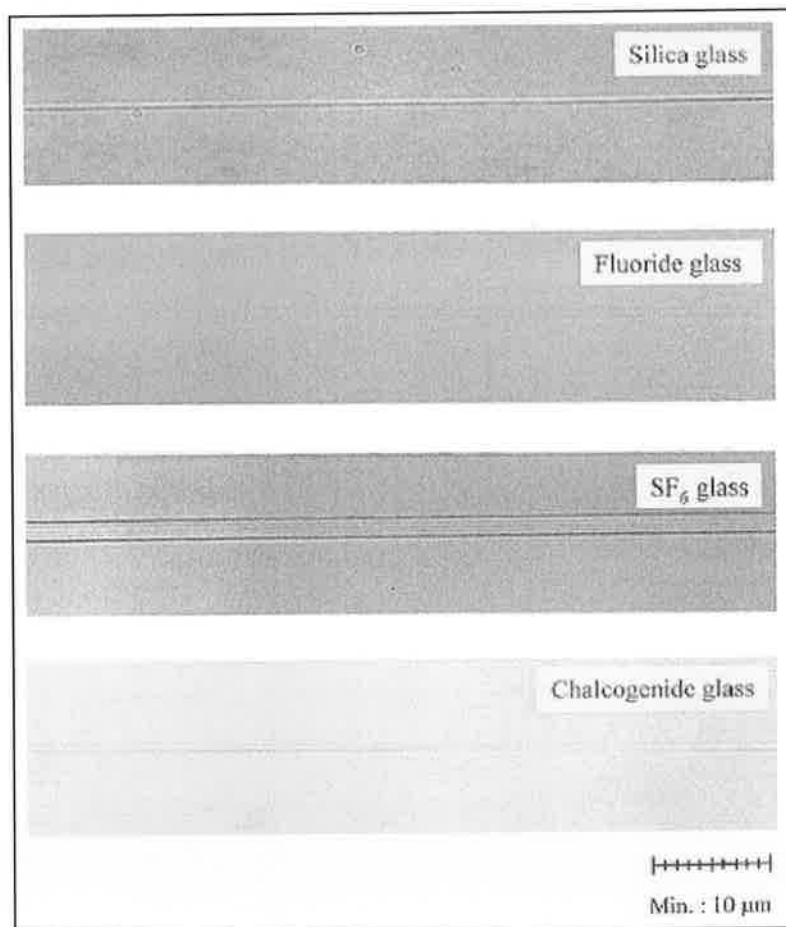


Figure 1.8: Waveguides fabricated using a Ti:Sapphire laser (810 nm) at 120 fs, 200 kHz mode locked pulses, and an average power of 975 mW [111].

1.6.3 Inspection methods

The purpose of post-microfabrication inspection is to determine the scale and nature of the effects of the laser irradiation at the focal spot inside the material. This can help a lot in understanding the nature of the microfabrication process. Furthermore, it can also

determine the breakdown thresholds. The laser-induced effects can be detected as structural differences between the microfabricated regions and the surrounding material matrix. Different microscopic inspection and testing methods are used in this field. The simplest technique for defect measurement is to use an optical microscope [9, 39]. The image shown in figure 1.9 was taken with an optical microscope from the works of Schaffer et. al. [39]. The structures were produced with multiple 5 nJ, 30 fs laser pulses from a 25 MHz oscillator focused with a 1.4 *NA* objective lens. The laser pulses were incident perpendicular to the plane of the image, and the number of pulses incident on the sample increased, by factors of 10, from 10^2 on the left to 10^5 on the right [39].

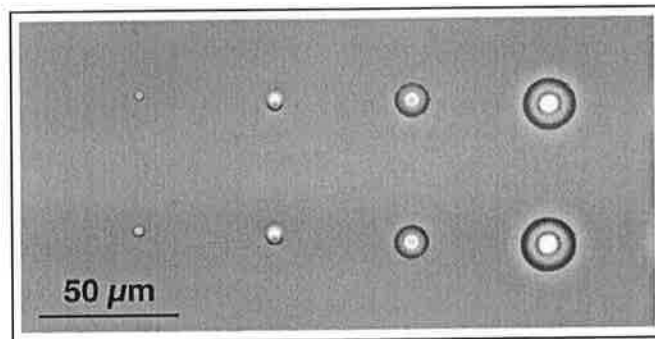


Figure 1.9: Optical microscope image of microfabricated structures in Corning 0211 glass [39].

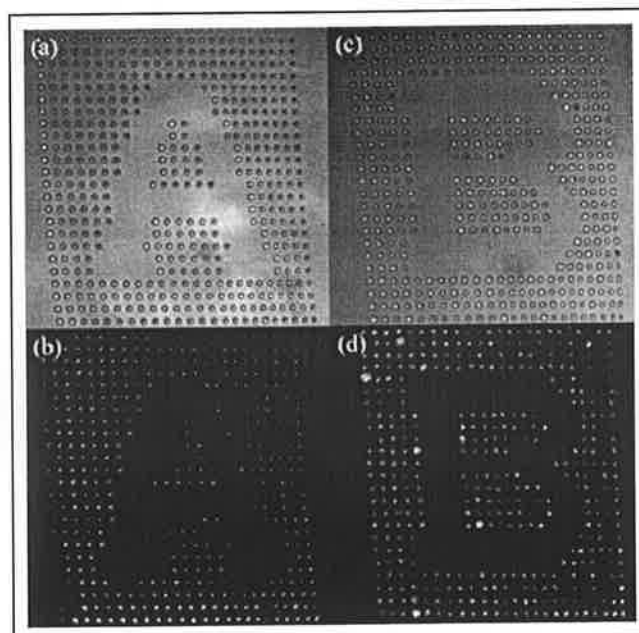


Figure 1.10: Void arrays: near surface (a) and (c) transmission microscopy; 15 μm deeper (b) and (d) confocal reflection microscopy [92].

Confocal laser scanning microscope (LSM) was also used for voxel examination [14]. Transmission and confocal reflection microscopy have also been used for the same purpose [92]. Results of this latter work are shown in figure 1.10 where multilayered arrays of voids were created in doped PMMA polymer. The first layer indicating the letter A, figure 1.10 (a) and (b) was recorded near the surface and the second layer indicating the letter B, figure 1.10 (c) and (d) was recorded with a separation of 15 μm in the depth direction.

The work done by Mazur's research group of Harvard University utilised a different inspection technique [11, 71-82, 85-87]. The image of the fused silica sample shown in figure 1.11(a) was taken by an optical microscope using transmitted light [82]. Later the sample was polished until the surface level revealed the internally recorded structures. Then a 30 nm gold coat was applied and the sample was viewed under a scanning electron microscope (SEM), which is shown in figure 1.11(b). SEM was also used by many other researchers for voxel examination such as [83]. Atomic force microscopy (AFM) was also reported by some other workers [82].

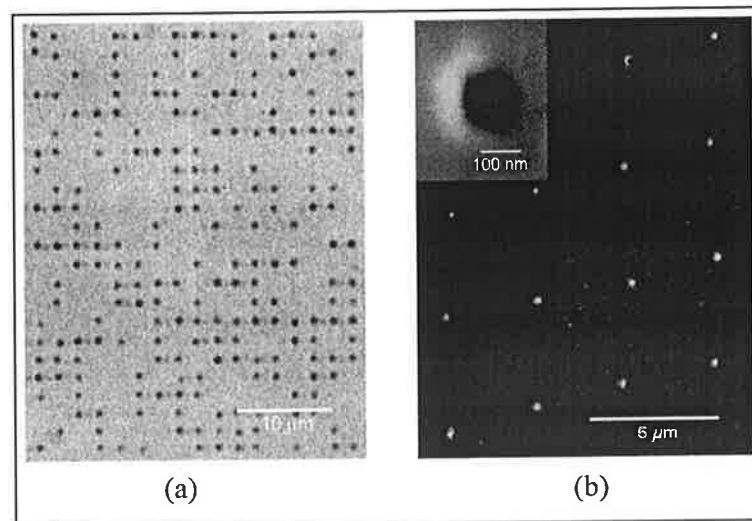


Figure 1.11: Binary data pattern stored in fused silica, (a) an optical microscope image and (b) a higher magnification SEM image [82].

Schaffer et. al. reported cleaving the sample after filling it with voxels instead of polishing to reveal the internally recorded structures [85]. Davis et. al. also used cleaving, and measured the refractive index change at the microfabricated regions with a microellipsometer [10]. Differential interference microscopy (DIC) was also reported as a measurement technique for the microfabricated structures [17, 39].

1.6.4 Use of short-wavelength lasers in industry

The results of the microfabrication process differ when it is applied in industrial systems. When the application deals with fabricating 3D graphic designs, the spot size becomes larger, on the order of hundreds of microns with larger focal depths [16]. The morphology of the microfabricated voxels in this case takes the form of irregular star-shapes. These shapes, as the one shown in figure 1.12, are better for viewing with the naked eye due to the large voxel size and refraction of light by the randomly/star-like shaped voxels.

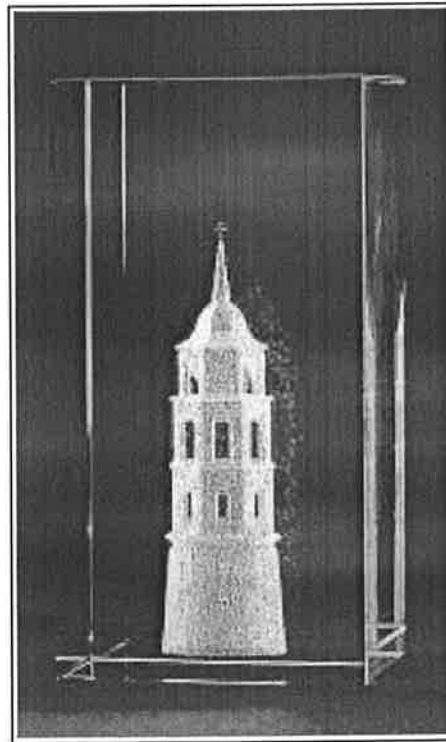


Figure 1.12: A 3D novelty shape marked inside BK7 [16].

There are a number of well established and growing companies in the field of intravolume glass laser marking as it is commercially referred to. A company based in Lithuania, EKSMA Co., produces compact systems for intravolume glass laser marking [16]. They employ Nd:YAG lasers and a typical system comes with control software that enables the user to control the marking quality and positioning inside the transparent samples. The specifications of one of their systems are listed in table 1.1.

Table 1.1: Specifications of a laser marking system (EKSMA Co.) [16]

Size of marking field	100×100×100 mm
Mark size quality	Adjustable from 100 – 200 μm in xy direction, 200 – 400 μm in z direction. (for BK7 glass).
Positioning accuracy	Up to $\pm 15 \mu\text{m}$.
Average marking speed	Up to 300 voxels/s.
Input file formats	dxf, 3ds, bmp, pcx
The size of the marking transparent samples	Maximum size 400×400×200 mm, one surface of the object must be plain and polished, absorption less than 0.01 cm^{-1} @ 532 nm.
Type of laser	Nd:YAG, diode pumped, air cooled

Some manufacturers developed systems that are capable of producing high precision intravolume ablation. Figure 1.13 shows Y-branch holes produced by Nakaya et. al. of Namiki Precision Jewels Co. Ltd. and cited by Washio [112]. The work involved laser processing of glass using a high repetition rate femtosecond laser and chemical etching to produce micro holes with smooth surfaces, having mean roughness R_a of 4.5 nm.

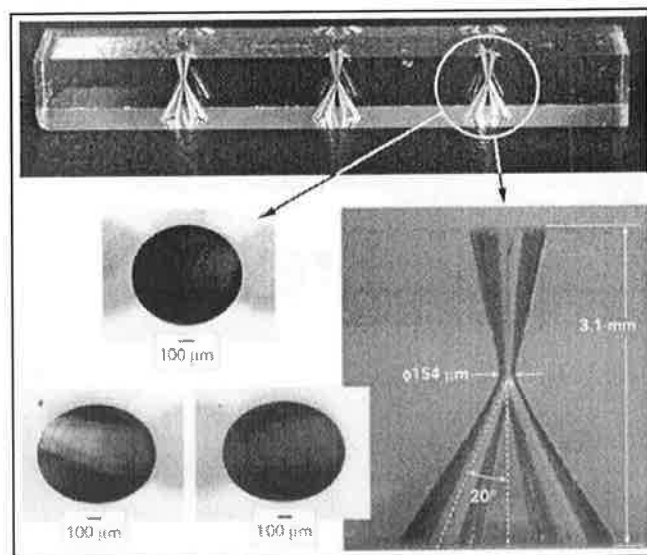


Figure 1.13: Y-branch holes produced by femtosecond laser and chemical etching [112].

Similarly, Leong reported that femtosecond lasers can be used for etching inside glass [110]. According to the author, femtosecond laser etching is a more flexible method than using UV lasers which require UV-sensitive glass for photosensitisation. This micromachining method of transparent materials has very little heat effects, as

illustrated in figure 1.14, where the material is etched away rather than ablated. With capabilities far surpassing conventional laser ablation, complex 3D micro-features can be manufactured [110].

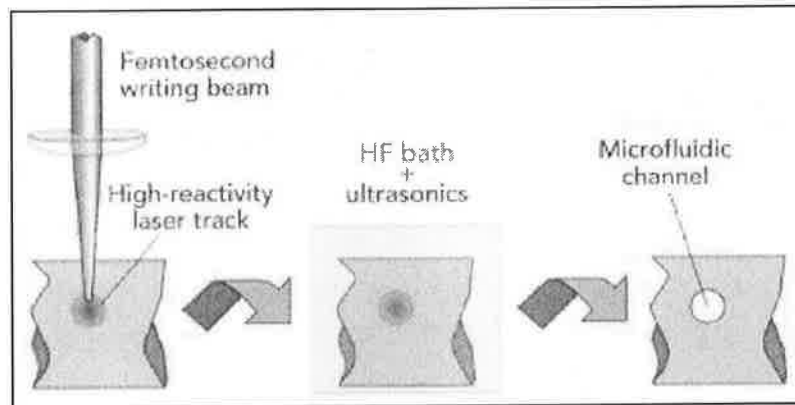


Figure 1.14: Schematic of femtosecond laser etching [110].

Various laser fabricated optical devices covering the range from simple straight waveguides to more sophisticated arrays of interferometric devices have been reported by many industries [110]. Figure 1.15 shows a helical waveguide created inside glass. The process can be automated and controlled precisely to provide more complex and multilayered designs compared to conventional lithographic techniques. These designs include rapid prototyped micro-optical and microfluidic components [110].

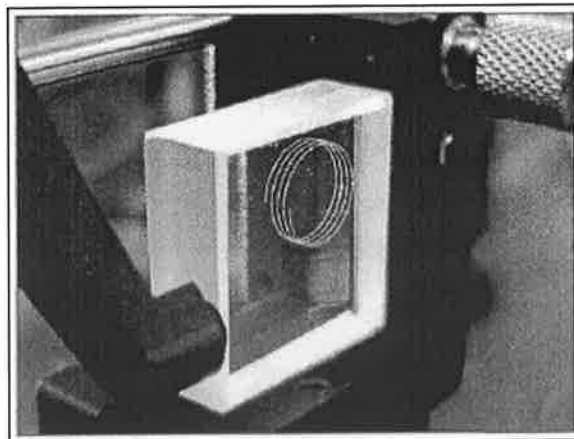


Figure 1.15: Helical waveguide [110].

1.6.5 Alternative focusing method in commercial systems

During the course of study, a visit was arranged to Crystalix Europe in Dublin [115]. According to Mr. E. Saridja, the technical coordinator, the beam focusing in their systems was achieved using mirrors to intersect laser beams inside the glass work piece.

The focal spot was at the intersection of the two beams. This method gave larger focal depth and overcame the effective focal depth (Rayleigh range) problems faced when using long focal length lenses. The employed mirror control system was sophisticated but enabled repeatable and a controllable intravolume markings. Figure 1.16 shows a schematic depiction of their system which worked as follows. The laser beam was generated from the laser head (1) with the required emission parameters. Then the beam expander/collimator (2) controlled the beam diameter according to the desired voxel size. The expanded/collimated beam (3) was then passed through a beam splitter (4) that split the beam into two beams; each carried half of the power of the original beam. Each beam was then reflected by the mirrors (5 and 6) to intersect inside the glass work piece (7) to create a voxel. For safety reasons a transparent (to the human eye) safety shield (8) covered the work piece table. The moving part of the system was enclosed in the dashed lines. The system employed an Nd:YAG laser and was capable of processing high resolution (30,000 pixels) 3D images inside crystal cubes ranging up to (5×5×5 inch) within approximately 4 minutes.

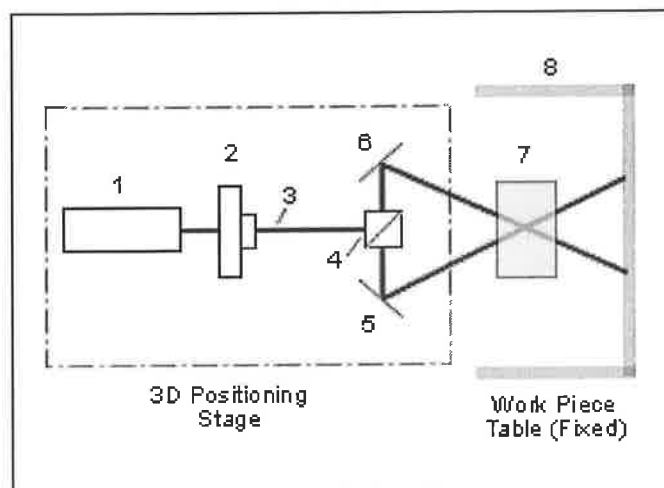


Figure 1.16: Schematic of Crystalix laser marking system configuration [115].

The 3D geometry data for the image to be produced was obtained using a Computed Tomography (CT) scanner and camera. The software controlling the laser marking system combined the tomography data and the digital image of the 3D geometry, which were then merged in the image processing software.

1.7 Surface microfabrication

1.7.1 Using short wavelength lasers

The fabrication of microchannels and MEMS has been the centre of active industrial and academic research activities over the past 50 years [116]. Henry et. al. reported a number of techniques for fabricating microchannels such as mask lithography, injection moulding, embossing and direct laser ablation [117]. The authors compared microchannels fabricated using a chemical imprinting method and laser ablation by an excimer laser. They found that the chemically modified channels had better surface quality than the laser ablated ones. However, this chemical process was more complicated and required a printed mask and a number of steps.

Most of the studied surface laser ablation applications of dielectric and transparent materials were based on the use of short wavelength and short pulse width lasers. One of the previous works related to microchannel fabrication was reported by Sauvain et. al. [44]. In their work, the channels were produced on the surface of BK7 glass using a Nd:YAG laser and were then etched using a 12% HF solution for 15 minutes [44]. Surface ablation of borosilicate glass (140 μm thick) was carried out by Matsuoka et. al. using a Q-switched Nd:YAG laser [30]. In particular, they fabricated rectangular through holes of approximately (200 \times 400 μm) that could be used in flat panel displays [30]. Microchannels were fabricated in the surface of polymers and glasses using different short wavelength nanosecond and femtosecond pulsed lasers as an alternative to conventional methods [45, 116, 118-120]. Yung et. al. studied the effect of defocusing on the kerfs' shapes of the microchannels, deeper channels were produced when the laser was focused underneath the surface [116].

Pervolaraki et. al. investigated laser surface ablation and microchannel fabrication using nanosecond Nd:YVO₄ laser (1064 and 532 nm) in polyimide, gold foils and silicon. The investigated laser parameters were pulse repetition frequency, fluence, and scanning speed. It was found that with the second harmonic (532 nm) and using high *PRF*, low fluence and high scanning speeds produced the best features of polyimide microchannels in terms of surface quality and amount of microcracks [109].

McGinty et. al. reported the fabrication of microtrenches or microchannels on the surface of polystyrene (PS), polycarbonate (PC) and polymethylmethacrylate (PMMA). The authors used excimer (193 nm), Nd:YAG and Nd:YVO₄ (266 and 355 nm) lasers. The effects of the laser processing parameters (pulse energy, scan speed, pulse repetition frequency and the number of passes) on the geometry (sidewall angles), surface roughness and ablation rates were studied using a statistical design of

experiments. The process was assessed and a prediction equation was obtained from the statistical analysis that can predict the resulting channel dimensions in terms of the process parameters [25, 100].

1.7.2 Surface microfabrication using CO₂ lasers

Little research has been conducted with long wavelength lasers especially CO₂, to examine microfabrication in transparent materials. This could be due to the fact that CO₂ lasers are not as precise microfabrication tool as picosecond and femtosecond short wavelength lasers. Probably one of the major draw backs of CO₂ laser processing is the induced microcracks in glasses.

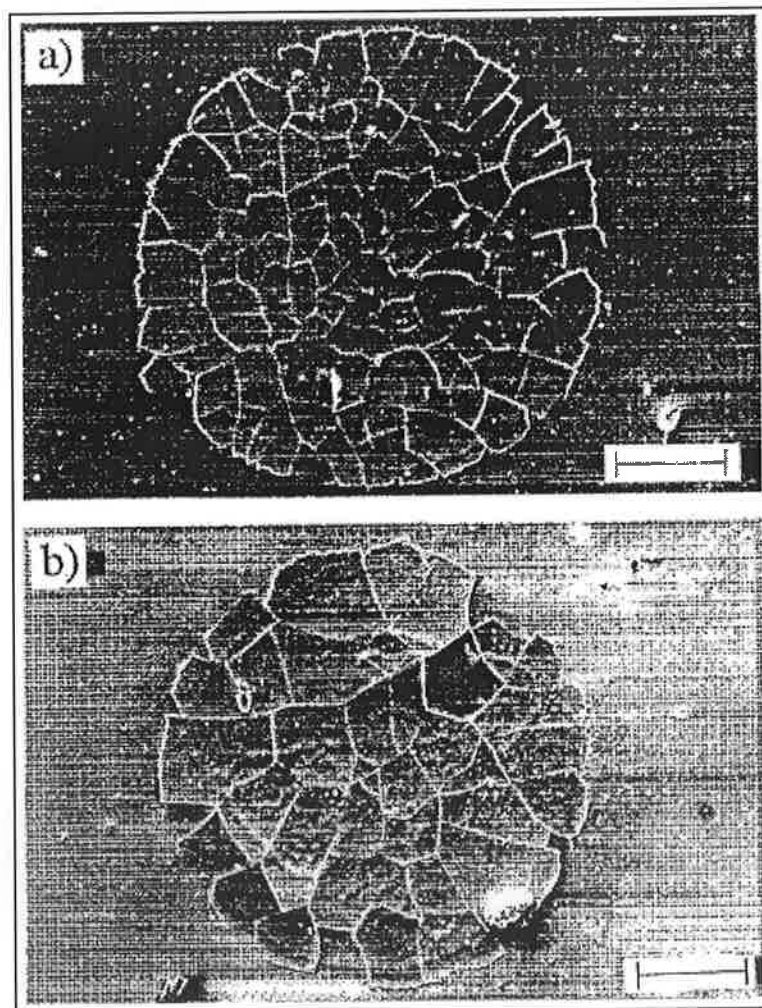


Figure 1.17: SEM micrographs of TEA CO₂ laser-irradiated soda-lime glass at:
(a) 15 J/cm² and (b) 10 J/cm². Scale = 200 μm [84].

Allcock et. al. studied the induced microcracks in 1.5 mm thick soda-lime glass upon irradiation with a pulsed 28 W CO₂ laser [84]. The laser beam was focused to a 0.8 mm spot size producing a maximum fluence of 18 J/cm². Above a certain minimum fluence,

all glass samples suffered surface cracking and this happened at least 120 ms after the exposure to the laser beam. They found that the size of the generated islands in the exposure zone was dependant on the fluence as shown in figure 1.17. The cracked islands remained attached to the surface even though the generated shock wave was measured to travel at a maximum speed of 1014 m/s and a minimum speed of 552 m/s. The authors attributed the crack formation to the residual stresses caused by thermal cycling in the glass. Moreover, loss of sodium and other gases during the exposure to the laser irradiation adds to the mechanism of crack formation. According to the authors, soda-lime glass contains dissolved gases which are liberated at around 1000 °C. These gases are typically 50% H₂O, 33% SO₂, 12% O₂ and 3% CO₂. The escape of such gases during irradiation causes the formation of blow holes in the surface which could also assist the formation of microcracks.

Kozhukharov et. al. also studied the microcrack formation in potassium-boron silicate glass due irradiation by CO₂ laser [61]. Their study was of a qualitative nature and did not provide a scientific explanation to any mechanisms. The authors suggested, similar to the explanation of Allcock et. al., that microcracks such as the one shown in figure 1.18 were due to the radial thermal tension caused by high temperature gradients.

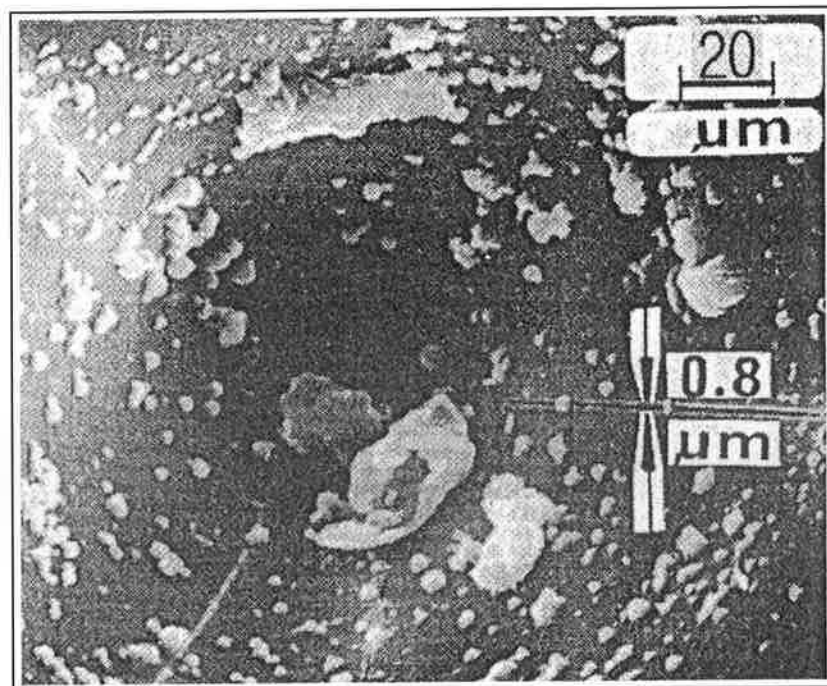


Figure 1.18: A 0.8 um microcrack induced in glass by CO₂ irradiation [61].

Other workers have also reported that the source of microcracks was the thermal stresses resulting from high temperature gradients [47, 48]. These thermal stresses have

been described to have the following nature: $\sigma \propto \alpha \cdot E \cdot \delta T$, where σ is the stress, α is the thermal expansion coefficient, E is Young's modulus and δT is the temperature gradient [47, 84]. If the induced tensile stress exceeded the fracture limit, cracks will be initiated at the surface. Buerhop et. al. observed that soda-lime glass fractured after being irradiated for 40 s with a 10 W CO₂ laser beam that had an intensity of 60 W/cm², which is much lower than the minimum 10⁶ W/cm² breakdown threshold given earlier by Radziemski et. al. [36, 47].

There are a number of advantages that may attract the use of CO₂ lasers in microfabricating or ablating the surface of transparent materials. Firstly, the CO₂ laser radiation is strongly absorbed by many transparent materials with Si – O bonds [47, 61, 102, 121, 122]. Consequently, induced damage or ablation may be produced at relatively low laser intensities with CO₂ lasers [37, 50]. The second advantage is that the cost of using short wavelength lasers, plasma etching or wet chemical etching is higher than using a CO₂ laser for micromachining transparent dielectrics [19, 123]. The next subsections illustrate some microfabrication results obtained with CO₂ laser microfabrication on the surface of transparent materials by both the research and the industrial communities.

1.7.3 Use of CO₂ laser in research

When a CO₂ laser is focused on the surface or within a transparent material, it can be used in fabricating microchannels, MEMS [19, 32], light waveguides [124], data storage [42], surface texturing [42, 64] and glass marking for manufacturing or novelty purposes [20]. CO₂ lasers have been used by Kuo et. al. [42] and Bennett et. al. [64] for surface texturing by creating laser bumps on the surface of glass and ceramic substrates. Bennett et. al. studied the relation between the pulse energy and the bump heights under different conditions of chemical strengthening, annealing of glass and the number of pulses. The bumps dimensions (height and width) had a non-linear increasing relationship with the pulse energies [74]. Sysoev et. al. [124] produced elliptical cross-section waveguides by heating quartz using the intersection of two and four CO₂ laser beams. Depending on the intersection method, different levels of ellipticity of the waveguides were achieved. They found that the use of a pulsed CO₂ laser provided faster heating and produced more controlled shapes than using CW CO₂ laser beams [124]. Wang et. al. [19] used a 1.4 W CO₂ laser focused to about a 100 μ m spot size to fabricate microchannels and microfluidic devices on the surface of PMMA. They

scanned the laser beam along the same path a number of times to avoid overheating of the samples. The produced channels ranged between 300 to 350 μm in width and the number of scans was used to control the aspect ratios.

Even though silicon absorbs more efficiently at short wavelengths and is almost transparent at a 10.6 μm , Chung et. al. used a CO_2 laser for micromachining the surface of silicon by placing the silicon substrate on top of a glass sheet [123]. The authors have only simply explained that the glass sheet has increased the absorption of silicon at the CO_2 laser emission wavelength.

Post-irradiation chemical etching of glass or transparent materials was reported earlier by some authors and shown to be a high quality surface finishing technique [110, 112]. Schaffer et. al. explained that microfabrication could be used to induce thermally-driven chemical changes inside the bulk of a sample [39]. The solubility of the material could be thereby thermally changed. It was suggested that free-standing three-dimensional structures could be fabricated by this route [39]. Juodkazis et. al. reported successful use of etching in PMMA after irradiating it with femtosecond laser pulses [14]. The etching was done using a water solution of methyl-iso-butyl-ketone (MIBK) 1:20 by volume under ultrasonic shake for 5 minutes. The result was the development of internally recorded microchannels by wet etching.

Zhao et. al. reported that they used a CW 9.95 W CO_2 laser focused to a diameter of 28 μm to create micro-grooves on the surface of fused silica glass (Corning HPFS 7980) [32]. The samples were rotated at different speeds using a spindle in front of the laser beam. Speed was the only variable in the study from the standpoint of laser fabrication. However, they later wet etched the samples using a buffered hydrofluoric acid (BHF) and different etching times. The widths and depths of the grooves ranged between (15.2 - 23.2 μm) and (0.053 - 4.072 μm) respectively. The heat affected zones had new physical and chemical properties that allowed wet etching to remove the altered material from these zones. Wet chemical etching as a subsequent step to the laser irradiation forms a possible approach to enhance the quality of surface processed by CO_2 lasers. However, it adds complication and safety hazards to the process. Furthermore, the microfabrication process then becomes a non-direct machining process.

1.7.4 Use of CO_2 lasers in industry

Georgi et. al. of Jenoptik Automatisierungstechnik GmbH discussed the latest developments in industrial processing of glass using lasers [46]. They developed an Elementary Volume Ablation (EVA) system using a low power CO_2 laser that could be

applied in bio-medical, microfluidic and semiconductor technologies. The CO₂ laser was modulated by an optical system to produce a pulsed beam in the kHz range. 2D and 3D cutting, structuring, drilling and ablating of the glass was possible to acceptable levels of accuracy and avoiding cracking or molten glass warps. They reported that layers of 5 to 20 μm were ablated from the glass surface per pass of the beam. Their motive was that CO₂ lasers are cheaper to buy than excimer or Nd:YAG lasers. Figure 1.19 from their publication shows structures ablated on the surface of glass [46].

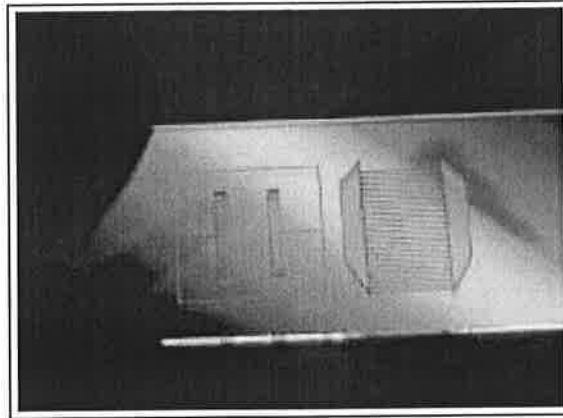


Figure 1.19: Structures ablated in the surface of glass using CO₂ laser [46].

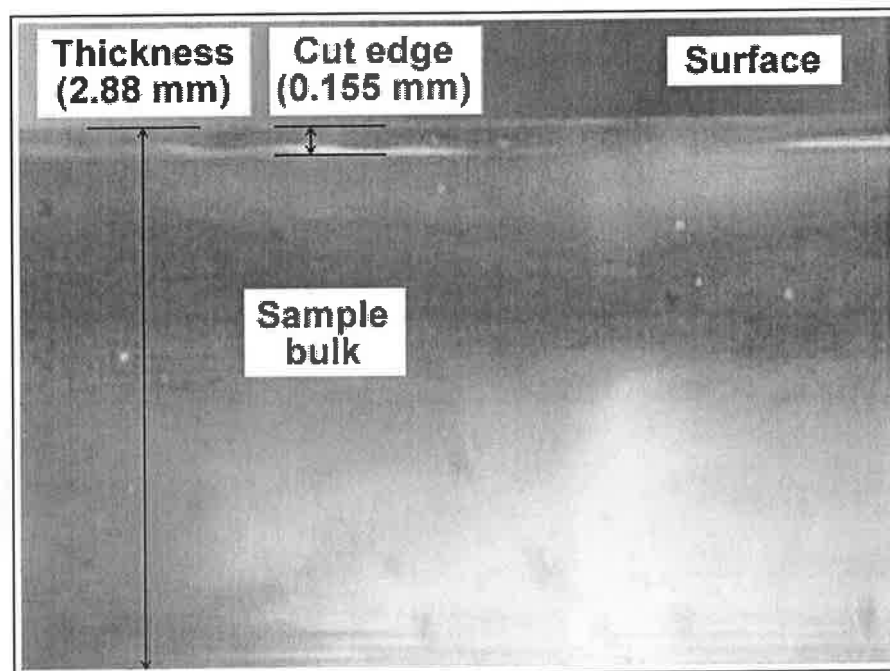


Figure 1.20: Glass cut edge with a CO₂ laser, water aerosol and cooling technique, improved after [46].

Geissler of Schott Spezialglas GmbH presented glass cutting by CO₂ laser to be efficient since it emits radiation of 10.6 μm [125]. The laser energy is directly absorbed

at the glass surface. The laser power was converted into heat with penetration depths of 50 μm [125]. This method is particularly appropriate for cutting glasses approximately up to 2 mm thick. The typical fields of application include electronic, display and biotechnology assay fabrication [125]. Both authors described the laser cutting process [46, 125]. The cutting was technically achieved by heating the glass using the laser beam along the cut line and afterwards applying defined cooling using a cooling agent (water aerosol) [46]. Due to the quick heating followed by the fast cooling, tensions induced within the glass resulted in a vertical and smooth fracture along the cutting line without any edge chips or microcracks [125]. Figure 1.20 shows a glass cut edge produced using this technique with a CO_2 laser taken from [46].

Synard Inc., USA offer a range of low power CO_2 lasers specially designed for surface processing or marking of dielectric materials such as polycarbonate, glass, quartz and stones [126]. Among the marking applications they reported are marking data matrix codes on CRT glass, shown in figure 1.21 (a), marking intricate designs on glass, shown in figure 1.21 (b), and marking glass to resemble sand blasting, shown in figure 1.22. On this latter application, the company reported that by selecting the proper laser marking parameters, the laser marks can resemble those made by sand blasting on plain soda lime and tempered glass. Lasers offer distinct advantages over sand blasting, eliminating airborne dust particles as well as the need for restrictive masks where CO_2 lasers mark glasses by micro-fracturing the surface of the material.

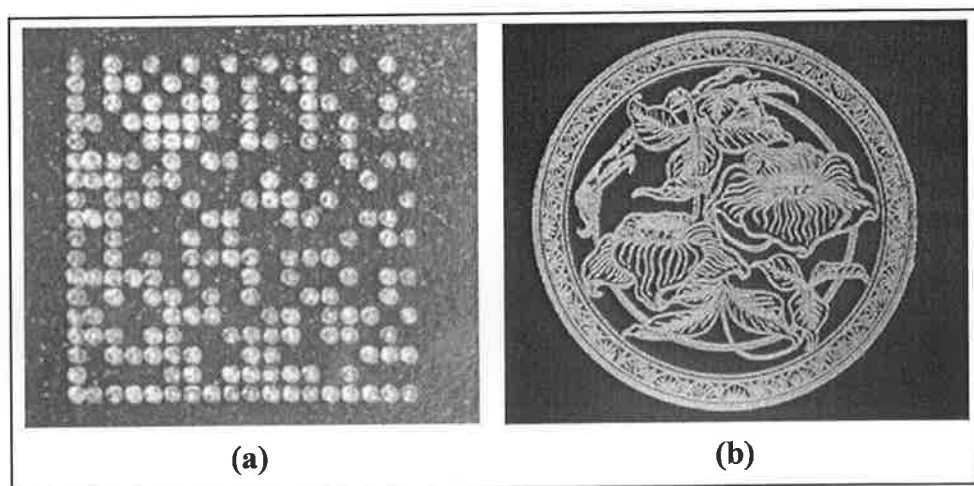


Figure 1.21: Glass marking with CO_2 laser (a) a close-up of a 2.26 cm^2 2D code marked on CRT monitor glass with 25 W in 2.6 seconds, and (b) a design marked on glass using 20 W, a 125 mm focal length lens and a scanning speed of 114 cm/min [20].

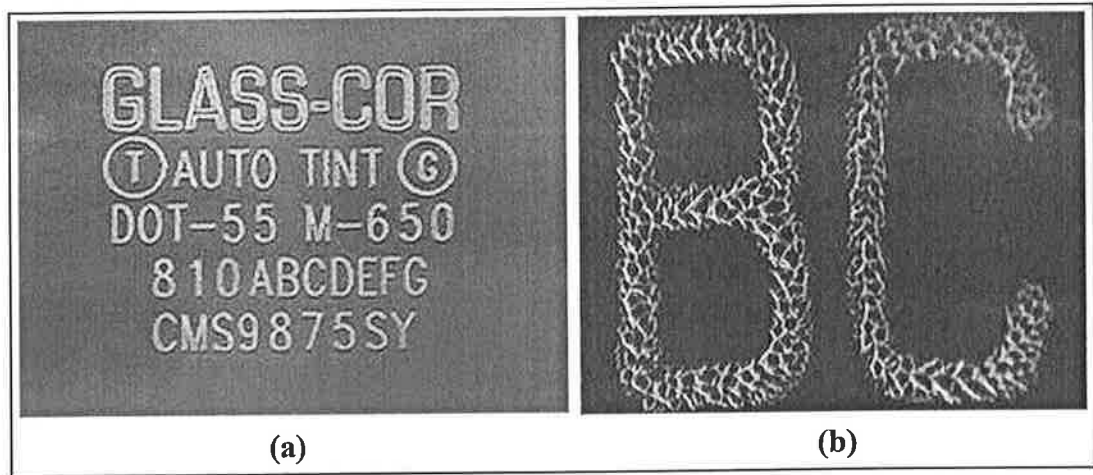


Figure 1.22: Surface marking of glass using a 10 W CO₂ laser at a speed of 76 cm/s, (a) general image view and (b) an extreme close-up of text marking shows that the line width of the mark is 252 μm, with a crack depth penetration of 51 μm [20].

1.8 Transparent materials for this study

The study of laser microfabrication of polycarbonate and soda-lime glass is presented in this thesis. The structure, physical, thermal and optical properties were of concern as these influenced the interaction of the materials with the laser irradiation. The following discussion presents the properties of both materials.

1.8.1 Polycarbonate

Polycarbonate is an amorphous thermoplastic, which means that it softens repeatedly when heated and hardens when cooled. Thermoplastics melt at relatively high temperatures and as they cool below a glass transition temperature they may become brittle. However, polycarbonate does not become as brittle as many other thermoplastics below the glass transition temperature. Polycarbonate consists of monomeric units forming chains that have rigid segments and flexible joints. The chains are directly attached to each other by weak Van der Waal forces. At any temperature above absolute zero, segments of the chains are in continual motion, coiling, uncoiling and twisting [127]. Polycarbonate's chemical formula is C₁₆H₁₄O₃ and the bonding structure of a polycarbonate unit is shown in figure 1.23 [128].

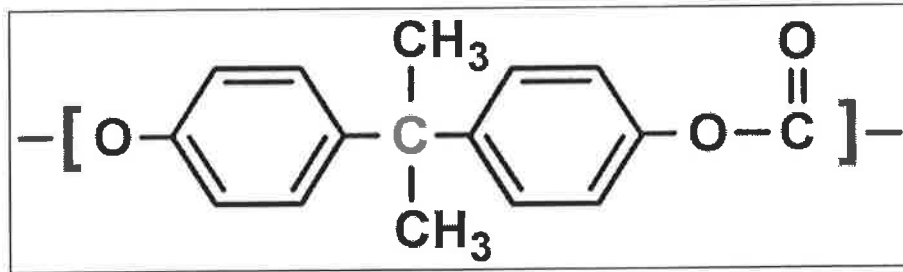


Figure 1.23: The bonding structure of polycarbonate, after [25, 128].

It was of particular importance in this thesis work to investigate the strength of the bonds of the constituents of polycarbonate. This was useful in understanding the laser-material interaction and the ionisation potentials of polycarbonate using the photon energy associated with the laser emission wavelength. The ionisation potential is defined as the least amount of energy, expressed in electron volts (eV), necessary to remove an electron from a free unexcited atom (or additional electron from an ionised atom) [129]. The ionisation potential or the dissociation energy controls the threshold breakdown energy of the material [101]. Table 1.2 lists the types of bonds existing in the polycarbonate molecule and the corresponding potential ionisation energy needed to break each bond [25].

The photon energy associated with a laser is estimated from $E_{PH} = hf$, where h is Planck's constant (4.1356×10^{-15} eV.s) and f is the frequency of the laser emission related to the wavelength λ through, $f = c/\lambda$, where c (3×10^8 m/s) is the speed of light [54]. Using the above relations, E_{PH} at $1.064 \mu\text{m}$ (wavelength of Nd:YVO₄ laser) is approximately equal to 1.17 eV. Theoretically, it may seem from these values that multiphoton absorption and ionisation is the mechanism taking place in breaking the bonds of polycarbonate, as breaking the weakest bond C – C requires the absorption of about three photons. However, as was indicated earlier, the process is dependent on other parameters such as the laser pulse width and impurities in the material [11].

Table 1.2: Dissociation energies of polycarbonate bonds [25].

Bond	E_D (eV)
C – C	3.62
C – O	3.74
C – H	4.30
C = C	6.40
C = O	11.09

Moreover, Radziemski et. al. stated multiphoton ionisation becomes less significant at large wavelengths (greater than $\sim 10 \mu\text{m}$) [36]. Another observation is that breaking the bonds in table 1.2 will always produce carbon molecules which may take different forms. However, the discussion of these is beyond the scope of this study.

Conditions such as the molecular weight or heating rates may vary during the manufacturing of polymers. This makes the determination of the polymeric materials' properties, especially the thermal properties, difficult and dependent on the manufacturing process [130]. Therefore, the properties of polycarbonate were gathered from different sources while trying to look for consistencies of the recorded values among the sources. Table 1.3 lists the optical and thermal properties of polycarbonate.

Table 1.3: The thermal and optical properties of polycarbonate.

Property	Value	Reference	Remarks
Optical properties			
Refractive index, n	1.583 – 1.586	[131]	
% transmittance	89	[25]	at $1 \mu\text{m}$
Thermal properties			
Density, ρ (g/cm^3)	1.17 – 1.45	[131]	
Thermal conductivity, k ($\text{W}/\text{m}\cdot^\circ\text{C}$)	0.19 – 0.21	[131]	
Specific heat, C_P ($\text{J}/\text{g}\cdot^\circ\text{C}$)	1 – 1.2	[131]	
Thermal diffusivity, α (cm^2/s)	1.39	$\alpha = k/\rho \cdot C_P$ [130]	Calculated from average values of k , ρ and C_P
Melting temperature, T_M ($^\circ\text{C}$)	≈ 150	[131, 132]	Based on T_M [132] and T_{MAX} service in air [131]

1.8.2 Soda-lime glass

Pure silica glass consists of SiO_4 tetrahedra that share its four corner oxygen ions with neighbours. These tetrahedras form part of a continuous random network, as shown in figure 1.24.

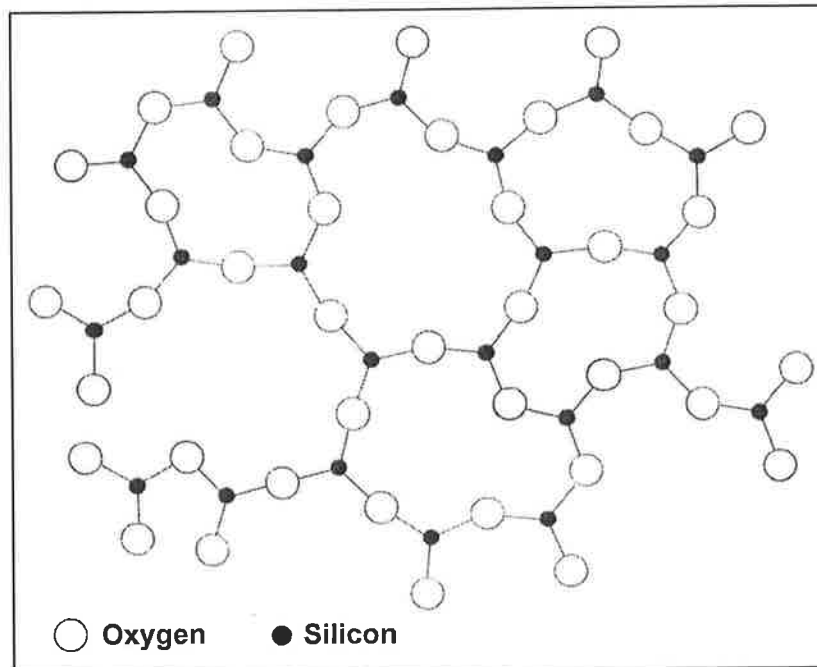


Figure 1.24: Random network of pure silica glass [62].

In soda-silica glass, the addition of monovalent ions such as Na_2O disrupts the continuity of the network [62]. These are usually called network modifiers because they make the network more complex so that when the components cool from liquid to solid, it is more difficult for the atoms to arrange themselves in suitable configurations for crystallisation to occur [133].

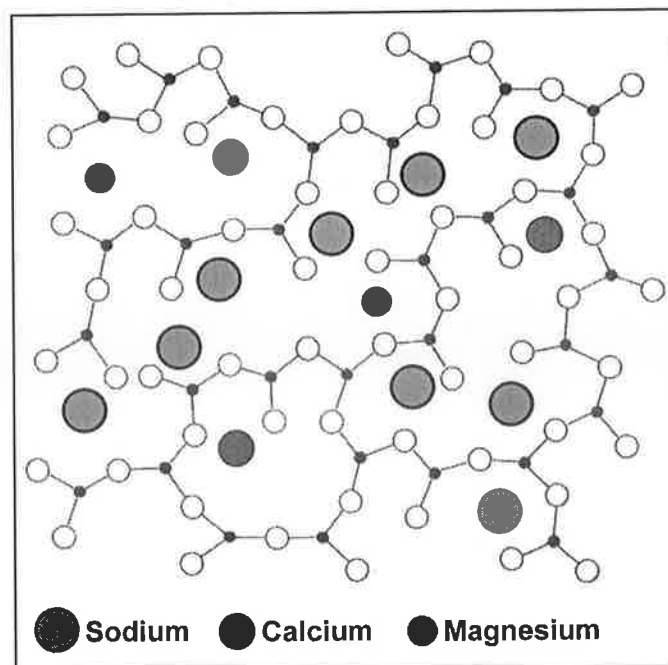


Figure 1.25: Two-dimensional analogue of soda-lime glass, after [62, 133].

The added sodium ions occupy some of the spaces in the network near non-bridging oxygen ions so as to preserve local electrical neutrality. For each monovalent metal ion introduced, one of the links in the network is broken and two non-bridging oxygen ions are produced, see figure 1.25. Soda-lime glass is the most common glass type based on soda-lime silicate (sodium calcium silicate) system shown in figure 1.25. This type of glass is cheap, chemically durable, and relatively easy to melt and form. The composition of soda-lime glass varies slightly depending on the manufacturer [62]. The typical composition of soda-lime glass is (73%SiO₂ - 15%Na₂O - 7%CaO - 4%MgO - 1%Al₂O₃) and it has a corning number of 0800 and a Kimble (Owens-Illinois) number of R-6 [134]. Some of its many applications are containers, windows, lamps, lenses, tableware, data storage disks, printed circuit substrates, photographic plates, substrates, wafers and optical windows [62, 134, 135]. Table 1.4 lists the most commonly quoted properties of soda-lime glass.

Table 1.4: The thermal and optical properties of soda-lime glass.

Property	Value	Reference	Remarks
Optical properties			
Refractive index, n	1.46	[62]	
% transmittance	≈70	[62]	at 1 μm
% transmittance	Negligible	[102, 121]	at 10 μm
Thermal properties			
Density, ρ (g/cm³)	2.5	[134]	
Thermal conductivity, k (W/m.°C)	1.06	[134]	Within the range 0 °C and 100 °C
Specific heat, C_p (J/g.°C)	0.87	[134]	Within the range 25-175 °C
Thermal diffusivity, α (cm²/s)	4.8736×10 ⁻³	$\alpha = k/\rho \cdot C_p$ [134]	Calculated from average values of k , ρ and C_p
Softening point (°C)	≈700	[62]	
Melting temperature, T_M (°C)	≈1000	[134, 138]	
Vaporisation temperature, T_V (°C)	≈3427	[36]	Based on ablation threshold calculations.

The properties in table 1.4 were taken from a number references. The thermal properties of lime soda glass were mainly taken from Bansal et. al. [134], as those values were obtained based on scientific experimentation and are regularly referred to by other workers [136, 137].

In pure silica the photon energies needed to ionise the Si-O-Si bond are in the range of 10 eV. However, ionisation occurs at lower photon energies in soda-lime glass than in fused silica [63]. Photoionisation in typical alkali-silicate glasses, such as soda-lime glass is affected by the dissociation energy of the alkali oxides [101] and requires photons to have an energy greater than ~6 eV, which corresponds to a wavelength ($\lambda < 210$ nm) [63]. However, nonlinear MPI may take place at larger laser wavelengths using high power intensity pulses leading to the breakdown of alkali-silicate glass [63]. Similar to the calculations performed earlier for polycarbonate show that, E_{PH} at 10.6 μm wavelength is approximately 0.117 eV. This photon energy is much less than 6 eV and MPI for this case would require the absorption of about 50 photons simultaneously, which is highly improbable according to [36]. It is more probable that the seed electrons for breakdown are provided by ionisation of the alkali oxides bonds which require less energy for ionisation [36].

1.9 Study focus and objectives

1.9.1 Literature summary

The mechanisms, findings and applications explained above are based on the induced structural changes and ablation of dielectric materials due to the nonlinear laser-deposition of energy. Research carried out to date in this field has been able to utilise and characterise the effects of microfabrication using a wide range of laser systems and inspection techniques. There have been many studies on the physics of the breakdown phenomena. However, a general process map or theory is not firmly established yet [11, 14, 39]. The large number of process variables in the reported experimental work has made it difficult to compare the reported experimental findings with each other and with a particular damage theory [8, 53]. Moreover, the determination of the actual damage thresholds as a function of material and laser properties with proposed damage theories is not complete [53]. A lot of application research has been carried out using short wavelength lasers.

Research on the use of CO₂ lasers for the microfabrication of transparent materials was limited. However, some industries have been able to utilise them and demonstrate their

potential in the field [20, 46, 125]. The cost effectiveness of CO₂ laser systems was frequently emphasised by the groups who used them. This indicates the competence and the potential of such laser systems in producing parts at lower prices. Furthermore, since CO₂ lasers are well known industrially and they require less sophisticated setups, their productivity can be readily increased to match industrial levels.

1.9.2 Hypothesis

It was hypothesised at the start of this work that the direct writing of voxels inside polycarbonate, soda lime glass, fused silica and sapphire was possible with a Nd:YVO₄ laser. It was also hypothesised that it was possible to directly write microchannels on soda lime glass with a CO₂ laser system. It was further hypothesised that a thermal model could be developed to allow microchannel topology prediction from the CO₂ laser microfabrication process. Hence the work, in this thesis, is divided into two main parts which are briefly summarised as follows.

The first laser system was a Nd:YVO₄ laser, which emits at a wavelength of 1.064 μm and has a maximum average power of 2.5 W with a characteristic 80 ns pulse width. This system was designed and integrated from a number of hardware parts and its control software was developed for three-dimensional microfabrication by focusing the laser beam using an achromat lens inside polycarbonate samples. The process was studied based on the laser emission parameters effects on the resulting structural dimension and morphology inside polycarbonate. The process control parameters were taken as the laser beam's average power, the pulse repetition frequency and the number of pulses delivered to the sample. Moreover, the laser beam was tightly focused using an oil-immersion microscope objective lens for microfabrication in fused-silica, soda-lime glass and sapphire samples. The breakdown thresholds were obtained for the experimented materials with the respective focusing techniques.

The second and main part of the study was done using a CO₂ laser system. This laser emits at a wavelength of 10.6 μm , has a maximum average power of 1500 W with a maximum pulse repetition frequency of 5000 Hz and controllable pulse width (26 μs – minimum). This system was used to fabricate microchannels on the surface of soda-lime glass sheets. Similarly, the effects of the process control parameters on the resulting microchannels dimensions and morphologies were studied. The process control parameters were taken as the average laser power, the pulse repetition frequency and the translational speed of the samples. Moreover, the defocusing of the laser beam (i.e. the focal point position relative to the sample's surface) was also investigated during the

initial stages of the study. The conducted experiments and the analysis of the results were performed using the design of experiments technique. In addition, the process was also mathematically modelled to enhance the understanding of the process by the means of three-dimensional transient temperature distributions in the samples due to heat deposition from a pulsed point source.

As this field is still evolving, researchers usually use different terminologies or parameters when reporting the induced changes in the material such as breakdown, ablated zone size or morphology. This causes a lot of confusion as the laser intensity, for instance, on its own does not explicitly include the pulse energy and fluence and vice versa. Accordingly, this study follows a systematic method in studying the relation between morphology and scale and the processing parameters. The breakdown threshold could still be referred to using the laser intensity, for instance, but the other process parameters such as the emission wavelength, laser beam mode, focusing technique, laser power, pulse repetition frequency, pulse duration, number of pulses, sample's translation speed, etc. must be carefully reported.

1.9.3 Aims of the study

The aims of this study can be summarised as follows:

- 1- To build and integrate the parts of a Nd:YVO₄ laser system. This included building a positioning stage to facilitate three-dimensional microfabrication.
- 2- To build the software for generating build files from computer aided designs, as well as controlling and monitoring the laser irradiation and the three-dimensional positioning stage.
- 3- To study the laser process parameters' effects on internal microfabricated structures in polycarbonate samples.
- 4- To use a CO₂ laser for fabricating microchannels on the surface of soda-lime glass sheets.
- 5- To study this process using a design of experiments, in order to investigate the effects of the laser processing parameters on the resulting microchannels' dimensions and shapes.
- 6- To thermally model the process using an analytical method, in order to simulate the effects of the process parameters. This was proposed to be helpful in understanding the morphologies of the channels.

1.9.4 Thesis outline

It was deemed, for effective reading, that some theoretical concepts be discussed at the relevant locations in the thesis and not in this chapter. This was mainly because these concepts were not fundamentals of the process under investigation. For instance, the theory behind the stepper motors was illustrated in the hardware setup chapter. Furthermore, there is a substantial number of theoretical definitions and extra details of the work presented in the appendices.

Each chapter in this thesis ends with a brief summary outlining the achievements and findings that were established. The hardware and software setups used for conducting the experimental work are presented in chapter 2. Since the work carried out in this study was obtained from two distinct laser systems and process, there are two experimental work and results chapters. Chapter 3 presents the experimental work and results obtained from internal microfabrication in transparent materials using the Nd:YVO₄ laser system. Chapter 4 presents the experimental work and results achieved from microchannel fabrication on soda-lime glass using the CO₂ laser system. Chapter 5 presents the thermal mathematical model developed for simulating the thermal field generated during the microchannel fabrication process. Chapter 6 presents an overall discussion of the study and concludes with highlighting the most important findings and recommendations for future research work.

Chapter 2

Hardware and Software Setup

Part I: Hardware Setup

2.1 Introduction

This chapter discusses the hardware and software setups used in the course of this study. The first part of this chapter discusses the Nd:YVO₄ laser hardware setup developed for the internal microfabrication in transparent materials. Moreover, the CO₂ laser system utilised for microchannels fabrication on the surface of glass sheets is presented. The control and CAD manipulation software codes are then explained in the second part of the chapter. The chapter is intended to present the necessary knowledge of the laser systems used in this work. A substantial amount of detailed illustrations can be found in designated appendices that are referred to in respective locations.

2.2 Nd:YVO₄ laser system

A laser system was developed for three dimensional internal fabrication in transparent materials. The system was developed around a Spectra Physics T-series (T20 - V80 - 106Q) Nd:YVO₄ laser. From the early stages of the system design, it was clear that a table to hold the system parts was a necessity. The design of the table was such that a maximum work piece size of 90 by 90 by 90 mm could be accommodated.

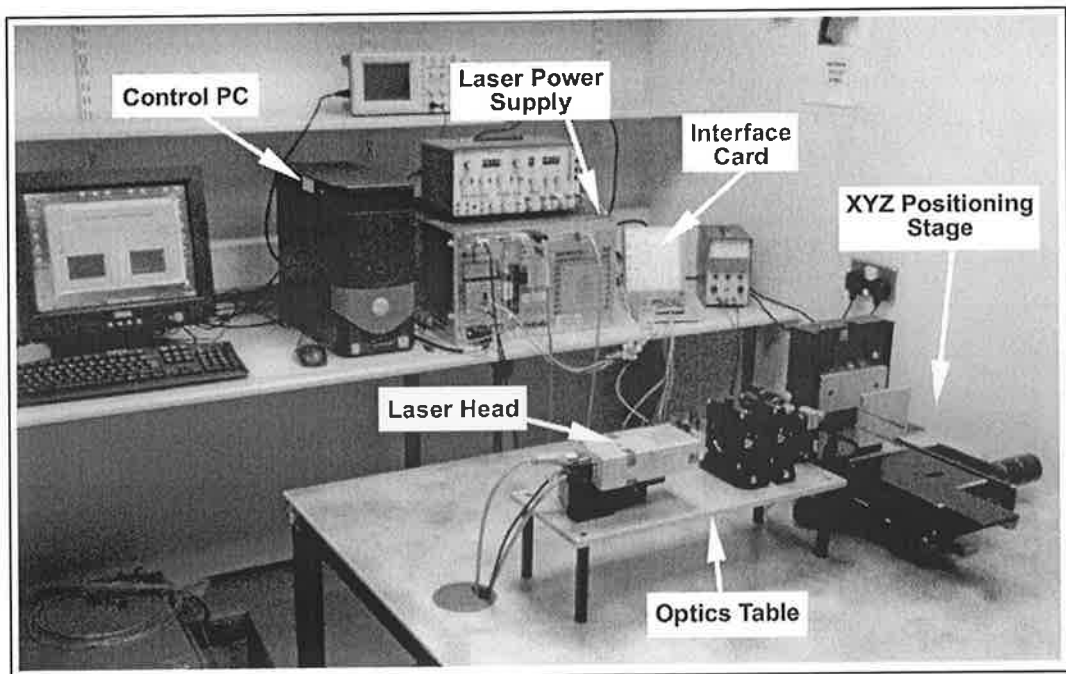


Figure 2.1: The complete laser system components.

This required the modification of the stepper motor frame sizes. The table was fabricated from 6 mm thick aluminium sheet. This rig table size was designed to accommodate the optical components, motor drivers and provide adequate work space. The rig cover was fabricated from sheet and structural aluminium components. Figure 2.1 shows the integrated laser system components built as part of this study.

2.2.1 Process layout

The process layout is shown in figure 2.2, the CAD designs were developed and processed using a controlling PC. The PC was also used to automatically control the process. The control of the laser emission was established via RS232 communication between the PC and the Nd:YVO₄ laser's power supply. The laser's power supply transmitted the emission parameters to the laser head and hence to the external optics. To facilitate 3D fabrication, the PC was used to control a 3D positioning stage. The positioning stage was composed of 3 orthogonal slide way frames (x, y and z), that were actuated via three stepper motors. The stepper motors were controlled via 3 motor drivers.

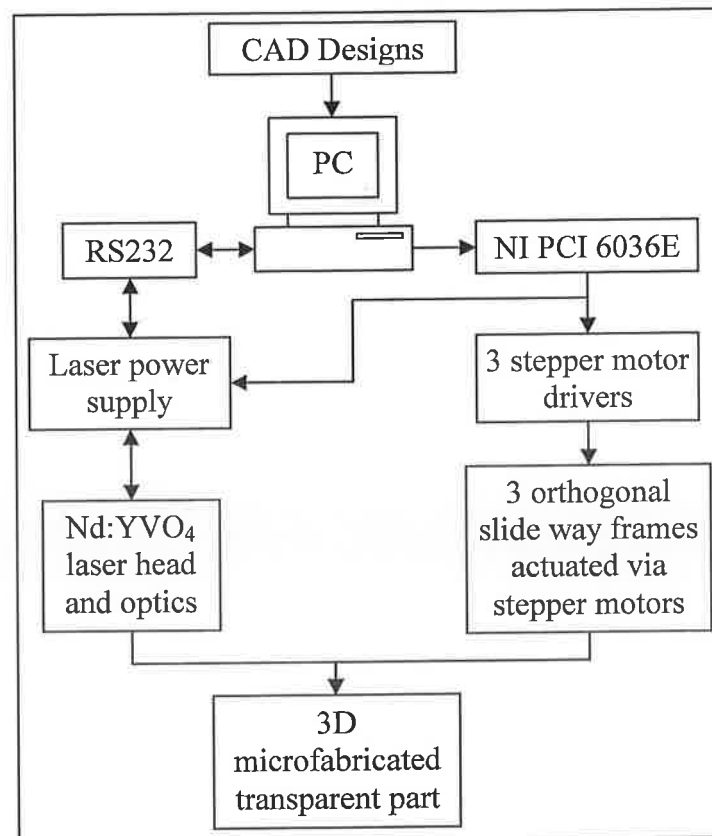


Figure 2.2: Process flow chart for the developed microfabrication system.

The motors drivers were controlled using a PCI 6036E series National Instruments interfacing card that transmitted positioning control signals to the 3 stepper motor drivers. The PCI card was also used to control the frequency and the number of laser pulses triggered at the target material. Laser emission and 3D positioning were carried out in synchronised cycles in order to only irradiate the desired locations within the transparent material. The following sections of this chapter include the details and the function of the different system parts indicated in figure 2.2.

2.2.2 The laser system specifications

Yttrium-vanadate (YVO₄) is a crystal doped with neodymium, grown by the Czochralski (CZ) technique [139]. The YVO₄ bar can have up to 3% of neodymium doping. Based on the technical data available in laser handbooks, Nd:YVO₄ lasers are rare earth ion lasers that are made for small and efficient applications, they have less temperature control requirements. One major advantage of Nd:YVO₄ lasers is the ability to retain short pulse output even at very high repetition rate frequency (PRF). YVO₄ lasers are diode-pumped with two or four diode bars and can produce an output power of about 35 W at 1064 nm. Table 2.1 presents a reference summary of the Nd:YVO₄ laser characteristics [139, 140].

Table 2.1: Summary of Nd:YVO₄ laser characteristics from literature [139]

Active Medium	Nd-doped YVO ₄ crystal
Output Wavelength*	1064 nm
Power Range	8 W – 35 W
Pulsed or CW	Both
Excitation	Optical (Diode-pumped)
Polarization	Unpolarized or linear

The laser used for this part of the study was the Spectra Physics T-Series laser and is shown in figure 2.3. This is a diode-pumped, fibre coupled, solid-state laser system incorporating a proprietary coupling technology to a high power laser diode bar. The V-style laser heads use Neodymium doped Yttrium Vanadium Oxide (Nd:YVO₄) as the active, or lasing medium. Vanadate has a high absorption coefficient, high gain, and short upper state lifetime making it attractive for high power and short pulse operation.

* most common wavelength

IBM Ireland bought a quantity of these T-Series lasers from Spectra Physics for use as laser-texturing tools, some of which were donated to Dublin City University.

The Nd:YVO₄ laser was first used in the 1960's for laser rods in lamp-pumped solid state resonators. A major drawback of Vanadate in those days was its fragility, making it difficult to manufacture long rods. It was virtually abandoned as a commercial laser medium. However, the advent of diode pumped solid-state laser technology in the 1980's enabled the use of small laser crystals [141].

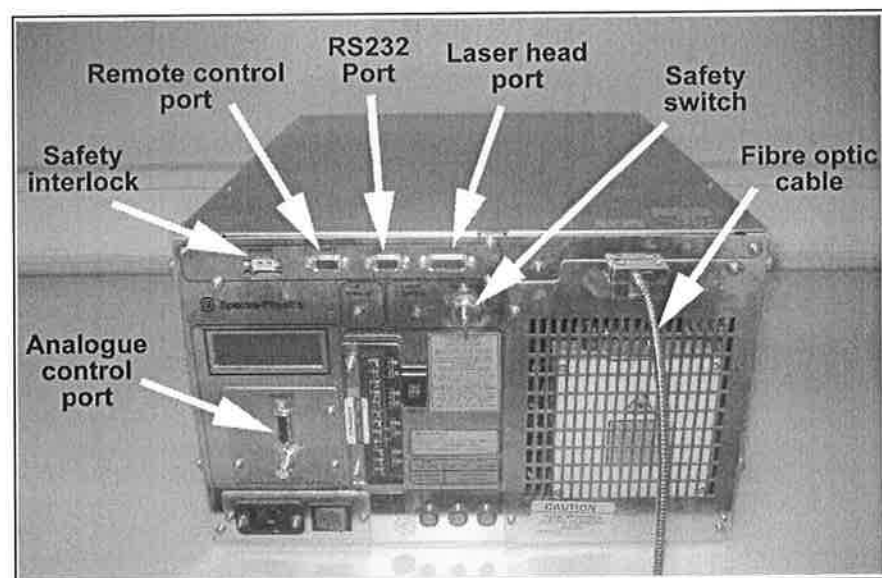


Figure 2.3: Spectra Physics laser power supply used in this work.

Originally, the T-Series system was controlled through an RS232 serial port using a simple DOS based program. Alternatively, control could be established using analogue and TTL signals. These signals can be sent to an analogue control port on the power supply [141].

Diode pumped laser design

Spectra Physics T-series laser systems are solid-state lasers, which are pumped by high power fibre coupled laser diode bars. This proprietary coupling technology, called *FCbar*TM, is unique to the T-Series products. *FCbar*TM designs maintain the high efficiency of an end pumped configuration and maintains excellent mode properties without thermal aberration [141]. Laser diodes combine very high brightness, high efficiency, monochromaticity and compact size in a near-ideal source for pumping solid-state lasers. These sources have replaced arc lamps as light pumps, and they have provided new capabilities such as narrower single-frequency emission and much shorter

Q-switched and mode-locked pulses as shown in figure 2.4. The pump source emission spectrum of a laser diode is very narrow and almost monochromatic compared to krypton arc lamp and a black body sources. Krypton arc flash lamps are used in alternative laser systems [141].

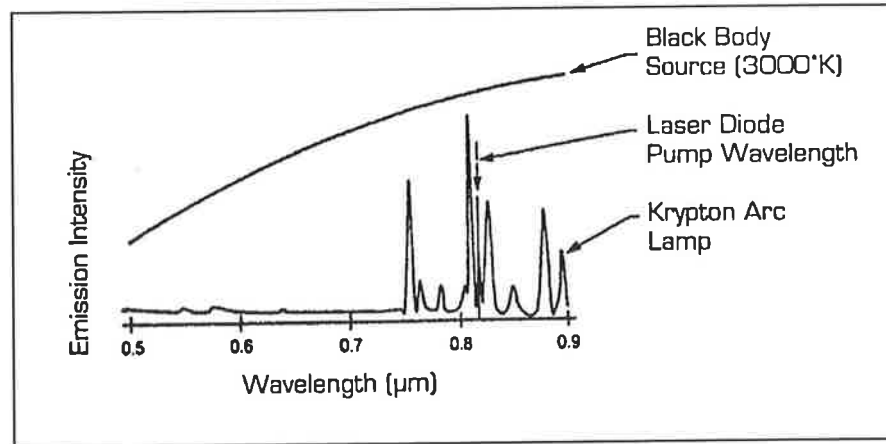


Figure 2.4: Monochromaticity of the emission spectra using a laser diode compared with krypton arc lamp and a black body source [141].

Model nomenclature explanation

The model numbers for the T-Series laser systems are descriptive, and give fundamental performance information for the system. The following example describes the coding of the laser type used in this work.

T20 - V80 - 106Q

Power Supply – Laser Head – Output Emission

T20: the letter ‘T’ designates the ‘Total’ thermal management system incorporated into the power supply. The numbers designate the total available diode pump power in that supply. The number ‘20’ designate that the laser can supply up to 20 Watts, with the addition of a second laser diode bar to the supply.

V80: the letter ‘V’ designates the resonator design of the laser head that is a folded v-shaped cavity with a single pump input. The digits 80 designate the pulse width, which has a nominal value of 80 ns at 110 kHz pulse repetition frequency *PRF*.

106Q: the number ‘106’ represents the output wavelength that is equal to 1064 nm. The letter ‘Q’ indicates that the laser head is Q-switched [141]. Table 2.2 contains the performance characteristics of the laser as given in the catalogue.

Table 2.2: The Nd:YVO₄ laser characteristics [141].

Beam characteristics	
Wavelength	1064 nm
Pulse energy, 110 kHz	>18 μ J
Pulse width, 110 kHz	80 ns
Average power, 110 kHz	<2.5 Watt
Maximum <i>PRF</i>	1 MHz max
Spatial mode	<i>TEM</i> ₀₀
Propagation characteristics	
Polarization	>100:1, vertical
Beam diameter at waist	0.6 mm \pm 10%
Beam divergence, half angle	<1.3 mrad

2.2.3 Controlling PC interface

The PC is a Dell with a P4 processor and Windows XP as the operating system. The computer included the control codes of the laser power supply as well as the control codes of the other system parts. The control of the laser operation was achieved through the serial communication port RS232 on the PC. The design of the serial communication cable is illustrated in appendix B.1.1. The laser power supply was connected to the PC via the RS232 communication cable and to the laser head by three cables:

- a) The laser head data cable (for laser head and gate control),
- b) The RF frequency cable (for laser pulse frequency), and
- c) The fiber optic cable, which carries the pumped diode light from the laser power supply to the laser head.

The PC and the laser power supply were also interfaced via the NI PCI 6036E series card for controlling the frequency and number of the Q-switched laser pulses.

Operation procedure

The following are the steps that should be followed for proper operation of the laser system.

- 1- The rig's cover doors must be closed.
- 2- Switch on the laser power supply and monitor any warming up messages appearing on the LCD display on the front panel of the laser power supply.
- 3- Warming takes around 15 minutes then the following message displays

BOOT COMPLETE
LASER DIODE OFF
POWER MODE READY

- 4- Run the LabVIEW control code and set the required emission parameters.
- 5- If the settings include a change in the diode temperature, a minimum 5 minutes settling time must be allowed to reach the desired temperature.
- 6- When the diode temperature reaches the required value, the laser diode can be turned ON.
- 7- Emission will not start until the positioning code is run; as the purpose was to irradiate specific 3D locations in the samples. When the positioning and laser firing control software has finished building the part the emission will stop. However, the laser diode is still ON, so it must be switched OFF from the control code.

Q-Switching

The Q-switch operation required two TTL logic signals (the Q-switch frequency and the Q-switch trigger). The two signals listed in table 2.3 were fed from the PCI 6036E card into the control port on the laser power supply.

Table 2.3: Q-Switching pin connections.

Analogue Port Pin	PCI 6036E Pin	Signal function
17 (External Q-Switch Gate)	2 (GPCTR0_OUT)	Q-switching frequency signal. TTL (internal pull up to +5V)
21 (External Q-Switch Trigger)	16 (DIO6)	Q-switching triggering (ON/OFF). TTL (internal pull up to +5V)
24 (Digital Reference Ground)	9 (DGND)	

The general purpose counter GPCTR0 on board the PCI 6036E card was used to supply the frequency that drove the Q-switching and also the pulses to the stepper motors for motion control. An advantage of this was that the laser emission was only triggered after the required position (to be microfabricated) was reached. Another advantage of using this single pulse control was that it was possible to generate a finite number of Q-switching pulses [142]. This was necessary for laser beam fluence control on each spot as discussed in section 3.2.2.

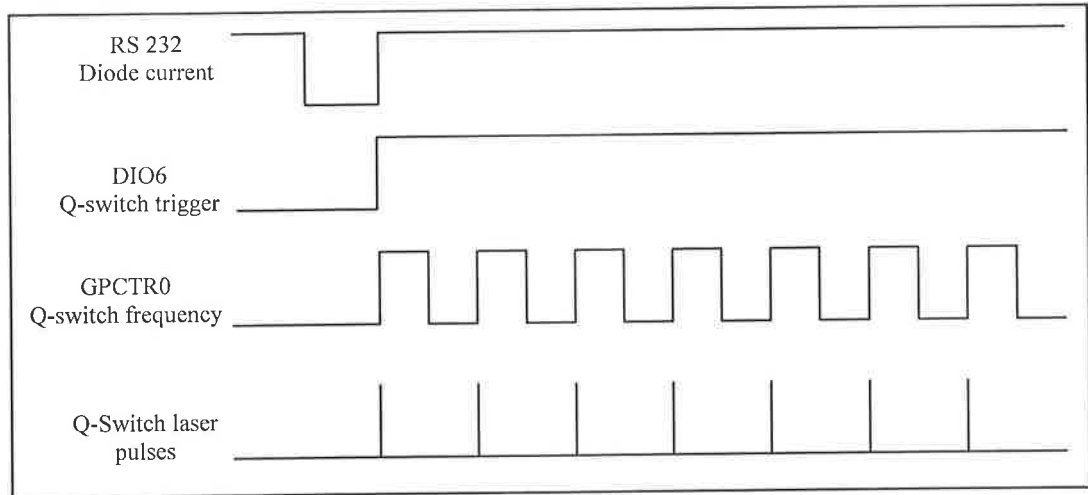


Figure 2.5: Q-Switch pulses generation diagram.

The software control of the Q-switching process is shown in figure 2.5. The Q-switching control required the following:

- 1- The internal pulse repetition frequency PRF of the laser power supply was set to 0 via RS232 communication. This was necessary for the microprocessor to enable the external trigger. This was performed when the laser emission settings were chosen from the LabVIEW laser control code.
- 2- The laser head's gate was then set to ON. This was also performed from the LabVIEW laser control code settings.
- 3- The laser diode was then switched on (controlled from the LabVIEW code via the RS232 cable). This is shown in by the signal at the top of figure 2.5.
- 4- The laser emission was started by sending a high TTL signal from DIO6 to the Q-switch trigger pin. This is described by the second signal in figure 2.5.
- 5- The Q-switching frequency was then set to the desired value, supplied through GPCTR0. This is described by the pulse train in the third signal from top in figure 2.5.

The resulting Q-switched laser pulses are represented by the signal at the bottom of figure 2.5. It can be seen that, as long as the laser diode is on, the pulses were only triggered when the states of both the Q-switch trigger and the Q-switch frequency were high.

2.2.4 The laser external optics

The optical components were placed in one straight line orthogonally to the laser beam. They were located on an optics plate elevated by 13.5 cm from the rig's table so that the

laser beam passes through the centre of the sample displacement capability along the z-axis stepper motor. The optics plate is shown in figure 2.6. The pumped laser light was delivered to the laser head by a fiber optic cable. The external optics used in the system, are explained below according to the propagation path of the laser beam.

Laser head

The laser head is a V-style that is designed for applications requiring short to moderate pulse durations at high PRF with superior pulse-to-pulse stability. The laser head is conductively cooled through a base plate. Ambient temperatures must be kept within 18 - 35°C [141].

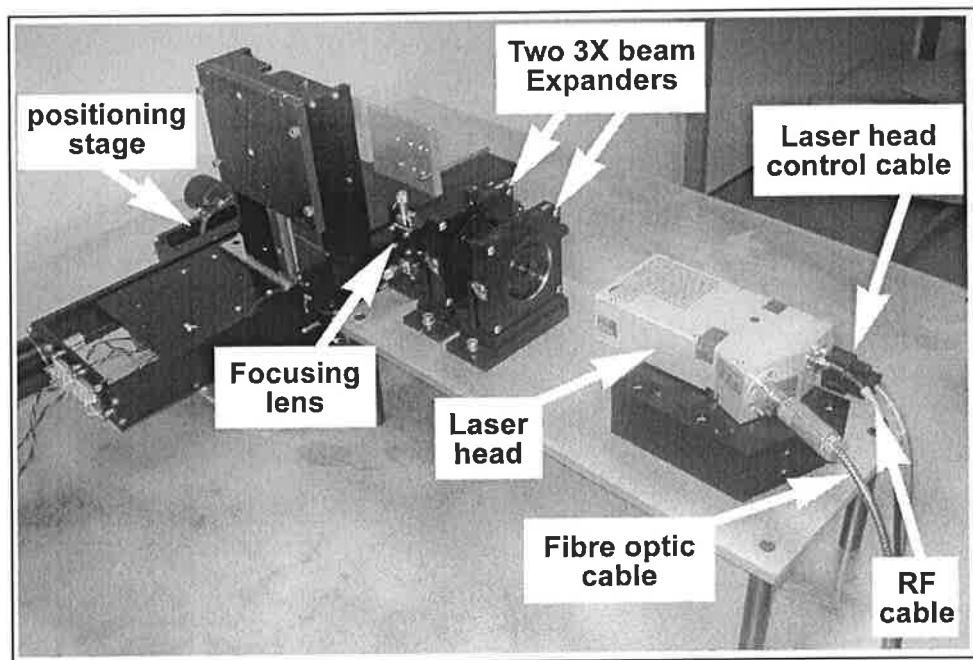


Figure 2.6: Optics plate top and side view.

Beam expander

The laser beam then passes through a variable 3X beam expander, which permitted adjustments of the laser beam diameter at the focusing lens entrance [143]. For the initial stages of experimental work, one beam expander was used. However, when a (100X / NA 1.25) microscope objective lens was used at a later stage of this study, two beam expanders were utilised, which produced a total expansion magnitude capability of 9X.

2.2.5 Focusing methods

Two methods were employed for focusing the laser beam into the target material. The first method utilised an achromat lens triplet that had a focal depth of, $f = 25.6$ mm. This method was used for 3D microfabrication in polycarbonate, since it produced a relatively large depth of field. The lens was mounted on a fine-adjustable x-y-z translating stage. Fine adjustment was needed to centre the beam on the lens and achieve optimum focus of the laser beam [143]. The second method utilised a microscope objective lens that had a numerical aperture, $NA = 1.25$, which was used with immersion oil. This method was used for tight focusing of the laser beam to enable 2D fabrication inside thin glass slides/sheets. The relative positioning of the optical components and the focal region parameters calculations of both focusing methods are presented in the following sections.

Optics relative positioning

Gaussian laser beam spreading phenomenon takes place when a laser beam is focused, expanded or propagated freely through air. Figure 2.7 shows how the laser beam has a curvature along its propagation direction, z . The beam radius along the propagation line can be calculated as a function of the distance z , and is given by,

$$w(z) = w_o \left[1 + \left(\frac{\lambda \cdot z}{\pi \cdot w_o^2} \right)^2 \right]^{1/2} \quad (2.1)$$

Where w_o is the initial beam radius at the focus or at the output of the beam expander, and λ is the emission wavelength.

The Rayleigh range, Z_R , can be defined as the distance over which the beam radius spreads by a factor of $\sqrt{2}$, see figure 2.7. The Rayleigh range is important in determining the relative positioning of optical components to ensure proper propagation of the laser beam with minimum losses and is given by [65],

$$Z_R = \frac{\pi \cdot w_o^2}{\lambda} \quad (2.2)$$

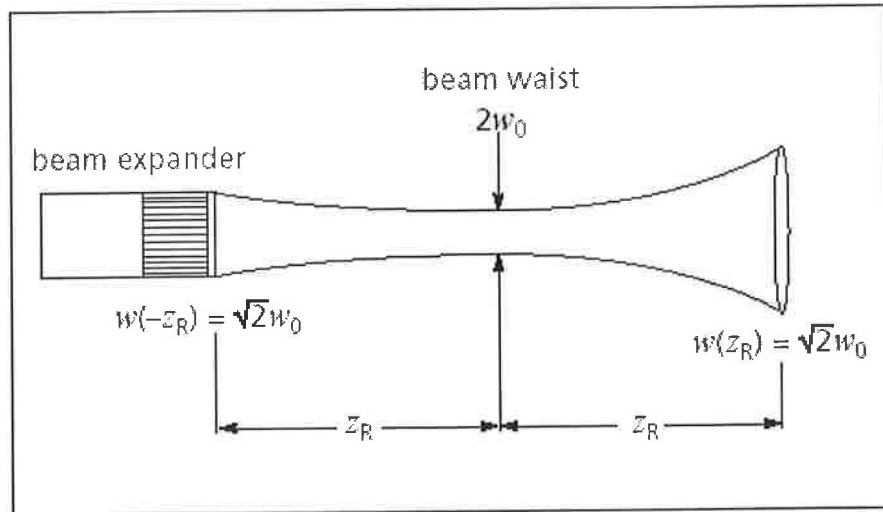


Figure 2.7: Rayleigh range of the laser beam propagation [65].

It can be verified from equation 2.1 that, the beam radius obtained at $z = Z_R$ reduces to $w = \sqrt{2} w_0$. The relative positioning in this study of the optical components was based on the calculations of the Rayleigh range of the laser beam using equations 2.1 and 2.2. The following sections describe the calculations of the beam dimensions throughout the propagation from exiting laser head till being focused in the sample using two different methods. Each of the methods described below was utilised for a specific part of the experimental work.

2.2.6 Achromat lens focusing

Figure 2.8 shows the optical components setup using the achromat lens focusing method. Table 2.4 lists the values of the beam propagation parameters as well as the optical components specifications. The shaded cells in table 2.4 indicate the values of the parameters used for the optical components and their relative separation. The other cells show the maximum spreading of the laser beam based on the Gaussian beam propagation. The 2X expansion capability of the beam expander was used with the achromat lens focusing method. It can be seen from table 2.4 that the chosen values for Z_1 and Z_2 are smaller than the maximum calculated Rayleigh range values Z_{1R} and Z_{2R} respectively. The separation between the components was based on the spreading of the beam calculations and they were positioned within the acceptable ranges of the beam propagation.

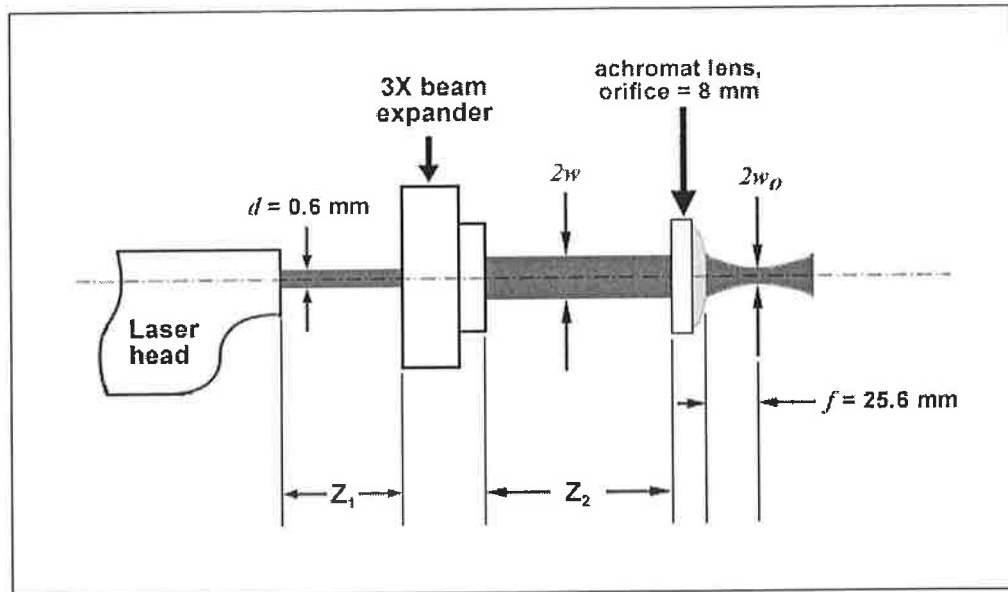


Figure 2.8: Optical components setup for the achromat lens focusing.

Table 2.4: Beam propagation parameters for achromat lens configuration.

Parameters	Units (μm)	Radii (μm)	Stage
Beam Dia, d	600	300	From laser head
Wavelength	1.064		
Z_{1R}	176273.90		Between laser head and beam expander
Beam Dia at Z_{1R}	848.53	424.26	
Z_1	95000		
Beam Dia at Z_1	681.59	340.79	
Beam expander	2X		After beam expander
Expanded Beam Dia	1363.18	681.59	
Z_{2R}	909890.53		
Beam Dia at Z_{2R}	1927.82	963.91	
Z_2	115000		After focusing
$2w$	1374.02	687.01	
f of lens	25600		
$2w_0$	38.05	19.03	
Z_{eff} of focal area	± 708.94		

2.2.7 Practical spot size calculations

This section presents the determination of the spot size experimentally and comparing it the analysis from the OEM's laser beam specifications. A variable-contrast, resin-coated and monochrome photographic paper (JESSOPE) was used to measure the expanded beam's size. As mentioned previously, the beam was expanded by a factor of two using the tuneable 3X beam expander. The measured beam expansion at a distance of 115 mm from the beam expander was 1.36 mm as can be seen in figure 2.9. This measurement agrees with the calculated beam diameter value $2w = 1.37$ mm listed at Z_2 in table 2.4. The expanded beam diameter, defined based on the $1/e^2$ definition [65], which is about

86.5% of the beam width, indicate that the beam diameter should be 1.18 mm. The beam's diameter according to the OEM specifications is 0.6 mm \pm 10% as it exits the laser head [141]. Based on the \pm 10% tolerance of beam diameter, the expanded beam diameter ranged between 1.32 and 1.08 mm. On average, the resulting beam diameter was 1.2 mm. This experimental value of the beam's diameter is in good agreement with the specifications of the laser system and the beam expander.

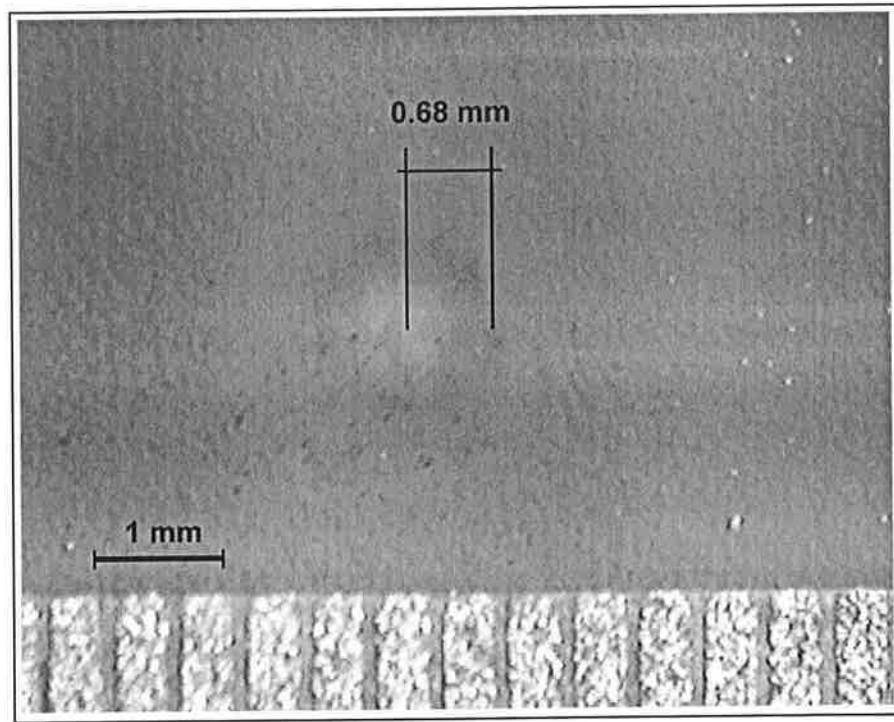


Figure 2.9: Beam size on photographic paper at 115 mm from the expander.

The laser emission wavelength was 1064 nm. Based on the experimental measurement of the beam diameter, the beam waist radius, w_o , at the focus is given by equation 1.4.

$$w_o = \frac{\lambda f}{\pi \cdot w} = \frac{1064 \times 10^{-3} \times 25.6 \times 10^3}{\pi \times \frac{1.18 \times 10^3}{2}} = 14.69 \mu\text{m},$$

and this gives the area affected by the focused beam by:

$$A = \pi \cdot w_o^2 = \pi \times (14.69)^2 = 677.9 \mu\text{m}^2.$$

On the other hand, the beam waist radius based on the OEM's average expanded beam diameter is given by

$$w_o = \frac{\lambda f}{\pi \cdot w} = \frac{1064 \times 10^{-3} \times 25.6 \times 10^3}{\pi \times \frac{1.2 \times 10^3}{2}} = 14.45 \mu\text{m},$$

and this gives the area affected by the focused beam by:

$$A = \pi.w_o^2 = \pi \times (14.45)^2 = 655.97 \mu\text{m}^2.$$

From the above comparison, there was effectively no difference between the experimental and theoretical values of the beam waist at the focus. Thus, the theoretical values of the expanded beam and focal size (1.2 mm and 14.45 μm respectively) were used in the experimental intensity and energy fluence calculations performed section 3.2.2.

2.2.8 Spherical aberration calculations

A simple lens with a spherical surface does not bring parallel light rays entering it at different distances from its centre (or axis) to precisely the same focal point, as shown in figure 2.10. This spreading out of the focus is called spherical aberration, and for a Gaussian beam TEM_{00} can be calculated from the following relation [65]:

$$S.A. = \frac{0.067 \times f}{(f/\#)^3} \quad (2.3)$$

where $f/\#$ is the f-number of the lens is the ratio between the focal depth and the lens diameter at the inlet [102]. In this case the laser beam does not fill the lens diameter, so the f-number is then taken to be the focal ratio f/D (the ratio between the focal depth and the diameter of the laser beam at the inlet of the lens).

The parameters of focusing the laser beam using the achromat lens were:

- 1- Focal depth $f = 25.6$ mm.
- 2- Beam diameter = 1.2 mm.
- 3- Focal ratio $f/D = f/\# = 21.33$

$$S.A. = \frac{0.067 \times 25.6}{(21.33)^3} = 1.77 \times 10^{-4} \text{ mm} = 0.177 \mu\text{m}.$$

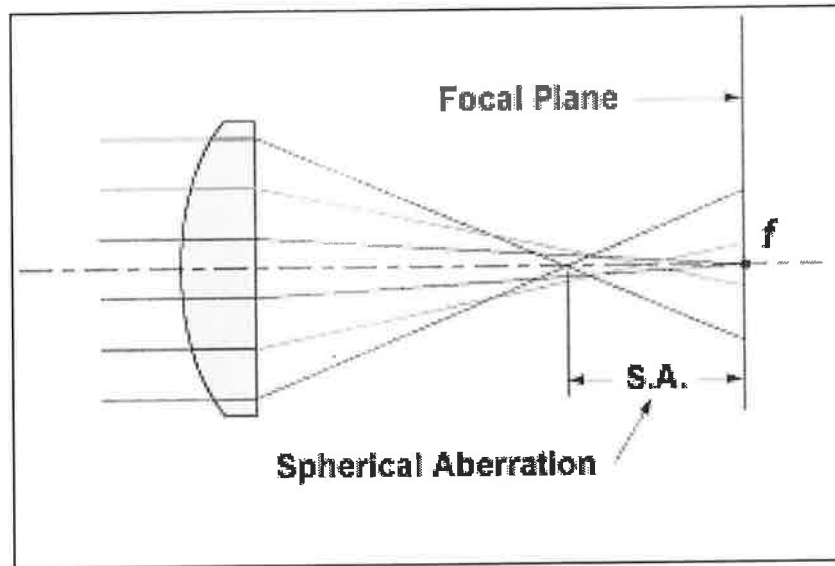


Figure 2.10: Spherical aberration in a basic lens, after [65].

2.2.9 Microscope objective lens focusing

In addition to the achromat lens focusing method used to carry out the experiments for voxels dimensional analysis, an objective lens was used to tightly focus the laser beam inside thin glass samples. The objective lens was used to achieve high intensities at the focus with which materials with higher melting points could be machined, such as soda lime glass, fused silica and sapphire. As shown in figure 2.11, an objective lens with a numerical aperture, $NA = 1.25$ and a magnification of X100 was used with immersion oil to focus the laser beam inside a microscope slide (fused silica, 2 mm thick).

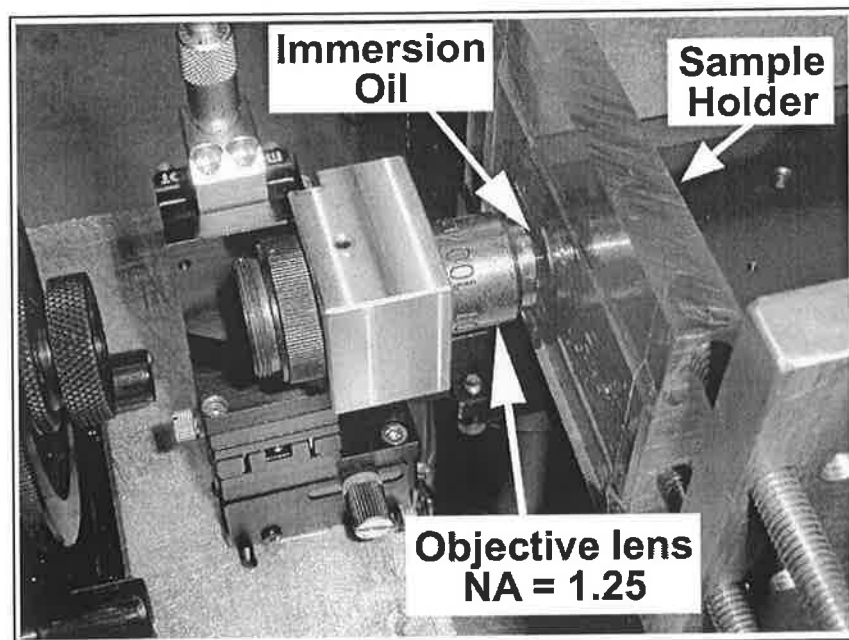


Figure 2.11: Laser beam focusing using an objective lens.

The refractive index, n , is related to NA by, $NA = n \cdot \sin \theta$, where θ is the half-angle of the maximum cone of light that can enter or exit the lens [65, 144]. The refractive index of air is 1 ($n_{air} = 1$), while the typical refractive index of immersion oil is 1.6 ($n_{oil} = 1.6$) [144, 145]. Based on these facts and the relation between NA and n [144], the use of immersion oil with the lens increases the efficiency of laser beam collection by increasing the refractive index and hence NA to a value as high as 1.6 [145]. An additional advantage of using oil is that it produces a better matching to the refractive index of the sample, which is known to reduce emission losses [144].

The relative positioning of the optical components in this case can be determined using the same law of Gaussian beam propagation explained earlier. However, in the light of the objective lens beam collection characteristics, there are slight differences with regards to the focusing of the beam using an objective lens. The f-number ($f/\#$) of the lens is given by [65, 145],

$$f/\# = \frac{1}{2NA} \quad (2.4)$$

The f-number was defined in equation 2.3. Combining both equations 2.3 and 2.4, the following is obtained,

$$\frac{f}{w} = \frac{1}{NA} \quad (2.5)$$

where w is the beam radius at the lens inlet and in this case, $w = f \cdot NA$. When this value is used in equation 1.4, it gives a focal spot radius of,

$$w_o = \frac{\lambda}{\pi \cdot NA} = 0.32 \frac{\lambda}{NA} \quad (2.6)$$

The focal spot diameter has a size limit of $D = 0.61 \lambda / NA$ [144, 145], which agrees with the derivation of equation 2.6 performed above. The optical resolution limit was also given by $D = 0.5 \lambda / NA$ [34]. This relation shows that the higher NA the smaller the spot size and the closer it becomes to the emission wavelength [34, 144]. Figure 2.12 shows the optical components and arrangement used with objective lens focusing. The two beam expanders were set to their maximum 3X beam expansion.

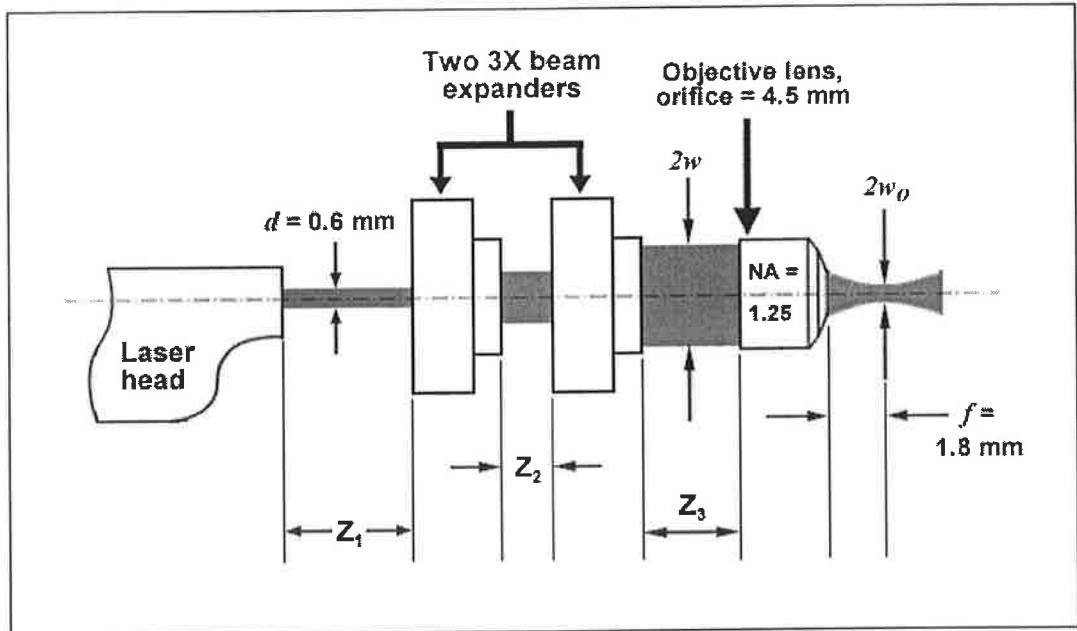


Figure 2.12: Optical components parameters of the new setup.

Table 2.5 lists the values of the beam propagation parameters as well as the optical components specifications. The shaded cells in the table indicate the values of the parameters used for the optical components and their relative separation. The other cells show the maximum spreading of the laser beam based on the Gaussian beam propagation. It can be seen from table 2.5 that the chosen values for Z_1 , Z_2 and Z_3 are smaller than the maximum calculated Rayleigh range values Z_{1R} , Z_{2R} and Z_{3R} respectively. The separation between the components was based on the spreading of the beam calculations and they were positioned within the acceptable ranges of the beam propagation. The beam diameter at the input of the objective lens was taken to be equal to the orifice of the lens since the orifice diameter was smaller than the expanded beam diameter.

Table 2.5: Beam propagation parameters for objective lens configuration.

Parameters	units (μm)	Radii (μm)	Stage
Beam Dia, d	600	300	From laser head
Wavelength	1.064		
Z_{1R}	176273.90		Before beam expander 1
Beam Dia at Z_{1R}	848.53	424.26	
Z_1	95000		
Beam Dia at Z_1	681.59	340.79	
Beam expander #1	3X		
Expanded B. Dia #1	2044.76	1022.38	Between beam expander 1 and 2
Z_{2R}	2047253.69		
Beam Dia at Z_{2R}	2891.73	1445.87	
Z_2	20000		
Beam Dia at Z_2	2044.86	1022.43	
Beam expander #2	3X		After beam expander 3
Expanded B. Dia #2	6134.58	3067.29	
Z_{3R}	18427041.69		
Beam Dia at Z_{3R}	8675.61	4337.81	
Z_3	50000		
Beam Dia at Z_3	6134.61	3067.30	After objective lens
Orifice = $2w$	4500	2250	
Lens NA	1.25		
$2w_o$	0.82	0.41	
Focal depth, f	1800		
Z_{eff} of focal area	0.33		

Equation 2.5 was used to estimate the depth of the focus inside the material shown in figure 2.12 and table 2.5. Equation 2.6 was used to calculate the focal spot size in this part of the study.

2.2.10 3D positioning stage

Building a controllable 3D positioning stage was necessary for fabricating 3D shapes in transparent materials. 3D fabrication can be achieved by scanning the focused laser beam inside the transparent material. Three (2-Phase-1.8°/step, VEXTA PH268-21M2) stepper motors were chosen to be the actuators of the 3D positioning stage due to their accuracy and relatively easy control requirements. The 3D positioning stage consisted of three stepper motors and associated stages placed orthogonally to one another as shown in figure 2.13.

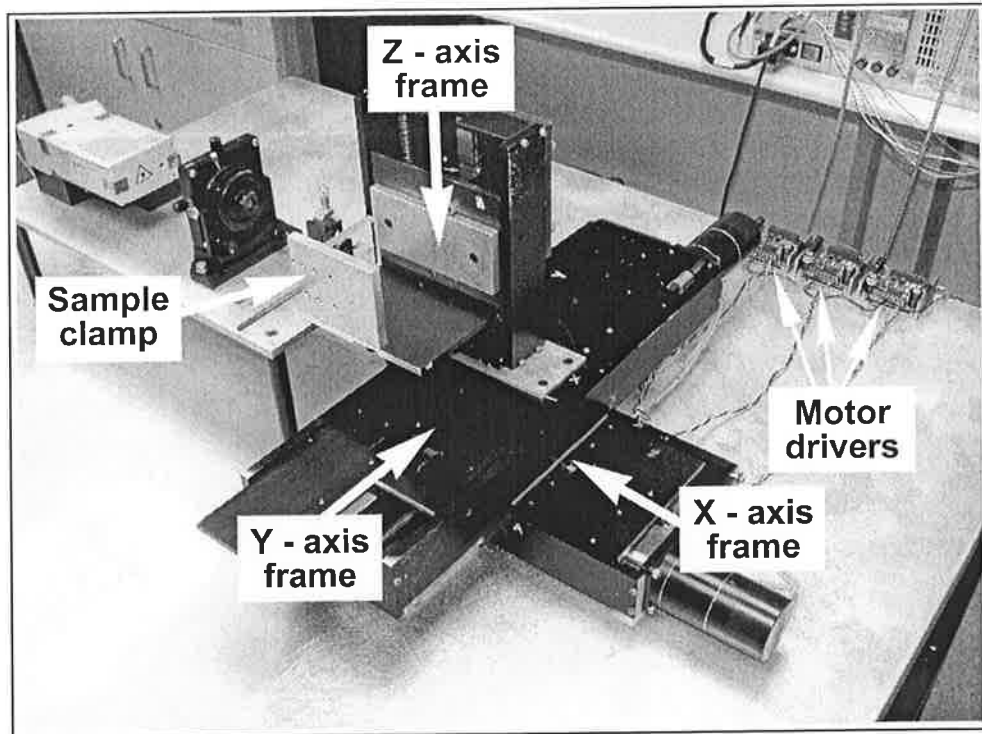


Figure 2.13: The 3D positioning stage built for this work.

The control block diagram of the stepper motors is shown in figure 2.14. Each motor was framed and coupled to a lead screw that converted the rotational motion into a linear motion.

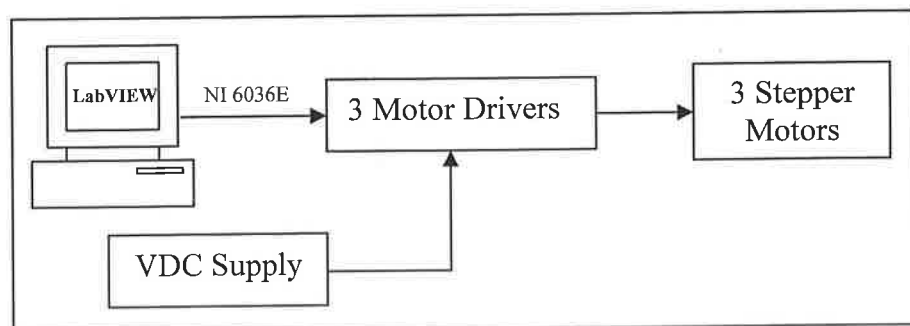


Figure 2.14: Stepper motor control block diagram.

A stepper motor is different from other motor types in the way it can be operated. To operate an AC or DC motor in the simplest case it is usually connected to a voltage supply. However, stepper motors require more than a voltage supply. They need an electronic digital pulse signal to move the motor shaft in steps. Physically, more than the electric pulse is needed, an electronic circuit, usually called the motor driver, is necessary to make the communication between the control signals and the motor windings. Each pulse in the signal will make the shaft to turn by one step; this is called the *step angle*. By sending a continuous pulse train to the stepper motor, it runs

continuously as if it was a DC or an AC motor. Stepper motors are used for precise position control by controlling the number of pulses. The step number S of a stepper motor can be defined as the number of steps required for the motor's shaft to rotate by 360° [146]. The step angle θ_s is a manufacture characteristic of the motor and is related to the step number by:

$$S = \frac{360}{\theta_s} \quad (2.7)$$

The stepper motors used in this work had $\theta_s = 1.8^\circ/\text{step}$, the step number based on equation 2.7 is then $S = 200$ steps. This means that the number of steps required to complete one shaft revolution is 200 steps. Figure 2.15 shows the basic mechanical setup of the stepper motor motion frame. As mentioned earlier, the rotational motion is converted into linear motion by the means of a lead screw and a follower. The linear displacement D caused by the lead screw is related to the number of pulses of the electric control signal by the relation:

$$D = \frac{p}{S} \times N \quad (2.8)$$

where, p is the lead screw pitch and N is the number of pulses sent to the stepper motor.

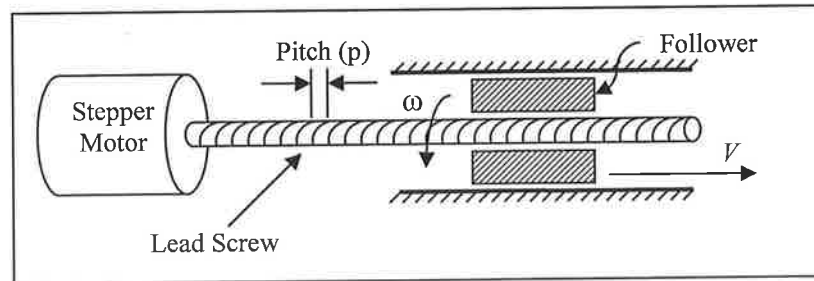


Figure 2.15: A basic set up of a stepper motor system.

It is clear from equation 2.8 that one complete rotation ($N = S = 200$) will produce a linear displacement equal to the pitch of the lead screw. The lead screws used in this work had a pitch, $p = 1/4" = 6.35$ mm. The rotational speed ω (rev/s) of the stepper motor is related to the electric signal's frequency f (Hz) by:

$$\omega = \frac{360}{S} \times f \quad (2.9)$$

The linear speed V (mm/s) caused by the lead screw is related to the frequency f by:

$$V = \frac{P}{S} \times f \quad (2.10)$$

The positioning resolution of the stepper motor is the smallest linear distance that the stepper motor / lead screw setup can achieve. It is clear from equation 2.8 that this displacement is a result of one single pulse. Displacement accuracy D_{AC} can be expressed as:

$$D_{AC} = \frac{P}{S} \quad (2.11)$$

With the specifications demonstrated above, the stepper motors gave a positioning accuracy $D_{AC} = 6.35/200 = 31.75 \mu\text{m}$. However, advances in the electronics technology made it possible to further increase the stepper motor's positioning resolution [147]. The step number can be increased using the motor driver board; this technique is called (microstepping) [147]. The motor driver basically works on regulating the level of the current running in the stepper motor winding. This in turn increases the number of steps required for one full revolution. The motor driver used with the positioning system in this work was an Intelligent Motion Systems, Inc. motor driver board (IM483) [147]. This driver can be set to microstep resolutions as high as 51,200 microstep/rev (i.e. 256 microsteps/ conventional step). The microstep number in this work was set to 51,200 microsteps/rev. It can be seen from equation 2.11 that the positioning resolution was thereby increased as a result to $D_{AC} = 6.35/51,200 = 0.124 \mu\text{m}$.

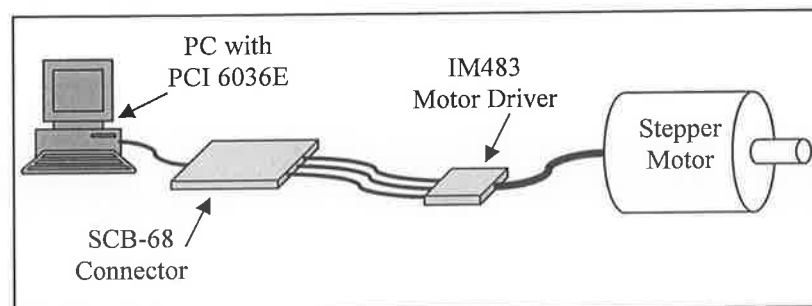


Figure 2.16: Schematic connection of a stepper motor to the control PC.

National Instruments™ has a range of interfacing boards, the PCI 6036E interfacing board [142] and the SCB-68 external connector [148] were used as the means of communication between the control PC and the motor drivers and hence the stepper motors. Each motor was connected to the PC in the same manner as shown in figure

2.16. The motor driver received 3 signals from the PC through the PCI 6036E and SCB-68 connector. Those signals were:

- 1- Frequency: a 5 VDC square signal from a counter on the PCI 6036E device. The frequency of this signal determined the positioning speed and the number of pulses determined the amount of displacement.
- 2- Enable: a 5 VDC digital logic signal; it toggled the status of the motor between ON and OFF modes.
- 3- Direction: a 5 VDC digital logic signal; it toggled the direction of rotation between CW and CCW.

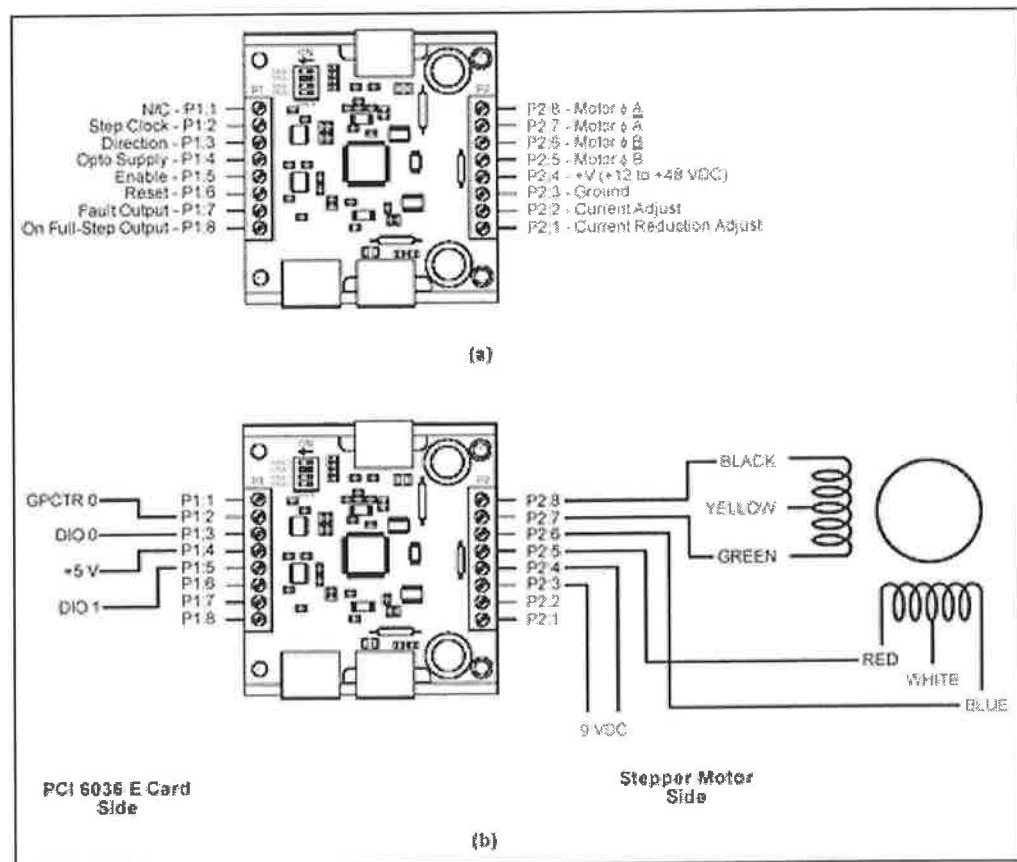


Figure 2.17: Stepper motor driver, (a) Pins configuration and (b) one motor's connection.

The workspace of the 3D positioning stage was designed to be 90 by 90 by 90 mm. The windings of each motor were wired to the IMS483 and figure 2.17 shows the pin connection configuration of the x axis driver and how it was connected to the motor. The control signals came from the PCI 6036E card as shown in figure 2.17. The pulse source was shared among the 3 motors. In order to control the positioning, each motor

was operated while the other two were disabled. Table 2.6 lists the pin connections between all the motor drivers and the PCI 6036E card.

Table 2.6: Motor driver – PCI 6036 E pin connections

Motor driver pin	X motor	Y motor	Z motor	Description
P1:2	CPCTR 0	CPCTR 0	CPCTR 0	Pulse source
P1:3	DIO 0	DIO 2	DIO 4	Direction
P1:4	+5 V, Fused	+5 V, Fused	+5 V, Fused	Opto supply
P1:5	DIO 1	DIO 3	DIO 5	Enable/Disable

2.3 CO₂ laser system hardware and specifications

The second part of the study was based on the use of a CO₂ laser. CO₂ lasers are very versatile and practical [66, 126] and produce an output in far infrared region (over 10,000 nm). A wide range of CO₂ lasers are available, which produce power outputs ranging from low-power (Watt ranges) to high-power lasers (kW ranges) used in material processing applications [126, 149]. Carbon dioxide lasers are available in pulsed and / or CW outputs. Table 2.7 provides a quick reference summary of the CO₂ laser characteristics from the literature [22].

Table 2.7: Summary of CO₂ laser characteristics from literature [22]

Active Medium	Carbon Dioxide Gas
Output Wavelength*	10.6 μm
Power Range	10 W – 5,000 W
Pulsed or CW	Both
Excitation	Electrical (10,000-50,000 V)
Polarization	Unpolarized

In this study, a Rofin DC-015 diffusion-cooled CO₂ slab laser system was used to fabricate microchannels on the surface of soda lime glass sheets. The optical resonator of the laser, shown in figure 2.18, is formed by the front and rear mirrors and two parallel RF-electrodes. Excitation of the laser gas takes place in the RF field between the water-cooled electrodes. The heat generated in the gas is dissipated by the water-cooled (diffusion-cooled) electrodes. Thus, the conventional gas circulation systems

* most common wavelength

involving roots blowers or turbines are not required. A beam shaping module is integrated into the laser head and produces a high quality round symmetrical beam. The resonator design produces a 45° linearly polarized beam [149].

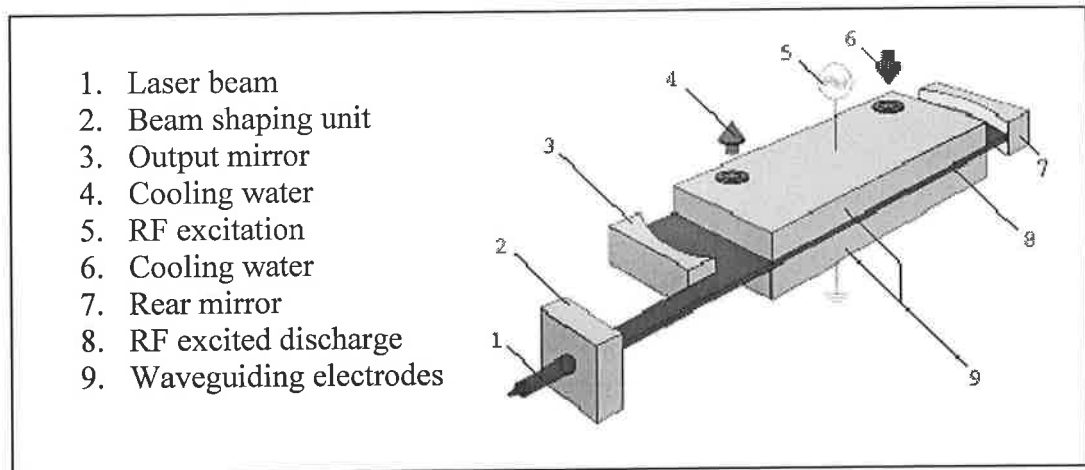


Figure 2.18: The CO₂ laser resonator configuration [149].

The laser beam mode is TEM_{00} and has a quality factor $K > 0.9$, giving M^2 value of 1.11. The M^2 is a dimensionless beam propagation parameter and it is equal to 1 for a perfect Gaussian beam [65]. The beam diameter was 20 mm at the laser output, diverging to 25 mm at 10 m distance. The focussed spot size and depth of focus depend on the focal length of the lens used. The laser beam is usually equal to 22 mm at the inlet of the focusing lens [150]. The focused spot diameter can be calculated from the real beam propagation equation [65].

$$D_o = \frac{\lambda \cdot f \cdot M^2}{\pi \cdot D} \quad (2.12)$$

Equation 2.12 is similar to the equations used in the calculations performed in section 2.2.7 except for the multiplication by the M^2 factor. Using the numerical values of the parameters in equation 2.12, the beam diameter at the focus becomes,

$$D_o = \frac{10.6 \times 10^{-3} \times 127 \times 1.11}{\pi \times 22} = 0.09 \text{ mm} = 45 \text{ } \mu\text{m}.$$

The calculations agree with an excel file received from the Rofin technical support. The excel file allowed calculation of spot diameter and the depth of focus $L_{5\%} = 0.32 \text{ mm}$, which is the depth of focus at 5% of focus diameter expansion. Figure 2.19 shows the laser system components. This laser system was a laser cutting machine that came with

a CNC motion system and it was used without any modifications. Table 2.8 lists the laser system and laser beam specifications.

Table 2.8: CO₂ laser system specifications [149-151].

Laser system specifications	
Wavelength	10.6 μm
Average power capacity	1500 W
Operation mode	CW / Pulsed
PRF range	2 - 5000 Hz
Pulse width range	26 μs – 125 ms
Laser beam specifications	
Spatial mode	TEM ₀₀
Beam quality factor, <i>K</i>	> 0.9
Beam propagation parameter, <i>M</i> ²	1.11

2.3.1 Controlling the CO₂ laser system

The CO₂ laser operation was controlled from the control console provided with the system. This console allowed the control of the laser beam's power, pulse repetition frequency and the translation speed by keying in their numerical values. The PRF of the laser pulses was controlled by dividing the principal frequency of the laser's master clock. The CO₂ laser system has a characteristic principal frequency of 4 MHz, which is modulated to set the value of the pulse repetition frequency PRF. There are two dimensionless parameters (from the control console) that can be used to accomplish this, namely, the period and the divide. The PRF is then given by $PRF = F_{fund} / (period \times divide)$, where F_{fund} is the principal frequency of the laser. The period parameter is the period of the resulting pulses and the divide parameter is a factor used to divide F_{fund} and also controls the duty cycle of the pulse. For example if a divide of 40 was used, then the principal frequency clock will be divided to become $4 \text{ MHz} / 40 = 100 \text{ kHz}$. This clock feeds the period clock, and if the period clock is 1000 then the output laser pulses frequency becomes, $100 \text{ kHz} / 1000 = 100 \text{ Hz}$ [152]. Alternatively, the laser system can be controlled using the main power supply; however that operation would not be synchronised with the motion control system [153]. It is worth mentioning here that once the control console is used, it overrides the setting on the main laser control unit.

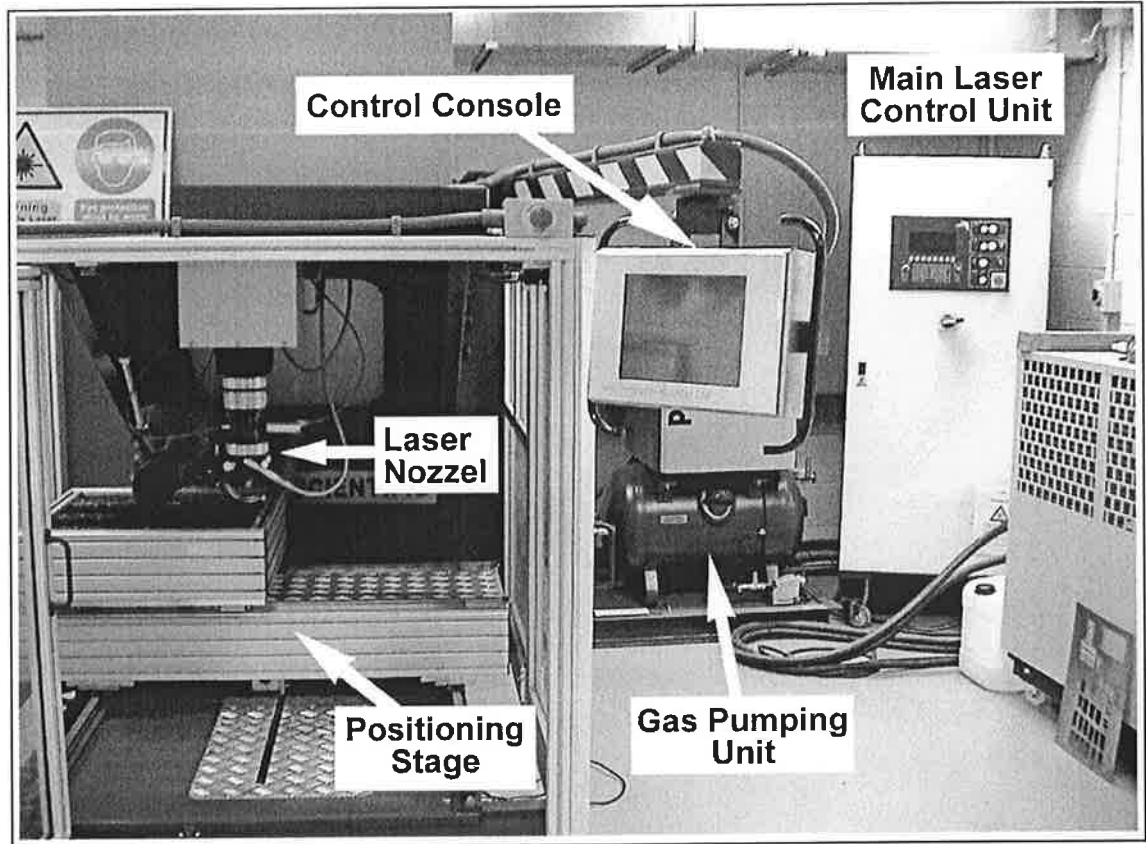


Figure 2.19: The CO₂ laser system used in this study.

2.3.2 The motion control system

The laser system came with a MTI 0505 Scientific motion system [153]. The motion system, shown in figure 2.19, consisted of a machining table that provided XY cutting area / envelope of 50 cm × 50cm. The motion resolution provided via the optical rotary encoders was 1.25 μm. The XY positioning speed ranged from 1 mm/min to 5 m/min, and the acceleration at the beginning of the motion could be as high as 2 m/s². The control console is a full colour touch screen TFT display, which was used for the simultaneous control of the motion system and the laser power supply. The laser beam was focused onto the moving samples by a high pressure 5” FL lens which was a part of a nozzle assembly. The nozzle assembly was guided by vertical linear variable displacement transducers (LVDT) and provided 150 mm of vertical height or focal position adjustments [153].

Part II: Software Setup

2.4 Introduction

The Nd:YVO₄ laser system designed and built in this work was similar in operation to a rapid prototyping machine. This involved the design and development of both the hardware set up and control software. This part of the chapter presents the developed control software for the Nd:YVO₄ laser system. The steps required to produce a 3D design in a transparent material using the developed system are as follows:

- 1 3D image design using any design software package, such as AutoCAD.
- 2 Exporting the 3D design as a stereolithography (STL) file, this is the common format to rapid prototyping (RP) systems.
- 3 Manipulating the 3D STL file to produce a 3D sliced build file.
- 4 Controlling the position of the work piece in 3D based on the data in the build file.
- 5 Operating the laser system for laser emission at suitable power/frequency ratings necessary to cause micro-fabrication in the transparent material.

Steps 4 and 5 were operated in a synchronised cyclic manner. Each of these steps will be discussed in detail in the sections below. Figure 2.20 shows the flow of the entire production process.

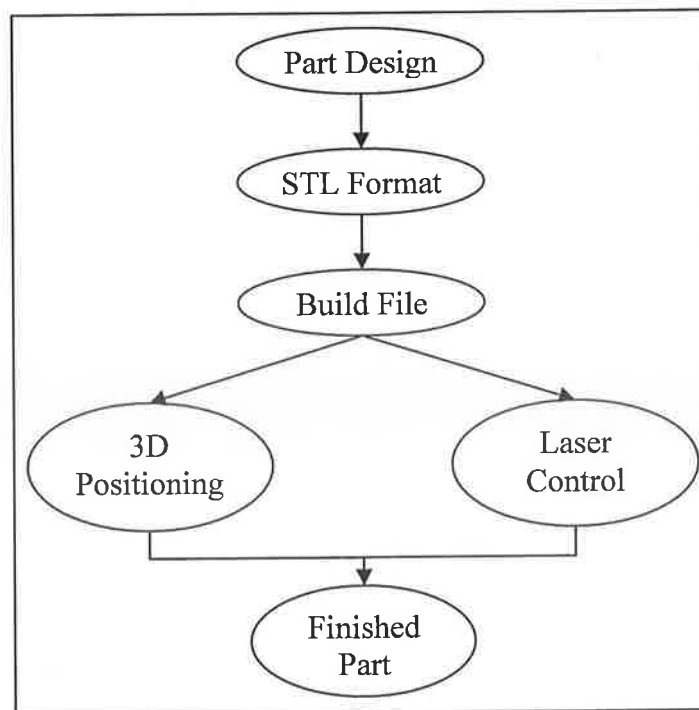


Figure 2.20: Flow chart of the system's production process.

The software control of the system can be divided into three main parts: CAD manipulation, sample position control, and laser control. LabVIEW was utilised in developing the three parts.

2.5 CAD manipulation codes

The part to be produced was designed in a CAD software. AutoCAD and Microstation were used as the CAD design environments for this work. The design must be a solid/surface object in order to be convertible to STL format that relates to "stereolithography" which is the method of layered manufacturing invented by 3D Systems™. STL is the file format used by rapid prototyping systems that allows translating the CAD model data into a file format that could be interpreted by rapid prototyping machinery, and thus physical prototype can be created [155]. After the model design is completed it can be exported to an STL file using the STLOUT command in AutoCAD.

2.5.1 STL file format

It is important to discuss the format of STL files as a ground for understanding the mathematical and numerical representation of the model. STL employs a method of representing the surfaces of a CAD model as a closed volume mesh comprised of triangles [156], this method is called "tessellation", see figure 2.21 for a sample tessellated model. Each triangle is referred to as a "facet" that is defined by 3 vertices and a normal vector to the facet surface. These facets' data are used by a slicing algorithm to determine the cross sections of the 3D shape to be built [157]. There are two important requirements to ensure proper processing of an STL file. First, triangle vertex ordering is used to identify interior or exterior surfaces. An order is assigned to each vertex, where a clockwise vertex ordering indicates an interior surface. The right-hand rule states that the vertices of each facet must be ordered so that when the fingers of the right hand pass from point one through point two to point three, the thumb will point away from the solid object [158]. This rule is illustrated in figure 2.22. The second rule is the vertex-to-vertex rule. Each triangle must share two vertices with each of its adjacent triangles. In other words, a vertex of one triangle cannot lie on the side of another [159, 160] as illustrated in figure 2.23.

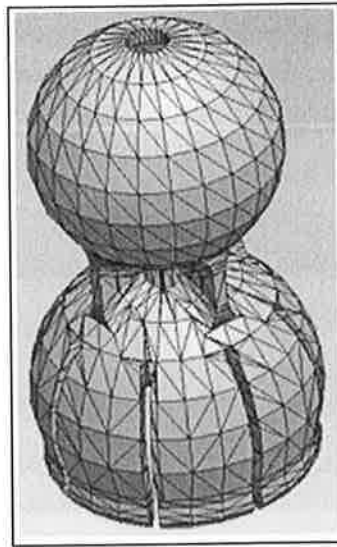


Figure 2.21: A sample tessellated solid model [156].

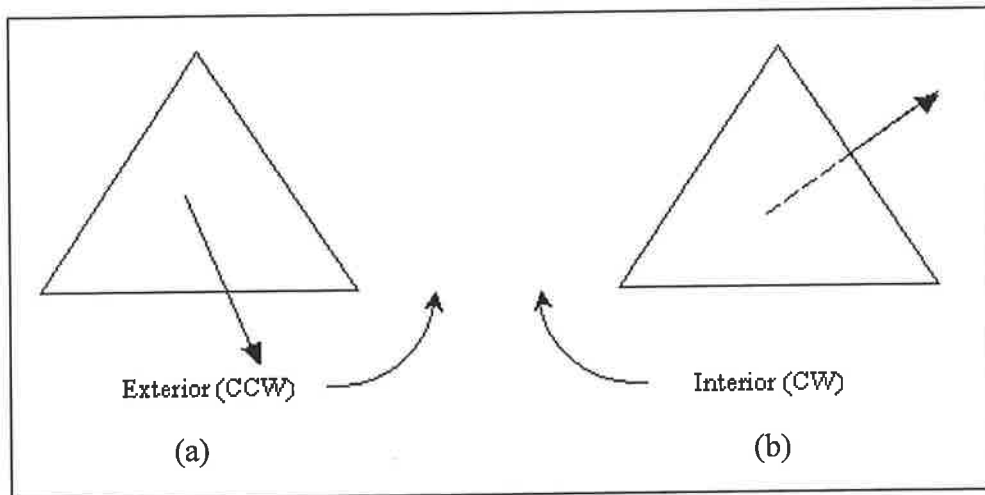


Figure 2.22: Right-hand rule, (a) illustrates an exterior surface and (b) an interior surface.

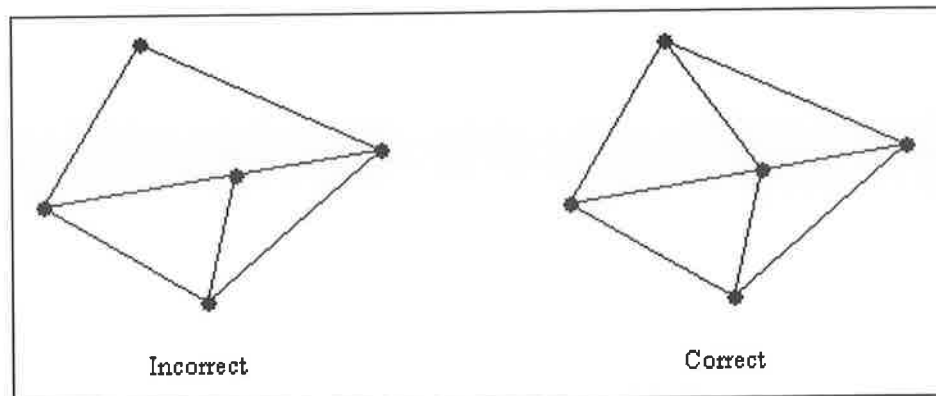


Figure 2.23: The vertex-to-vertex rule. The left figure shows a violation of the rule and a correct configuration is shown on the right.

The object represented must also be located in the positive x, y and z portion of 3D space. In other words, all vertex coordinates must be positive-definite (non-negative and non-zero) numbers. The STL file does not contain any scale information; the coordinates are in arbitrary units. Typically, an STL file is saved with the extension “STL,” case-insensitive. ASCII and Binary STL files are the two types of STL files that are commonly used. Both types store 3D facets and their normals. ASCII STL files have one advantage in that they are easy to read with most text editors. Binary STL files, on the other hand, are more compact and faster for the computer to read [159]. The design of this system was based on the ASCII STL format. These two formats are described separately in what follows.

2.5.2 STL ASCII format

The ASCII STL format has the following syntax:

solid *name*

$$\left\{ \begin{array}{l} \mathbf{facet\ normal} \ n_i \ n_j \ n_k \\ \mathbf{outer\ loop} \\ \mathbf{vertex} \ v1_x \ v1_y \ v1_z \\ \mathbf{vertex} \ v2_x \ v2_y \ v2_z \\ \mathbf{vertex} \ v3_x \ v3_y \ v3_z \\ \mathbf{endloop} \\ \mathbf{endfacet} \end{array} \right\}^+$$

endsolid *name*

Bold face indicates a keyword; these must appear in lower case. Note that there is a space in “facet normal” and in “outer loop,” while there is no space in any of the keywords beginning with “end.” Indentation must be with spaces; tabs are not allowed. The notation, “{...}+,” means that the contents of the brace brackets can be repeated one or more times. Symbols in italics are variables which are to be replaced with user-specified values. The numerical data in the *facet normal* and *vertex* lines are float numbers, for example, (1.1×10^{-3}) . A *facet normal* coordinate may have a leading minus sign; a *vertex* coordinate may not [157]. An ASCII STL sample file of a triangle (three vertices) is shown as follows.

```

solid test
facet normal -0.006623 -0.026361 0.999631
  outer loop
    vertex 25.624990 50.786594 17.745050
    vertex 24.960028 50.800739 17.740273
    vertex 25.595644 51.446274 17.727461
  endloop
endfacet
facet normal -0.002423 -0.215967 0.976398
  outer loop
    vertex 25.624990 50.786594 17.745050
    vertex 25.613110 50.155865 17.884531
    vertex 24.960028 50.800739 17.740273
  endloop
endfacet
facet normal 0.024105 -0.241428 0.970119
  outer loop
    vertex 24.942366 50.173779 17.896738
    vertex 24.960028 50.800739 17.740273
    vertex 25.613110 50.155865 17.884531
  endloop
endfacet
endsolid test

```

Notes:

- The length of the normal vector is 1
- The vertices follow the right hand rule
- The numbers are float values

2.5.3 STL binary format

The binary format uses the IEEE integer and floating point numerical representation.

The syntax for a binary STL file is as follows:

Bytes	Data type	Description	
80	ASCII	Header No data significance	
4	unsigned long integer	Number of facets in file	
	4	float	i for normal
	4	float	j
	4	float	k
	4	float	x for vertex 1
	4	float	y
	4	float	z
	4	float	x for vertex 2
	4	float	y
	4	float	z
	4	float	x for vertex 3
	4	float	y
	4	float	z
	2	unsigned integer	Attribute byte count

The notation, “ $\{\dots\}^+$,” means that the contents of the brace brackets can be repeated one or more times. The attribute syntax is an optional element in the STL, which may be used to specify a certain colour or tool to be used for fabricating that a specific vertex [157]. The attribute syntax was not documented in the formal specification above.

2.5.4 Read STL code

Having studied the STL format and the meaning of the data that it contains, now we can explain the method used to produce a build file from the STL file format. The technique is known as the “slicing method” [158]. Our build file is going to be significantly different from other build files commonly employed in stereolithography. The reason behind this is that our aim is to optically store the model, in the form of voxels, inside the transparent substrate. However, in other RP processes the aim is to produce a part or a prototype that has the same geometry and dimensions of the CAD model, i.e. physically separated from the substrate. This usually requires additional parts in the build file, such as model placement, orientation and support generation and assignment of build and recoat attributes [158]. The build file generated in this work was mainly based on the slicing of the tessellated model, i.e. the STL file. The following section discusses the algorithm used for slicing and the LabVIEW code developed to achieve that.

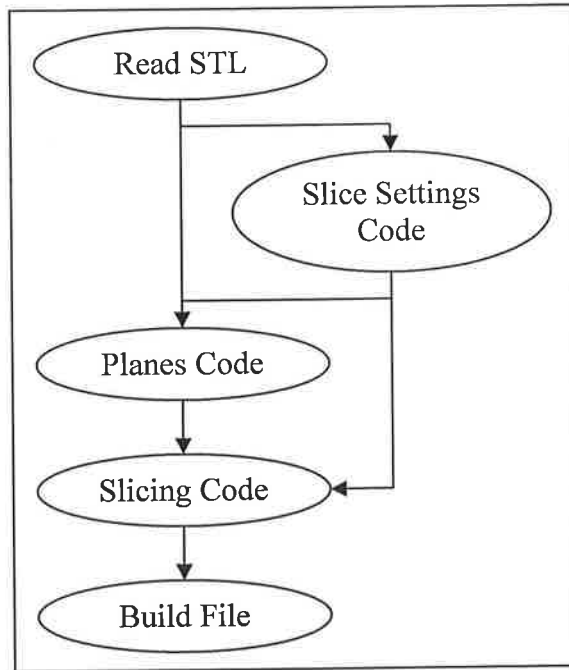


Figure 2.24: CAD file manipulation code flow chart.

The CAD manipulation code is composed of a group of codes. Each code performs a specified function, all leading to one goal that is to produce a build file. The program's flow chart is illustrated in figure 2.24. The function of this code was to read the STL file and filter out the necessary data needed for the slicing to be performed on the design. It saves the filtered data in a text file. Filtering the necessary data is essential because it provided the data for the slicing process. For slicing, only the coordinates of the three vertices that define each facet (triangle) on the surface are needed. The rest of data contained in the STL file was filtered, which also reduced the size of the file. The input and output variables used in this program are shown in figure 2.25. The illustration of using the code and how it works can be found in appendix B.2.1.

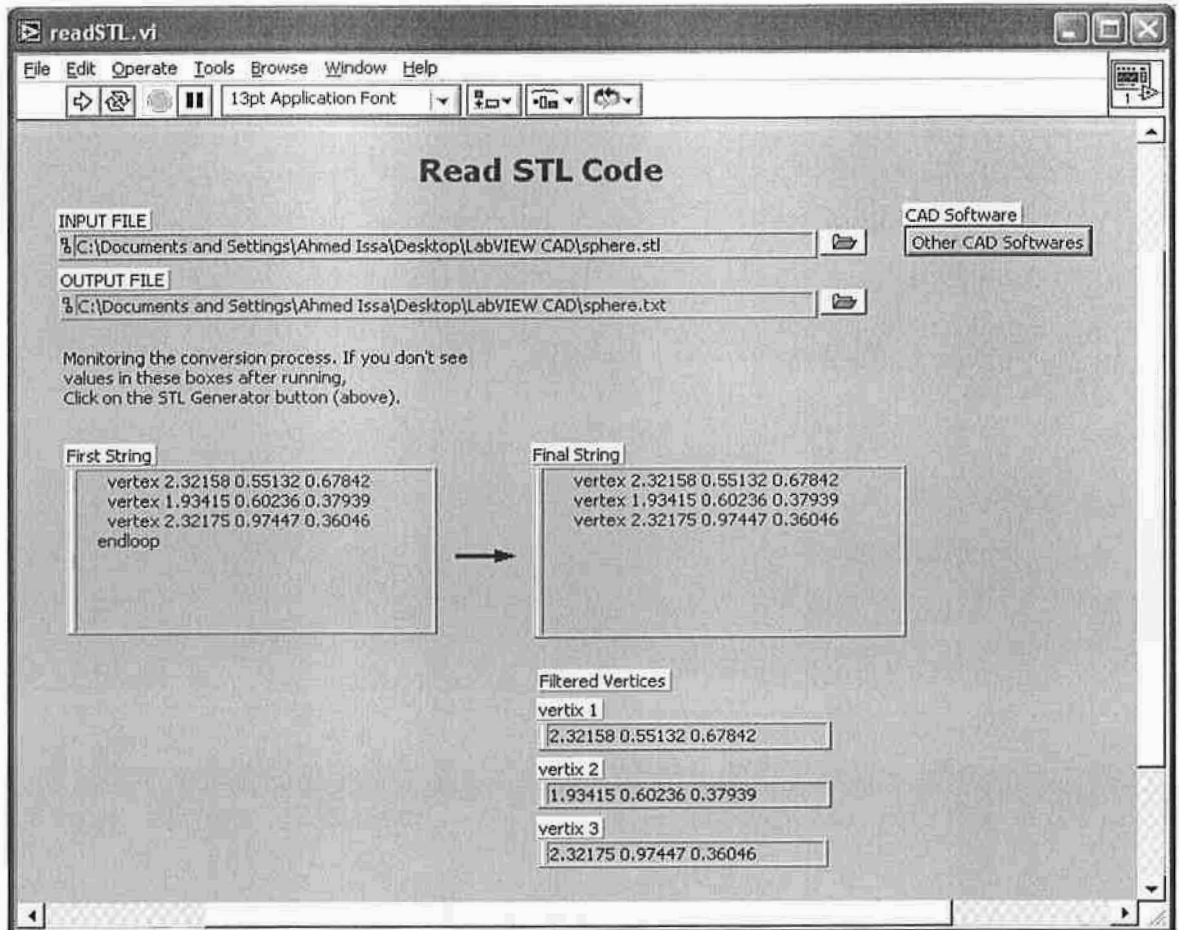


Figure 2.25: Read STL code front panel.

Figure 2.26 (a) shows the unprocessed STL format with the extra details. Figure 2.26 (b) shows the text file format output after processing the STL file. After this stage the program deals with this text file, called “source file” hereafter.

<pre> solid sphere facet normal -0.13 -0.13 -0.98 outer loop vertex 1.50000 1.50000 0.00000 vertex 1.50000 1.11177 0.05111 vertex 1.11177 1.50000 0.05111 endloop endfacet facet normal 0.13 0.13 -0.98 outer loop vertex 1.50000 1.50000 0.00000 vertex 1.50000 1.88823 0.05111 vertex 1.88823 1.50000 0.05111 endloop endfacet facet normal -0.13 0.13 -0.98 outer loop vertex 1.11177 1.50000 0.05111 vertex 1.50000 1.88823 0.05111 vertex 1.50000 1.50000 0.00000 endloop endfacet facet normal 0.13 -0.13 -0.98 outer loop vertex 1.88823 1.50000 0.05111 vertex 1.50000 1.11177 0.05111 vertex 1.50000 1.50000 0.00000 endloop endfacet facet endsolid </pre>	<pre> 1.50000 1.50000 0.00000 1.50000 1.11177 0.05111 1.11177 1.50000 0.05111 end 1.50000 1.50000 0.00000 1.50000 1.88823 0.05111 1.88823 1.50000 0.05111 end 1.11177 1.50000 0.05111 1.50000 1.88823 0.05111 1.50000 1.50000 0.00000 end 1.88823 1.50000 0.05111 1.50000 1.11177 0.05111 1.50000 1.50000 0.00000 end eof </pre>
(a)	(b)

Figure 2.26: STL file filtering: (a) Original 4 facets vertex information, and (b) Reduced text file showing the same facet vertex information.

2.5.5 Slice settings code

In this code the user defines the slicing parameters that are going to be used in processing the design. The front panel of this code is shown in figure 2.27. The parameters are the direction of slice and the layer spacing. The process parameters and the XYZ data taken from the source file are fed into another two sub-codes. The actual slicing is done in the Planes.vi and Intersection.vi sub-codes. Appendix B.2.2 illustrates how to use this code and how it works.

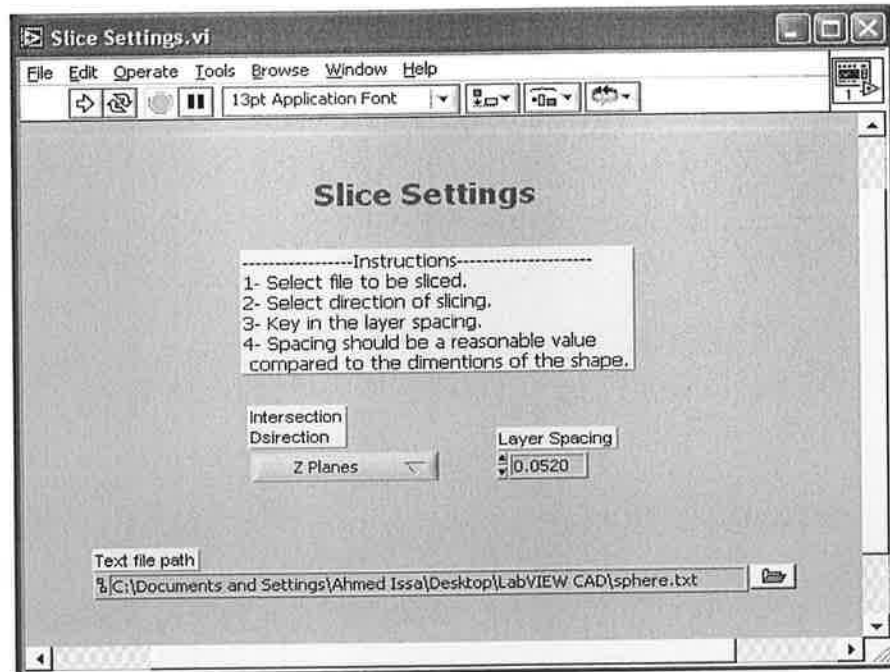


Figure 2.27: Slice Settings code front panel.

2.5.6 Planes code

This code takes its inputs from the slice settings code. The inputs are (X values, Y values, Z values and Layer Spacing). This code develops the CAD envelope (maximum and minimum XYZ-coordinates). According to the CAD envelope and the layer spacing it will generate 3 sets of slicing planes (X Planes, Y Planes and Z Planes). This code is self executing; it needs no instructions from the user. See figure 2.28 for the front panel and diagram of the code. The slicing planes are then used in the Slicing code. The details of how this code works can be found in appendix B.2.3.

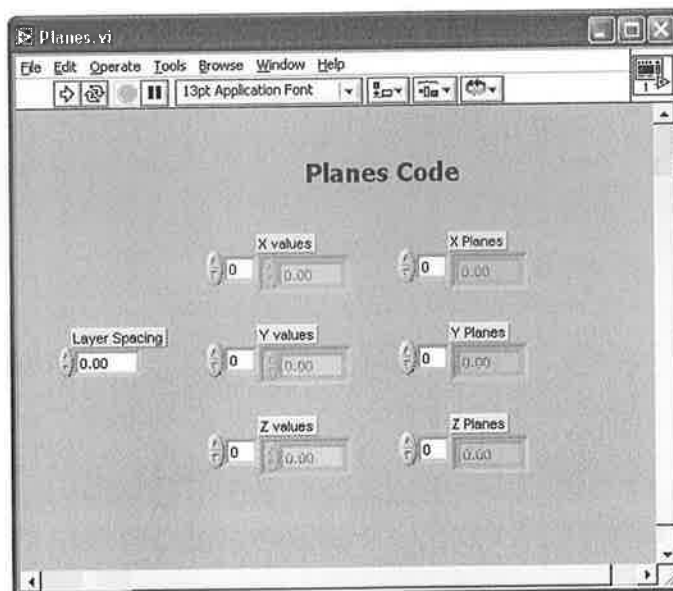


Figure 2.28: Planes code front panel.

2.5.7 Slicing code

The slicing can be described as passing an array of planes through the designed part or CAD geometry. Those planes are parallel and have constant increments in values in one of the major axes direction, for example z planes, see figure 2.29. The intersections of each plane with the tessellated (faceted) surface of the part will form planar contours, see figure 2.30. These planar contours are the basis of any RP or stereolithographic manufacturing process.

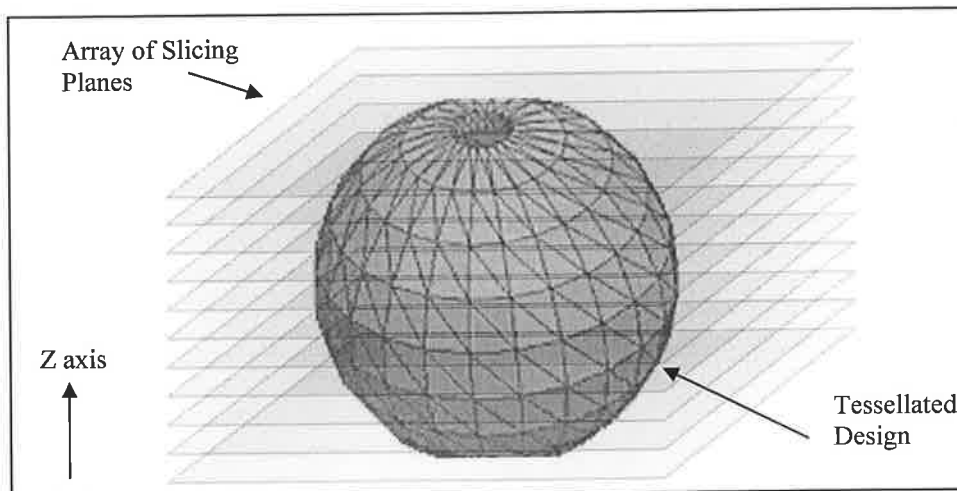


Figure 2.29: Slicing concept using Z planes.

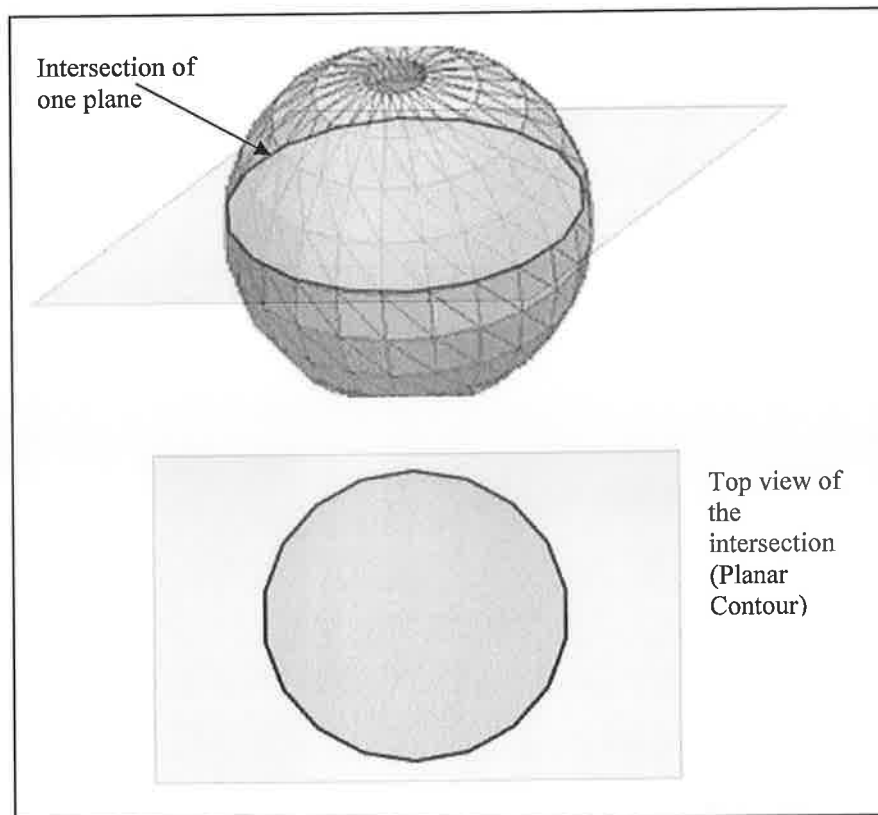


Figure 2.30: Single plane slice (planar contour).

Appendix B.2.4 illustrates the mathematical background necessary for understanding the line-plane intersection in 3D space. This concept of line-plane intersection illustrated in the theory of appendix B.2.4 was used in the Slicing code developed in this work. This code launches automatically after the Slicing Settings and the Planes codes terminate, taking inputs from both:

- Facets Data: (X, Y and Z values) taken from the Slicing Setting code.
- Slicing Direction: (X, Y and Z Direction) taken from the Slicing Setting code.
- Slicing Planes: (X, Y and Z Planes) taken from the Planes code.
- Mark Spacing: usually equals $2 \times (\text{Layer Spacing})$ taken from the Planes code. This parameter is a numerical value. The layer spacing is entered by the user in the Slice Settings.vi code, see figure 2.27. This is the spacing between planes taken through the CAD file of the object. The points where a plane intersects a facet on the surface of the object are used as positions within the physical part for voxel fabrication. If the plane cuts a face at an angle such that the distance between these points is larger than the Layer Spacing, the software segments this distance to produce a more homogeneous distribution of voxels within the object. The segments separation is set by the Mark Spacing parameter.
- Build File Path: defines the path and name of the build file, a default value saves the build file on the desktop, typically, with the name (data.txt).

The slicing code has two main sub-codes, namely, Segment code and Filter code. Appendix B.2.5 contains the illustration of how the slicing code and its sub-codes work. Figure 2.31 shows the difference brought by segmenting the distances between point-pairs resulting from the slicing plane intersection with one facet.

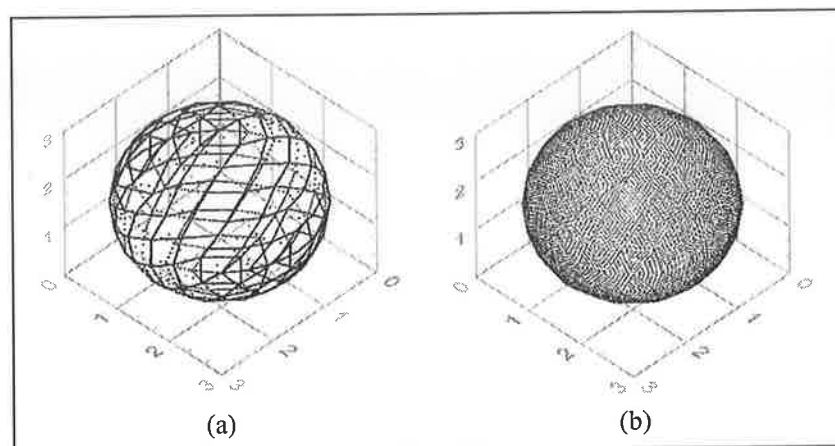


Figure 2.31: Significance of segmentation, (a) slicing without segmentation and (b) slicing with segmentation.

Repeated intersection points are generated after slicing, due to the edge-to-edge characteristic of the STL file format shown in figure 2.32. The repeated points are filtered by the Filter sub-code.

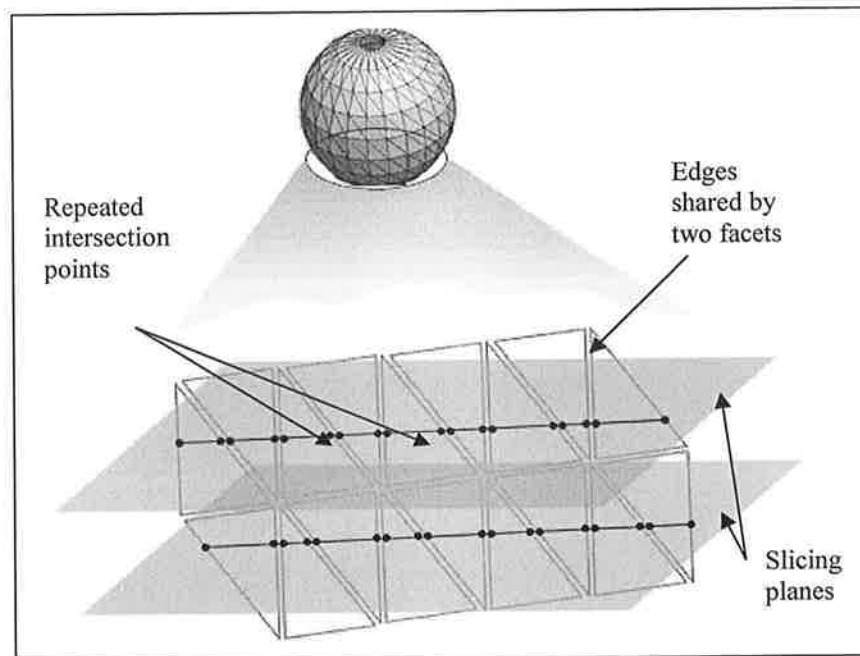


Figure 2.32: Filtering the repeated intersection points is necessary.

After the segmentation and the filtering of the points is done, the resulting set of points belonging to the slicing plane form a planar contour as shown in figure 2.33.

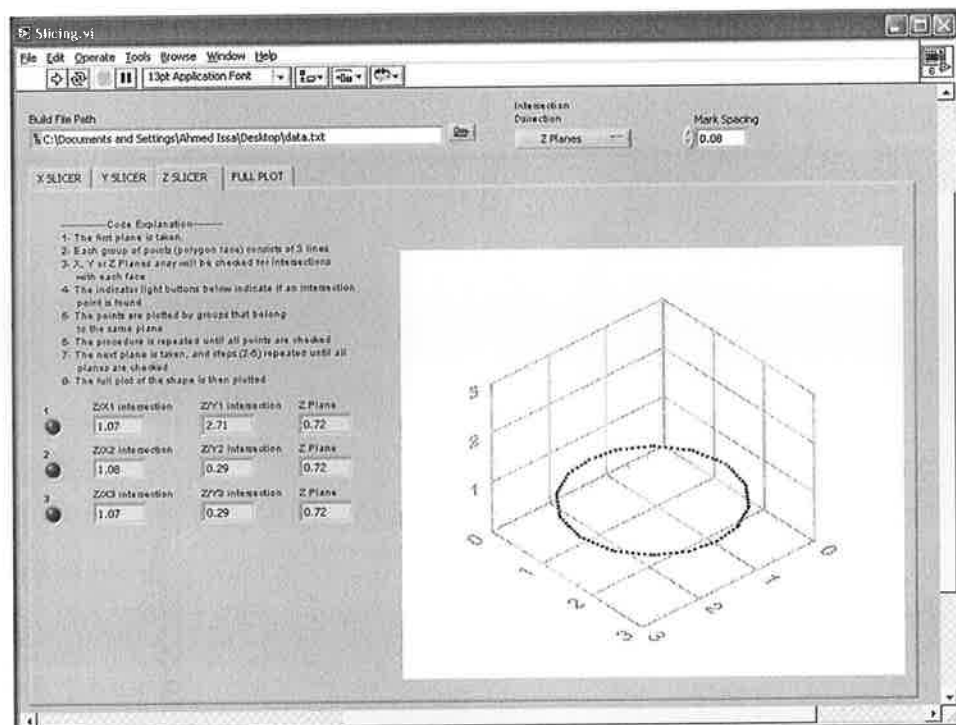


Figure 2.33: Sample planar contour of a sphere.

The combination of the generated planar contours gives the fully sliced 3D CAD design, which can be written to a build text file. As shown in figure 2.34, each planar contour data points are grouped together and a line reading “PLANE” designates the end of the planar contour data points. The complete sliced sphere geometry treated in this illustration is shown in figure 2.35. The flow chart of the slicing code is shown in figure 2.36.

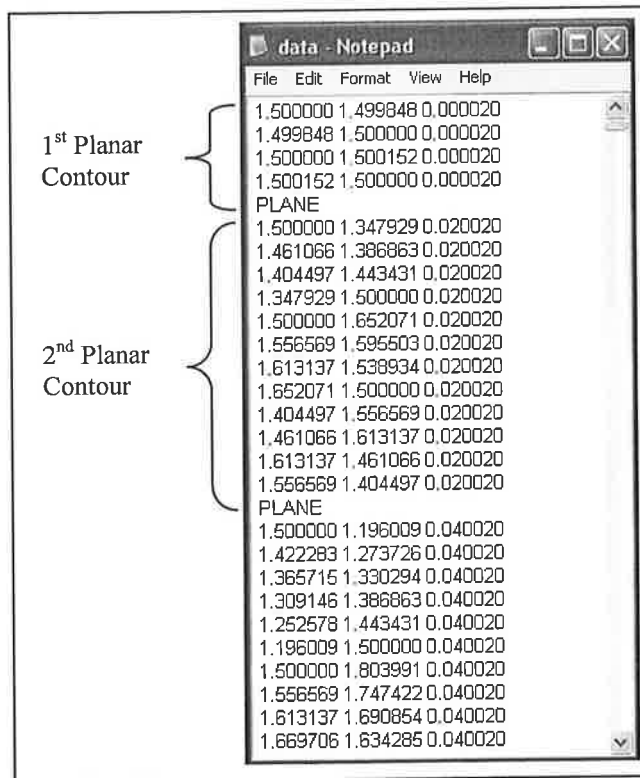


Figure 5.34: Part of the sphere build file.

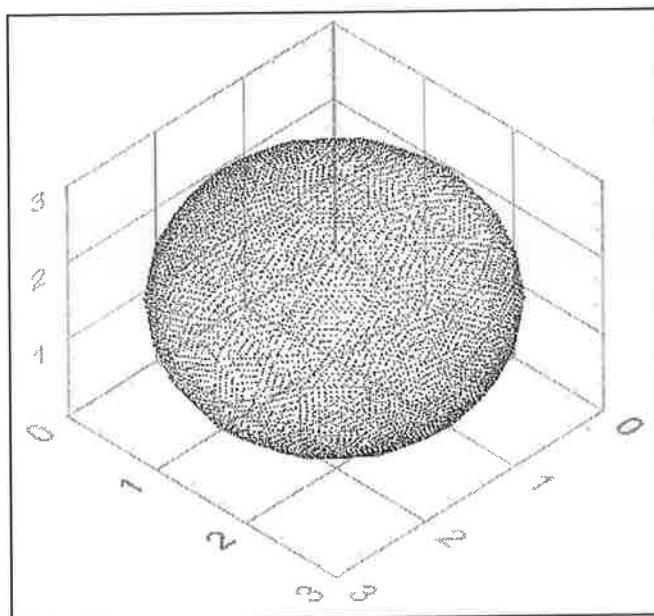


Figure 2.35: Full plot of the sphere.

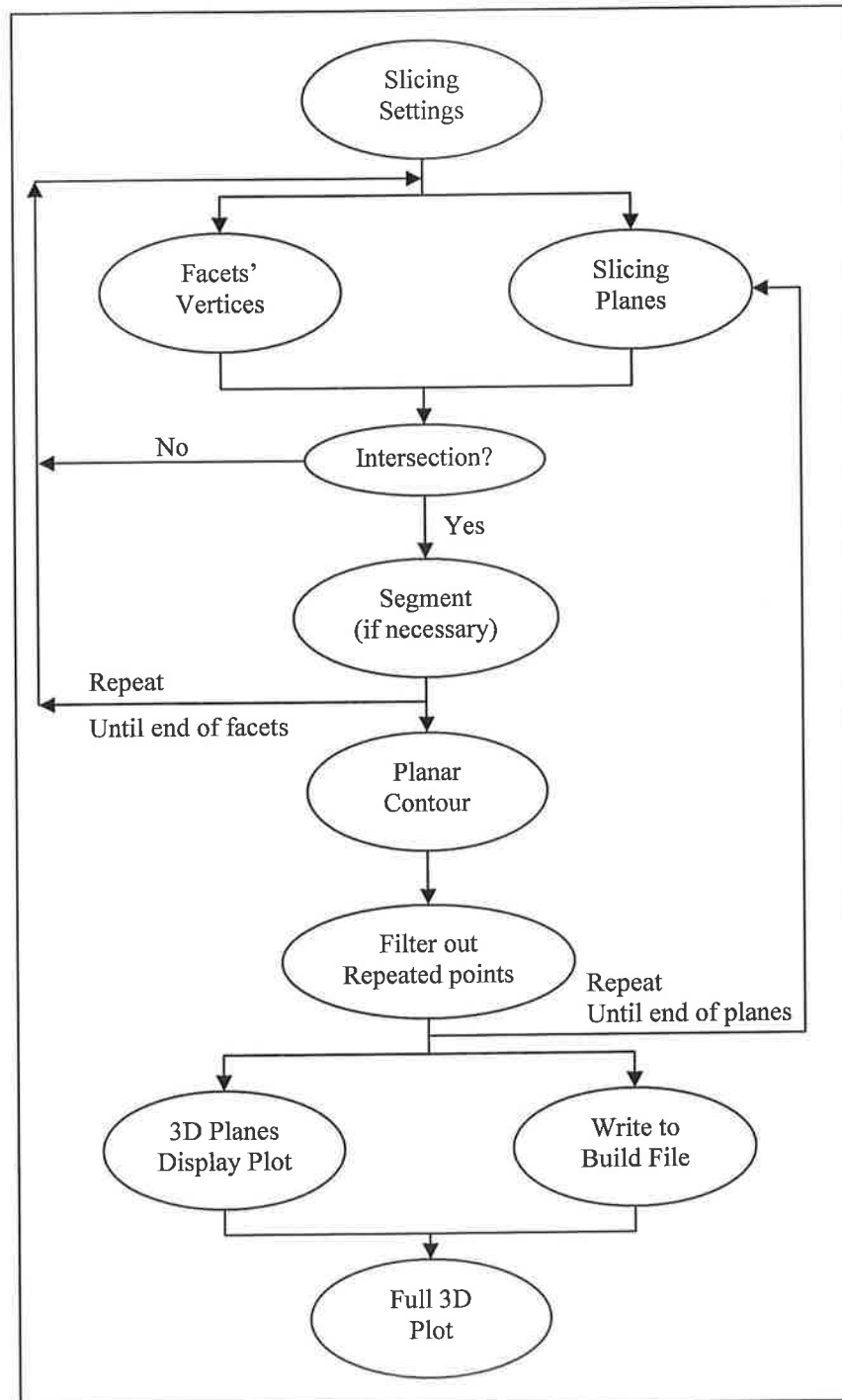


Figure 2.36: Flow chart of the Slicing Code.

2.6 Position control code

After the CAD design has been manipulated and converted from STL format into a build file, the next step is to build the part. This requires the control of the laser emission and the 3D position of the work piece, as shown in figure 2.20. In this section the position control code is discussed. Stepper motors were utilised for moving the sample on the 3D positioning stage. The code that controls the positioning stage was developed in this work using LabVIEW. The mathematical relations discussed in

section 2.2.10 were used in the control code of the 3D positioning stage. The position can be controlled using equation 2.8. Equation 2.9 was used to calculate the suitable frequency for driving the stepper motor which corresponded to a suitable linear speed. Figure 2.37 shows the front panel and diagram of the position control code. Illustrations of how to use this code and how it works are found in appendix B.2.6.

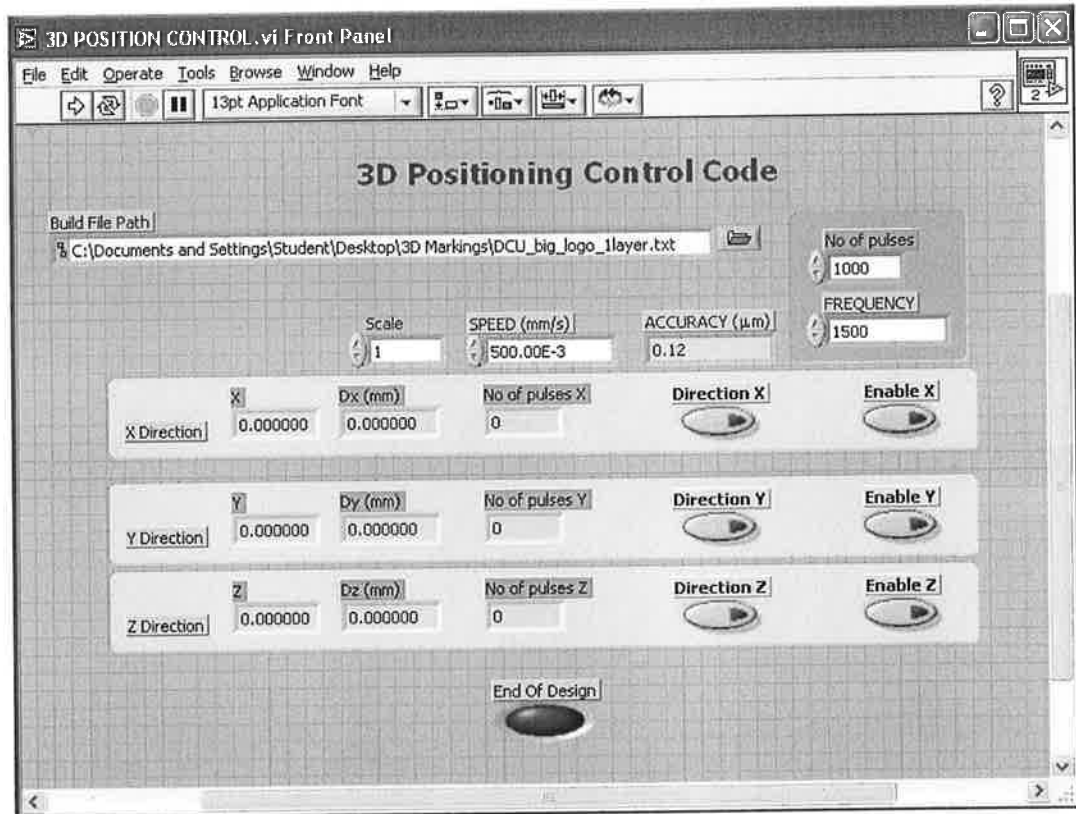


Figure 2.37: Position control code front panel.

Upon running the code, it will start the positioning process immediately reading the x, y and z coordinates from the build file. Figure 2.38 shows the flow chart of the positioning code. More details on the outputs of the codes and the pin connections from the PCI 6036E board to the stepper motor drivers can be found in appendix B.2.6.

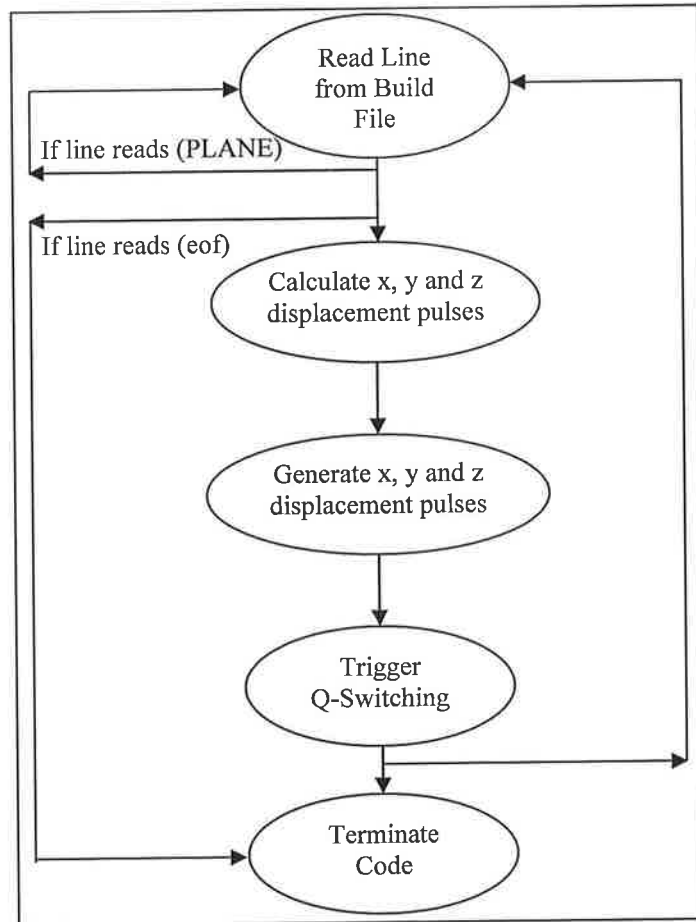


Figure 2.38: Flow chart of the positioning code.

2.7 Laser control codes

The operation of the Nd:YVO₄ laser was originally done using the T-Remote control or the T-Soft control program supplied by the OEM. Both methods did not provide a proper comprehensive control of the laser. For example, Q-switching was not possible using these methods. The development of a new code for controlling the laser operation was necessary. Serial communication with the T-Series laser power supply unit was possible and as explained in section 2.2.3, all the operation parameters can be controlled via RS232. This was the basis of the control method used with the system. This section presents the serial communication syntax set by the OEM, and based on this syntax the control code developed in LabVIEW.

2.7.1 RS232 communication codes

Commands to the T-Series power supply consist of strings of ASCII characters. Each command is terminated by a semicolon. Multiple commands can be issued in a single string. Full discussion of the communication syntax can be found in appendix B.1.2. The first step in developing the control code was to test all the read and write

commands. For that purpose, a simple serial port read-write LabVIEW code was developed. Important characteristics of the serial data communication were discovered in this stage:

Serial Port Configuration: this is necessary for the communication to properly take place. As specified in the laser catalogue, the default settings are:

9600 Baud.

No Parity Bits.

8 Data Bits.

1 Stop Bit.

Data Flow Control is request to send and clear to send (RTS/CTS). This is further explained in appendix B.1.1.

Figure 2.39 shows the serial port configuration VI (Virtual Instrument). Note: "ASRL1::INSTR" designated the configurations to COM1 port on the PC. The same configurations are used throughout the control code.

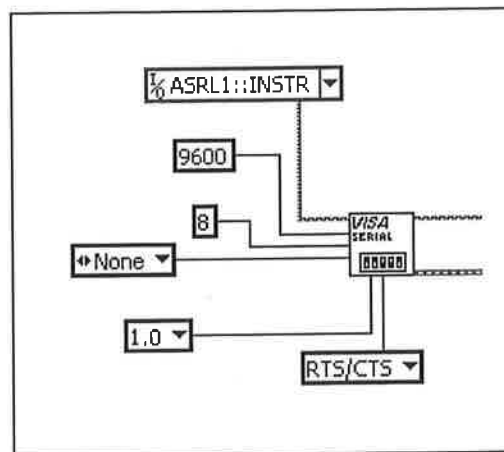


Figure 2.39: Serial port configuration in LabVIEW.

Data Overflow: one major problem in serial communication. Data is transmitted from the laser power supply to the PC in series (i.e. rows of bytes). Due to delays in the RS232 communication buffers, the beginning and end of the received string is shifted as shown in figure 2.40. This problem is most evident in a read string and was solved in the following ways:

- 1- Clearing/resetting the communication buffer when communication is no longer needed (i.e. the termination of the sub-codes and/or the main code).
- 2- Adding software controlled time delays to counter-balance this buffer delay. Various experiments revealed the value of this delay ($T_d = 100$ ms in each loop).

- 3- Searching the received string for specific characters that mark the data received, for example as character (A) marks the current reading, whereas character (P) marks the power reading. This solution can be used when the contents of the received string are previously known. This solution was used in the main code that monitors the operation parameters such as the Diode Current (C1), Power (P), Temperature (T1) and PRF (Q).

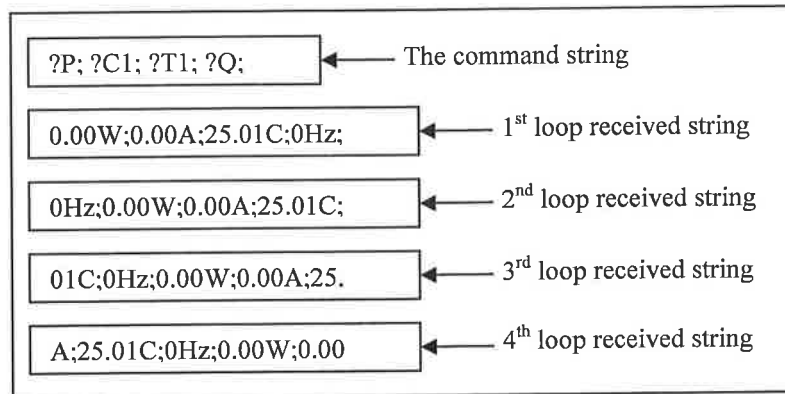


Figure 2.40: Received data overflow in the serial port buffer.

Write Commands: the commands that set the operating parameters such as (diode temperature, diode current and diode ON/OFF) have to be sent once, instead of continuously sending them. The memory in the laser power supply unit will save these settings. This will also help to reduce the possibility of overflow to occur.

NOTE: the read and write strings contain the data in a specific format set by the manufacturer. The strings data is converted in the code so as to make it look familiar to the user. For example:

C1:1154; will set the diode current to (11.54 A).

M0; will set the diode pump regulation mode to (Current Mode).

G1; will gate the Q-switch to (ON)

The user deals with the syntax in brackets, while the string conversion is performed behind the scene. The command syntax was tested thoroughly and the desired commands for control were selected. These commands will be listed in the respective locations they were used in the code. The control code consists of 3 main sub-codes (Laser calibration, Settings before operation and Laser control). The following discussion explains the use and the working principle of each part. In order to operate the laser, the control code is first run.

2.7.2 Initial settings code

This code runs automatically when the Laser Control.vi code is run. The front panel of this code appears in the middle of the screen, as shown in figure 2.41. This code reads the initial values of the operation parameters from the laser power supply unit. Table 2.9 contains a list of the parameters and the corresponding string commands sent to the serial port.

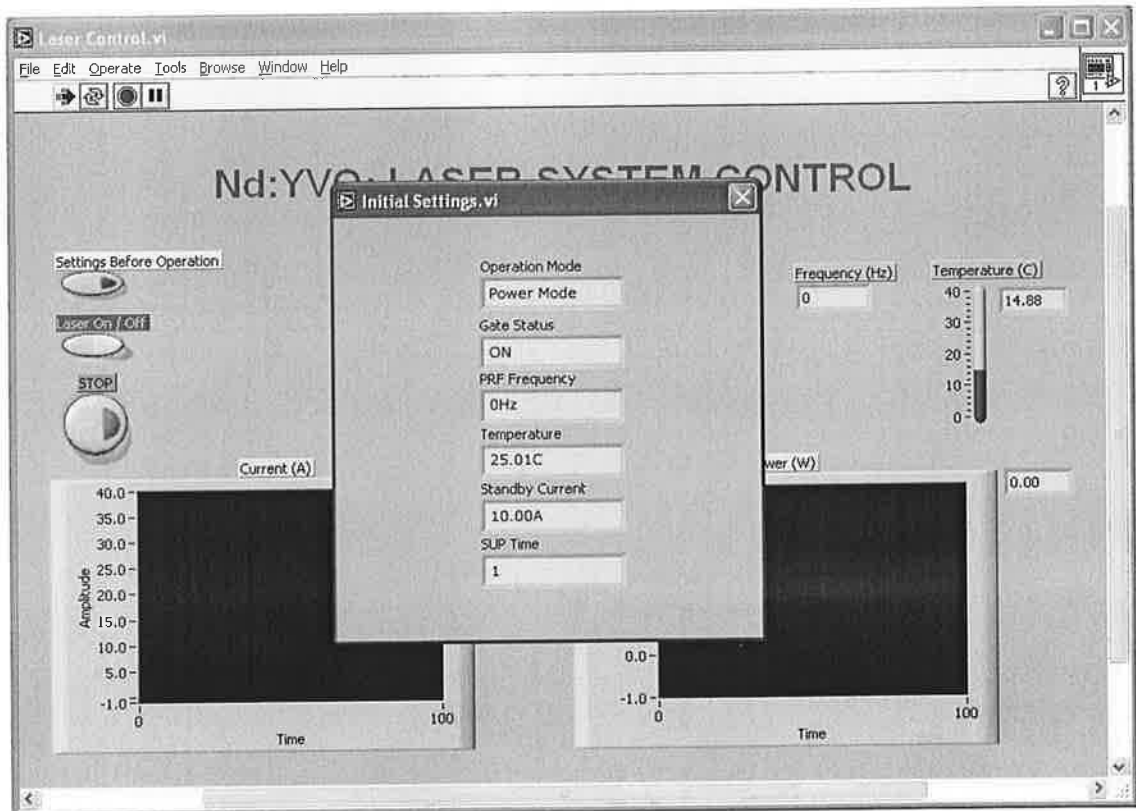


Figure 2.41: Initial settings code front panel displayed on stand up.

Table 2.9: Initial settings parameters and string commands.

Parameter	Sent command	Received string	Displayed value
Operation Mode	?M;	0 or 1	Current Mode or Power Mode
Gate Status	?G;	0 or 1	OFF or ON
PRF Frequency	?Q;	0-1000000Hz	0-1000000Hz
Temperature	?T1;	14.90-40.00C	14.90-40.00C
Standby Current	?STB;	0.00-37.80A	0.00-37.80A
Sup Time	?SUP;	0-8000	0-8000

All the readings are concatenated into a string that is written to a text file. This file is used later in the “Setting before operation” code, and it can be a useful parameter reference after the use of the laser. The naming of the initial settings files follows a certain format (CLB Hour-Minute Day-Month-Year.txt), for example the file (CLB 19-

15 20-07-04.txt) was created at 7:15pm on 20-July-2004. A sample initial settings file is shown in figure 2.42. The code terminates and the front panel closes automatically.

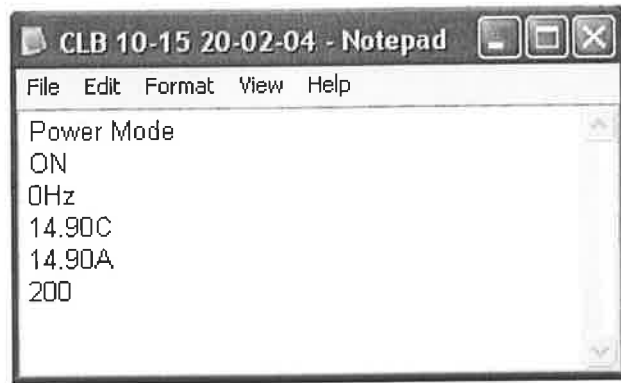


Figure 2.42: Sample initial settings file.

2.7.3 Settings before operation code

After the calibration code panel closes, the operator is back at the front panel of the Laser Control.vi code. The code now is running and displaying the current, power and temperature levels of the laser diode as shown in figure 2.43 the laser emission parameters can be changed by clicking on the Settings before operation button.

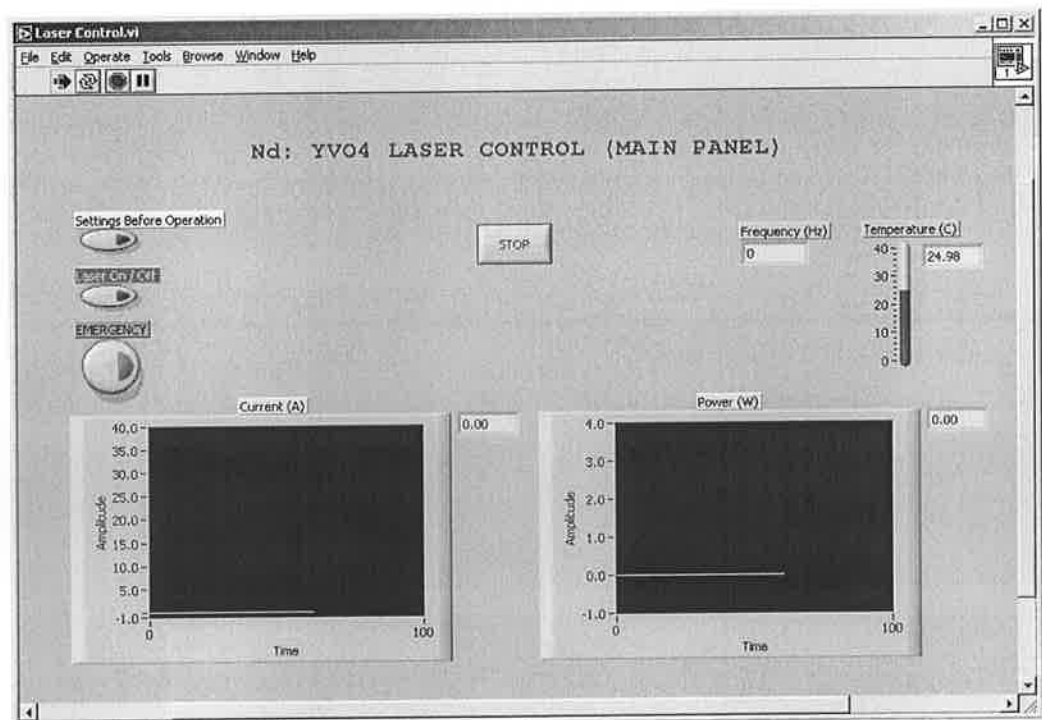


Figure 2.43: Laser Control code front panel.

When this button is clicked the front panel of the Settings code will appear in the middle of the screen as shown in figure 2.44. Listed on the left are the initial parameters'

readings taken by the initial settings code. The initial values are read from the initial settings text file created previously. On the right are the same parameters if the operator wishes to make any changes in their values. Note that there are no initial values for the diode current and power, because the diode is usually off when the program is first run. The EXIT button must be clicked after the operator is done with setting the parameters' values. The new settings are sent in a single string to the laser power supply unit via the serial port and the front panel closes. The calibration code procedure in serial port communication and parameter conversion is followed in this code.

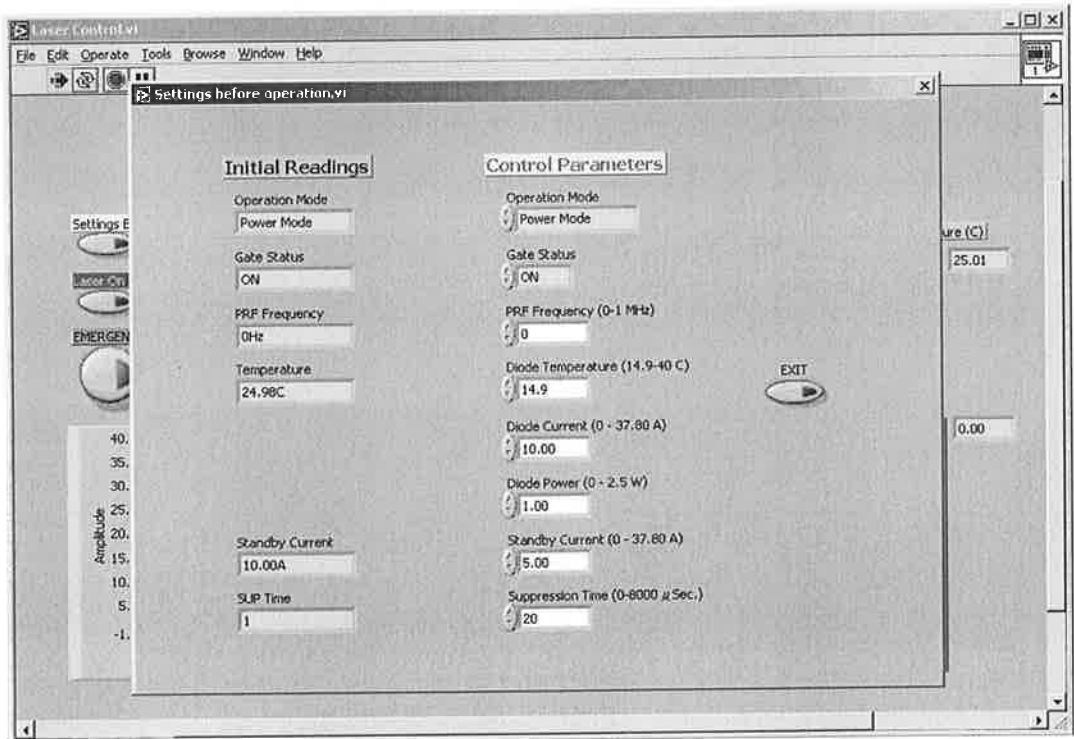


Figure 2.44: Front panel of the Settings Before Operation code.

Table 2.10 contains a list of the control parameters and the string commands sent to the serial port.

Table 2.10: Settings parameters and string commands.

Parameter	Sent command	Value Range
Operation Mode	M0; M1;	Current Mode Power Mode
Gate Status	G0; G1;	OFF ON
PRF Frequency	Qnnnnnnn;	0-1000000 Hz
Temperature	T1:nnn;	14.90-40.00 C
Diode Current	C1:nnnn;	0.00-37.80 A
Diode Power	Pnnnn;	0.00-2.50 A
Standby Current	STB:nnnn;	0.00-37.80 A
Sup Time	SUP:nnnn;	0-8000 μs

2.7.4 Laser control code

The laser control code is the main code that contains the Initial Settings and Settings codes. However, these codes should be executed before the laser emission takes place. The front panel of the Laser Control.vi code shown in figure 2.43 contains monitoring displays and control button, which indicate the following:

Monitoring Displays:

- 1- Laser diode current graph and digital display.
- 2- Laser diode power graph and digital display.
- 3- Laser diode temperature scale and digital display.
- 4- Laser emission Pulse Rate Frequency *PRF* digital display.

Control Buttons:

- 1- Settings Before Operation. This opens the setting code front panel as explained previously.
- 2- Laser ON/OFF. This switches the laser emission ON or OFF.
- 3- EMERGENCY. For emergency stop, it stops the emission and terminates the program all at once.
- 4- STOP. For normal stop of the program after the operator switches the laser diode off.

Table 2.11 contains the list of the displayed parameters in the Laser Control code and the corresponding string commands sent to the serial port.

Table 2.11: Laser Control parameters and string commands.

Parameter	Sent command	Value Range
Diode Current	?C1;	0.00-37.80 A
Diode Power	?P;	0.00-2.50 A
PRF Frequency	?Q;	0-1000000 Hz
Temperature	?T1;	14.90-40.00 C
Diode ON/OFF	D0; D1;	OFF ON

2.7.5 Laser switch code

The Laser ON/OFF button when clicked will open the front panel of Diode Switch code shown in figure 2.45. This is a small code that asks the operator to confirm the action of switching ON or OFF the laser diode. It also sends the command to the serial port only once, this reduced the command load on the serial port buffer. Once the operator clicked the confirm button, the command was sent and the front panel closed. The laser

emission then started at the pre-specified settings. Figure 2.46 shows the front panel of the laser control code after the laser emission was turned on.

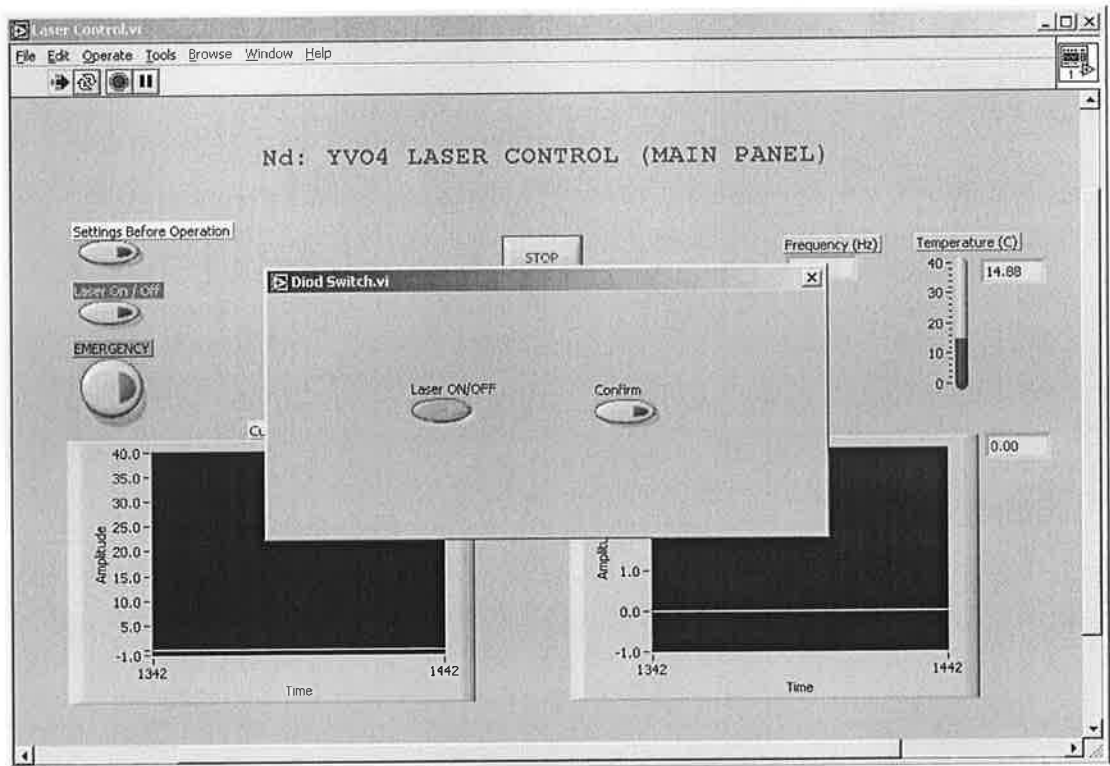


Figure 2.45: The front panel of the Diode Switch code displayed on stand up.

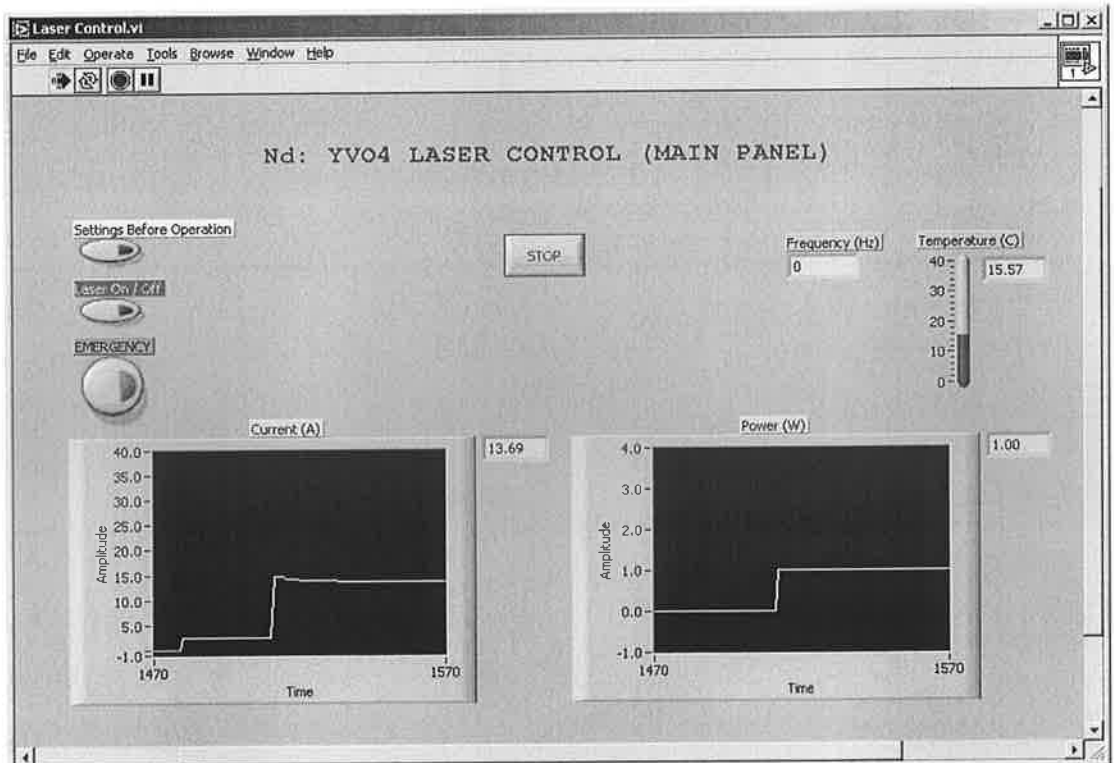


Figure 2.46: The front panel of the Laser Control code while laser diode is ON.

Summary

The development of the hardware and software of the Nd:YVO₄ laser system were demonstrated. The two different focusing techniques and related calculation were also presented in this chapter. This system was used for internal microfabrication and 3D CAD fabrication in transparent materials as will be presented in chapter 3. Moreover, the CO₂ laser system specification and hardware were illustrated. This system will be used for fabricating microchannel on the surface of soda-lime glass samples as will be demonstrated in chapter 4.

Chapter 3

Nd:YVO₄ Laser Experiments

3.1 Introduction

Three different experiments were carried out on the Nd:YVO₄ laser system. The objective of the first experiment was to understand and analyse the microfabrication process and its control parameters. The second and third experiments verified the three dimensional positioning and the laser control from the software and the hardware perspectives. The main objective of the second and third experiments was the dimensional analysis of the three dimensional CAD microfabrication process.

3.2 Microfabrication experiments

These experiments were carried out to draw a relation between the laser beam parameters and the morphology of the microfabricated voxels inside polycarbonate samples.

3.2.1 The equipment used

- 1- The laser system developed and explained in section 2.2.
- 2- Polycarbonate samples of 5mm thickness.
- 3- Optical microscope for inspection (Me F2 universal camera microscope made by Beuhler Omnimet Enterprise [161] with a quantitative image analyser [162]).
- 4- Polishing apparatus to facilitate side inspection.
- 5- Control PC and LabVIEW control codes explained in sections 2.5 to 2.7.

3.2.2 Pulse energy and fluence calculations

The Nd:YVO₄ laser had a characteristic pulse width of 80 ns [141]. The following equations were used to calculate the pulse energy at different average laser powers and pulse repetition frequencies PRF [22].

$$\text{Duty cycle} = \text{Pulse width} \times PRF \quad (3.1)$$

$$\text{Peak power} = \text{Average power} / \text{Duty cycle} \quad (3.2)$$

$$\text{Pulse energy} = \text{Peak power} \times \text{Pulse width} \quad (3.3)$$

To calculate the pulse energy using these equations the values of PRF and average power were needed. In fact, these two parameters were used as process control parameters in the design of experiments. Laser fluence can be defined as the laser pulse energy deposited per unit area, and it is measured in (J/cm^2) [83]. The accumulated fluence due to a number of laser pulses, N , is therefore given by:

$$F = N \frac{E_p}{A} \quad (3.4)$$

where, E_p is the pulse energy and A is the focal spot area. The evaluation of the above equations can be tedious if one has to perform them for each sample produced. So, a LabVIEW code was developed to evaluate them. The front panel of this code is shown in figure 3.1. The code simply employs the equations used for focal spot area and pulse energy calculations to calculate the accumulated fluence value (J/cm^2).

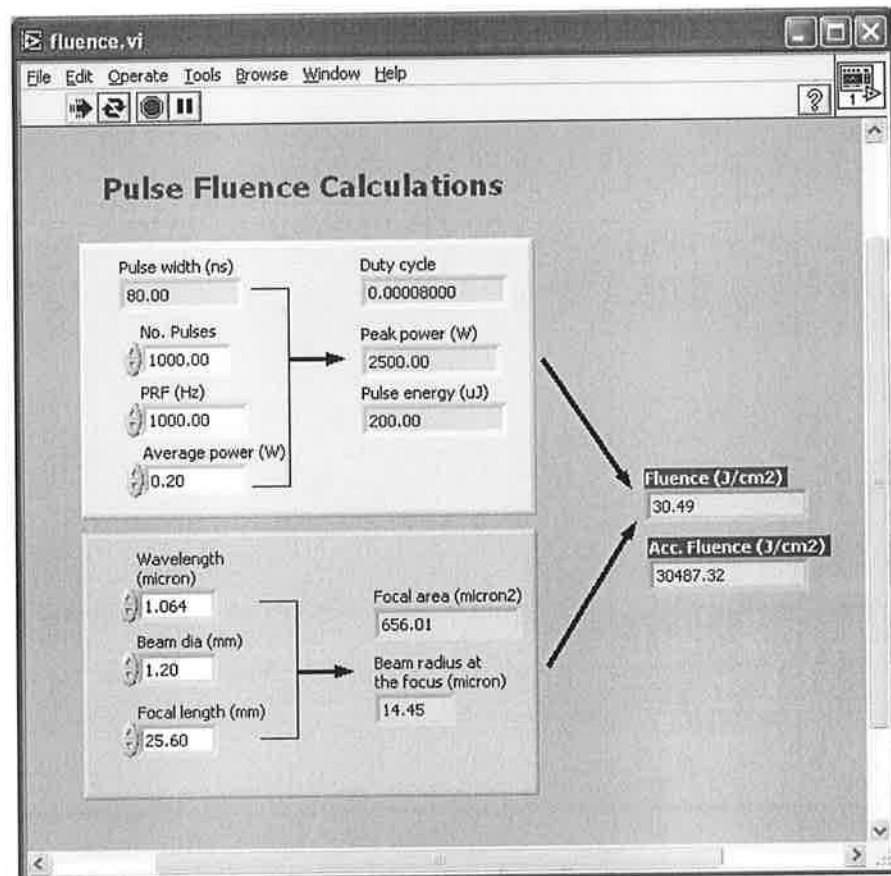


Figure 3.1: Front panel of the fluence calculations code.

3.2.3 Experiment design

At the beginning of this work, screening experiments were conducted based on literature readings and trial and error. The objective of these experiments was to select the process control parameters. The minimum laser power that could be generated was 0.1 W. The breakdown threshold in polycarbonate was observed using a minimum $P = 0.15$ W and maximum $PRF = 5000$ Hz. Increasing the PRF value reduced the pulse energy and no breakdown was observed after 5000 Hz. Laser power values higher than 0.5 W were noticed to cause burning of the samples.

The laser control variables of this experiment were then chosen to be *PRF*, the average laser power *P* since they set the pulse energy value. The number of pulses, *N*, triggered on each voxel location was selected as a control parameter based on its expected effect from the accumulated fluence expression in equation 3.4. The aim of the design of experiment was to examine changes in the average voxel size as these three parameters changed. Moreover, to draw a relation between these control parameters and the morphology of the microfabricated voxels. In order to achieve this, rows of voxels were fabricated inside polycarbonate sheets of 5 mm thickness. Each row consisted of 40 voxels separated by 200 μm and fabricated with the same parameter settings. Table 3.1 lists the parameter combinations that were examined. Each cell in the table refers to the parameters at which each row of voxels was fabricated, indicating the number of pulses triggered at each frequency and power setting.

Table 3.1: Microfabrication experiment parameters.

<i>P</i> (W)	<i>PRF</i> (Hz)														
	1000			2000			3000			4000			5000		
0.2	1k	2k	3k	2k	4k	6k	3k	6k	9k	4k	8k	12k	5k	10k	15k
0.3	1k	2k	3k	2k	4k	6k	3k	6k	9k	4k	8k	12k	5k	10k	15k
0.4	1k	2k	3k	2k	4k	6k	3k	6k	9k	4k	8k	12k	5k	10k	15k
0.5	1k	2k	3k	2k	4k	6k	3k	6k	9k	4k	8k	12k	5k	10k	15k

3.2.4 Fabrication of samples

One polycarbonate sheet was used for each power rating. This meant that each sample contained 15 rows. However, three rows were used for each group. Each group shared the same *PRF* value. Figure 3.2 shows the contents of the samples. Each row within a group separated from the others by 500 μm . Each group was separated from the others by 2 mm. This range of separation made the microscopic inspection task easier, because three rows could be captured in one image.

3.2.5 Experimental procedure

- 1- The laser system was switched ON and it was checked that the laser diode was OFF.
- 2- The polycarbonate sheet workpiece was mounted in the workpiece clamp.
- 3- The laser control code was run and the laser parameters were set to produce the desired average power. The laser diode was then turned ON.
- 4- The positioning code was run with the build file to fabricate a row of voxels.
- 5- After the completion of the building process, the laser diode was switched OFF.

6- The positioning code was then run to produce the separation between the rows.

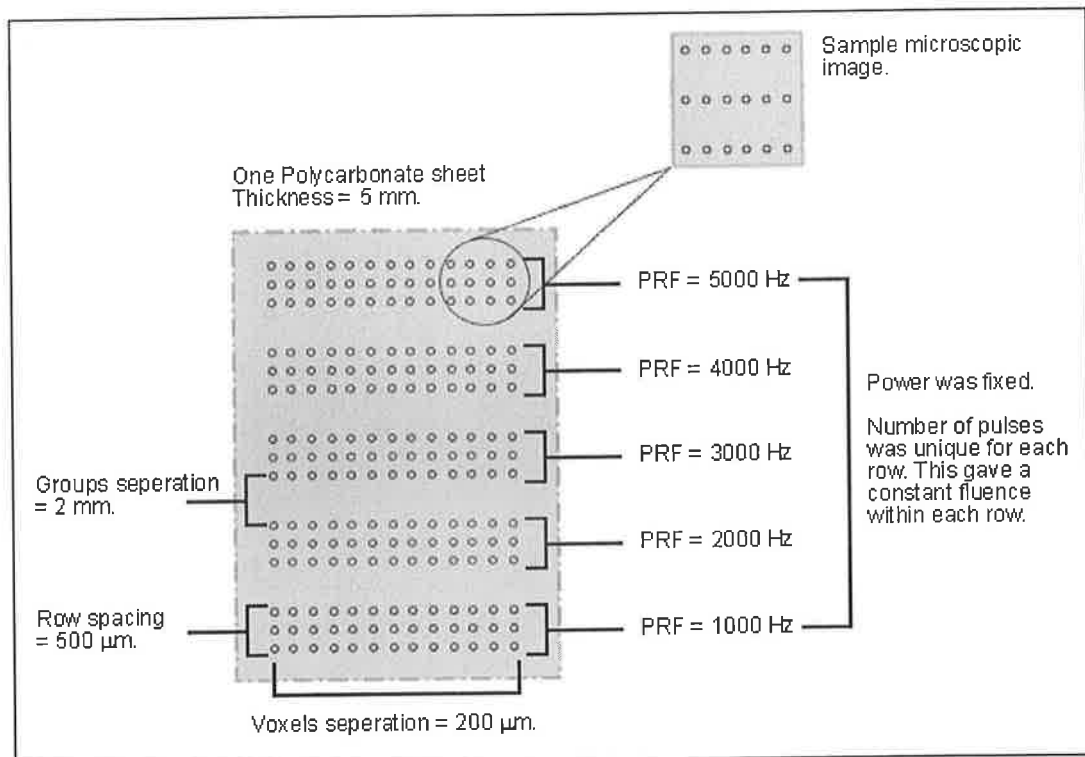


Figure 3.2: Illustration of a sample's subsets and microfabricated voxels' settings.

- 7- Steps 3 to 6 were repeated until a group of 3 rows was fabricated. The number of laser pulses was set for each row separately.
- 8- The laser diode was turned OFF. The positioning code was run again to make the separation between groups.
- 9- Steps 3 to 8 were repeated with a new *PRF* value for each group until all the rows on the workpiece were fabricated.
- 10- The laser diode was switched OFF. A new polycarbonate sheet was mounted and the same procedure was followed. Four separate workpieces were required to produce voxels with the four chosen *P* settings, 0.2, 0.3, 0.4 and 0.5 W, see table 3.1.

3.2.6 Inspection of the samples

The inspection was performed under an optical microscope using a 5X objective lens. The voxel diameters, as viewed from the top / laser firing direction, were measured under the microscope taking the most clearly edge defined voxels fabricated in each row. In the case of voxels having star-like shapes, the diameter was defined in a subjective manner, as the flakes were a result of propagating thermal stresses/cracks. Hence, they could not be considered in the voxel size measurement. As shown in figure

3.3(a), a circle was located at the centre the star. The diameter of the circle was defined by the closest non-affected material matrix based on the refractive index/colour difference. In the case of the circular or confined shaped voxels, the diameter was defined by a circle that covers the heat affected zone as the one shown in figure 3.3(b). Both voxels in figure 3.3 were cloned on the bottom of the figure for clear visualisation. At least the average of 5 voxels was calculated, and the average of a maximum 8 voxels was calculated in some cases. Some of the voxels in the sample images had a fuzzy shape; this is due to the focusing limitations of the microscope objective lens, keeping in mind that the voxels have a 3D shape. The star-like shaped voxels produced in this study provided better visualisation with the naked eye under the room light.

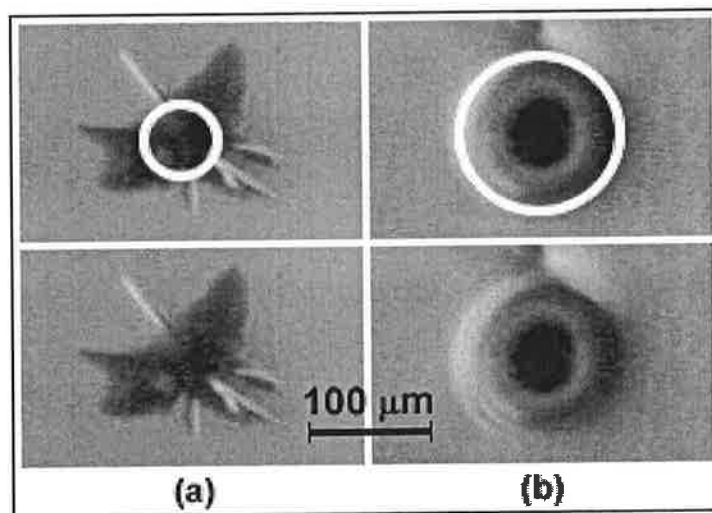


Figure 3.3: Voxel diameter definition, (a) star-shaped voxel, and (b) circular voxel.

Tables 3.2 – 3.6 include the images of the voxels microfabricated using $P = 0.2$ W, with the corresponding operation parameters. The rest of the results and images are included in appendix C.1. The fluence and the accumulated fluence were also calculated and listed. In table 3.2, taking the sample image as the starting point from the left, the next column shows the number of pulses for the row of voxels in the sample image. The calculated fluence per pulse is the third column, the accumulated fluence in the fourth and the average voxel diameter is listed in the last column to the right, all corresponding to the row of voxels in the image.

Table 3.2: Microfabrication results at $P = 0.2\text{W}$, $PRF = 1000\text{ Hz}$ and $E_p = 200\mu\text{J}$.

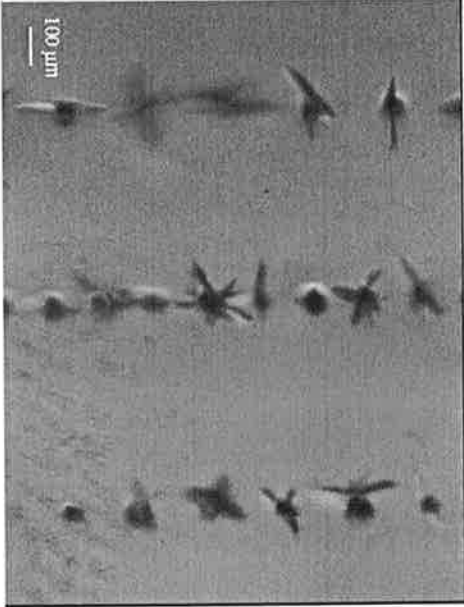
Microscopic image	No. of Pulses	Pulse Fluence (J/cm^2)	Acc. Fluence (J/cm^2)	Av. voxel Dia (μm)
	3,000	30.49	91461.95	78
	2,000		60974.63	63.25
	1,000		30487.32	47.5

Table 3.3: Microfabrication results at $P = 0.2\text{W}$, $PRF = 2000\text{ Hz}$ and $E_p = 100\mu\text{J}$.

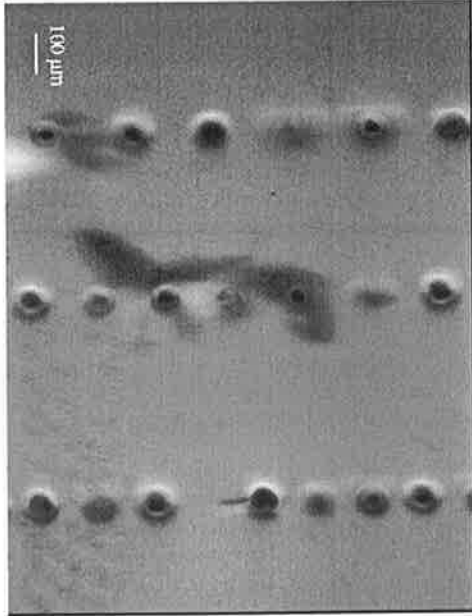
Microscopic image	No. of Pulses	Fluence (J/cm^2)	Acc. Fluence (J/cm^2)	Av. voxel Dia (μm)
	6,000	15.24	91461.95	91.29
	4,000		60974.63	83.29
	2,000		30487.32	81

Table 3.4: Microfabrication results at $P = 0.2W$, $PRF = 3000$ Hz and $E_p = 66.67\mu J$.

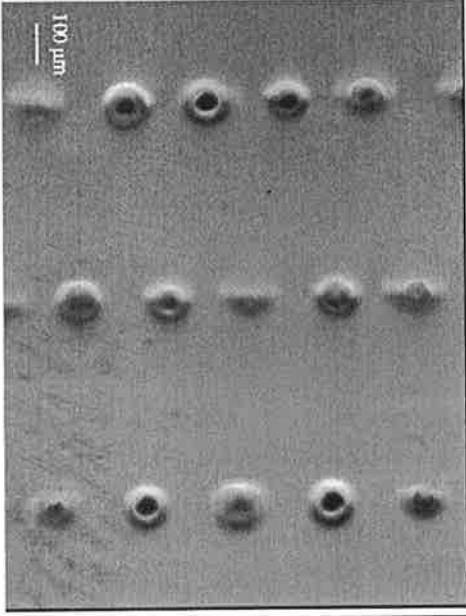
Microscopic image	No. of Pulses	Fluence (J/cm^2)	Acc. Fluence (J/cm^2)	Av. voxel Dia (μm)
	9,000	10.16	91461.95	114.6
	6,000		60974.63	105
	3,000		30487.32	99.6

Table 3.5: Microfabrication results at $P = 0.2W$, $PRF = 4000$ Hz and $E_p = 50 \mu J$.

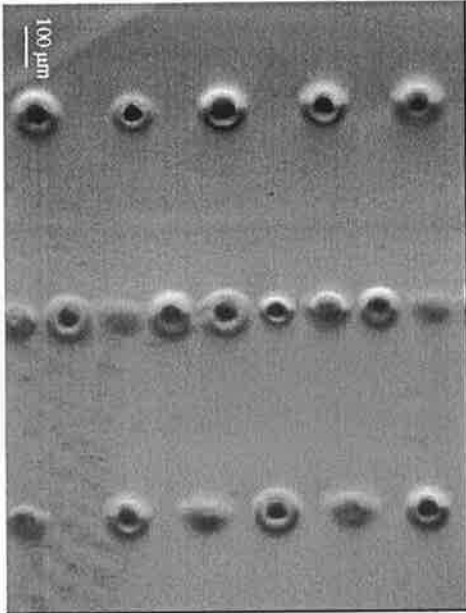
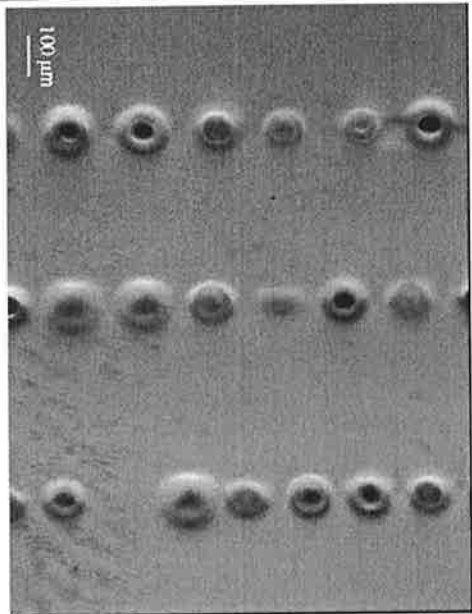
Microscopic image	No. of Pulses	Fluence (J/cm^2)	Acc. Fluence (J/cm^2)	Av. voxel Dia (μm)
	12,000	7.62	91461.95	117.6
	8,000		60974.63	110.4
	4,000		30487.32	98.4

Table 3.6: Microfabrication results at $P = 0.2\text{W}$, $PRF = 5000\text{ Hz}$ and $E_p = 40\mu\text{J}$.

Microscopic image	No. of Pulses	Fluence (J/cm^2)	Acc. Fluence (J/cm^2)	Av. voxel Dia (μm)
	15,000	6.1	91461.95	125.5
	10,000		60974.63	117.67
	5,000		30487.32	103.17

3.2.7 Microfabricated voxel morphology analysis

In terms of the voxel morphology, the laser pulses tended to have an explosive or a hammering effect on the material at low frequencies [68, 163]. This was evident from the star-like shapes of the voxels at low PRF values ranging from 1000 to 2000 Hz. The time separation between successive laser pulses allowed the material around the focus to cool down before the thermal energy can be deposited into the surrounding area. This also caused the loss of the seed electrons necessary for avalanche ionization to take place.

At higher frequencies, the process seemed to result more confined and uniform voxel shapes suggesting faster thermal energy deposition into the material surrounding the focus. If we consider one voxel, as shown in figure 3.4 (a), this voxel was microfabricated using $P = 0.2\text{ W}$, $PRF = 1000\text{ Hz}$, and 1000 pulses. The voxel in figure 3.4 (b) was fabricated using $P = 0.2\text{ W}$, $PRF = 3000\text{ Hz}$ and 3000 pulses (both voxels were cloned on the right in these figures for clear visualisation). The control parameters' settings in both cases, lead to an accumulated fluence of $30487.32\text{ J}/\text{cm}^2$. Despite having the same accumulated fluence, the sizes and morphologies of the two voxels are evidently different. In the first case, where a low PRF was used, a hammering effect of the laser deposition produced the star-like shape of the voxel. Whereas, in the second case the shape was circular and more confined, suggesting a uniform heat deposition

mechanism. From this observation, the accumulated fluence could not have been the only process control parameter affecting the process. Therefore, it is not sufficiently accurate to only quote the accumulated fluence value when carrying out such analysis. It is also necessary to quote the laser processing parameters such as the average laser power, pulse repetition frequency, pulse width and the number of pulses.

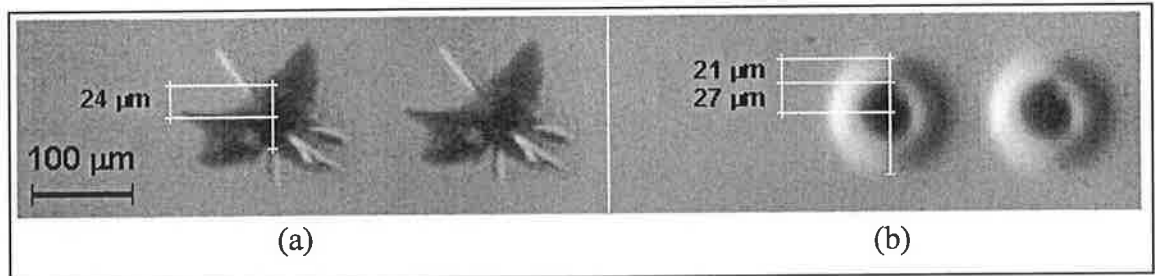


Figure 3.4: Microfabricated voxel morphology, (a) star-like voxel at low *PRF* effect, (b) spherical shape voxel at higher *PRF*.

Heat deposition melts the material at the focal region. After solidification the material around the voxel is denser giving it a higher refractive index. In figure 3.4 (b), the refractive index change was gradual; the black circle (having a radius of $26.8 \mu\text{m}$) represents the maximum refractive index change at the middle of the voxel. The ring (having a thickness of $21 \mu\text{m}$) and surrounding the centre has a lighter colour that gradually fades into the matrix colour representing a gradual refractive index change as we move away from the centre [163, 164].

At the beginning of this chapter, calculations were presented of the beam diameter at the focus. The diameter at the focus was found equal to ($2 \times 14.45 = 28.9 \mu\text{m}$). However, the minimum average voxel diameter obtained in this work was $47.5 \mu\text{m}$. This was expected due to the effect of incubation and the use of many pulses to create each voxel. The amount of accumulated fluence deposited into the material exceeded by the order of thousands the amount expected from a single pulse.

3.2.8 Microfabricated voxel size analysis

Figures 3.5 – 3.8 show the effect of the accumulated fluence on the voxel diameter at the preset *PRF* values using the average laser powers of 0.2, 0.3, 0.4, 0.5 W respectively. As can be observed from the curves, the accumulated fluence has a proportionally increasing effect on the voxel diameter.

Similar accumulated fluence values can be obtained using different combinations of pulse energies and number of pulses, see equation 3.4. For each power value presented

in figures from 3.5 to 3.8, a range of accumulated fluence was obtained. For a specific accumulate fluence in one of these figures, the graphs represent the same amount of thermal energy deposited into the material but at different rates. The *PRF* values of 1000, 2000, 3000, 4000 and 5000 Hz controlled the rate at which the energy was deposited into the focus and transferred to the surrounding regions. Increasing *PRF* resulted in an increase in the average voxel diameter indicating a direct proportionally increasing relationship between the *PRF* and the voxel size. The jumps in average voxel size among the curves in these figures indicate that the pulse energy also has an effect on the voxel diameter. Moreover, the pulse energy is dependent on the average power and *PRF*. This means that the same fluence delivered to the voxel using different pulse energies might induce different voxel diameters. It has also been observed in the previous section that this can affect the shape of the voxel. This observation further supports that the accumulated fluence is not the only parameter affecting the process.

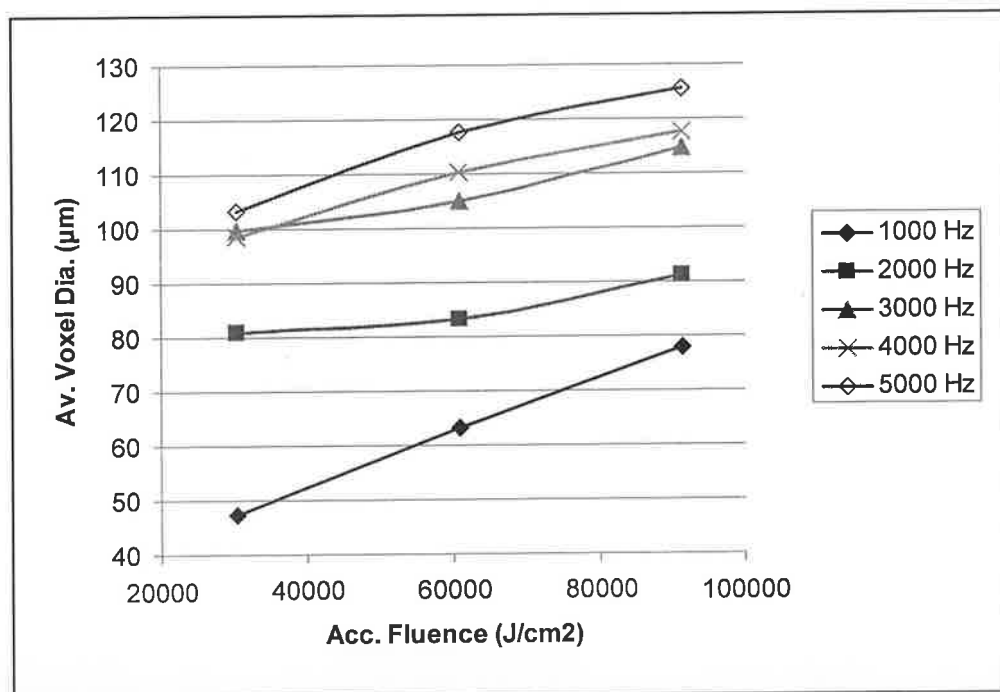


Figure 3.5: *PRF* effect on voxel size at $P = 0.2$ W.

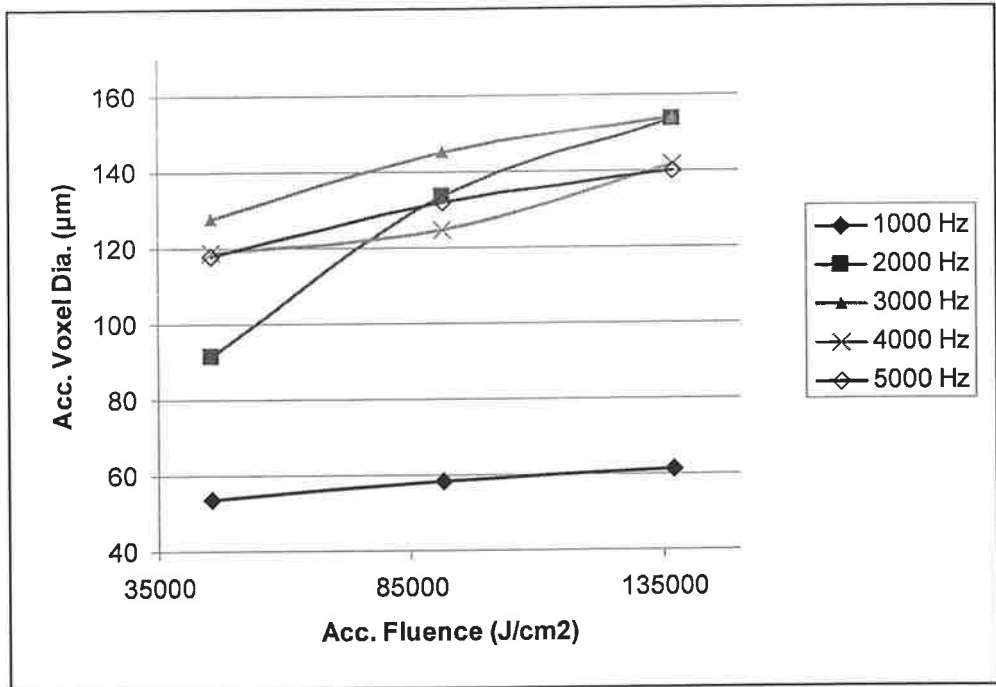


Figure 3.6: *PRF* effect on voxel size at $P = 0.3$ W.

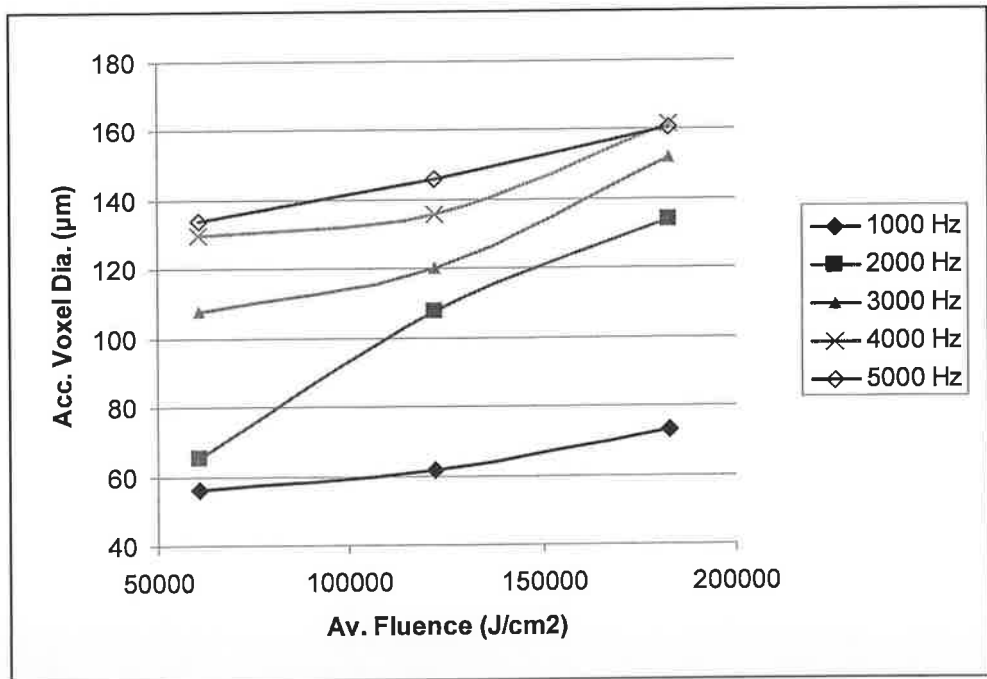


Figure 3.7: *PRF* effect on voxel size at $P = 0.4$ W.

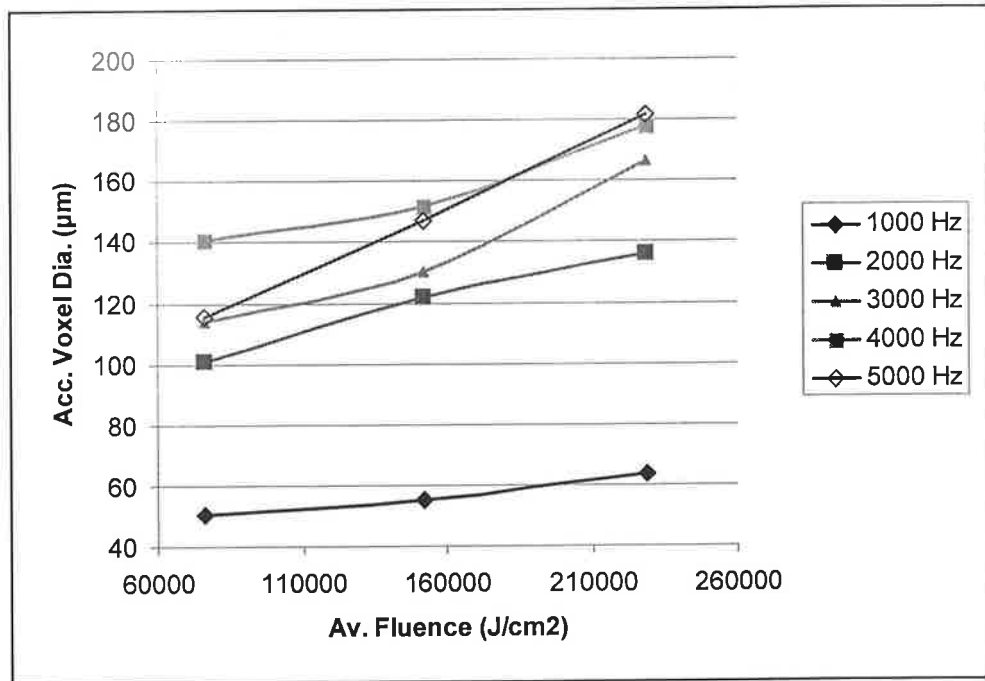


Figure 3.8: *PRF* effect on voxel size at $P = 0.5$ W.

Another result can be drawn from the experimental data, which is the relation between the average voxel diameter and the number of laser pulses. Figure 3.9 displays the effect of increasing the number of pulses on the average voxel diameter fabricated at different power values that were investigated in this work. The voxels seem to have a strong direct relationship with the number pulses. However, the relation seems to saturate or become weaker as the trend lines that best describe the results data were logarithmic. This indicated that the voxels have reached a limit of size growth. This limit depends on the focusing lens, the heat dissipation properties of the material or a non-linearity in the relation between the heat deposition and the voxel growth. It can also be observed from the figure that increasing the average power caused an increase in the average voxel diameter. This can be readily observed from the separation between the curves that describe each power rating results, starting from $P = 0.2$ W at the bottom and ending at $P = 0.5$ at the top of the figure.

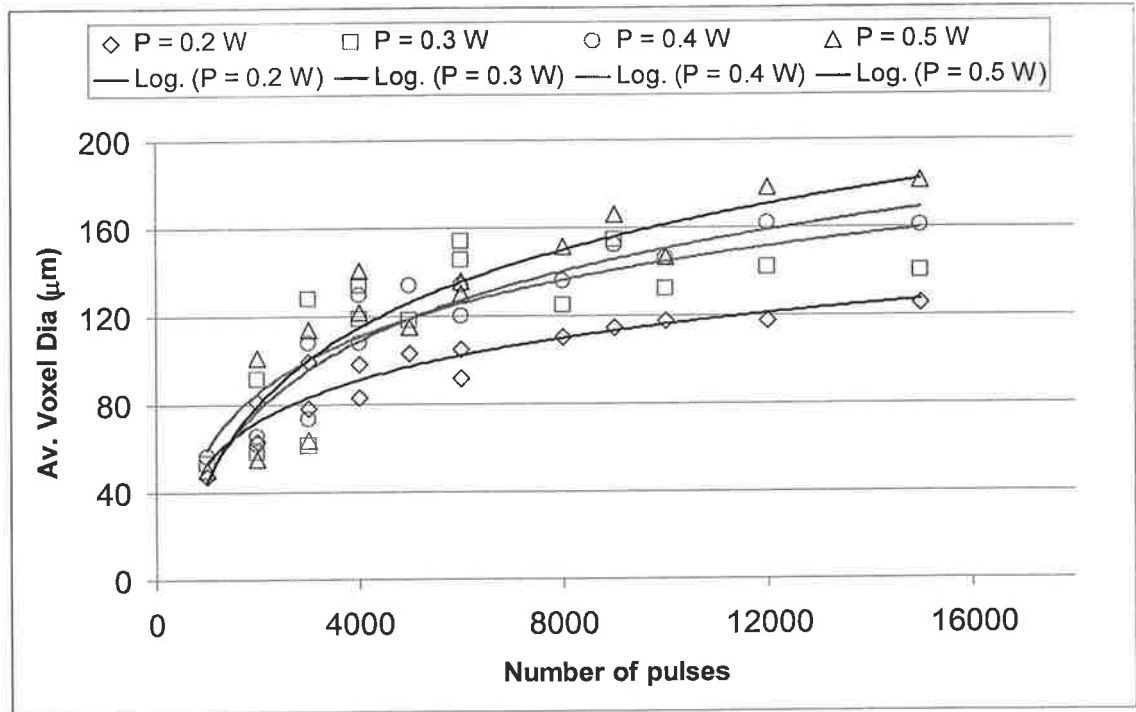


Figure 3.9: Number of pulses effect on voxel diameter at different power values.

3.2.9 Side view microscopic inspection

Figure 3.10 shows the side views of 3 voxels microfabricated inside a polycarbonate sample (thickness = 10 mm). The voxels were produced using:

$P = 0.3$ W,

$PRF = 4000$ Hz, and

No. of pulses, $N = 4000$.

To reveal the voxel images from the side face of the sample; it took approximately 2 hours to hand polish one sample using the following polishing steps:

- 1- P1200 SiC.
- 2- 6 micron diamond.
- 3- 3 micron diamond.
- 4- 1 micron diamond.
- 5- 0.005 micron colidal silicon (Alumina).

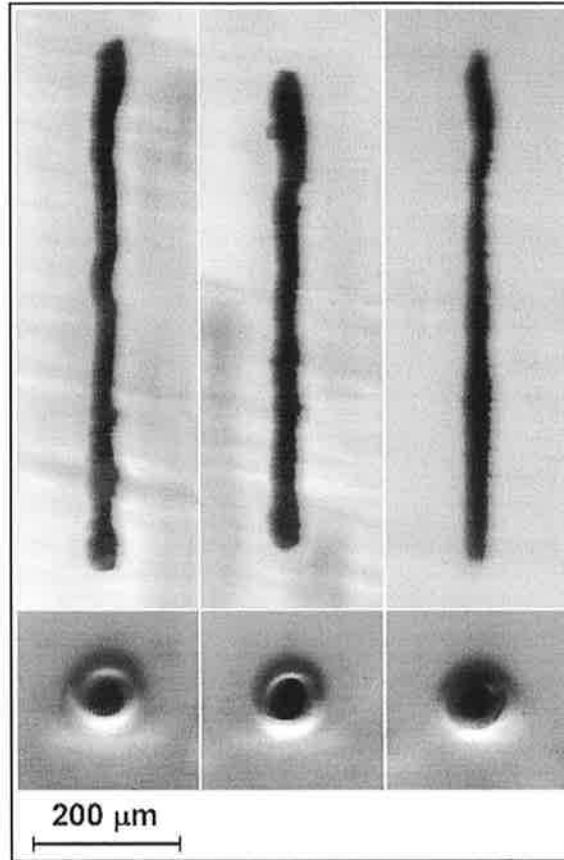


Figure 3.10: Side images of microfabricated voxels, laser beam propagation was from the bottom of the image.

The lengths of the three voxels of image 3.10 from left to right were 735, 665 and 708 μm respectively and the average length was 703 μm . The fact that these voxels were fabricated along a line was not due to spherical aberrations. The expected spherical aberration as calculated in section 2.2.8 was equal to 0.177 μm . The effective focal range of laser intensity above the material breakdown threshold was along this line. Similar to the calculations performed in section 2.2.6, calculations of the effective or the Rayleigh range of the focal depth, showed that the effective depth of focus Z_R is equal to 825 μm . The Z_R can be calculated from the following relation [65],

$$Z_R = \frac{\pi \cdot w_o^2}{\lambda} \quad (3.5)$$

where, w_o is the beam radius at the focus, and λ is the emission wavelength. A LabVIEW code was built to perform these calculations along with side view beam profile and intensity calculations. The front panel of this code is shown in figure 3.11. The Rayleigh range is measured, equally, about the focal spot, so that the total Rayleigh range is approximately equal to $\pm 825 \mu\text{m}$ and is shown for this case in bottom-right plot

of figure 3.11 (red-coloured). This value is about twice the length of the structures in figure 3.10 indicating that self-focusing could have taken place. When focused inside a transparent material and upon the start of breakdown, the beam is further focused to a smaller range due to self-focusing effect [8]. Coarse focusing was noticed to produce longer structures from the side views and tighter beam focusing produced shorter side view lengths. Moreover, the laser power was noticed to enlarge the length of the structures due to high laser intensities achieved in the material depth.

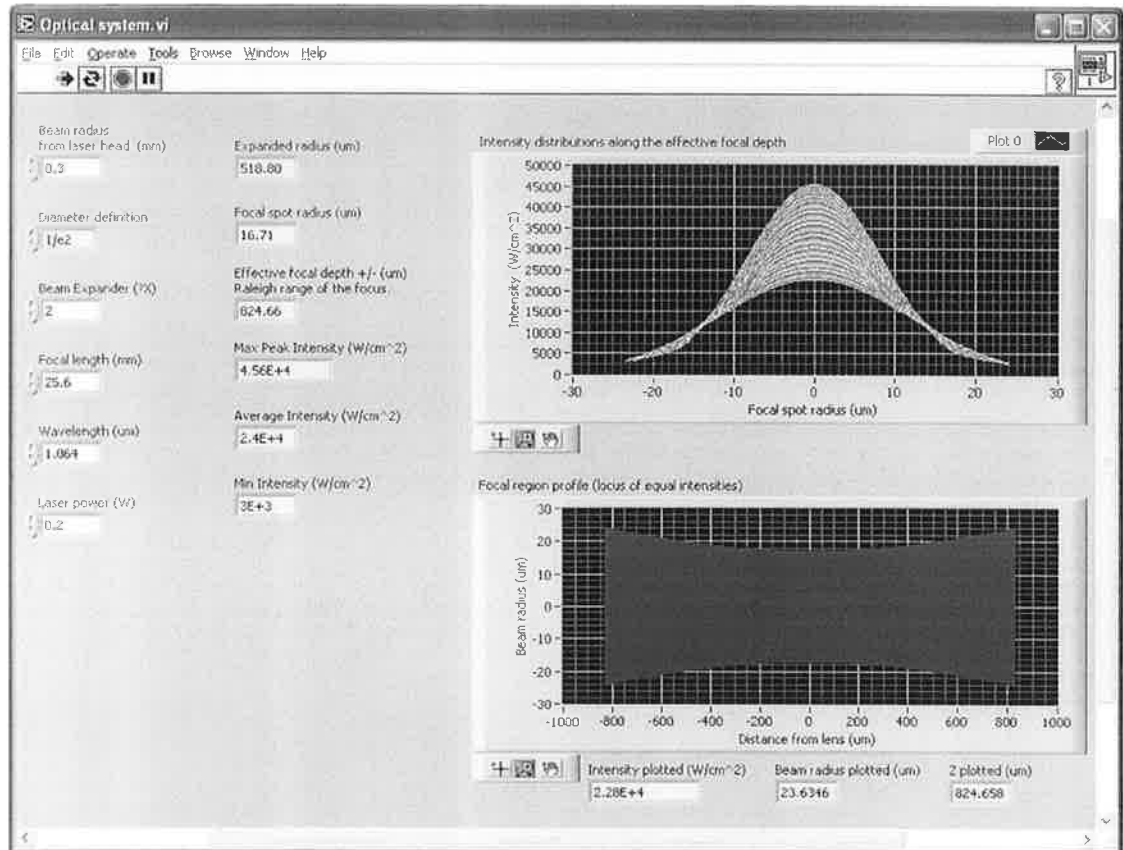


Figure 3.11: Front panel of the intensity profile calculations code.

3.2.10 General discussions on the microfabrication experiment

Accumulated fluence cannot be considered as the control parameter of the process. However, it can be treated as the common control parameter [12, 13] along with the other control parameters that were investigated in this study. The voxels microfabricated at low frequencies take star-like shapes. This shape gives better and appealing visualisation to the naked eye. The voxels will illuminate under the room light due to the light refraction/scattering caused by the large refractive index change, which makes them better for 3D novelty or marking applications.

Cracks around the microfabricated voxels at high powers are due to high thermal stresses or high rates of heating and cooling [68, 35]. The high energy pulse has an effect of thermal shock on the lattice around the focus resulting in random cracking. Although not as good for novelty purposes, it was found that more uniformly spherical voids were achieved at medium powers and *PRF* values. If tight focusing, short pulse width and high frequency laser are used, the effect will be localised and of very short time duration. This could allow a more confined voxel shape and size to be produced [11, 54]. Higher average power ratings were seen to result in sample burning. The process has a nonlinear nature which depends on the initiating of or seed electrons that cause the excitation of other electrons. If the seed electrons do not exist in the focal region then microfabrication will not take place or will give unexpected results. Moreover, the initiation of microfabrication might depend on impurities in the material that will break their bonds faster causing the successive melting of the material. Further research is needed in this field to understand the nature of the process, especially the threshold values for breakdown in different transparent materials subjected to laser pulses. This is necessary in order to model and control the process.

3.3 Dimensional analysis experiments

The aim of this experiment was to verify the function of the 3D positioning system. To investigate the positioning accuracy in 2D, microscopic images were obtained in the microfabrication experiment for set positional displacements. Figure 3.12 shows the image of a row of voxels microfabricated using $P = 0.2 \text{ W}$ at $PRF = 4000 \text{ Hz}$. The voxels were expected to be spaced by $200 \mu\text{m}$. The short vertical lines represent the expected centre location of each voxel. As can be observed from the image, the middle voxel is shifted to the left by approximately $10 \mu\text{m}$. The rest of the voxels were quite accurately spaced by $200 \mu\text{m}$.

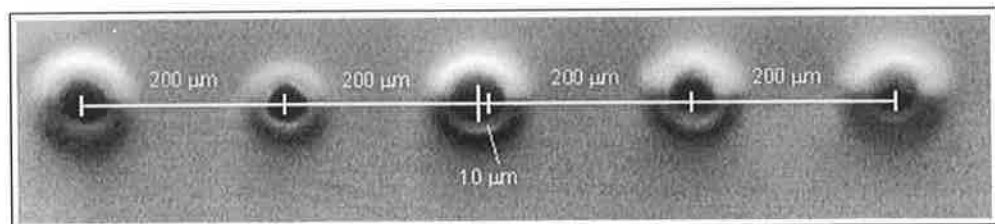


Figure 3.12: Spatial resolution of microfabricated voxels.

The positioning system has a resolution of $0.124 \mu\text{m}$ as derived in section 2.2.10. The expected error can then be estimated. The number of pulses required to achieve a

displacement of 200 μm is $200 / 0.124 = 1612.90$ pulses that is rounded to 1613 pulses. Using 1613 pulses the displacement achieved should be $1613 \times 0.124 = 200.012 \mu\text{m}$. So the expected error can be in the range of $\pm 0.012 \mu\text{m}$. It is clear from figure 3.12 that the positioning error is not expected. This error corresponds to $10 / 0.124 = 81$ pulses approximately. This error may be a result of an error from the counter controlling the stepper motor drivers. The positioning control code calculates the number of pulses required to achieve a particular displacement. The number of pulses was sent to the counter on board the PCI 6036E card.

To further study the positioning error, voxels were produced in a polycarbonate sample at repeated fixed displacements along the y and the z-directions to investigate the amount of deviations from the expected displacements using a positioning speed of 20 $\mu\text{m/s}$. The laser power used was $P = 0.5 \text{ W}$, $PRF = 5000 \text{ Hz}$ and the number of pulses at each voxel position, $N = 5000$. The positioning stage was dictated to translate in the y and z-directions using a build file that is included in appendix C.4 As can be seen in figure 3.13, the sample was translated, forward and backward, in the y-direction at 100 μm , 400 μm and 500 μm . In the z-direction it was translated by 1000 μm .

Six identical rows of voxels were produced inside the polycarbonate sample and the averages of the displacements were taken. Consequently, the average positioning errors and percentage errors were calculated as shown in tables 3.7 and 3.8. In the y-direction, a maximum average percentage error of 7.92 % occurred at the displacements of 400 μm . However, in the z-direction the average percentage error occurred was 4.29 %. The error nature from tables 3.7 and 3.8, is systematic. This can be a direct result of mechanical friction in the stepper motor lead screw and bearings. The addition of a position transducer would most likely reduce the amount of error and/or make it more uniform for all ranges of displacements. The actual microscopic images of the error detection samples are included in appendix C.3.

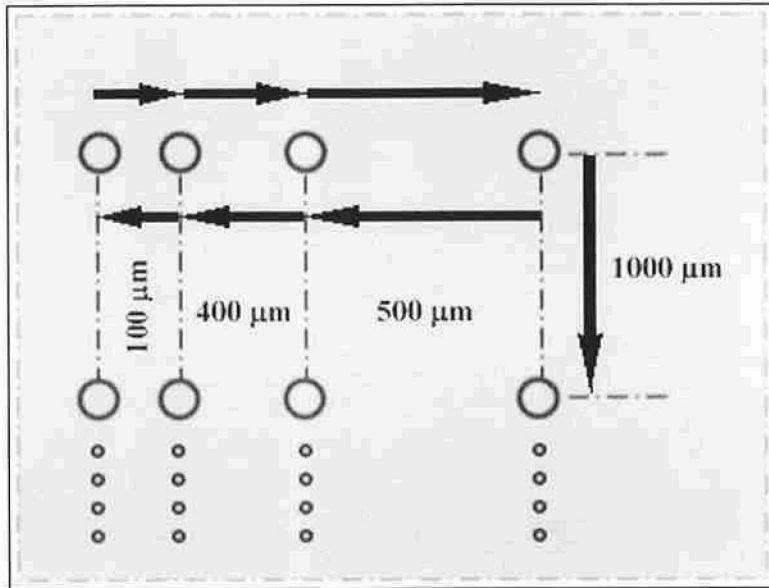


Figure 3.13: Contents of the error checking sample.

Table 3.7: Error analysis of displacements in the y-direction

Sample	Theoretical position (µm)	No. stepper pulses	Expected displacement (µm)	Measured displacement (µm)	Error	% Error
Sample 1	100	805	99.5	100.95	-1.45	-1.46
	400	3225	399.9	367.62	32.28	8.07
	500	4031	499.9	472.4	27.5	5.50
Sample 2	100	805	99.5	97.1	2.4	2.41
	400	3225	399.9	369.5	30.4	7.60
	500	4031	499.9	474.3	25.6	5.12
Sample 3	100	805	99.5	102.9	-3.4	-3.42
	400	3225	399.9	369.5	30.4	7.60
	500	4031	499.9	476.2	23.7	4.74
Sample 4	100	805	99.5	102.9	-3.4	-3.42
	400	3225	399.9	371.4	28.5	7.13
	500	4031	499.9	478.1	21.8	4.36
Sample 5	100	805	99.5	100.9	-1.4	-1.41
	400	3225	399.9	367.6	32.3	8.08
	500	4031	499.9	470.5	29.4	5.88
Sample 6	100	805	99.5	102.9	-3.4	-3.42
	400	3225	399.9	363.8	36.1	9.03
	500	4031	499.9	474.3	25.6	5.12
Average % Errors						
Displacement 1 (100 µm)	-1.78	31.66333		7.92	5.12	
Displacement 2 (400 µm)	-1.78	25.6		25.6		
Displacement 3 (500 µm)						

Table 3.8: Error analysis of displacements in the z-direction

Sample No.	Theoretical position (μm)	No. of stepper pulses	Expected displacement (μm)	Measured displacement (μm)	Error	% Error
Height 1	1000	8063	999.8	935.2	64.6	6.46
Height 2	1000	8063	999.8	950.5	49.3	4.93
Height 3	1000	8063	999.8	950.5	49.3	4.93
Height 4	1000	8063	999.8	971.4	28.4	2.84
Height 5	1000	8063	999.8	977.1	22.7	2.27
					Average Error	Average % Error
					42.86	4.29

3.4 Three dimensional CAD microfabrication

This experiment is carried out to verify the function of the CAD manipulation code and the 3D positioning system. The DCU logo was developed in 3D and exported as STL file format. The STL file was then sliced using the code developed and explained in sections 2.5 to 2.7. Figure 3.14 shows the steps followed to perform the slicing on the object and get a build file.

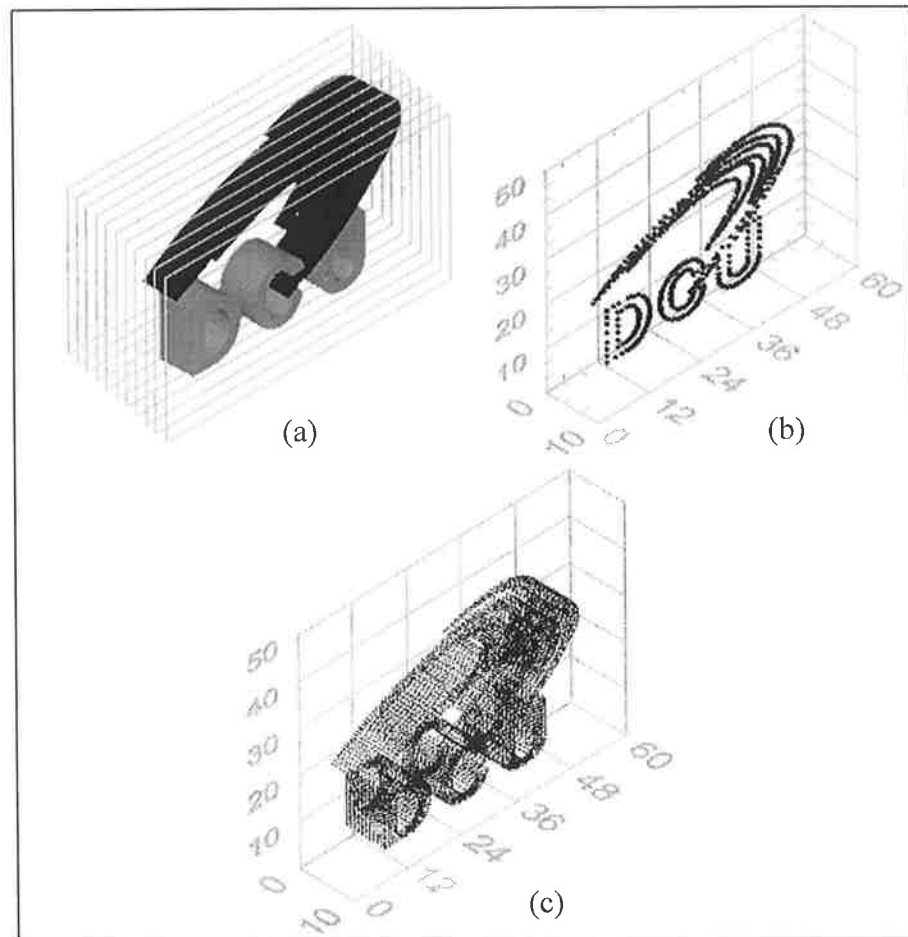


Figure 3.14: Steps leading to the final 3D sliced object (a) CAD design, (b) one planar contour and (c) fully sliced design.

One planar contour was picked up for this experiment. This plane contained 1046 coordinates (i.e. voxels). A build file containing these single plane coordinates was used to fabricate this shape in a polycarbonate sheet. The result is consistent with the expected shape and details. Figure 3.15 shows the image of the DCU logo fabricated inside a 10 mm thick polycarbonate sample.

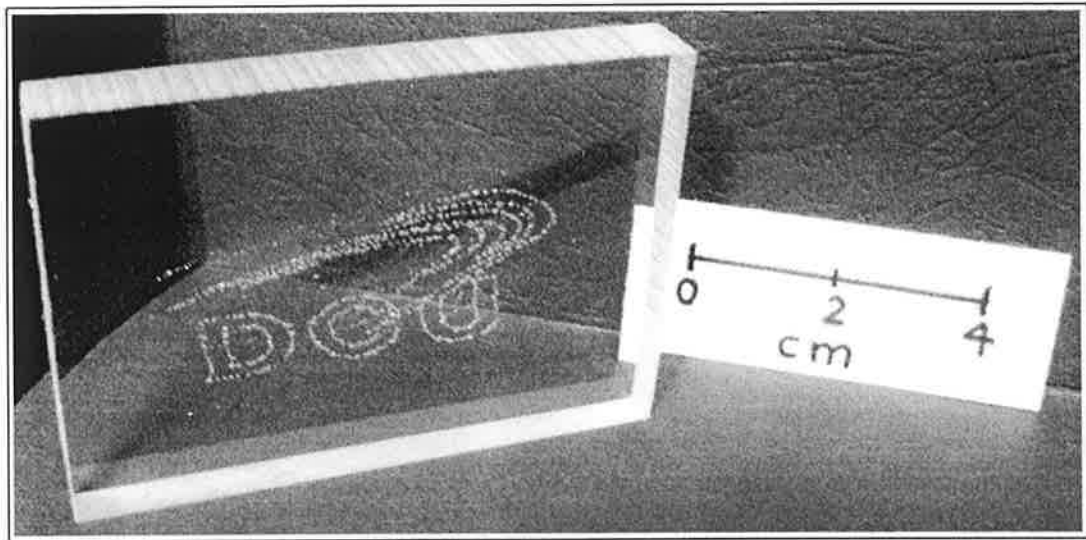


Figure 3.15: DCU logo fabricated inside polycarbonate.

3.5 Microfabrication with microscope objective lens

As presented in section 2.2.9, an objective lens of $NA = 1.25$ was also used to focus the laser beam in transparent samples. The focal calculated spot size was approximately $1 \mu\text{m}$. This tight focal spot size enabled microfabrication of materials that could not be microfabricated with the achromat lens focusing method. Voxels were produced in soda-lime glass, fused silica and sapphire samples. The aim of the study at this stage was to fabricate microchannels or waveguides that could be used in biomedical or telecommunication applications. However, this objective could not be met with the current laser system as will be presented in the overall discussion in section 3.6. Therefore, only some of the results obtained from this focusing technique are briefly presented in this section.

Figure 3.16 shows the voxels produced in a 2 mm thick soda-lime glass sheet using $P = 0.15 \text{ W}$ and $PRF = 1000 \text{ Hz}$. These settings produced a pulse energy of $150 \mu\text{J}$, which corresponded to the breakdown threshold energy in soda-lime glass. The laser intensity was $I = 19.1 \times 10^6 \text{ W/cm}^2$ and the pulse fluence was $F_p = 1.91 \times 10^4 \text{ J/cm}^2$. Interestingly, these settings produced the same breakdown threshold for fused silica. The voxels in figure 3.16 had approximate diameters of $5\text{--}10 \mu\text{m}$ and the number of pulses did not seem to have a noticeable effect on their size. One voxel produced using the same settings is shown in figure 3.17. The size of this voxel is many times smaller than the ones produced by commercial novelty 3D microfabrication systems ($100 - 200 \mu\text{m}$) [16]. It was also observed that the formation of these voxels was repeatable from shot to shot. This is due to the relatively higher intensity and energy fluence in this case which increased the probability of initiation of breakdown per laser shot. However, they were

always surrounded by microcracks that had star-like shapes. The induced structural changes by nanosecond laser micromachining always include microcracks or shock-induced shearing phenomena as reported in [35, 68]. Microcracking may also be explained in terms of the loss of excited photons, as the time separation between successive nanosecond pulses is higher than the time needed for the photons to convert their absorbed energy into heat [50]. Hence the focal region will have its heat conducted or diffused away before the second pulse arrives to excite more electrons, photons and generate heat. This causes a shocking effect in the focal region. Moreover, maybe the ionisation potential of the dissociated molecules by the first pulse is higher and therefore the growth of such structures is terminated.

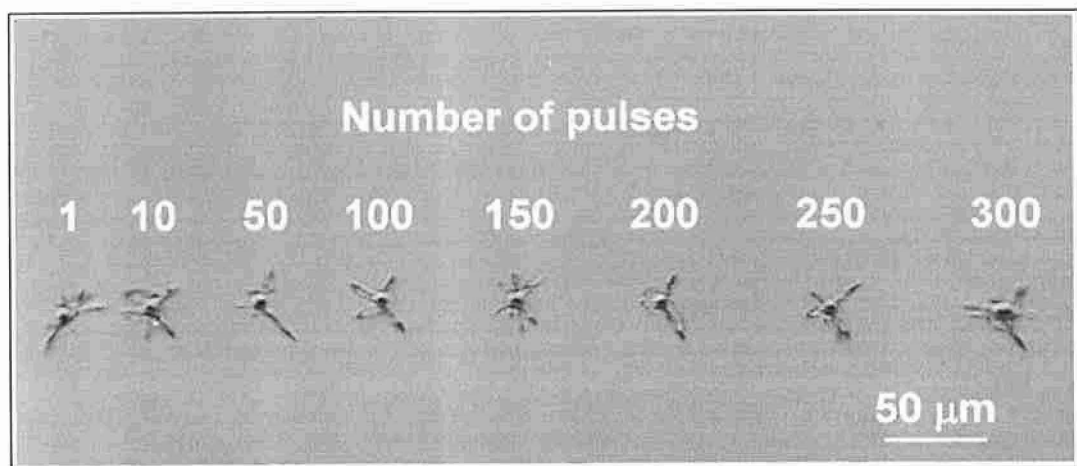


Figure 3.16: Voxels produced inside a 2 mm thick soda-lime glass sheet.

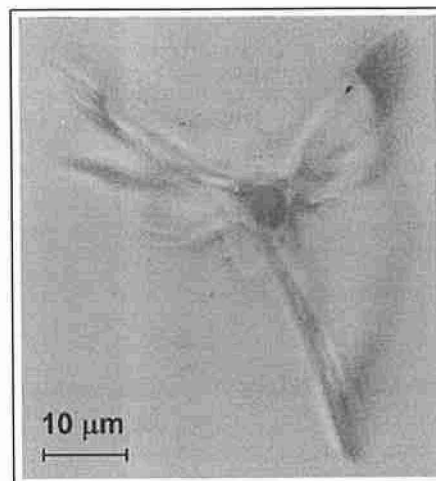


Figure 3.17: One voxels produced using 200 pulses inside a 2 mm thick soda-lime glass sheet.

Figure 3.18 shows a smaller version of the DCU logo presented in figure 3.15 earlier. The logo was fabricated using 1000 data points from a CAD file using $P = 2$ W, $PRF = 18$ kHz, and 100 pulses triggered at each data point. The positioning speed was $200 \mu\text{m/s}$. The sample was illuminated with a flash light to reveal the internal produced voxels, which could not be readily seen with naked eye.

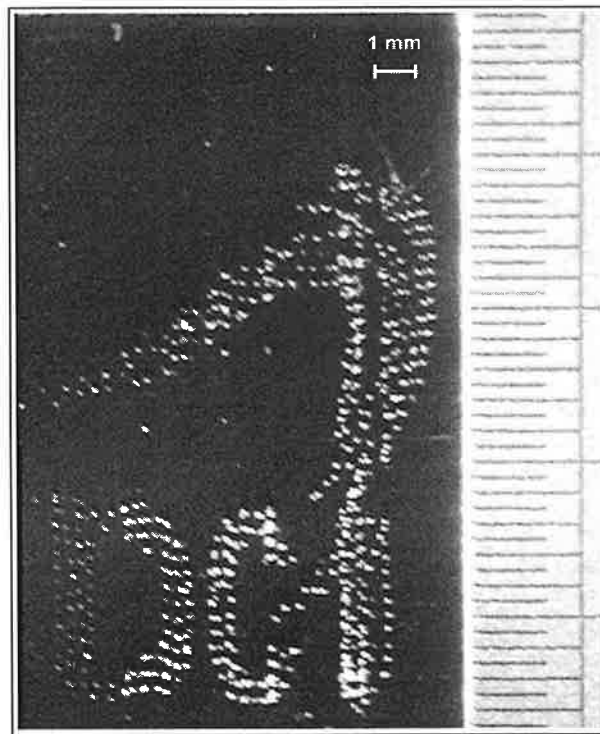


Figure 3.18: DCU logo microfabricated inside a 2 mm thick soda-lime glass sheet.

Attempts have been carried out to produce microchannels or waveguides inside a 2 mm thick fused silica microscope slide. The processing parameters were $P = 2.5$ W, $PRF = 20000$ Hz, and translational speed = $12 \mu\text{m/s}$ with a positioning resolution of $0.124 \mu\text{m}$. The sample was scanned along a fixed path in front of the laser beam a number of times to produce the microchannels. The sample was illuminated with a flash light to reveal the internal produced structures. As shown in figure 3.19, the upper waveguide has a width about $34 \mu\text{m}$ and was produced using one scan. The lower waveguide has a width of $55 \mu\text{m}$ and was produced using 7 scans along the same path.

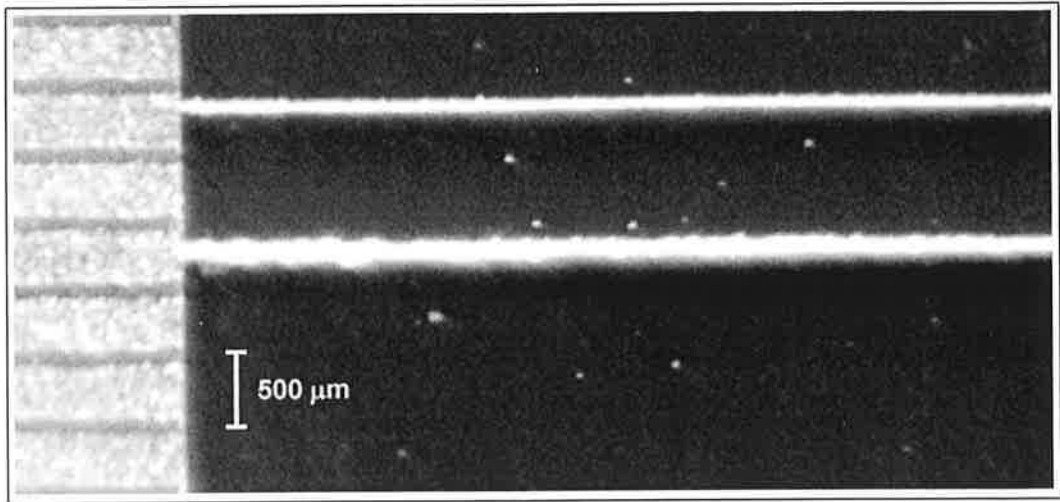


Figure 3.19: Two waveguides fabricated in a 2 mm thick fused silica sheet.

Figure 3.20 shows the side view of the upper waveguide in figure 3.19. The incident laser beam was focused from the top of the image. It can be seen that the waveguide was fabricated at an approximate distance of 220 μm underneath the sample's surface. However, the calculated focal depth in table 2.5 of section 2.2.9 was 1.8 mm. This suggests that the immersion oil enhanced the laser beam collection. Moreover, self-focusing can also reduce the focal depth inside transparent materials.

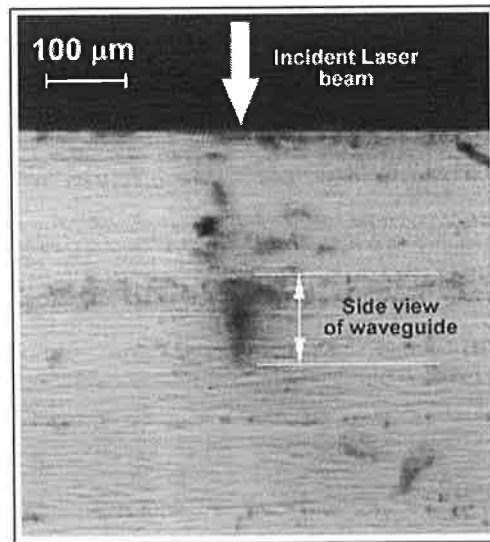


Figure 3.20: Side view of the upper waveguide in figure 3.19.

Figure 3.21 shows the microscopic images of the same waveguides presented in figure 3.19. The morphology of these waveguides was not regular as can be seen from the figure.

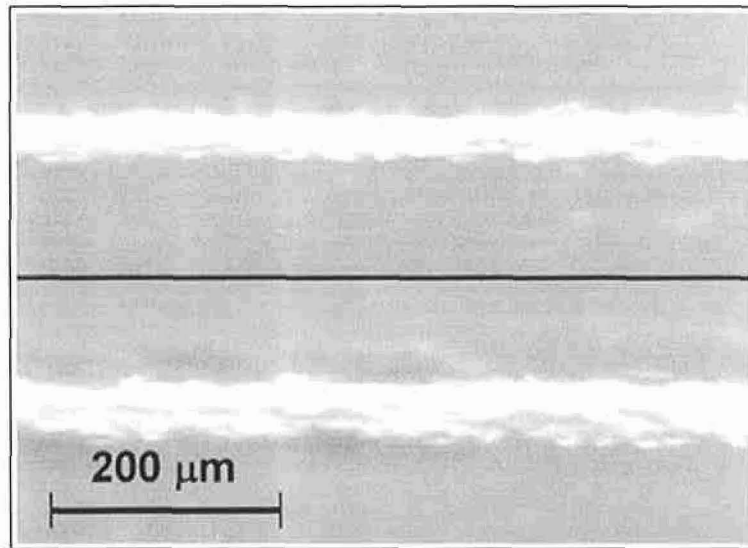


Figure 3.21: Microscopic image of the two waveguides from figure 3.19.

Figure 3.22 (a) and (b) show the images of voxels produced on the surface and inside a sapphire sample respectively. The processing parameters were $P = 2.5$ W, $PRF = 10,000$ Hz, and $N = 100$ pulses. The resulting pulse energy was $E_p = 250$ μ J. The laser intensity was calculated as $I = 3.2 \times 10^8$ W/cm² and the pulse fluence was $F_p = 3.2 \times 10^4$ J/cm². It was observed that the fluence breakdown threshold in the case of sapphire was about two times higher than that for soda-lime and fused silica. Moreover, the breakdown was not stable from shot to shot (i.e. some voxels were not fabricated). The morphologies obtained from the sapphire experiment showed less cracks surrounding the actual voxel. Table 3.9 summarises the breakdown thresholds and laser processing parameters used to produce them in the experimented transparent materials in this chapter.

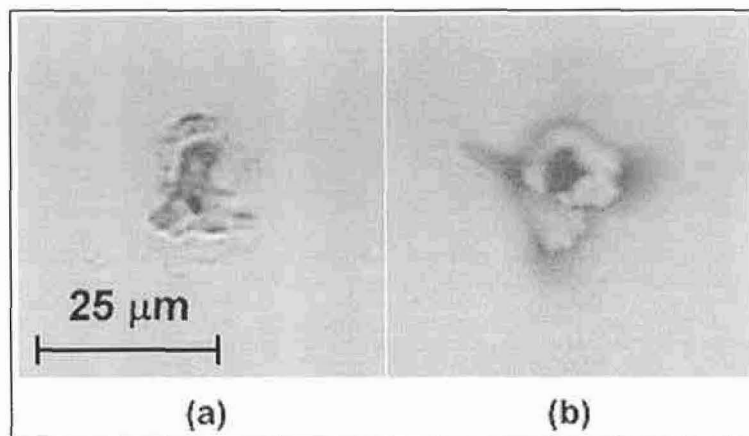


Figure 3.21: Voxels in sapphire, (a) on the surface and (b) inside the sample.

Table 3.9: Breakdown thresholds summary for tested materials.

Material	Focusing method	Spot size (μm)	P (W)	PRF (Hz)	E_p (μJ)	F_p (J/cm^2)	I (W/cm^2)
Polycarbonate	Achromat lens	28.9	0.15	5000	30	4.57	2.3×10^4
Soda-lime glass	Objective lens	1	0.15	1000	150	1.91×10^4	1.9×10^7
Fused silica			0.15	1000	150	1.91×10^4	1.9×10^7
Sapphire			2.5	10000	250	3.2×10^4	3.2×10^8

3.6 Overall Discussions

The experiments carried out on the system were aimed to verify its function and suitability for internal microfabrication in transparent materials. The microfabrication experiments performed on the polycarbonate samples showed a potential in the system to further expand the scope of the project in the future. The system despite the positioning errors mentioned earlier, is capable of inducing internal optical damage in polycarbonate.

The achromat focusing method employed gave a high Rayleigh range which distributed the laser pulse energy along the propagation direction and produced high aspect ratio structures. This result may be beneficial for some applications such as internal microchannel fabrication. Some experiments were carried out to fabricate channels in polycarbonate samples. However, they were not successful as the material was carbonised in the focal regions and could not be chemically etched away after laser processing. Details on these microchannel fabrication trials can be found in appendix C.5. If a special polymeric material is used with adequate post-laser chemical etching then cleaner channel cavities may be produced. The developed system was efficient for fabricating 3D shapes in polycarbonate as the fractured focal regions offered an enhanced visibility under room light due to reflection of light from the thermally altered voxels.

The accumulated fluence was related, as a common control factor of the process, to the microfabricated voxel diameter. The size of the voxel tends to increase with the increase of the accumulated fluence. However, similar accumulated fluence can be achieved using different combinations of pulse energies (i.e. average laser power and PRF values) and number of pulses. This indicates that accumulated fluence could not be considered as the process control parameter on its own. Similarly, the pulse energy, laser intensity or power cannot be, individually, taken as parameters inducing

breakdown or affecting the process outcomes. In order to have an accurate explanation of the process, it is necessary to bear in mind and record the values of all the process parameters, as it is their combined affect that determines or helps explaining the results. The microfabricated structures contained cracking due to the relatively wide pulse widths as introduced in the literature chapter. Moreover, these pulses also had relatively high energies and low pulse repetition frequencies. These limits were system related and could not be rectified with the current system setup. Therefore, the fabrication of structures of high precision was not possible.

Summary

The developed Nd:YVO₄ laser system showed a potential in decorative markings in polycarbonate and possibly with designed polymers it may be possible to fabricate internal microchannels or waveguides. The effects of the process parameters on the produced voxel shapes and sizes were assessed. Microscope objective lens focusing has enabled microfabrication of smaller voxel sizes in materials with higher melting points. Experimented materials included soda-lime glass, fused silica and sapphire.

Chapter 4

CO₂ Laser Experiments

4.1 Introduction

In this chapter the results from experiments conducted with the CO₂ laser and the procedures carried out to achieve those results are discussed. The objective of this part of the study was to fabricate microchannels on the surface of commercial soda lime glass sheets. The chapter starts by discussing the equipment used, the experimental procedures and the investigation techniques. In section 4.4 the design of microchannel fabrication experiments is discussed. Statistical variance analysis (ANOVA) of the results obtained from the design of experiments is explained. Mathematical models for width, depth and surface roughness were derived from the statistical analysis using response surface methodologies (RSM) are then presented.

4.2 Equipment and materials used

The equipment and materials used in this experimental work are listed below.

- 1- The CO₂ laser system presented in section 2.3,
- 2- Optical microscope and camera imaging system (Me F2 universal camera microscope made by Beuhler Omnimet Enterprise [161] with a quantitative image analyser [162]). The widths of the channels were measured under a confocal optical microscope and Buhler image analysis system which was calibrated to 0.1 micron,
- 3- Scanning electron microscope (LE0440 stereo scan [165]),
- 4- In-house built laser surface profile scanning system and gold scan coater (Pirani 501 SIX sputter coater, BOC Edwards [166]), and
- 5- Soda lime glass sheets (two millimetres thick).

4.3 Screening experiment

In any attempt to study a process systematically and precisely using the design of experiments techniques, screening experiments are often conducted [167, 168]. Screening experiments were carried out with the CO₂ laser system in order to understand the process and to decide on the process control parameters, the ranges of the control parameters and the response parameters that could be measured. The method followed for the screening experiments was to randomly test combinations of laser emission parameters, which included maximum and minimum settings where appropriate. This trial and error method was repeated with appropriate optical microscope inspection of the samples until the significant control parameters and their ranges were decided. Figure 4.1 shows a schematic of the process control parameters. The main laser emission parameters used as the control parameters for this study were,

- 1- The average power of the laser beam, P (W),
- 2- The pulse repetition frequency of the laser beam, PRF (Hz), and
- 3- The translation speed of the glass sample, U (mm/min).

The effect of focal depth, Df (mm) which is the distance between the laser spot focus plane and the sample's surface was also examined. Df was taken to be negative when the laser spot focus plane lay underneath the surface. After initial screening experiments with this parameter it was fixed at $Df = 0$ mm for the more refined design of experiments. Microchannels were also produced using $Df = -2$ and 2 mm.

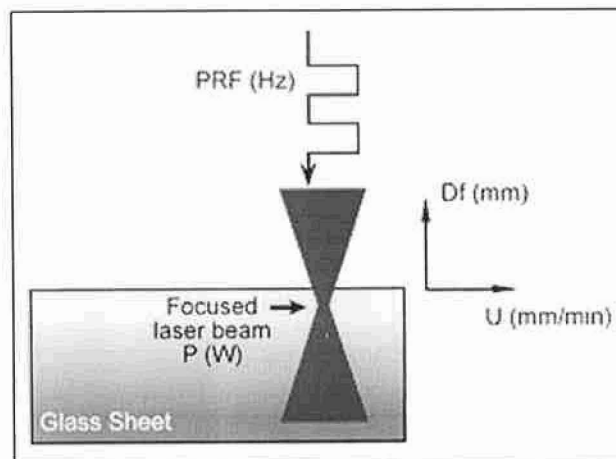


Figure 4.1: Process control parameters, laser beam power, P , pulse repetition frequency, PRF , translation speed, U , and focus depth, Df .

As stated earlier, another objective of the screening experiments was to pick the response parameters. These were the microchannels' dimensional parameters to be studied as a direct effect of changing one or more control parameters. Figure 4.2 shows a schematic of a typical microchannel illustrating the response parameters.

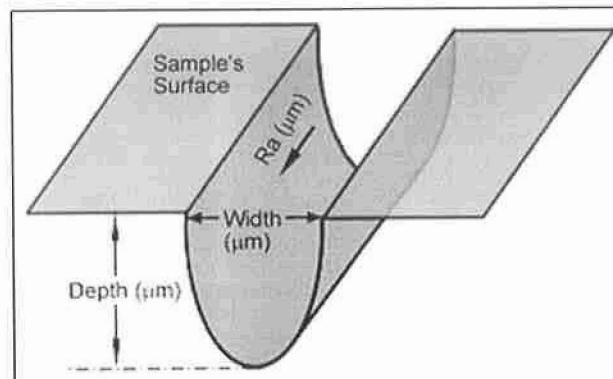


Figure 4.2: Microchannel schematic indicating response parameters measured: the channel's width, depth and roughness.

The microchannels' response parameters chosen and measured were the channel's width (μm), depth (μm) and roughness (μm) along its main longitudinal axis. As a result of the screening experiments, the ranges of the process control parameter to be investigated were decided and are listed in table 4.1. The limits of these parameters that the system is capable of are also shown in this table.

Table 4.1: Control parameters ranges.

Parameter	System capability range		Process range investigated in detail	
	P (W)	0	1500	18
PRF (Hz)	2	5000	160	400
U (mm/min)	0	5000	100	500

4.4 Design of experiments

Based on the results and control parameters ranges chosen from the screening experiments a three-level, 3^n , factorial design of experiments was produced. The number of control parameters, n , was equal to 3 for this work. The PRF was controlled by fixing the period factor to 500 and changing the divide as explained in the section 2.3.1. The divide was varied between 20 and 50. As a result the PRF was experimentally varied between 400 and 160 Hz respectively. The centre value of the PRF in this design of experiments corresponded to the centre value of the divide 35, which produced a $PRF = 228$ Hz. This PRF centre value was not equal to the arithmetic average $(160+400)/2 = 280$ Hz of the minimum and maximum PRF . This was taken into consideration in the statistical analysis of the results using the software tool. Table 4.2 shows the levels of the control parameters and the corresponding coding of these.

Table 4.2: Control parameters levels and their corresponding DoE coding.

Parameter	Actual			Coded		
	Low	Mid	High	Low	Mid	High
P (W)	18	24	30	-1	0	1
PRF (Hz)	160	228	400	-1	-0.433	1
U (mm/min)	100	300	500	-1	0	1

Table 4.3 contains the list of experiments conducted. The list covers all the possible combinations of the control parameters. For repeatability analysis, five extra experiments were repeated at the centre points of the investigated ranges, so that the

total number of experiments conducted was $3^3 + 5 = 32$. These five extra experiments were repetitions of the conditions for experiment number/channel number 14 and are listed in table 4.3 as experiment numbers/channel numbers 28 to 32. The run order, shown in the second column of the table is a software randomly generated sequence of execution to minimise systematic errors. This random run order was used to fabricate the channels, however, the upcoming discussion of the channels will refer to the numbering sequence in the left-most column.

4.5 Experimental procedure

The procedure of carrying out the experiments is listed below.

- 1- The soda lime sheet was mounted on the translation bed of the CO₂ laser using sellotape.
- 2- A reference point near the bottom left corner of the glass sheet was set. This was the starting position of the first channel.
- 3- The processing parameters from the run order row in table 4.3 were input.
- 4- To initiate laser cutting, the laser beam and the translation bed were simultaneously and automatically switched on by the motion system's PLC to fabricate a 15 mm long channel.
- 5- The sample was brought back to the reference point and then displaced to a new reference point. This was done by moving the translation bed by a 10 mm distance in the direction perpendicular to the channel's axis.
- 6- Steps 3 to 5 were repeated until all the parameters' combinations in table 4.3 were processed.
- 7- Using a water proof marker, the samples' names, date and channel number were carefully marked.
- 8- The glass sheet was cut to smaller sizes of approximately 100×100 mm (in order to fit in the inspection device chambers). Cutting was done with the channel side down on compliant paper by spraying a small amount of lubrication oil (WD-40) on the back surface of the sheet and scribing using a glass cutting tool (Silberschnitt) and a metallic rule. Cutting was done on the back surface so as to not cause cracking along the channels and to prevent oil contamination inside the channels.
- 9- The samples were cleaned using water to remove all the dust and debris on the surface.

- 10- The samples' images, straight down on the channel, were taken the using the optical microscope and some of the samples were examined using the scanning electron microscope.
- 11- The channels were then scanned using the laser surface profile scanning system. The system has a laser scanning head and hence gold coating was necessary for each sample for about 500 seconds.
- 12- The channel parameters were then measured for each channel using the LabVIEW GUI of the scanning system. This system captured the three dimensional profile of the channels.
- 13- The measured data were entered in Excel spreadsheet files, to carry out the statistical analysis and modelling of the process.

Table 4.3: Design of experiments.

Ordered Expt. No.	Run	P (W)	PRF (Hz)	U (mm/min)
1	25	18	160	100
2	16	24	160	100
3	22	30	160	100
4	8	18	228	100
5	31	24	228	100
6	29	30	228	100
7	27	18	400	100
8	28	24	400	100
9	18	30	400	100
10	1	18	160	300
11	30	24	160	300
12	32	30	160	300
13	26	18	228	300
14	9	24	228	300
15	4	30	228	300
16	15	18	400	300
17	14	24	400	300
18	20	30	400	300
19	10	18	160	500
20	19	24	160	500
21	3	30	160	500
22	2	18	228	500
23	21	24	228	500
24	7	30	228	500
25	13	18	400	500
26	24	24	400	500
27	12	30	400	500
28	5	24	228	300
29	11	24	228	300
30	6	24	228	300
31	17	24	228	300
32	23	24	228	300

4.6 Optical microscope inspection

The optical microscope was used first to estimate the widths of the channels. Figure 4.3 shows a microscopic image of microchannel 10 and the remaining channels' microscope images are included in appendix D.1. Channel quality from these images was judged based on the amount of microcracks around the channel. The microcracks are a result of thermal stress due to the steep gradients of temperatures combined with the low conductivity of glasses. The quality of the channels was not a response parameter in the response surface study, however, it was observed for recommendations on the best parameters settings at which channels could be produced in the future.

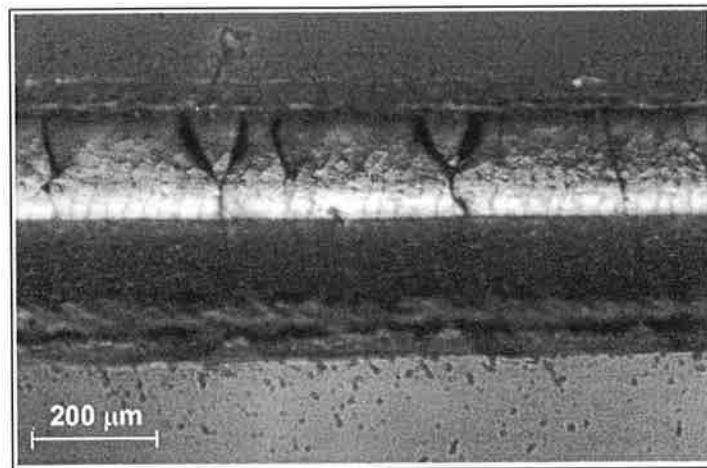


Figure 4.3: Microscopic image of microchannel 10.

4.7 Scanning electron microscope

Scanning electron microscope was used to study the structural changes in the material regions surrounding some of the microchannels. This inspection helped in judging the quality of the channels similar to the case of optical microscope imaging. Figure 4.4 shows an SEM image of microchannel 19. The laser scan direction in the image was from right to left. The channel shape consisted of repeating helical features along the channel axis. The source of these features will be discussed in details in chapter 6. The image shows some microcracks or peeling structures around the ablated channel, which was a result of thermal stress. A build up zone can be identified by the raised edges around the channel boundaries.

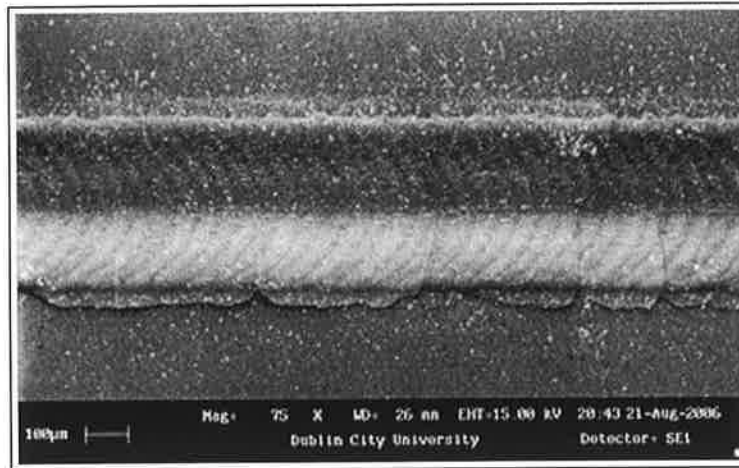


Figure 4.4: SEM image of microchannel 19.

4.8 Laser profileometer inspection

The laser scanning profileometer system was used as the main inspection method. The scanner enabled the measurement of the three channel dimensional parameters. The laser profileometer, shown in figure 4.5, is a non-contact profile inspection system that was developed by another research study in DCU [169].

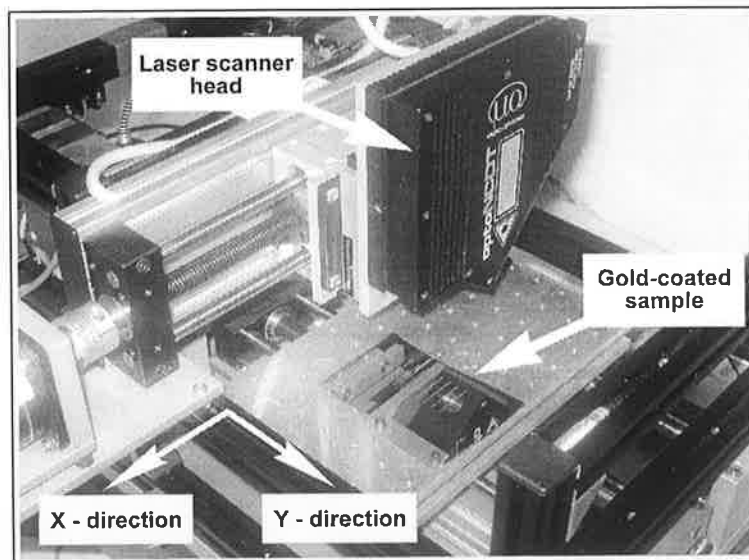


Figure 4.5: The 3D laser profileometer.

4.8.1 Length measured from each channel

A fixed length was scanned from each channel, which was calculated based on the maximum translation speed combined with the minimum *PRF* values used in the experiments. The calculation of this distance is depicted in figure 4.6, which shows an array of disks, each representing a glass volumetric element affected/ablated due to one laser pulse.

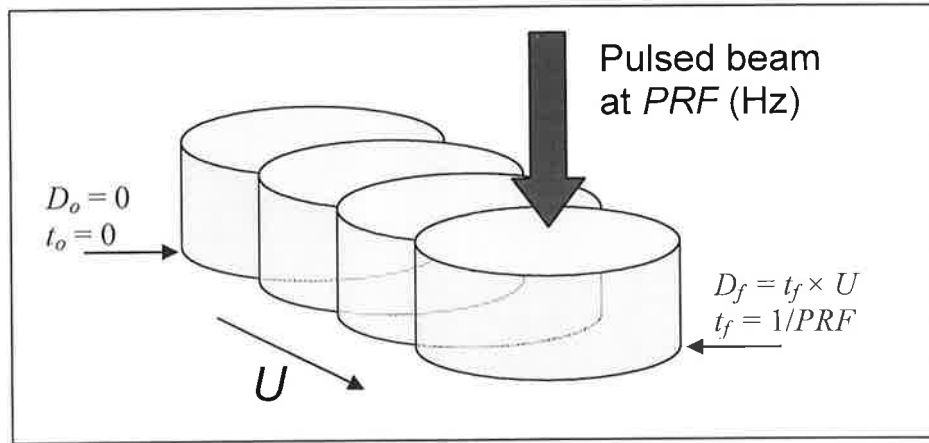


Figure 4.6: Schematic of the length covered by a laser pulse; effect of PRF and U .

The periodic nature of the laser source suggests that the channel dimensions and geometry will repeat along the axis of ablation, so that scanning and analysing the area covered by one laser pulse should capture most of the channel dimensional data. In this work a distance covering at least one pulse ablated region was scanned from the channels fabricated. The calculation of the distance covered by one laser pulse is analogous to the calculation of the feed of the conventional mechanical machining processes, as will be treated in section 4.9.4. The minimum PRF value of 160 Hz gave a pulse duration, $t_f = 1/PRF = 6.25 \times 10^{-3}$ s. When this was used with the maximum translational speed examined, $U = 500$ mm/min = 8.333 mm/s, the distance covered by the laser beam during the pulse time was maximum and given by $D_f = t_f \times U = 52.08$ μ m/pulse. Based on the calculations above, a length of 48.75 μ m was scanned off each channel, except for channels 19, 20 and 21, where 58.5 μ m was scanned off these channels. The reason for this, was that these were the only channels fabricated using the minimum PRF and maximum U resulting in the 52.08 μ m as per the calculation above.

4.8.2 Profile scanning procedure and software

The front panel of the profile scanning code is shown in figure 4.7. This code was used to control the motion of two stepper motors which moved the sample in the x and y-directions underneath the scanner in a raster scanning pattern. The stepper motors displaced the glass sheet sample to designated coordinates dictated by the number of stepping pulses. The minimum resolution obtained from one pulse with this system was 0.039 μ m [169]. In this study, 50 pulses were used to translate the glass sample to each location at which a z-axis (height) data point was recorded. This displacement value was inserted in the “number of pulses” control dialogue box as can be seen in figure 4.7. The resultant lateral resolution from this setting was $0.039 \times 50 = 1.95$ μ m in both x and y-

directions. The resolution and the area scanned settings were also chosen with time of scan in mind. Each scan took approximately one hour to complete and the number of scans performed in this study was 86 scans (54 scans for the screening experiments, 27 for the refined DoE, and 5 for the repeatability in the DoE).

The microchannels were mounted on the scanner bed underneath the laser head such that the channel's main axis was parallel to the x-axis as shown in figure 4.8. Once the control program, shown in figure 4.7 was run, the 3D scanner system automatically scanned the channel.

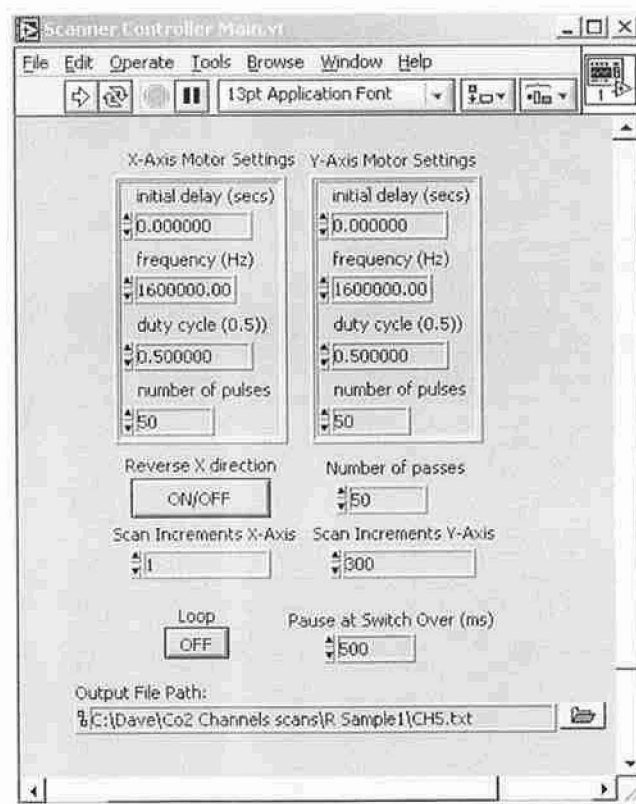


Figure 4.7: 3D profile scanner controller code front panel.

Figure 4.8 shows a schematic of the top view of a sample channel's scan with the locations of points at which topographic data were recorded. For illustrative purpose, figure 4.8 is an example of a channel's scan over an 11×11 raster scan pattern. The figure shows a scan area including 11×11 data points, whereas, in reality the scanned area included 25×300 data points. The scan was started at the location indicated in figure 4.8, where a data point was taken, then the y-motor automatically displaced the sample by $1.95 \mu\text{m}$ in the negative y-direction and stopped for 500 ms allowing another data point to be taken. This was repeated until the full width of the channel was scanned. The number of points to be displaced in the y-direction was controlled from

the “scan increments Y-axis” field on the front panel shown in figure 4.7. At the end of one scan path in the y-axis, the y-motor was automatically disabled and the x-axis motor displaced the sample in the x-direction by $1.95 \mu\text{m}$ where another data point was taken and the y-motor was again enabled. The number of individual displacement increments in the x-axis was controlled by “scan increments X-axis” field in figure 4.7, which was kept equal to 1 to conserve an equal scan resolution in both directions. The y-motor then automatically repeated the same scanning procedure in the reverse direction, see figure 4.8. This procedure was repeated until the number of passes across the x-axis was equal to the “number of passes” field on the front panel of figure 4.7. The number of passes controlled the length of the channel to be scanned in the x-direction, which was calculated earlier to be either 48.75 or $58.5 \mu\text{m}$. These distances were covered using $48.75/1.95 = 25$ passes and $58.5/1.95 = 30$ passes respectively, which were the values used for the scans performed in this study. On the other hand, the number of scan increments in the y-direction was changed each time to suit the channel’s width being measured. In figure 4.7, the number of scan increments in the y-direction is set to 300 increments; this is equal to a displacement of $585 \mu\text{m}$ in the y-direction.

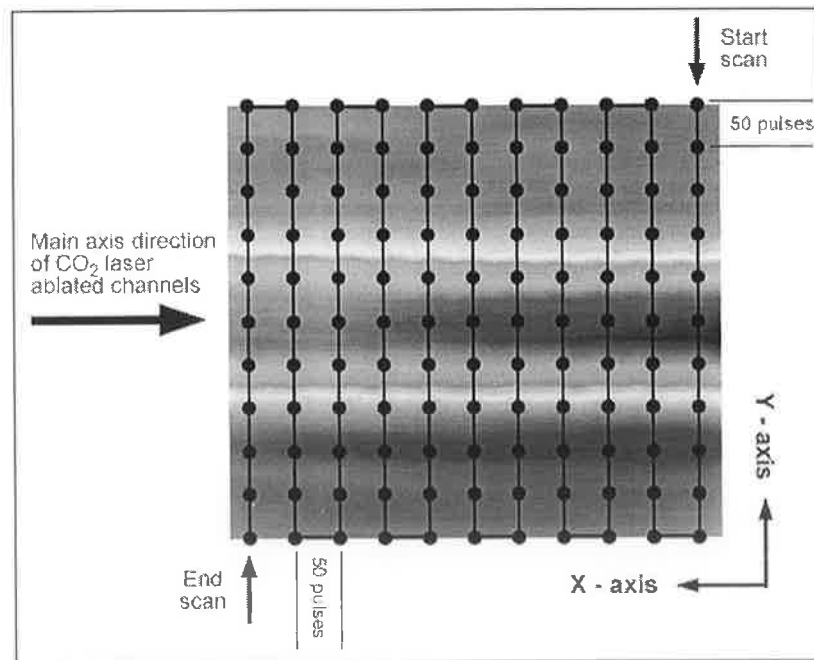


Figure 4.8: Schematic of top view of sample channel scan with data points illustrated.

The dialogue boxes shown in figure 4.7 controlled the resolution and displacement of the sample in both x and y-direction, while the scanning laser head allowed the height measurements as voltages to be recorded at each location. These voltage readings were written to a text file in the form of a 1D-array at the end of each scan across the

channel's width. The readings of the successive scans across the channels were appended to the same file, so that at the end of the scan, the file contained a 2D-array. This 2D array contained the data representing the 3D profile of the channel. It should be noted at this stage that the output height readings were registered as voltages that had three significant figures after the decimal point. The sensitivity of the laser head was $500 \mu\text{m}/\text{V}$ [169, 170], which meant that the height voltage data had to be multiplied by 500 in order to convert them to μm units. The resolution of the z-axis or the laser head was $0.25 \mu\text{m}$ as given in the specification sheet. However, the voltage readings obtained were given to an accuracy of three significant figures after the decimal point. This meant that the smallest voltage value of 0.001 V gave a measurement resolution of $0.001 \times 500 = 0.5 \mu\text{m}$, which was in turn the smallest detectible height reading this study. The isometric view of a sample channel is presented in figure 4.9. This figure shows that the voltage reading, black-coloured, on the z-axis were multiplied by $500 \mu\text{m}/\text{V}$ to convert them to the red-coloured μm readings. The original x and y - axes readings, black-coloured, in figure 4.9 are the scan counts or increments in both directions as explained earlier. The adjacent axes reading, red-coloured, are converted to μm after multiplying by $1.95 \mu\text{m}/\text{increment}$.

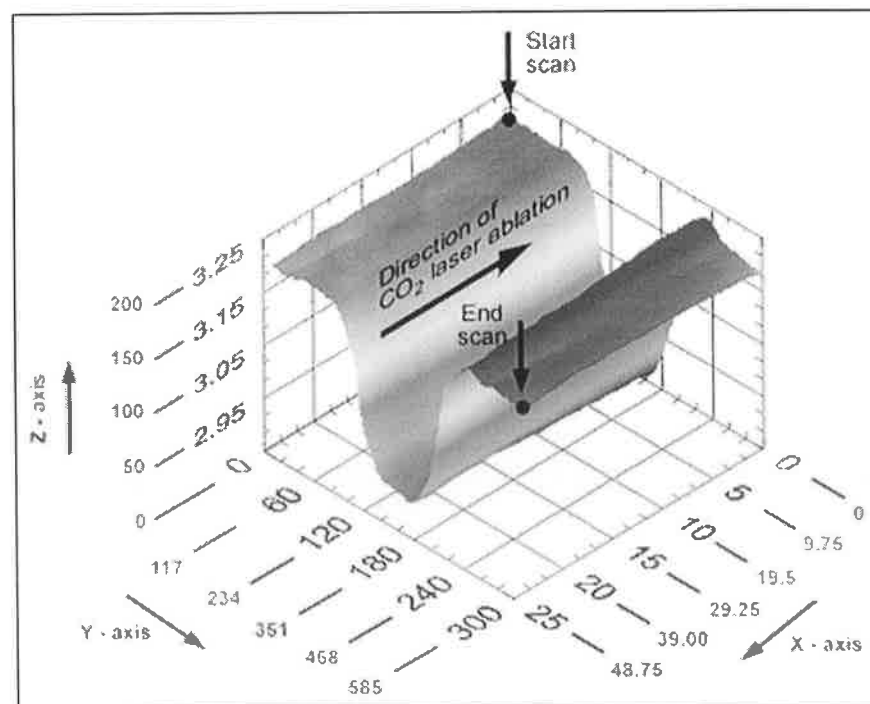


Figure 4.9: A sample channel before aspect ratio correction.

The true aspect of the channel can not be seen from figure 4.9 as the range of the z and y-axes scale are not the same. In order to be able to visualise and compare the channels,

the z and y-axes ranges were set to (0-585 μm) for all the 3D channel scans. The isometric view of the same channel with the corrected aspect is shown in figure 4.10 note that both the y and z – axes have the same displacement scaling and length.

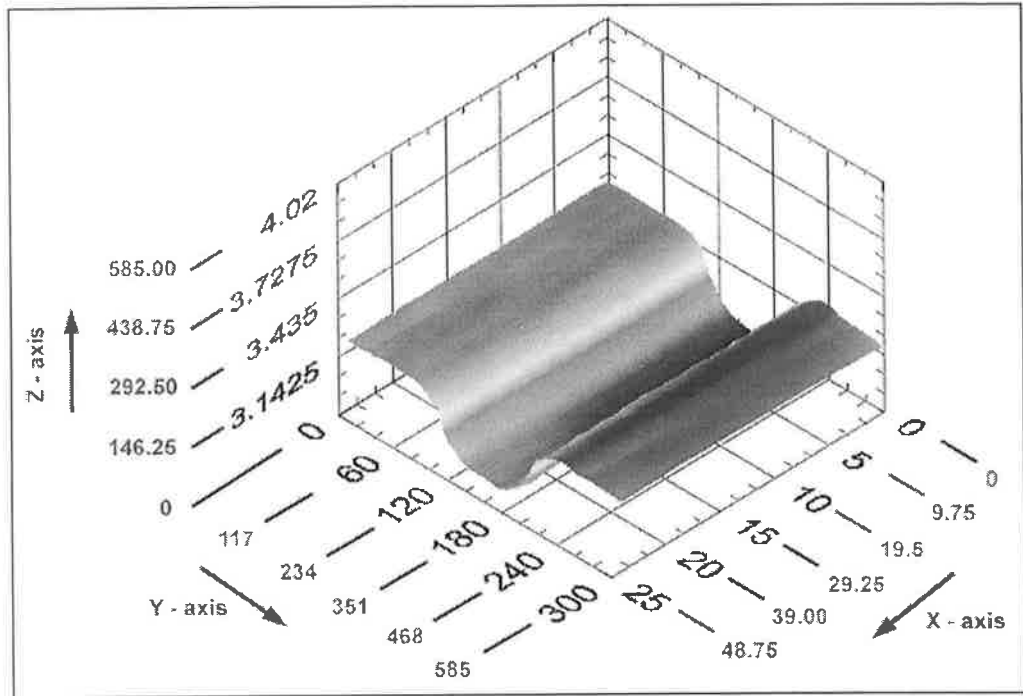


Figure 4.10: Sample channel with corrected aspect ratio.

The heights or the voltage readings represented the relative heights of the surface profile. The “relative” term here means that all heights were measured with respect to the minimum height scanned on a particular surface. Consequently, to measure heights, the difference between the minimum height and the heights at all points was calculated. This issue and the measurement of distances in the lateral directions are dealt with in greater detail in section 4.8.4. It should only be clarified here that, on the z-axes readouts, the minimum displacement value was set as zero. The scanning and image modification procedure illustrated in this section was performed on the scans of all the channels produced for this work. The only parameter that was changed was the scan increments in the y-axis to accommodate different channel widths.

4.8.3 Measurements and calculations of the channel parameters

Figure 4.11 indicates the three parameters that were measured from a sample channel. Knowing the x, y and z-axes data in the 3D plot, the distance between any two points can be calculated by multiplying by the appropriate calibration factor as explained earlier.

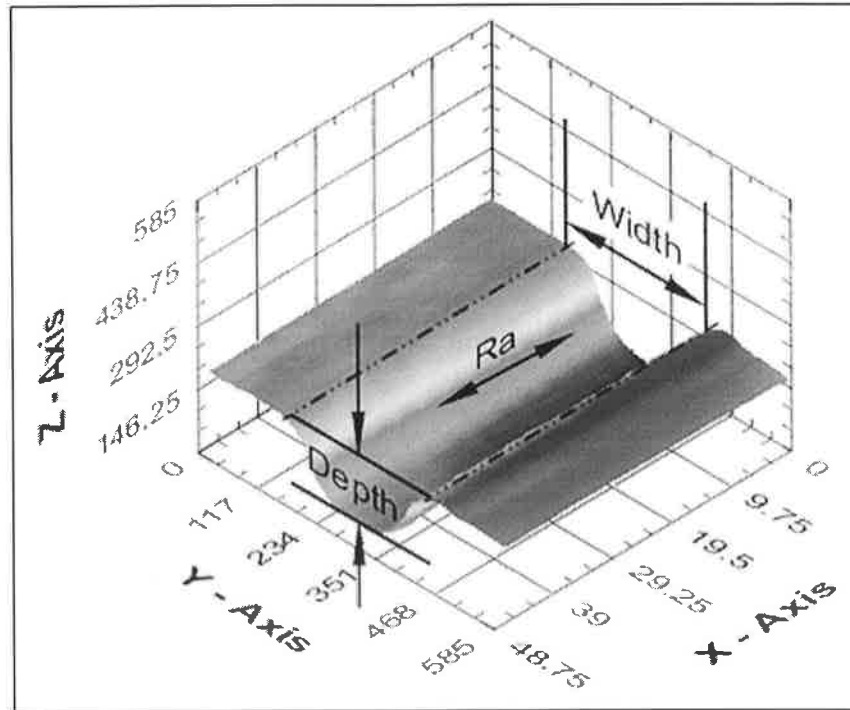


Figure 4.11: Microchannel parameters measurements, scan of CH 14.

4.8.4 Channel width measurement

The point pair, between which the width was measured, was picked using the cursors and by looking at all views of the channel. This was necessary because sometimes the channel axis was slightly tilted or irregular. Moreover, in some channel scans, the build up zone was higher than the unprocessed glass surface. In a couple cases, channels 16 and 25, where the 3D scan could not provide accurate judgement of the channel's width, the measurement was assisted by the aid of the microscopic images. The microscopic images of the channels are shown in appendix D.1.

Generally, the unprocessed glass surface was first found by moving the cursors in the z-direction when viewing the scanned surface edge in the direction of the x-axis, examples are shown in figures (b) of appendix D.2. Then the channel's isometric view was examined and the cursors moved again in the x and y-direction only until the locations defining the highest points on opposite edges of the channel were found. This pair of points was recorded and the displacement between them was recorded as the channel width. This procedure was repeated for three different locations along the channel width. This procedure was repeated for three different locations along the channel axis and the average was calculated. Appendix D.3 shows the three width measurements and the average channel widths found from this work. Figure 4.12 shows the front panel of the LabVIEW code developed for the measurement of both the width and depth of the channels.

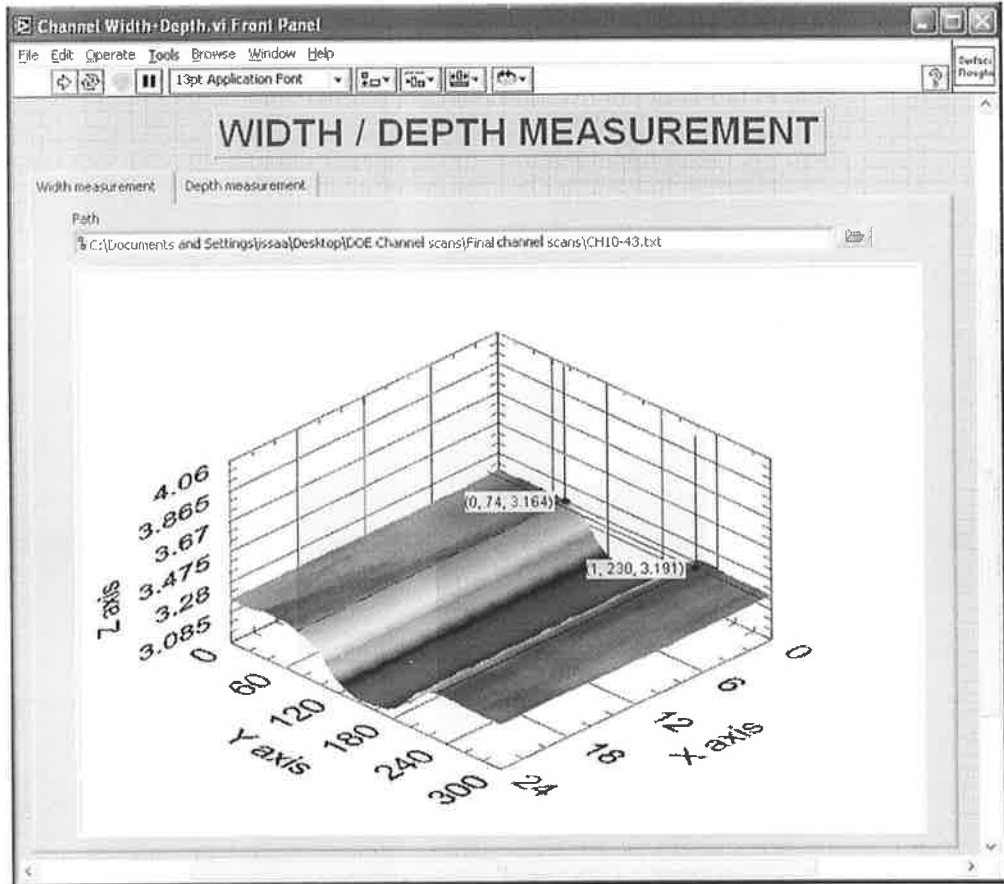


Figure 4.12: Front panel of the width and depth measurement code.

Figure 4.13 shows a sample channel 3D surface viewed in the width measurement window. As can be seen from the figure there is a cursor defining the unprocessed glass surface level, called “Top level” and has dashed coordinate lines. The surface is represented by the darkened XY plane in the figure. Three pairs of cursor co-ordinates were used to define and measure the channel’s geometry.

Each cursor in figure 4.13 has a flag which contains the three coordinate readouts, x, y, and z respectively. Looking at the y-coordinates of the first pair of cursors at the back of the channel plot ($x = 0$), the distance between them is $(198-61) \times 1.95 = 267.15 \mu\text{m}$. This calculation was repeated for the remaining two pairs and the average was taken as mentioned earlier. Each pair of cursors had the same x-coordinate, as can be seen in figure 4.13. This allowed easy comparison of co-ordinate pairs and introduced negligible error in the width measurement.

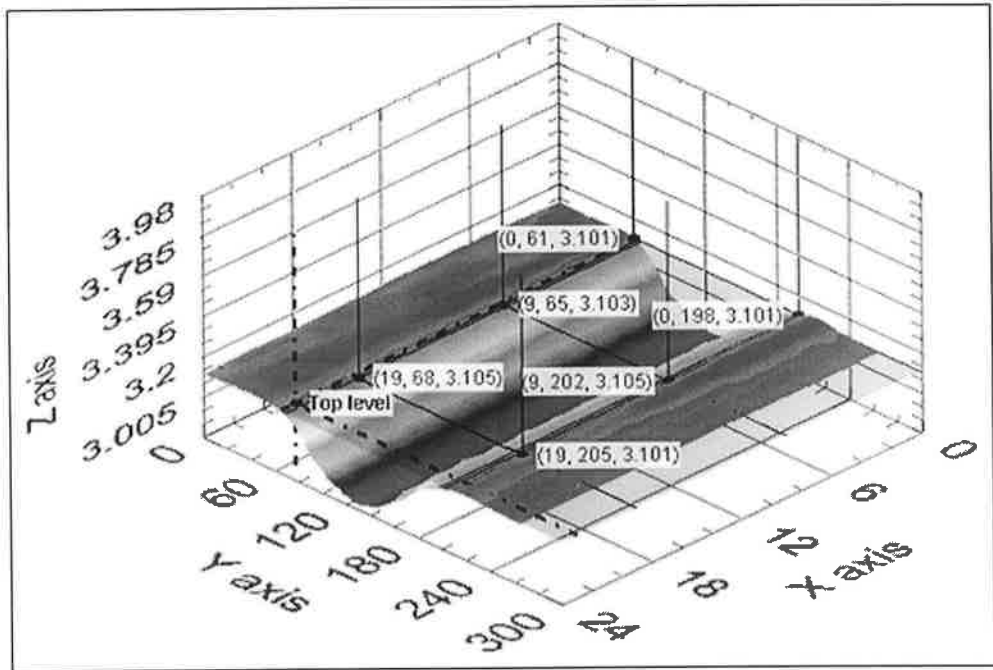


Figure 4.13: Sample channel width measurement procedure.

Figure 4.14 shows the top view of this sample channel. The cursor flags are clearer from this view and it can also be noted that the channel's axis is slightly tilted with respect to the scan direction. To accommodate this tilt during measurements the y-coordinates of the cursor pairs are not equal. It can be seen, in figure 4.14, that the cursors are distributed along the darkened surface intersection with the 3D scan surface.

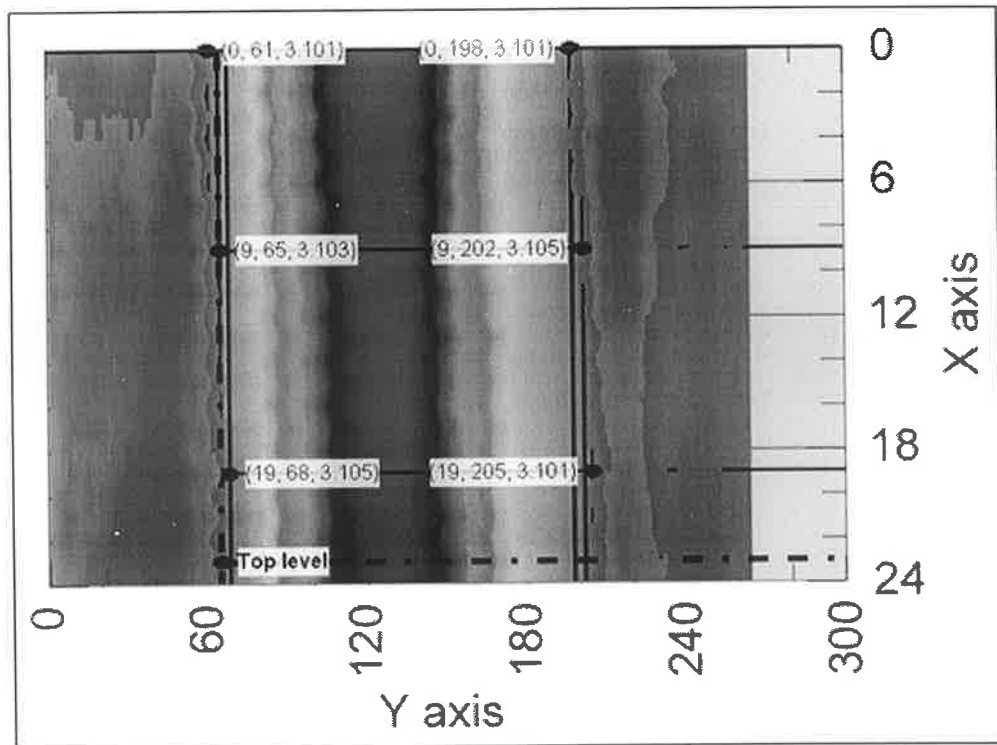


Figure 4.14: Top view of a sample channel width measurement procedure.

Figure 4.15 shows the front view of the same channel without changing the cursor's locations. The flags for the pairs of cursors are not visible in figure 4.15. This shows that the width measurements were taken at the level of the unprocessed glass surface, which was at approximately 3.13 mV in this example.

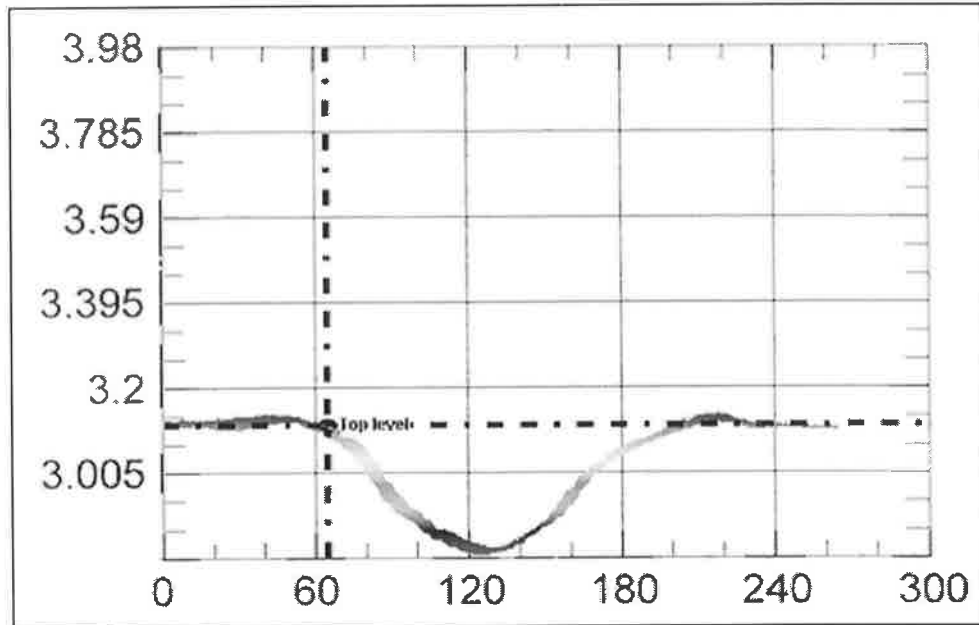


Figure 4.15: Front view of a sample channel's width measurement.

Throughout this procedure, the channel top view was checked to ascertain that the cursor pairs actually represented logical/fair measurements as was the case of the top view of the channel in figure 4.14. The cursor pairs' locations were estimated from the isometric and front views; however, it was necessary to refine the locations of the cursor pairs from the top view, where the darkened surface indicated an accurate illustration of the channel's width. This method was the same for the measurements taken from all the channels.

4.8.5 Channel depth measurement

The depth measurements were taken using the same GUI shown in figure 4.12. The procedure was similar in nature to the channel width measurement; however, the distances were measured in this case between 3 cursors that lied on the top level plane and three other cursors at the bottom of the channel and distributed along the channel's axis. The "Top level" cursor here was, normally, kept at the same coordinates as for the width measurement procedure. However, in some cases, such as channels 3, 6 and 12, it was slightly varied to correspond with the average surface height depending on the

severity of the build up zone. Figure 4.16 shows the isometric view of the sample channel from the previous two figures but with the depth measurement cursors in place. The z-coordinates of each pair of cursors were compared and multiplied by the conversion factor. For instance, the cursor pair at the back of the channel ($x = 0$) gave a depth equal to $(3.101 - 2.815) \times 500 = 143 \mu\text{m}$.

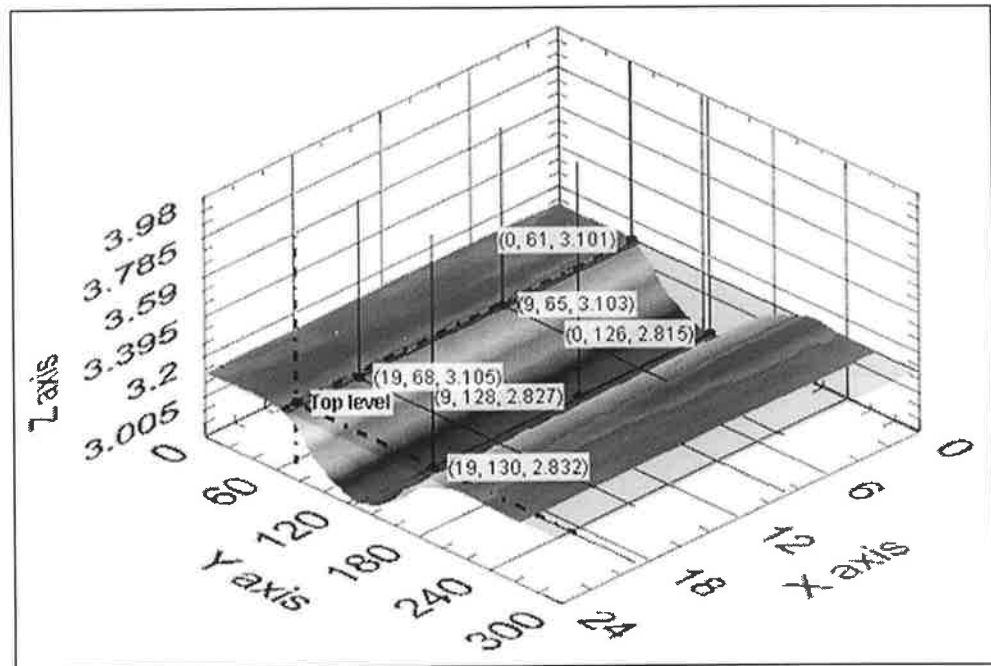


Figure 4.16: Sample channel depth measurement procedure.

Figure 4.17 is another isometric view of this sample channel, in which the cursor pairs are illustrated in a clearer manner. Each pair of cursors in figure 4.17 had the same x-coordinate as illustrated for the width measurement procedure. Three depth measurements were obtained from this procedure and the average was calculated. The measurements of the three depth measurements and the average channel depths are listed in appendix D.4.

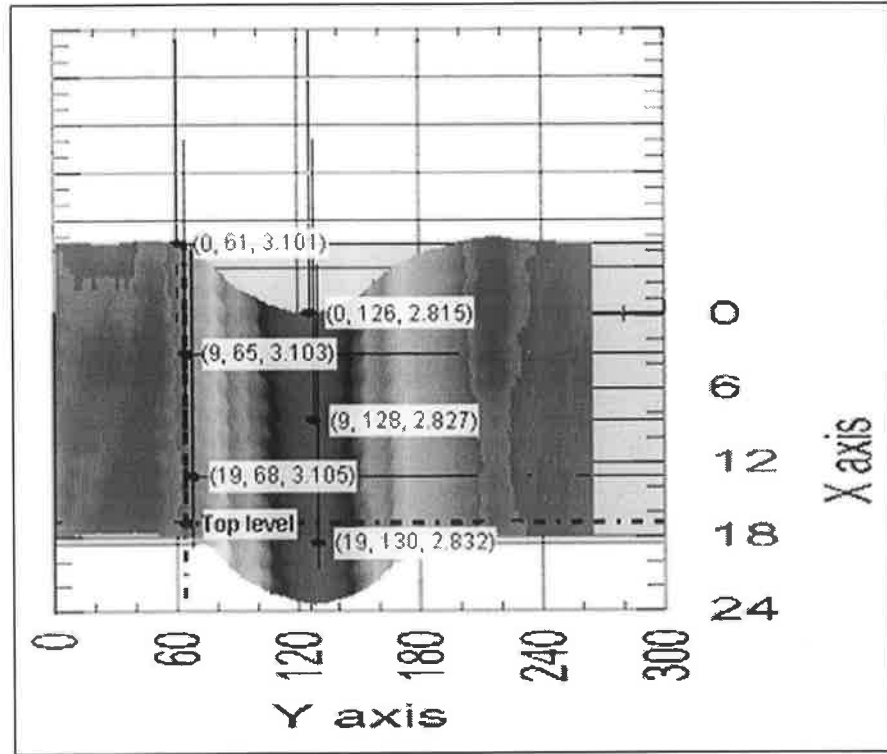


Figure 4.17: Auxiliary view of a sample channel's depth measurement procedure

In a similar manner to the width measurement, the side view of the channel was checked to make sure that the three cursors in the centre of the channel lied at the bottom of the channel. Figure 4.18 shows the side view of the same sample channel of figure 4.17. It can be seen that the three cursors are located at the bottom the channel.

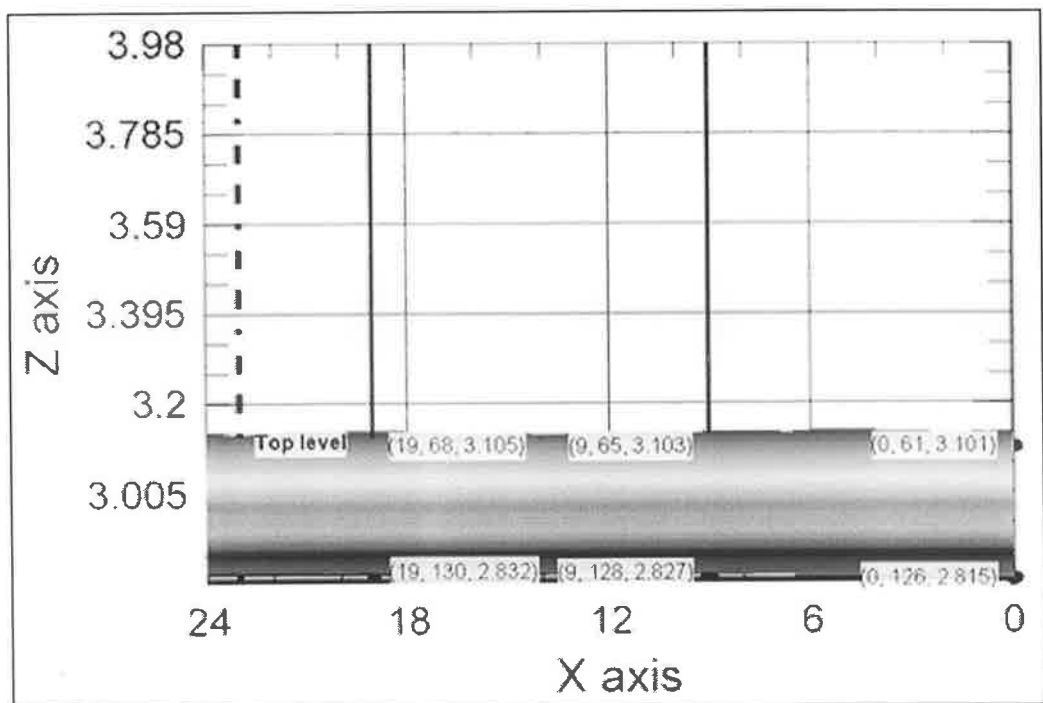


Figure 4.18: Side view of a sample channel's depth measurement procedure.

4.8.6 Surface roughness measurement

The channel surface roughness was measured using a LabVIEW code that was developed for a previous study on surface defect detection using the laser triangulation method [171]. This code was modified to suite the application sought here. The roughness was measured along three lines parallel to the x-axis. Two lines were taken along the centres of the sides of the channels and the third along the bottom of the channels. Figure 4.19 shows a sample channel with one of these lines parallel to the x-axis. The y-coordinate of this line, equal to 93 here, was used in the other part of the code shown in figure 4.20. This code extracts the profile along this line, which is the full length of the channel, and computes a number of surface quality parameters. The calculated surface quality parameters are the average roughness Ra , the RMS roughness Rq , the kurtosis Rku and the skewness Rsk [172]. These parameters are defined in Appendix D.6. These are shown in the fields on the right of figure 4.20. Only the value of Ra was taken as the surface quality measure in this study. The three Ra values, for these profiles indicated, were taken and the average was calculated for each channel. The results for Ra measurements and the remaining above mentioned surface quality measurements are shown in appendix D.5.

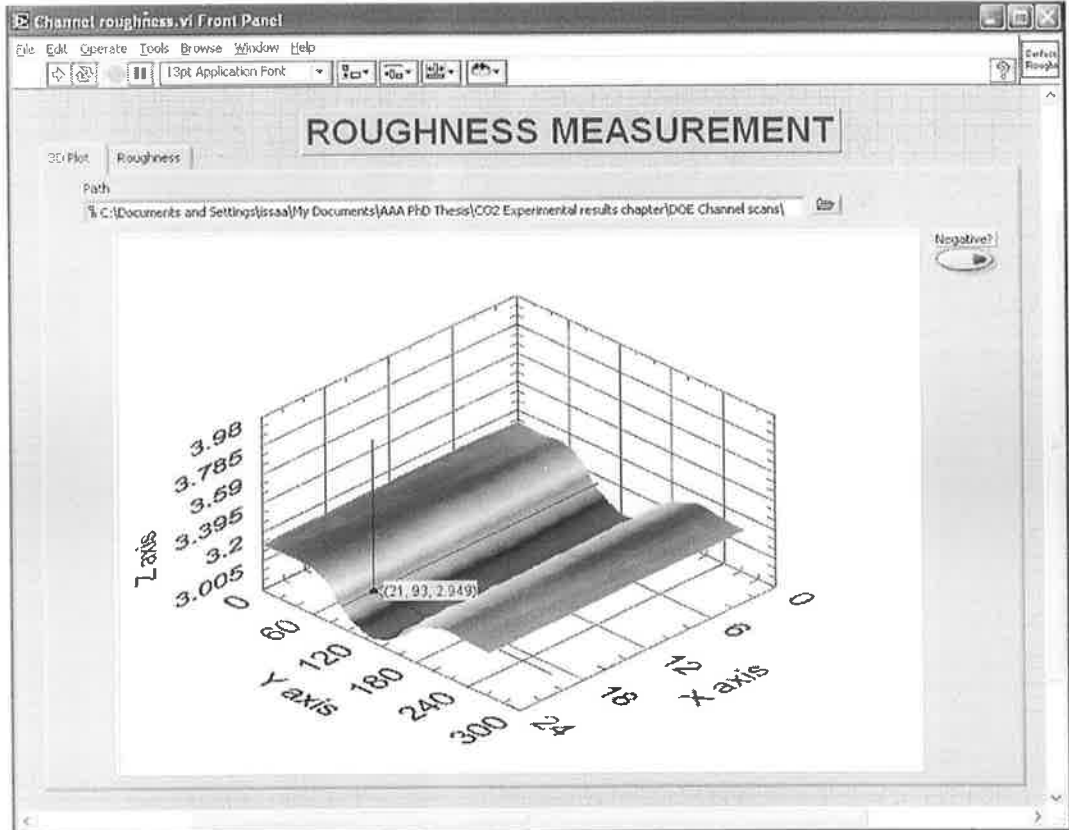


Figure 4.19: Roughness measurement code showing a profile line.

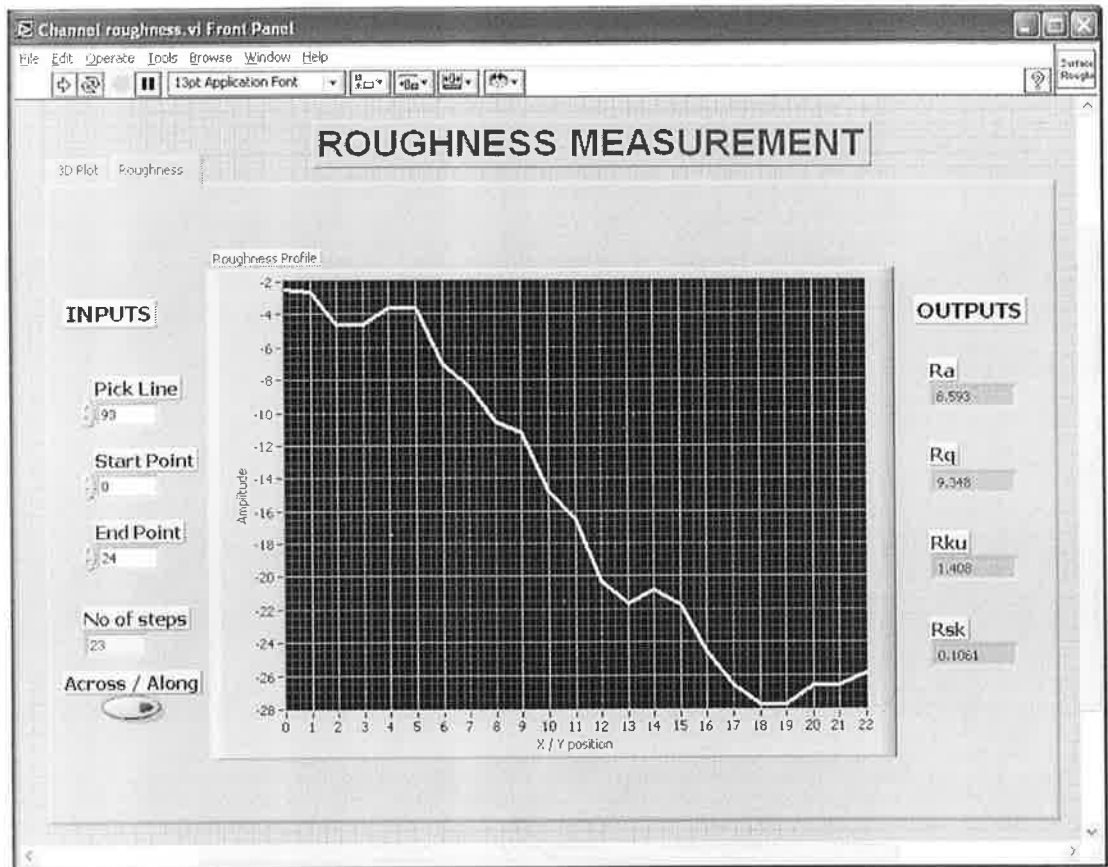


Figure 4.20: Roughness measurement code showing the roughness profile.

Based on the procedures described above three measurements and the average of the response parameters (width, depth and Ra) were obtained from the three dimensional profile scans. Initially, the statistical analysis of variance (ANOVA) of the results was carried out using the three measurements for each response parameter. The statistical analysis of variance was also done using the average values of these response parameters. The magnitudes, trends, mathematical models and the statistical measures obtained in both cases were very close. Hence, for efficient and concise presentation, the ANOVA of the average measurements was used and presented in this study. Table 4.4 contains the average responses from the channels fabricated at $Df = 0$ mm.

Table 4.4: Microchannel experiments results.

Ordered Expt. No.	Run	P (W)	PRF (Hz)	U (mm/min)	Width (μm)	Depth (μm)	Ra (μm)
1	25	18	160	100	315	213	7
2	16	24	160	100	320	279	6
3	22	30	160	100	365	379	13
4	8	18	228	100	248	120	5
5	31	24	228	100	271	225	2
6	29	30	228	100	332	320	12
7	27	18	400	100	163	26	11
8	28	24	400	100	213	120	3
9	18	30	400	100	327	256	6
10	1	18	160	300	308	135	2
11	30	24	160	300	324	202	5
12	32	30	160	300	351	296	5
13	26	18	228	300	231	45	4
14	9	24	228	300	267	148	5
15	4	30	228	300	316	248	3
16	15	18	400	300	118	13	7
17	14	24	400	300	209	48	3
18	20	30	400	300	308	142	4
19	10	18	160	500	302	74	3
20	19	24	160	500	314	130	3
21	3	30	160	500	345	227	5
22	2	18	228	500	222	21	2
23	21	24	228	500	267	89	4
24	7	30	228	500	310	166	6
25	13	18	400	500	81	3	12
26	24	24	400	500	187	30	2
27	12	30	400	500	300	88	4
28	5	24	228	300	265	138	6
29	11	24	228	300	263	147	5
30	6	24	228	300	263	151	6
31	17	24	228	300	269	141	7
32	23	24	228	300	270	151	5

4.8.7 Other measurements

The aspect ratio of the channels (depth/width), channel shape and some quality factors were also calculated and included in appendix D.7. The same measurements were performed on the channels fabricated at $Df = -2$ mm and $Df = 2$ mm. These measurements, channel images and 3D profiles are included in appendices D.8.1 and D.8.2 respectively. These appendices also include a brief discussion on the reasons that prevented the inclusion of these results in the statistical analysis of results.

4.9 Statistical analysis of results

The data obtained from the analysis carried out on the scanned channels was used in a design of experiments analysis software and RSM was applied to the experimental data using the State-Ease Inc., Design-Expert V 7.0.0 statistical analysis software.

4.9.1 Design-Expert software and regression method

The Design-Expert software was used to carry out the analysis of variance, ANOVA, for testing the adequacy of the developed models. The statistical significance of the models and each of the model terms in the regression equation (model equation) were examined using the sequential F-test, lack-of-fit test. The Prob.>F (i.e. the p-value) of the model or the terms was computed by the software utilising the ANOVA technique. If the p-value does not exceed the level of significance (e.g. $\alpha = 0.05$) then the model is considered adequate within a confidence interval of $(1 - \alpha)$. Similarly, if the p-value for the lack-of-fit test exceeds the significance level and then the model may be considered to adequately fit the data [173]. The significance value in this study was taken to be ($\alpha = 0.05$) so that the developed models had a confidence interval of 95%.

The testing for the significance of the model terms and consequently their inclusion in the model equation was performed in the software using a stepwise regression method. This regression method develops a model that includes the possible model terms or their combinations one by one based on their correlation with the response parameter. The correlations of all the possible model terms are calculated first. The term with the highest correlation to the response is added. The regression coefficient of this term is tested (if it is high it remains in the model equation, otherwise it is eliminated). Assuming that this term was significant and included in the equation, the model equation is now adjusted to the effect this term and the correlations of the remaining terms are calculated again in accordance with this latter adjustment. The term with the highest correlation among the remaining terms is now treated the same way as the first term. The search for significant terms continues in this manner until all the remaining terms have insignificant coefficients or all the terms are included. However, during this process, the software regression procedure may look back and eliminate a term that was included at earlier stages depending on the changes in the correlations after each step. Hence, this term selection method is named (stepwise regression) [173].

The discussion and analysis in sections 4.9.2 to 4.9.4 were established around some statistical measures/terms that are explained in appendix D.9. As illustrated earlier, for

the width, depth and *Ra* models, the step-wise regression method was utilised with all the possible combinations of the control parameters except for the terms with cubic combinations because the evaluation of the results from the software indicated that the cubic terms were aliased for the ranges of the data obtained. The terms selected via the step-wise regression method lead to eliminating the insignificant model terms automatically. Eventually, the developed model equations only contained terms that had significant effects on the responses.

Three models for the channel width, depth and *Ra* were developed. The fitness of the third model, however, was not high as will be explained in section 4.9.4. A general summary of the response values is listed in table 4.5

Table 4.5: General result notes.

Response	Units	Minimum	Maximum	Mean	Std. Dev.
<i>Width</i>	µm	81	365	270.1	64.9
<i>Depth</i>	µm	3	379	149.1	94.0
<i>Ra</i>	µm	2	13	5.4	2.9

4.9.2 Width model results

Modelling and analysis of variance for width

Table 4.6 shows the calculated ANOVA results with the significance for the width model and each of the parametric terms in the model. The F value is a test for comparing model/term variance with residual variance. If the variances are close to each other, the ratio will be close to one and it is less likely that the term has a significant effect on the response. If the p-value is greater than 0.10 then the term is generally regarded as not significant. In table 4.6, the only not significant terms was the lack of fit, which is a good indicator [173]. The predicted R-squared and the adjusted R-squared should be within 0.20 of each other. Otherwise there may be a problem with either the data or the model. Adequate precision ratios greater than 4 indicate adequate model discrimination [173].

Table 4.6 shows, at the bottom, the adequacy measures R^2 , adjusted R^2 and predicted R^2 . All the adequacy measures are close to 1, and in reasonable agreement indicating an adequate model [167, 174]. The adequate precision, shown at the bottom of the table too, is greater than 4 indicating adequate model discrimination. Furthermore, this indicates that the model is capable of navigating the design space [173]. The R^2 value of about 0.998 indicates that about 99.8% of the variability in the data is explained by the

model. This fact combined with the satisfactory residual analysis further indicates that the model is a very good fit to the data and that the channel width, within the investigated range of parameters, can be predicted.

Table 4.6: ANOVA results of the width model.

Source	Sum of Squares	df	Mean Square	F Value	p-value Prob > F	Significance
Model	134380.6	10	13438.06	865.2653	< 0.0001	significant
<i>P</i>	60733.51	1	60733.51	3910.58	< 0.0001	significant
<i>PRF</i>	59742.72	1	59742.72	3846.784	< 0.0001	significant
<i>U</i>	321.7703	1	321.7703	20.71852	0.0002	significant
<i>P</i> × <i>PRF</i>	16969.5	1	16969.5	1092.652	< 0.0001	significant
<i>P</i> × <i>U</i>	350.6954	1	350.695	22.581	0.0001	significant
<i>PRF</i> × <i>U</i>	868.8444	1	868.844	55.944	< 0.0001	significant
<i>P</i> ²	934.8291	1	934.829	60.193	< 0.0001	significant
<i>PRF</i> ²	2949.218	1	2949.218	189.898	< 0.0001	significant
<i>P</i> × <i>PRF</i> × <i>U</i>	540.4032	1	540.403	34.796	< 0.0001	significant
<i>P</i> ² × <i>U</i>	373.778	1	373.778	24.067	< 0.0001	significant
Residual	326.142	21	15.531			
Lack of Fit	281.309	16	17.582	1.961	0.235	not significant
Pure Error	44.833	5	8.967			
Cor Total	134706.7	31				
R-Squared		0.998	Adj R-Squared		0.996	
Pred R-Squared		0.992	Adeq Precision		122.522	

Equation 4.1 shows the process model calculated from the experimental results within the investigated ranges of parameters.

$$\begin{aligned}
 \text{Width} = & 929.1719 - 35.375 \times P - 2.18455 \times PRF - 0.45144 \times U + 0.034057 \times P \times PRF + \\
 & + 0.053512 \times P \times U - 0.00167 \times PRF \times U + 0.714387 \times P^2 + 0.001768 \times PRF^2 + \\
 & + 5.54 \times 10^{-5} \times P \times PRF \times U - 0.00134 \times P^2 \times U
 \end{aligned}
 \tag{4.1}$$

Using the model's equation can only give predictions of the width as a result of using any combinations of control parameters within the investigated range of process parameters ($18 \leq P \leq 30$ W, $160 \leq PRF \leq 400$ Hz and $100 \leq U \leq 500$ mm/min). Table 4.7 shows the actual versus predicted value of the investigated combinations of the control parameters in this design of experiments. The right-most column lists the residual values.

Table 4.7: Actual vs predicted and the residual from the width model.

CH. No.	Run	P	PRF	U	Actual Value	Model Predicted Value	Residual
1	25	18	160	100	315	314.5666	0.433373
2	16	24	160	100	320	318.6257	1.37425
3	22	30	160	100	365	364.4541	0.545897
4	8	18	228	100	248	249.761	-1.76104
5	31	24	228	100	271	269.9743	1.025693
6	29	30	228	100	332	331.9568	0.043192
7	27	18	400	100	163	158.839	4.160997
8	28	24	400	100	213	219.9128	-6.91276
9	18	30	400	100	327	322.7558	4.244244
10	1	18	160	300	308	308.2837	-0.28373
11	30	24	160	300	324	319.5214	4.478632
12	32	30	160	300	351	353.1949	-2.1949
13	26	18	228	300	231	234.2824	-3.2824
14	9	24	228	300	267	266.1923	0.807692
15	4	30	228	300	316	320.5381	-4.53812
16	15	18	400	300	118	120.1005	-2.10054
17	14	24	400	300	209	204.2991	4.700855
18	20	30	400	300	308	310.9336	-2.93364
19	10	18	160	500	302	302.0008	-0.00083
20	19	24	160	500	313	320.417	-7.41699
21	3	30	160	500	345	341.9357	3.064293
22	2	18	228	500	222	218.8038	3.196246
23	21	24	228	500	267	262.4103	4.589691
24	7	30	228	500	310	309.1194	0.880573
25	13	18	400	500	81	81.36208	-0.36208
26	24	24	400	500	187	188.6855	-1.68553
27	12	30	400	500	300	299.1115	0.888467
28	5	24	228	300	265	266.1923	-1.19231
29	11	24	228	300	263	266.1923	-3.19231
30	6	24	228	300	263	266.1923	-3.19231
31	17	24	228	300	269	266.1923	2.807692
32	23	24	228	300	270	266.1923	3.807692

Graphical results for width

Figure 4.21, shows that the collected data points were scattered along the trend line relating the predicted and the actual values. This observation agrees that the model has a good fitness value.

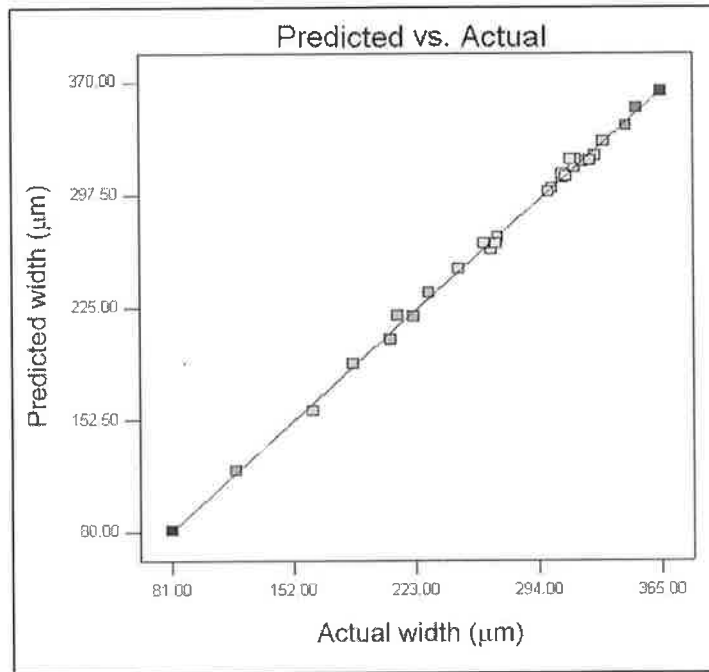


Figure 4.21: Actual versus predicted width values.

Figure 4.22, shows a cubic representation of the investigated levels of the control parameters along with the measured and predicted width values by the model. The actual measurements are indicated by italic numbers within square brackets, for instance [81]. In agreement with the good fitness of the model shown in figure 4.21, it can be seen in the cubic representation that predicted values are in accord with the actual measurements.

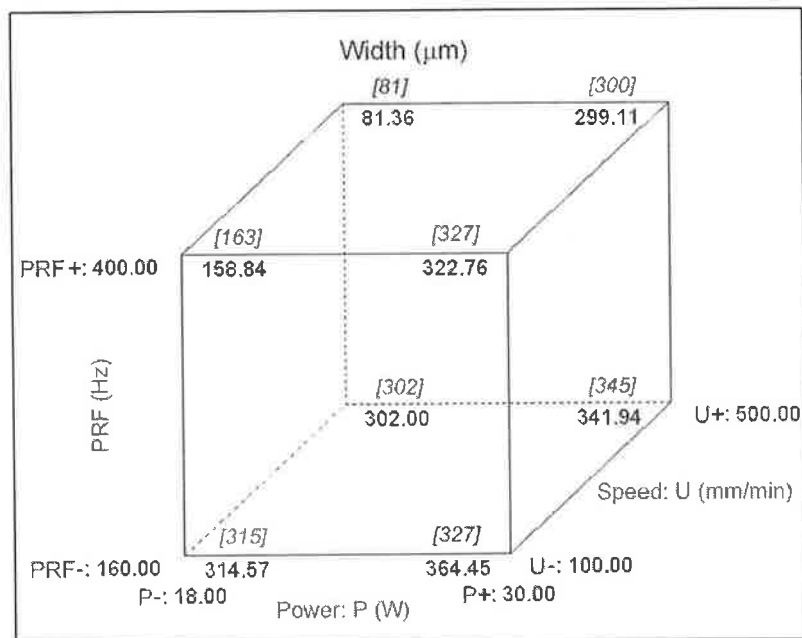


Figure 4.22: Cubic representation of the design points and the experimental and width model results.

Figure 4.23 shows the perturbation plot of the channel width data at the experimented mid values of the control parameters. The perturbation plot enables the comparison of the effects of all the control parameters at a particular point in the design range. The response is plotted by changing only one parameter over its range while holding of the other parameters constant. This tool is very useful in observing the interactive effects of parameters on the response [173]. The x-axis of the plot shows the relative positions of the chosen levels of the parameters to the coded scale. The slopes of the curves show how each parameter affects the response. In figure 4.23, the point selected in the design range was the central point (process parameters for microchannel 14) at $P = 24$ W, $PRF = 228$ Hz and $U = 300$ mm/min.

The figure indicates that the power P has the strongest direct proportional effect on the width, while the PRF has an inversely proportional effect which is slightly smaller than the effect of P . The combination of these two effects is a direct result of the fact that both parameters set the value of the pulse energy $= P / PRF$, which in turn controls the amount of heat delivered to the glass sheets. The lines describing the effects of the parameters on the width are curved due to the quadratic terms in the model.

The speed, as expected too, has an inverse relationship with the width. High translation speeds, within the range investigated, produced relatively narrower channel widths. This is related to the fact that more heat diffused into the material at lower speeds. Changing the set point chosen earlier did not change the nature of the parameters' effects; it only affected the steepness of the slopes (i.e. the relative effect strengths of the parameters). For example, the effect of speed, shown in figure 4.23, becomes larger when $P = 18$ W and $PRF = 400$ Hz were chosen.

The combination of parameters settings is vast and hence, the graphical representations (perturbation plots, contours and 3D plots) in the forthcoming discussion were all based on the same reference point ($P = 24$ W, $PRF = 228$ Hz, and $U = 300$ mm/min), which represents the mid point of the experimented parameter ranges.

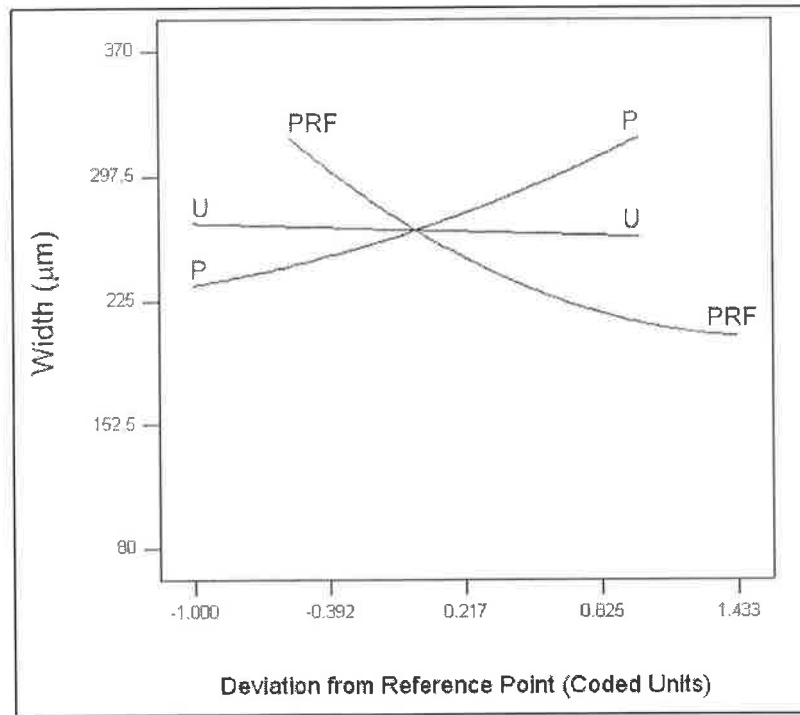


Figure 4.23: Perturbation plot of the process control variables' effects on the width.

Table 4.8 lists the relative effects of the model parameters on the response in a numerical representation, called the “Coefficient Estimate”. The coefficient estimate is a regression coefficient representing the expected change in response per unit change in a certain design factor when all remaining factors are held constant. This numerical representation also shows the interaction of the parameters' effect on the response. For instance, it can be seen that $P \times PRF$ has the strongest interaction effect on the response. The interesting effects of the parameters on the response are illustrated later in this section by the means of contour and 3D surface plots.

Table 4.8: Relative effects of the process model parameters on width.

Term	Coefficient Estimate
P	58.94
PRF	-57.61
U	-7.36
$P \times PRF$	36.48
$P \times U$	5.49
$PRF \times U$	-8.26
P^2	11.22
PRF^2	25.46
$P \times PRF \times U$	7.97
$P^2 \times U$	-9.67

The following figures 4.24 – 4.29, show the combined effects of two parameters, at a time, on the width. These figures show the effect of changing the two selected parameters on the response, while the third parameter is held constant. As explained for the perturbation concept, the third parameter could be changed, however, it was again held at the same value chosen for the perturbation figure. The red spheres on these graphs indicate the design points (i.e. the investigated combinations of control parameters). It can be noticed, particularly on the 3D plots, that these spheres are located very close to the surfaces, which meant that the model fits the data points to a good extent. These figures, do not present effects that are different from the ones shown earlier in the perturbation figure. However, they offer a visual aid to the selection of desired ranges of the parameters by observing their effects in terms of the numerical values of the response. Furthermore, they are useful in the process of optimising the ranges processing parameters to meet certain response criterion for example. Based on these facts, and to avoid redundancy, the comments made on each figure will be brief, as well as the discussions of the results from the depth and Ra models. Figure 4.24 the contour plot of the effect of P and PRF on the channel width. Each contour curve represents the combinations of the two parameters that will predict a constant channel width value. This width value is viewed inside the box located at the middle of each contour curve. It can also be seen from the contour plot that P has a direct proportional effect on the predicted width, while PRF has an inverse proportional effect.

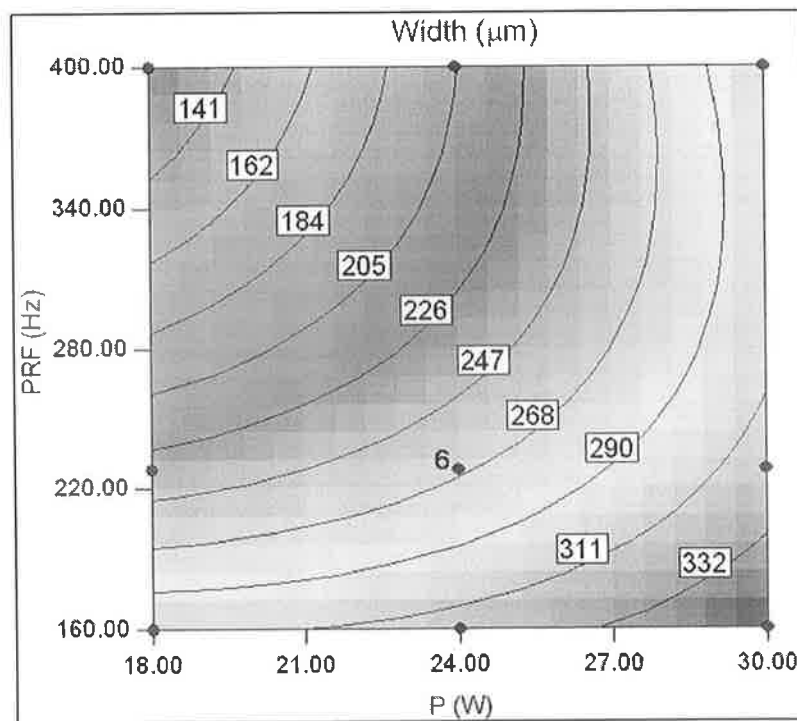


Figure 4.24: P and PRF contour showing the interactive effect on the width.

Figure 4.25 holds the same data as figure 4.24, except that it has the P and PRF values on the lateral axes and the predicted width on the vertical axis. An extra advantage of the 3D plot is that it is easier to visualise how the effect of one of the parameters changes by changing the value of the other parameter. For example, consider the effect of PRF at $P = 30$ W, which is the curve lying on the PRF -Width plane at the back of the plot. When this is compared to the PRF effect at $P = 18$ W represented by the curve lying on the PRF -Width plane on the front of the plot, it can be seen the PRF effect is stronger in the latter case. These observations are possible to make from the contour plot, however, they are not as straightforward.

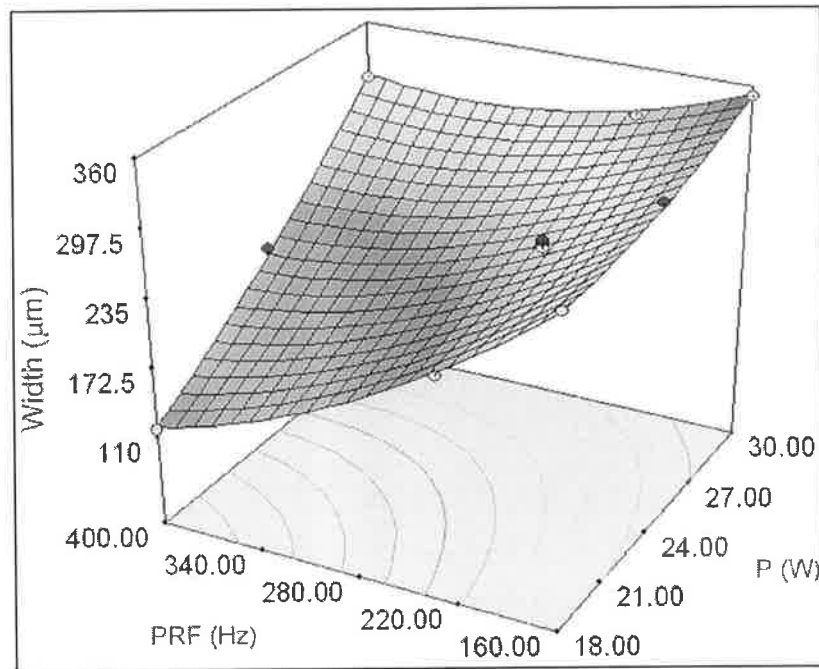


Figure 4.25: 3D view of the interactive effect of P and PRF on width.

Figures 4.26 and 4.27 show that both P and U have a direct proportional effect on the width. However, P has stronger effect than U . This means that variations in P will result in larger changes in the width than the ones resulting from even large changes in U .

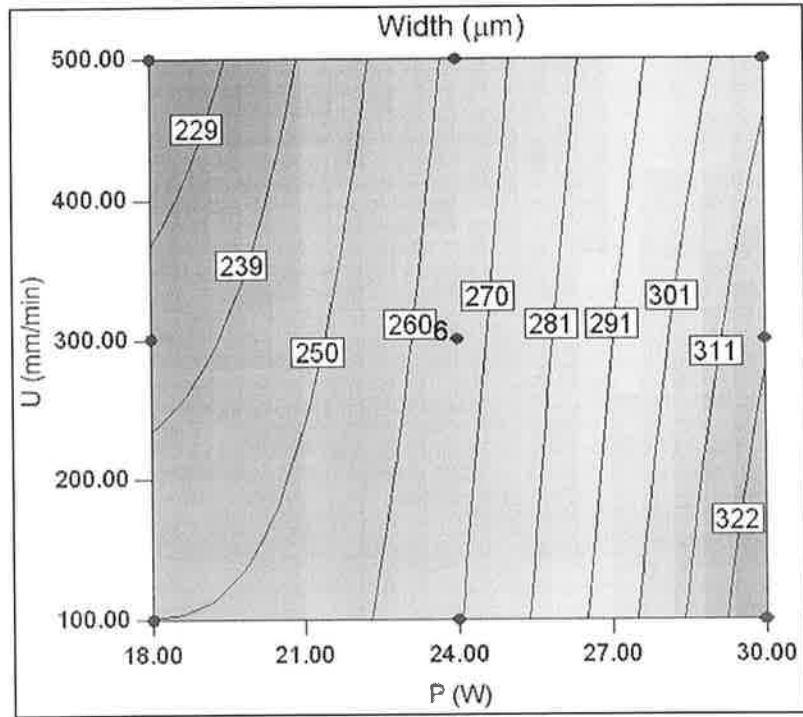


Figure 4.26: P and U contour showing the interactive effect on the width.

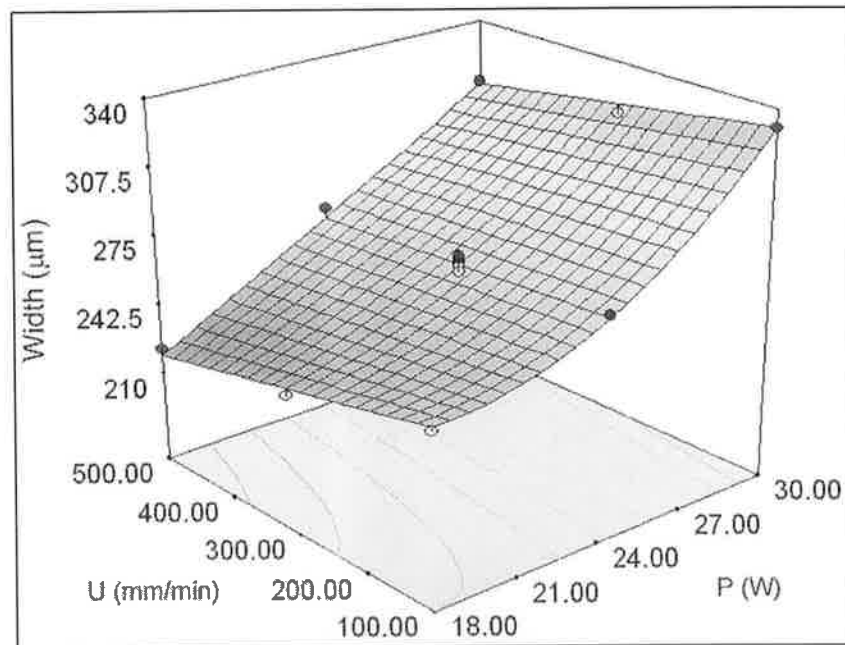


Figure 4.27: 3D view of the interactive effect of P and U on width.

Figures 4.28 and 4.29 show that both PRF and U have inversely proportional effects on the width. Similarly, PRF has stronger effect on the response than U exhibits.

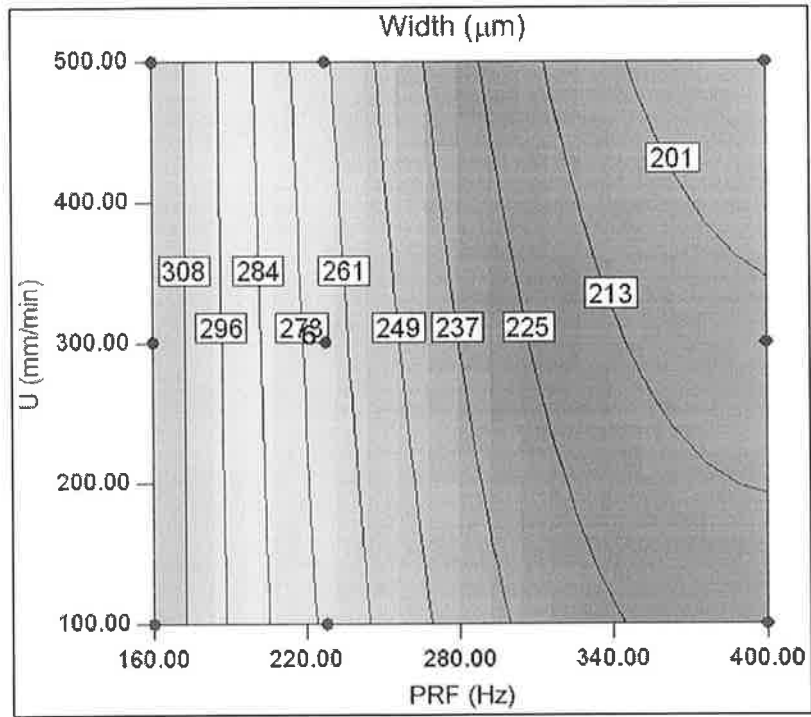


Figure 4.28: *PRF* and *U* contour showing the interactive effect on the width.

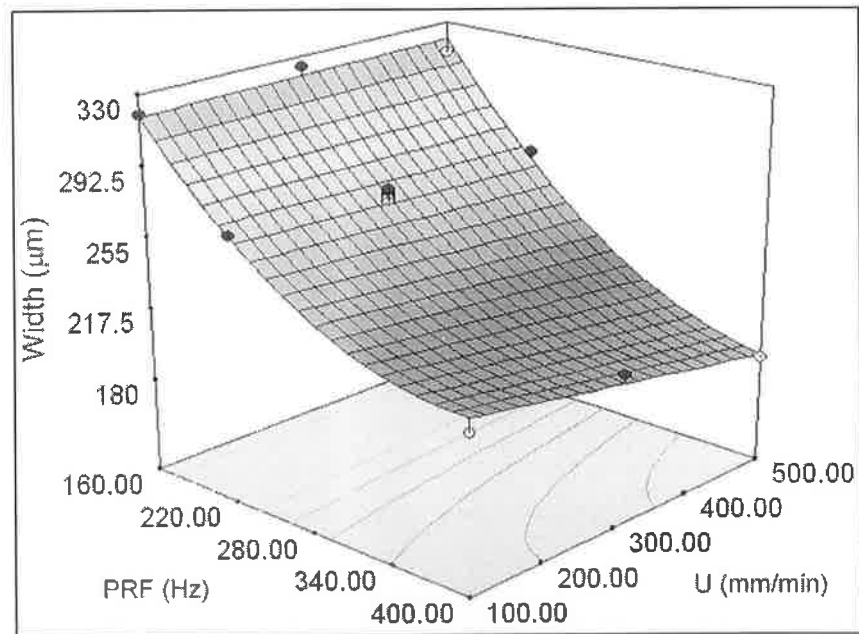


Figure 4.29: 3D view of the interactive effect of *PRF* and *U* on width.

4.9.3 Depth model results

Modeling and analysis of variance for depth

For the depth model, the step-wise regression method was also utilised with all the possible combinations of the control parameter except for the terms with cubic combinations because the evaluation of the results from the software indicated that the cubic terms were aliased for the ranges of the data obtained. The terms selected along

with the step-wise regression method lead to eliminating the insignificant model terms automatically [173]. Table 4.9 shows the calculated ANOVA results with the significance for the depth model and each of the terms in the model.

Table 4.9: ANOVA analysis of depth model

Source	Sum of Squares	df	Mean Square	F Value	p-value Prob > F	significance
Model	281132.4	11	25557.49	291.041	< 0.0001	significant
<i>P</i>	30830.76	1	30830.76	351.091	< 0.0001	significant
<i>PRF</i>	81204.5	1	81204.5	924.732	< 0.0001	significant
<i>U</i>	62469.1	1	62469.1	711.379	< 0.0001	significant
<i>P</i> × <i>PRF</i>	108	1	108	1.230	0.2806	not significant
<i>P</i> × <i>U</i>	4714.455	1	4714.455	53.687	< 0.0001	significant
<i>PRF</i> × <i>U</i>	2193.298	1	2193.298	24.976	< 0.0001	significant
<i>P</i> ²	825.476	1	825.476	9.400	0.0061	significant
<i>PRF</i> ²	3033.713	1	3033.713	34.547	< 0.0001	significant
<i>U</i> ²	678.938	1	678.938	7.732	0.0115	significant
<i>P</i> × <i>PRF</i> × <i>U</i>	2270.681	1	2270.681	25.858	< 0.0001	significant
<i>P</i> × <i>PRF</i> ²	639.447	1	639.447	7.282	0.0138	
Residual	1756.282	20	87.814			
Lack of Fit	1612.282	15	107.485	3.732	0.0764	not significant
Pure Error	144	5	28.8			
Cor Total	282888.7	31				
R-Squared	0.994		Adj R-Squared		0.990	
Pred R-Squared	0.980		Adeq Precision		65.381	

In table 4.9, the *P*×*PRF* term is not significant as can be seen from its p-value that is larger than 0.1, however this term was automatically added to support the hierarchy of the model. The step-wise regression method detected that this model term was not significant but it was required by other significant model terms, in this case, these dependant terms were *P*×*PRF*×*U* and *P*×*PRF*². The other non-significant term was the lack of fit, which is a good indicator. The table also shows that the adequacy measures *R*², adjusted *R*² and predicted *R*² are all close to 1, and in reasonable agreement indicating an adequate model [167, 174]. The adequacy precision is greater than 4 indicating adequate model discrimination. Furthermore, this indicates that the model is capable of navigating the design space [173]. The *R*² value of about 0.994 indicates that about 99.4% of the variability in the data is explained by the model. This fact combined with the satisfactory residual analysis further indicates that the model is a very good fit to the data and that the channel depth, within the investigated range of parameters, can be predicted. Equation 4.2 shows the process model calculated from the experimental results within the investigated ranges of parameters.

$$\begin{aligned}
\text{Depth} = & 794.4823 - 16.715 \times P - 4.95908 \times PRF - 0.95849 \times U + 0.133888 \times P \times PRF + \\
& + 0.01502 \times P \times U + 0.00327 \times PRF \times U + 0.298387 \times P^2 + 0.006283 \times PRF^2 + \\
& + 0.000244 \times U^2 - 0.00011 \times P \times PRF \times U - 0.00019 \times P \times PRF^2
\end{aligned}
\tag{4.2}$$

Using the model's equation can only give predictions of the depth as a result of using any combinations of control parameters within the investigated range of process parameters ($18 \leq P \leq 30$ W, $160 \leq PRF \leq 400$ Hz and $100 \leq U \leq 500$ mm/min). Table 4.10 shows the actual versus predicted values of the investigated combinations of the control parameters in this design of experiments. The right-most column lists the residual values.

Table 4.10: Actual versus predicted of the design points.

CH. No.	Run	P	PRF	U	Actual Value	Model Predicted Value	Residual
1	25	18	160	100	213	210.9483	2.051676
2	16	24	160	100	279	283.9735	-4.97347
3	22	30	160	100	379	378.4825	0.517518
4	8	18	228	100	120	123.513	-3.51303
5	31	24	228	100	225	217.1329	7.867079
6	29	30	228	100	320	332.2367	-12.2367
7	27	18	400	100	26	23.69725	2.302751
8	28	24	400	100	120	123.4097	-3.40974
9	18	30	400	100	256	244.6061	11.3939
10	1	18	160	300	135	132.086	2.913978
11	30	24	160	300	202	201.3441	0.655914
12	32	30	160	300	296	292.086	3.913978
13	26	18	228	300	45	61.34409	-16.3441
14	9	24	228	300	148	141.9355	6.064516
15	4	30	228	300	248	244.0108	3.989247
16	15	18	400	300	13	3.752688	9.247312
17	14	24	400	300	48	67.01075	-19.0108
18	20	30	400	300	142	151.7527	-9.75269
19	10	18	160	500	74	72.70759	1.29241
20	19	24	160	500	130	138.1986	-8.19858
21	3	30	160	500	227	225.1734	1.826568
22	2	18	228	500	21	18.65901	2.340986
23	21	24	228	500	89	86.22192	2.778082
24	7	30	228	500	166	175.2687	-9.26869
25	13	18	400	500	3	3.291998	-0.292
26	24	24	400	500	30	30.09564	-0.09564
27	12	30	400	500	88	78.38314	9.616855
28	5	24	228	300	138	141.9355	-3.93548
29	11	24	228	300	147	141.9355	5.064516
30	6	24	228	300	151	141.9355	9.064516
31	17	24	228	300	141	141.9355	-0.93548
32	23	24	228	300	151	141.9355	9.064516

Graphical results for depth

Figure 4.30, shows that the collected data points were scattered along the trend line relating the predicted and the actual values. This observation means that the model has a good fitness value.

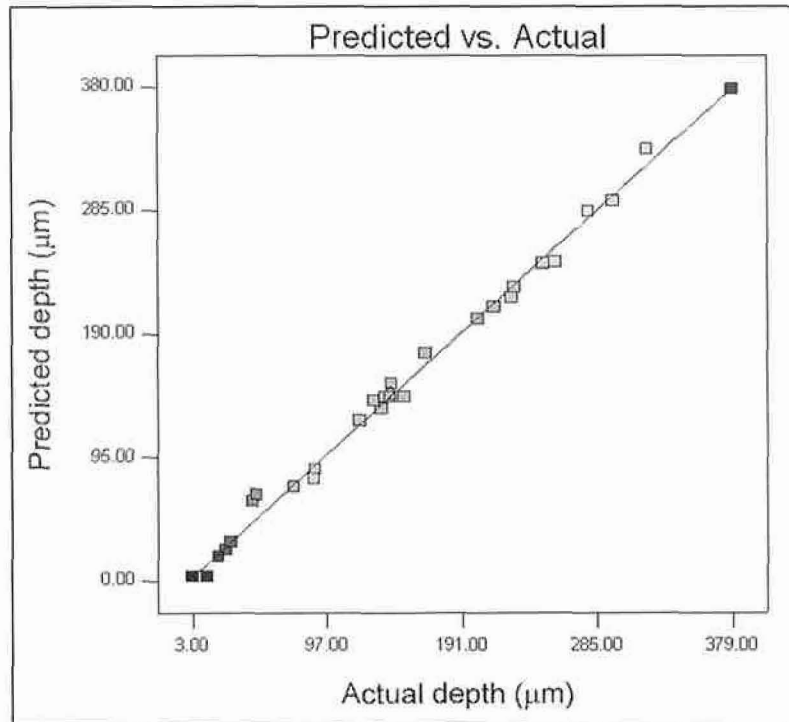


Figure 4.30: Actual versus predicted scattering of the data points.

Figure 4.31, shows a cubic representation of the investigated levels of the control parameters along with the measured and predicted depth values by the model. The actual measurements are indicated by italic figures within square brackets. The predicted and actual values on the design points shown in the cubic representation are in agreement, indicating that the model is accurate.

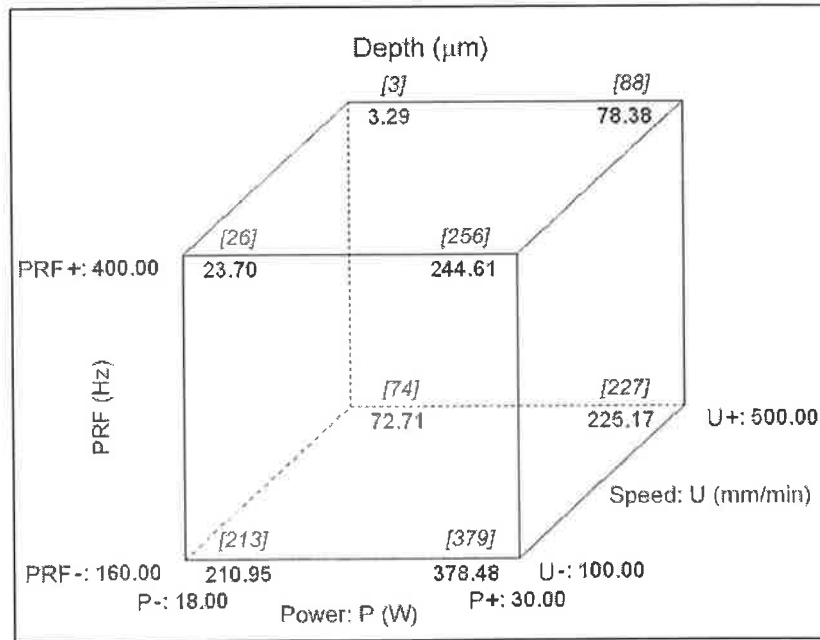


Figure 4.31: Cubic representation of the design points and the experimental and depth model results.

The perturbation of the process parameters in figure 4.32 was obtained at the same point location ($P = 24$ W, $PRF = 228$ Hz, and $U = 300$ mm/min). The figure shows that P has a direct proportional effect and it had the strongest effect on the depth. The second strongest effect was due to PRF , which has an inverse proportional effect on the depth. Similar to their effect on the width, the combination of these two effects is a direct result of the pulse energy = P / PRF . The speed U had an inverse effect on the depth.

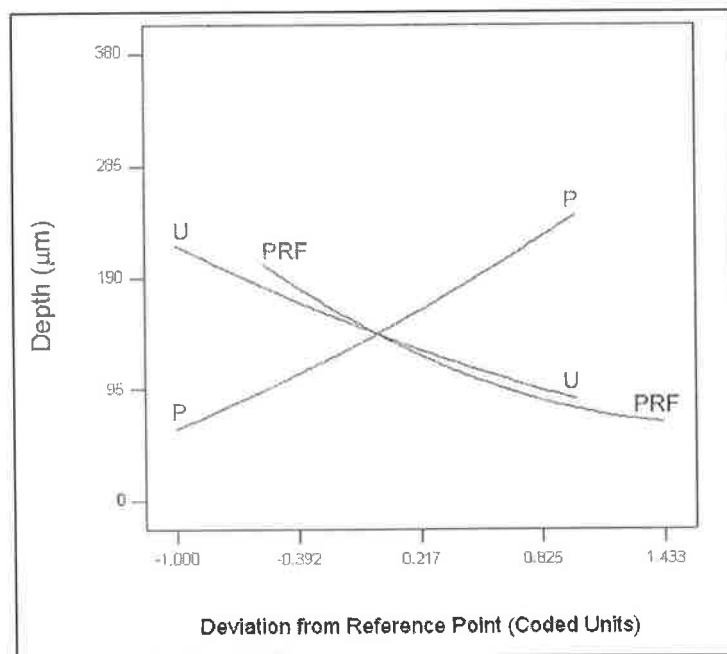


Figure 4.32: Perturbation plot of the process control variables' effects on the depth.

Table 4.11 lists the relative effects of the model parameters on the response in a numerical representation. It can be seen that PRF^2 and $P \times U$ have the strongest interaction effects on the depth. The interesting effect of the parameters on the response will be illustrated by the means of contour and 3D surface plots.

Table 4.11: Relative effects of the process model parameters on depth.

Factor	Coefficient Estimate
P	93.05
PRF	-67.17
U	-59.77
$P \times PRF$	-3
$P \times U$	-20.11
$PRF \times U$	13.12
P^2	10.74
PRF^2	26.28
U^2	9.74
$P \times PRF \times U$	-16.34
$P \times PRF^2$	-16.05

The following figures 4.33 – 4.38, show the combined effects of two parameters, at a time, on the depth. The red spheres on these graphs indicate the design points, and their locations on the 3D plots mean that the model fits to a good extent the data points. Figure 4.33 the contour plot of the effect of P and PRF on the channel depth. It can be seen from the contour plot that P has a direct proportional effect on the predicted depth, while PRF has an inverse proportional effect.

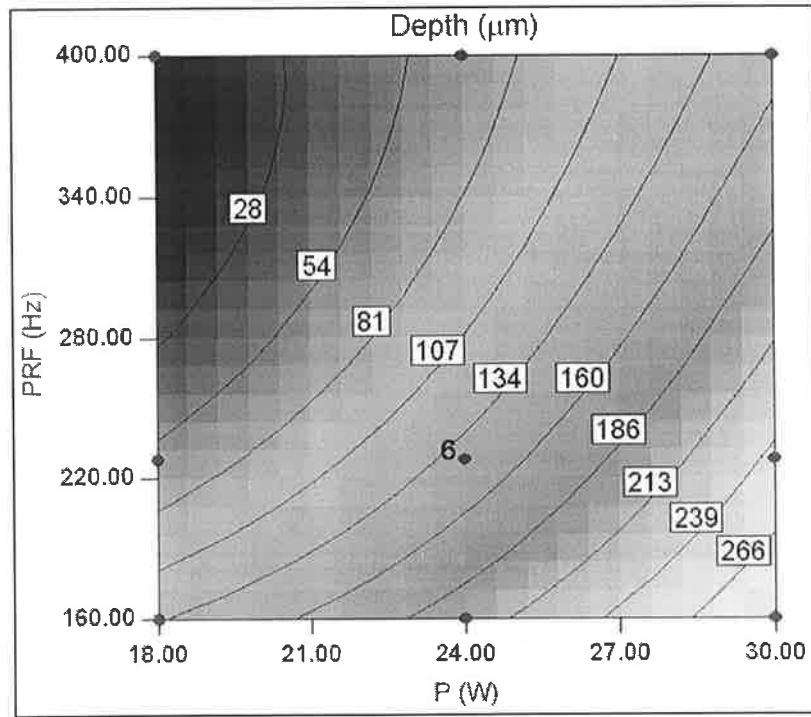


Figure 4.33: P and PRF contour showing the interactive effect on the depth.

The 3D plot in figure 4.34 shows that as P is increase the channel depth increases. The opposite effect is induced by changing the value of PRF . The deepest channel depths were produced when using high P in combination with low PRF settings, while holding U constant, in this case at its mid-range = 300 mm/min.

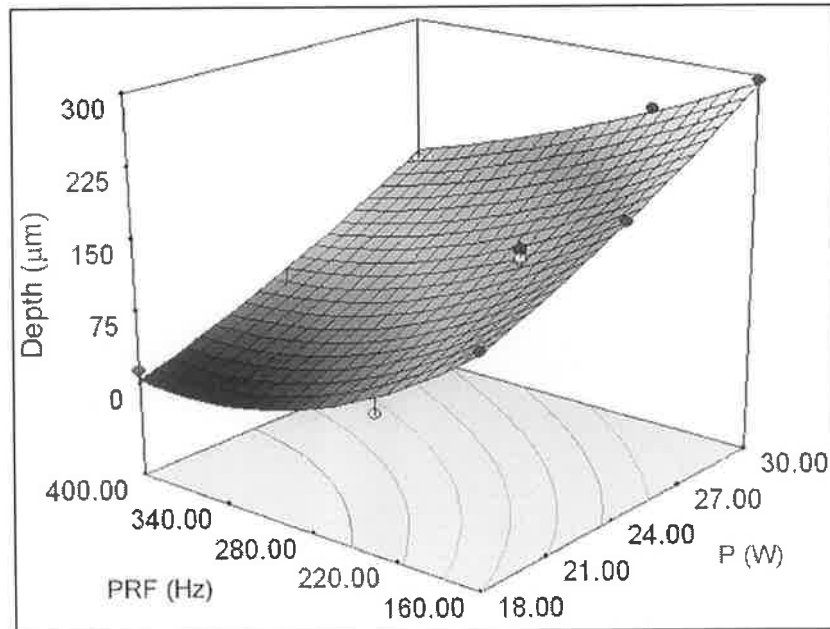


Figure 4.34: 3D view of the interactive effect of P and PRF on depth.

Figures 4.35 and 4.36 show that P has a direct proportional effect on the depth, while U has an inversely proportional effect. However, P has stronger effect than U . In a similar to their effect on the width, small changes in P will affect the depth in a magnitude larger than changes induced by changes in U .

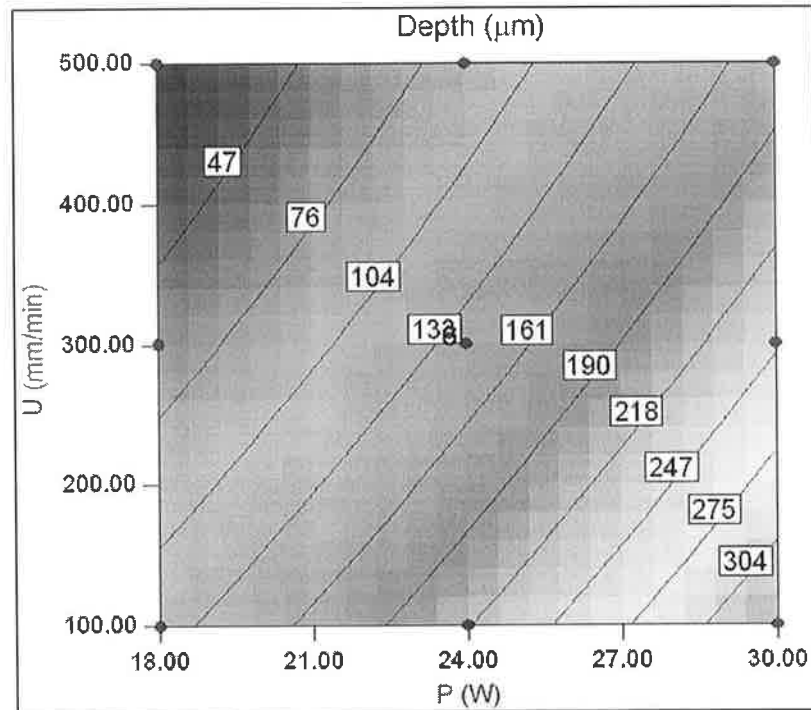


Figure 4.35: P and U contour showing the interactive effect on the depth.

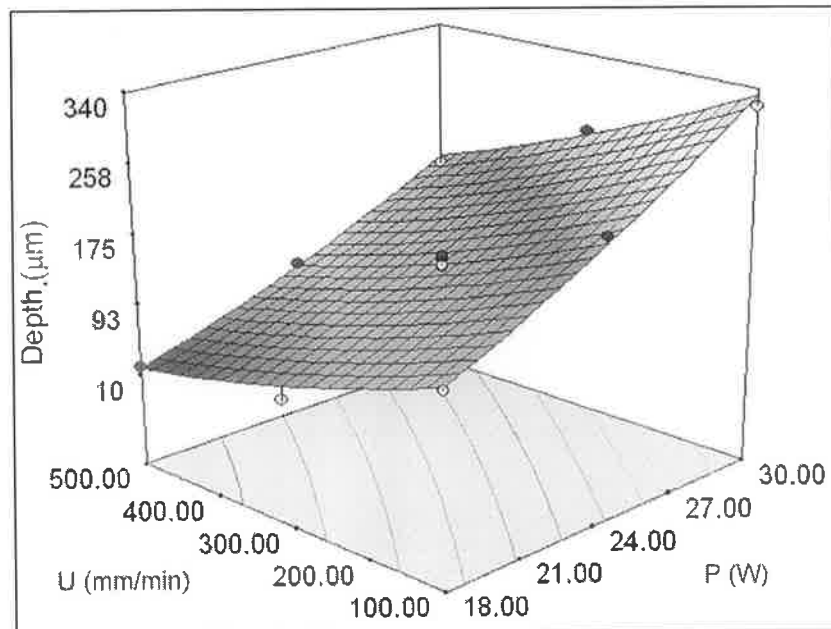


Figure 4.36: 3D view of the interactive effect of P and U on depth.

Figures 4.37 and 4.38 show that both PRF and U have inversely proportional effects on the depth. Similarly, PRF , as can be seen from the slopes of the contour lines and the 3D surface, has a stronger effect on the depth than U exhibits.

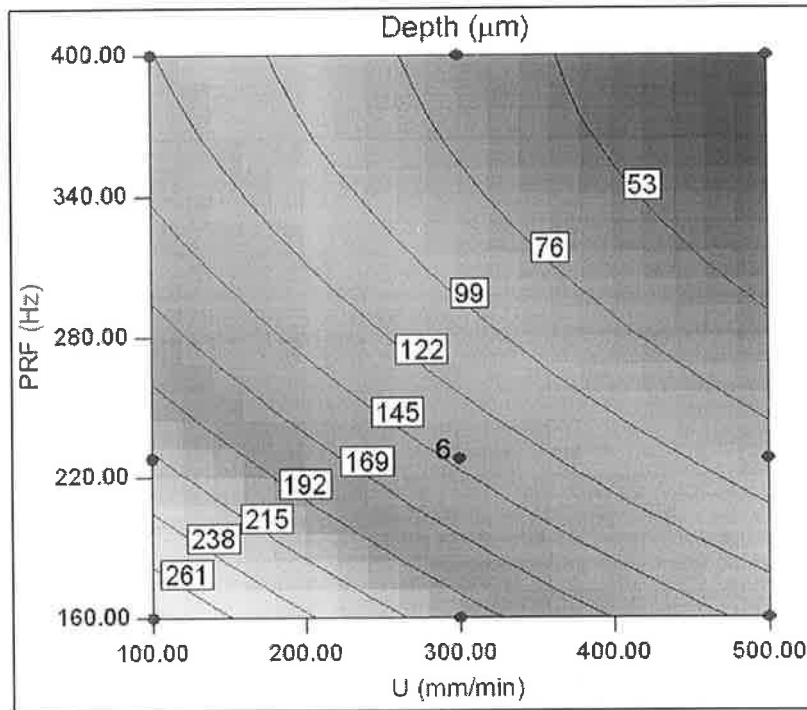


Figure 4.37: PRF and U contour showing the interactive effect on the depth.

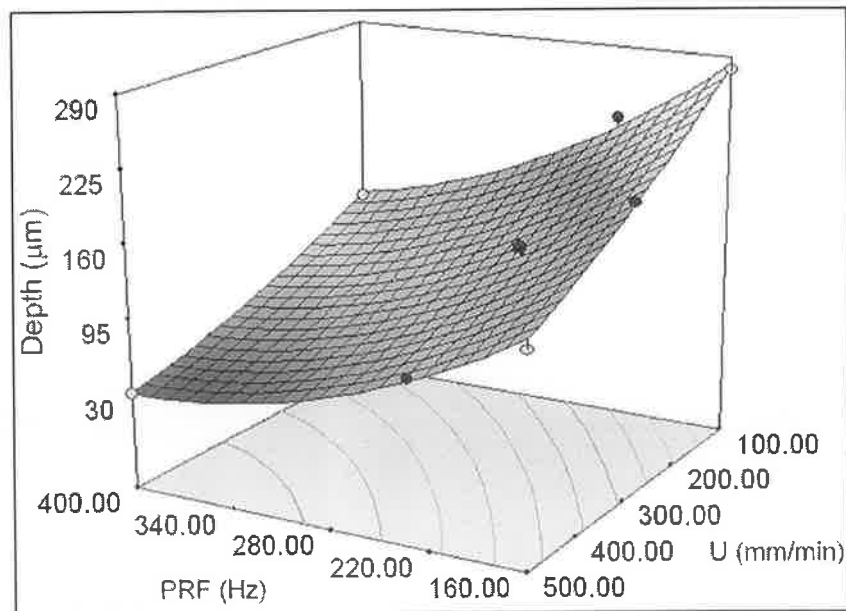


Figure 4.38: 3D view of the interactive effect of PRF and U on depth.

4.9.4 Ra model results

When attempting to model a certain process using statistical means, such as ANOVA, process related knowledge is very essential. This is important because statistical figures

and measures alone cannot, without process knowledge, be used to make process-related judgments. Additionally, results obtained from statistical procedure on scientific or engineering contexts do not always produce logical conclusions. The surface roughness, as opposed to channel width and depth, is relatively harder to anticipate in terms of the process parameters. In other words, the discussion of the width and depth statistical results was based on the amounts or rates of heat deposited into the material. The later were easy to visualise in terms of P , PRF and U , as combinations of the three parameters can lead to educated estimates of parameters such as pulse energies, material removal rates or respective irradiation times. Hence, a discussion of this process's surface roughness, the proposed process parameters to affect the roughness and estimating calculations of the roughness are introduced in this section. Following this discussion, the experimental roughness results will be presented and discussed.

Machining-induced surface roughness

Laser fabrication of the channels, performed in this study, is considered a machining process and the laser beam, to a certain extent, can be treated as a conventional machining tool. This treatments takes into consideration the unique properties of laser machining, most important of which in this context, is the fact that there is no physical contact between the laser beam and the material being machined.

The channel making process involves a moving sample and a stationary laser beam. The laser beam is, pulsed so it can be treated as a single-point tool that is rotating/reciprocating around/along its axis while stationary relative to the translation direction of the sample. Milling and drilling using single-point tools are, hypothetical, examples of such a machining process. Besides the depth of cut, tool geometry and material, the combination of the sample's speed and the feed of the machining tool are the most important factors contributing to the surface finish quality [175]. It is also worth mentioning that there is no optimal combinational setting of the sample speed and the feed. Different combinations of speed and feed can produce similar effects on the surface roughness and suitable settings can be obtained from experimentation or specific tables [170, 176].

Feed is the amount of material processed/removed for each revolution or per pass of the tool over the sample. Feed is measured in units of length/revolution, length/pass, length/tooth, length/time, or other appropriate unit for the particular process [176]. In

accord with the process parameters under investigation, the feed's unit will be recorded in $\mu\text{m}/\text{pulse}$. The feed has been used in the calculations of the scan length of the channels based on figure 4.6. The same expression used for the feed at that stage will be employed in this discussion. The feed, f , in ($\mu\text{m}/\text{pulse}$) is given by,

$$f = U / PRF \quad (4.3)$$

The ideal (theoretical) surface roughness from a specific process is a function of only feed and tool geometry. It represents the best possible finish which can be obtained for a given tool shape and feed. It can be achieved only if the built-up-edge, chatter and inaccuracies in the machine tool movements are eliminated completely [175]. For a sharp tool without nose radius, the maximum height of unevenness, R_{MAX} , shown in figure 4.39, is given by,

$$R_{MAX} = \frac{f}{\cot \alpha + \cot \beta} \quad (4.4)$$

where f is the feed,

α is the major cutting edge angle, and

β is the working minor cutting edge angle.

Where the laser beam is treated to be uniform and of Gaussian distribution, the angles α and β become virtually equal. Using this assumption and substituting equation 4.3 in equation 4.4, the expression for R_{MAX} becomes,

$$R_{MAX} = \frac{U}{2 \times PRF \times \cot \alpha} \quad (4.5)$$

Equation 4.5 can be used to define the best average surface roughness, R_a , using this expression,

$$R_a = \frac{R_{MAX}}{4} = \frac{U}{8 \times PRF \times \cot \alpha} \quad (4.6)$$

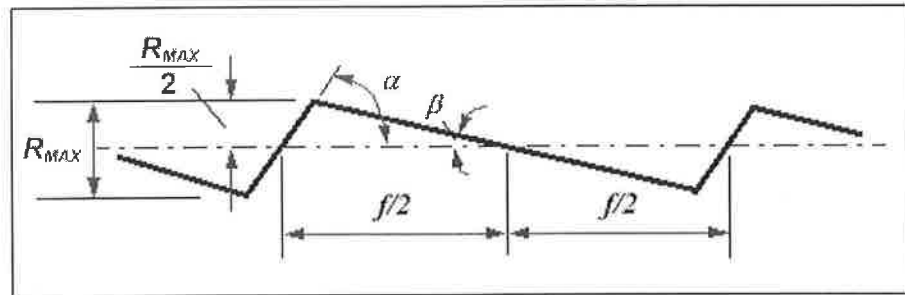


Figure 4.39: Idealised model of surface roughness, after [175].

Equation 4.6 shows that, ideally, the surface roughness depends on the sample's speed, pulse repetition frequency and the focused laser beam geometry. The latter parameter is usually assumed to be constant, however, the first two parameters were considered as changing process parameters in this study. Based on equation 4.6, U is directly proportional and PRF is inversely proportional to the roughness. Investigation of figure 4.6 shows that both parameters affect the stretching and compaction of the disks representing laser irradiated regions. As mentioned earlier, the combination of both parameters sets the expected surface finish quality. Generally speaking, however, increasing speed and fixing PRF increases the roughness. On the other hand, increasing PRF and fixing U decreases the surface roughness. It is worth mentioning with practical conventional cutting tools, Ra becomes proportional to f^2 . This still preserves the effects of the involved process parameters, but yet it accounts for the radius of the tool corner [175]. As mentioned earlier, the depth of cut is another parameter that may affect the machined surface roughness. Keeping in mind that laser processing is a non-contact process; the depth of cut may not have as a significant effect on the roughness as it does in conventional machining processes. An analogous parameter to the conventional depth of cut may be possible to develop for this process. The depth of cut using laser may depend on the pulse energy, pulse width, material properties, and laser emitting wavelength. This parameter's effect will however be indirect on the surface roughness, because it is involved in an interaction with the combination of U and PRF . However, for simplicity, it is proposed that higher pulse energies will contribute to high surface roughness.

Modelling and analysis of variance for Ra

Table 4.12 shows the ANOVA results obtained from the channels Ra measurements. The step-wise regression method was also utilised, in this case, with all the possible combinations of the control parameter except for the terms with cubic combinations

because the evaluation of the results from the software indicated that the cubic terms were aliased for the ranges of the data obtained.

Table 4.12: ANOVA analysis of Ra model

Source	Sum of Squares	df	Mean Square	F Value	p-value Prob > F	significance
Model	160.908	8	20.113	4.251482	0.0030	significant
<i>P</i>	0.083	1	0.0832	0.017588	0.8956	not significant
<i>PRF</i>	0.523	1	0.5233	0.110606	0.7425	not significant
<i>U</i>	0.217	1	0.2168	0.045807	0.8324	not significant
<i>P</i> × <i>PRF</i>	73.487	1	73.487	15.53332	0.0007	significant
<i>P</i> × <i>U</i>	8.333	1	8.333	1.76146	0.1975	not significant
<i>PRF</i> × <i>U</i>	12.385	1	12.385	2.617859	0.1193	not significant
<i>P</i> ²	23.228	1	23.228	4.909849	0.0369	significant
<i>P</i> ² × <i>U</i>	9	1	9	1.902377	0.1811	not significant
Residual	108.811	23	4.731			
Lack of Fit	105.478	18	5.860	8.789826	0.0122	significant
Pure Error	3.333	5	0.667			
Cor Total	269.719	31				
R-Squared		0.597	Adj R-Squared			0.456
Pred R-Squared		0.0596	Adeq Precision			8.683

It can be seen from the p-values in table 4.12 that three main process parameters are considered not significant. They were added to the model terms in the regression procedure to support the hierarchy of the model. In other words, there were other significant parameters that depended on them. The significant parameters in table 4.12 were *P*×*PRF* and *P*². This could be possible for the range of the processing parameters used in the study. The lack of fitness, however, was significant as can be seen from its p-value. This meant that the model is not able of predicting the design points. Furthermore, the adequacy measures R², adjusted R² and predicted R² are not close to 1. The adjusted R² and predicted R² are not in agreement, and the difference between them is larger than 0.2, which meant that there may be a problem with the data [173]. An explanation of the behaviour of the collected data and the proposed reason and the possible solutions to overcome it will be presented later in this section.

Graphical results for the Ra

Figure 4.40 shows the distribution of the actual versus model-predicted Ra values. It can be seen that the data points are scattered around the trend line suggesting the poor fitness of the model.

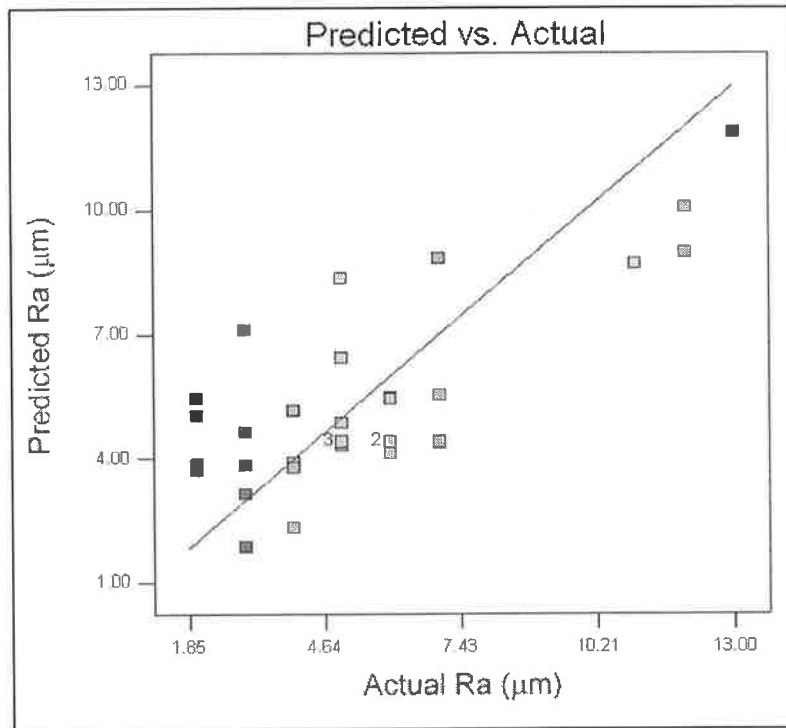


Figure 4.40: Actual versus predicted scattering of the data points.

Figure 4.41 shows the effects of the process parameters on Ra . The figure shows that P has a non-linear effect on Ra , it is inversely proportional to Ra at low values of PRF and U , while it has the opposite effect at high values of PRF and U within the investigated range of parameters. Most importantly, are the effects of PRF and U , which can be seen from the figure to contradict with the expected behaviour from equation 4.6. According to the model, PRF is directly proportional to Ra while U is inversely proportional. Moreover, from the graphical analysis tools in the software, at high P values, both PRF and U have an inversely proportional effect on Ra . This latter effect is shown in figure 4.42.

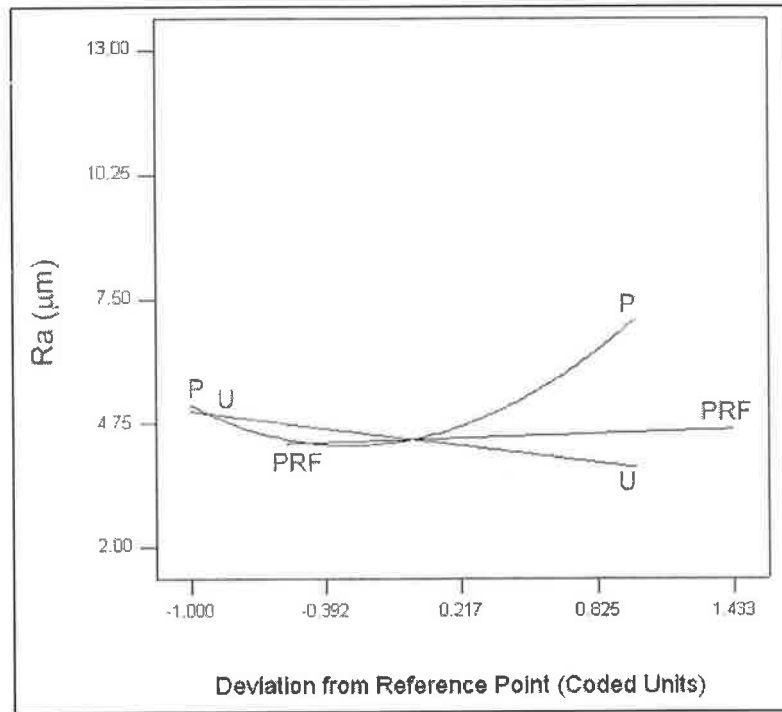


Figure 4.41: Perturbation plot of the process control variables' effects on Ra .

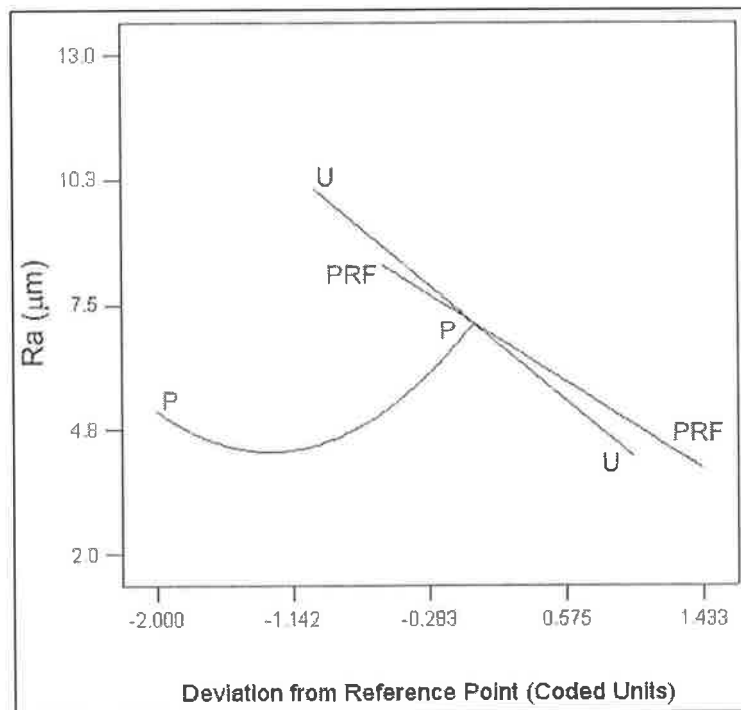


Figure 4.42: Perturbation plot of the process control variables' effects on Ra at high P values.

Table 4.13 lists the relative effects of the model parameters on the response in a numerical representation. It can be seen that $P \times PRF$ and P^2 have the strongest interaction effects on the depth; these were the only significant terms in the model. Interestingly, PRF and U have stronger effects than P . However, again their effects

contradict with expectations from engineering knowledge. Due to the lack of fitness in the model, only the interactive effect of PRF and U will be presented in this section.

Table 4.13: Relative effects of the process model parameters on Ra

Term	Coefficient Estimate
P	-0.069
PRF	0.16
U	-0.19
$P \times PRF$	-2.40
$P \times U$	-0.83
$PRF \times U$	0.99
P^2	1.72
$P^2 \times U$	-1.5

Figure 4.43 shows the 3D surface representing the effects of PRF and U on the Ra as predicted by the statistical model at the mid-range of P . It can be seen from the figure that at high U values increasing PRF causes increases in Ra . On the other hand, increasing PRF at low values of U decreases Ra . Similarly, the effect of U changed from directly proportional to inversely proportional by changing PRF from high to low values. As briefly mentioned earlier, this behaviour of the two parameters changes when the level of P changes.

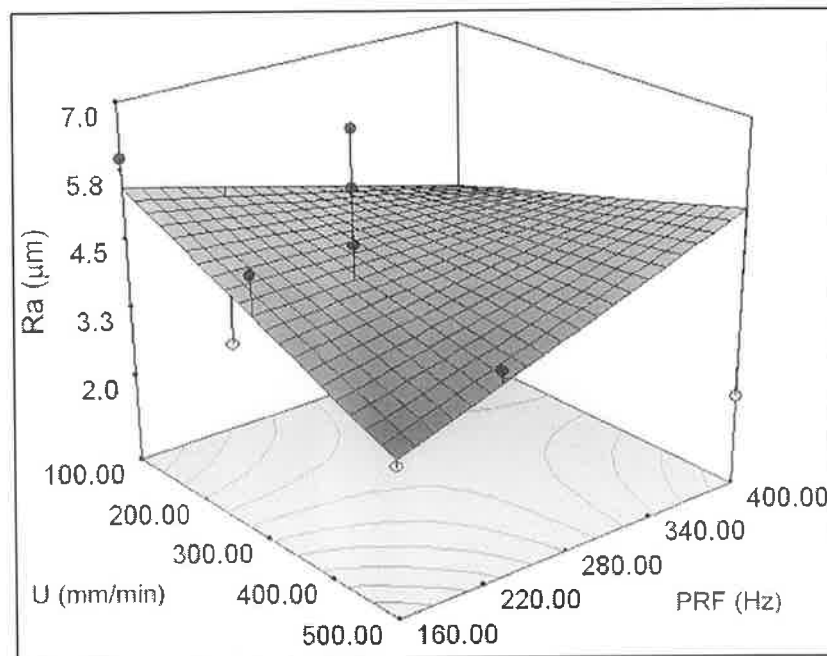


Figure 4.43: 3D view of the interactive effect of PRF and U on Ra .

Figure 4.44 is the 3D surface of PRF and U effect as P is fixed at its lowest value. When P is low, PRF has an inversely proportional effect on Ra at all values of U . Similarly, U affect Ra in a similar manner, however, its effect becomes weak as PRF is increased. Figure 4.45 on the other hand, shows the effects of PRF and U on Ra at high values of P . According to figure 4.45, PRF is directly proportional to Ra at all values of U . On the contrary, U has an inversely proportional effect on Ra at all values of PRF .

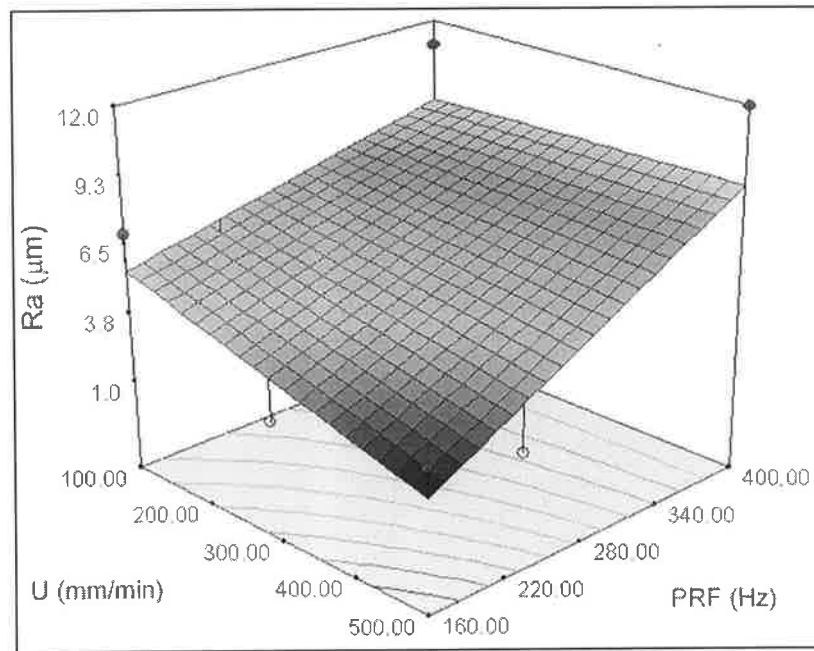


Figure 4.44: 3D view of the interactive effect of PRF and U on Ra at low P .

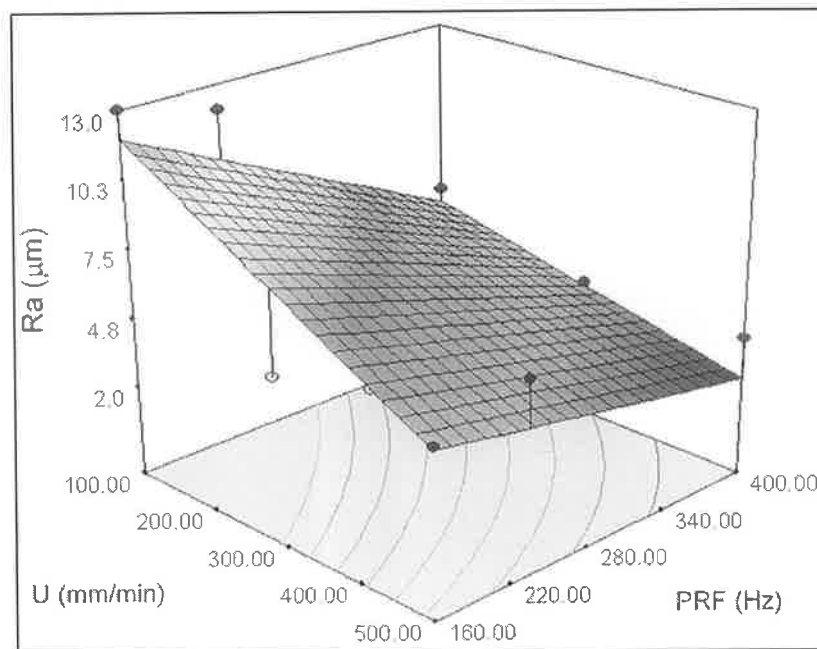


Figure 4.45: 3D view of the interactive effect of PRF and U on Ra at high P .

Looking at the results in table 4.14, the repeated experiments Ch 14, 28 – 32, the Ra values are consistent and in agreement. However, based on the discussion of figures 4.43 to 4.45 and by looking at the remaining Ra values in table 4.14 does not lead to general variance trend. For insets with constant U and PRF , the power did not seem to have a certain effect on Ra . Trends sought here could be a combination of linear or curved, directly or inversely proportional. Similarly, trying to detect the effects of U or PRF independently, did not lead to any uniform or regular trend. The data scatter in table 4.14 takes more or less a random shape that does not follow the changes in the process parameters. This very fact, made the task of statistically modelling the Ra results very difficult.

Table 4.14: Actual versus predicted of the design points.

Standard Order	Run	P	PRF	U	Actual Value	Predicted Value	Residual
1	25	18	160	100	7	5.53764	1.46236
2	16	24	160	100	6	5.481502	0.518498
3	22	30	160	100	13	11.86766	1.132338
4	8	18	228	100	5	6.432623	-1.43262
5	31	24	228	100	2	5.01611	-3.01611
6	29	30	228	100	12	10.04189	1.958106
7	27	18	400	100	11	8.696404	2.303596
8	28	24	400	100	3	3.838942	-0.83894
9	18	30	400	100	6	5.423777	0.576223
10	1	18	160	300	2	3.69446	-1.69446
11	30	24	160	300	5	4.304989	0.695011
12	32	30	160	300	5	8.357815	-3.35782
13	26	18	228	300	4	5.147913	-1.14791
14	9	24	228	300	5	4.398067	0.601933
15	4	30	228	300	3	7.090518	-4.09052
16	15	18	400	300	7	8.824294	-1.82429
17	14	24	400	300	3	4.633499	-1.6335
18	20	30	400	300	4	3.885001	0.114999
19	10	18	160	500	3	1.85128	1.14872
20	19	24	160	500	3	3.128476	-0.12848
21	3	30	160	500	5	4.847968	0.152032
22	2	18	228	500	2	3.863203	-1.8632
23	21	24	228	500	4	3.780023	0.219977
24	7	30	228	500	6	4.139141	1.860859
25	13	18	400	500	12	8.952184	3.047816
26	24	24	400	500	2	5.428056	-3.42806
27	12	30	400	500	4	2.346224	1.653776
28	5	24	228	300	6	4.398067	1.601933
29	11	24	228	300	5	4.398067	0.601933
30	6	24	228	300	6	4.398067	1.601933
31	17	24	228	300	7	4.398067	2.601933
32	23	24	228	300	5	4.398067	0.601933

The software suggested that transformation of the signal might improve the modelling task. This suggestion was performed by modelling the Rq , which is the RMS roughness instead of the Ra . This had no effect on the resulting model significance, which indicated that the transformation was not the solution to this problem.

Reasons for lack of fit of Ra model

The magnitudes of the Ra measurements were small in comparison with the fabricating laser beam's radius at the focus, which was approximately 45 μm . This fact made it very difficult to observe any regular variance within the investigated range of the process control parameters. If the fabricating laser beam's geometry is small in comparison with the fabricated channels geometry, it might be possible to make observations and conclusions on Ra . Furthermore, the statistical model here tends to fit data that disagrees with the expected behaviour of Ra 's relation to process parameters, particularly PRF and U . This theoretical behaviour is supported by simulation results that will be explained in section 6.4.2, which agree with the theory explained earlier and lead to equation 4.6.

Suggestions

The range of the processing parameters can be narrowed down to modify the Ra model and make it able to fit the collected data and represent Ra with good accuracy. Within a narrower range of the same processing parameters, a regular variance could be observed. Ra values recorded in this study fell within a range of (2-13 μm), with a mean value of 4.41 μm , a median of 5 μm and a mode of 7.50 μm . Consequently, the Ra values observed with the ranges investigated are acceptable for fluids that have relatively large particles sizes. Based on the results achieved in this section, the Ra values were used to make judgments on the quality of the channels produced. Comments on the quality of the channels based on Ra values and other qualitative parameters are listed in appendix D.7.

Summary

Microchannels of widths that range between (81 to 365 μm), depths that range between (3 to 379 μm) and Ra that range between (2 to 13 μm) were fabricated on the surface of soda-lime glass sheets. The microchannels had a range of acceptable cross-sectional shapes. The process control parameters were taken as the laser power, P , pulse repetition frequency, PRF and the translational speed, U . The process was statistically

modelled in terms of these control parameters. It was found that the width and depth of the channels were directly proportional to P . On the other hand, the width and depth of the channels were inversely proportional to PRF and U . The mathematical models for width and depth may be used to predict the dimensions of the channels before production. The process may also be optimised for producing microchannels of desired dimensions and probably more intricate shapes (e.g. curved or circular channels). The surface roughness, Ra , data of the channels did not enable a good fit to the statistical model. The reasons for that were discussed in section 4.9.4. The mathematical model developed in the next chapter and the discussions of chapter 6 will emphasise the theoretical concepts of the expected Ra trends as a function of the process control parameters.

Chapter 5

Thermal Mathematical Model

5.1 Introduction

In addition to the experimental results illustrated in chapter 4, a thermal mathematical model has been developed and used to simulate the microchannels fabrication process using the same CO₂ laser processing parameters discussed in the experimental work chapter. The 3D channel geometrical simulations obtained from this mathematical model enabled the measurement of the same response parameters obtained from the experimental analysis, namely, the width, depth and surface roughness. Accordingly, a comparison between the experimental and simulation results could be established. Although this comparison is not entirely accurate due to limitations in the mathematical model itself, morphological aspects and relative dimensional contrast could be drawn. Of particular importance the trends of the expected surface roughness due to the periodic nature of the laser source is compared to the *Ra* statistical model obtained in section 4.9.4. This is of particular importance due to the lack of fit of the derived *Ra* model.

By nature, mathematical models are rigid to some extent, since they tend to express a phenomena or a process in a single equation or a set of simultaneous equations. The flexibility of a model is vital as it can give room for nonlinearities in the process under investigation. On the other hand, the formulation and use of a thermal mathematical model is an attractive method for simulation since it can save a lot of computation efforts. Nevertheless, it is prone to a lot of assumptions that can introduce some misjudgements of reality.

The first sections of this chapter describe the problem under investigation and cite the possible methods of modelling it. Later sections describe the modelling steps such as the assumptions, boundary and initial conditions. Based on the general heat conduction equation and the assumptions, the analytical solution is then formulated. Furthermore, the computer programs developed for simulating the process are then described and the results obtained are presented.

5.2 Explanation of the mathematical model

The temperature distribution in a solid due to absorption of laser radiation is a function of both spatial and time coordinates, $T(x,y,z,t)$. The sample solid can be in motion relative to a fixed laser beam and has temperature dependant properties. If the heat is only transported in the solid by conduction (no radiation or convection) then the heat conduction equation can be expressed in a coordinate system fixed with the laser beam [177, 178]. The general heat conduction equation in this case is given by,

$$\rho(T)c_p(T)\frac{\partial T(x,y,z,t)}{\partial t} - \nabla[k(T)\nabla T(x,y,z,t)] + \rho(T)c_p(T)U\nabla T(x,y,z,t) = Q(x,y,z,t) \quad (5.1)$$

where $\rho(T)$ in (kg/m³) is the mass density, $c_p(T)$ in (J/kg.°C) is the specific heat capacity at constant pressure and $k(T)$ in (W/m.°C) is the heat conductivity of the material. U in (m/s) is a constant translational velocity of the sample. $Q(x,y,z,t)$ is the heat supplied per unit time per unit volume (W/m³) [177, 178]. If the material properties were temperature independent (i.e. constants) then the heat conduction equation becomes,

$$\rho c_p \frac{\partial T(x,y,z,t)}{\partial t} - k\nabla^2 T(x,y,z,t) + \rho c_p U \nabla T(x,y,z,t) = Q(x,y,z,t)$$

$T(x,y,z,t)$ can be simply denoted by T keeping in mind that it depends on space and time dimensions. The gradients in equation 5.1 can be expressed as partial derivatives of the temperature with respect to space to maintain the unit balance on both sides of the equation. Furthermore, if the sample is translated with a constant velocity along the x direction, as shown in figure 5.1, then the third term on the left side of the equation is differentiated with respect to x [178]. Equation 5.1 then becomes,

$$\rho c_p \frac{\partial T}{\partial t} - k \left[\frac{\partial^2 T}{\partial x^2} + \frac{\partial^2 T}{\partial y^2} + \frac{\partial^2 T}{\partial z^2} \right] + \rho c_p U \frac{\partial T}{\partial x} = Q(x,y,z,t)$$

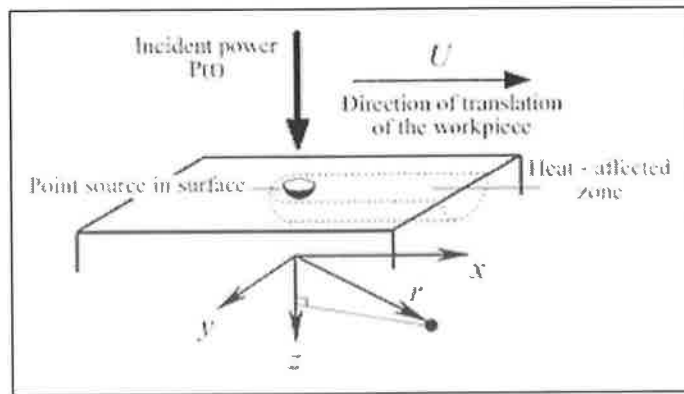


Figure 5.1: Heat point source in the surface of the workpiece.

In the case of heat flowing through a solid without heat generation within that solid; the heat conduction equation will reduce to the heat conduction equation for a homogeneous isotropic solid [178,179]. The equation can then be expressed as,

$$\rho c_p \frac{\partial T}{\partial t} - k \left[\frac{\partial^2 T}{\partial x^2} + \frac{\partial^2 T}{\partial y^2} + \frac{\partial^2 T}{\partial z^2} \right] + \rho c_p U \frac{\partial T}{\partial x} = 0$$

if the equation is divided by ρc_p and rearranged, then it can be written as,

$$\frac{\partial T}{\partial t} + U \frac{\partial T}{\partial x} = \alpha \left(\frac{\partial^2 T}{\partial x^2} + \frac{\partial^2 T}{\partial y^2} + \frac{\partial^2 T}{\partial z^2} \right) \quad (5.2)$$

where, α (m^2/s) is the thermal diffusivity of the material equal to $k/\rho c_p$.

Solving equation 5.2 gives a transient heat or temperature distribution in the medium in the form $T(x,y,z,t)$. However, the solution is not unique to all cases and depends on a number of assumptions, initial conditions and boundary conditions. The assumptions made for the upcoming solution are:

- 1- The initial temperature is equal to the ambient temperature $T(x,y,z,0) = T_o$.
- 2- The medium is a slab of two parallel planes and heat enters from one plane at $z = 0$.
This solution is a heat conduction one, it requires that there is no heat losses by any means from the medium at its two planes, i.e. $\frac{\partial T}{\partial z} = 0$.
- 3- There are no phase changes in the medium. Although such a solution does not explicitly include the latent heat effects, it is still useful in estimating the penetration of the melting isotherms under the conditions of melting via conduction [102]. Moreover, the originator of this fundamental model recommended that this model is a reasonable method of tackling the problem [180]. Details of communications with the author can be found in appendix E.1.
- 4- The medium is a semi-infinite solid, meaning that the temperature variations in the region of interest do not affect the temperatures in regions considered to be far a way from it, such as the bottom plane. The significance of this assumption has been experimentally verified, during the screening experiments stage, by applying the same conditions on different thicknesses (2 mm to 6mm) and obtaining the same result.

Similar assumptions were made by Buerhop et. al. [47]. Based on these assumptions, equation 5.2 can be solved for a time-dependent heat source (i.e. pulsed laser beam). The incident laser beam modelled as a time-dependent point heat source at (0,0,0). The

solution of equation 5.2 given by [179] and based on the mathematical models described by [178] for slabs of harmonic temperatures.

$$T(x, y, z, t) = T_o + \frac{P(t)}{2\pi k r} \exp \left[i\omega t + \frac{U}{2\alpha} \left(x - r \sqrt{1 + \frac{4\alpha\omega i}{U^2}} \right) \right] \quad (5.3)$$

where, $P(t)$ is the time dependent power input.

ω is the fundamental frequency of the power input = $2\pi PRF$.

r is the radial distance from the power source = $\sqrt{x^2 + y^2 + z^2}$.

The derivation of equation 5.3 is illustrated in appendix E.2. The square root taken in equation 5.3 must be the one with a positive real part. A pulsed laser power input as the one shown in figure 5.2 was used in the model. This power source has a period $t_o = 1/PRF$ and is given in the interval $-1/2 t_o \leq t < 1/2 t_o$ by

$$P(t) = \begin{cases} P_o t_o / \tau & |t| < 1/2 \tau \\ 0 & 1/2 \tau < |t| < 1/2 t_o \\ P_o t_o / 2\tau & \text{otherwise} \end{cases}$$

where, P_o (W) is the average power and τ (s) is the pulse width. $P_o t_o / \tau$ is the peak power of the laser pulse, and $P_o t_o / 2\tau$ is the arithmetic mean of the jumps in the pulse function, necessary for the mathematical formulation of the Fourier series describing the power function [181].

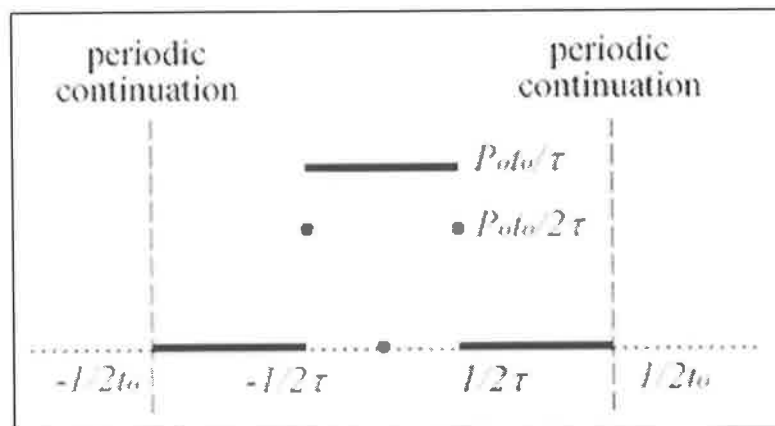


Figure 5.2: The pulsed power input given by equation 5.4.

As mentioned earlier, the power function can be described in terms of a Fourier series of the form

$$P(t) = P_o + \sum_{n=1}^{\infty} a_n \cos \frac{2\pi n t}{t_o} = P_o + \sum_{n=1}^{\infty} a_n \operatorname{Re} \left(\exp \frac{2\pi n t}{t_o} i \right) \quad (5.4)$$

in which,

$$\begin{aligned} a_n &= \frac{2}{t_o} \int_{-\tau/2}^{\tau/2} \frac{P_o t_o}{\tau} \cos \frac{2\pi n t}{t_o} dt \\ &= \frac{2P_o t_o}{t_o \tau} \int_{-\tau/2}^{\tau/2} \cos \frac{2\pi n t}{t_o} dt = \frac{2P_o}{\tau} \times \frac{t_o}{2\pi n} \times \sin \frac{2\pi n t}{t_o} \Bigg|_{-\tau/2}^{\tau/2} \\ &= \frac{P_o t_o}{\pi n \tau} \left(\sin \frac{2\pi n \tau}{2 t_o} - \sin \frac{-2\pi n \tau}{2 t_o} \right) \\ a_n &= \frac{2P_o t_o}{\pi n \tau} \sin \frac{\pi n \tau}{t_o} \end{aligned}$$

An integration error was discovered at the stage of calculating the parameter a_n [179]. This error was discovered during re-deriving the Fourier series representation of the power signal based on standard formulae [181]. The corrected equations were agreed by the author in personal communication [180]. Having calculated a_n , the power function of the heat source in the form of Fourier series becomes,

$$P(t) = P_o + \frac{2P_o t_o}{\pi \tau} \sum_{n=1}^{\infty} \frac{1}{n} \sin \frac{n\pi\tau}{t_o} \cdot \operatorname{Re} \left(\exp \frac{2\pi n t}{t_o} i \right) \quad (5.5)$$

Substituting equation 5.5 into equation 5.3 gives

$$\begin{aligned} T(x, y, z, t) &= T_o + \frac{P_o}{2\pi k r} \exp \left[\frac{U}{2\alpha} (x-r) \right] + \\ &+ \frac{P_o t_o}{\pi^2 k r \tau} \sum_{n=1}^{\infty} \frac{1}{n} \sin \frac{n\pi\tau}{t_o} \operatorname{Re} \left(\exp \left[\frac{2n\pi t}{t_o} i + \frac{U}{2\alpha} (x-r\sqrt{1+i n \operatorname{Si}}) \right] \right) \end{aligned}$$

where,

$\operatorname{Si} = \frac{8\pi \alpha}{t_o U^2}$ is Simon's number [179] that characterises a periodic solution with period t_o

and was substituted in equation 5.3. When taking the real parts of the exponential and the square root, the equation gives

$$\begin{aligned}
T(x, y, z, t) = & T_o + \frac{P_o}{2\pi k r} \exp\left[\frac{U}{2\alpha}(x-r)\right] + \\
& + \frac{P_o t_o}{\pi^2 k r \tau} \sum_{n=1}^{\infty} \frac{1}{n} \sin \frac{n\pi\tau}{t_o} \exp\left[\frac{U}{2\alpha}(x-r \text{Sn})\right] \times \\
& \times \cos\left(\frac{2n\pi t}{t_o} - \frac{U r n \text{Si}}{4 \alpha \text{Sn}}\right)
\end{aligned} \tag{5.6}$$

where $\text{Sn} = \sqrt{\frac{1 + \sqrt{1 + n^2 \text{Si}^2}}{2}}$.

Equations 5.6 consists of three terms, the first term is the initial temperature, T_o . The second term is an exponential term that dictates the magnitude of the temperature at a specific location. The third term is the Fourier series, which controls the harmonics of the temperature variations at each location. Investigating the limits of equation 5.6, the following can be observed:

- 1- The temperature approaches the initial condition, T_o , as r the radial distance, approaches infinity in all directions. This is evident from the exponential functions in the second and third terms. As r becomes significantly high, the indices of the exponents are dominated by negative large numbers, which in turn gives them a value that approaches zero. Moreover, in the second and third terms r appears in the denominator of the constant coefficient to the left of the exponential and the series. This means that this magnitude will also approach zero as r approaches infinity.
- 2- Similarly, the same terms can be investigated with paying attention to the effect of very small r . It can be noted that the temperature approaches a very high value as r becomes very small; this takes place at the initial stages of the pulse. This temperature will be equal to infinity if r is zero, in other words at a location (0,0,0). This was avoided in accordance with advice received from Dowden [180]. The temperatures were simulated in this work at a minimum radial distance calculated from (0,0,1) μm . The significance of this observation is that the maximum temperatures appear at the centre of the point heat source and at the initial stages of the pulse time.

These observations satisfy the initial conditions and assumptions stated at the beginning of the solution. It can be observed from equation 5.6 that the variable parameters can be restricted to P_o , t_o , τ and U . with such a restriction, equation 5.6 was used to calculate

the temperature distribution in the glass sheets, $T(x, y, z, t)$, based on the process parameters, power, PRF , pulse width and speed. Other methods of obtaining solutions similar to equation 5.6 are given using Fourier series, complementary error functions and using Laplace transforms in [178].

5.3 Process considerations

5.3.1 Material under experiments

As mentioned in the experimental chapter, sheets of lime-soda glass were used in this part of the study. The properties and structure of soda-lime glass were presented in the literature chapter. For convenience, table 5.1 lists the properties of soda-lime glass relevant to this chapter.

Table 5.1: Thermal properties of soda-lime glass.

Density, ρ (kg/m ³)	Thermal conductivity, k (W/m.°C)	Specific heat capacity, C_p (J/kg.°C)	Thermal diffusivity, α (m ² /s)
2500	1.06	870	4.8736×10^{-7}

5.3.2 Laser-material interaction

Based on the laser intensity range used in this work (0.3 - 0.5 MW/cm²), the plasma formed is a laser-supported combustion plasma (LSC). During the initial stages of the pulse, LSC plasma starts to form, shielding up to 90 % the incident power from the target [36]. However, as the plasma begins to expand radially, the coupled energy increases to 50 % [36, 50]. The radiative losses in this plasma scheme are typically 15 to 20 % of the incident power. There is a significant amount of energy consumed to raise the glass to its melting and consequently to its vaporisation temperature. These amounts of energies are called the latent heat of melting and vaporisation, respectively. Simple calculations can show the amount of energy needed to raise the focal volume to the vaporisation temperature. The amount of heat required to reach the vaporisation temperature, T_v , equals $C_p.(T_v - T_o) = 870.(3427 - 22) = 2,962,350$ J/kg. The amount of heat required to raise the temperature of the vapour to approximately 10 times the vaporisation temperature, T_s , was also calculated. This allowed an approximation of the energy required to ablate the material in order to form the channel, as per the procedure followed by other workers [36]. This energy was calculated as $C_p.(T_s - T_v) = 870.(34270 - 3427) = 26,833,410$ J/kg. This approximates the energy required for ablation without

the need for knowledge of the latent heat energies. The scale length of diffusion was obtained from, $L_D = \sqrt{\alpha \cdot \tau}$, where α and τ are the thermal diffusivity and the laser pulse width [36]. The average pulse width used in this work was 1.53125 ms, so that $L_D = 27.32 \mu\text{m}$ was the average depth affected by the heat wave diffused per a single pulse. The volumetric mass affected by the heat wave can be calculated from, $m = \rho \cdot \pi \cdot r^2 \cdot L_D$, where r is the laser beam radius. The average heated mass, m , was equal to 4.345×10^{-10} kg. This mass was multiplied by the two energy values calculated above, which gave the amount of energies required to bring this irradiated volume to its vaporisation temperature and then to being ablated. These were 1.287 mJ for heating the volume to its vaporisation temperature and 11.659 mJ for ablation.

In this study the laser beam's power, P , was varied between 18 and 30 W, and the pulse repetition frequency, PRF , was varied between 160 and 400 Hz, this resulted in minimum and maximum pulse energies of 45 and 187.5 mJ respectively. Table 5.2 lists the minimum and maximum pulse energies produced in this study and the minimum percentages of these needed for breakdown.

Table 5.2: Energy percentages needed for breakdown.

Experimental energy (mJ)	% For heating	% For ablating	% Total
45	2.86	25.91	28.77
187.5	0.69	6.22	6.91

The breakdown threshold energy, E_{th} , was observed at 45 mJ, which corresponded to a fluence, $F_{th} = E_{th} / \pi \cdot r^2 = 707.55 \text{ J/cm}^2$. A channel that was used to identify the breakdown threshold in this work is shown in figure 5.3 (a). The surface cracks in this figure were produced using $P = 18 \text{ W}$, $PRF = 400 \text{ Hz}$ and $U = 8.333 \text{ mm/s}$, which corresponds to the first row in table 5.2 and to channel 25 from table 4.4. The structural changes in this image suggest that about 29 % of the incident power was necessary to initiate ablation; the remainder of the power was shielded by the induced plasma. At higher fluences, wider and deeper structural changes, as shown in figure 5.3 (b), were produced. This channel was produced using $P = 30 \text{ W}$, $PRF = 160 \text{ Hz}$ and $U = 8.333 \text{ mm/s}$. These settings correspond to the second row in table 5.2 and channel 21 from table 4.4. The larger dimensions in the channel in figure 5.3 (b) suggest that more than about 7 % of the energy was coupled to the sample. The longer pulse duration from the

processing parameters to produce the channel in figure 5.3 (b) would be expected to allow time for the heat to diffuse and further energy to be coupled to the target [36, 50].

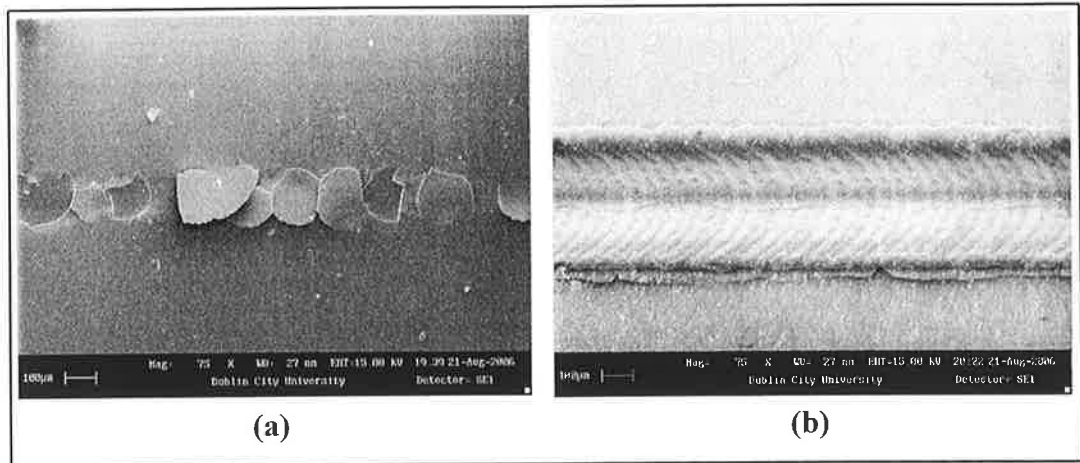


Figure 5.3: SEM image of (a) minimum fluence channel 25, and (b) maximum fluence channel 21.

Based on the total percentages in table 5.2, plasma shielding theory, radiative losses associated with the LSC plasma scheme, and simulation trial and error procedures on experimental data, an average 25 % of the incident beam's power was calculated as being delivered to the sample. This 25 % of the incident power was used for solving the thermal mathematical model. Based on the pulse energy range shown in table 5.2, the mathematical model would in some cases, over-estimate or under-estimate the channel dimensions. This would not affect the predicted channel shape; however, it has implicitly reduced the complexity of analysis compared to taking phase changes into account in the mathematical model [102, 182].

5.4 Process simulation

All the simulated results and graphics were achieved using a number of LabVIEW software codes built for this part of the study. To solve equation 5.6, the laser power source was assumed to be stationary at the coordinate (0,0,0) at all instances of time and the sample was translated in the x direction at a constant velocity U [179]. Three main LabVIEW codes were developed, the first code simulates planar thermal isotherms, the second code, based on the first one, simulates the three-dimensional geometries of the channels and the third code simulates thermal histories, for prolonged time durations, at specified coordinates as the sample translates past the laser beam. The discussion of these simulation codes is given in the following sections.

5.4.1 Planar isotherms

This code is discussed in greater depth as the other simulation codes in this chapter are based on it. A planar isotherm is a numerical / graphical display of the temperature distribution on one plane of the sample. Since the sample was translated in the x-direction, the x-coordinate or the variable x in equation 5.6 depended on the time, t . Consequently, for temperature distribution in any z-plane in the sample, only the time and the y- coordinates were needed to solve equation 5.6. Hence, a 2D mesh in time and space (t,y) was constructed. The size of the mesh was defined by two parameters, the first being the pulse duration, $t_o = 1/PRF$, which ensures the calculation of the temperature distribution due to a full laser pulse. The second element was a sufficiently large value of the y-coordinate to cover half of the expected heat affected zone's width (i.e. half the channel's width). Only half the channel was modelled due to the symmetry of the solution and the increased speed of computation. The grid size of the y-mesh was variable according to the grids' location with respect to the heat source. This was necessary, due to the nonlinear relation between the temperature and the space coordinates from the exponential terms in equation 5.6. Higher temperature gradients were expected as one move towards the heat source, and so smaller mesh elements were needed to show such changes. In other words, as we moved towards the point heat source in the y-direction, equation 5.6 had to be solved at closer points. Figure 5.4 shows the mesh generated for a length of 200 μm and a mesh element size of 1 μm . Note that the closer one moves towards $y = 0$, the smaller the element size becomes. Figure 5.5 shows the mesh generated for the time direction where $t = 1/PRF$. As can be seen, the element size of the time / x-axis mesh was of a regular element size, as there were no steep temperature gradients in the x-direction that needed extra elements to show their effects.

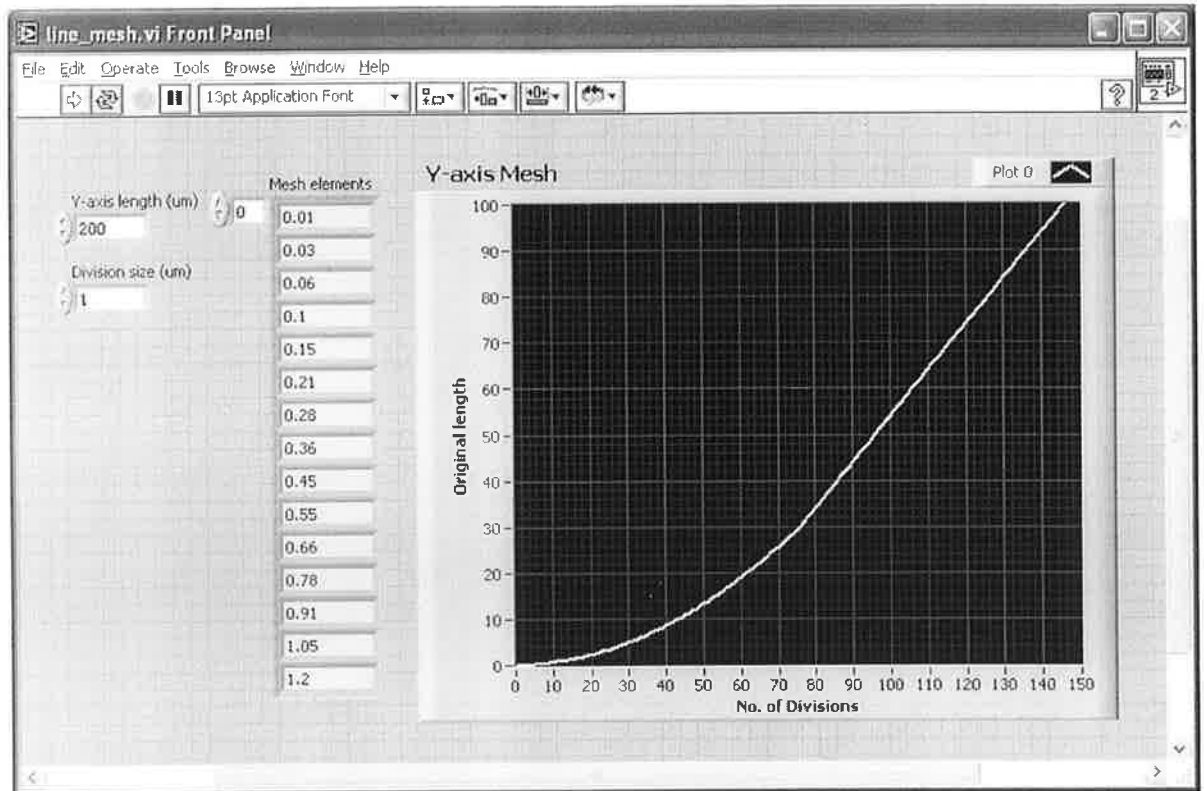


Figure 5.4: Mesh elements generated for the Y-axis.

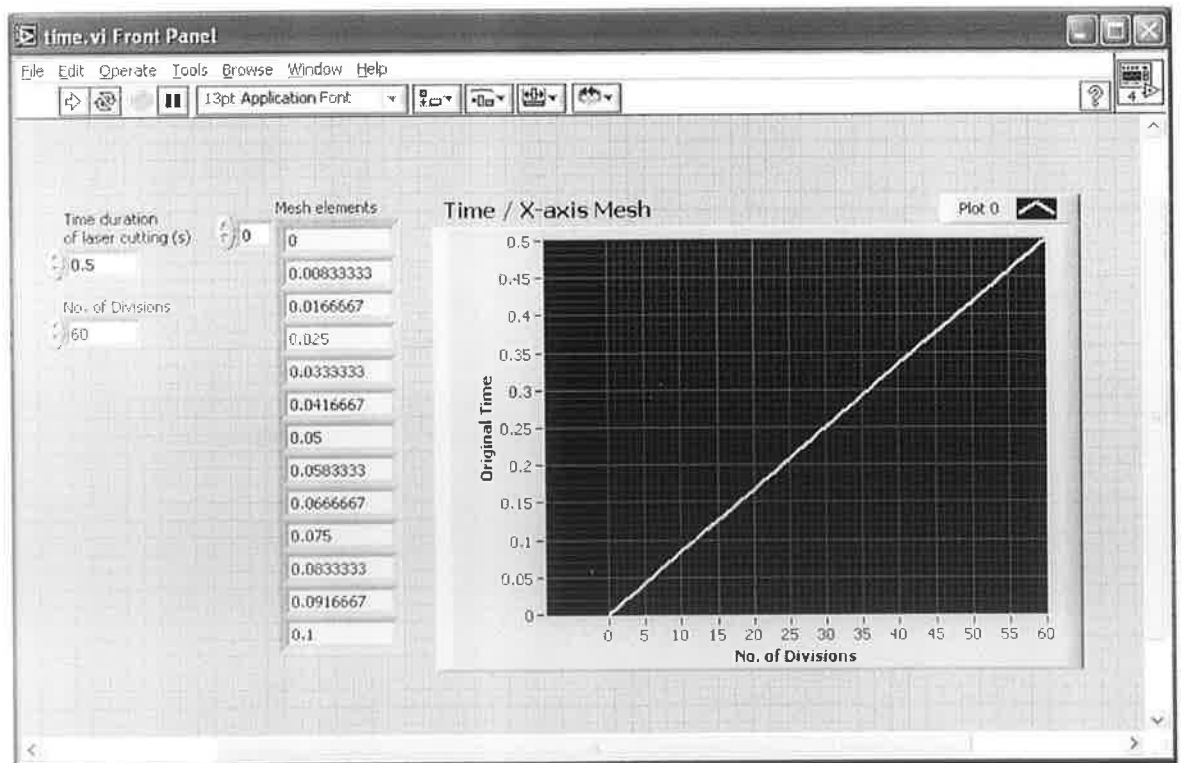


Figure 5.5: Mesh elements generated for the X-axis

Figure 5.6 shows a schematic of the mesh generated to simulate one pulse isotherm on a sample. Although the figure is presenting results that are discussed later, it is helpful in

visualising the need for changing elements sizes in the mesh. It can be seen from figure 5.6 that the mesh elements sizes changes in the y-direction, while a constant mesh element size was maintained in the x-direction. It can also be noted that the temperature distribution through half of the area can be simulated since the solution is symmetrical about the y-axis.

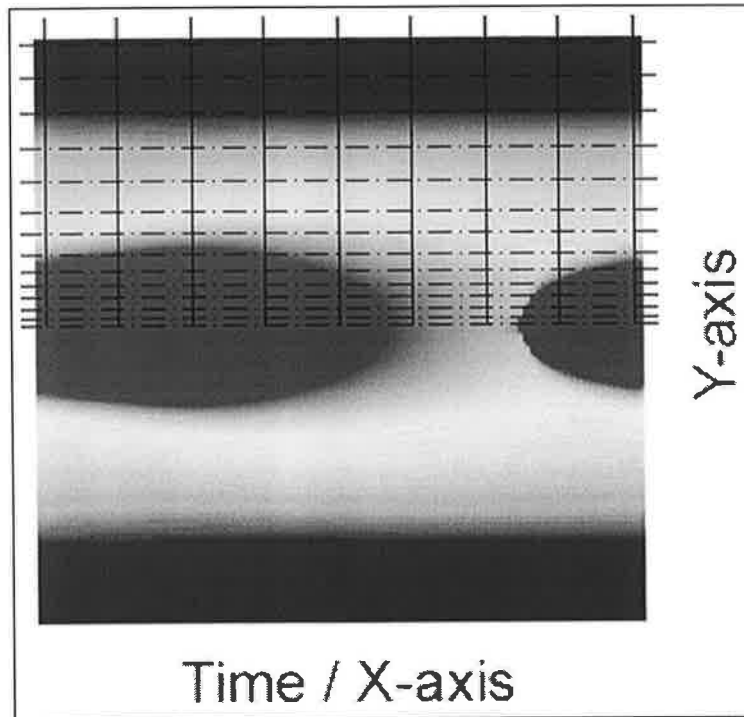


Figure 5.6: Schematic of the mesh generated for simulating planar isotherms.

This code starts by allowing the user to select the material subjected to the laser irradiation. A pop up window appears with a list of materials along with their properties that were previously saved in a text file in a tabulated format. Figure 5.7 shows the material selection code. Once the desired material was selected and the button at the bottom of the front panel in figure 5.7 clicked, the window closes and the user is back at the main front panel of the simulation code shown in figure 5.8. The user can then fill the fields on the front panel with the desired values to be used in the solution of equation 5.6. The fields are divided into two categories, namely, the process parameters and the solution parameters. The process parameters are the power, P (W), the pulse repetition frequency, PRF (Hz), the pulse duration, τ (s), and the translational speed, U_x (mm/s). Displayed to the right of these control parameters are the name, thermal conductivity and thermal diffusivity of the material obtained from the selection code.

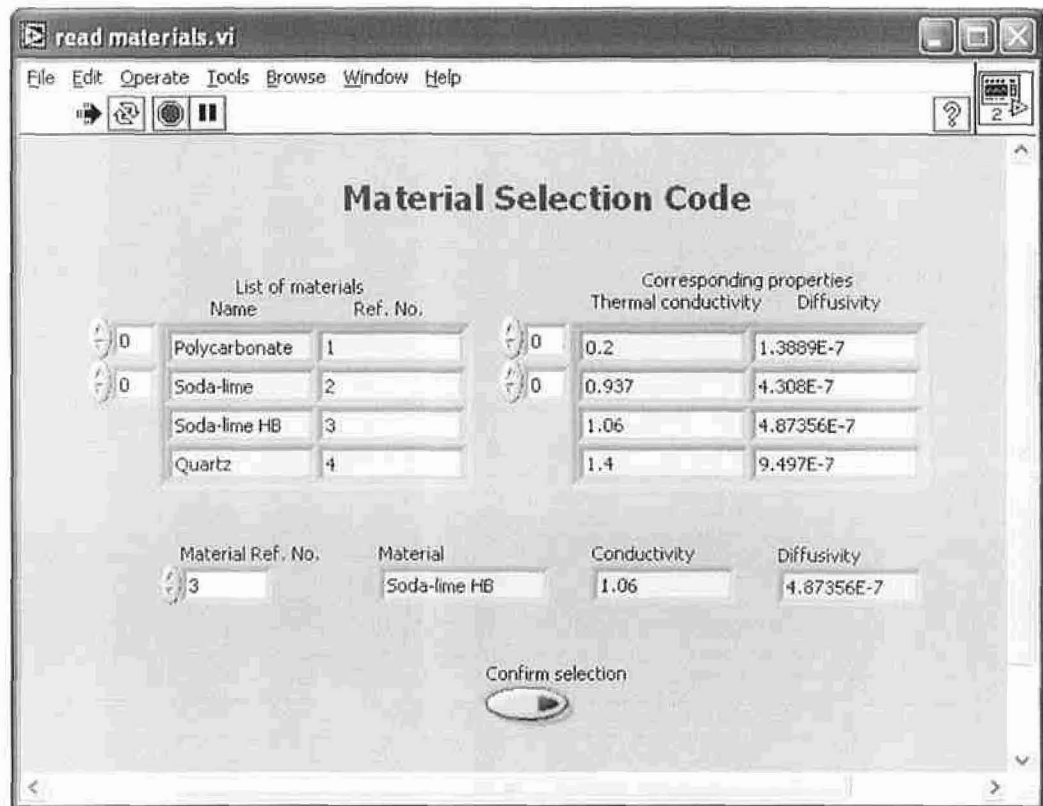


Figure 5.7: Front panel of the material selection code.

The solution parameters included the number of the terms in the Fourier series, taken to be equal to 500 in all the simulations performed in this study. Another solution parameter was the number of pulses to focus on, i.e. how many times the solution will be duplicated after the first pulse. The user can also specify the mesh size and mesh element sizes. The first mesh dimension defines the range of the y-axis to be simulated. The second mesh dimension is automatically defined by the inverse of the *PRF* value which is the pulse duration. The location on the x-axis was specified and kept at 1 μm throughout the simulations in this work to make sure that the temperature will not tend to infinity. Moreover, the truncation temperature above which the temperatures were given the same value was specified. The level of the isotherm plane was specified from the value of *z*, which can be changed to investigate the temperature distribution on various depths of the sample. The user can choose the values to be displayed on the x-axis, either time or displacement values. The user can also specify the text file name to which the simulation data will be written. Finally, the button at the bottom "Run Analysis" is clicked to start the simulation. The progress of the process can be monitored from the blue coloured bar at the bottom-right of the front panel.

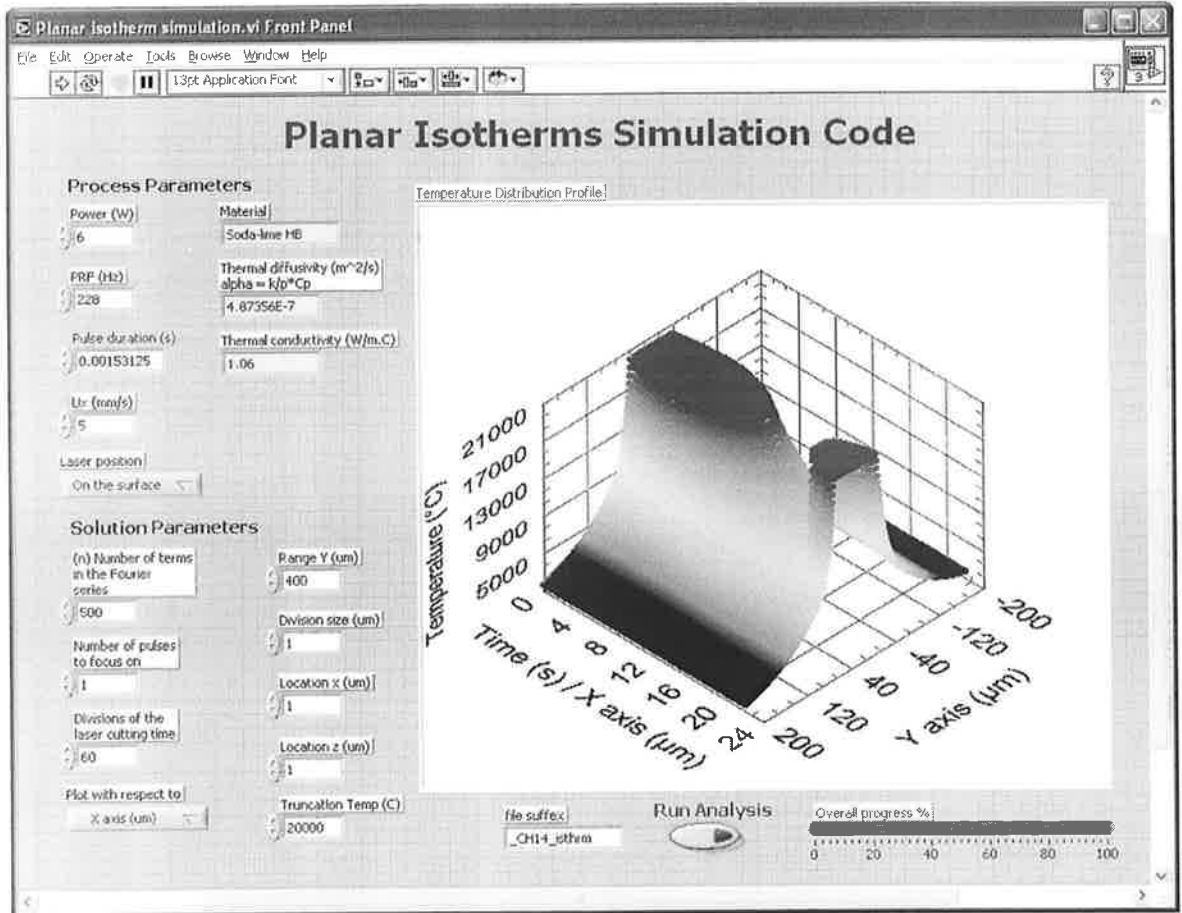


Figure 5.8: Front panel of the planar isotherm simulation code.

Once the analysis started, two sub-codes calculated the mesh elements as explained earlier and based on the user inputs from the front panel. Since the solution is symmetric about the y-axis, the planar isotherms were simulated for half of the y-range mesh dimension, which saved half of the execution time. The solution was independent of the mesh size, since equation 5.6 was solved at each point in the mesh. Since the solution was carried out in a two dimensional space ($y, t / x$), the code consisted of two main loops, each iterating on the mesh elements. The first value from the array containing the y-mesh value was taken in the first loop. The second loop was an inset of the first loop and it iterated through the array elements of the t-mesh. Equation 5.6 was solved inside the inner loop and the temperature value along with the ($y, t / x$) coordinates were written to a text file. The inner loop terminated when all the t / x array values were examined, then the outer loop took the next value from the y-mesh array and the same sequence was repeated until all the values in the y-mesh array were examined.

Figure 5.9 shows the predicted isotherms of three laser pulses at plane $z = 1 \mu\text{m}$ and $x = 1 \mu\text{m}$. The laser processing parameters used were, $P = 24 \text{ W}$, $PRF = 228 \text{ Hz}$, $\tau =$

1.53125 ms, and $U = 5$ mm/s. The mesh was generated for $t = (0 \text{ to } t_0) = (0 \text{ to } 1/228 \text{ s})$ and $y = (0 \text{ to } 400 \text{ } \mu\text{m})$. These settings are similar to the settings used to produce channel 14 in the experimental study. The resulting isotherm was reflected about the x-axis to give the full temperature distribution. The solution is also periodic in time, so that solving for, t_0 , seconds was sufficient and the results were repeated for the proceeding pulses. As explained earlier, the temperature tends to a very high value as r approaches 0 or its smallest examined value, so the temperatures were truncated at a sufficiently high value, for example 20,000 °C. As shown in figure 5.9, the readings of the x-axis can be represented by time (red-coloured) as well as length readings (black-coloured). Both readings can be interpreted to have to the same meaning, however, for convenience, the x-axis readings will be represented by length readouts (m or μm). The laser ablation direction is taken from $x = 0$ to $x =$ a value corresponding to the pulse termination time, in this case, $x = (1/228) \times 5000 = 4.386 \times 10^{-3} \times 5000 = 21.92 \text{ } \mu\text{m}$. This value can be seen on both time and length readouts of the x-axis in figure 5.9.

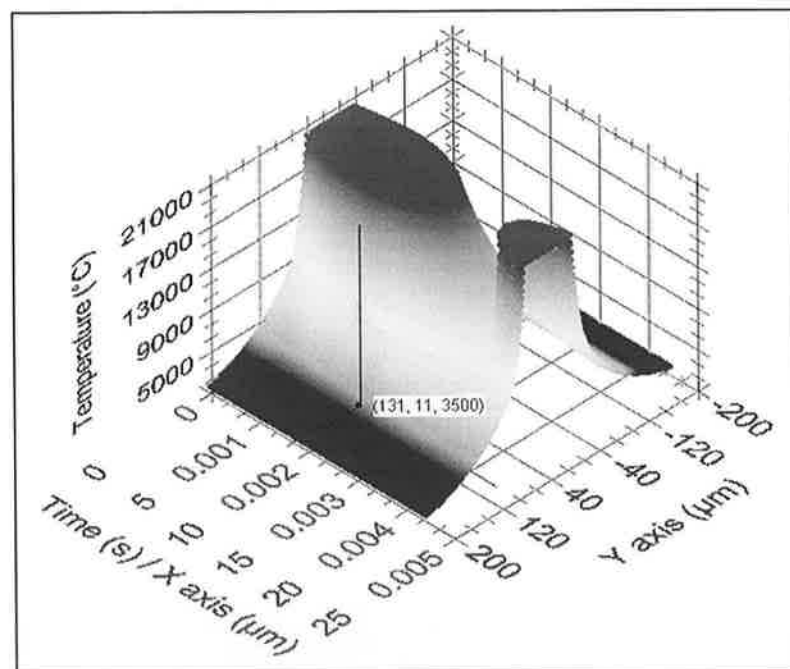


Figure 5.9: Channel 14: 3D isotherm of one pulse at $z = 0$

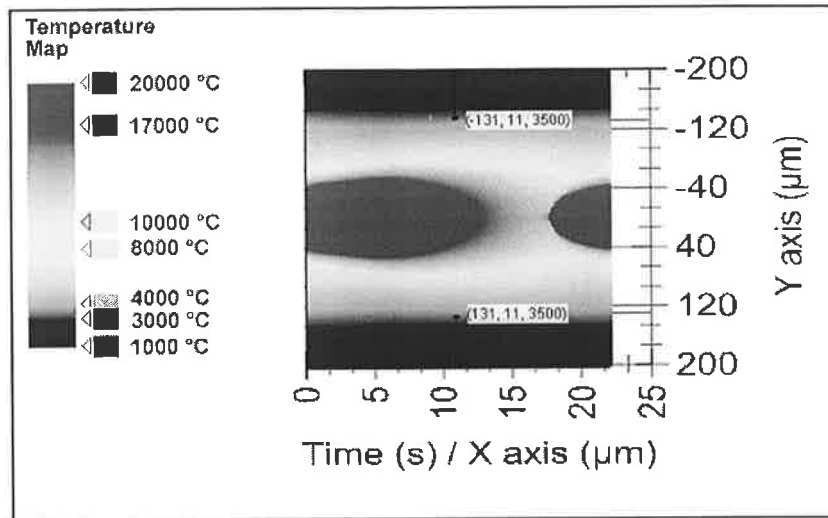


Figure 5.10: Channel 14: Top view of isotherm of one pulse at $z = 0$

The cursor in figure 5.9 was located in such a way to show the evaporation isotherm at temperature = 3500 °C. This is an important isotherm and was used in predicting the 3D geometry of the channels explained in the next section. Figure 5.10 shows the top view of the same isotherm of figure 5.9. The ablation direction in figure 5.10 was taken from left to right and the symmetry of the solution can be observed from the cursors lying on the evaporation isotherms. The temperature legend in figure 5.10 shows the temperature values in terms of colour gradients. Temperatures increase for points closer to $y = 0$, i.e. closer to the point heat source.

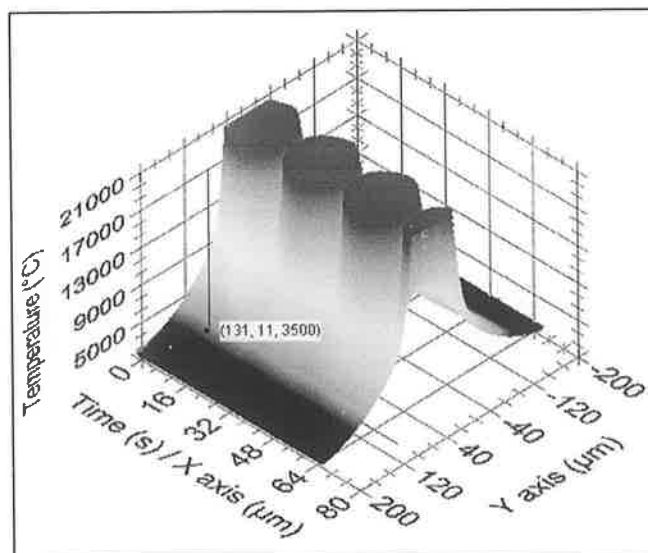


Figure 5.11: 3D isotherms of three pulses of channel 14.

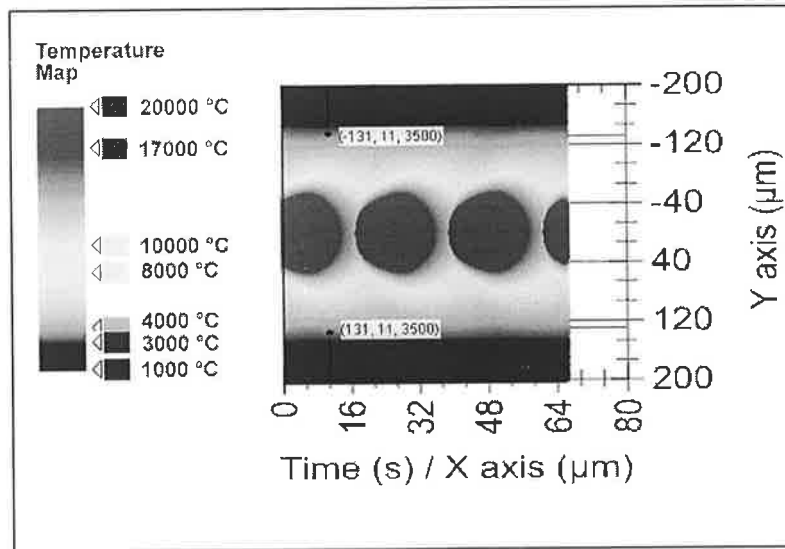


Figure 5.12: Top view of three pulses isotherms of channel 14.

As has been mentioned earlier, the solution derived from equation 5.6 is periodic in time. Figure 5.11 and 5.12 show the isotherms of three pulses calculated for the same processing parameters of channel 14. The isotherm of figure 5.9 has been produced three times and is shown in the isotherms in figures 5.11 and 5.12.

Similarly figure 5.13 (a) and (b) show the isotherms of 10 and 20 pulses, respectively, produced by the same parameters. Interestingly, the harmonic effects produced by each pulse seem to have a curved shape. Those shapes were observed in this work to be concaved against the direction of ablation. The latter observation is discussed in comparison with some microscopic images of the experimental channels in section 6.3 of discussion chapter.

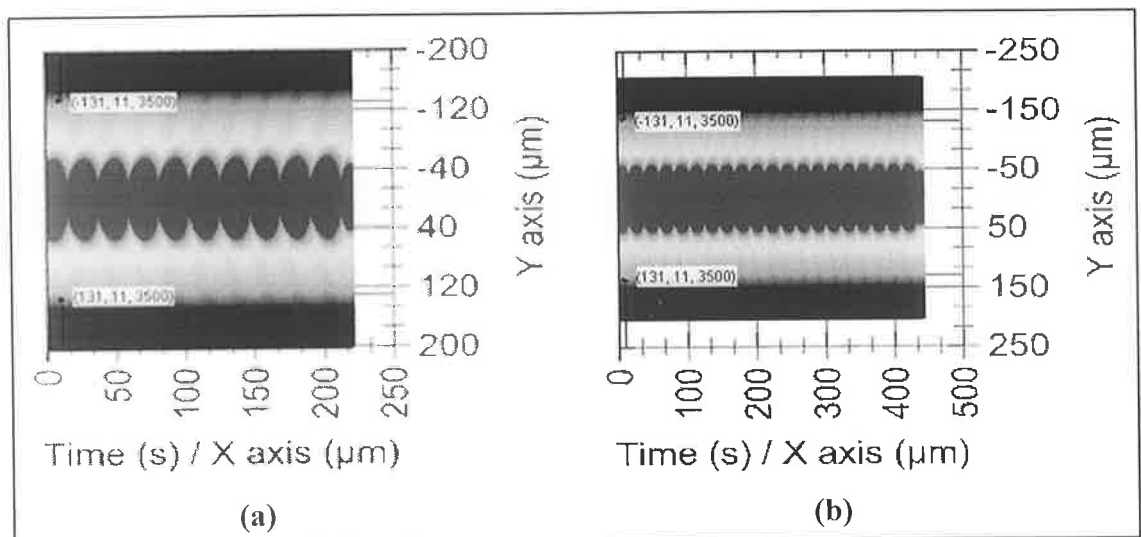


Figure 5.13: Channel 14 isotherms of (a) 10 pulses and (b) 20 pulses

5.4.2 Channel 3D geometry

The 3D geometry prediction is based on the prediction of the planar isotherms explained earlier. Instead of solving for a single z-plane, the simulation procedure was repeated for all z-planes until the maximum values of temperature per each isotherm fell below a set vaporisation value. This temperature value was taken to be the vaporisation temperature T_v . There is a vaporisation isotherm in each plane, as shown in figure 5.9 and 5.10, as long as the maximum temperature in that plane is more than T_v . All the coordinates, in the plane, corresponding temperature values greater than T_v represent locations of the ablated material. So the data points with temperatures closest to T_v were extracted to produce the channel surface data. This procedure was repeated for z values ranging between $z = 0$ and $z = \text{depth of channel}$. The later value of z was decided, manually and by trial and error, when the maximum temperature in that plane was less than T_v . A code was built to iterate through the range of z planes calculating the isotherms, in each iteration, and writing the data points corresponding the processed location to a text file. The solution took a long time, hence again half of the channel width was simulated and the solution was reflected about the y-axis when the 3D channel geometry was viewed. On average it took around 3 hours to simulate one pulse induced 3D geometry from each channel settings.

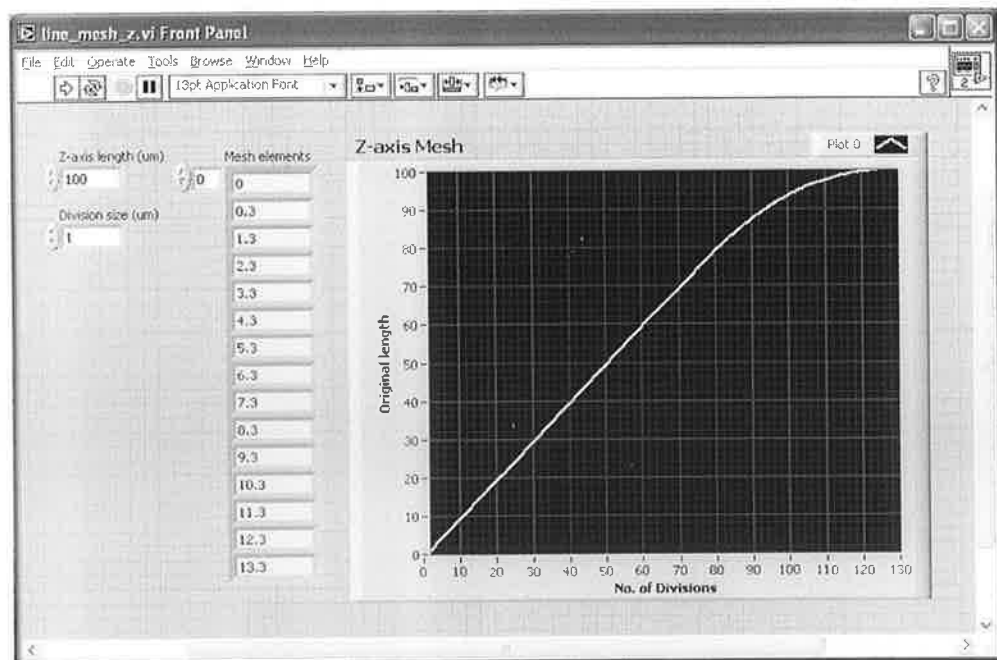


Figure 5.14: Mesh elements generated for the Z-axis.

The temperature had steep gradients as one moved closer towards the depth of the channel. Hence, a mesh code similar to the y-mesh code was used. Figure 5.14 shows

how the grid size will become smaller when the value of z becomes larger. In the case shown in figure 5.14, a mesh size of $100\ \mu\text{m}$ was used with a mesh element size of $1\ \mu\text{m}$. The mesh element size was reduced to fractions of $1\ \mu\text{m}$ as we moved closer to maximum z value. The sign of these elements was inverted after they were used in the simulation code to satisfy the requirements of equation 5.6 of points lying underneath the sample's surface.

The front panel of the 3D channel geometry code is shown in figure 5.15. It looks similar to the isotherm simulation code. There is no 3D plot viewer in this code because real-time viewing of the results requires more processing time and memory. The truncation temperature can be specified before the simulation starts and it was fixed at $3500\ ^\circ\text{C}$ for all simulations.

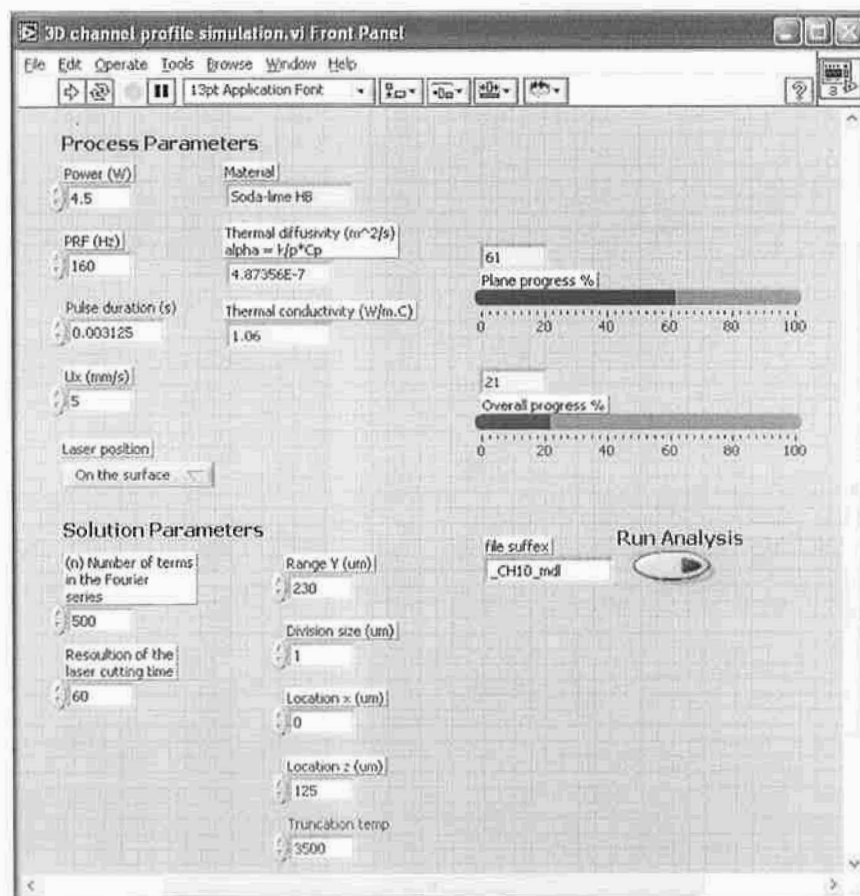


Figure 5.15: Front panel of 3D simulation code.

Usually the simulation was run the first time with a large mesh dimensions and element sizes in both the y and z directions to get a quick idea on the 3D channel geometry. Then when the width and depth of the channel were roughly estimated from this step, the simulation was run again with appropriate mesh dimensions and a small elements

size. The element size was also fixed for all simulations and was equal to 1 μm . There are two progress bars in this code one of them shows the progress per planar isotherm while the other shows the overall progress. The data points were written to the text file during the course of simulation. Depending on the dimensions of the simulated channel, the resulting data file sizes were usually high. The minimum data file size was 27.5 MB for channel 19 and the maximum was 122.9 MB for channel 9.

The data files resulting from the simulation code shown in figure 5.15 were used by another code to view the 3D geometry of the channel. This viewing code, shown in figure 5.16, iterates through the temperature data belonging to each plane. Each planar data at this stage represent the ablated regions, thus picking the minimum temperature readings in each plane will result the boundaries of the channel in that plane. Searching for minimum values of temperatures in all planes and plotting the corresponding x,y and z coordinates of these points resulted the 3D geometry of the channel. The simulations were performed for the 27 experimental settings presented in table 4.3 in section 4.5. The 3D geometries of the simulated channels are shown in appendix E.3.

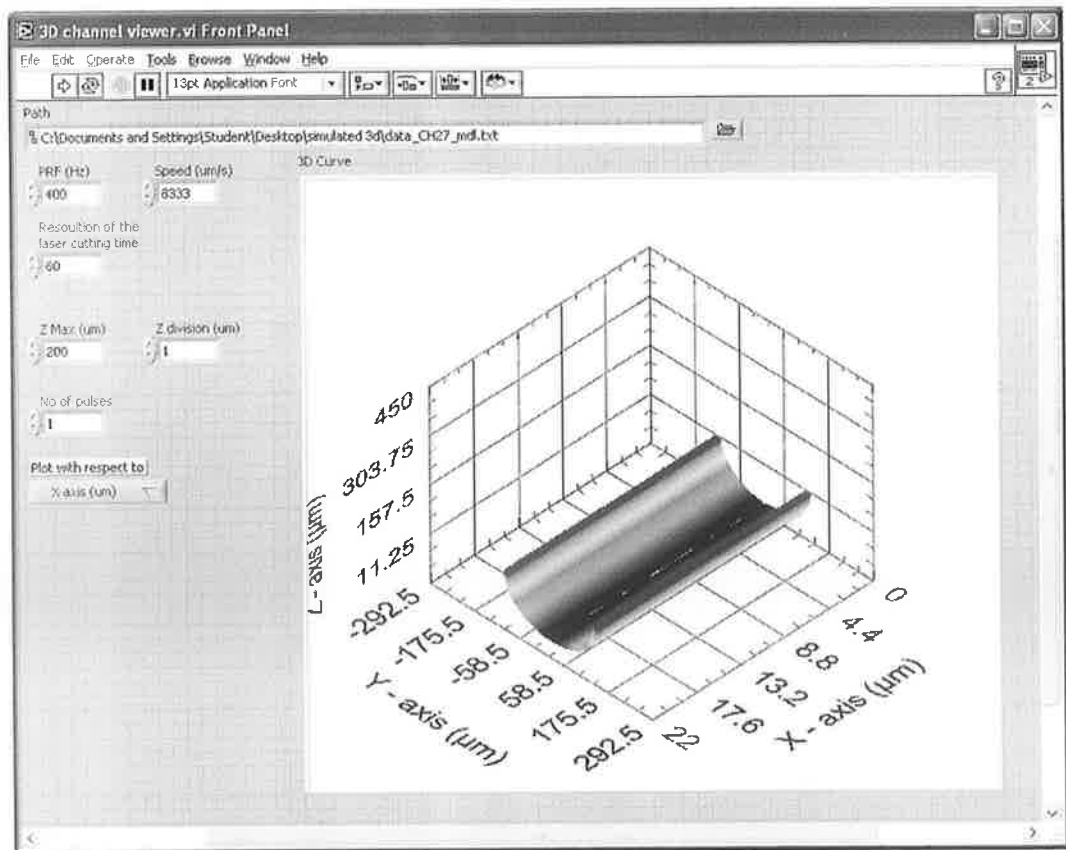


Figure 5.16: Front panel of the 3D channel viewing code.

The channel width, depth and surface roughness parameters can also be calculated from the predicted 3D geometries as the one shown in figure 5.16. Furthermore, another code was developed to change the distinctive 3D points shown in figure 5.16 to one surface showing the 3D geometry of the channel. This was useful in calculating the Ra values of the simulated 3D channel. The channel width, depth and Ra numerical data obtained from the simulations are listed in appendix E.4. In those cases where the measured Ra was equal to zero in appendix E.4, it meant that the Ra value was very small. These zero Ra values were due to the very small differences in the simulated height measurements, which when were converted from 3D coordinates to surface data they were detected as equal values. This effect was a result of the fact that the mesh element size in the z-direction was not small enough to detect height changes at the bottom of the simulated channel in those cases.

5.4.3 Thermal history

The laser power source is assumed to be on (0,0,0) at all instances of time. The temperature changes at particular constant points in the sample may be simulated as the sample is translated in the x direction. The resulting temperature readings can be thought of as probe or thermocouple readings fixed at those locations of interest. They are referred to as thermal histories because they show the temperature change or times that usually exceed the pulse duration. Since the workpiece is translated in the x direction at a constant velocity, U , the x values change with time based on a Eulerian coordinate, according to $x = a + t \times U$, where, a , is the initial x location and, t , is the time elapsed since the beginning of translation [179]. Equation 5.6 can also be solved to predict the thermal history of specific points in the plane of interest. This can be useful in monitoring how the temperatures change at those points over a period of time which exceeds the pulse duration and enables the study the heating and cooling rates which can be useful in estimating the resulting microstructures due to laser irradiation. Figure 5.17 shows thermal histories for four points at $y = 10, 150, 500$ and $1000 \mu\text{m}$. These thermal histories are obtained from the planar isotherm of figure 5.9 corresponding to the processing parameters of channel 14. The initial x coordinate was set so that it crossed the laser point source at $t = 0.2$ seconds. The temperatures were calculated for a total time of 2 seconds so at the traversing speed of $5000 \mu\text{m/s}$ the y points were a perpendicular distance of $9000 \mu\text{m}$ behind the laser point source.

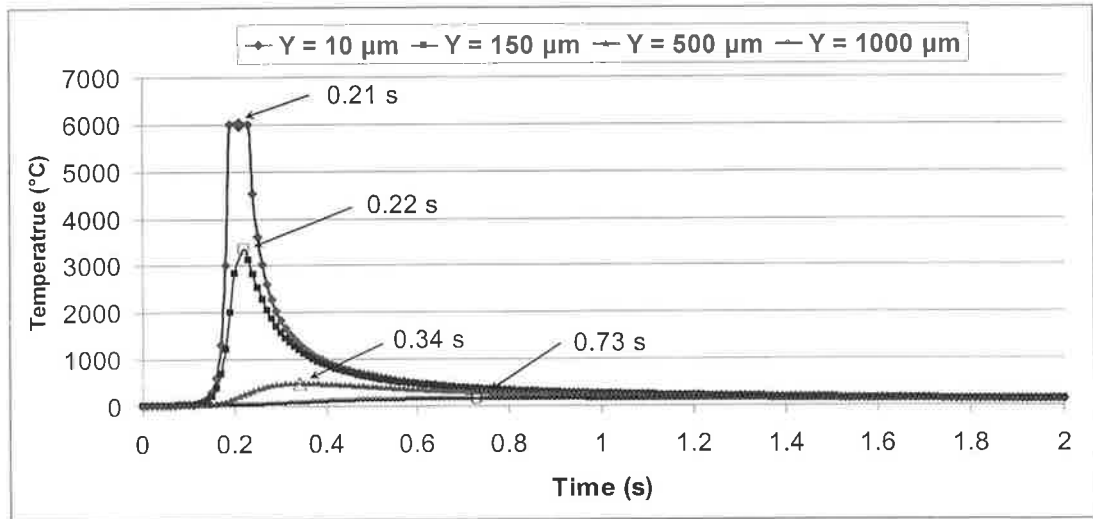


Figure 5.17: Thermal histories of four points on the surface of glass sheet.

The maximum temperature at point $y = 10 \mu\text{m}$ occurred at the truncated $6,000 \text{ }^\circ\text{C}$. The maximum temperatures were reached at 0.21, 0.22, 0.34 and 0.73 seconds for the points $y = 10, 150, 500$ and $1000 \mu\text{m}$, respectively. This indicates that substantial time duration is required for heat diffusion from the heat source. The temperature falls below $3500 \text{ }^\circ\text{C}$ as the y value becomes more than $130\text{-}150 \mu\text{m}$. This may also be noted from the isotherms in figures 5.9 and 5.10. It can also be noted that the cooling rates are different for the four points in figure 5.17, this may be used to estimate the resulting microstructure in those regions.

Summary

The microchannel fabrication process was thermally modelled. The analytical thermal mathematical model was used in a computer program to simulate the process. The graphical and numerical simulation results are presented in appendix E.3 and E.4. The thermal model seems to underestimate or overestimate the dimensions of the channels due to the embedded assumptions used to derive the model. However, the results presented in this chapter and the appendices show that there are similarities between experimental results and simulations from the morphological perspective. In the next chapter, this similarity will be emphasised and used to describe the change in Ra trends with the process parameters.

Chapter 6

Discussions and Conclusions

6.1 Introduction

This chapter presents the discussion of the results obtained from the experimental and simulation studies. The chapter starts by presenting a discussion on the experimental results using a different analysis from the statistical analysis that was presented in section 4.9. This discussion is based the effects of indirect process parameters (i.e. calculated parameters) on the channel dimensions as well as ablation rates. This discussion is intended to support the knowledge gained in chapter 4. The subsequent part of the chapter establishes a comparison between the simulated and the experimental results. The comparison is intended to understand the morphological nature of the microchannels, support the trends of the experimental results obtained and enhance understanding the process parameters effects. Overall conclusions on the study and future work recommendations are finally drawn based on the discussions.

6.2 Indirect process response parameters

In chapter 4, the effects of P , PRF and U on the width, depth and Ra of the microchannels have been covered. That analysis was beneficial from the stand point of fabrication of the channels and process modelling in terms of these parameters. Laser intensity, I (W/cm^2), pulse energy, E_P (J), laser fluence, F (J/cm^2), and pulse fluence per meter, F_M (J/cm) are indirect process parameters, which are calculated from the process control parameters. Moreover, ablation rates can be derived with the width and depth of the channels. These ablation rates can be treated as response parameters and the effect of the indirect process parameters on them can be studied. The investigation of these parameters' effects is beneficial for enhancing the understanding the process, and estimating the process time, cost, and efficiency.

6.2.1 Indirect parameters' equations

The laser intensity, pulse energy, and pulse fluence have been defined in equations 1.3 to 1.7. The pulse fluence per meter can be calculated from,

$$F_M = E_P / f \quad (6.1)$$

where f is the pulse feed (m/pulse) defined in equation 4.3. It is worth noting that calculations of this parameter per one pulse or per the whole length of the channel will yield the same values. Based on that, the measurement unit for this parameter can be J/m instead of $J.pulse/m$. This parameter gives the amount of energy delivered to each length unit in the direction of ablation.

As mentioned earlier, a number of ablation rates may be calculated, and may be categorised according to the measured quantity. In this case, the ablated quantities can be either volume or mass. In order to calculate the channel volume, the general shape of the channels' cross-sectional area was considered to be trapezoidal as shown in figure 6.1. The calculation of the cross-sectional area required the measurement of a new channel parameter that is the bottom width, W_B . The bottom width was measured from the 3D scans of the channels following the same procedure as with the top channel width, W_T . The values of W_B are listed in table F.1. The cross-sectional area shown in figure 6.1 is given by, $A = 0.5 d (W_T + W_B)$ where d is the depth of the channel.

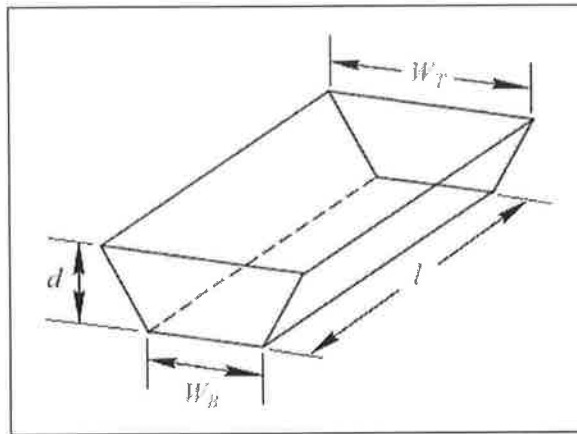


Figure 6.1: Channel cross-sectional area shape.

The calculated volume ablation rates were, the total ablated volume, V (μm^3), the ablated volume per pulse V_P ($\mu\text{m}^3/\text{pulse}$), ablated volume per second V_S ($\mu\text{m}^3/\text{s}$), and the ablated volume per Joule V_J ($\mu\text{m}^3/\text{J}$). Similarly, the mass ablation rates were the total ablated mass, M (g), the ablated mass per pulse M_P (g/pulse), ablated mass per second M_S (g/s), and the ablated mass per joule M_J (g/J). The total ablated volume can be calculated from:

$$V = A \times l \quad (6.2)$$

where l is the full length of the channel. The number of pulses required to fabricate the full length of the channel was, $N = l \times PRF / U$. Hence, the ablated volume per pulse can be calculated from:

$$V_P = V / N \quad (6.3)$$

The ablated volume per second can be obtained:

$$V_s = V_p \times PRF \quad (6.4)$$

The removal rate per Joule can be defined from the following equation:

$$V_J = V_p / E_p \quad (6.5)$$

The mass ablation rates can be calculated directly from the volumetric ablation rate by multiplying the later parameters by the density of the material, ρ ($\text{g}/\mu\text{m}^3$), giving the total ablated mass, $M = \rho \times V$, ablated mass per pulse, $M_p = \rho \times V_p$, ablated mass per second, $M_s = \rho \times V_s$, and ablated mass per Joule, $M_J = \rho \times V_J$.

A distinction should be made between these ablation rates as some of them refer to the effect of one laser pulse and others refer to the effect taken from the fabrication of the whole channel. The calculation of total ablation rates from those rates corresponding to single parameters would yield the same values. For instance, if the ablated mass per joule was to be calculated for the whole channel then it requires the division of the total ablated mass by the total amount of energy used, this will yield the same value obtained from dividing the ablated mass per pulse by the pulse energy. As a matter of fact, the switching between both parameters uses the multiplication and division of the number of pulses simultaneously. As a result of this, for volume and mass calculations, there is one main overall ablation rate for each and the remaining rates are per pulse.

Finally, the total energy, E_T , used to fabricate the channel can be obtained from the multiplication of the pulse energy by the number of pulses, and is given by,

$$E_T = N \times E_p \quad (6.6)$$

This parameter may be used in calculating the cost and efficiency of channel fabrication. For summary and convenience reasons, table 6.1 lists the indirect process parameters, the ablation rates, the unit used to express them in this study and their implication. The parameters listed in table 6.1 were calculated for the channel results used in the DoE. The calculations of these are shown in table F.2 and F.3.

Table 6.1: Indirect process parameters and ablation rates.

Parameter	Symbol	Unit	Significance
Indirect process parameters			
Intensity	I	kW/cm^2	Laser power (per focal area)
Pulse energy	E_P	mJ	Energy (per pulse)
Pulse fluence	F	kJ/cm^2	Energy fluence (per pulse)
Fluence per length	F_M	J/cm	Energy fluence (per unit length)
Volume ablation rates			
Ablated volume	V	μm^3	Ablated volume (total)
Ablated volume/pulse	V_P	$\mu\text{m}^3/\text{pulse}$	Ablated volume (per pulse)
Ablated volume/second	V_S	$\mu\text{m}^3/\text{s}$	Ablated volume (per second)
Ablated volume/Joule	V_J	$\mu\text{m}^3/\text{J}$	Ablated volume (per Joule)
Mass ablation rates			
Ablated mass	M	g	Ablated mass (total)
Ablated mass/pulse	M_P	g/pulse	Ablated mass (per pulse)
Ablated mass/second	M_S	g/s	Ablated mass (per second)
Ablated mass/Joule	M_J	g/J	Ablated mass (per Joule)

The effects of the indirect process parameters on the width and the depth of the channel will be discussed first. Later, the effects on the ablation rates will be presented and discussed. However, it is important to make an important note on the nature of the indirect process parameters. As these parameters are from a limited set of process parameters P , PRF and U , their effects have similarities. This can be observed from the way these parameters change in table F.2. It can be seen that the laser intensity has a similar trend as the fluence per length. Similarly, the pulse energy has a similar effect as that of the pulse fluence. According to this nature, the effects of the similar parameters will be investigated simultaneously, by plotting curves with two horizontal axes, each representing one of the parameters. There is a substantial number of figures that have two horizontal axis titles presented in this chapter. In those cases, the horizontal axis readings are those of the lower axis title.

6.2.2 Parameters effects on channel width and depth

As can be seen from table F.2 the range of the laser intensity and the fluence per length is fixed for insets of processing parameters having a fixed PRF and U values. Hence the effect of intensity and fluence per length is best seen by plotting the responses for a

fixed value of U and observing the effect of changing PRF . Figures 6.2 to 6.4 show the effect I and F_M on the channel width and figures 6.5 to 6.7 show their effect on the channel depth. Each figure represents responses obtained at a fixed U value. It can be seen that the range of I and F_M changes between the figures, but remains the same for the three PRF values plotted in each figure.

Two important observations can be made by inspecting figures 6.2 to 6.7. Firstly, by looking at each curve representing a fixed PRF value, as the intensity or the fluence per length increases, the width and depth increase. The second observation, by looking at the curves representing the PRF values in each curve, it can be seen that increasing the value of PRF decreases the width and depth. These comply with the parameters effects observations made earlier in the DoE analysis.

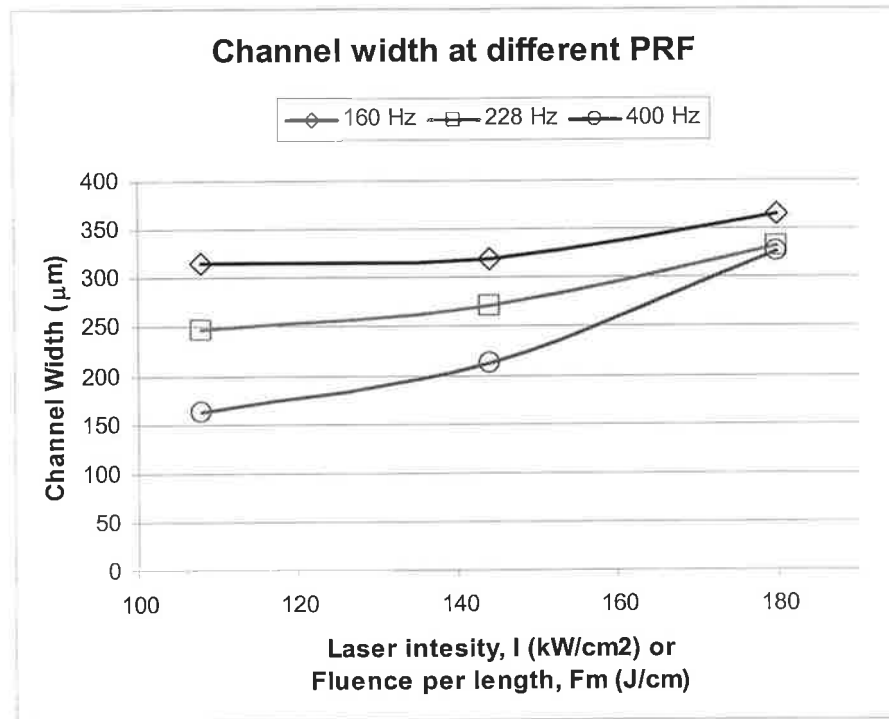


Figure 6.2: I and F_M effect on channel width at $U = 100$ mm/min and different PRF values.

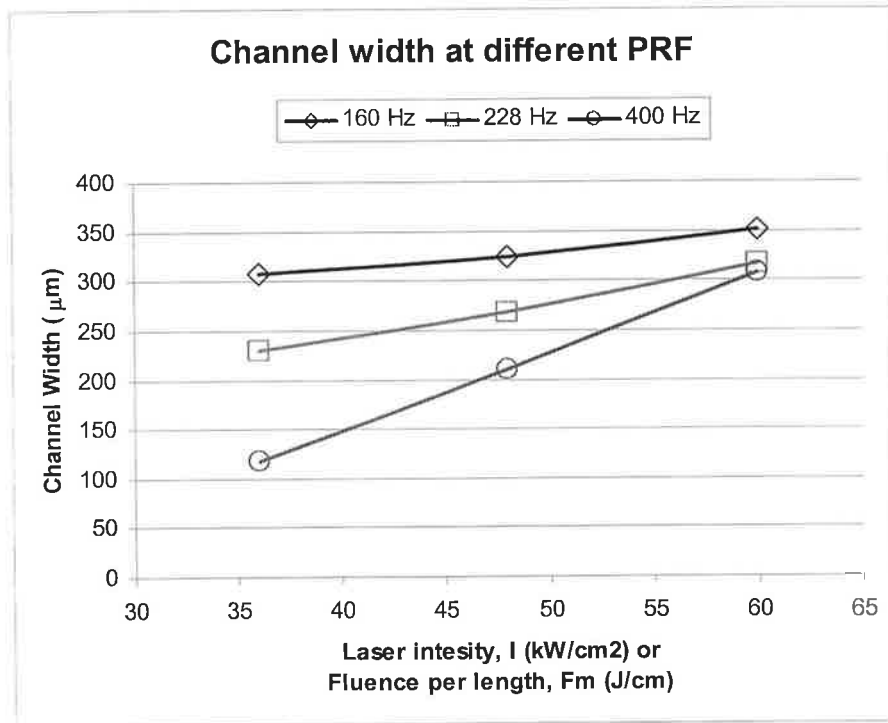


Figure 6.3: I and F_M effect on channel width at $U = 300$ mm/min and different PRF values.

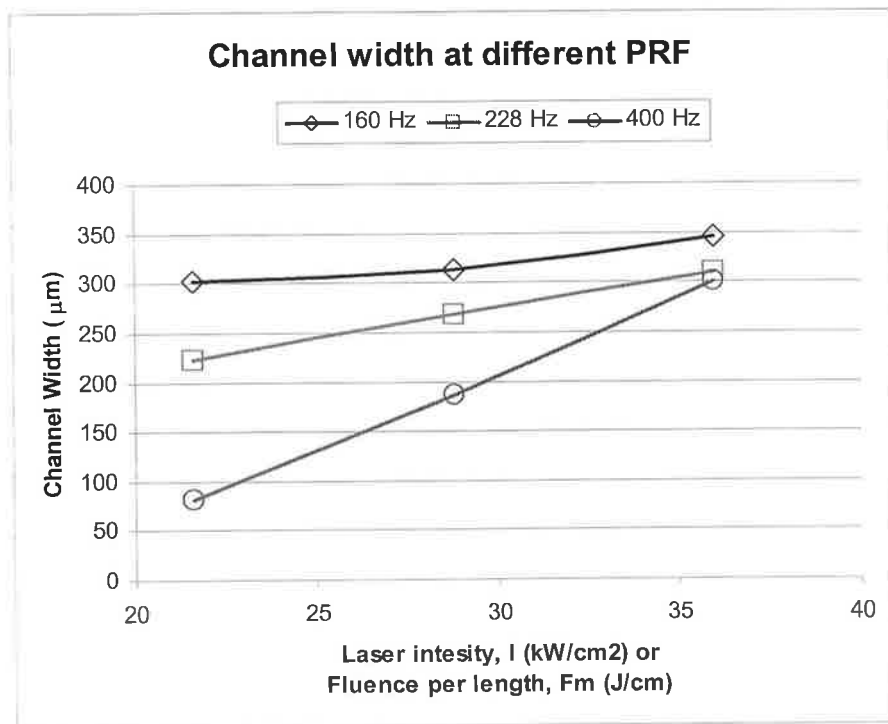


Figure 6.4: I and F_M effect on channel width at $U = 500$ mm/min and different PRF values.

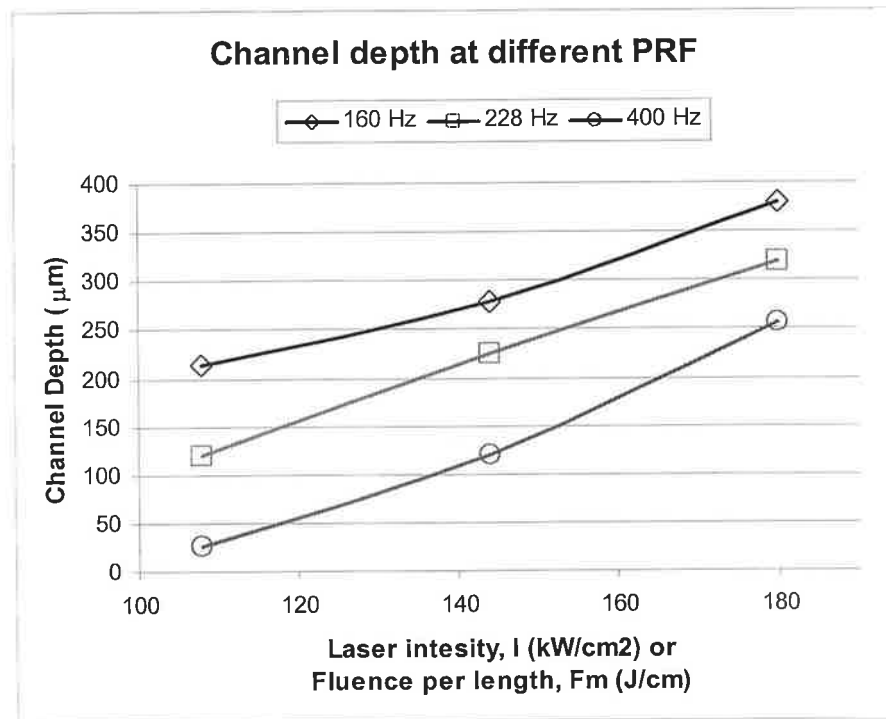


Figure 6.5: I and F_M effect on channel depth at $U = 100$ mm/min and different PRF values.

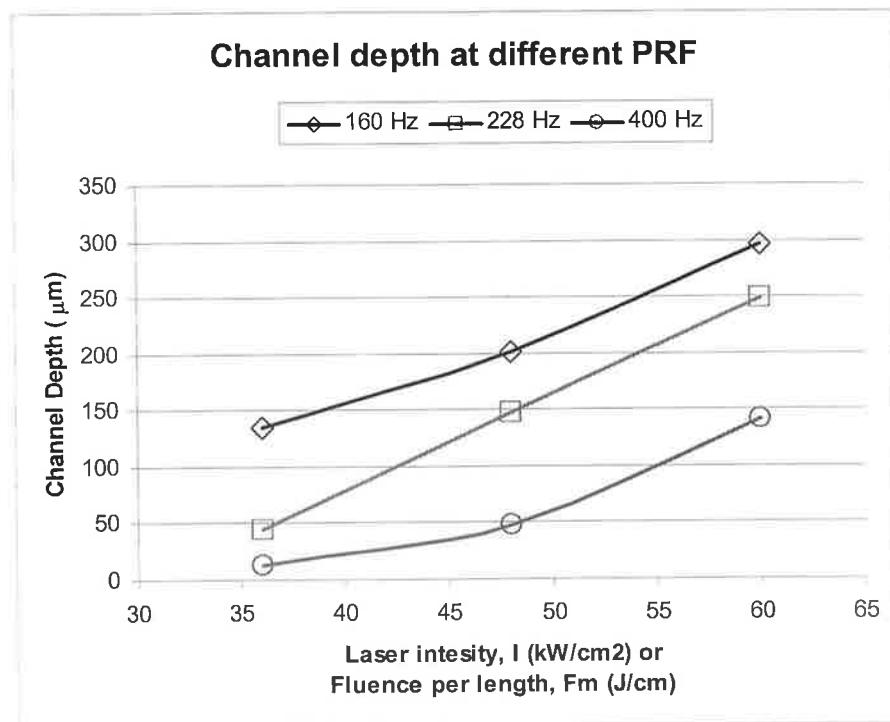


Figure 6.6: I and F_M effect on channel depth at $U = 300$ mm/min and different PRF values.

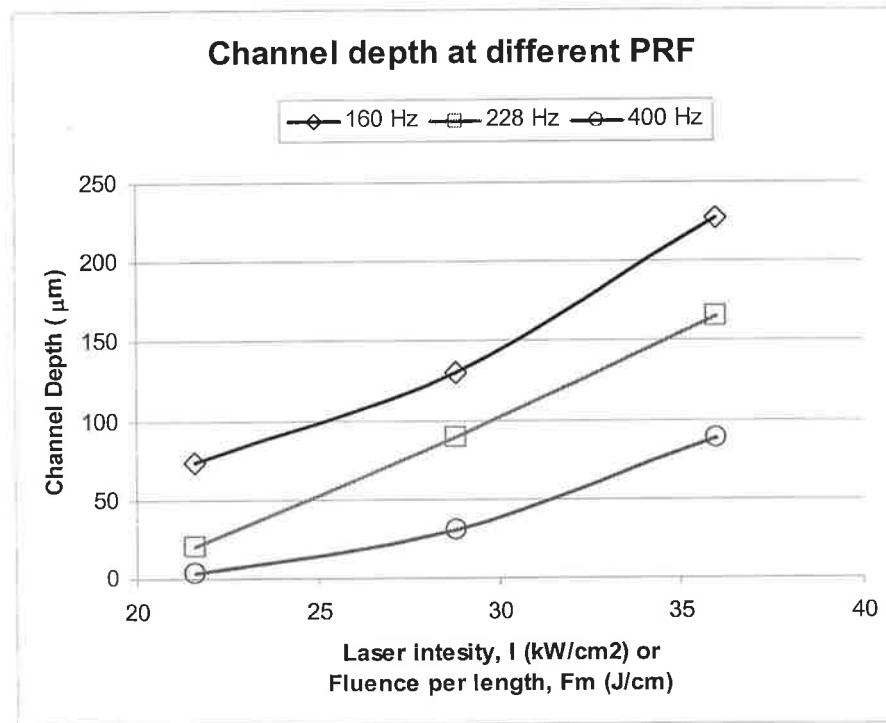


Figure 6.7: I and F_M effect on channel depth at $U = 500$ mm/min and different PRF values.

Another interesting relation can be studied between the pulse energy or fluence and the channel width and depth. The pulse energy and fluence give a fixed range for all values of PRF . This range repeats for each inset having the same U value as can be seen from tables F.1 and F.2. Both parameters have the same effect and their effect can be studied simultaneously. Figure 6.8 shows the effect of E_p and F on the channel width and figure 6.9 shows their effect on the channel depth. It can be seen from both figures that increasing E_p and F increases the width and depth for all values of U represented by the three curves in each figure. If the relation between the three curves in each figure is studied, it can be seen that decreasing the speed causes an increase in the channel width and depth. These observations are in agreement with the ones obtained earlier from the analysis on the DoE. There are slight differences between the effects of E_p and F on width and depth. Firstly, the effect of U on the width seems to be less than its effect on the depth, as can be seen from the vertical separation between the curves in figures 6.8 and 6.9. Moreover, the effect of E_p and F on the width seems to be saturating or converging as it increases in the case of the depth.

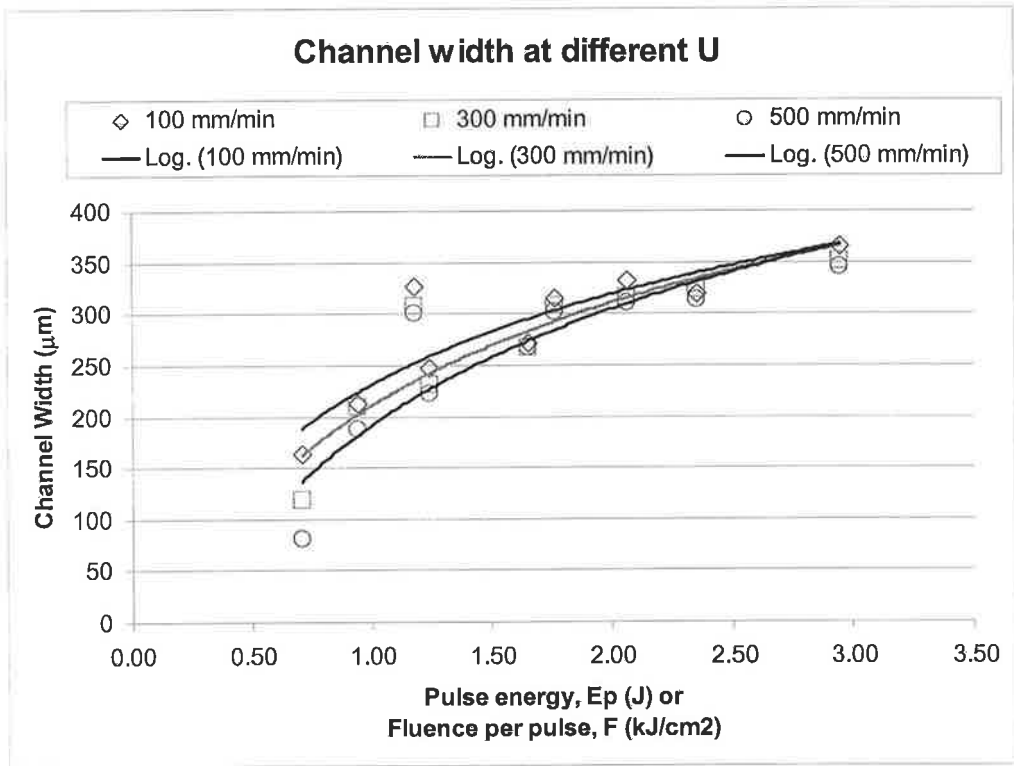


Figure 6.8: E_p and F effect on channel width for different U values.

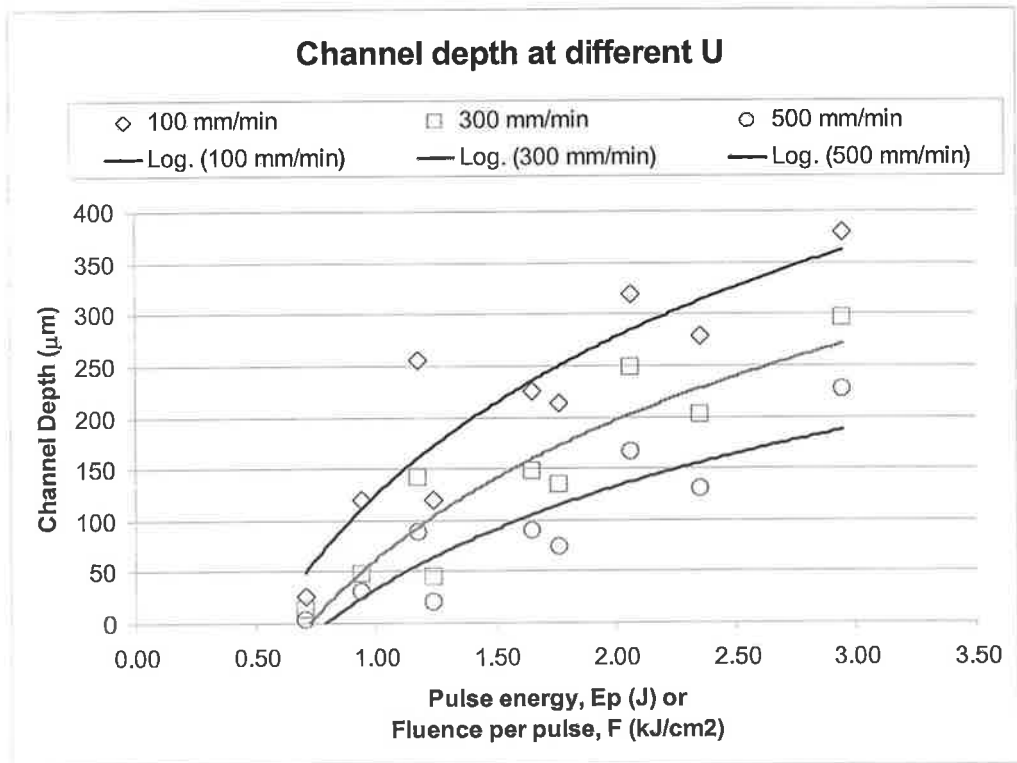


Figure 6.9: E_p and F effect on channel depth for different U values.

6.2.3 Parameters effects on the ablation rates

It was found that the considering the effect of E_p and F on the ablation rates provides broad observations as compared to studying three separate figures for the effect of I and F_M . An individual example will be illustrated to show the effect of I and F_M at the end of this section. Figure 6.10 shows the effect of changing E_p and F on the total ablated volume from the channels. It can be seen that over the investigated range of E_p and F , the total ablated volume is directly proportional to the increase in the process parameters. This, in fact, was expected since increases in these parameters meant corresponded to an increase in the total amount of heat input to the material. Furthermore, the trend curves representing the data scatter for each U setting in figure 6.10 shows that decreases in the speed result an increase in the ablated volume. This is a direct effect of larger number of pulses required to fabricate the channels at low speed and hence the larger amount of total energy deposited.

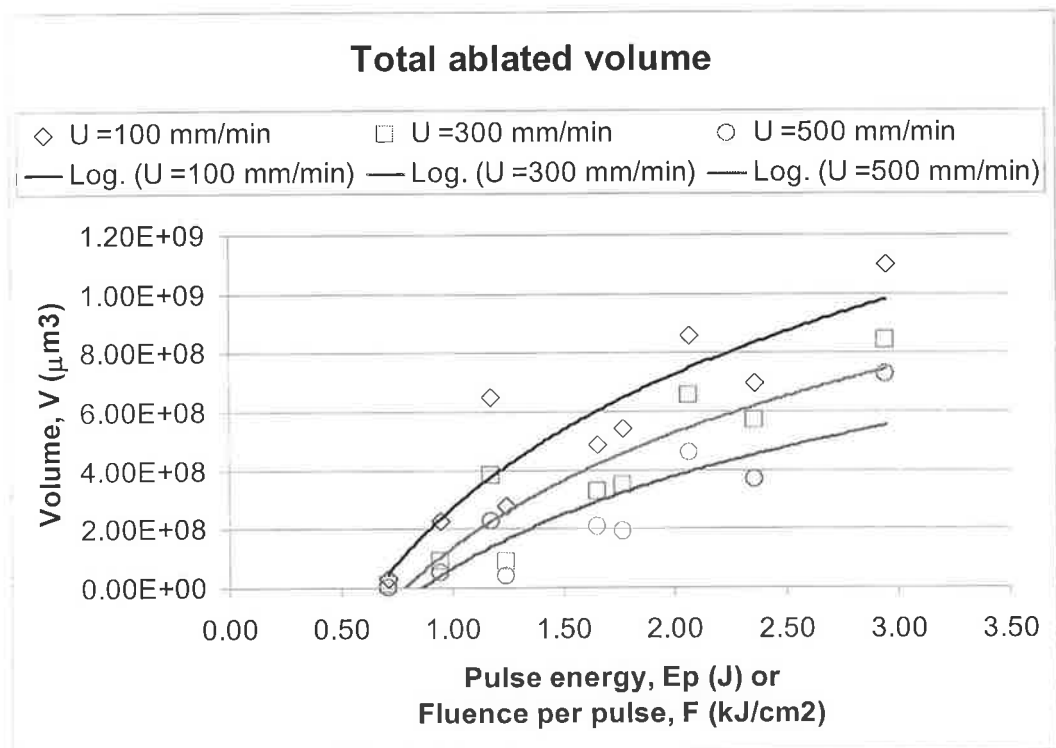


Figure 6.10: E_p and F effect on total ablated volume at different U values.

In terms of the total ablated mass, figure 6.11 shows that the effect of changing E_p and F on the total ablated mass. This figure shows the same effect of the process parameters as observed in figure 6.10.

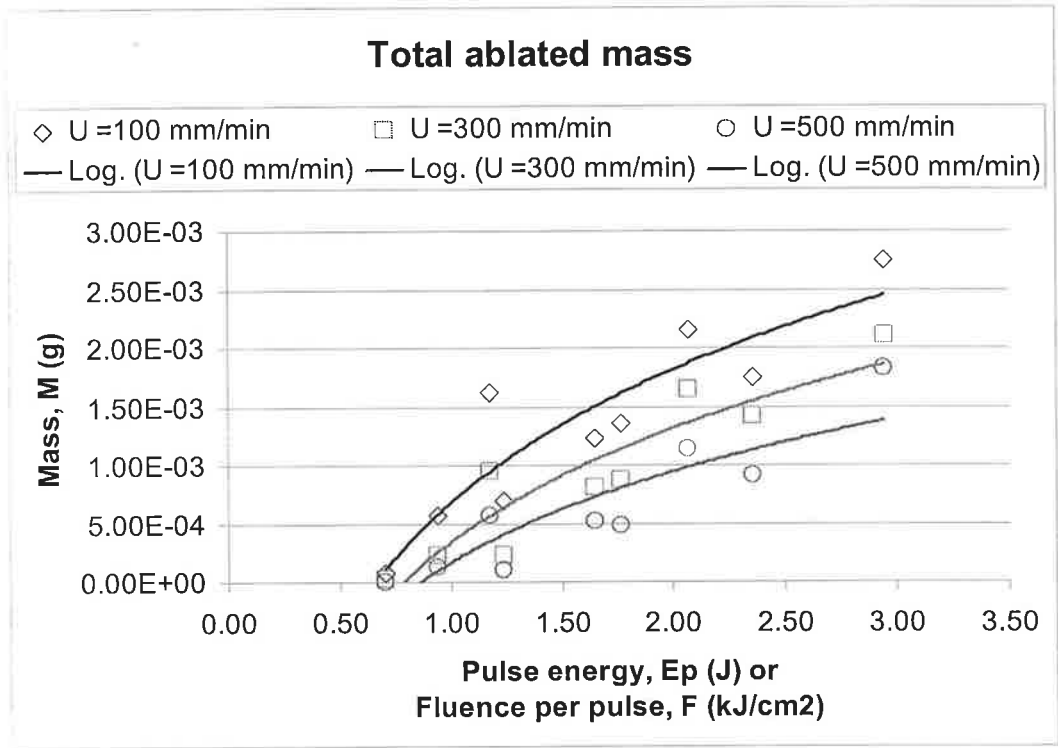


Figure 6.11: E_p and F effect on total ablated mass at different U values.

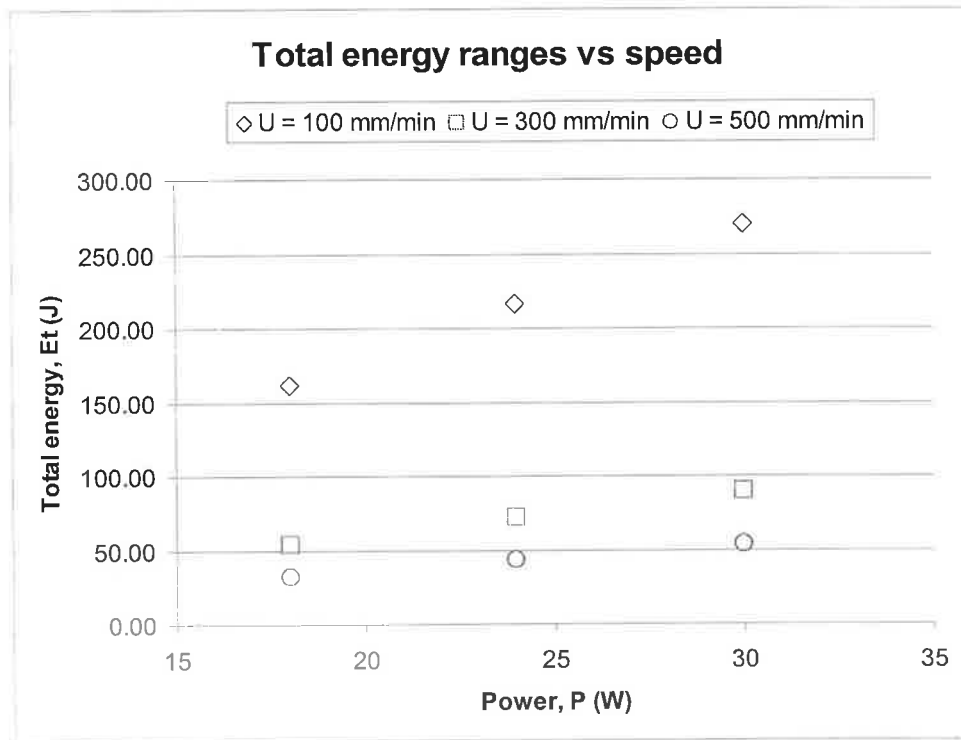


Figure 6.12: Ranges of total energy deposited for different P settings.

This very effect of U on the ablation rates can be studied by illustrating its effect on the total amount of heat delivered to material. The total energies are shown in table F.3, but it is easier to observe from figure 6.12, which shows all the possible total amounts of

energy calculated from the experiments, plotted versus the range of P , I or F_M . It can be seen that for higher U values the amount of energy becomes less. This is a direct result of the less number of pulses delivered to the material at those speed settings.

The effects of E_p and F on the ablation rates per pulse, second or Joules might be misinterpreted from the first glance. Take figure 6.13 for instance, which shows the effect of E_p and F on the ablated volume per pulse, V_p . It can be seen by looking at each trend line individually that the ablation rate increases as these process parameters are increased. If the three curves representing the different U values are contrasted, then it can be seen that high U values result in higher ablation rates. This contradicts with the results shown earlier and with the expected results from general engineering knowledge. However, this behaviour is again due to the speed effect on the feed, the number of pulse and the total energy deposited in to the material as shown in figure 6.12. The levels of the trend lines in figure 6.13 will change to become exactly the same as those of figure 6.10 if multiplied by the respective number of pulses. The number of pulses needed to fabricate each channel is listed in table F.2. Based on this, relations such as the ones shown in figure 6.13 are not absolute or conclusive, but relative, and cannot be directly compared. It can be said, from figure 6.13 that pulses delivered at higher speed ablated more material, but in a collective observation, the material removed from the channels at those settings was less according to figure 6.10. Figures like 6.13 provide some interesting information on comparing the different settings from the efficiency point of view, such as which settings provide the best ablation rates per pulse, second or Joule. The relations between E_p and F and the remaining volume and mass ablation rate measures are illustrated in figures 6.14 to 6.18 and possess the same nature of effects.

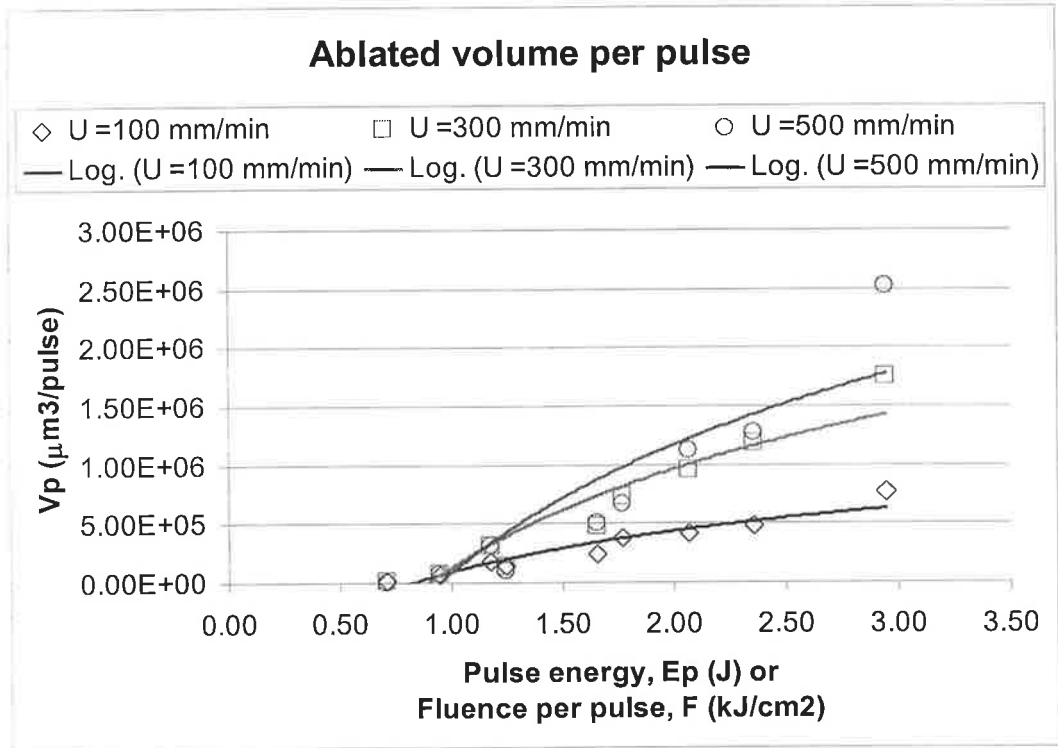


Figure 6.13: E_p and F effect on ablated volume per pulse at different U values.

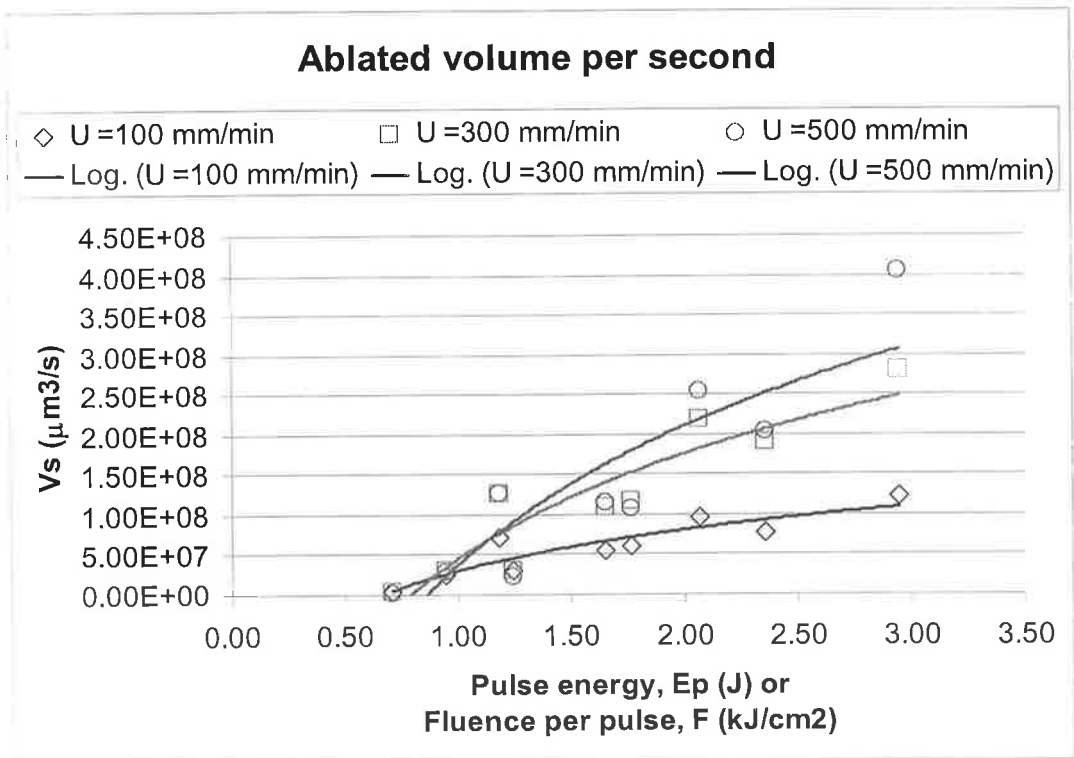


Figure 6.14: E_p and F effect on ablated volume per second at different U values.

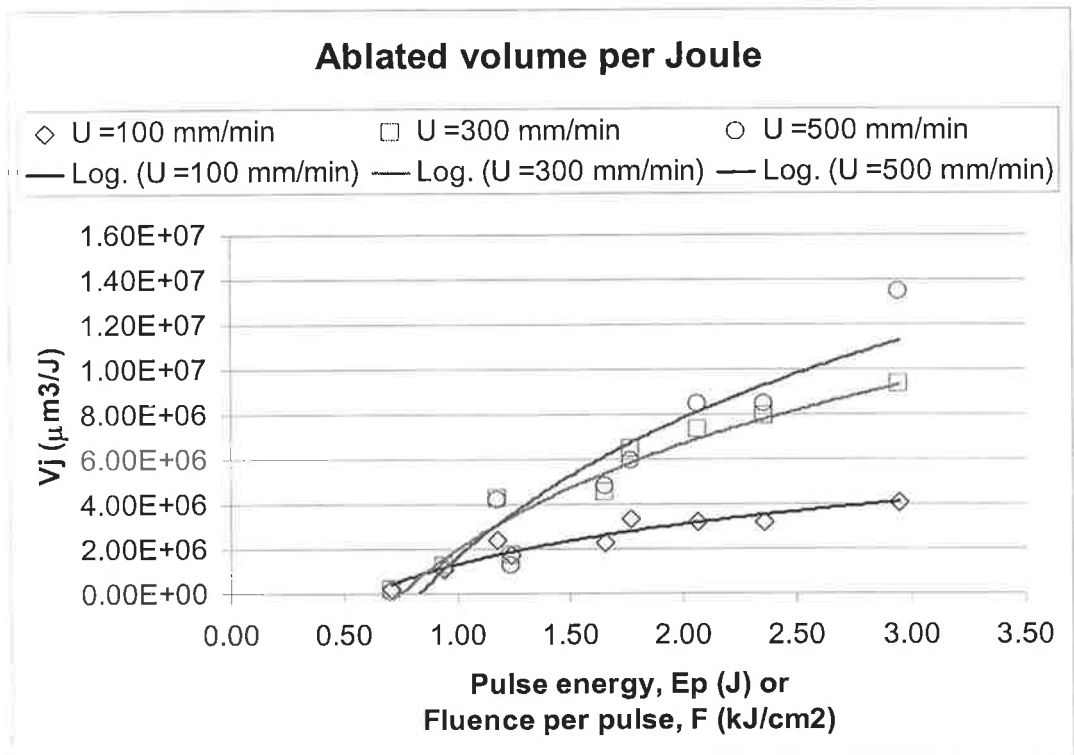


Figure 6.15: E_p and F effect on ablated volume per Joule at different U values.

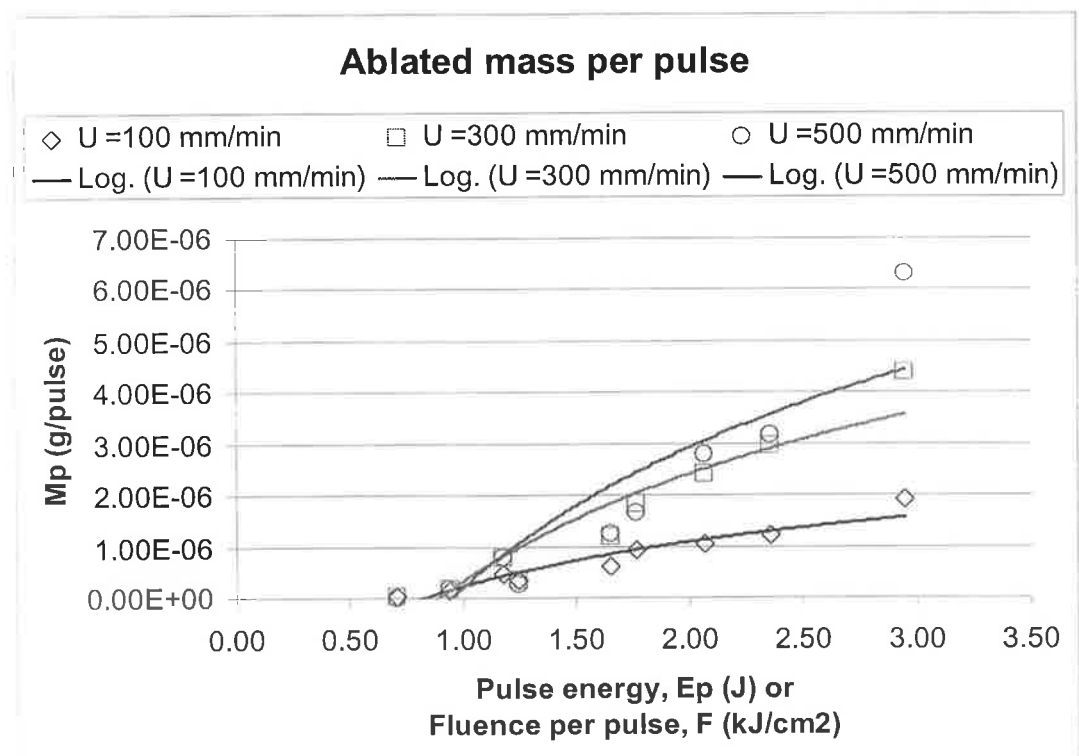


Figure 6.16: E_p and F effect on ablated mass per pulse at different U values.

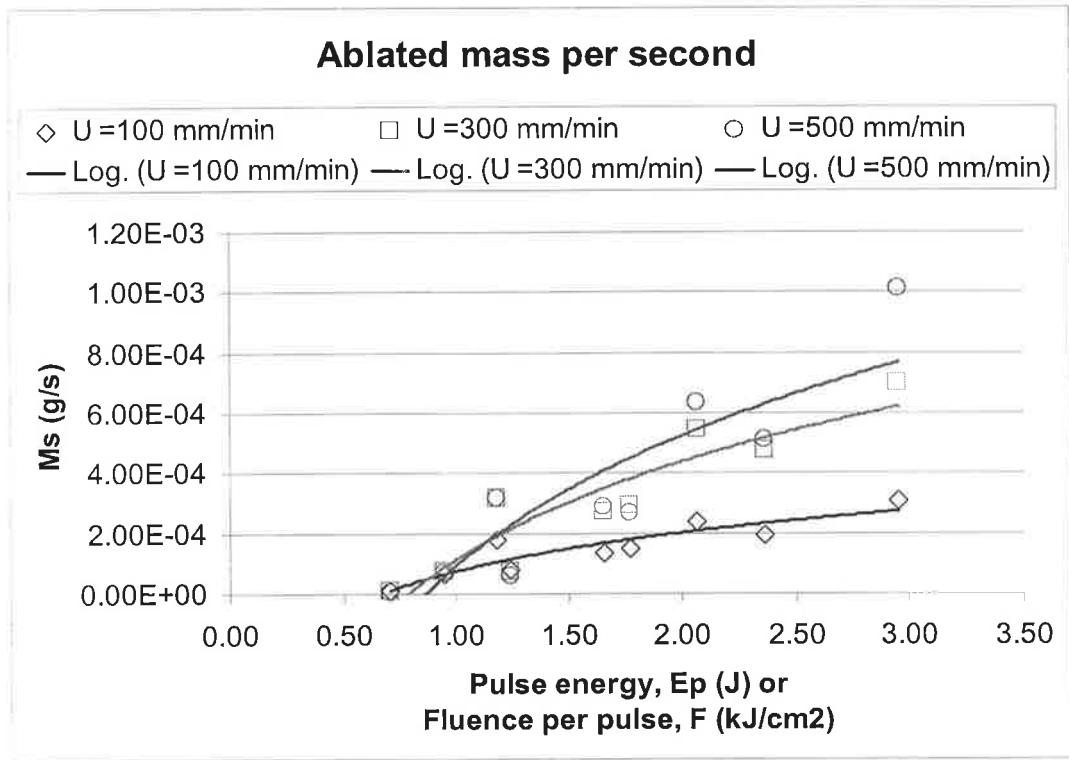


Figure 6.17: E_p and F effect on ablated mass per second at different U values.

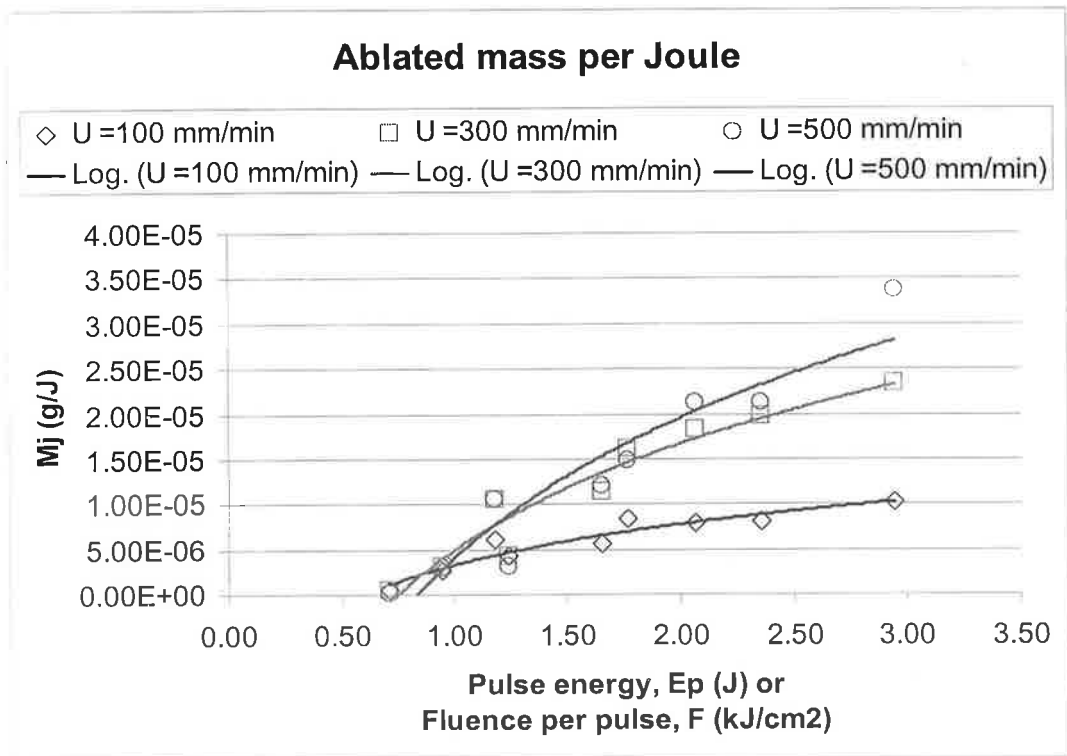


Figure 6.18: E_p and F effect on ablated mass per Joule at different U values.

The relation with the ablation rates that can be discussed is that with the laser intensity I and fluence per length F_M . Because each ablation rate would require three different

figures to contrast it with I and F_M , only one case will be illustrated. Figures 6.19 to 6.22 show the effect of I and F_M on the volume ablation rates calculated at a fixed $U = 100$ mm/min. It can be seen that the nature of the effect is similar to the ones shown in figures 6.2 to 6.7. This is the case for the other ranges of U and for the mass ablation rates too. The ablation rates increase as of I or F_M increase and they also increase as the PRF is decreased.

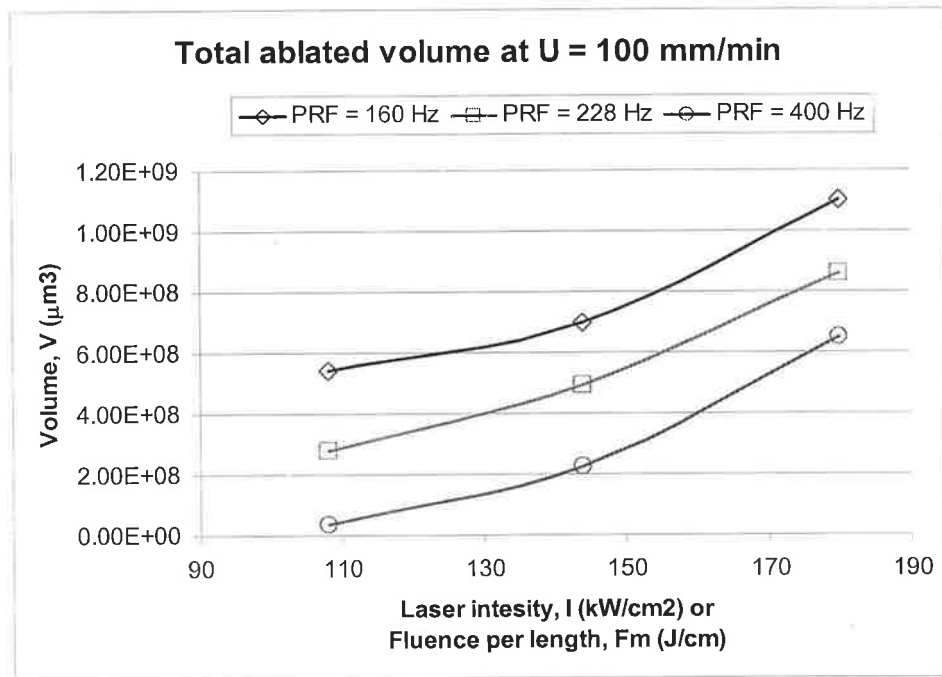


Figure 6.19: Effect of I and F_M on the total ablated volume at $U = 100$ mm/min.

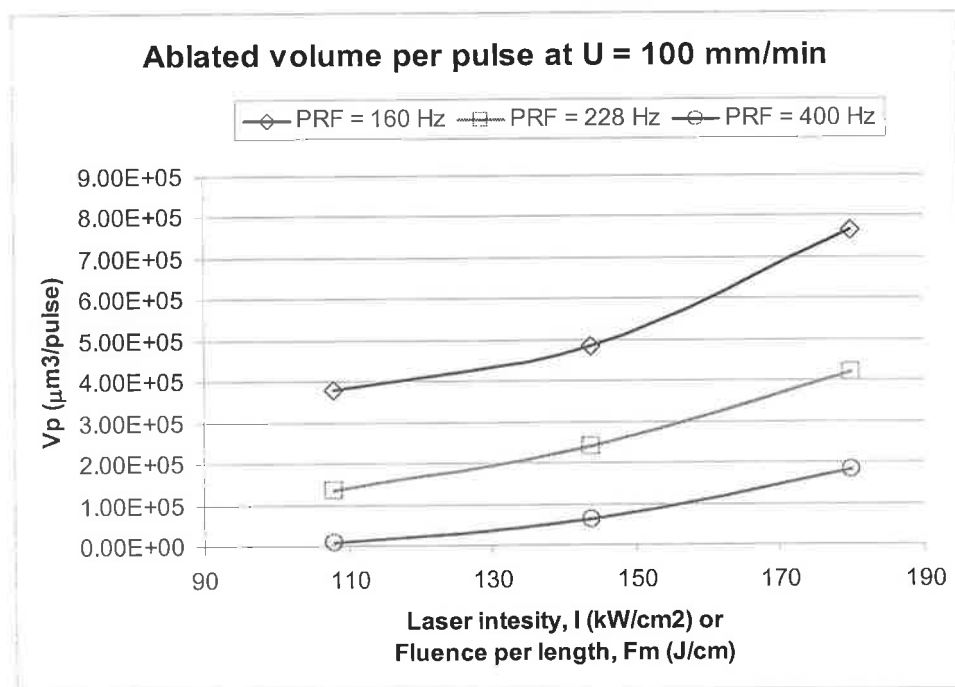


Figure 6.20: Effect of I and F_M on the ablated volume per pulse at $U = 100$ mm/min.

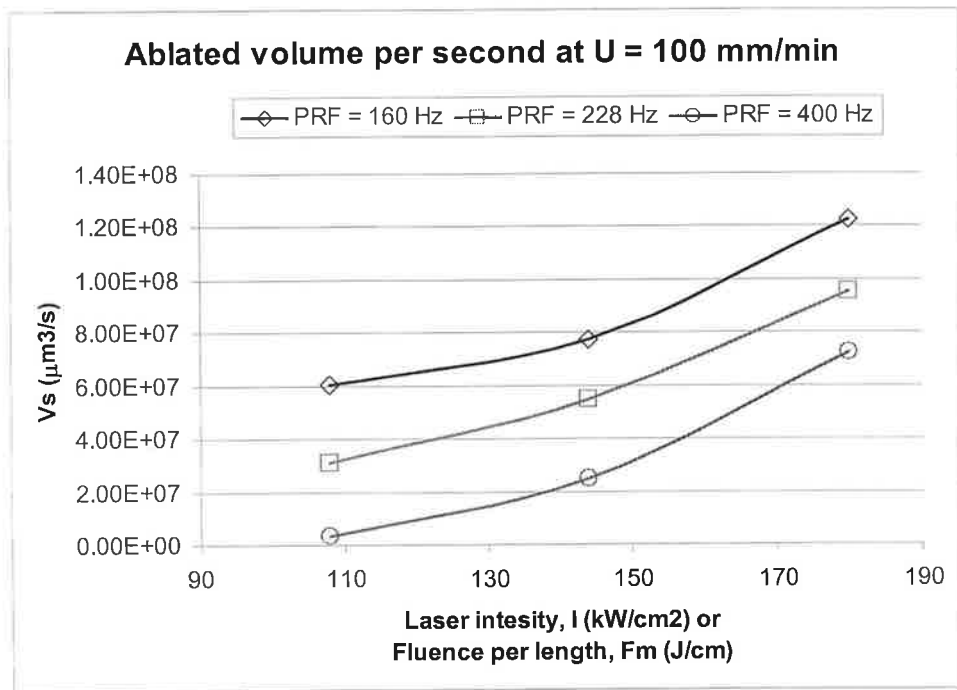


Figure 6.21: Effect of I and F_M on the ablated volume per second at $U = 100$ mm/min.

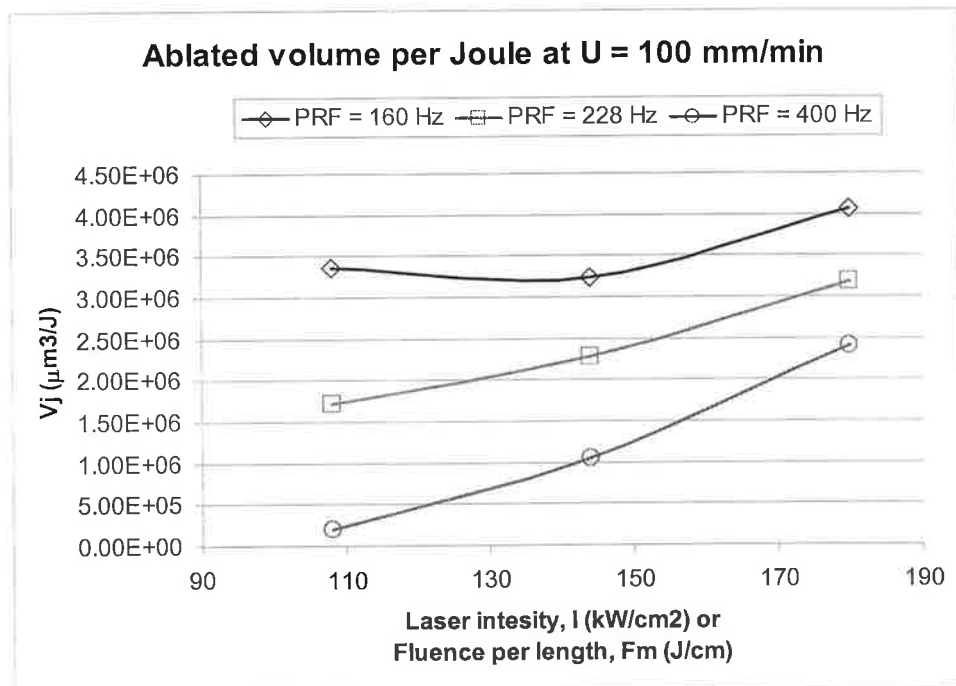


Figure 6.22: Effect of I and F_M on the ablated volume per Joule at $U = 100$ mm/min.

6.3 Simulated versus experimental morphology

This section presents the similarity found between the experimental and simulation results from morphological and surface nature stand points. The periodic nature of the pulsed laser beam source suggests that the resulting ablated regions will have a periodic nature. This can be seen from the simulated isotherms in figures 5.11 to 5.13 and the

simulated 3D channel profiles in appendix E.3. This periodic nature was also found in the SEM or 3D scans of the experimental channels. This nature had a particular clarity in channels that were produced using relatively higher feed rates, that is to say they were fabricated using high translational speed combined with low *PRF* settings. Examples of these are channels 10 to 15 and 19 to 24, and their microscopic images are in appendix D.1.

Figure 6.23 (a) and (b) show the SEM image simulated isotherm respectively for channel 21. The length taken from the SEM image corresponded to 450 μm to have equal scales of the SEM image and simulation, so that a direct comparison can be drawn. The direction of the laser ablation is taken from right to left in both images. It can be seen that the simulation underestimates the channel's width, which can also be numerically seen in table E.3. Figure 6.23 (a) contains about 9 periodic surface features corresponding to 9 laser pulses. This number of pulses and the separation between them agrees to a good extent with the simulated 8 pulses in figure 6.23 (b). Furthermore, the shape and the concavity direction of the surface features are similar in both images. The same observation can be made on the results obtained from the other channels mentioned above.

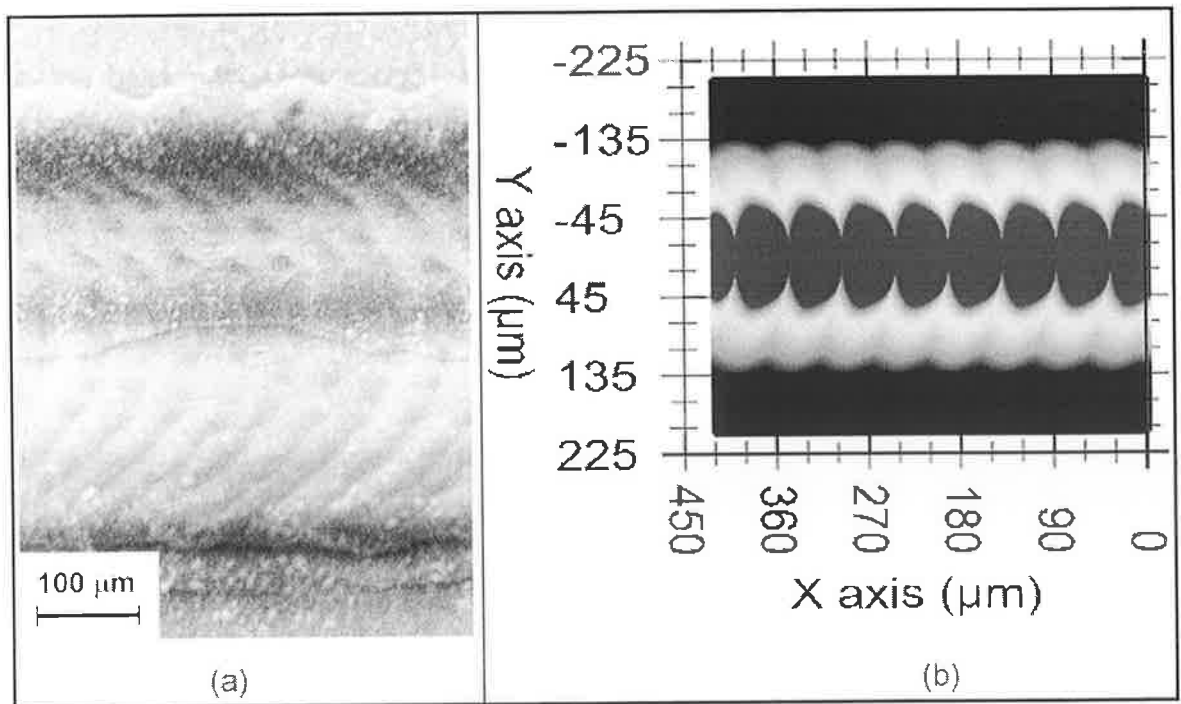


Figure 6.23: Comparison of channel 21, (a) SEM image and (b) simulated isotherms.

The results obtained from channel 19, 20 and 21 are interesting since they were fabricated using the highest feed rate and the periodic surface features were the clearest

from the microscopic, SEM images and 3D scans. The Ra from these channels was the highest amongst all simulation measurements in table E.3. A close investigation of the microscopic images of these channels shows that the separation between the successive features due to laser pulses was consistent. The calculated separation between the successive pulses from equation 4.3 was around $52 \mu\text{m}$ for all these channels. This agrees to a very good extent with measurements that can be made from the images and scans of channels 19 to 21. Figures 6.24 to 6.26 show the side views of the 3D scans of three pulses from each of channels 19, 20 and 21 respectively. The periodic features can be observed by looking the bottom of the channels. The separation between the valleys in figure 6.24 to 6.26 can be roughly estimated, by dividing the scanned length by 3, as $155/3 = 51.7 \mu\text{m}$. The separation between the successive pulses from the simulated 3D profiles can be obtained by repeating the same profile a number of times and for this particular case it was equal to about $52 \mu\text{m}$.

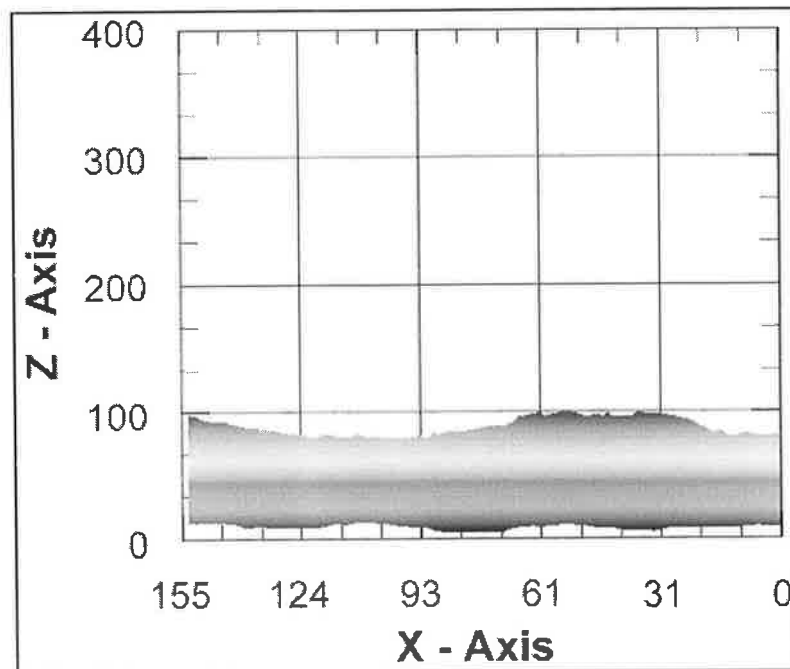


Figure 6.24: Side view of three pulses from channel 19.

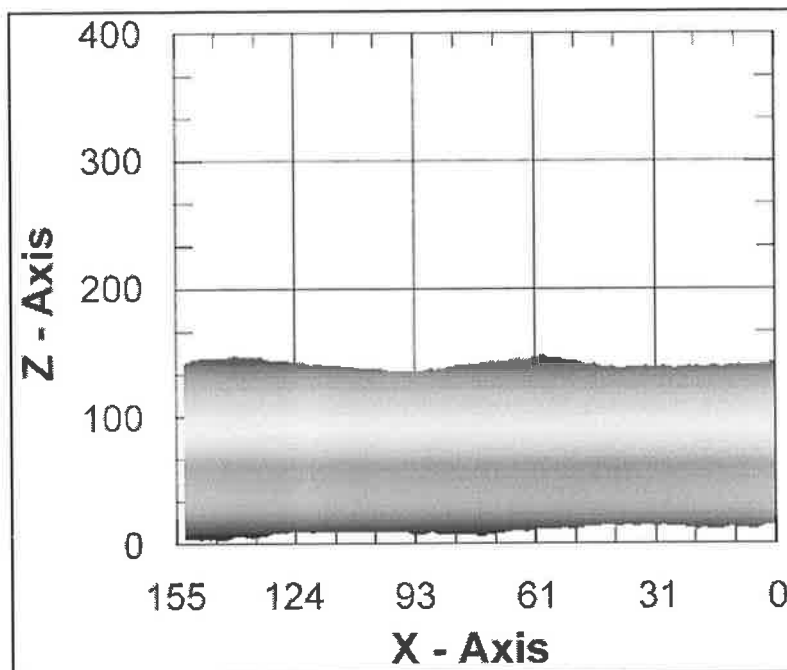


Figure 6.25: Side view of three pulses from channel 20.

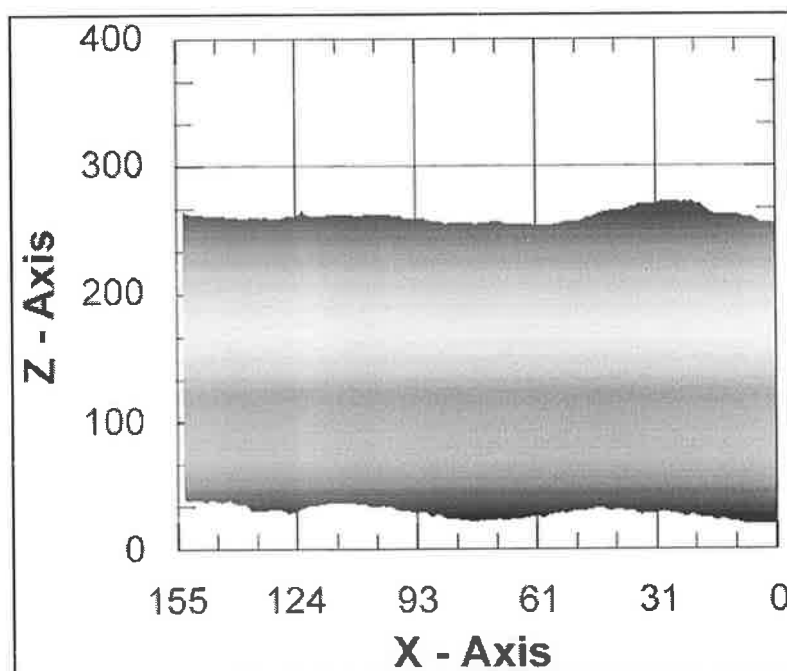


Figure 6.26: Side view of three pulses from channel 21.

Figures 6.27 to 6.29 show the top views of 20 simulated pulses of channels 5, 14 and 23 respectively. The figures also present the microscopic image of each channel opposite to the simulated profiles. The scale of the simulated images was changed maintaining the proportions between the x and y axes. As a result, the scales of the microscopic and simulated images are equal for direct comparison. The lengths of the simulated channels were different because they had fixed P and PRF settings but different U settings. The

simulation settings and responses of these channels are shown in tables E.1 and E.2. In figures 6.27 to 6.29, the laser propagation direction was from the top to the bottom. Hence, the periodic features were concaved up in both the simulated and the microscopic images. Comparing the figures and the numerical results in tables E.2 and E.3 shows that the speed had a directly proportional effect on the surface roughness. The effect of *PRF* on the channel morphology or *Ra* was also detected and presented in the next section.

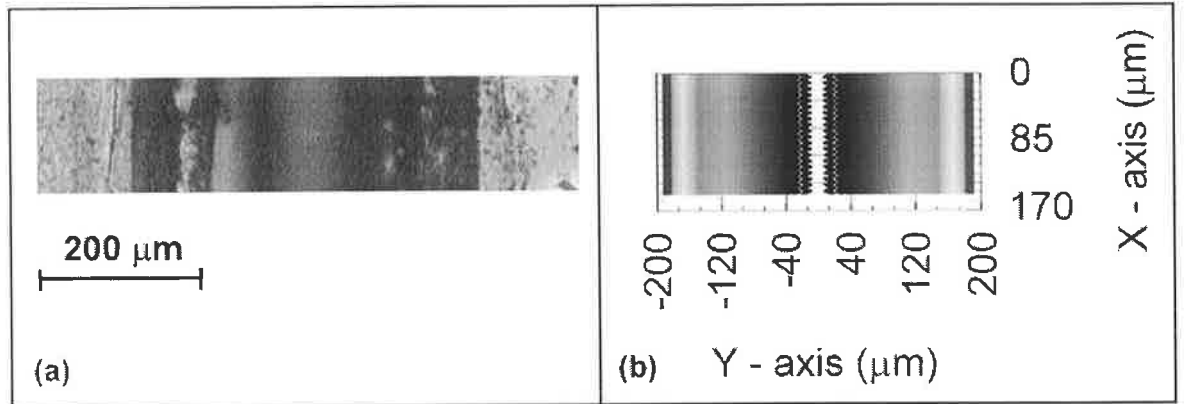


Figure 6.27: Channel 5 comparison (a) microscopic and (b) simulated image.

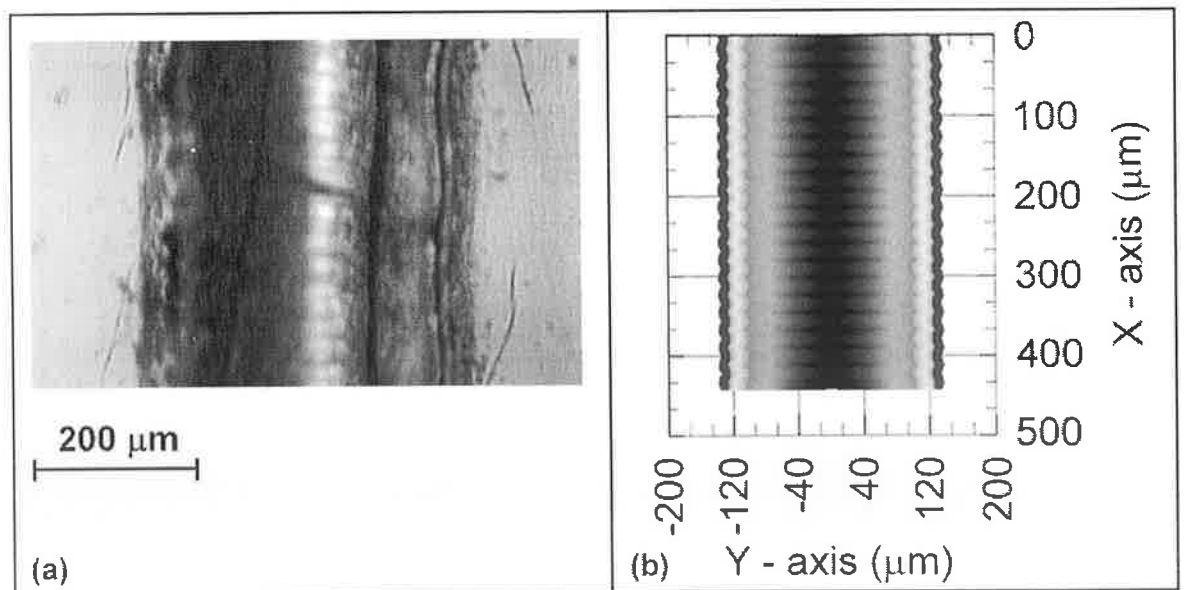


Figure 6.28: Channel 14 comparison (a) microscopic and (b) simulated image.

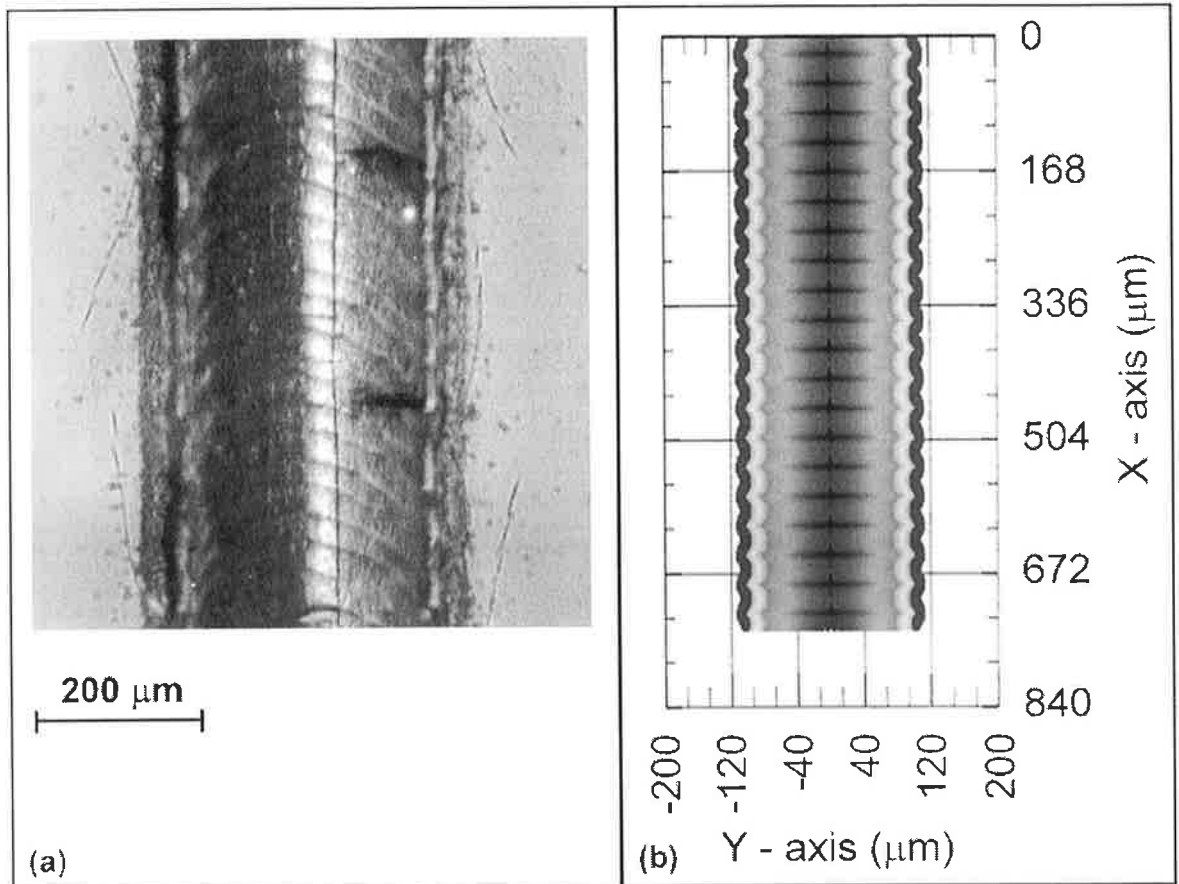


Figure 6.29: Channel 23 comparison (a) microscopic and (b) simulated image.

6.4 Comparative process parameters' effects

The process parameters' effects on the simulated results can be studied in a similar manner to the discussion of the experimental results in section 4.9. The effect of each parameter can be studied individually or a common parameter can be chosen to perform this investigation. The pulse energy can be treated as the common process parameter through which the effects of the other parameters can be investigated. The same responses are going to be treated in this section and at the beginning the effect of each parameter on the results are illustrated. Later on, the general trends of the parameters' effects are shown. All discussion performed in this section are compared to the obtained experimental results.

6.4.1 Width and depth trends

Figures 6.30 and 6.31 show the effects of P and PRF on the channel width and depth respectively. The figures were taken from the simulated results at a fixed speed of 8.333 mm/s. The results from the other two speed levels are similar in nature, but different in magnitude, see figures F.1 and F.2. It can be seen in figures 6.30 and 6.31 that P has a

directly proportional effect on the width and depth. PRF on the other hand, has an inverse relation with the width and depth. This agrees with the experimental results presented in figures 6.4 and 6.7. It can also be seen from the slopes and separation between the curves that P has a stronger effect than PRF on the both depth and width. For instance, in figure 6.30, changing P from 18 to 30 W at $PRF = 400$ Hz caused a change in the width from about 180 to 235 μm . On the other hand, changing PRF from 160 to 400 Hz at $P = 18$ W caused the width to reduce from about 192 to 180 μm . The same observation applies to other combinations of P and PRF in figures 6.30 and 6.31. This strength of effects also agrees with the statistical effect results obtained from the ANOVA results in tables 4.8 and 4.11.

Despite the magnitude differences between the experimental and simulated results of the width and the depth of the channels, the trends of the parameters effects on the width and the depth agree with the experimental data. The differences between the actual and simulated results could be attributed to the assumptions imbedded in the thermal model.

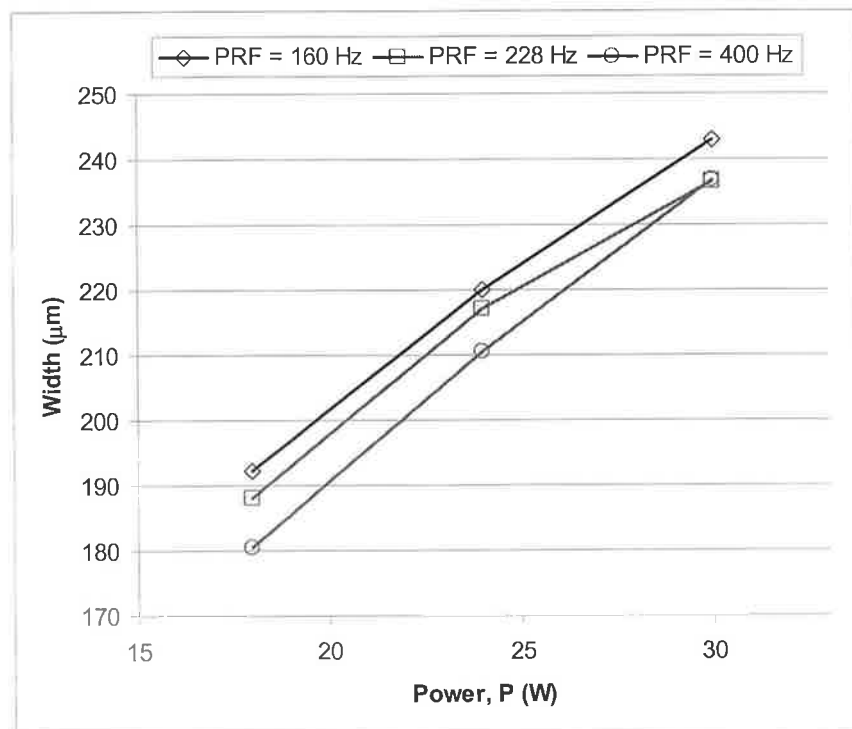


Figure 6.30: PRF and P effects on channel width at $U = 500$ mm/min.

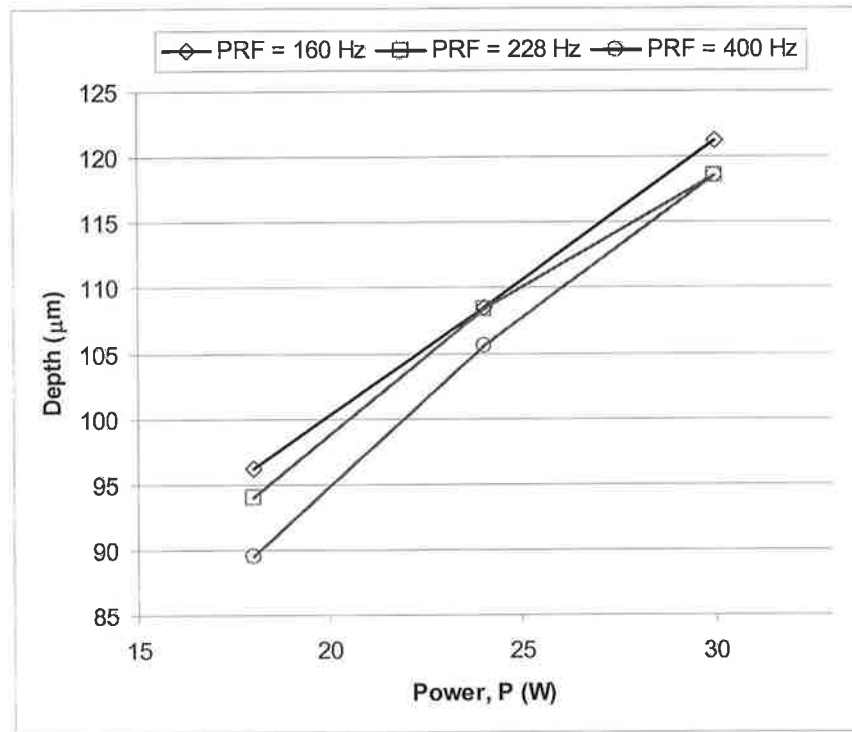


Figure 6.31: *PRF* and *P* effects on channel depth at $U = 500$ mm/min.

Plotting the simulated data versus a common parameter such as the pulse energy enables the investigation of the effects of all the parameters in one plot. Figures 6.32 and 6.33 show the simulated width and depth data versus the pulse energy. The figures show that increasing the pulse energy, which is dependant on P and PRF , increases the channel width and depth. Increasing the speed, U , on the other hand, causes a decrease in the channel width and depth. These results agree with the experimental results presented in figures 6.8 and 6.9.

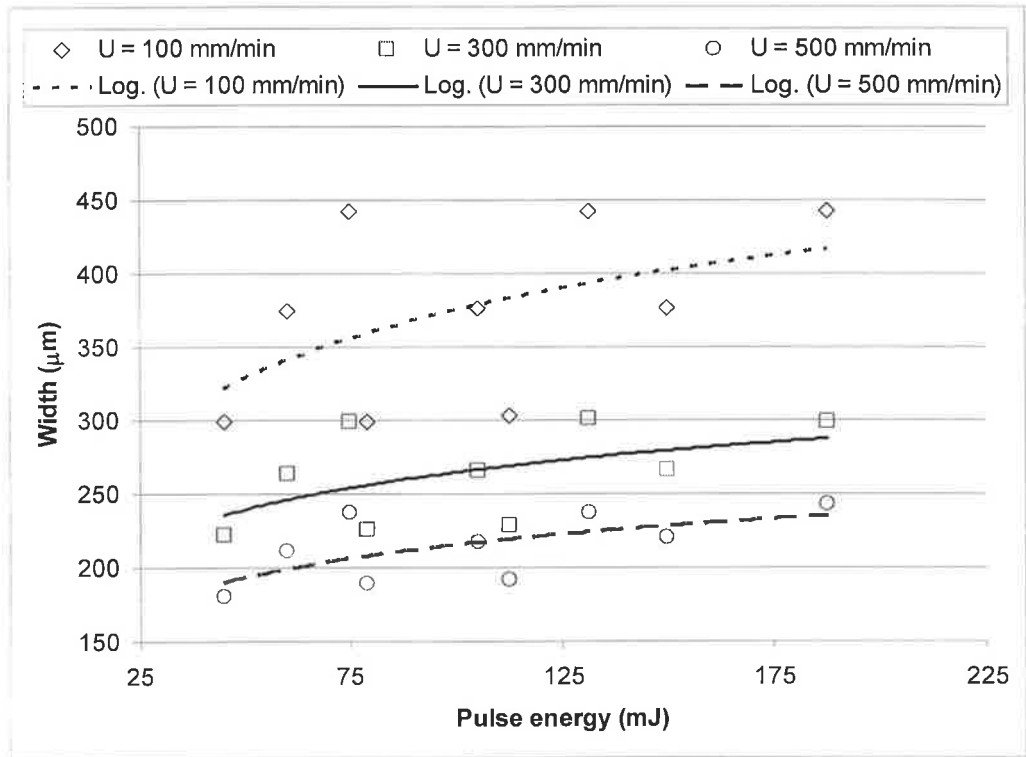


Figure 6.32: Pulse energy effect on simulated channel width.

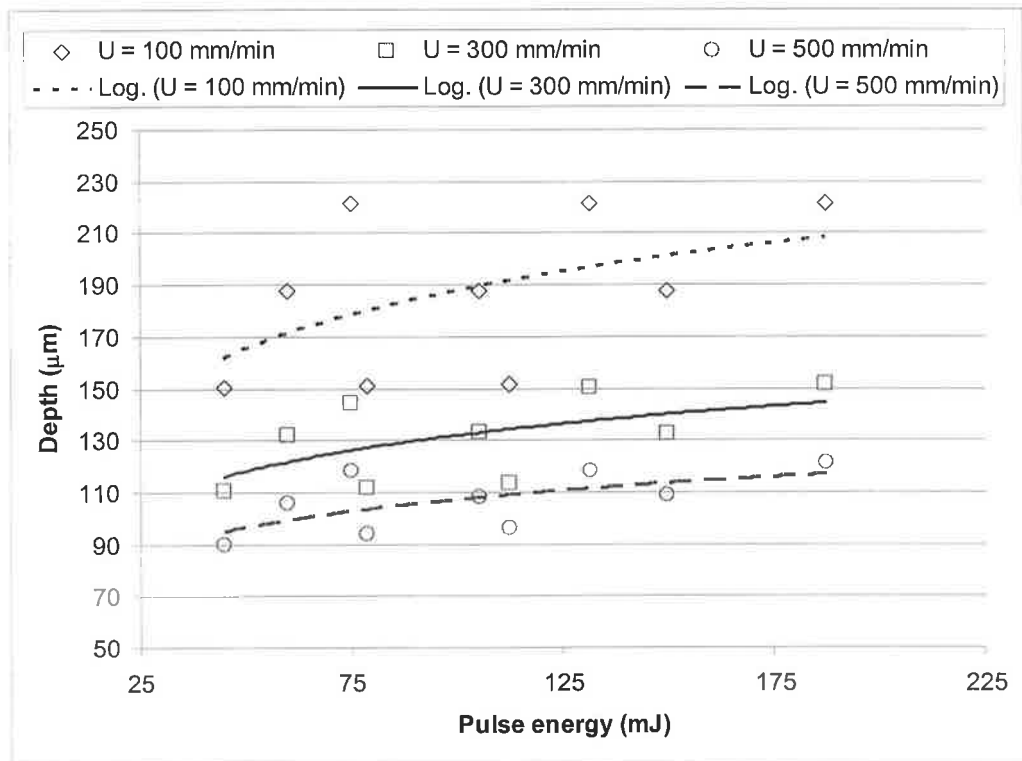


Figure 6.33: Pulse energy effect on simulated channel depth.

6.4.2 *Ra* trend based on simulation results

One of the aims of thermal modelling and simulation study was to investigate the change of *Ra* with the process parameters. The *Ra* predicted results from numerical simulation are presented in table E.2. Investigating the trend of *Ra* with each parameter reveals the following three observations:

- 1- *Ra* decreases by increasing *PRF* for fixed values of *P* and *U* values. This can be seen by comparing channels sharing the same *P* and *U* values. For instance comparing the trends of *Ra* for channel (10, 13, 16) to (11, 14, 17) and (12, 15, 18).
- 2- *Ra* increases by increasing *U* for fixed values of *P* and *PRF*. This can be seen by comparing channels sharing the same *P* and *PRF* values. For instance comparing the trends of *Ra* of channels (1, 10, 19) to (2, 11, 20) and (3, 12, 21).
- 3- *Ra* decreases by increasing *P* for fixed values of *PRF* and *U*. This can be seen by comparing channels sharing the same *PRF* and *U* values. For instance comparing the *Ra* values of channels (1, 2, 3), (10, 11, 12) and (19, 20, 21) separately.

The effects of *P*, *PRF* and *U* on simulated *Ra* are shown in figures 6.34 to 6.36. Each figure illustrates the effects of *P* and *PRF* on *Ra* at a fixed value of *U*. It can be seen that *P* and *PRF* are inversely proportional *Ra*. It can also be seen, by comparing the three figures that *U* has a directly proportional effect on *Ra*. The effect of *PRF* and *U* on *Ra* is of particular importance due to their larger effect. It can be seen from figures 6.34 to 6.36 that their effects agree with the expected theoretical effects that were presented in section 4.9.4. This supported that the actual experimental results showed rather a random and more complicated non-regular variance and could not be simply modelled.

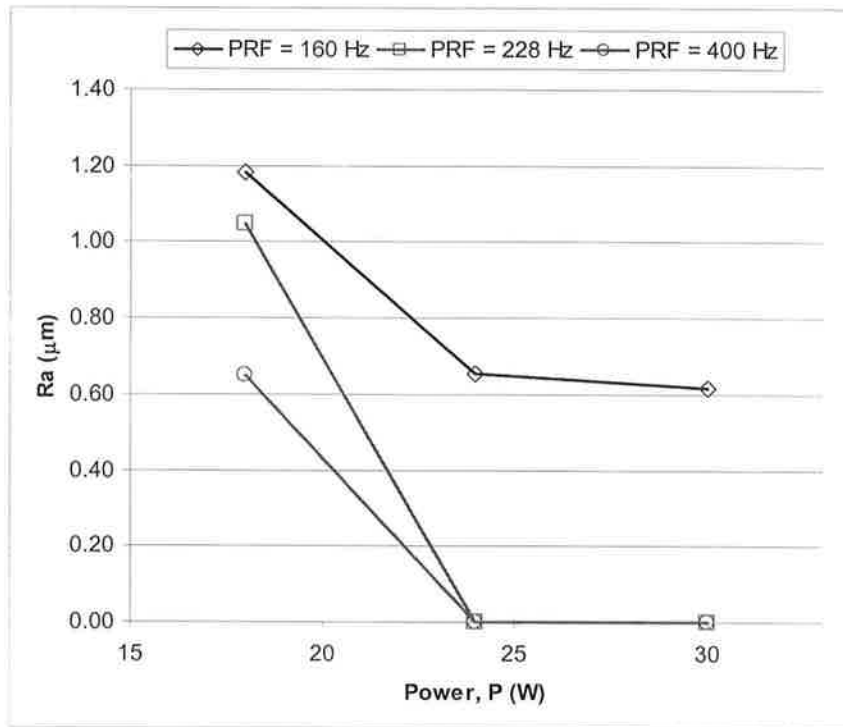


Figure 6.34: PRF and P effects on Ra at $U = 100$ mm/min.

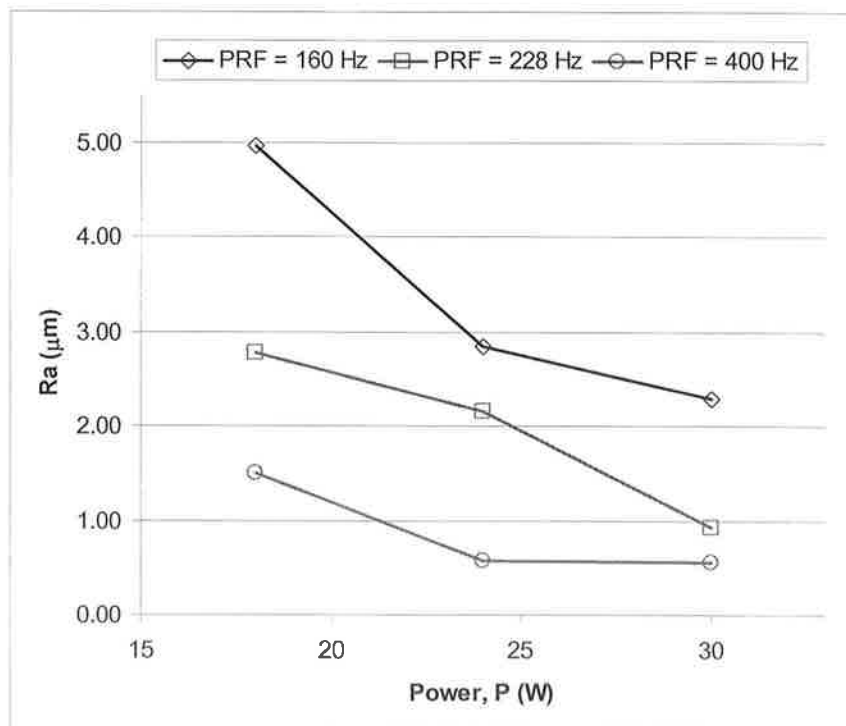


Figure 6.35: PRF and P effects on Ra at $U = 300$ mm/min.

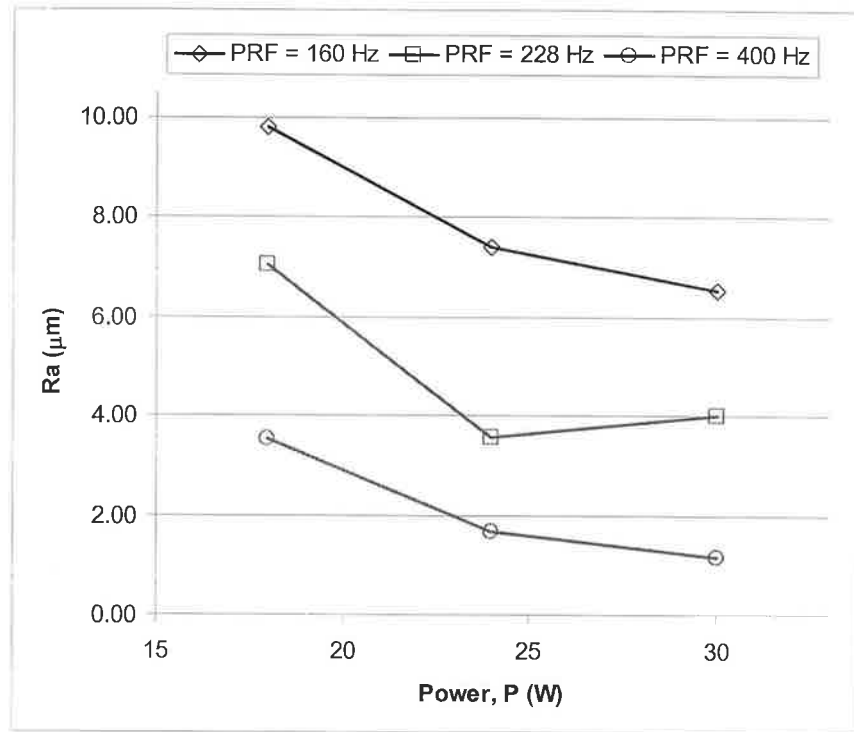


Figure 6.36: *PRF* and *P* effects on *Ra* at *U* = 500 mm/min.

The third observation above can be explained by considering the thermal deposition gradients. Increasing the power for fixed *PRF* values resulted in higher pulse energies delivered using the same *PRF*. The thermal mathematical model was based on heat conduction, and the resulting temperature gradients for high pulse energies were not as steep as they were in the case of relatively smaller pulse energies. This meant that this higher energy was distributed more uniformly over the length affected by each laser pulse. As a result the simulated ablated regions were distributed more uniformly in the *x*, *y* and particularly in the *z* direction. This effect can be seen by inspecting the simulated 3D profiles or the numerical results from simulations of the channels noted in point 3 above. These can be found in appendices E.3 and E.4 respectively.

Plotting the *Ra* simulated data versus the pulse energy enabled the general trends of *Ra* to be investigated as the process parameters are changed. Figure 6.37 shows that, in general, both the pulse energy and *U* are directly proportional to *Ra*.

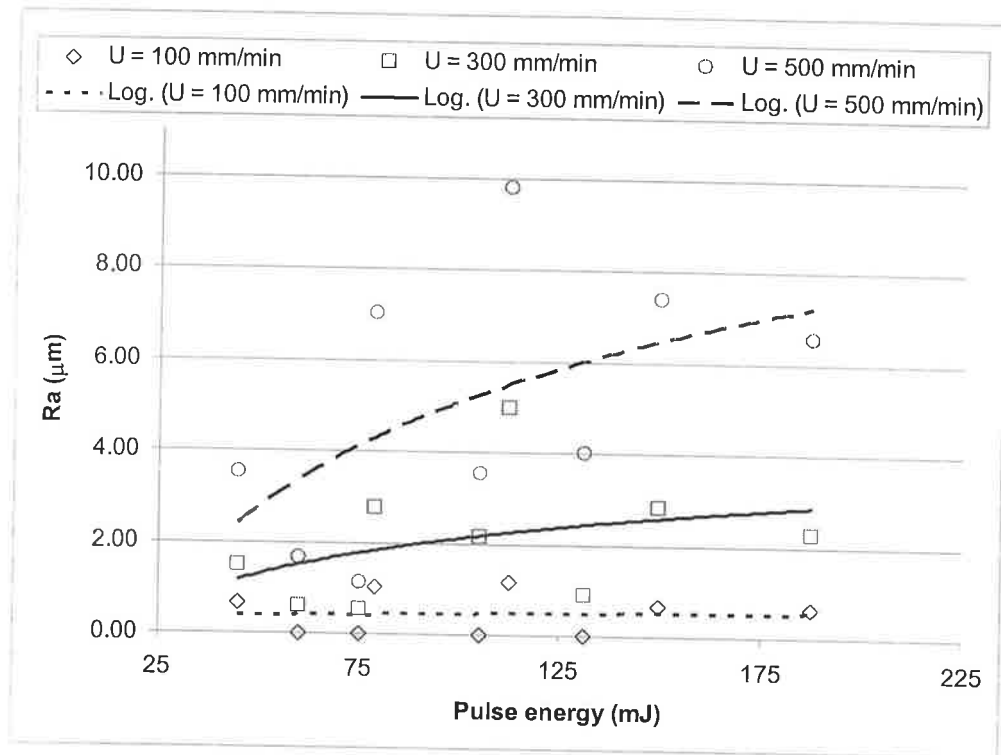


Figure 6.37: Pulse energy effect on simulated channel Ra .

6.5 General discussion

The analysis performed in section 6.2 representing the ablation rates and the effects of the indirect process parameters agreed with the DoE data that were used to produce the statistical process models. These data can be used in future studies of the channel fabrication efficiencies. The process parameters can be looked at from different perspectives and can take different forms such as the analogy among the P , I and F_M . The results can be presented in terms of any of these parameters without affecting the magnitudes. However, the essence of cause and effect can be investigated differently. For instance, when the channel width or ablation rates are plotted versus the laser power, the investigator will be thinking of the process parameter used or to be used. The breakdown thresholds of the material can be considered by plotting the channel width or ablation rate versus the intensity or fluence. The same applies to the interchangeable use of E_p and F as the control parameters. The total energy consumed may be used to calculate the total cost of channel fabrication, which may be used to optimise the fabrication ranges along with other optimisation criteria.

The assumptions in the mathematical model, based on the process dealt with, are acceptable. The understanding displayed in this work came in different forms, from basic engineering knowledge, to design of experiments study, and finally to process simulation. The three parts, combined, can be used to explain this process. Despite the

differences between the simulated and experimental results in some cases, the simulation results were useful in predicting the resulting channel profiles and the general trends of the response change with process parameters.

6.6 Conclusions and future recommendations

The results obtained from the Nd:YVO₄ laser internal microfabrication experiments showed that the system has a potential for internal marking in decorative applications. The process has been studied and knowledge of the effect of the process parameters on the resulting size and morphology of the structures has been gained. The extension of this system's capabilities to precision fabrication of microchannels or waveguides is possible. This can be achieved by a number of different ways:

- 1- Using specially doped polymers and glasses that could be chemically treated after irradiation with laser pulses to produce better quality structures.
- 2- Using an external oscillator in order to double or triple the frequency of the laser beam and consequently reduce its wavelength and enhance the focusability. Another alternative is to use a short wavelength femtosecond or picosecond laser. This could lead to even higher intensities or fluences combined with lower pulse energies than the ones obtained with the microscope objective lens in this work. This would allow for higher precision microfabrication to be achieved.
- 3- The laser may also be applied in stereolithography where a photo-curable resin solution is used instead of a solid transparent material.
- 4- One or all the above stated recommendations would require enhancing the positioning control software and hardware setup of the system to achieve a positioning accuracy comparable to the focal spot size (i.e. micrometer or below).

The results obtained from the CO₂ laser fabrication experiments were very useful in determining the microchannel shapes and dimensions. A great deal of knowledge has been gained from the design of experiments study. The effects of the process parameters have been assessed and the thermal mathematical model simulations have aided in understanding how these parameters interact and affect the results. The simulations were of particular benefit in assessing the effects of the parameters on the morphologies of the produced channels. Future work in this regard may involve the following:

- 1- The use of the fabricated microchannels in microelectromechanical devices (MEMS), optical telecommunication systems or micro-sensors.

- 2- Narrowing the ranges of the process parameters in order to produce channels with optimum shapes and dimensions and possibly fabricating more intricate channel shapes.
- 3- The use of the ablation rates results in estimating the cost of the process and compare to other processes such as sanding or chemical etching, bearing in mind other advantages of all the processes involved in the comparison such as the accuracy and the range of shapes that can be produced.
- 4- The study of the depth of focus effect individually as a process parameter. Furthermore, using the results obtained from $Df = +2$ mm in a future study on the codes or decorative markings on the surfaces of different glass types.
- 5- The use of a high speed thermal imaging system to help in understanding the breakdown mechanism in this process. This may be beneficial in assessing the thermal stresses causing the micro-cracks.

References

- [1] J. Hecht. The Laser Guidebook. McGraw-Hill, 1986.
- [2] F.G. Bachmann, Industrial laser applications, Applied Surface Science, Vol. 46, pp. 254 – 263, 1990.
- [3] D. Bratton, D. Yang, J. Dai and C. K. Ober, Recent progress in high resolution lithography, Polymers for Advanced Technologies, Vol. 17, pp. 94 – 103, January-2006.
- [4] M. G. Alonso-Amigo, Polymer Microfabrication for Microarrays, Microreactors and Microfluidics, Journal of the Association for Laboratory Automation, Vol. 5, Issue 6, pp. 96-101, December-2000.
- [5] T. Lippert, Laser application of polymers, Adv Polym. Sci., Vol. 168, pp. 51–246, 2004.
- [6] C. R. Giuliano, Laser-induced damage to transparent dielectric materials, Applied physics letters, Vol. 5(7), 137-139, October-1964.
- [7] R. Y. Chiao, E. Garmire and C. H. Townes, Self-trapping of optical beams, physical review letters, Vol. 13(15), 479-482 October-1964.
- [8] R. M. Wood, R. T. Taylor and R. L. Rouse, Laser damage in optical materials at 1.06 μm , Optics and Laser Technology, Vol. 6, 105-111, June-1975.
- [9] D. Homolle, S. Wielandy, A. L. Gaeta, N. F. Borrelli and C. Smith, Infrared photosensitivity in silica glasses exposed to femtosecond laser pulses, Opt. Lett., Vol. 24, pp. 1311 – 1313, 1999.
- [10] K. M. Davis, K. Miura, N. Sugimoto and K. Hirao, Writing waveguides in glass with a femtosecond laser, Opt. Lett., Vol. 21, pp. 1729 – 1731, 1996.
- [11] C.B. Schaffer, A. Brodeur and E. Mazur, Laser-induced breakdown and damage in bulk transparent materials induced by tightly focused femtosecond laser pulses, Meas. Sci. Technol., Vol. 12, pp. 1784 – 1794, 2001.
- [12] P. R. Herman, K. P. Chen, Sandy Ng, J. Zhang and Dragan Coric, Photosensitivity in glasses: comparing ultrafast lasers with vacuum-ultraviolet lasers, Conf. on Lasers and Electro-Optics, Tech. Digest, pp. 490 – 491, 2001.
- [13] P. R. Herman, K. P. Chen, P. Corkum, A. Naumov, Sandy Ng and J. Zhang,

Advanced lasers for photonic device microfabrication, Riken Review No. 32, Focused on Laser Precision Microfabrication LPM2000, pp. 31 – 35, January, 2001.

- [14] S. Juodkazis, K. Yamasaki, A. Marcinkevicius, V. Mizeikis, S. Matsuo, H. Misawa and T. Lippert, Microstructuring of silica and polymethylmethacrylate glasses by femtosecond irradiation for MEMS applications, *Mat. Res. Soc. Symp. Proc.*, Vol. 687, pp. B5.25.1 - B5.25.6, 2002.
- [15] V. Mizeikis, H.-B. Sun, A. Marcinkevicius, J. Nishii, S. Matsuo, S. Juodkazis and H. Misawa, Femtosecond laser micro-fabrication for tailoring photonic crystals in resins and silica, *Journal of Photochemistry and Photobiology A: Chemistry*, Vol. 145, pp. 41 – 47, 2001.
- [16] EK SMA Co., Laser, optics, electronics, Glass Master Series Catalogue, www.eksma.com, access date: August - 2003.
- [17] J. H. Strickler and W. W. Webb, Three-dimensional optical data storage in refractive media by two-photon point excitation, *Opt. Lett.*, Vol. 16, pp. 1780 – 1782, 1991.
- [18] M. H. Hong, B. Luk'yanchuk, S. M. Huang, T. S. Ong, L. H. Van and T. C. Chong, Femtosecond laser application for high capacity optical data storage. *Appl. Phys. A*, Vol. 79, pp. 791–794, 2004.
- [19] S.-C. Wang, C.-Y. Lee and H.-P. Chen, Thermoplastic microchannel fabrication using carbon dioxide laser ablation, *Journal of Chromatography A*, Vol. 1111, pp. 252 – 257, 2006.
- [20] Synrad Inc. – USA website, http://www.synrad.com/search_apps/materials/Glass_Quartz.htm, accessed on 10 – February – 2007.
- [21] J. T. Luxon, D. E. Parker, and P. D. Plotkowski. *Lasers in Manufacturing: An Introduction of the Technology*. IFS Ltd, 1987.
- [22] D. Beach, A. Shotwell, Paul Essue. *Applications of Lasers and Laser Systems*. Prentice Hall Inc., 1993.
- [23] B. Hitz, J. J. Ewing and J. Hecht, *Introduction to laser technology*, third edition, IEEE Press, New York, 2001.
- [24] J. J. Zayhowski, Passively Q-switched Nd:YAG microchip lasers and applications, *Journal of Alloys and Compounds*, Vol. 303 – 304, pp. 393 – 400, 2000.
- [25] S. McGinty, G. M. O'Connor and T. J. Glynn, A comparative study of channel

formation in polymer materials using VUV and UV nano-second laser sources for use in micro-fluidic applications, Opto-Ireland 2005: Optoelectronics, Photonic Devices, and Optical Networks (Dublin), Proc. of SPIE, Vol. 5825, pp.622-633, April-2005.

- [26] Liu X, Du D, Mourou G. Laser ablation and micromachining with ultrashort laser pulses. IEEE J. Quantum Electron., Vol. 33(10), pp. 1706 – 16, 1997.
- [27] L. Shah, M. Richardson, J. Tawney and K. Richardson, Femtosecond micro-machining of high index and photo-sensitive glasses in air, Conference on Lasers and Electro-Optics (CLEO 2000), pp. 613-614, May-2000.
- [28] D. Du, X. Liu, G. Korn, J. Squier and G. Mourou, Laser-induced breakdown by impact ionization in SiO₂ with pulse widths from 7 ns to 150 fs, Appl. Phys. Lett., Vol. 64, pp. 3071 – 3073, 1994.
- [29] J. T. Luxon, D. E. Parker, Industrial lasers and their applications, Printice-Hall Inc., New Jersey, 1985.
- [30] Y. Matsuoka, K. Wake, T. Nagashima and N. Iehisa, Glass processing using the fourth harmonic of nanosecond pulse Nd:YAG laser, Appl. Phys. A, Vol. 87, pp. 81–85, 2007.
- [31] B. S. Shin, J. Y. Oh and H. Sohn, Theoretical and experimental investigations into laser ablation of polyimide and copper films with 355-nm Nd:YVO₄ laser, J. Mat. Proc. Tech., Vol. 187-188, pp. 260-263, 2007.
- [32] J. Zhao, J. Sullivan, T. D. Bennett, Wet etching of silica glass after CW CO₂ laser treatment, Applied Surface Science, Vol. 225, pp. 250 – 255, 2004.
- [33] J. B. Lonzaga, S. M. Avanesyan, S. C. Langford, and J. T. Dickinson, Color center formation in soda-lime glass with femtosecond laser pulses, Journal of Applied Physics, Vol. 94, No. 7, pp. 4332 – 4340, October – 2003.
- [34] F. Beinhorn, J. Ihlemann, K. Luther and J. Troe, Plasma effects in picosecond-femtosecond UV laser ablation of polymers, Appl. Phys. A, Vol. 79, pp. 869-873, 2004.
- [35] P. R. Herman, H. Higaki, E. Rouillon and R. S. Marjoribanks, Pondermotive-driven “acceleration” of etch rates for short-pulse laser micromachining of transparent glasses, Conference on Lasers and Electro-Optics (CLEO 1998), pp. 524-525, May 1998.
- [36] L. J. Radziemski and D. A. Cremers, Laser-induced plasmas and applications, Marcel Dekker Inc., New York, 1989.
- [37] J. C. Miller, Laser Ablation: Principles and Applications, Springer-Verlag-

Berlin 1994.

- [38] J. C. Hwang, Femtosecond Laser-Induced Damage for Micromachining of Transparent Materials, Senior Thesis, Harvard University, Department of Chemistry and Physics, April-2002.
- [39] C.B. Schaffer, J. F. Garcia and E. Mazur, Bulk heating of transparent materials using a high repetition-rate femtosecond laser, *Appl. Phys. A*, Vol. 76, pp. 351 – 354, 2003.
- [40] M. E. Fermann, A. Galvanauskas and G. Sucha, *Ultrafast lasers: technology and applications*, Marcel Dekker Inc., New York, 2003.
- [41] A. Desai, D. Bökenkamp, X. Yang, Y.-C. Tai, E. Marzulff and S. Mayo, Microfluidic sub-millisecond mixers for the study of chemical reaction kinetics, *International Conference on Solid State Sensors and Actuators. TRANSDUCERS '97*, Vol. 1, pp. 167 – 170, Chicago, 1997.
- [42] D. Kuo, S. D. Veirk and G. Rauch, Laser zone texturing and glass-ceramic substrates, *IEEE Transactions on Magnetics*, Vol. 33, No. 1, pp. 944-949, January-1997.
- [43] D. J. Beebe, R. J. Adrian, M. G. Olsen, M. A. Stremmer, H. Aref and B.-H. Jo, Passive mixing in microchannels: fabrication and flow experiments, *Mecanique & Industries*, Vol. 2, No. 4, pp. 343 – 348, 2001.
- [44] E. Sauvain, J. H. Kyung and N. M. Lawandy, Photoinduced micron scale maskless etching in transparent glasses, *IEEE Lasers and Electro-Optics Society Annual Meeting*, Vol. 2, pp. 137 – 138, 31-Oct.-3 Nov-1994.
- [45] S. Nikumb, Q. Chen, C. Li, H. Reshef, H. Y. Zheng, H. Qiu and D. Low, Precision glass machining, drilling and profile cutting by short pulse lasers, *Thin Solid Films*, Vol. 477, pp. 216 – 221, 2005.
- [46] S. Georgi, Separating and structuring of brittle material by the use of laser radiation, *Glass Processing Days*, pp. 551 – 553, 2003.
- [47] C. Buerhop, B. Blumenthal, R. Weissmann, N. Lutz and B. Biermann, Glass surface treatment with excimer and CO₂ lasers, *Applied Surface Science*, Vol. 46, pp. 430 – 434, 1990.
- [48] S. J. Qin and W. J. Li, Process characterization of fabricating 3D micro channel systems by laser-micromachining, *Sensors and Actuators A*, Vol. 97 – 98, pp. 749 – 757, 2002.
- [49] J. F. Ready, *Effects of high-power laser radiation*, Academic Press, Inc., 1971.
- [50] Y.-I. Lee, K. Song and J. Sneddon, Laser-induced breakdown spectrometry,

Nova Science publishers, Inc., 2000.

- [51] C.-H. Fan and J. P. Longtin, Modeling optical breakdown in dielectrics during ultrafast laser processing, *App. Optics*, Vol. 40, pp. 3124-3131, 2001.
- [52] E. N. Glezer, M. Milosavljevic, L. Huang, R. J. Finlay, T.-H. Her, J. P. Callan and E. Mazur, 3-D optical storage and engraving inside transparent materials, *Ultrafast Phenomena X*, Ed. by P. F. Barbara, J. G. Fujimoto, W. H. Knox and W. Zinth, pp. 157 – 158, Berlin, 1996.
- [53] A. Vaidyanathan, T. W. Walker and A. H. Guenther, The relative roles of avalanche multiplication and multiphoton absorption in laser-induced damage of dielectrics, *IEEE Journal of Quantum Electronics*, Vol. QE-16(1), 89-93, January-1980.
- [54] D. C. Giancoli. 3rd ed. *Physics*. Prentice Hall Inc., 1991.
- [55] D. W. Fradin, E. Yablonovitch and M. Bass, Confirmation of an electron avalanche causing laser-induced bulk damage at 1.06 μm , *Applied Optics*, Vol. 12 (4), pp. 700-709, April-1973.
- [56] C. B. Schaffer, *Interaction of Femtosecond Laser Pulses with Transparent Materials*, PhD Thesis, Department of Physics, Harvard University, May-2001.
- [57] B. C. Stuart, M. D. Feit, A. M. Rubenchik, B. W. Shore and M. D. Perry, Laser-induced damage in dielectrics with nanosecond to subpicosecond pulses, *Phys. Rev. Lett.*, Vol. 74, pp. 2248 – 2251, 1995.
- [58] M. Bass and D. W. Fradin, Surface and Bulk Laser-Damage Statistics and the Identification of Intrinsic Breakdown Processes, *IEEE Journal of Quantum Electronics*, Vol. QE-9, No. 9, pp. 890 – 896, September-1973.
- [59] E. Kocher, L. Tschudi, Jurg Steffen and G. Herziger, Dynamics of laser processing in transparent media, *IEEE Journal of Quantum Electronics*, Vol. QE-8, No. 2, pp. 120 – 125, February-1972.
- [60] C. S. Ake', H. Sobral, M. V. Muniz, L. E.-Alarco'n and E. Camps, Characterization of laser ablation plasmas by laser beam deflection, *Optics and Lasers in Engineering*, Vol. 39, pp. 581–588, 2003.
- [61] V. Kozhukharov, D. Dimitrov and D. Tonchev, Integration of CO₂ laser radiation with glasses, *Infrared Physics*, Vol. 29, No. 2 – 4, pp. 415 – 422, 1989.
- [62] D. G. Holloway, *The physical properties of glass*, Wykeham Publication Ltd., London, 1973.
- [63] L. A. Siiman and L. B. Glebov, Color center generation in sodium-calcium

- silicate glass by nanosecond and femtosecond laser pulses, *Laser-Induced Damage in Optical Materials: 2005*, Proc. of SPIE, edited by G. J. Exarhos, A. H. Guenther, K. L. Lewis, D. Ristau, M. J. Soileau and C. J. Stolz, Vol. 5991, pp. 599112-1 - 599112-5, 2005.
- [64] T. D. Bennett, D. J. Krajnovic, L. Li and D. Wan, Mechanisms of topography formation during CO₂ laser texturing of silicate glasses, *J. of Applied Physics*, Vol. 84, No. 5, pp. 2897 – 2905 , September-1998.
- [65] Melles Griot, *The practical application of light*, Catalogue X.
- [66] *ASM Handbook, Volume 16 – Machining*, 9th edition, ASM-International, 1997.
- [67] K. Miura, H. Inouye, J. Qiu, T. Mitsuyu and K. Hirao, Optical waveguides induced in inorganic glasses by a femtosecond laser, *Nuclear Instruments and Methods in Physics Research B*, Vol. 141, pp. 726 – 732, 1998.
- [68] R. S. Marjoribanks, Y. Kerachian, P. R. Herman, S. Camacho-Lopez, and M. Nantel, Pulsetrain 'burst' machining: ultrafast-laser microprocessing at ultrahigh (>100 MHz) pulse-rates, *Conference on Lasers and Electro-Optics CLEO '01*, pp. 575-576, May-2001.
- [69] R. R. Gattaa, L. R. Cerami and E. Mazur, Micromachining of bulk glass with bursts of femtosecond laser pulses at variable repetition rates, *Optics Express*, Vol. 14, No. 12, pp. 5279 – 5284, June-2006.
- [70] K. S.-Tinten, J. Bialkowski, A. Cavalleri, D. von der Linde, A. Oparin, J.M.-t.-Vehn and S. I. Anisimov, Transient states of matter during short pulse laser ablation, *Phys. Rev. Lett.*, Vol. 81 No. 1, pp. 224-227, July-1998.
- [71] C.B. Schaffer, A. Brodeur, J. F. Garcia and E. Mazur, Micromachining bulk glass using femtosecond laser pulses with nanojoule energy, *Opt. Lett.*, Vol. 26, pp. 93 – 95, 2001.
- [72] C.B. Schaffer, N. Nishimura and E. Mazur, Thresholds for femtosecond laser-induced breakdown in bulk transparent solids and water, *Proceedings of SPIE*, Vol. 3451, *Time Structure of X-Ray Sources and Its Applications*, Ed. By A. K. Freund, H. P. Freund and M. R. Howells, pp. 2 – 8, San Diego, CA, 1998.
- [73] C.B. Schaffer, A. O. Jamison, J. F. Garcia, J. B. Ashcom and E. Mazur, Morphology and mechanisms of femtosecond laser-induced structural change in bulk transparent materials, *Conf. on Lasers and Electro-Optics (CLEO)*, pp. 445 – 446, Baltimore, MD, 2001.
- [74] E. N. Glezer and E. Mazur, Ultrafast-laser driven micro-explosions in

- transparent materials, *Appl. Phys. Lett.*, Vol. 71, pp. 882 – 884, 1997.
- [75] C.B. Schaffer, A. O. Jamison and E. Mazur, Morphology of femtosecond laser-induced structural changes in bulk transparent materials, *Appl. Phys. Lett.*, Vol. 84, pp. 1441 – 1443, 2004.
- [76] J. Ashcom and E. Mazur, Femtosecond laser-induced microexplosions in transparent materials, *LEOS*, pp. 300 – 301, San Diego, 2001.
- [77] C.B. Schaffer, E. N. Glezer, N. Nishimura and E. Mazur, Ultrafast laser induced microexplosions: explosive dynamics and sub-micrometer structures, *Photonics West*, pp. 36 – 45, San Jose, 1998.
- [78] E. N. Glezer, L. Huang, R. J. Finlay, T.-H. Her, J. P. Callan, C.B. Schaffer and E. Mazur, Ultrafast laser-induced microexplosions in transparent materials, *28th Annual Boulder Damage Symposium*, pp. 392 – 403, Boulder, 1996.
- [79] M. Lenzer, J. Kruger, S. Sartania, Z. Cheng, Ch. Spielmann, G. Mourou, W. Kautek and F. Krausz, Femtosecond optical breakdown in dielectrics, *Phys. Rev. Lett.*, Vol. 80, No. 18, pp. 4076 – 4079, 1998.
- [80] C.B. Schaffer, A. Brodeur, N. Nishimura and E. Mazur, Microscopic bulk damage in dielectric materials using nanojoule femtosecond laser pulses, *Quantum Electronics and Laser Science (with CLEO)*, pp. 232, Baltimore, 1999.
- [81] C.B. Schaffer, A. Brodeur, N. Nishimura and E. Mazur, Laser-induced microexplosions in transparent materials: microstructuring with nanojoules, *Photonics West*, pp. 143, San Jose, 1999.
- [82] E. N. Glezer, M. Milosavljevic, L. Huang, R. J. Finlay, T.-H. Her, J. P. Callan and E. Mazur, 3-D optical storage inside transparent materials, *Opt. Lett.*, Vol. 21, pp. 2023 – 2025, 1996.
- [83] D. V. Tran, H. Y. Zheng, Y. C. Lam, V. M. Murukeshan, J. C. Chai and D. E. Hardt, Femtosecond laser-induced damage morphologies of crystalline silicon by sub-threshold pulses, *Optics and Lasers in Engineering*, Vol. 43, pp. 977 – 986, 2005.
- [84] G. Allcock, P. E. Dyer, G. Elliner and H. V. Snelling, Experimental observation and analysis of CO₂ laser-induced microcracking of glass, *Journal of Applied Physics*, Vol. 78, No. 12, pp. 7295 – 7303, December-1995.
- [85] C.B. Schaffer and E. Mazur, Micromachining using ultrashort pulses from a laser oscillator, *Optics and Photonics News*, Vol. 12, pp. 20 – 23, 2001.
- [86] C.B. Schaffer, A. Brodeur, J. F. Garcia, W. A. Leight and E. Mazur,

- Micromachining optical waveguides in bulk glass using a femtosecond laser oscillator, Technical Digest: Conf. on Lasers and Electro-Optics (CLEO), pp. 375 – 376, San Francisco, 2000.
- [87] C.B. Schaffer, A. Brodeur, J. F. Garcia and E. Mazur, Micromachining of bulk glass with tightly-focused femtosecond laser pulses, IEEE LEOS Annual Meeting, pp. 183, San Francisco, 1999.
- [88] Y. Kawata, H. Ishitobi and S. Kawata, Use of two-photon absorption in a photorefractive crystal for three-dimensional optical memory, Opt. Lett., Vol. 23, pp. 756 – 758, 1998.
- [89] A. Toriumi, S. Kawata and M. Gu, Reflection confocal microscope readout system for three-dimensional photochromic optical data storage, Opt. Lett., Vol. 23, pp. 1924 – 1926, 1998.
- [90] D. Day, M. Gu and A. Smallridge, Use of two-photon excitation for erasable – rewritable three-dimensional bit optical data storage in a photorefractive polymer, Opt. Lett., Vol. 24, pp. 948 – 950, 1999.
- [91] G. Zhou, M. J. Ventura, M. R. Vanner and M. Gu, Use of ultrafast-laser-driven microexplosion for fabricating three-dimensional void-based diamond-lattice photonic crystals in a solid polymer material, Opt. Lett., Vol. 29, pp. 2240 – 2242, 2004.
- [92] D. Day and M. Gu, Formation of voids in a doped polymethylmethacrylate polymer, Appl. Phys. Lett., Vol. 80, pp. 2404 – 2406, 2002.
- [93] M. Gu, J. O. Amistoso, A. Toriumi, M. Irie and S. Kawata, Effect of saturable response to two-photon absorption on the readout signal level of three-dimensional bit optical data storage in a photochromic polymer, Appl. Phys. Lett., Vol. 79, pp. 148 – 150, 2001.
- [94] K. Yamasaki, S. Juodkazis, M. Watanabe, H.-B. Sun, S. Matsuo and H. Misawa, Recording by microexplosion and two-photon reading of three-dimensional optical memory in polymethylmethacrylate films, Appl. Phys. Lett., Vol. 76, pp. 1000 – 1002, 2000.
- [95] M. Watanabe, S. Juodkazis, H.-B. Sun, S. Matsuo and H. Misawa, Two-photon readout of three-dimensional memory in silica, Appl. Phys. Lett., Vol. 77, pp. 13 – 15, 2000.
- [96] M. Watanabe, S. Juodkazis, H.-B. Sun, S. Matsuo, H. Misawa, M. Miwa and R. Kaneko, Transmission and photoluminescence images of three-dimensional memory in vitreous silica, Appl. Phys. Lett., Vol. 74, pp. 3957 – 3959, 1999.

- [97] K. Miura, J. Qiu, H. Inouye, T. Mitsuyu and K. Hirao, Photowritten optical waveguides in various glasses with ultrashort pulse laser, *Appl. Phys. Lett.*, Vol. 71, p. 3329 – 3331, 1997.
- [98] D. K. Y. Low and L. Li, An investigation into melt flow dynamics during repetitive pulsed laser drilling of transparent media, *Optics and Laser Tech.*, Vol. 33, pp. 515 – 522, 2001.
- [99] M. Rothschild, D. J. Ehrlich and D. C. Shaver, Effects of excimer laser irradiation on the transmission, index of refraction, and density of ultraviolet grade fused silica, *Appl. Phys. Lett.*, Vol. 55, pp. 1276 – 1278, 1989.
- [100] S. McGinty, G. M. O'Connor and T. J. Glynn, Development of a prediction equation for depth, aspect ratio and trench roughness pertaining to excimer laser ablation of polymer materials, *Opto-Ireland 2005: Photonic Engineering (Dublin)*, *Proc. of SPIE*, Vol. 5827, pp. 515-526, April-2005.
- [101] M. Watanabe, Y. Kuroiwa and S. Ito, Study of femtosecond laser ablation of multicomponent glass, *Reports Res. Lab. Asahi Glass Co. Ltd.*, Vol. 55, pp. 27 – 31, 2005.
- [102] W. W. Duley, *Laser processing and analysis of materials*, Plenum Press, New York, 1982.
- [103] W. A. Tolbert, I.-Y. S. Lee, D. E. Hare, X. Wen and D. D. Dlott, Ultrafast dynamics of photothermal polymer ablation, on *Laser Ablation: Mechanisms and Applications – II*, Knoxville, TN, (April - 1993). *Proc. edited by: J. C. Miller and D. B. Geohengan*, *AIP Conference Proceedings 288*, AIP Press, New York, 1994.
- [104] D. V. Tran, H. Y. Zheng, Y. C. Lam, V. M. Murukeshan, J. C. Chai, D. E. Hardt, Femtosecond laser-induced damage morphologies of crystalline silicon by sub-threshold pulses, *Optics and Lasers in Engineering*, Vol. 43, pp. 977–986, 2005.
- [105] T. Dumont, T. Lippert, A. Wokaun and P. Leyvraz, Laser writing of 2D data matrices in glass, *Thin Solid Films*, Vol. 453 – 454, pp. 42 – 54, 2004.
- [106] M. J. Soileau, W. E. Williams, N. Mansour and E. W. Van Stryland, Laser-induced damage and the role of self-focusing, *Optical Engineering*, Vol. 28 (10), pp. 1133-1144, October-1989.
- [107] A. L. Gaeta, Self-focusing of ultrashort pulses above the threshold for catastrophic collapse, *Quantum Electronics and Laser Science Conference 1999*, pp. 163 – 164, May-1999.

- [108] F. Raimondi, S. Abolhassani, R. Brtüsich, F. Geiger, T. Lippert, J. Wambach and J. Wei, Quantification of polyimide carbonization after laser ablation, *Journal of Applied Physics*, Vol. 88, No. 6, pp. 3659 – 3666, 2000.
- [109] M. Pervolarki, P. E. Dyer and P. Monk, Ablation studies using a diode-pumped Nd:YVO₄ micro-laser, *Appl. Phys. A*, Vol. 79, pp. 849 – 854, 2004.
- [110] K. H. Leong, Innovative glass processing, Industrial Laser Solutions, www.industrial-laser.com, Technology Report, pp. 24 – 26, September-2004.
- [111] K. Hirao and K. Miura, Writing waveguides and gratings in silica and related materials by femtosecond laser, *Journal of Non-crystalline Solids*, Vol. 239, pp. 91 – 95, 1998.
- [112] K. Washio, Microfabrication feast, Industrial Laser Solutions, www.industrial-laser.com, Conference Report, pp. 30 – 33, August-2004.
- [113] M. Will, S. Nolte, J.-P. Ruske, A. Tünnermann and F. Wunderlich, Properties of waveguides manufactured with fs-laser pulses in transparent materials, *Conference on Lasers and Electro-Optics (CLEO '01)*, pp. 491, May-2001.
- [114] M. Kamata, M. Obara, R. R. Gattass, L. R. Cerami and E. Mazur, Optical vibration sensor fabricated by femtosecond laser micromachining, *App. Phys. Lett.*, Vol. 87, pp. 051106-1 – 051106-3, 2005.
- [115] E. Saridja, Technical Coordinator at Crystallix Europe - Dublin, e-mail: emre@crystalixeuropa.com, Visit date: February-2004.
- [116] K. C. Yung, S. M. Mei and T. M. Yue, Rapid prototyping of polymer-based MEMS devices using UV YAG laser, *Journal of Micromechanics and Microengineering*, Vol. 14, pp. 1682 – 1686, 2004.
- [117] A. C. Henry, E. A. Waddell, R. Shreinder and L. E. Locascio, Control of electroosmotic flow in laser-ablated and chemically modified hot imprinted poly(ethylene terephthalate glycol) microchannels, *Electrophoresis*, Vol. 23, pp. 791 – 798, 2002.
- [118] H. Y. Zheng, H. Liu, S. Wan, G. C. Lim, S. Nikumb and Q. Chen, Ultrashort pulse laser micromachined microchannels and their application in an optical switch, *Int. J. Adv. Manuf. Technol.*, Vol. 27, pp. 925 – 929, 2006.
- [119] J. Rossier, A. Schwarz, F. Reymond, R. Ferrigno, F. Bianchi and H. H. Girault, Microchannel networks for electrophoretic separations, *Electrophoresis*, Vol. 20, pp. 727 – 731, 1999.
- [120] J. Rossier, F. Reymond and P. E. Michel, Polymer microfluidic chips for electrochemical and biochemical analysis, *Electrophoresis*, Vol. 23, pp. 858 –

867, 2002.

- [121] J. O. Isard, Surface reflectivity of strongly absorbing media and calculations of the infrared emissivity of glass, *Infrared Physics*, Vol. 20, pp. 249 – 256, December-1979.
- [122] C. McAtamney, A. Cronin, R. Sherlock, G. M. O'Connor and T. J. Glynn, Reproducible Method for Fabricating Fused Biconical Tapered Couplers Using a CO₂ Laser Based Process, *Proc. of the third International WLT – conference on Lasers in Manufacturing 2005*, Munich, Edited by E. Beyer, F. Dausinger, A. Ostendorf and A. Otto, (ISBN 3-00-016402-2), pp. 673-678, June-2005.
- [123] C. K. Chung, M. Y. Wu, J. C. Wu, Y. C. Sung and G. R. Huang, Silicon micromachining by CO₂ laser, *Proceedings of the 1st IEEE International Conference on Nano/Micro Engineered and Molecular Systems*, pp. 1445-1448, Zhuhai-China, January-2006.
- [124] V. K. Sysoev, B. P. Papchenko, and S. Ya. Rusanov, Production of quartz light guides with an elliptical cross-section using CO₂ laser, *Glass and Ceramics*, Vol. 61, No. 3 - 4, 2004.
- [125] H.-G. Geissler, Challenge of development and potential for glass processing by laser technology, *Glass Processing Days*, pp. 100 – 102, 2003.
- [126] Synrad Inc. – USA website,
<http://www.synrad.com/Applications/marketing.htm>, accessed on 10 – February – 2007.
- [127] H. F. Mark, N. M. Bikales, C. G. Overberger, G. Menges and J. I. Kroschwitz, *Encyclopedia of polymer science and engineering*, Vol. 9, John Wiley & Sons Inc., 1985.
- [128] <http://www.polymerprocessing.com/polymers/PC.html>, date: 07 – Sep. – 2005.
- [129] G. W. C. Kaye and T. H. Laby, *Tables of physical and chemical constants*, 16th edition, Longman, 1995.
- [130] H. F. Mark, N. M. Bikales, C. G. Overberger, G. Menges and J. I. Kroschwitz, *Encyclopedia of polymer science and engineering*, Vol. 16, John Wiley & Sons Inc., 1985.
- [131] <http://www.matweb.com/SpecificMaterial.asp?bassnum=O3100&group=General>, access date: 7 – September – 2005.
- [132] <http://www.plasticsusa.com/pc.html>, access date: 7 – September – 2005.
- [133] <http://www.pilkington.com/about+pilkington/education/chemistry+of+glass.htm>, access date: 23 – September – 2006.

- [134] N. Bansal and R. Doremus, Handbook of glass properties, Academic Press Inc., Orlando, 1986.
- [135] Valley design corporation website resources,
<http://www.valleydesign.com/sodalime.htm>, access date: 19 – May – 2006.
- [136] Flex-o-Lite Inc. website resources,
<http://www.flexolite.com/literature/BOL%20GENERAL%20PROPERTIES.pdf>, access date: 19 – May – 2006.
- [137] Pilkington Group Limited website resources, Lime-soda glass technical information,
<http://www.pilkington.com/resources/ats129swproperties20050715.doc>, access date: 01 – June – 2006.
- [138] <http://www.lenntech.com/Glass.htm>, access date: 05 – July – 2006.
- [139] C. E. Webb and J. C. Jones. Handbook of Laser Technology and Applications, Volume II: Laser design and laser systems, Institute of Physics Publishing Ltd, UK, 2004.
- [140] M. J. Weber, Handbook of Laser Wavelengths, CRC Press, 1999.
- [141] Spectra Physics Lasers Inc. T-Series Q-Switched Nd:YVO₄ Laser Systems User Manual, September 1997.
- [142] National Instruments, PCI E Series User Manual, July 2002.
- [143] IBM Ireland, Laser Texturing Tool Manual.
- [144] Renishaw, www.renishaw.com, Product note from the Spectroscopy Products Division, SPD/PN/088, Issue 1.1, June 2003.
- [145] M. Young, Optics and lasers: an engineering physics approach, Springer-Verlag – Berlin, 1977.
- [146] T. Kenjo, Stepping Motors and Their Microprocessor Controls, Clarendon Press, 1984.
- [147] Intelligent Motion Systems, Excellence in Motion™ IM483 Operating Instructions, December 2002.
- [148] National Instruments. SCB-68 68-Pin Shielded Connector Block User Manual. December 2002.
- [149] Rofin website, <http://www.rofin.com/index-e.htm>, accessed on 27-January-2007.
- [150] Email communication with the Rofin technical support, Derek Hughes, D.Hughes@rofin-baasel.co.uk, Tue, 28 Mar 2006.
- [151] Rofin DC-015 CO₂ laser operation manuals.
- [152] Email communication with the Mechtro. technical support, J. S. Maulson,

Mechtro@aol.com, Wed, 22 Mar 2006.

- [153] Email communication with the Rofin technical support, Derek Hughes, D.Hughes@rofin-baasel.co.uk, Mon, 13 Mar 2006.
- [154] Laser motion system catalogue, Mechatronic Industries Ltd., MTI, Unit 4, Doncaster road, Kirk Sandall Industrial Estate, Doncaster, DN3 1HP, UK.
- [155] Ing. Anton Petík, PhD, Faculty of Manufacturing Technologies of the Technical University Košice with headquarters in Prešov.
- [156] SICAM Corporation website, www.sicam.com, date: November – 2003.
- [157] Ennex Corporation website, <http://www.ennex.com/~fabbers/StL.asp>, access date: November – 2003.
- [158] Paul F. Jacobs, Stereolithography and other RP&M Technologies: from Rapid prototyping to Rapid Tooling, ASME Press, 1996.
- [159] <http://www.tacc.utexas.edu/~reyes/titanium/stl/stlmarch17.htm>, access date: November – 2003.
- [160] G. B. Thomas and R. L. Finney, Calculus and Analytic Geometry, Sixth Edition, Addison Wesley Publishing Company, 1985.
- [161] Operating instructions for the Me F2 universal camera microscope, BUEHLER, Ltd.
- [162] Image analysis training manual, BUEHLER Ltd., 1999.
- [163] Issa, A., Brabazon, D., and Hashmi, M.S., Computer control of Nd:YVO₄ laser system for 3 dimensional microfabrication in polymers, 6th Conference on Rapid Design, Prototyping, and Manufacture, June 2005, Edited by D.M. Jacobson, A.E. Rennie, C.E. Bocking, X-CD Technologies, pp. 35 - 44, ISBN 0-9737783-1-8.
- [164] Issa, A., Brabazon, D., and Hashmi, M.S., Three Dimensional microfabrication in polycarbonate using nano-second laser pulses, 8th Annual Sir Bernard Crossland Symposium, Queens University Belfast, pp. 11-28, 6th and 7th April 2005, ISBN 1898012733.
- [165] Stereoscan 440 operator manual, Cannin electron microscope, Leica Cambridge Ltd, Cambridge, England, 1994.
- [166] Scan coat six sputter coater, Installation and maintenance instructions, BOC Edwards, UK.
- [167] D. C. Montgomery, Design and analysis of experiments, 2nd edition, John Wiley and Sons Inc., 1984.
- [168] Y. Dodge, Analysis of Experiments with Missing Data, John Wiley and Sons

Inc., 1985

- [169] D. Collins, Development of a laser based surface profilometer using the principle of optical triangulation, M.Eng. Thesis, School of mechanical and manufacturing engineering, Dublin City University, 2005.
- [170] OptoNCDT 2000, Intelligent laser optical displacement sensor, Instructions manual, Micro-Epsilon, Messtechnik, Germany.
- [171] M. A. Kamal, Development and characterisation of a novel optical surface defect detection system, M.Eng. Thesis, School of mechanical and manufacturing engineering, Dublin City University, 2005.
- [172] ASME, Surface Texture (Surface Roughness, Waviness, and Lay), B46.1, the American Society of Mechanical Engineers, New York, 1995.
- [173] Design-Expert software, V7, user's guide, Technical manual, Stat-Ease Inc., Minneapolis, MN, 2005.
- [174] D. M. Grove and T. P. Davis, Engineering, quality and experimental design, Longman, 1998.
- [175] <http://www.mfg.mtu.edu/cyberman/quality/sfinish/terminology.html>, accessed on 31-03-2007.
- [176] http://www.efunda.com/processes/machining/chip_formation_2.cfm, accessed on 31-03-2007.
- [177] D. Bäuerle, Laser processing and chemistry, 3rd edition, Springer-Verlag, Berlin, 2000.
- [178] H. S. Carslaw and J. C. Jaeger, Conduction of heat in solids, Oxford University Press, Oxford, 1959.
- [179] J. M. Dowden, The mathematics of thermal modelling: an introduction to the theory of laser material processing, Chapman and Hall CRC, New York, 2001.
- [180] Email communication with Prof. J. M. Dowden, Department of mathematical sciences, University of Essex, UK, Dates 31 – May to 6 – June 2006.
- [181] E. Kreyszig, Advanced engineering mathematics, 8th edition, John Wiley and Sons Inc., 1999.
- [182] Issa, A., Brabazon, D., and Hashmi, S., 3D transient thermal modelling of laser micro-channel fabrication in lime soda glass, Journal of Materials Processing Technology, Accepted March 2006.
- [183] M. D. Seyer, RS-232 Made Easy: Connecting Computers, Printers, Terminals, and Modems, Prentice-Hall, 1984.

Appendices

Appendix A – Band Theory of Solids

A.1 From energy levels to bands

If two hydrogen atoms approach each other, the wave functions overlap, and the two 1s states (one for each atom) divide into two states of different energy. Figure A.1a shows this situation for 1s and 2s states for two atoms. If six atoms come together, as in figure A.1b, each of the states splits into six levels. If a large number of atoms come together to form a solid, each of the original atomic levels becomes a *band* as shown in figure A.1c. The energy levels are so close together in each band that they seem essentially continuous. From the band theory perspective, solids can be classified as conductors, insulators or semiconductors [54].

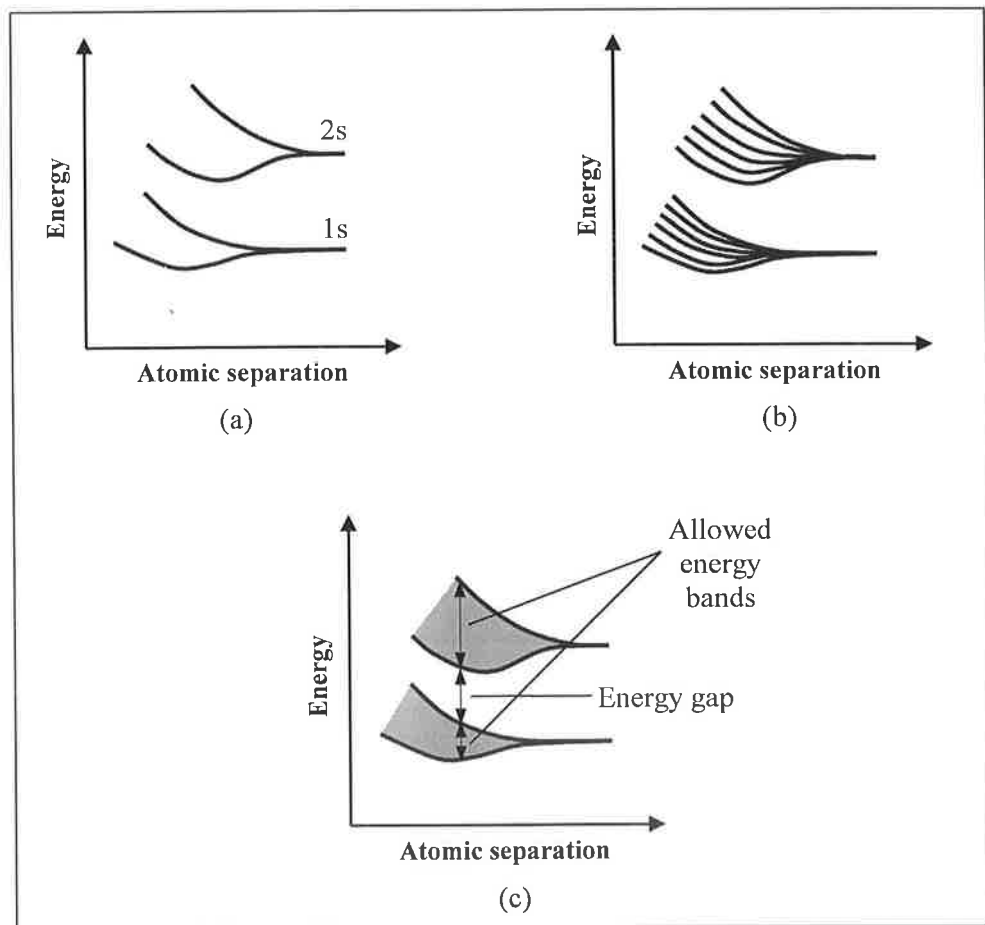


Figure A.1: The splitting of 1s and 2s atomic energy levels for (a) two atoms, (b) six atoms and (c) many atoms forming a solid, redrawn after [54].

A.2 Conductors

If the solid is a good conductor such as sodium, the highest energy band containing electrons is only partially filled, see figure A.2a. When a potential difference is applied across the material, electrons can respond by accelerating and increasing their energy,

since there are plenty of unoccupied states, of slightly higher energy available. Hence, a current flows readily and the solid is a good conductor.

A.3 Insulators

On the other hand, in a solid insulator material such as glasses or polymers, the highest band containing electrons is called the *valence band*, and it is completely filled. The next highest energy band, is called the *conduction band*, and it is separated from the valence band by a *energy gap*, E_g , of typically 5 to 10 eV, see figure A.2b. At room temperature (un-excited state), almost no electrons can acquire the 5 eV needed to reach the conduction band. When a potential difference is applied across the material, there are no available states accessible to the electrons, and no current flows. Hence, the material is a good insulator.

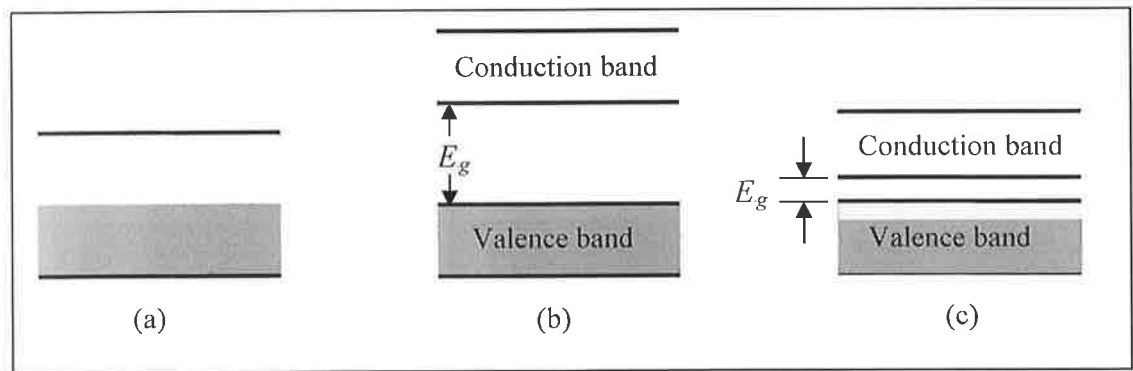


Figure A.2: Energy bands for (a) a conductor, (b) an insulator and (c) a semiconductor. Shading represents occupied states, after [54].

A.4 Semiconductors

In pure semiconductors such as silicon or germanium, the bands are like those for insulators, except that the unfilled conduction band is separated from the filled valence band by a much smaller energy gap, E_g , typically on the order of 1 eV, see figure A.2c. The pale shading at the top of the valence band indicates that at room temperature, there will be a few electrons that can acquire enough thermal energy to reach the conduction band, and so a very small current can flow when a voltage is applied.

Appendix B – Extra Parts of Chapter 2

B.1 PC-Laser Serial Communication

B.1.1 RS232 cable design

The RS232 port on the laser power supply is designed to plug directly into any IBM AT-style computer. The data flow is hardware controlled. Data transmission from the supply is held off by a low on pin 7 (RTS). The power supply expects the host computer to suspend transmission when the power supply asserts a low at pin 8 (CTS) [183]. Table B.1 lists the pin connections of the RS232 cable suitable for communication with the laser power supply.

Table B.1: Serial communication cable design [141].

HOST DB-9	SIGNAL	DESCRIPTION	RS232
2	RXD	Receive Data	2
3	TXD	Transmit Data	3
5	GND	Ground	5
7	RTS	Request to Send	7
8	CTS	Clear to Send	8

B.1.2 RS 232 communication syntax

Commands to the T-Series power supply consist of strings of ASCII characters [141]. Each command is terminated by a semicolon. Multiple commands can be issued in a single string. The format of the read and write commands is listed below.

Read Command Vocabulary

?Cn; Reads diode currents:

n=1 for diode #1

n=2 for diode #2 (if present)

?H; Reads the status history array in the system memory.

The return string is a 17-byte string of hex data.

?S; Reads the last system status from power supply.

Returns numeric string from 1 to 3 bytes.

?Tn; Reads diode temperatures:

n=1 for diode #1

n=2 for diode #2 (if present)

?V; Reads software serial number. A 17-character string (including terminator) is transmitted to the host.

?M; One byte value between 0 and 3. reads the diode pump regulation mode.

?P; Reads laser output power (if available).

?Xkn; Reads diode **n** EEPROM information. Character **k** specifies information to be read from EEPROM. A character string is transmitted; length is information dependant, but includes the terminator character. The **n** defines diode 1 or 2, as above.

?X1n; reads diode serial number. A 17-character string is transmitted to the host.

?X2n; reads the diode ship date and transmits a 9-character string to the host.

?X3n; reads the diode operating temperature and transmits a 6-character string to the host

?X4n; reads the diode current limit and transmits a 6-character string to the host.

?X5n; reads diode initial operating current and transmits a 6-character string to the host.

?X6n; reads diode operating hours and transmits a 10-character string to the host.

?G; Reads gate status. Replies with 0 or 1.

?Q; Reads pulse repetition frequency (PRF) in units of Hz.

?STB; Reads standby current.

?SUP; Reads suppression rate.

Write Command Vocabulary

B1; Reboots the laser power supply without resetting communications.

Cm:nnnn; Sets the laser diode **m** current to **nnnn** in hundredth of Amps. Internal circuitry balances the currents in the diodes based on the set current limits. The set current limits will override this command.

Dn; Queues a diode ON/OFF event
n=0, DIODE OFF event queued.
n=1, DIODE ON event queued.

Fn; changes system into/from a sleep mode
n=0, system goes to sleep mode.
n=1, system goes back to normal from sleep mode.
Default=1.

Pnnnn; Sets the laser power in mW.

Tm:nnn; Sets the laser diode **m** temperature to **nnn** (n=0.1°C)

Mn; Sets the diode pump regulation mode.
(Diode must be OFF)
n=0, Current feedback.
n=1, Laser power feedback.

n=2, Diode power feedback.

n=3, Current feedback, Standby setting.

Q-switch Command Vocabulary

^C; Resets RS-232 communication buffers. **^C** is a key by pressing Ctrl+C, or by sending the Hex value – 0x03.

Q:nnnnnnn; Sets internal PRF to **nnnnnnn** Hz. Valid values for PRF are from 1 to 1,000,000. Values greater than 350, 000 yields cw operation.

Q:0; Sets the PRF source to EXTERNAL. With no external input on the ANALOGUE connector, the PRF will be set to zero.

Gn; Gates the Q-switch to ON or OFF.

SUP:nnnn; Part of the first pulse suppression routine, which runs at the beginning of any gated pulse train. This command sets the suppress time in microseconds. This is the time to the laser pulses from a GATE ON transmission, in which the diode current is lowered to STANDBY level, and Q-switch pulses are held off. Valid suppress times are from 0 to 8000 microseconds. A value of 0 will defeat the suppress routine.

STB:nnnn; Sets the STANDBY diode current in hundredths of Amps during the first pulse suppression routine. Valid standby currents are from 3 amps up to the lowest current limit value.

B.2 Nd:YVO₄ control system LabVIEW codes

B.2.1 Read STL code

How to use the code

- 1- INPUT FILE: the name and location of the STL file on the PC.
- 2- OUTPUT FILE: the required name and location of the output file. Usually is has the same details as the STL file; except that the extension is (.txt).
- 3- CAD Software: if AutoCAD was used to generate the STL file, this button has to be clicked.
- 4- When the program is run, readings should appear in the vertices indicators at the bottom of the front panel. This means the program is running without problems.

How the code works

- 1- It reads the first 7 lines in the STL file. These lines contain the coordinates of the first facet, they will for example read:

solid sphere

```
facet normal -0.13 -0.13 -0.98
  outer loop
    vertex 1.50000 1.50000 0.00000
    vertex 1.50000 1.11177 0.05111
    vertex 1.11177 1.50000 0.05111
  endloop
```

2- It looks for a matched string in these lines “outer loop”, this marks the beginning of the facet vertices’ details. Then it deletes the matched string and the preceding text. After that it passes the remaining string.

3- It looks for another matched string “endloop” in the remaining string; this marks the end of the facet vertices’ details. The program then deletes the match string and the text after this. After that it passes the remaining string.

4- The remaining string contains 3 lines, each line begins with the word “vertex” followed by 3 numbers that resemble the coordinates of the vertex. The words “vertex” are also deleted so that the string only contains 3 lines of coordinate readings.

5- A fourth line is added to the previous string, this line reads “end” marking the end of the first facet’s details. These 4 lines are written to an output text file.

6- This ends the first iteration in the program; the second loop iteration processes the following 7 lines from the STL file and so on. Steps 2 to 5 are repeated in each iteration.

7- This algorithm is followed till the last 7 lines are processed from the STL file. In this last loop an extra line is added to the string in step 5, reading “eof” which marks the end of file.

The program terminates its operation at the end of the STL file. The output text file contains all the facets’ details but in a reduced form. The size of the file is thus reduced by half and it is more easily used in the slicing program.

B.2.2 Slice Settings code

How to use the code

The input and output variables used in this program are shown in figure 2.27 in chapter 2. These include:

- 1- Intersection Direction: Defines the direction of slicing, the user can choose between X, Y and Z direction.
- 2- Layer Spacing: Defines the spacing between the slicing planes. The value chosen is usually a compromise between the best quality and a reasonable build file size.

3- Text file path: Defines the path of the source file generated from the Read STL code.

How the code works

1- It takes the first facet's data from the source file, and saves the X, Y and Z coordinates in 3 individual arrays.

2- Step 1 is repeated till the end of the source file. At the end we have 3 arrays (X-values, Y-values and Z-values).

3- The 3 arrays, the Intersection Direction and the Layer Spacing value are fed as inputs to the Planes code and the Slicing code.

B.2.3 Planes code

How the code works

Here the procedure is explained for generating Z Planes, it is exactly the same for the other two directions.

1- It finds the minimum and maximum values in the Z values arrays. The difference between them defines the length in the Z direction.

2- The length in Z direction is divided by the layer spacing; it gives the number of planes required.

3- The Z Planes are generated in a loop that has the count of the number of planes calculated in step 2. Starting with the minimum Z value and adding the layer spacing every time to the preceding value and saving the value in an array until the maximum Z value is reached.

B.2.4 Mathematical theory for slicing

First let us take a closer look at the mathematical side of the slicing process, and then we will proceed to explain the code structure. Slicing means to mathematically locate the intersection lines between each facet and the slicing plane. The group of intersection lines that belong to that plane are called the planar contour. Each facet is defined by 3 vertices; hence it could be represented by 3 line equations. If the slicing plane is to have an intersection with any facet, it means that it is intersecting two edges (lines), see figure B.1. This is the basic idea used in the developed code.

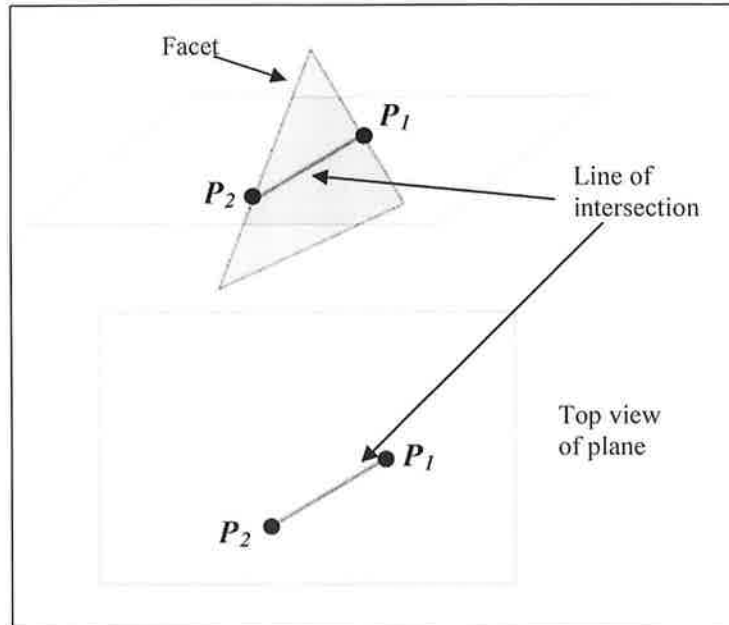


Figure B.1: Facet-plane intersection, P_1 and P_2 are the intersection points.

The following are the mathematical equations needed to define the points of intersection. The mathematical relations are found in [159].

Plane equation in 3D

Let us consider a random plane in 3D, figure B.2. To identify this plane we need a point that belongs to the plane (P) and a vector that is normal to the plane (\mathbf{N}).

If $P_p = (x_p, y_p, z_p)$, and $\mathbf{N} = A\mathbf{i} + B\mathbf{j} + C\mathbf{k}$

then the plane equation can be written as:

$$A(x-x_p) + B(y-y_p) + C(z-z_p) = 0 \quad (\text{B.1})$$

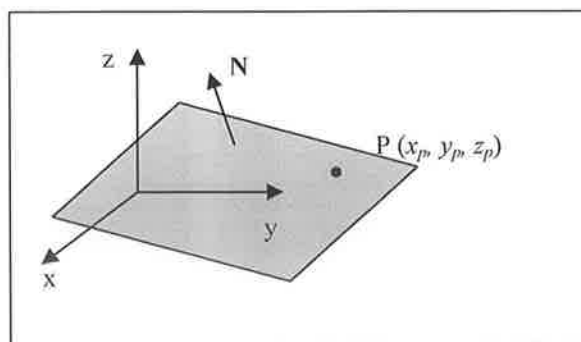


Figure B.2: Plane equation in 3D.

If we consider the case of a plane whose normal is parallel to one of the major axes. Say a plane with \mathbf{N} , parallel to the z axis, see figure B.3, then:

$$P = (0, 0, z_p),$$

$$\mathbf{N} = 0\mathbf{i} + 0\mathbf{j} + 1\mathbf{k} = \mathbf{k}, \text{ and}$$

$$0(x-0) + 0(y-0) + 1(z-z_p) = 0$$

The plane equation will take this form:

$$z = z_p \tag{B.2}$$

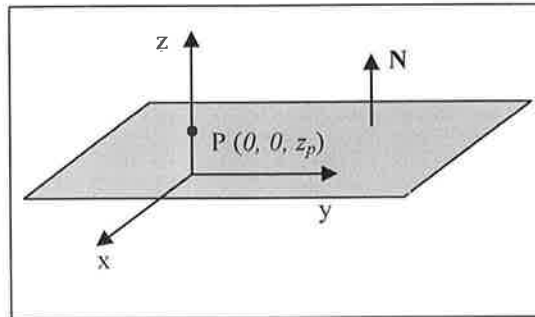


Figure B.3: A plane with normal parallel to the z axis.

Line equation in 3D

Two points or one point and a vector parallel to the line are required to write its equation in 3D. In our case we will use two points to write the equations. Let us consider the line in figure B.4. It passes through the points $P_0 = (x_0, y_0, z_0)$ and $P_1 = (x_1, y_1, z_1)$.

The vector equation of this line can be written as:

$$\mathbf{P}_0\mathbf{P}_1 = t.\mathbf{v} \tag{B.3}$$

where \mathbf{v} is a vector parallel to the line and $(0 \leq t \leq 1)$ is a scalar.

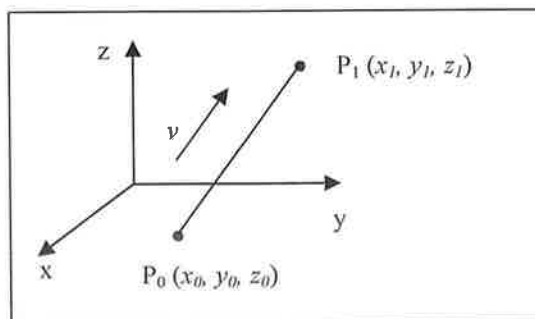


Figure B.4: Line equation in 3D.

however, $\mathbf{P}_0\mathbf{P}_1 = (x_1 - x_0)\mathbf{i} + (y_1 - y_0)\mathbf{j} + (z_1 - z_0)\mathbf{k}$

So the parametric equation of the line is written as:

$$\begin{aligned} x &= x_0 + (x_1 - x_0).t \\ y &= y_0 + (y_1 - y_0).t \\ z &= z_0 + (z_1 - z_0).t \end{aligned} \tag{B.4}$$

or in this form:

$$t = \frac{x - x_0}{x_1 - x_0} = \frac{y - y_0}{y_1 - y_0} = \frac{z - z_0}{z_1 - z_0} \quad (\text{B.5})$$

Note that if we substitute P_0 in equation B.5 will give $t = 0$. Substituting P_1 in the same equation will give $t = 1$. These are the endpoints of the line.

Intersection between a plane and a line in 3D

The intersection between a plane and a line in 3D can be a single point or it can be all the points of the line (if the line is along the plane), see figure B.5. The intersection can be found by simply substituting the line's equation into the plane's equation, this will give the value of t where $(0 \leq t \leq 1)$.

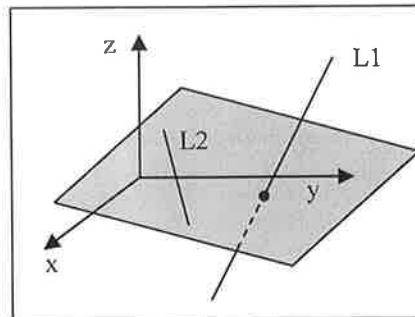


Figure B.5: Intersection between a line and a plane in 3D.

Example

This example illustrates the theory above. The plane in figure B.6 passes through $P = (0, 0, -2)$ and has a normal vector parallel to the z -axis. The plane passes through the line $P_1 = (-3, 2, -3)$ to $P_2 = (1, -1, 4)$. Find the equations of the plane and the line, and check if there is an intersection between them?

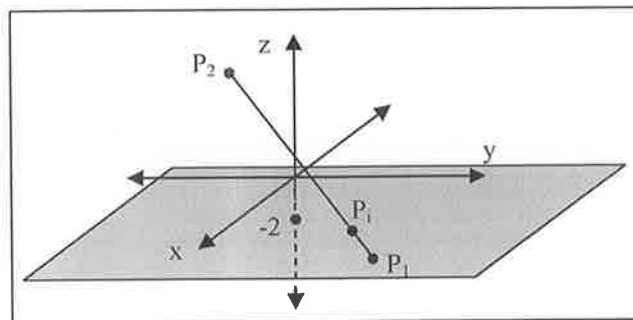


Figure B.6: Example

Solution:

The plane has a normal $\mathbf{N} = \mathbf{k}$ (parallel to z -axis)

Using this and $P = (0, 0, -2)$ into equation 5.1, gives

$$0(x-0) + 0(y-0) + 1(z-(-2)) = 0$$

$$z = -2$$

The line's equation can be given by equation B.4

$$x = -3 + (1-(-3)).t = -3 + 4t$$

$$y = 2 + (-1-2).t = 2 - 3t$$

$$z = -3 + (4-(-3)).t = -3 + 7t$$

to check for intersection we substitute the line equation into the plane's equation and find the value of t .

$$-3 + 7t = -2$$

$$t = 1/7$$

The value of t satisfies the condition ($0 \leq t \leq 1$) that means there is an intersection between the plane and the line. To find the intersection point, we substitute the value of t into the line's equation.

$$x = -3 + 4(1/7) = 17/7$$

$$y = 2 - 3(1/7) = 11/7$$

$$z = -3 + 7(1/7) = -2$$

So the point of intersection P_i ($17/7, 11/7, -2$).

B.2.5 Slicing code

How the code works

It is composed of three cases to perform slicing in X, Y and Z directions. The procedure here is explained for slicing in the Z direction, but it is exactly the same for the other two directions.

- 1- Take the first plane from Z Planes array.
- 2- Take the first three elements from (X, Y and Z values), representing the first facet's vertices:

$$V_1(x_1, y_1, z_1)$$

$$V_2(x_2, y_2, z_2)$$

$$V_3(x_3, y_3, z_3)$$

- 3- Three line equations can be generated, but that is not always necessary. The possibility of having an intersection with the plane is checked as follows:

- a) The plane's equation is always in the form of equation B.2, (e.g. $z = C$, where C is a constant).

b) Check is $z_1 \leq C \leq z_2$. If true then form the line V_1V_2 equation and solve for intersection with the plane as done in the previous example. If false then the equations will not be formed.

c) Check is $z_1 \leq C \leq z_3$. If true then form the line V_1V_3 equation and solve for intersection with the plane as done in the previous example. If false then the equations will not be formed.

d) Check is $z_2 \leq C \leq z_3$. If true then form the line V_2V_3 equation and solve for intersection with the plane as done in the previous example. If false then the equations will not be formed.

Note: At least two lines will have intersection with the plane, or none of them. If no intersection is found, go back to step 2 and take 3 new vertices to be checked.

e) Save the intersection points in a 2D array (2 rows and 3 columns). Each row contains the (x, y, z) coordinates of one intersection point.

Note: The z coordinate is constant = C.

4- **Segment code:** Segmentation of the distance between two intersection points is sometimes necessary when the distance is significantly large (i.e. distance $\geq 2 \times$ Mark Spacing) then the final shape of the design will be ill- represented, see figure 2.31 (a) and (b) in chapter 2. The Mark Spacing was taken to be $2 \times$ (Layer Spacing) based on trial and error procedure. This code is hidden and runs automatically. It takes the intersection points as an input. Its function is as follows:

a) Calculate the distance between the intersection points.

b) If the distance $\geq 2 \times$ (Mark Spacing) then the distance between the two points is segmented at a segment length = (Mark Spacing). The coordinates of the intermediate point(s) are calculated and returned in a new 2D array that contains the original and all intermediate points.

c) If the distance $< 2 \times$ (Mark Spacing) then return the original points without segmenting.

5- After segmenting, the points are saved in an array that will contain all the planar-contour points.

6- The loop will go back to step 2 and takes the 2nd facet's vertices. Steps 3-5 are repeated until all facets in the (X, Y and Z values) arrays are checked for intersection with the plane.

7- The loop ends here, with the result of all the intersection points with the 1st plane saved in the array in step 5.

8- **Filter code:** the tessellation technique has a basic important characteristic, which is the (edge-to-edge rule). This rule means that every facet edge can be shared with a single adjacent facet, see figure 2.32 in chapter 2 for illustration. This implies that the intersection points will be repeated, this will affect the size of the build file. The planar-contour array from step 7 is therefore sent as an input to another sub-code (Filter code), which runs automatically. It simply deletes all the redundant points in the array and returns it to the main program.

9- The filtered array entries are plotted on a 3D graph display. Figure 2.33 in chapter 2 shows a sample planar-contour plot of a sphere.

10- The contents of the filtered planar array are written to the build file, each line contains the x, y and z coordinates of one point. The text "PLANE" is placed below the last line to mark the end of the 1st planar-contour data. Figure 2.34 in chapter 2 shows a part of the sphere build file.

11- The code goes back to step 1 and takes the 2nd plane from the Z Planes array. Steps 2-10 are repeated generating the 2nd planar-contour and writing it to the same file below the previous data. This procedure is repeated until all the slicing planes are checked for intersections with the design.

12- Upon completion, the full design plot is displayed on a 3D graph display, see figure 2.35 in chapter 2. The last line in the build file is written as "eof".

B.2.6 Position Control code

How to use the code

The external voltage supply to the stepper motors has to be switched on. The following are the inputs and outputs of the code:

1- Build File Path: the name and location of the build file previously obtained from the CAD manipulation code.

2- Scale: this is an optional entry that is used to scale the build file coordinates in order to fabricate bigger or smaller parts from the same design.

3- SPEED: is a control of the positioning speed in (mm/s), this value will set the frequency of the signal sent to the motors.

4- FREQUENCY: this is the PRF setting of the triggered laser pulses.

5- Number of pulses: this is the number of pulses to be triggered at each point inside the sample using the set frequency.

6- ACCURACY: is an indicator of the positioning resolution in (μm), it is calculated from equation B.5.

The 3 yellowish boxes in the front panel contain indicators of the positioning process in X, Y and Z directions respectively. Since they are exactly the same for the 3 directions, only the indicators of the X direction are explained here:

7- X: displays the x-coordinate of the point being located, this reading comes from the build file.

8- Dx: displays the difference between the current and the previous x-coordinates. This represents the distance in millimetres that the work piece has to be displaced in the x direction.

9- No of pulses X: displays the number of pulses required to achieve the displacement Dx. This number is calculated from equation B.2.

10- Direction X: an LED indicator ON/OFF. It indicates the direction of displacement depending on the sign of Dx (positive Dx → ON, negative Dx → OFF).

11- Enable X: an LED indicator ON/OFF. If ON it indicates that the X-motor is operating, OFF indicates that the motor has reached the required position.

End Of Design: an LED indicator ON/OFF at the bottom of the front panel. If ON it indicates that the positioning process has finished. The status of this LED is on at the end of the build file.

How the code works

The following explains the code's execution algorithm:

1- At the beginning, the X, Y and Z coordinates are set to (0,0,0).

2- The 1st line from the build file is read, it contains X1, Y1 and Z1 (the coordinates of the 1st point).

3- If the line reads "PLANE" signifying the beginning of a new planar contour. Then go back to step 2.

4- Dx, Dy and Dz are calculated in the first loop they equal (X1-X, Y1-Y, Z1-Z) these values resemble the displacement required in the x, y and z directions respectively.

5- The pulse frequency "F" is calculated from equation B.4.

6- Px, Py and Pz are calculated from equation B.2, and represent the number of pulses to be generated in the x, y and z directions respectively.

Then the program enters into a structure that contains 3 sequences, each sequence performs the displacement in one direction. Taking the x direction for example:

(a) If Px is not equal to 0, the sequence will be executed. If Dx = 0 the program will jump to sequence-Y.

(b) A TRUE-Boolean signal (Enable X) is sent to DIO 1 which is the digital port on PCI 6036E connected to the enable pin on the motor driver.

(c) Depending on the sign of Dx, a Boolean signal (Direction X) is sent to DIO 0 which is the digital port on PCI 6036E connected to the direction input on the motor driver.

(d) Generate a pulse train that has Px number of pulses at F frequency on GPCTR 0, which is a counter output on the PCI 6036E. This pin is connected to the Step Clock Input pin on the motor driver.

(e) When the pulse train reaches the required number of pulses Px, the counter will reset and the Enable signal will turn to FALSE. The program proceeds to sequence-Y.

7- When the displacement has taken place in the 3 directions, a TRUE-Boolean is sent to DIO 6 which is connected to the analogue control socket on the laser power supply unit. This signal gates the Q-switching. Then a finite number of pulses are triggered at the current location using the setting from the number of pulses field.

8- The current X, Y and Z coordinates are saved in a shift register. They will take the place of the previous coordinates in the next loop. The code loops back to step 2.

9- This algorithm is repeated until the line read from the build file reads “eof”, the program will terminate its operation.

Table B.2: Positioning code output parameters and pin connections.

Code Parameter	PCI 6036E pin	Motor Driver / Laser Power pins	Task			
Px	GPCTR 0	Step clock X	Step pulse train to motor X			
Py	GPCTR 0	Step clock Y	Step pulse train to motor Y			
Pz	GPCTR 0	Step clock Z	Step pulse train to motor Z			
Enable X	DIO 1	Enable Input X	ON	OFF	OFF	Enable / Disable of motors.
Enable Y	DIO 3	Enable Input Y	OFF	ON	OFF	
Enable Z	DIO 5	Enable Input Z	OFF	OFF	ON	
Direction X	DIO 0	Direction Input X	Direction control of motor X			
Direction Y	DIO 2	Direction Input Y	Direction control of motor Y			
Direction Z	DIO 4	Direction Input Z	Direction control of motor Z			
Q-Switch	DIO 6	External Q-Switch Gate	Q-switch gate control to the laser power supply unit.			
No of pulses	GPCTR 0	Q- Switch frequency	Finite number of laser pulses			

Code's outputs and pin connections

There was only one counter GPCTR 0 available on the PCI 6036E board. The 3 motor drivers were connected to this counter; hence the motion could only be achieved in one direction at a time. Therefore, the Enable/Disable signal was used to make sure that the

pulse signal was not fed to the three drivers at the same time. Table B.2 lists the positioning code output parameters and their corresponding control pins on the motor drivers and the laser powers supply unit.

Appendix C – Extra Parts of Chapter 3

C.1 Experimental results from polycarbonate experiments

The tables C.1 – C.5 for the samples produced using the average power of 0.3 W.

Table C.1: Microfabrication results at $P = 0.3\text{W}$, $\text{PRF} = 1000\text{ Hz}$ and $E_p = 300\mu\text{J}$.

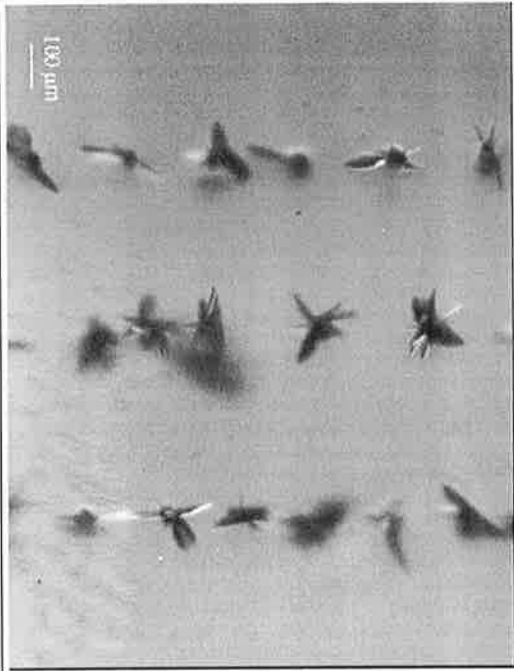
Microscopic image	No. of Pulses	Fluence (J/cm^2)	Acc. Fluence (J/cm^2)	Av. voxel Dia (μm)
	3,000	45.73	$\frac{137192.9}{2}$	61.33
	2,000		91461.95	58.17
	1,000		45730.97	53.5

Table C.2: Microfabrication results at $P = 0.3\text{W}$, $\text{PRF} = 2000\text{ Hz}$ and $E_p = 150\mu\text{J}$.

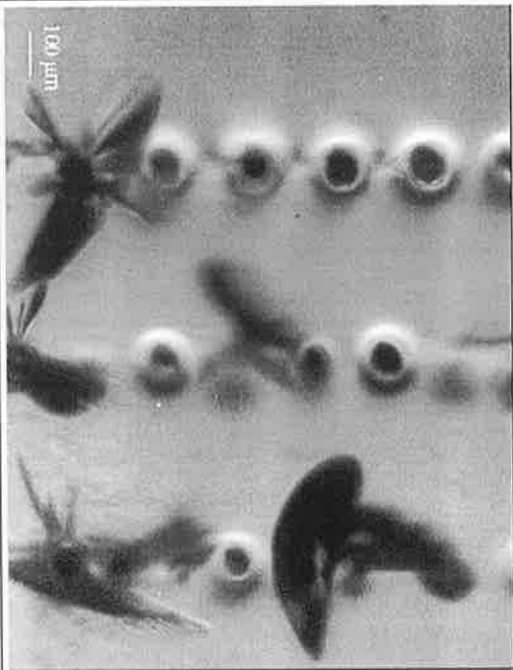
Microscopic image	No. of Pulses	Fluence (J/cm^2)	Acc. Fluence (J/cm^2)	Av. voxel Dia (μm)
	6,000	22.87	$\frac{137192.9}{2}$	153.8
	4,000		91461.95	133.8
	2,000		45730.97	91.4

Table C.3: Microfabrication results at $P = 0.3\text{W}$, $\text{PRF} = 3000\text{ Hz}$ and $E_p = 100\mu\text{J}$.

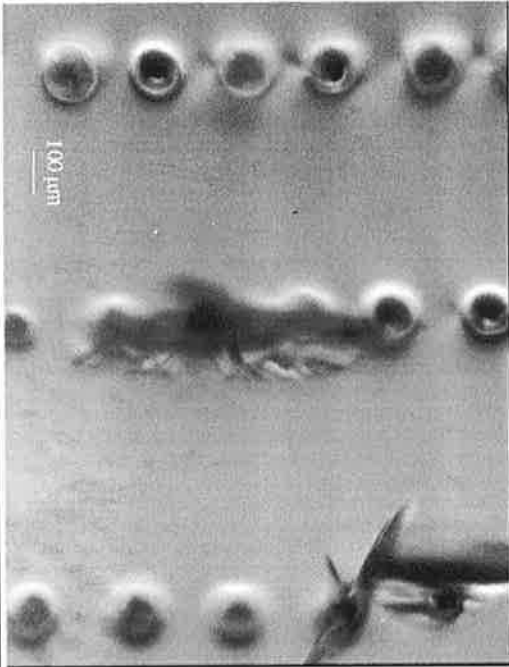
Microscopic image	No. of Pulses	Fluence (J/cm^2)	Acc. Fluence (J/cm^2)	Av. voxel Dia (μm)
	9,000	15.24	137192.9 2	154.4
	6,000		91461.95	145.4
	3,000		45730.97	127.6

Table C.4: Microfabrication results at $P = 0.3\text{W}$, $\text{PRF} = 4000\text{ Hz}$ and $E_p = 75\mu\text{J}$.

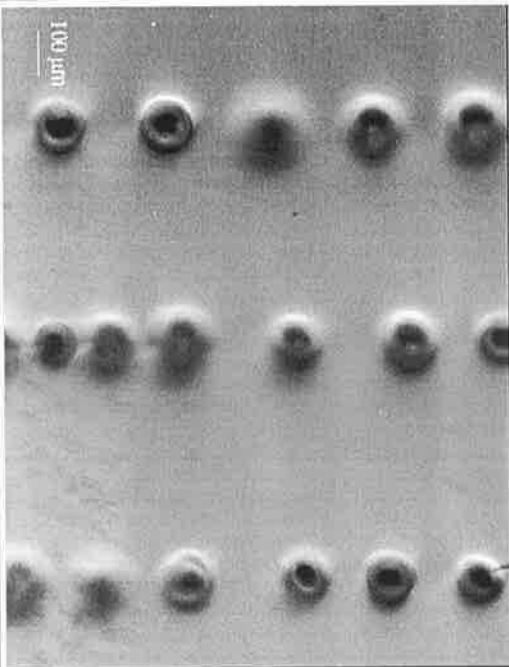
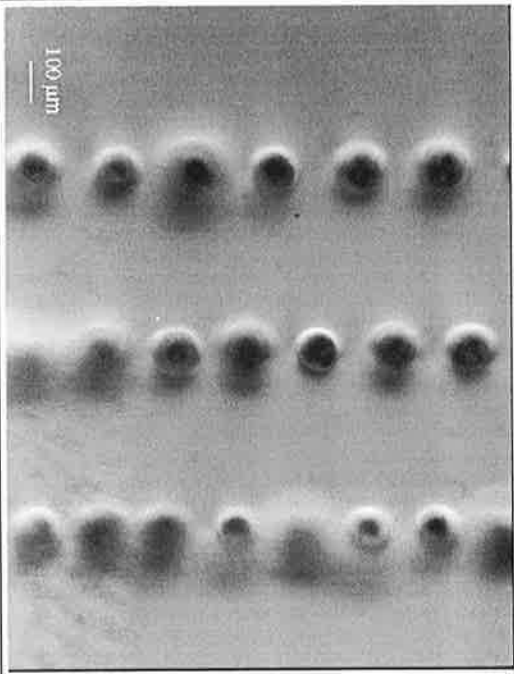
Microscopic image	No. of Pulses	Fluence (J/cm^2)	Acc. Fluence (J/cm^2)	Av. voxel Dia (μm)
	12,000	11.43	137192.9 2	142
	8,000		91461.95	124.67
	4,000		45730.97	119

Table C.5: Microfabrication results at $P = 0.3\text{W}$, $\text{PRF} = 5000\text{ Hz}$ and $E_p = 60\mu\text{J}$.

Microscopic image	No. of Pulses	Fluence (J/cm^2)	Acc. Fluence (J/cm^2)	Av. voxel Dia (μm)
	15,000	9.15	137192.9 2	140.13
	10,000		91461.95	132.13
	5,000		45730.97	118

The tables C.6 – C.10 for the samples produced using the average power of **0.4 W**.

Table C.6: Microfabrication results at $P = 0.4\text{W}$, $\text{PRF} = 1000\text{ Hz}$ and $E_p = 400\mu\text{J}$.


Microscopic image	No. of Pulses	Fluence (J/cm^2)	Acc. Fluence (J/cm^2)	Av. voxel Dia (μm)
	3,000	60.96	182923.8 9	73.17
	2,000		121949.2 6	61.83
	1,000		60974.63	56.33

Table C.7: Microfabrication results at $P = 0.4W$, $PRF = 2000$ Hz and $E_p = 200\mu J$.

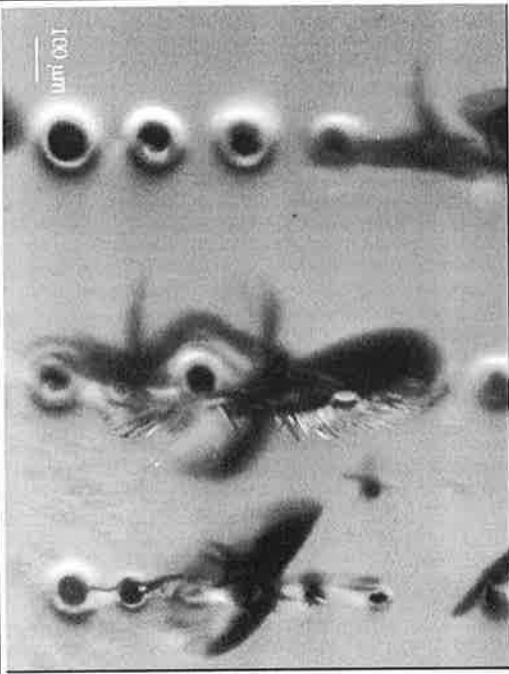
Microscopic image	No. of Pulses	Fluence (J/cm^2)	Acc. Fluence (J/cm^2)	Av. voxel Dia (μm)
	6,000	30.94	182923.8 9	134.1428 571
	4,000		121949.2 6	107.8571 429
	2,000		60974.63	65.28571 429

Table C.8: Microfabrication results at $P = 0.4W$, $PRF = 3000$ Hz and $E_p = 133.33 \mu J$.

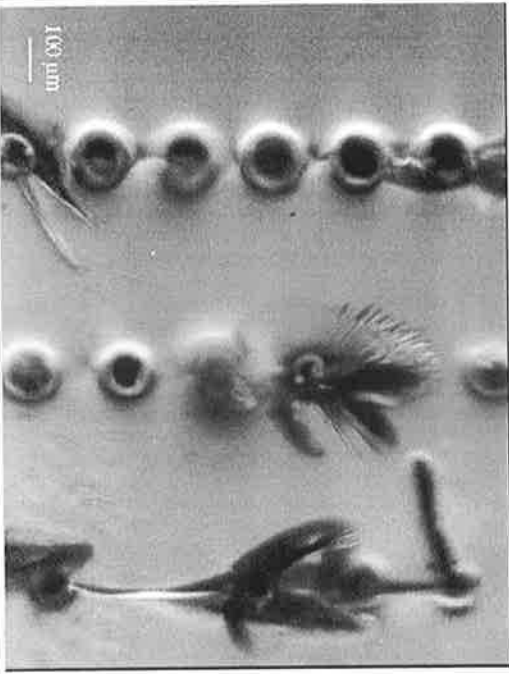
Microscopic image	No. of Pulses	Fluence (J/cm^2)	Acc. Fluence (J/cm^2)	Av. voxel Dia (μm)
	9,000	20.32	182923.8 9	152
	6,000		121949.2 6	120.17
	3,000		60974.63	107.83

Table C.9: Microfabrication results at $P = 0.4W$, $PRF = 4000$ Hz and $E_p = 100\mu J$.

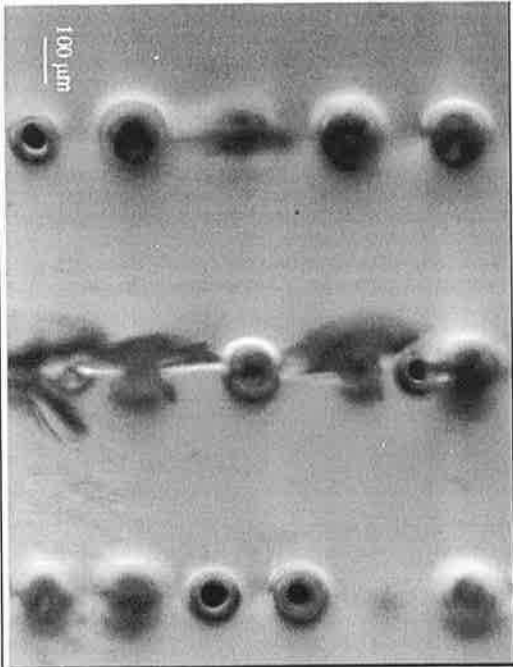
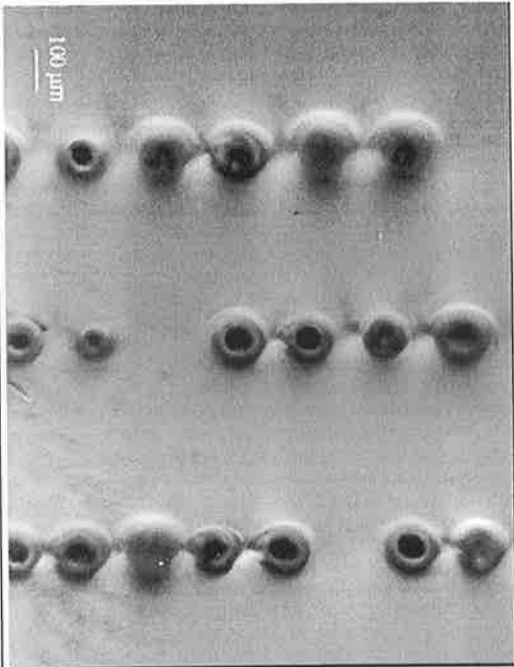
Microscopic image	No. of Pulses	Fluence (J/cm^2)	Acc. Fluence (J/cm^2)	Av. voxel Dia (μm)
	12,000	15.24	182923.8 9	161.6
	8,000		121949.2 6	136
	4,000		60974.63	129.6

Table C.10: Microfabrication results at $P = 0.4W$, $PRF = 5000$ Hz and $E_p = 80\mu J$.

Microscopic image	No. of Pulses	Fluence (J/cm^2)	Acc. Fluence (J/cm^2)	Av. voxel Dia (μm)
	15,000	12.19	182923.8 9	160.57
	10,000		121949.2 6	146
	5,000		60974.63	134.14

The tables C.11 – C.15 for the samples produced using the average **power of 0.5 W**.

Table C.11: Microfabrication results at $P = 0.5\text{W}$, $\text{PRF} = 1000\text{ Hz}$ and $E_p = 500\mu\text{J}$.


Microscopic image	No. of Pulses	Fluence (J/cm^2)	Acc. Fluence (J/cm^2)	Av. voxel Dia (μm)
	3,000	76.22	228654.8 6	63.4
	2,000		152436.5 8	55.2
	1,000		76218.29	50.4

Table C.12: Microfabrication results at $P = 0.5\text{W}$, $\text{PRF} = 2000\text{ Hz}$ and $E_p = 250\mu\text{J}$.

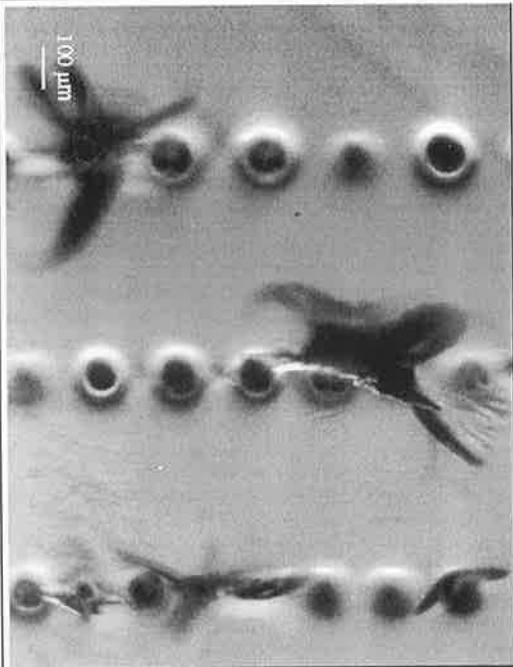
Microscopic image	No. of Pulses	Fluence (J/cm^2)	Acc. Fluence (J/cm^2)	Av. voxel Dia (μm)
	6,000	38.11	228654.8 6	135.83
	4,000		152436.5 8	121.67
	2,000		76218.29	101

Table C.13: Microfabrication results at $P = 0.5W$, $PRF = 3000$ Hz and $E_p = 166.67\mu J$.

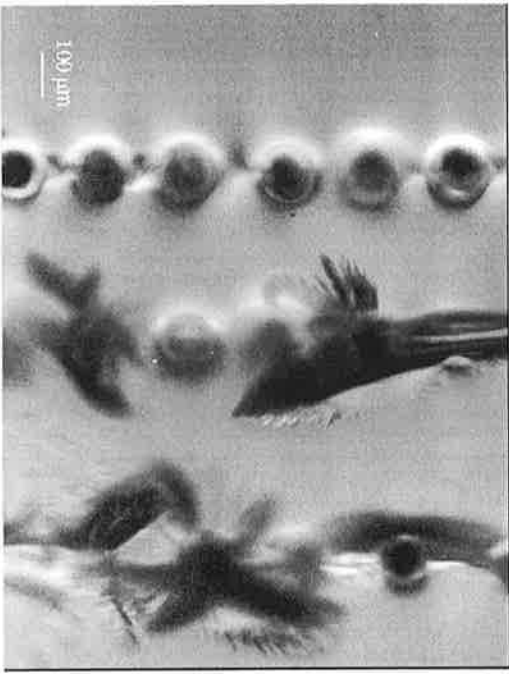
Microscopic image	No. of Pulses	Fluence (J/cm^2)	Acc. Fluence (J/cm^2)	Av. voxel Dia (μm)
	9,000	25.41	228654.8 6	166.33
	6,000		152436.5 8	130.33
	3,000		76218.29	113.83

Table C.14: Microfabrication results at $P = 0.5W$, $PRF = 4000$ Hz and $E_p = 125\mu J$.

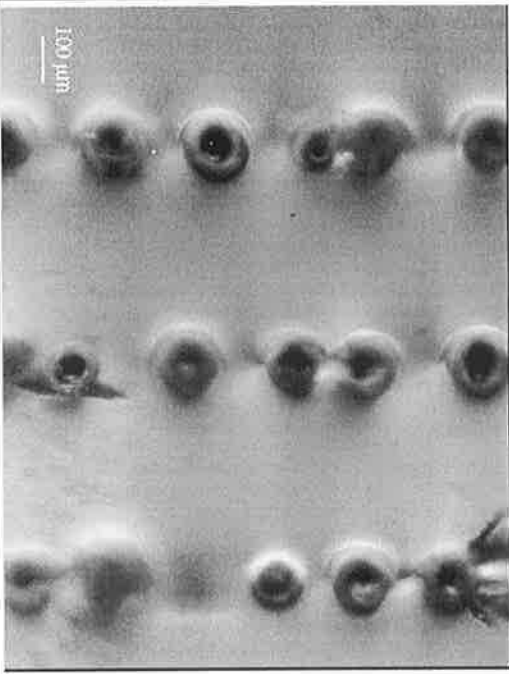
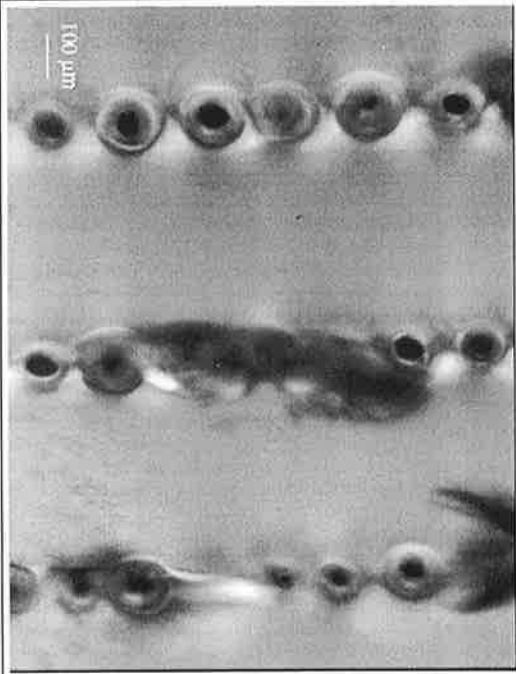
Microscopic image	No. of Pulses	Fluence (J/cm^2)	Acc. Fluence (J/cm^2)	Av. voxel Dia (μm)
	12,000	19.05	228654.8 6	178
	8,000		152436.5 8	151.6
	4,000		76218.29	140.8

Table C.15: Microfabrication results at $P = 0.5W$, $PRF = 5000\text{ Hz}$ and $E_p = 100\mu J$.

Microscopic image	No. of Pulses	Fluence (J/cm^2)	Acc. Fluence (J/cm^2)	Av. voxel Dia (μm)
	15,000	15.24	228654.8 6	181.4285 714
	10,000		152436.5 8	146.8571 429
	5,000		76218.29	115.4285 714

C.2 Build Files of Experiments

C.2.1 The build file used in the microfabrication experiment.

```

0      0      0
0      0.2    0
0      0.4    0
0      0.6    0
0      0.8    0
0      1      0
0      1.2    0
0      1.4    0
0      1.6    0
0      1.8    0
0      2      0
0      2.2    0
0      2.4    0
0      2.6    0
0      2.8    0
0      3      0
0      3.2    0
0      3.4    0
0      3.6    0
0      3.8    0
0      4      0
0      4.2    0
0      4.4    0
0      4.6    0
    
```

```
0 4.8 0
0 5 0
0 5.2 0
0 5.4 0
0 5.6 0
0 5.8 0
0 6 0
0 6.2 0
0 6.4 0
0 6.6 0
0 6.8 0
0 7 0
0 7.2 0
0 7.4 0
0 7.6 0
0 7.8 0
0 8 0
0 0 0
```

PLANE

eof

C.2.2 The build file to achieve 500 μm spacing between the rows in the microfabrication experiment.

```
0 0 0.5
```

PLANE

eof

C.2.3 The build file to achieve 2 mm spacing between the groups in the microfabrication experiments.

```
0 0 2
```

PLANE

eof

C.3 Images and build file of the error checking experiments

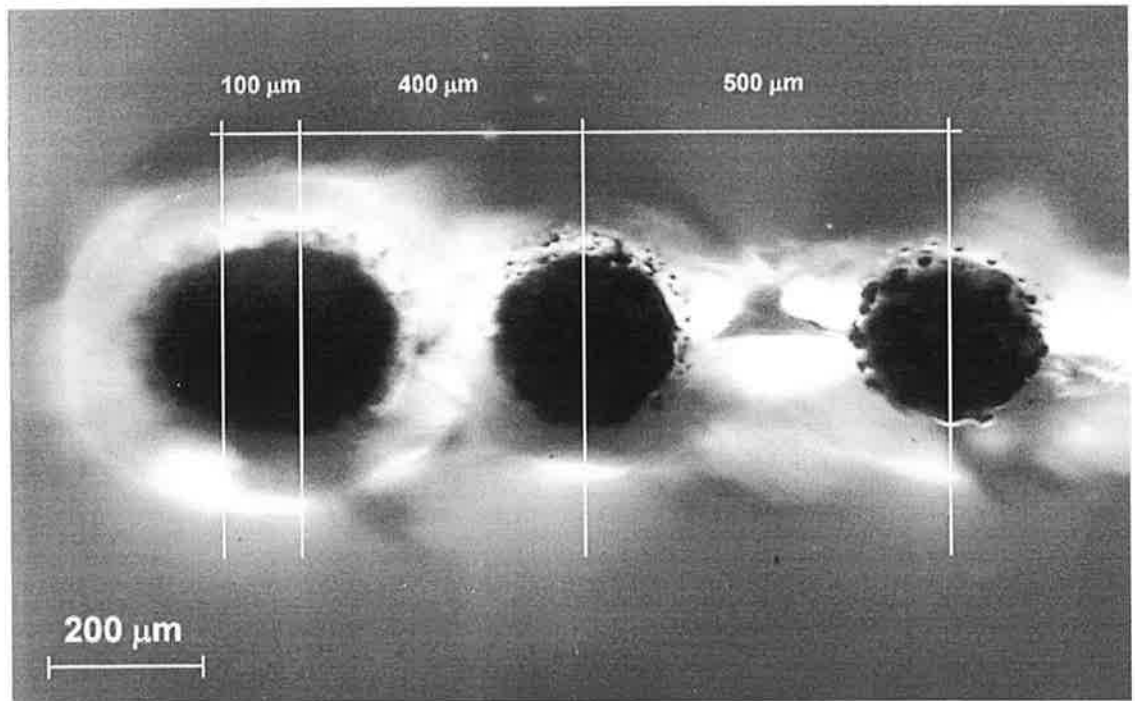


Figure C.1: Row 1 of the error checking sample

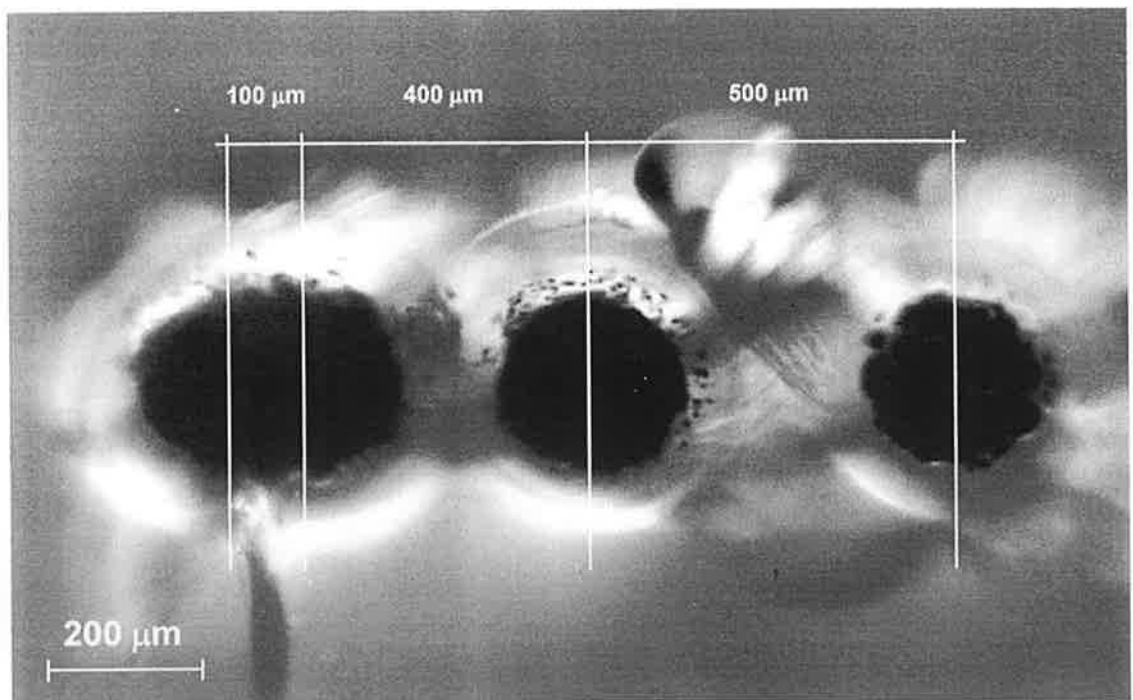


Figure C.2: Row 2 of the error checking sample

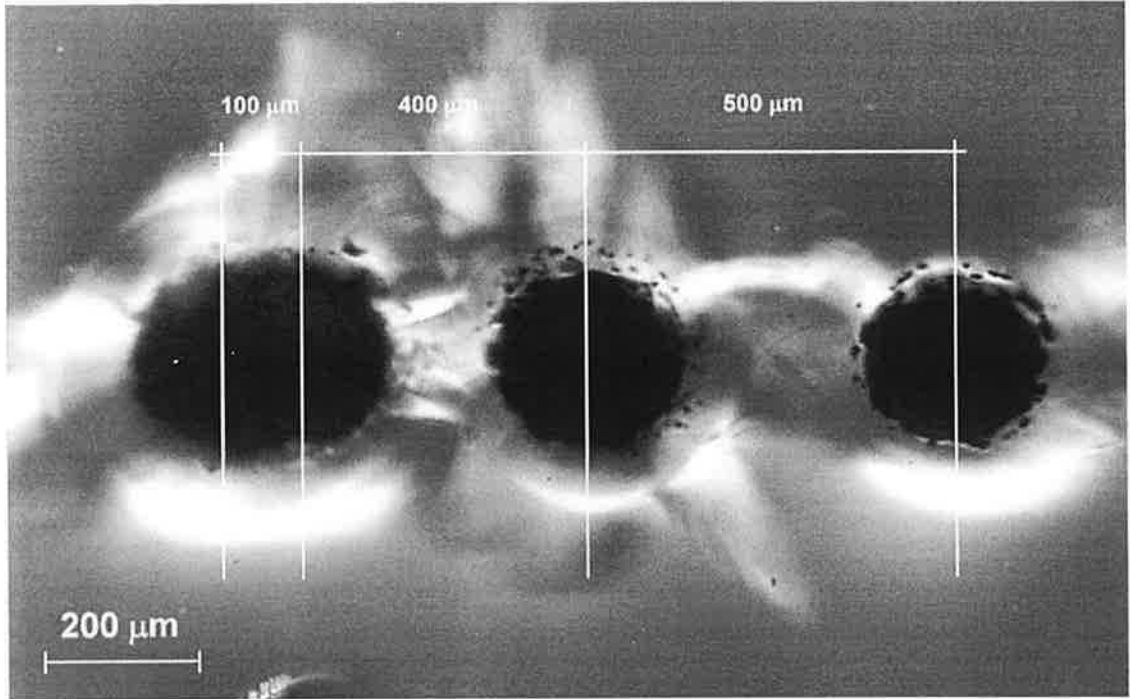


Figure C.3: Row 3 of the error checking sample

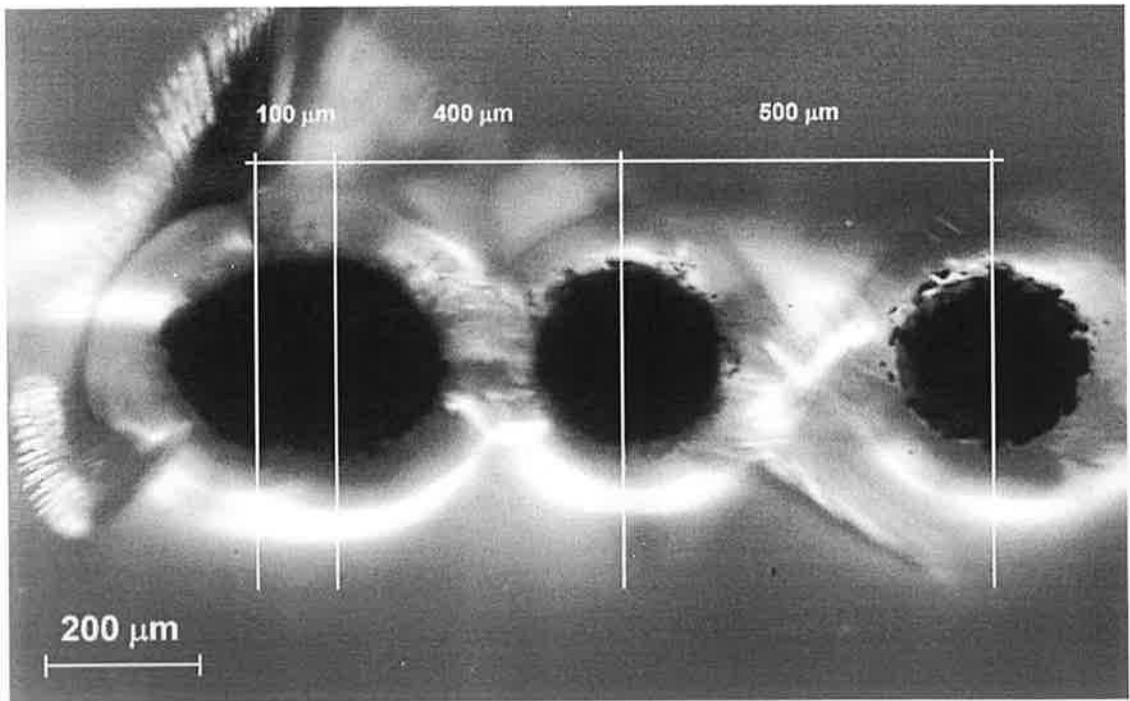


Figure C.4: Row 4 of the error checking sample

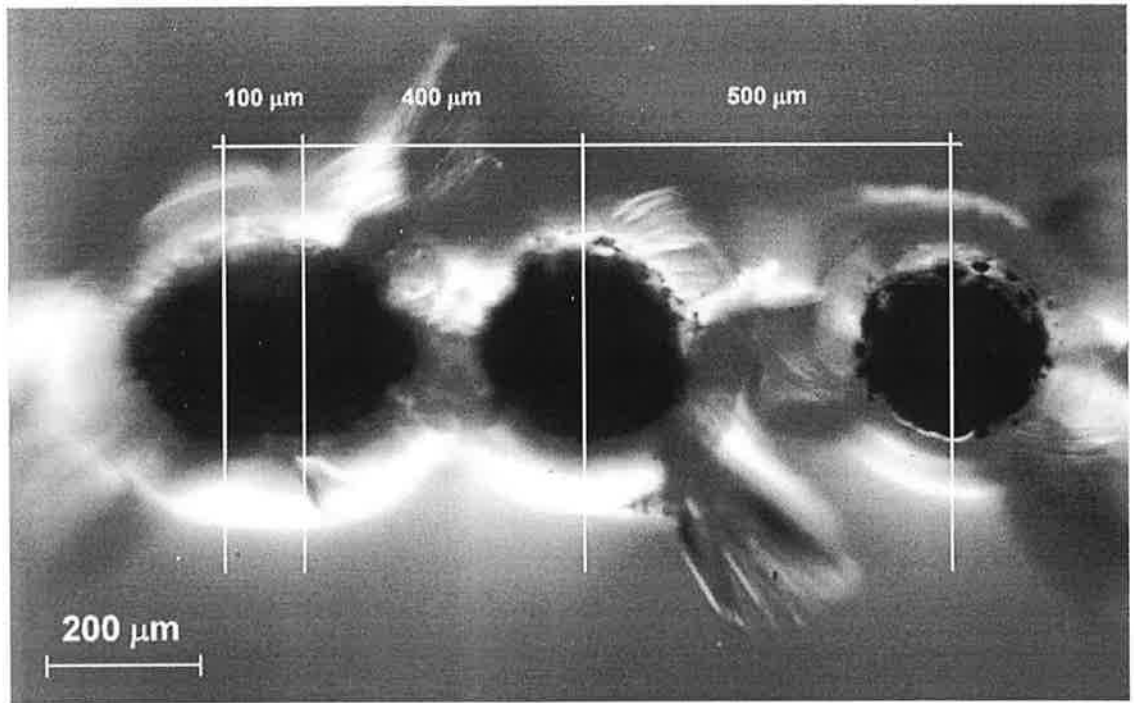


Figure C.5: Row 5 of the error checking sample

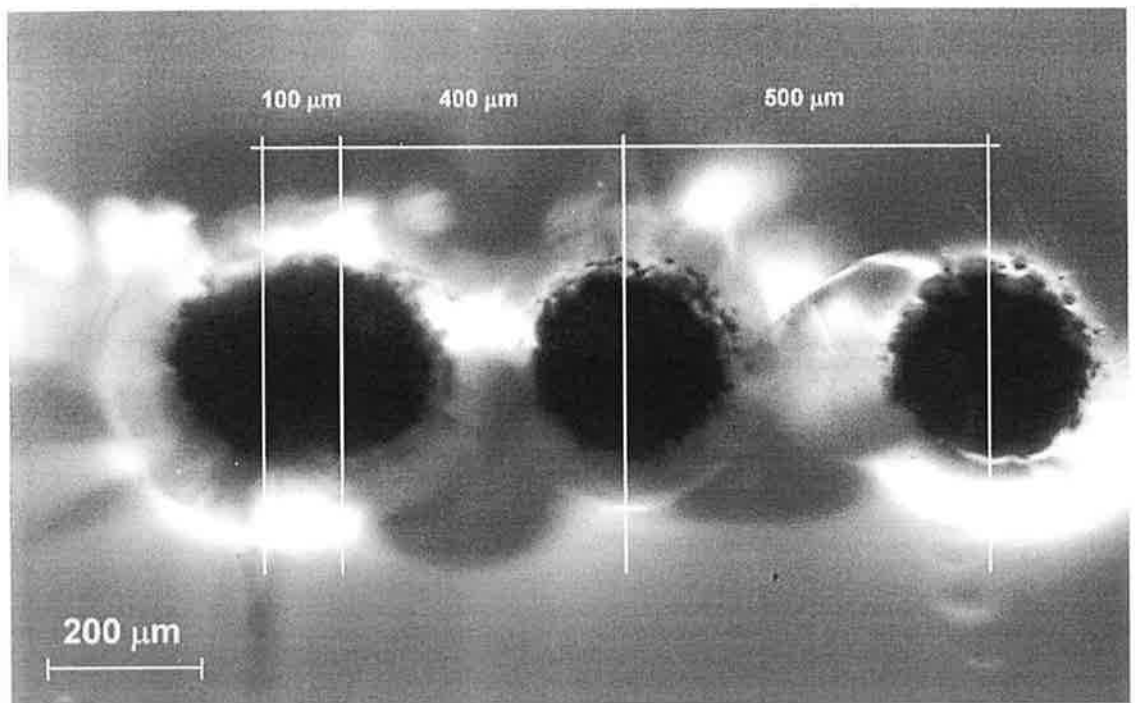


Figure C.6: Row 6 of the error checking sample

C.4 Build file of error checking experiment

X	Y	Z
0	0	0
0	0.1	0
0	0.5	0
0	1	0
0	0.5	0
0	0.1	0
0	0	0
0	0	1
0	0.1	1
0	0.5	1
0	1	1
0	0.5	1
0	0.1	1
0	0	1
0	0	2
0	0.1	2
0	0.5	2
0	1	2
0	0.5	2
0	0.1	2
0	0	2
0	0	3
0	0.1	3
0	0.5	3
0	1	3
0	0.5	3
0	0.1	3
0	0	3
0	0	4
0	0.1	4
0	0.5	4
0	1	4
0	0.5	4
0	0.1	4
0	0	4
0	0	5
0	0.1	5
0	0.5	5
0	1	5
0	0.5	5
0	0.1	5
0	0	5

eof

C.5 Internal microchannels in polycarbonate

Some experiments were carried out to fabricate microchannels inside polycarbonate samples using the developed Nd:YVO₄ laser system. The material was carbonised instead of ablated as can be seen in figures C.7 to C.10. Chemical etching in an ultrasonic bath was tried on these samples in order to reveal the internal channel structures. The used etching chemical was methyl-iso-butyl-ketone (MIBK) following the results of Juodkazis et. al. that were presented in chapter 1 [14]. However, the etching caused degradation of the actual polycarbonate material without any significant effect on the irradiated region. At this stage, it was decided that another laser system should be used.

The channels in figures C.7 to C.10 were fabricated by focusing the laser beam at the back of the sample through its front surface using the achromat lens focusing. The sample was then translated the beam propagation direction but away from the lens so that the irradiated regions do not block the beam propagation. The parameters used were $P = 1 \text{ W}$, $\text{PRF} = 10,000 \text{ Hz}$ with different scanning speeds quoted in the figure captions. Each image shows the microscopic images of the channel underneath the surface (left) and after polishing down to approximately the middle of its cross-section (right).

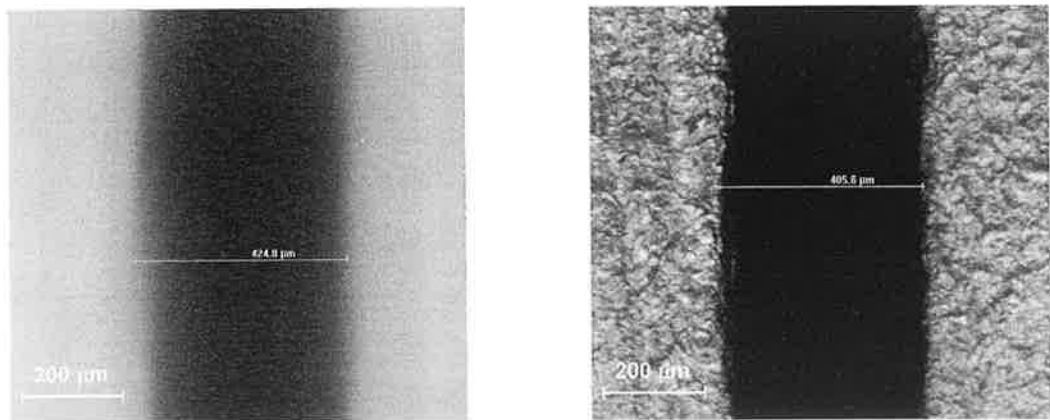


Figure C.7: Channel fabricated using $P = 1 \text{ W}$, $\text{PRF} = 10 \text{ kHz}$ and $U = 6.2 \text{ μm/s}$.

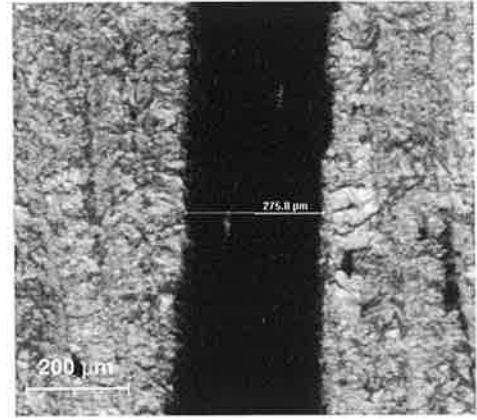
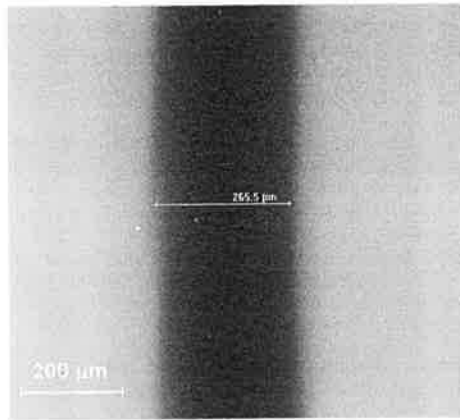


Figure C.8: Channel fabricated using $P = 1$ W, $PRF = 10$ kHz and $U = 25$ $\mu\text{m/s}$.

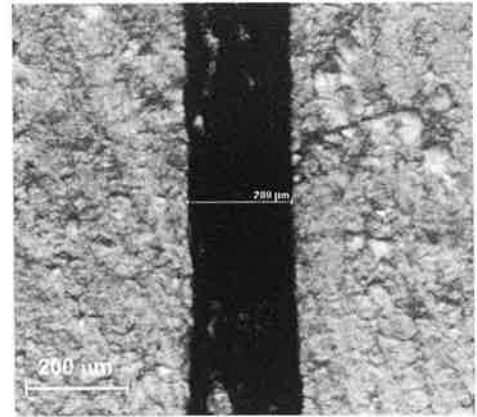
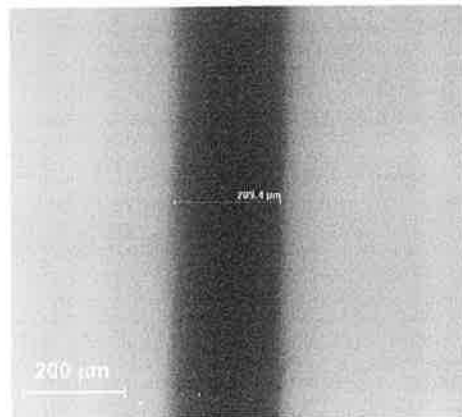


Figure C.9: Channel fabricated using $P = 1$ W, $PRF = 10$ kHz and $U = 62$ $\mu\text{m/s}$.

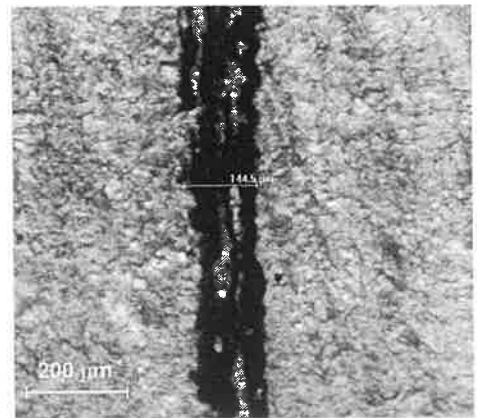
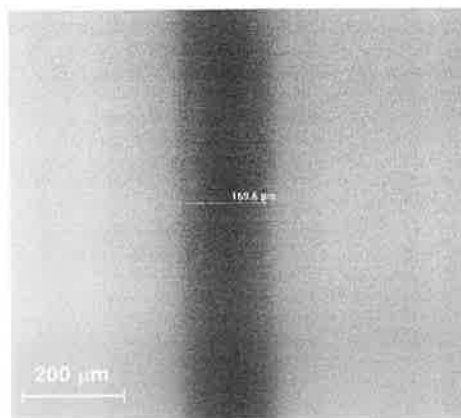


Figure C.10: Channel fabricated using $P = 1$ W, $PRF = 10$ kHz and $U = 124$ $\mu\text{m/s}$.

Appendix D – Extra Results from Chapter 4

D.1 Microscopic images of the channels fabricated at $D_f = 0$ mm.

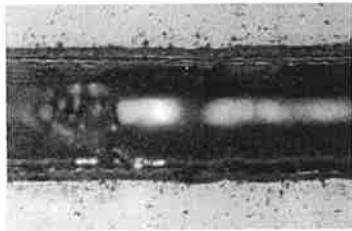
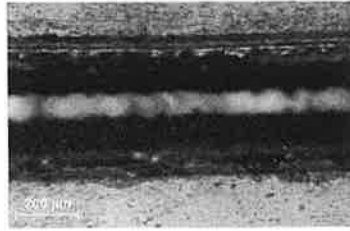
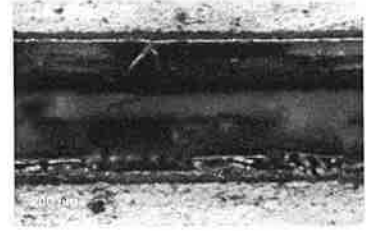


Figure 1: Channel 1



channel 2



channel 3

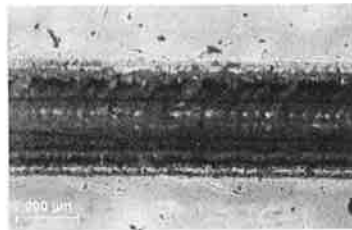
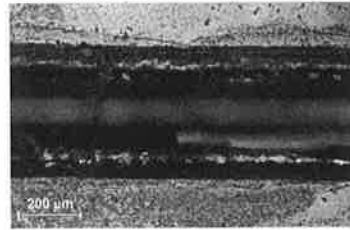
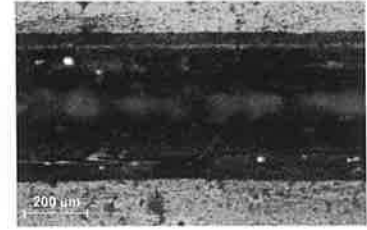


Figure 1: Channel 4



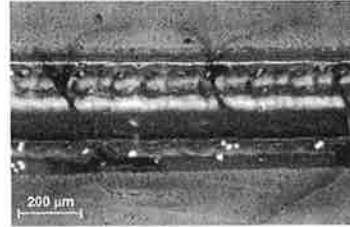
channel 5



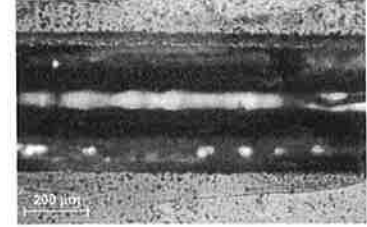
channel 6



Figure 1: Channel 7



channel 8



channel 9

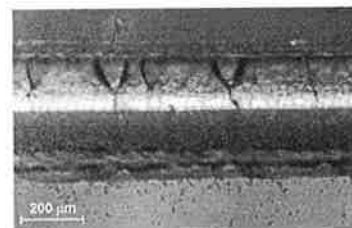
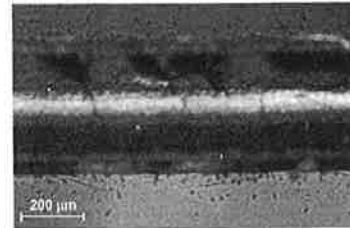
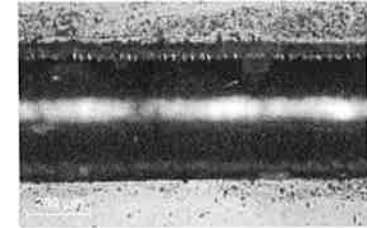


Figure 1: Channel 10



channel 11



channel 12

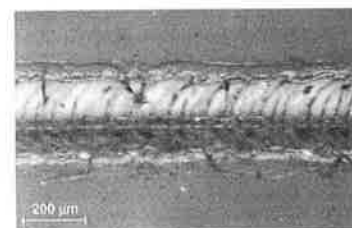
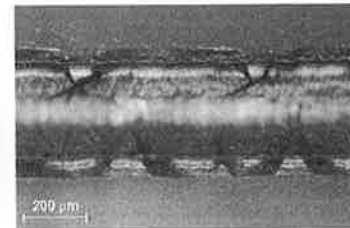
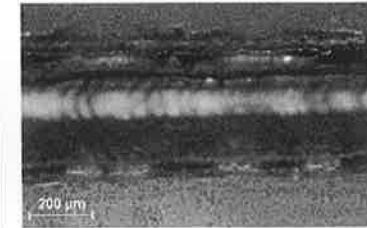


Figure 1: Channel 13



channel 14



channel 15

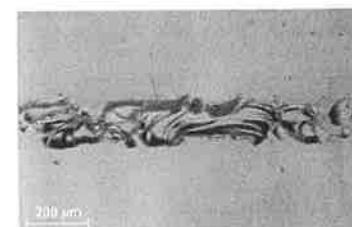
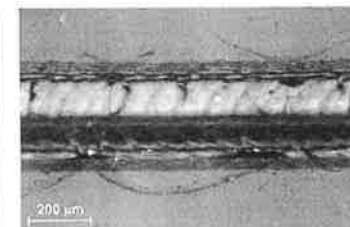
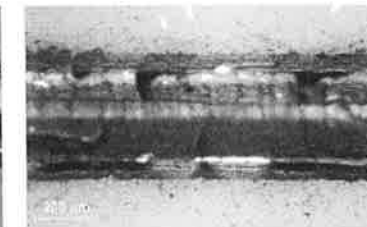


Figure 1: Channel 16



channel 17



channel 18

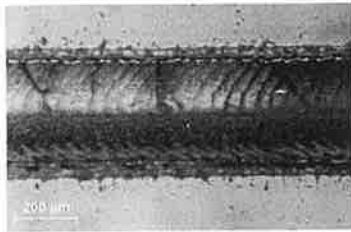
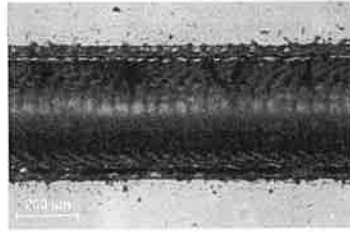
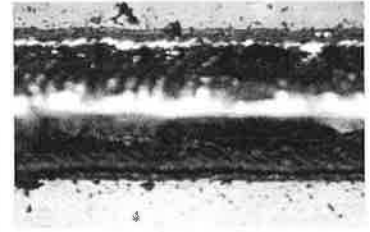


Figure 1: Channel 19



channel 20



channel 21

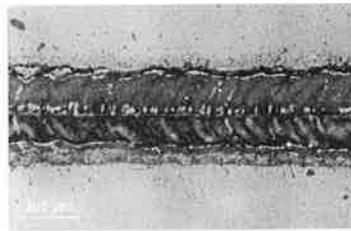
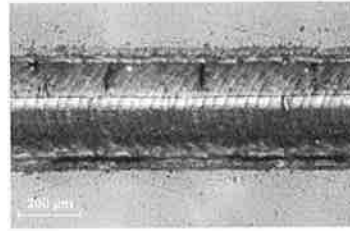
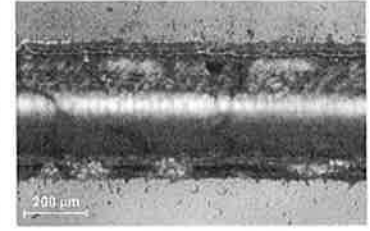


Figure 1: Channel 22



channel 23



channel 24

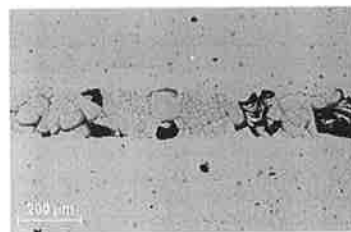
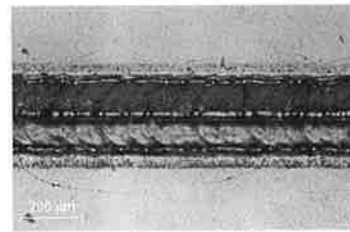
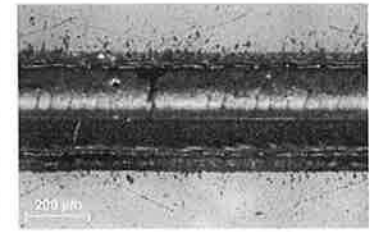


Figure 1: Channel 25



channel 26



channel 27

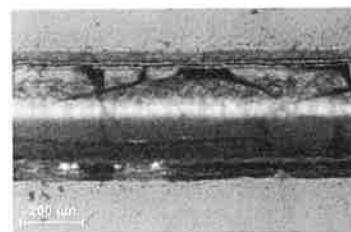
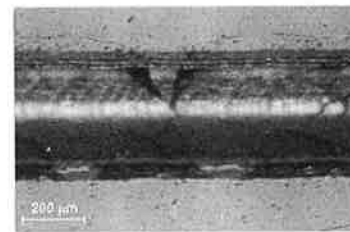
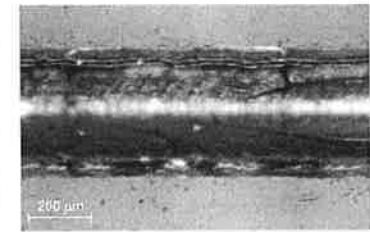


Figure 1: Channel 28



channel 29



channel 30

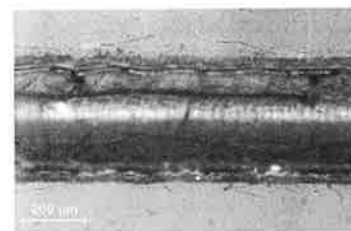
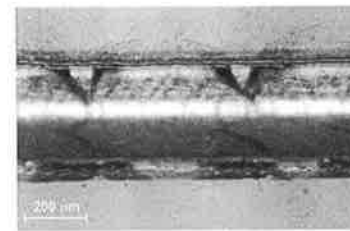


Figure 1: Channel 31



channel 32

D.2 3D profiles for microchannels at $D_f = 0$ mm.

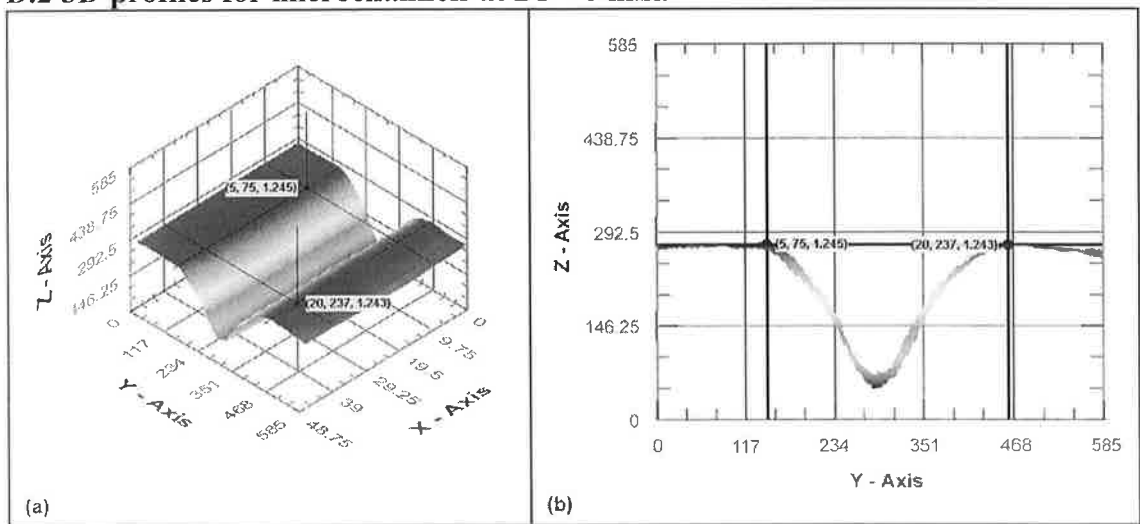


Figure 1: Channel 1, (a) isometric view and (b) front view.

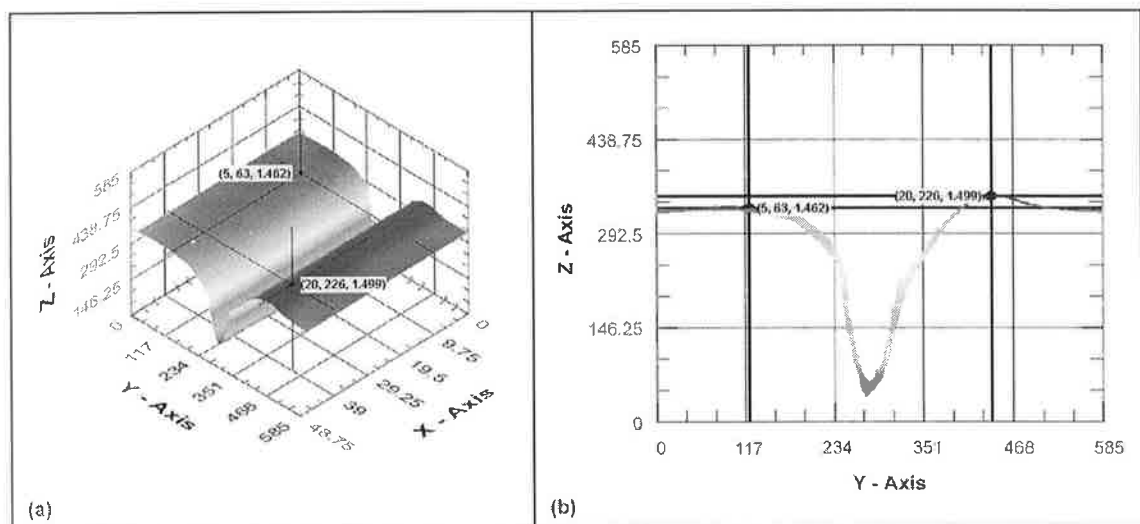


Figure 2: Channel 2, (a) isometric view and (b) front view.

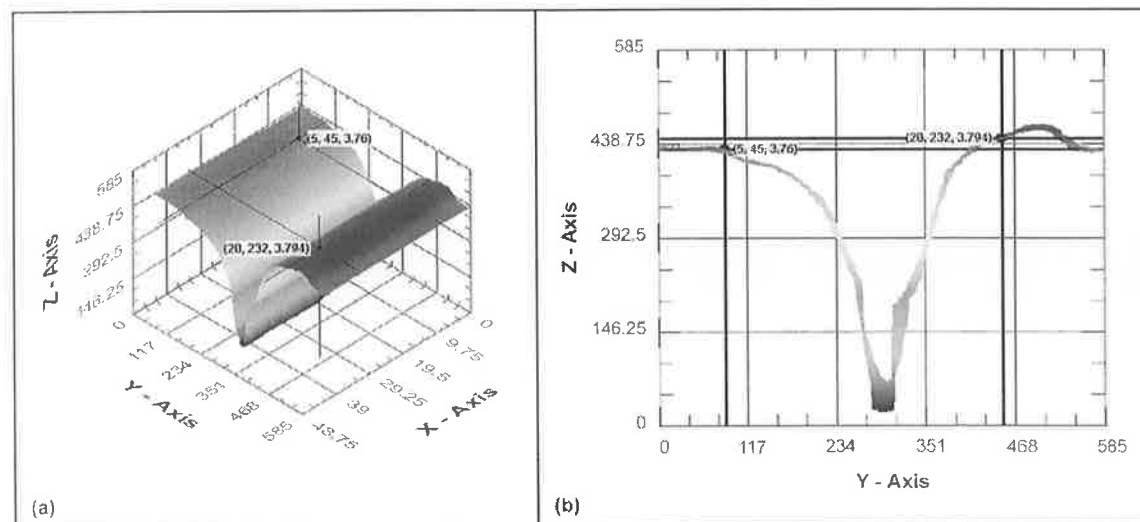


Figure 3: Channel 3, (a) isometric view and (b) front view.

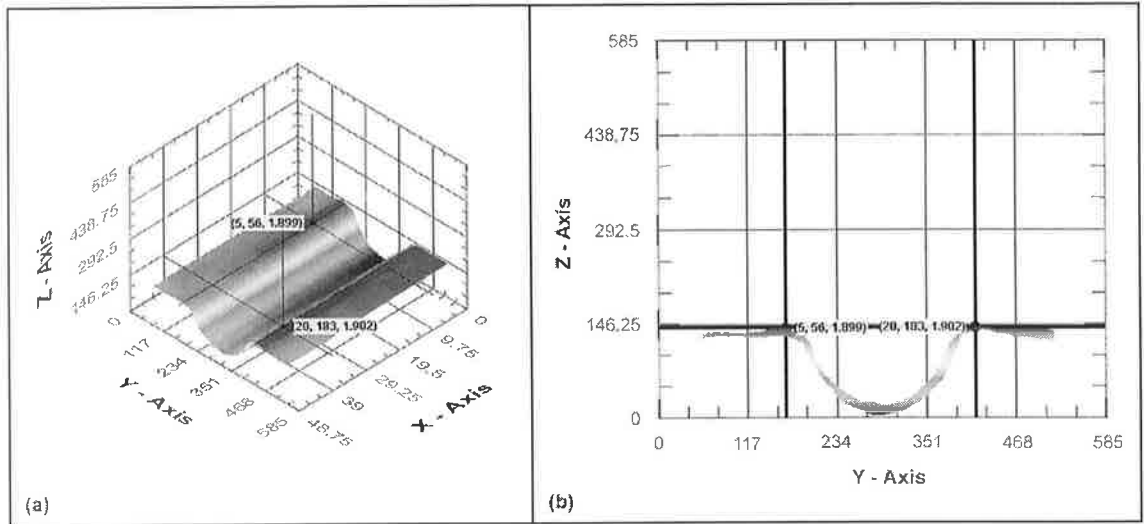


Figure 4: Channel 4, (a) isometric view and (b) front view.

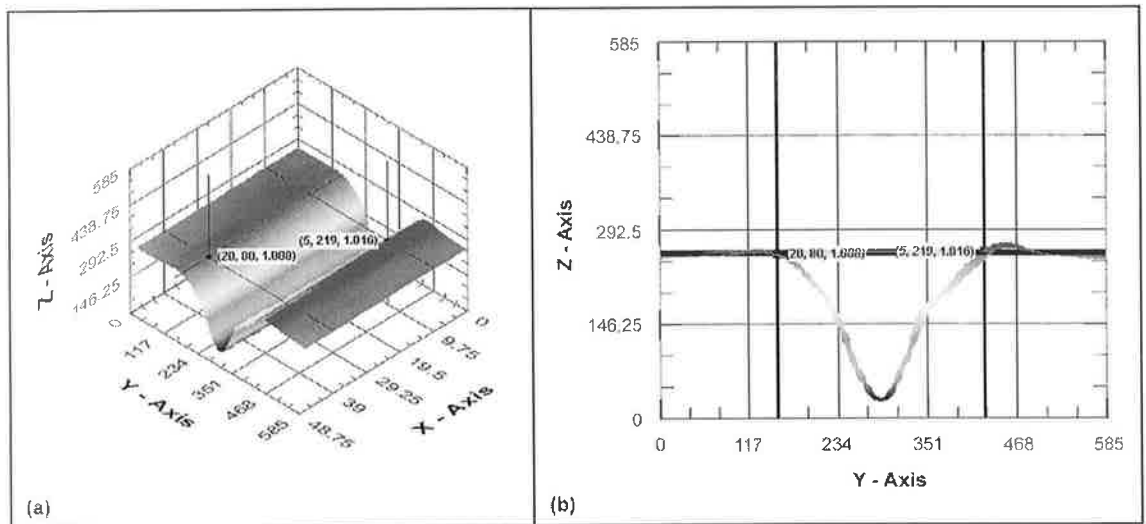


Figure 5: Channel 5, (a) isometric view and (b) front view.

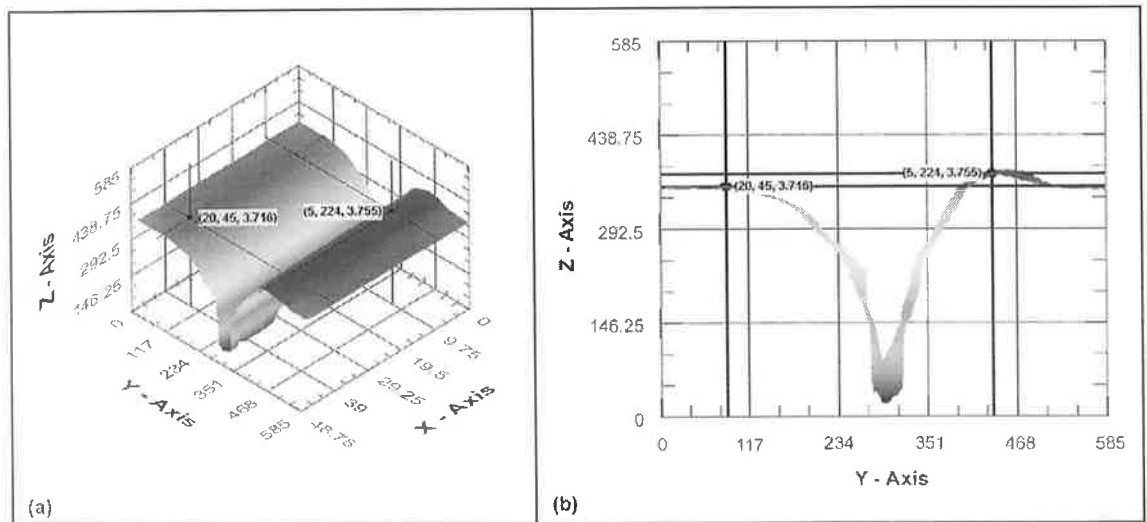


Figure 6: Channel 6, (a) isometric view and (b) front view.

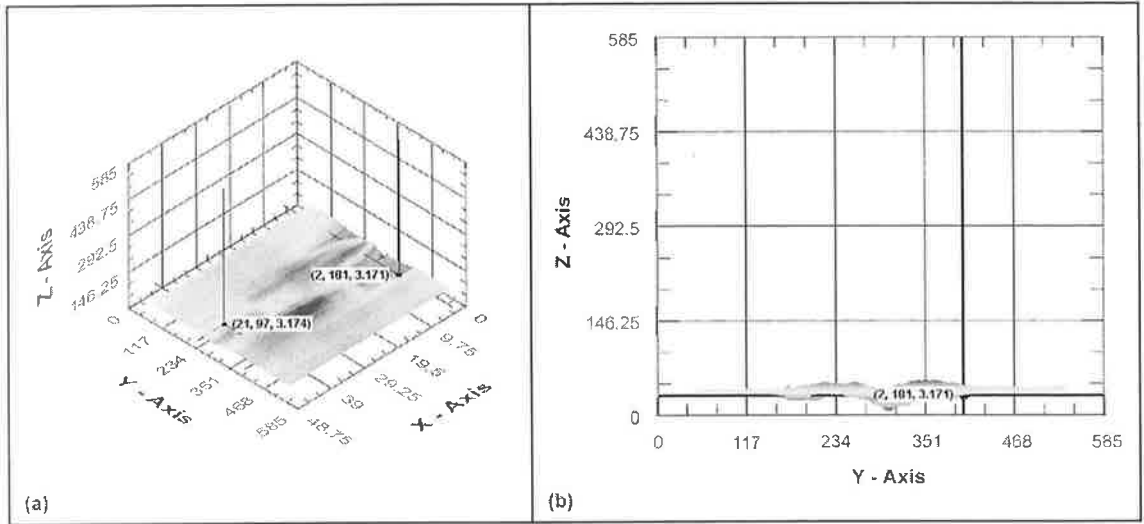


Figure 7: Channel 7, (a) isometric view and (b) front view.

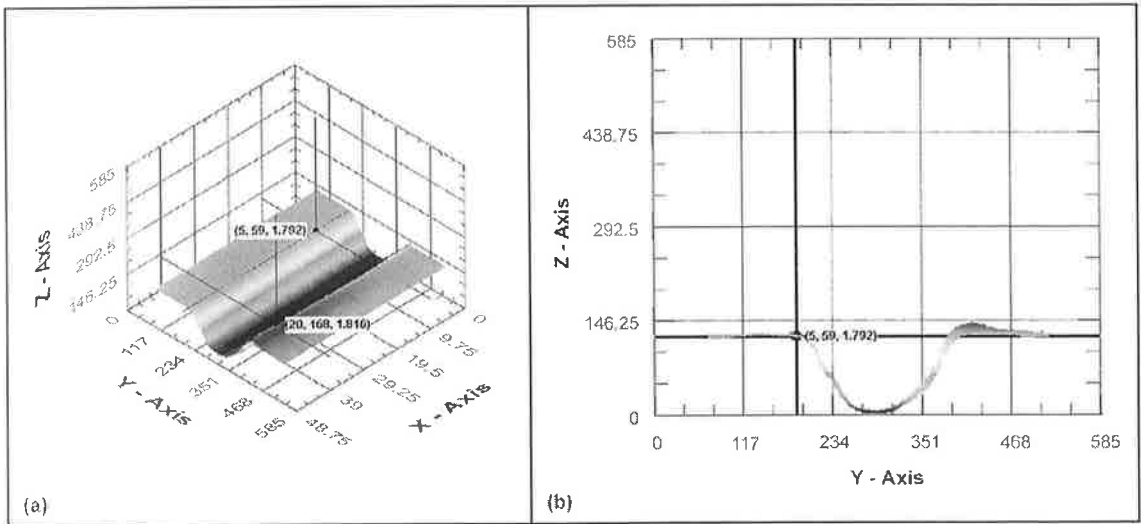


Figure 8: Channel 8, (a) isometric view and (b) front view.

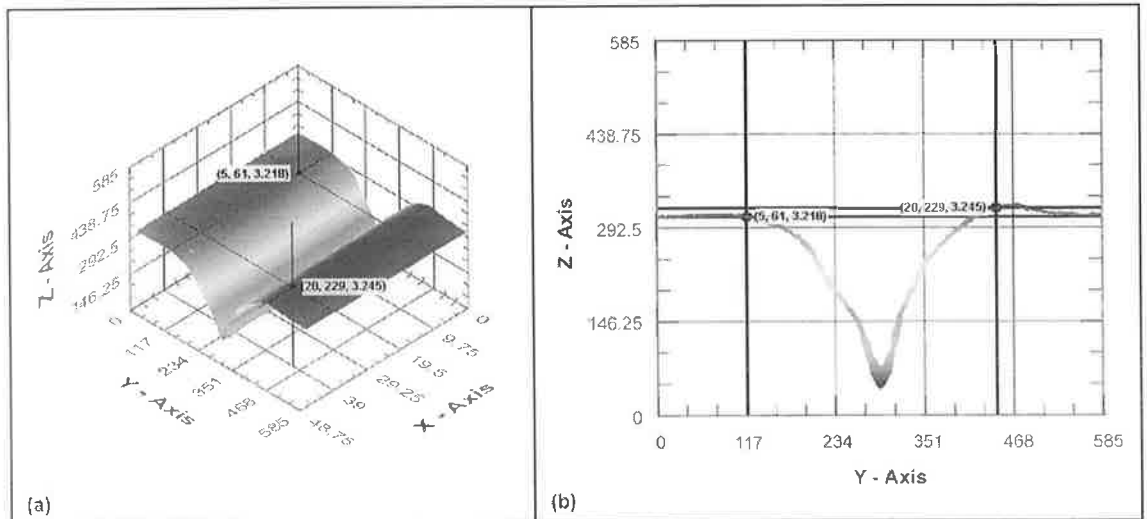


Figure 9: Channel 9, (a) isometric view and (b) front view.

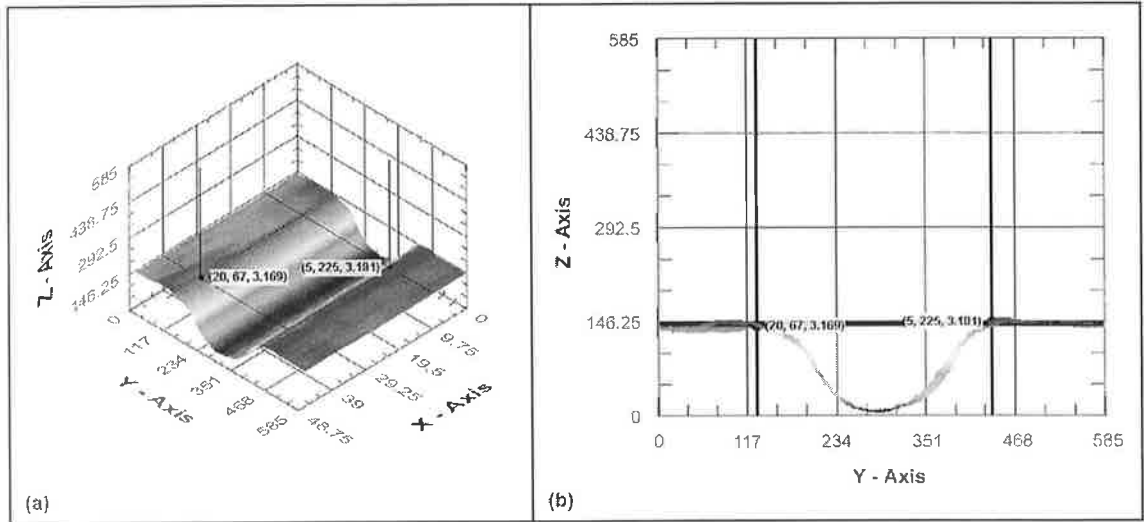


Figure 10: Channel 10, (a) isometric view and (b) front view.

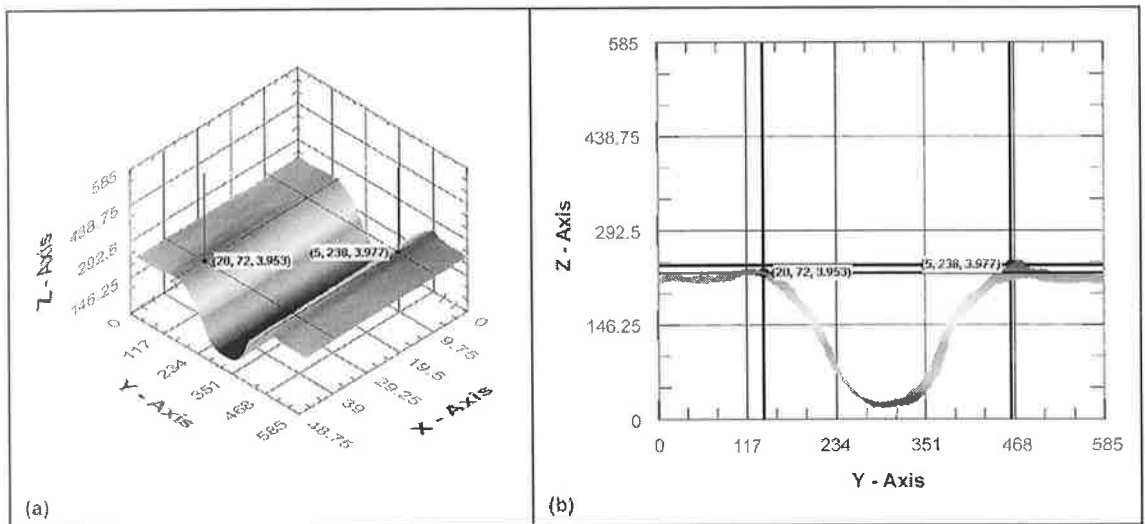


Figure 11: Channel 11, (a) isometric view and (b) front view.

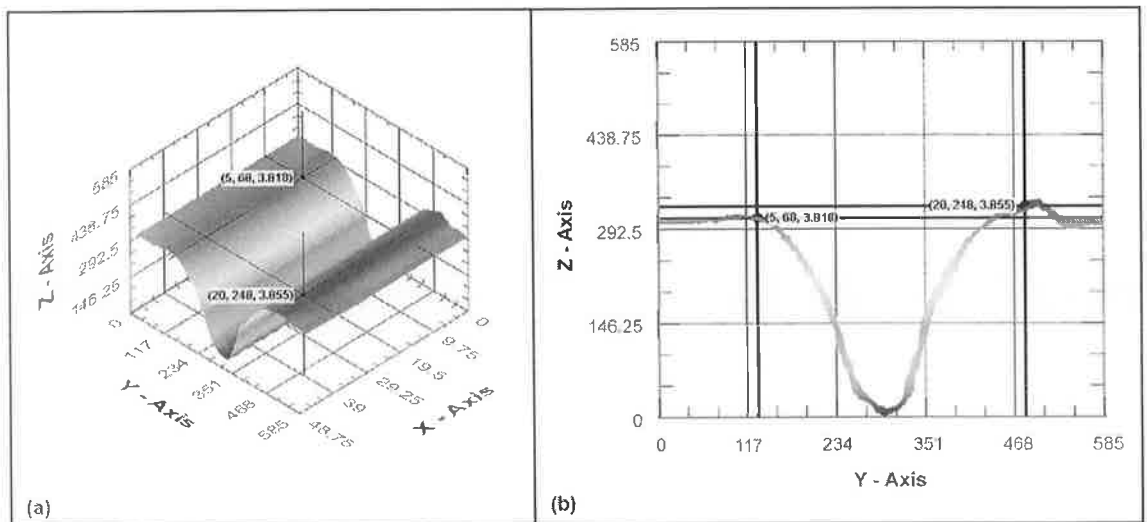


Figure 12: Channel 12, (a) isometric view and (b) front view.

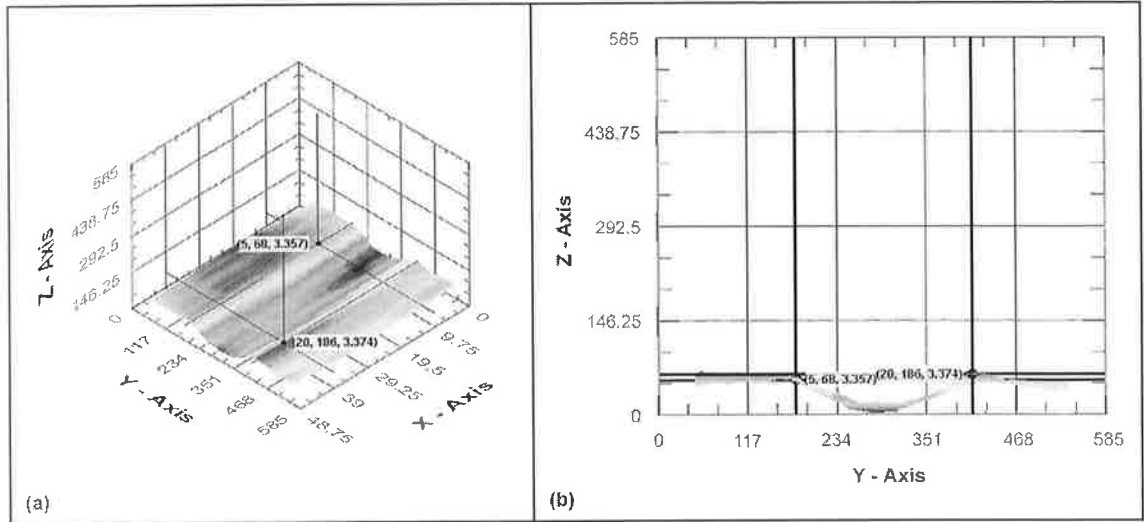


Figure 13: Channel 13, (a) isometric view and (b) front view.

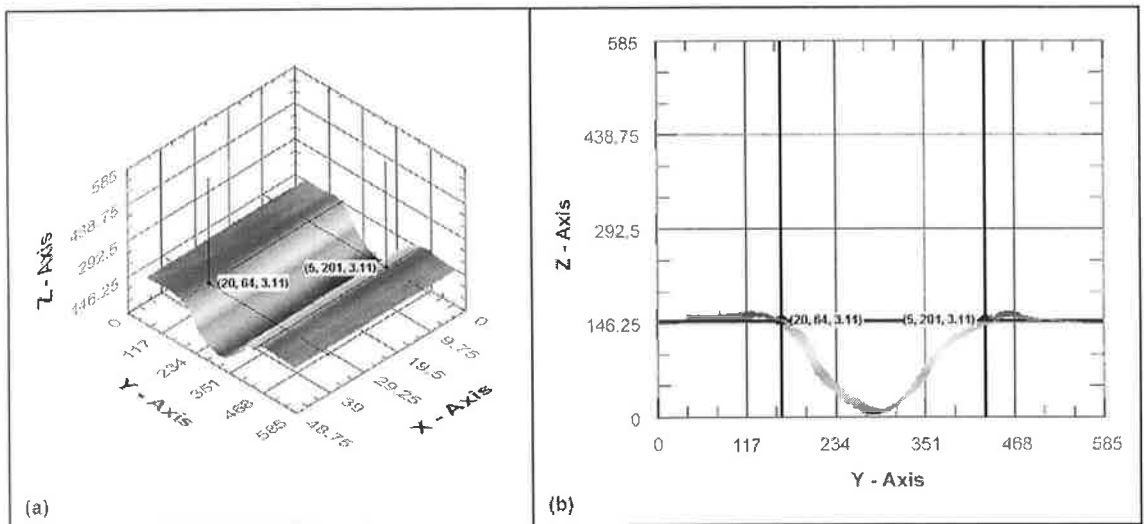


Figure 14: Channel 14, (a) isometric view and (b) front view.

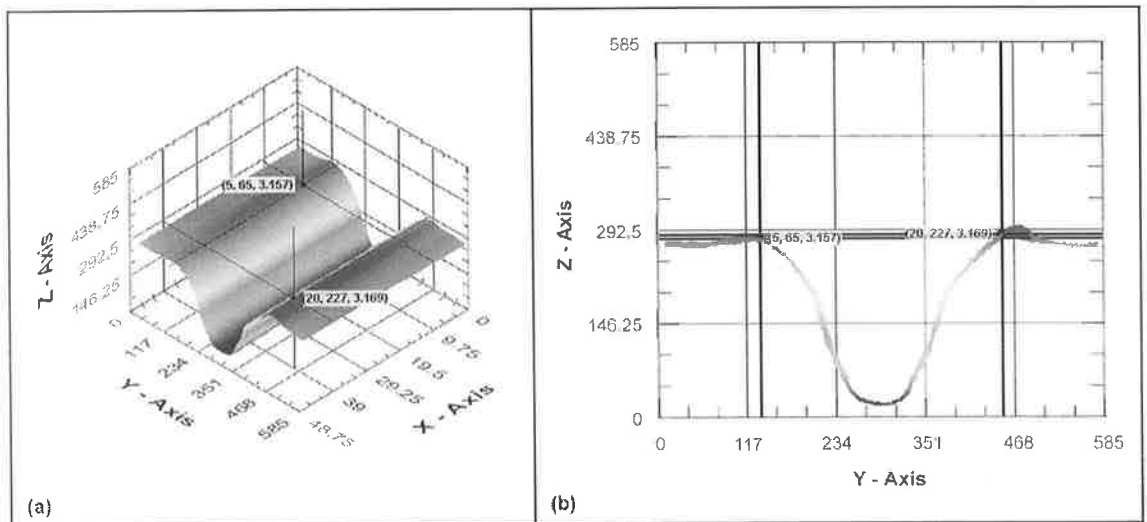


Figure 15: Channel 15, (a) isometric view and (b) front view.

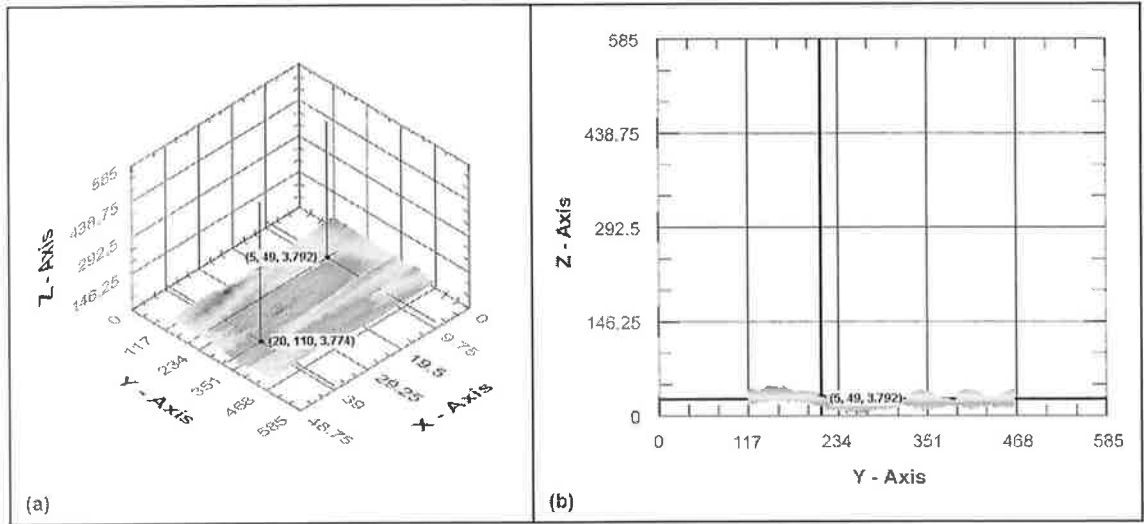


Figure 16: Channel 16, (a) isometric view and (b) front view.

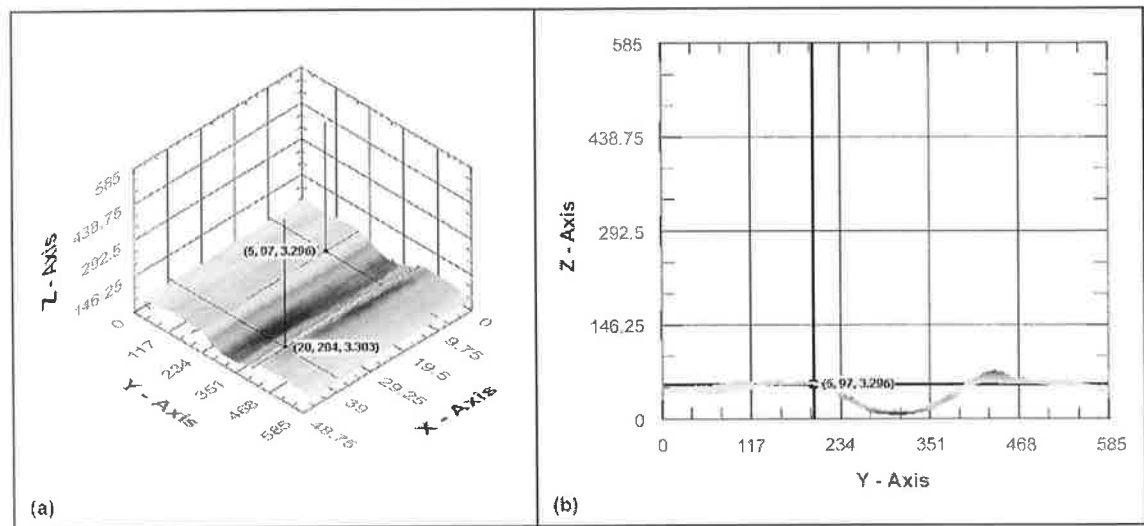


Figure 17: Channel 17, (a) isometric view and (b) front view.

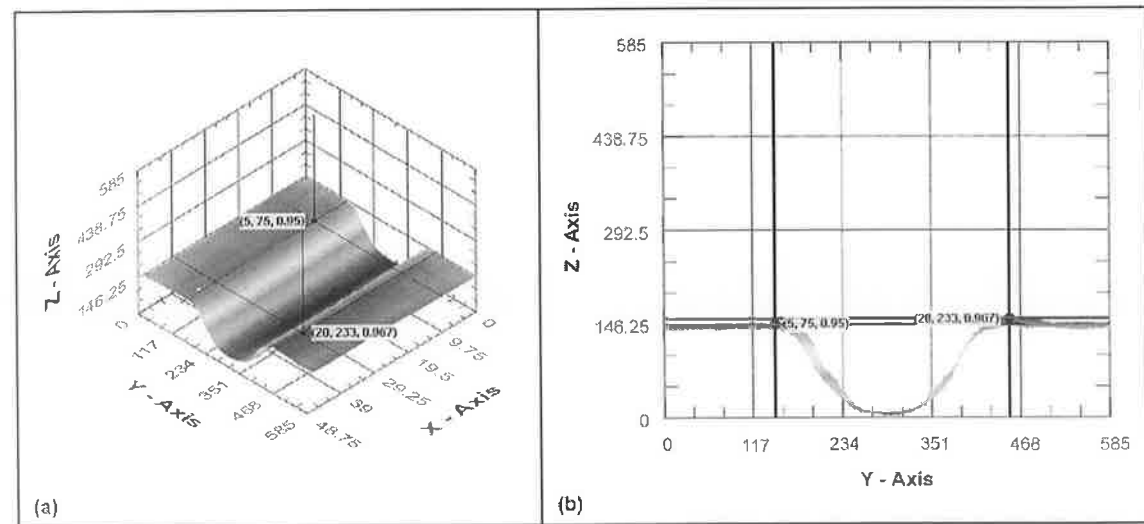


Figure 18: Channel 18, (a) isometric view and (b) front view.

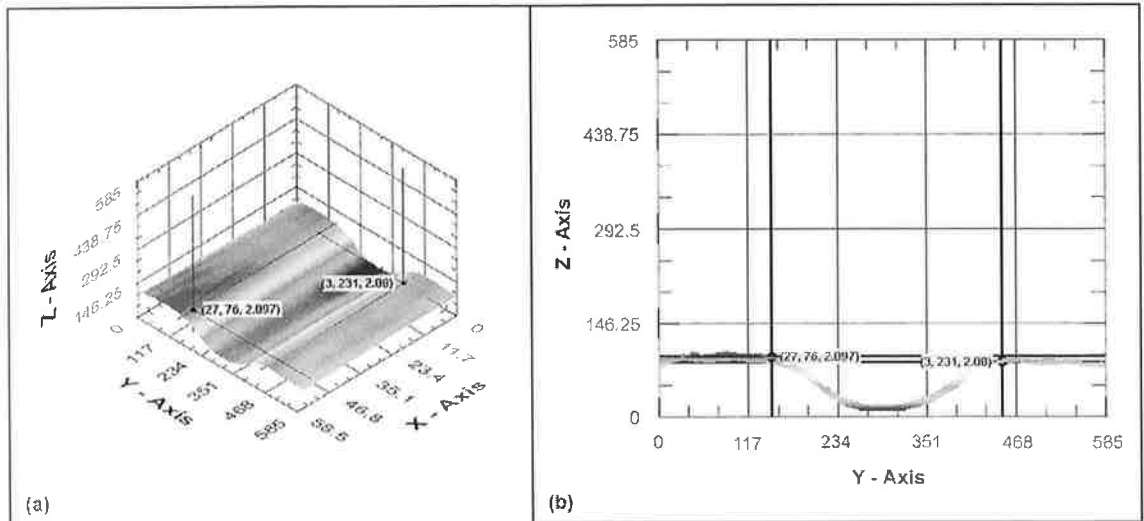


Figure 19: Channel 19, (a) isometric view and (b) front view.

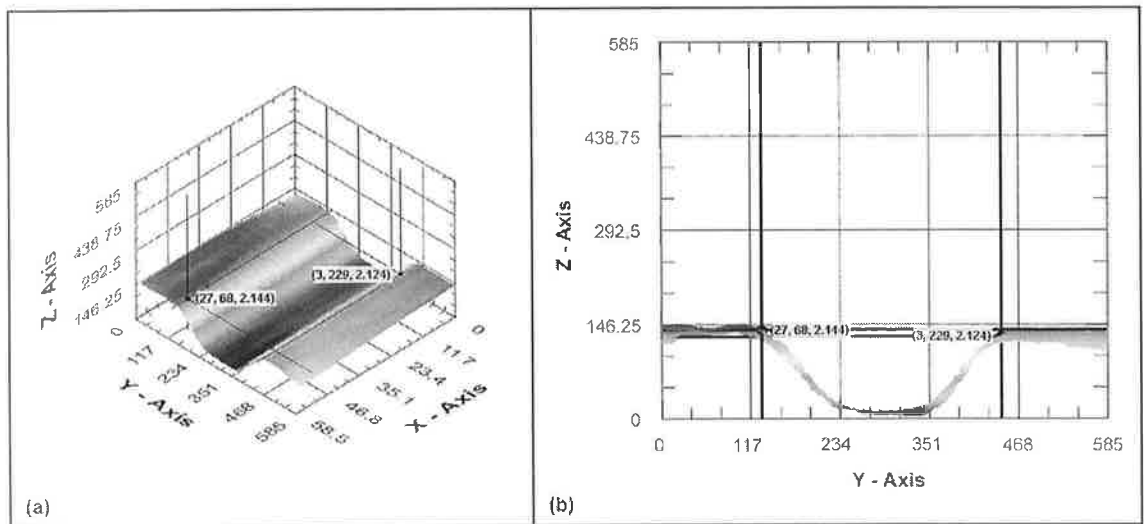


Figure 20: Channel 20, (a) isometric view and (b) front view.

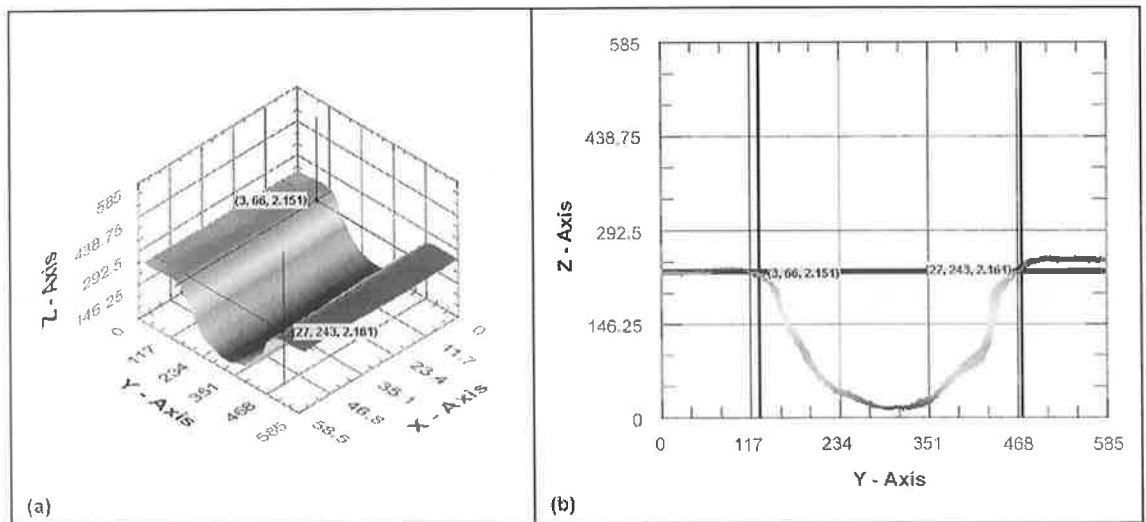


Figure 21: Channel 21, (a) isometric view and (b) front view.

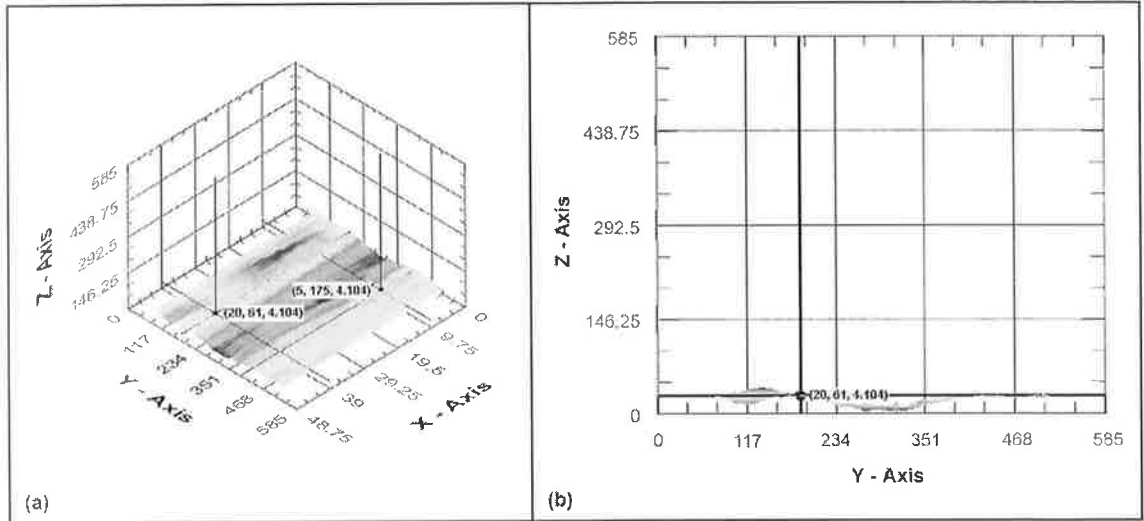


Figure 22: Channel 22, (a) isometric view and (b) front view.

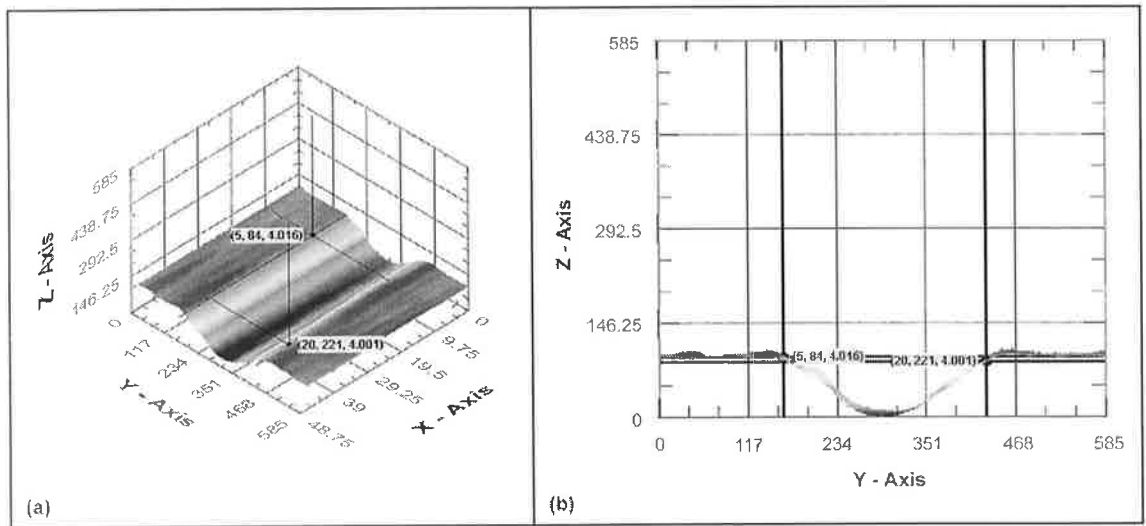


Figure 23: Channel 23, (a) isometric view and (b) front view.

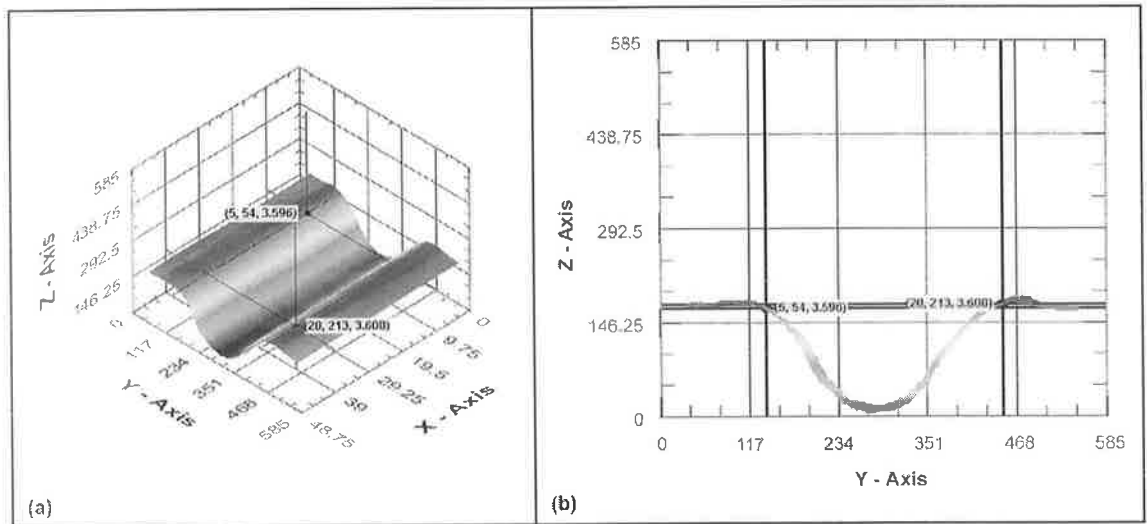


Figure 24: Channel 24, (a) isometric view and (b) front view.

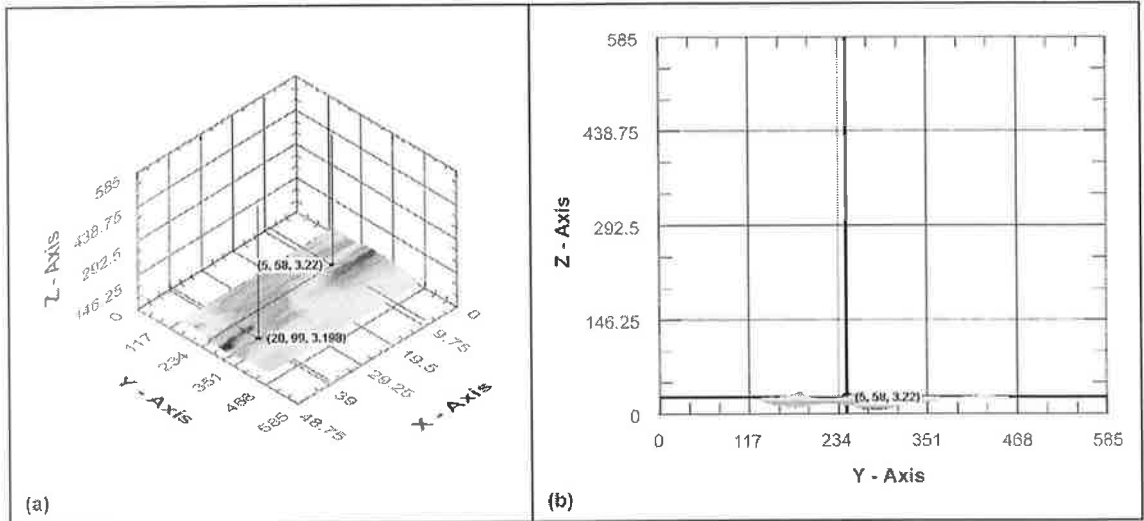


Figure 25: Channel 25, (a) isometric view and (b) front view.

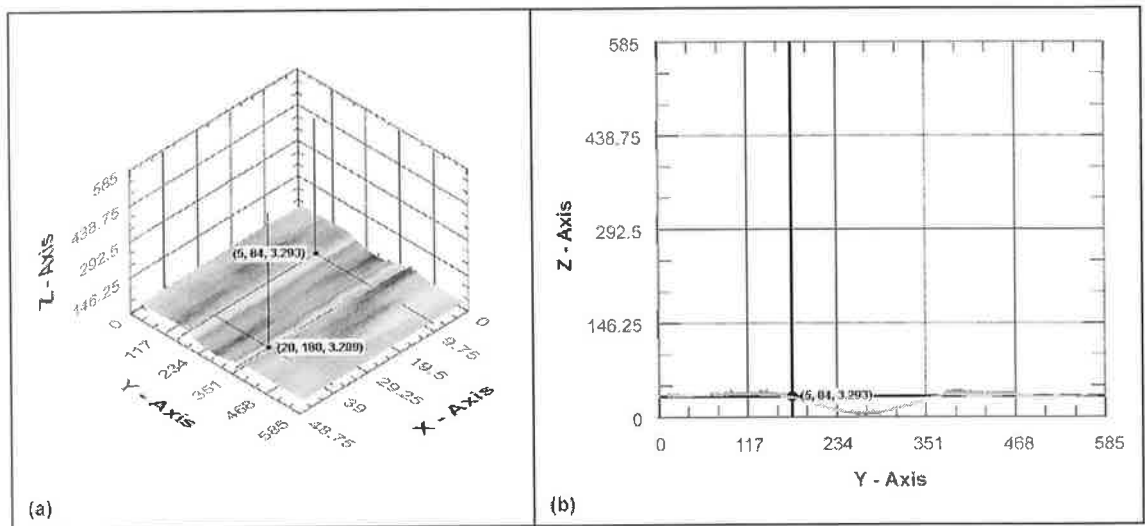


Figure 26: Channel 26, (a) isometric view and (b) front view.

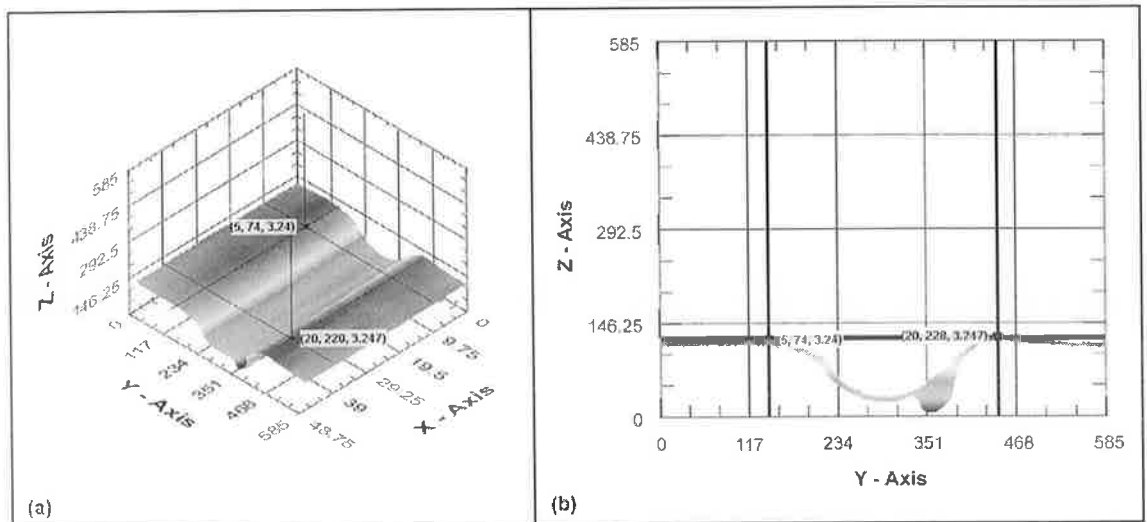


Figure 27: Channel 27, (a) isometric view and (b) front view.

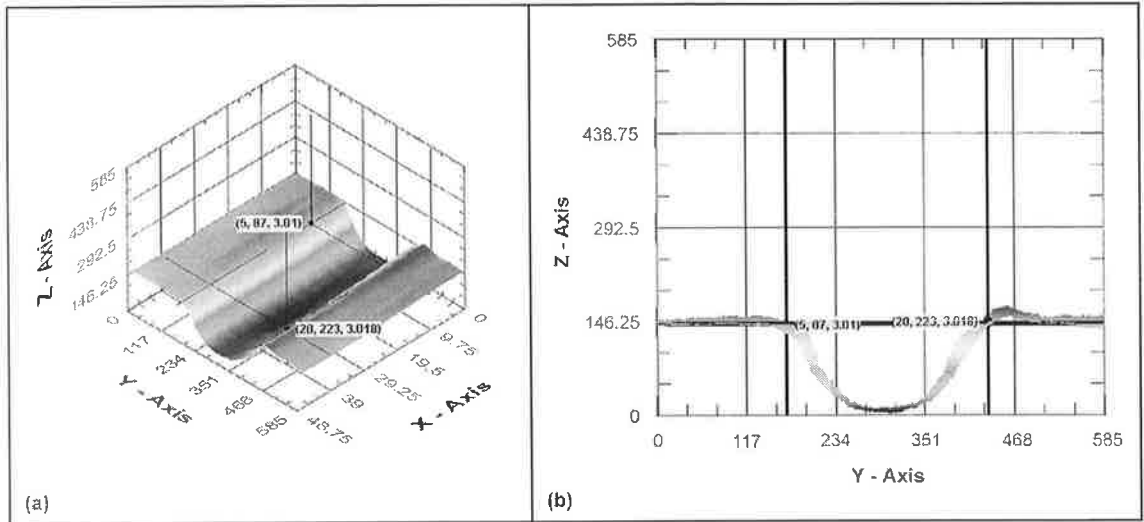


Figure 28: Channel 28, (a) isometric view and (b) front view.

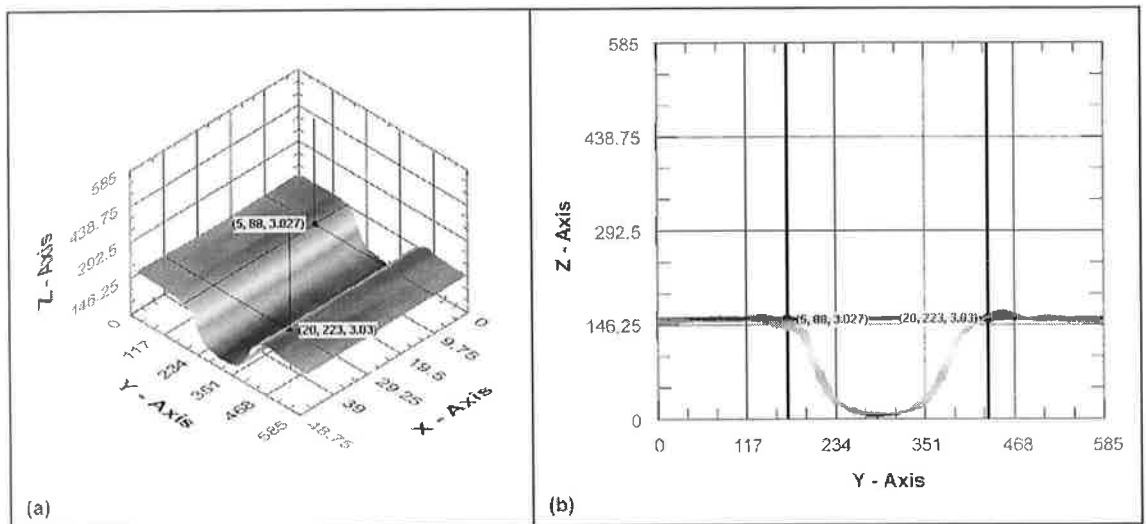


Figure 29: Channel 29, (a) isometric view and (b) front view.

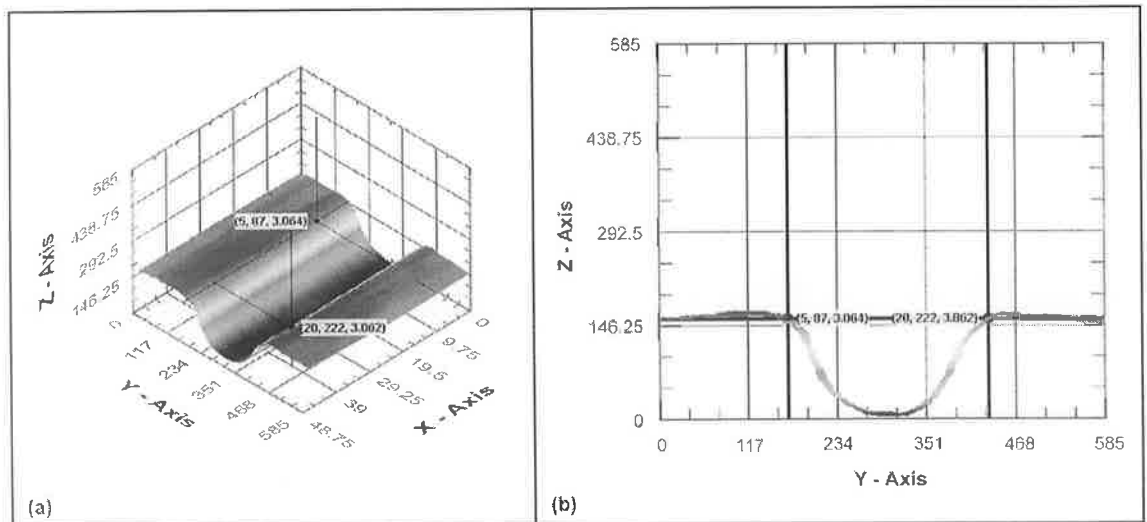


Figure 30: Channel 30, (a) isometric view and (b) front view.

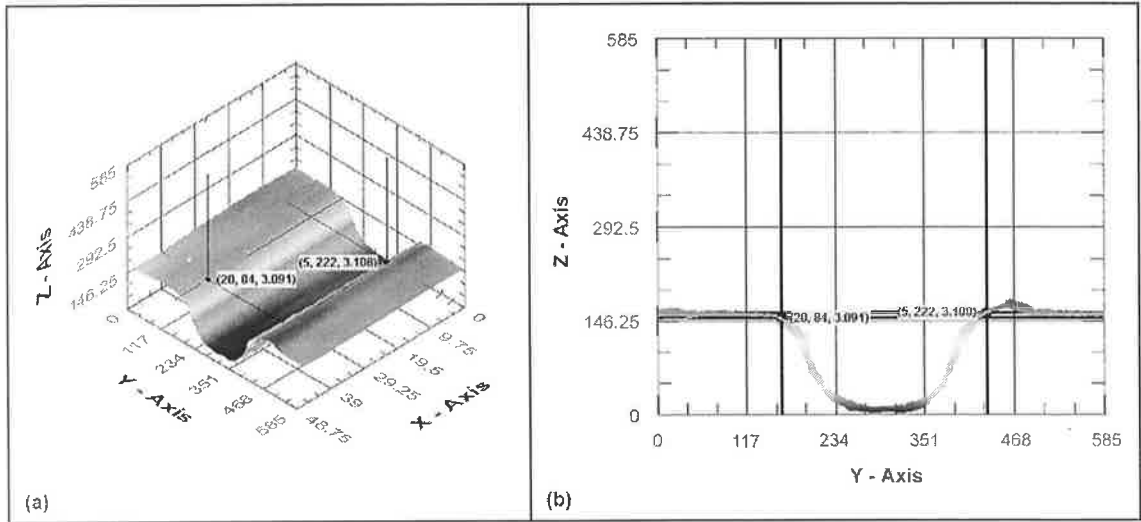


Figure 31: Channel 31, (a) isometric view and (b) front view.

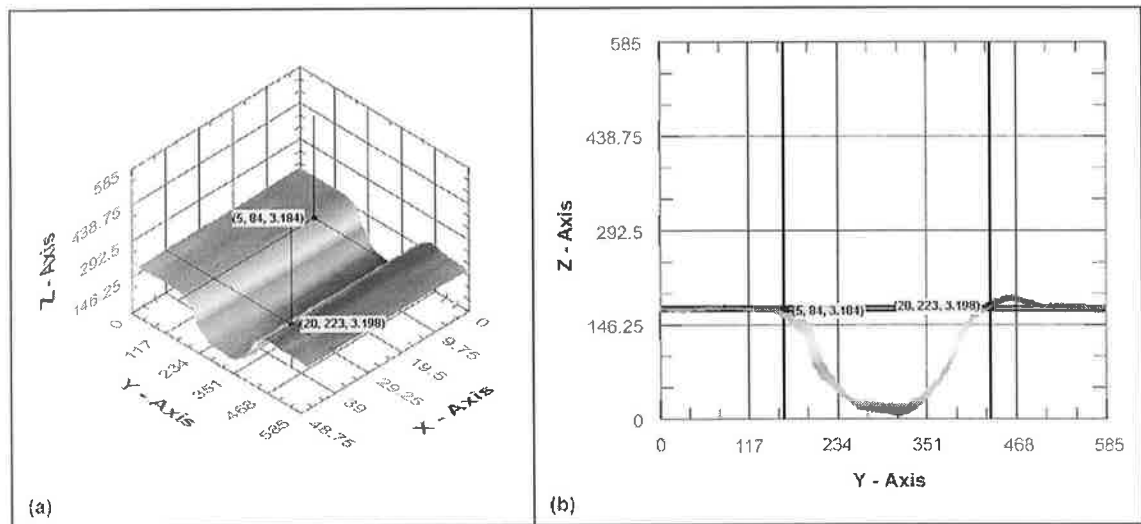


Figure 32: Channel 32, (a) isometric view and (b) front view.

D.3 Width results for microchannels at Df = 0 mm.

Table D.1: Width measurements of the channels.

Scan ID	DoE ID	Conv. Unit	Left1	Right1	Width1	Left2	Right2	Width2	Left3	Right3	Width3	Average	Rnd Average
34	1	1.95	75	236	313.95	75	237	315.9	75	237	315.9	315.25	315
35	2	1.95	63	226	317.85	63	227	319.8	62	227	321.75	319.8	320
36	3	1.95	45	232	364.65	46	232	362.7	45	233	366.6	364.65	365
31	4	1.95	56	183	247.65	55	183	249.6	57	183	245.7	247.65	248
32	5	1.95	80	218	269.1	80	219	271.05	80	220	273	271.05	271
33	6	1.95	54	224	331.5	53	223	331.5	54	224	331.5	331.5	332
28	7	1.95	97	181	163.8	98	180	159.9	97	181	163.8	162.5	163
29	8	1.95	59	168	212.55	60	169	212.55	59	168	212.55	212.55	213
30	9	1.95	61	229	327.6	61	228	325.65	61	229	327.6	326.95	327
43	10	1.95	67	225	308.1	66	224	308.1	67	225	308.1	308.1	308
44	11	1.95	72	238	323.7	72	238	323.7	72	238	323.7	323.7	324
45	12	1.95	66	246	351	66	247	352.95	66	245	349.05	351	351
40	13	1.95	68	186	230.1	68	186	230.1	68	187	232.05	230.75	231
41	14	1.95	64	201	267.15	65	202	267.15	64	201	267.15	267.15	267
42	15	1.95	65	227	315.9	65	227	315.9	65	227	315.9	315.9	316
37	16	1.95	49	110	118.95	49	110	118.95	50	110	117	118.3	118
38	17	1.95	97	204	208.65	96	203	208.65	97	205	210.6	209.3	209
39	18	1.95	75	233	308.1	75	233	308.1	75	233	308.1	308.1	308
52	19	1.95	77	232	302.25	77	232	302.25	77	232	302.25	302.25	302
53	20	1.95	69	230	313.95	69	230	313.95	68	229	313.95	313.95	314
54	21	1.95	66	243	345.15	66	243	345.15	66	243	345.15	345.15	345
49	22	1.95	61	175	222.3	62	176	222.3	61	175	222.3	222.3	222
50	23	1.95	84	221	267.15	84	221	267.15	84	221	267.15	267.15	267
51	24	1.95	54	213	310.05	54	213	310.05	54	213	310.05	310.05	310
46	25	1.95	58	99	79.95	58	100	81.9	58	99	79.95	80.6	81
47	26	1.95	84	180	187.2	84	180	187.2	84	180	187.2	187.2	187
48	27	1.95	74	228	300.3	75	229	300.3	75	228	298.35	299.65	300
82	28	1.95	87	223	265.2	88	224	265.2	87	222	263.25	264.55	265
83	29	1.95	88	223	263.25	87	223	265.2	88	222	261.3	263.25	263
84	30	1.95	87	222	263.25	87	222	263.25	87	222	263.25	263.25	263
85	31	1.95	84	222	269.1	84	222	269.1	84	222	269.1	269.1	269
87	32	1.95	84	223	271.05	85	223	269.1	85	223	269.1	269.75	270

D.4 Depth results for microchannels at Df = 0 mm.

Table D.2: Depth measurements of the channels.

Scan ID	DoE ID	Conv. Unit	Upper1	Lower1	Depth1	Upper2	Lower2	Depth2	Upper3	Lower3	Depth3	Average	Rnd Average
34	1	500	1.24	0.789	225.5	1.241	0.82	210.5	1.243	0.84	201.5	212.5	213
35	2	500	1.47	0.894	288	1.462	0.906	278	1.46	0.92	270	278.67	279
36	3	500	3.757	3.024	366.5	3.765	3.03	367.5	3.75	2.942	404	379.33	379
31	4	500	1.877	1.626	125.5	1.88	1.638	121	1.882	1.653	114.5	120.33	120
32	5	500	1.008	0.562	223	1.011	0.562	224.5	1.012	0.559	226.5	224.67	225
33	6	500	3.71	3.043	333.5	3.709	3.0481	330.45	3.71	3.12	295	319.65	320
28	7	500	3.181	3.123	29	3.181	3.14	20.5	3.182	3.123	29.5	26.33	26
29	8	500	1.794	1.558	118	1.794	1.553	120.5	1.794	1.553	120.5	119.67	120
30	9	500	3.225	2.686	269.5	3.225	2.715	255	3.225	2.739	243	255.83	256
43	10	500	3.174	2.908	133	3.174	2.902	136	3.174	2.905	134.5	134.5	135
44	11	500	3.943	3.542	200.5	3.943	3.543	200	3.943	3.535	204	201.5	202
45	12	500	3.806	3.208	299	3.806	3.211	297.5	3.806	3.221	292.5	296.33	296
40	13	500	3.357	3.257	50	3.357	3.276	40.5	3.357	3.269	44	44.83	45
41	14	500	3.115	2.817	149	3.123	2.827	148	3.125	2.832	146.5	147.83	148
42	15	500	3.137	2.642	247.5	3.137	2.638	249.5	3.135	2.639	248	248.33	248
37	16	500	3.787	3.757	15	3.787	3.755	16	3.787	3.773	7	12.67	13
38	17	500	3.301	3.203	49	3.298	3.204	47	3.296	3.201	47.5	47.83	48
39	18	500	0.945	0.663	141	0.948	0.667	140.5	0.962	0.676	143	141.5	142
52	19	500	2.09	1.94	75	2.09	1.942	74	2.09	1.943	73.5	74.17	74
53	20	500	2.142	1.882	130	2.142	1.88	131	2.142	1.883	129.5	130.17	130
54	21	500	2.17	1.718	226	2.17	1.715	227.5	2.17	1.713	228.5	227.33	227
49	22	500	4.102	4.062	20	4.103	4.063	20	4.102	4.058	22	20.67	21
50	23	500	4.016	3.843	86.5	4.0165	3.835	90.75	4.0152	3.834	90.6	89.28	89
51	24	500	3.608	3.274	167	3.611	3.285	163	3.613	3.28	166.5	165.5	166
46	25	500	3.198	3.19	4	3.198	3.193	2.5	3.198	3.192	3	3.17	3
47	26	500	3.298	3.24	29	3.3	3.241	29.5	3.299	3.235	32	30.17	30
48	27	500	3.225	3.042	91.5	3.22	3.049	85.5	3.225	3.049	88	88.33	88
82	28	500	3.018	2.737	140.5	3.018	2.744	137	3.019	2.748	135.5	137.67	138
83	29	500	3.025	2.727	149	3.025	2.734	145.5	3.025	2.734	145.5	146.67	147
84	30	500	3.065	2.762	151.5	3.069	2.769	150	3.069	2.764	152.5	151.33	151
85	31	500	3.1	2.819	140.5	3.101	2.82	140.5	3.106	2.82	143	141.33	141
87	32	500	3.186	2.892	147	3.186	2.879	153.5	3.18	2.873	153.5	151.33	151

D.5 Ra results for microchannels at Df = 0 mm.

Table D.3: Ra measurements of the channels.

Scan ID	DoE ID	Left	Center	Right	Average Ra	Rounded Ra
34	1	6.892	7.515	7.402	7.26966667	7
35	2	4.592	6.672	5.327	5.53033333	6
36	3	5.773	28.41	5.05	13.0776667	13
31	4	3.613	6.231	5.234	5.026	5
32	5	1.316	1.797	3.24	2.11766667	2
33	6	3.858	28.39	4.692	12.3133333	12
28	7	6.741	12.44	14.04	11.0736667	11
29	8	2.135	1.184	5.193	2.83733333	3
30	9	1.908	12.59	3.976	6.158	6
43	10	1.013	1.495	4.049	2.18566667	2
44	11	4.924	3.388	7.405	5.239	5
45	12	4.303	4.127	6.352	4.92733333	5
40	13	2.93	6.027	3.803	4.25333333	4
41	14	6.899	2.904	3.683	4.49533333	5
42	15	1.788	2.177	3.858	2.60766667	3
37	16	7.256	8.258	6.788	7.434	7
38	17	2.988	2.981	2.958	2.97566667	3
39	18	4.284	1.935	4.325	3.51466667	4
52	19	2.487	3.349	3.648	3.16133333	3
53	20	3.486	2.459	4.086	3.34366667	3
54	21	4.892	2.782	5.952	4.542	5
49	22	3.189	2.149	1.728	2.35533333	2
50	23	5.564	2.728	3.156	3.816	4
51	24	9.14	3.946	5.016	6.034	6
46	25	10.89	12.83	10.77	11.4966667	12
47	26	1.015	2.12	2.704	1.94633333	2
48	27	4.783	3.409	4.871	4.35433333	4
82	28	6.637	2.667	7.203	5.50233333	6
83	29	5.014	2.386	7.348	4.916	5
84	30	8.25	2.409	7.384	6.01433333	6
85	31	7.971	3.925	8.524	6.80666667	7
87	32	7.905	5.426	2.077	5.136	5

Table D.4: Rq measurements of the channels.

Scan ID	DoE ID	Left	Center	Right	Average Rq	Rounded Rq
34	1	7.193	8.551	10.35	8.698	9
35	2	6.38	7.565	6.384	6.7763333	7
36	3	6.502	28.82	6.308	13.876667	14
31	4	4.283	7.038	7.303	6.208	6
32	5	1.52	2.408	3.957	2.6283333	3
33	6	4.21	32.16	5.739	14.036333	14
28	7	7.664	14.39	15.85	12.634667	13
29	8	2.636	1.507	6.128	3.4236667	3
30	9	2.267	13.95	4.529	6.9153333	7
43	10	1.303	1.804	4.424	2.5103333	3
44	11	5.925	3.747	8.332	6.0013333	6
45	12	5.013	4.555	7.598	5.722	6
40	13	3.96	7.047	4.66	5.2223333	5
41	14	8.445	3.365	4.395	5.4016667	5
42	15	2.189	2.418	4.791	3.1326667	3
37	16	8.574	9.512	7.901	8.6623333	9
38	17	3.844	3.374	3.941	3.7196667	4
39	18	5.573	2.21	4.43	4.071	4
52	19	3.525	3.881	4.896	4.1006667	4
53	20	4.807	2.849	5.003	4.2196667	4
54	21	7.132	3.025	7.355	5.8373333	6
49	22	3.711	2.834	1.98	2.8416667	3
50	23	6.399	3.2	3.494	4.3643333	4
51	24	10.71	4.8	6.812	7.4406667	7
46	25	11.8	14.27	12.03	12.7	13
47	26	1.171	2.376	2.999	2.182	2
48	27	5.757	3.629	6.208	5.198	5
82	28	7.601	2.963	8.426	6.33	6
83	29	7.113	2.71	8.799	6.2073333	6
84	30	9.269	2.969	8.89	7.0426667	7
85	31	8.524	4.504	9.67	7.566	8
87	32	8.711	6.237	2.73	5.8926667	6

Table D.5: Rku measurements of the channels.

Scan ID	DoE ID	Left	Center	Right	Average Rku	Rounded Rku
34	1	1.266	1.859	3.762	2.29566667	2
35	2	4.438	1.585	2.311	2.778	3
36	3	1.765	1.069	4	2.278	2
31	4	2.494	1.745	3.213	2.484	3
32	5	1.891	2.866	2.61	2.45566667	3
33	6	1.586	2.049	2.121	1.91866667	2
28	7	2.036	2.045	1.747	1.94266667	2
29	8	2.915	2.878	2.307	2.7	3
30	9	2.27	1.738	1.72	1.90933333	2
43	10	3.403	2.594	1.541	2.51266667	3
44	11	2.059	1.614	1.837	1.83666667	2
45	12	1.956	1.59	2.416	1.98733333	2
40	13	3.447	1.888	3.013	2.78266667	3
41	14	2.174	1.702	2.743	2.20633333	2
42	15	3.156	1.694	2.685	2.51166667	3
37	16	2.526	2.537	2.198	2.42033333	2
38	17	2.763	1.661	4.065	2.82966667	3
39	18	3.664	1.839	1.185	2.22933333	2
52	19	4.43	2.366	3.968	3.588	4
53	20	4.361	1.939	2.108	2.80266667	3
54	21	3.245	1.614	2.997	2.61866667	3
49	22	1.868	3.42	1.845	2.37766667	2
50	23	2.235	2.442	1.485	2.054	2
51	24	2.319	2.51	4.116	2.98166667	3
46	25	1.441	1.574	1.612	1.54233333	2
47	26	1.82	1.815	1.715	1.78333333	2
48	27	3.108	1.322	2.698	2.376	2
82	28	2.254	1.597	2.322	2.05766667	2
83	29	5.44	1.635	2.674	3.24966667	3
84	30	1.762	2.143	2.159	2.02133333	2
85	31	1.31	2.097	1.715	1.70733333	2
87	32	1.505	1.875	3.415	2.265	2

Table D.6: Rsk measurements of the channels.

Scan ID	DoE ID	Left	Center	Right	Average Rsk	Rounded Rsk
34	1	0.2529	-0.5164	-1.109	-0.4575	-0.458
35	2	-1.676	0.1509	0.9649	-0.1867333	-0.187
36	3	0.01987	-0.1248	1.02	0.30502333	0.305
31	4	1.012	-0.1657	0.2853	0.3772	0.377
32	5	-0.2757	-0.5967	0.8695	-0.0009667	-0.001
33	6	0.449	0.8813	0.1402	0.49016667	0.490
28	7	0.2372	0.6848	0.597	0.50633333	0.506
29	8	-0.8134	-0.2202	-0.9023	-0.6453	-0.645
30	9	0.688	0.2643	0.5019	0.48473333	0.485
43	10	0.9891	0.7808	-0.0083	0.58720433	0.587
44	11	-0.4174	-0.1239	-0.3149	-0.2854	-0.285
45	12	0.3863	-0.0627	-0.7021	-0.1261667	-0.126
40	13	0.866	0.1828	-0.6384	0.1368	0.137
41	14	-0.1213	0.2214	-0.2421	-0.0473333	-0.047
42	15	1.024	0.4347	1.139	0.8659	0.866
37	16	-0.8116	-0.7204	-0.4496	-0.6605333	-0.661
38	17	0.2955	0.1002	1.497	0.6309	0.631
39	18	1.07	-0.3031	-0.1354	0.2105	0.211
52	19	1.609	0.9052	1.439	1.31773333	1.318
53	20	1.406	0.4056	0.2037	0.67176667	0.672
54	21	0.673	-0.064	-0.9108	-0.1005833	-0.101
49	22	0.2875	0.7706	-0.4265	0.21053333	0.211
50	23	-0.8474	-0.9308	-0.2153	-0.6645	-0.665
51	24	-0.8131	0.7078	-1.42	-0.5084333	-0.508
46	25	0.02413	0.138	0.2489	0.13701	0.137
47	26	-0.2395	0.212	-0.4928	-0.1734333	-0.173
48	27	1.141	-0.1635	-0.3732	0.20143333	0.201
82	28	0.888	-0.1403	-0.7515	-0.0012667	-0.001
83	29	1.648	0.01694	-0.6831	0.32728	0.327
84	30	-0.1052	-0.1075	-0.1066	-0.1064333	-0.106
85	31	-0.0792	0.7977	0.07372	0.26406667	0.264
87	32	0.3422	-0.4802	0.6345	0.1655	0.166

D.6 Surface parameters definitions

Average roughness, Ra

It is the arithmetic average of the absolute values of the profile height deviations recorded within the evaluation length and measured from the mean line [171]. As shown in figure 1, Ra can be digitally approximated by the sum of the absolute values of the profile heights $Z(x)$ divided by the number of data points, given by

$$Ra = (|Z_1| + |Z_2| + |Z_3| + \dots + |Z_N|) / N$$

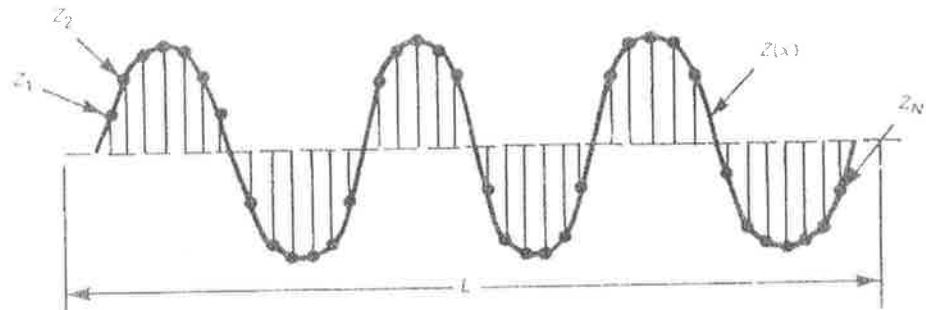


Figure 1: Illustration of the Ra calculation [171].

Root mean square (rms) roughness, Rq

It is the root mean square average of the profile height deviations taken within the evaluation length and measured from the mean line [171]. The digital approximation of Rq is given by

$$Rq = [(|Z_1|^2 + |Z_2|^2 + |Z_3|^2 + \dots + |Z_N|^2) / N]^{1/2}$$

Skewness, Rsk

It is a measure of the asymmetry of the profile about the mean line [171], see figure 2. The digital approximation of Rsk is given by

$$Rsk = \frac{1}{Rq^3} \cdot \frac{1}{N} \sum_{j=1}^N Z_j^3$$

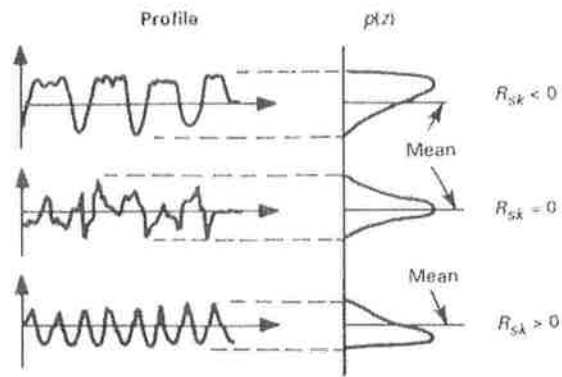


Figure 2: Three surface profiles with different Rsk [171].

Note: the amplitude density functions $p(z)$ of the surface heights are shown on right

Kurtosis, Rku

It is a measure of the peakedness of the profile about the mean line [171], see figure 3.

The digital approximation of Rku is given by

$$Rsk = \frac{1}{Rq^4} \cdot \frac{1}{N} \sum_{j=1}^N Z_j^4$$

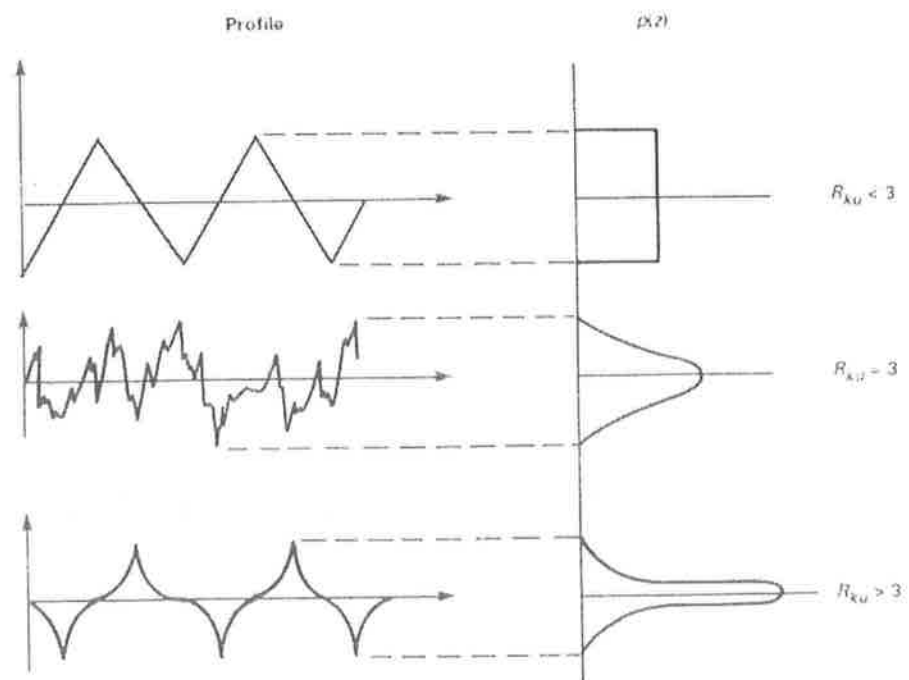


Figure 2: Three surface profiles with different Rku [171].

D.7 Quality and shapes of microchannels fabricated at Df = 0 mm.

Table D.7: General quality factors of the produced channels.

Scan ID	DoE ID	Average Width	Average Depth	Aspect Ratio	Quality of Ratio	Average Ra	Quality of Ra	Channel Shape	Quality of Shape
34	1	315	213	0.68	Fair	7	Fair	V	Fair
35	2	320	279	0.87	V. Poor	6	Fair	V	Poor
36	3	365	379	1.04	V. Poor	13	Poor	Deep V	Poor
31	4	248	120	0.49	V. Good	5	Good	U	V. Good
32	5	271	225	0.83	V. Poor	2	V. Good	V	Fair
33	6	332	320	0.96	V. Poor	12	Poor	V	Poor
28	7	163	26	0.16	Poor	11	Poor	--	V. Poor
29	8	213	120	0.56	V. Good	3	V. Good	U	V. good
30	9	327	256	0.78	Fair	6	Fair	V	Fair
43	10	308	135	0.44	V. Good	2	V. Good	U	V. Good
44	11	324	202	0.62	Good	5	Good	U	Good
45	12	351	296	0.84	Poor	5	Good	Deep U	Fair
40	13	231	45	0.19	V. Poor	4	Good	Surface U	Poor
41	14	267	148	0.55	V. Good	4	Good	U	V. Good
42	15	316	248	0.79	Poor	3	V. Good	U	Good
37	16	118	13	0.11	V. Poor	7	Fair	--	V. Poor
38	17	209	48	0.23	Poor	3	V. Good	Surface U	Poor
39	18	308	142	0.46	V. Good	4	Good	U	V. Good
52	19	302	74	0.24	Poor	4	Good	Surface U	Fair
53	20	314	130	0.41	Good	4	Good	U	Good
54	21	345	227	0.66	Good	6	Fair	U	V. Good
49	22	222	21	0.09	V. Poor	2	V. Good	--	V. Poor
50	23	267	89	0.33	Fair	4	Good	Surface U	Fair
51	24	310	166	0.53	V. Good	6	Fair	U	V. Good
46	25	81	3	0.04	V. Poor	12	Poor	--	V. Poor
47	26	187	30	0.16	Poor	2	V. Good	Surface U	Poor
48	27	300	88	0.29	Fair	4	Good	U	Good
82	28	265	138	0.52	V. Good	6	Fair	U	V. Good
83	29	263	147	0.56	V. Good	5	Fair	U	V. Good
84	30	263	151	0.57	V. Good	6	Fair	U	V. Good
85	31	269	141	0.53	V. Good	7	Fair	U	V. Good
87	32	270	151	0.56	V. Good	5	Fair	U	V. Good

D.8 Results and analysis of results obtained at Df = -2 and +2 mm.

Investigating the numerical and graphical results in appendix Df = -2 mm, it can be seen that the process produced deep structural changes. The following can be observed:

- 1- For Df = -2 mm, the laser beam was practically focussed at the bottom surface of the glass sheet. This resulted in deeper channels and narrower widths than the ones presented for Df = 0 mm in the experimental results chapter.
- 2- The channels had high aspect ratios and the cross-sectional areas were narrow V-shaped, which are possibly desirable in some applications such as scribing and cutting the glass.
- 3- The width and depth data trends with Df as a control parameter in this case were random or not regular. Hence, statistical modelling was not possible.

Furthermore, investigating the numerical and graphical results in appendix Df = +2 mm, it can be seen that the process produced superficial structural changes. The following can be observed:

- 1- Three channels were not fabricated because the intensity or the energy fluence of the laser beam was not high enough to cause ablation. The estimation of the dimensions of these channels would make the statistical analysis not very reliable.
- 2- The aspect ratios of these channels were low and the cross-sectional areas were wide U-shaped, which desirable in other applications such as glass marking.
- 3- The width and depth data trends with Df as a control parameter in this case were random or not regular. Hence, statistical modelling was not possible.

Generally, Df as a process parameter had an effect on the dimensions and the shapes of the channels. However, modelling of the responses obtained for both Df = -2 and Df = +2 mm was not possible, neither on their own (i.e. two separate model) nor when combined with the results of Df = 0 mm. In general terms, inspecting the results obtained for all settings of Df, the following effects can be concluded:

- 1- Df has a directly proportional relationship with the width of the channels.
- 2- Df has an inversely proportional relationship to the depth of the channels.
- 3- Df has an inversely proportional relationship to the aspect ratio of the channels.

D.8.1 Df = -2 mm channels' 3D scans

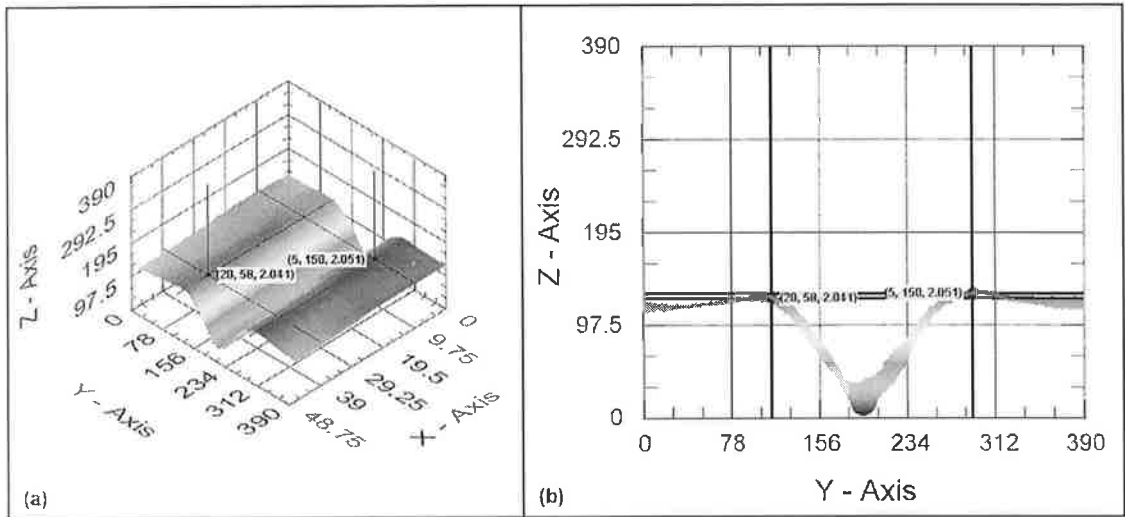


Figure 1: Channel 1, (a) isometric view and (b) front view

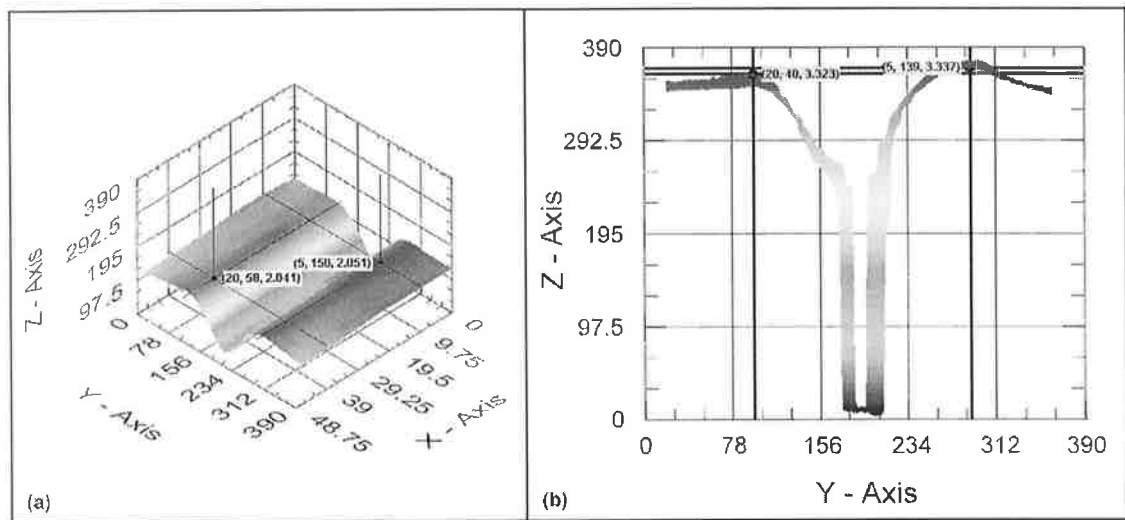


Figure 2: Channel 2, (a) isometric view and (b) front view

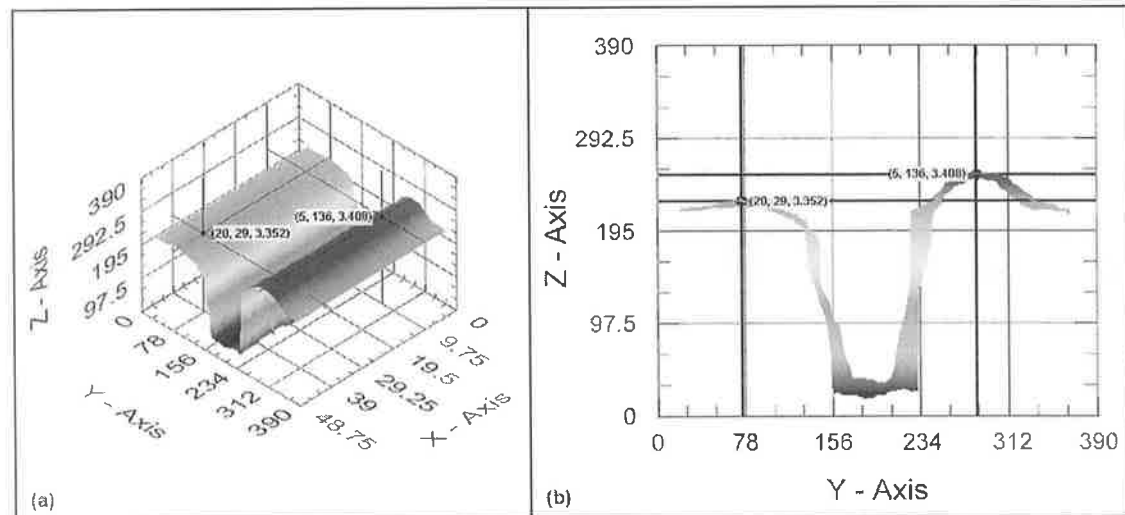


Figure 3: Channel 3, (a) isometric view and (b) front view

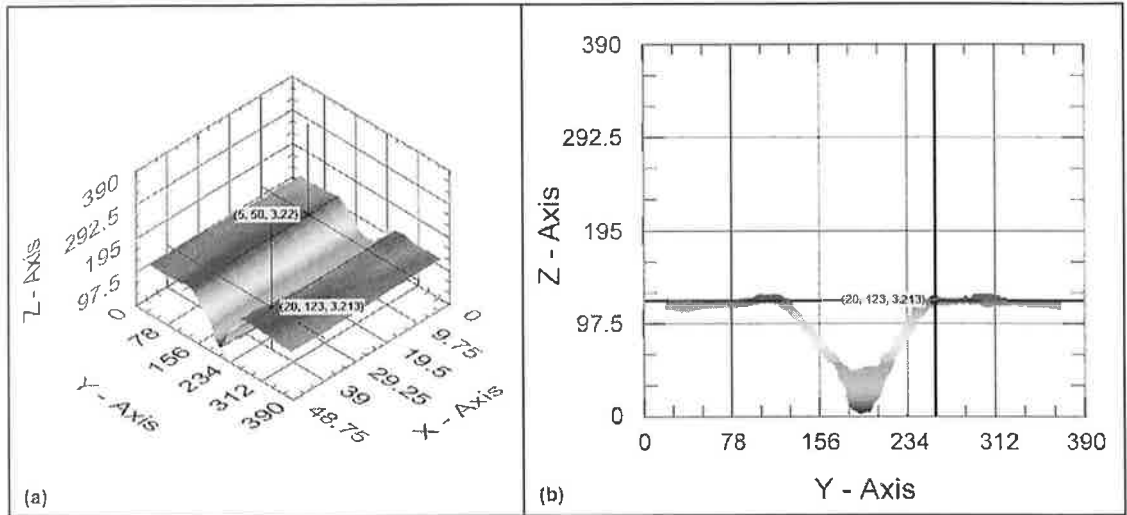


Figure 4: Channel 4, (a) isometric view and (b) front view

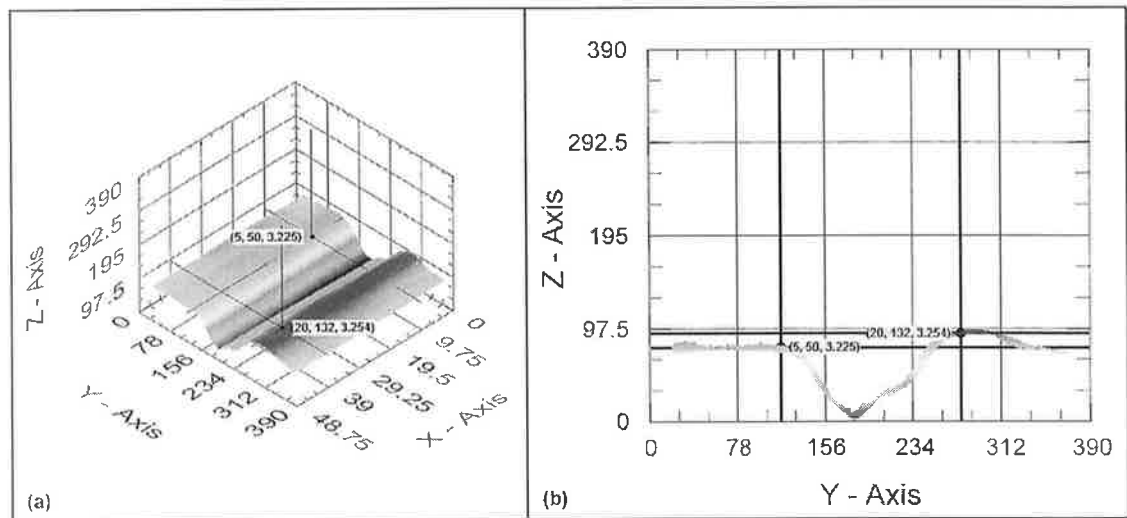


Figure 5: Channel 5, (a) isometric view and (b) front view

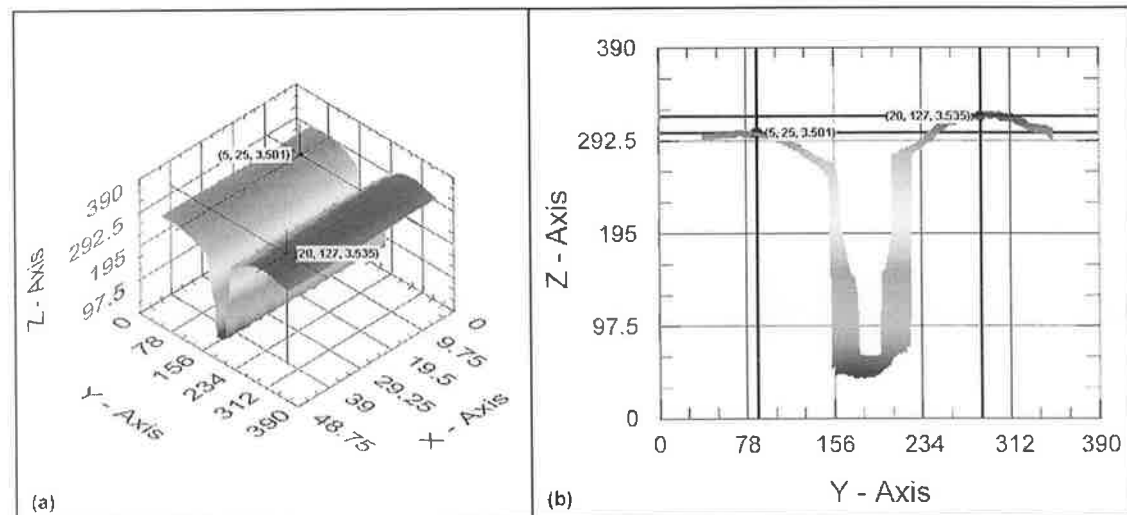


Figure 6: Channel 6, (a) isometric view and (b) front view

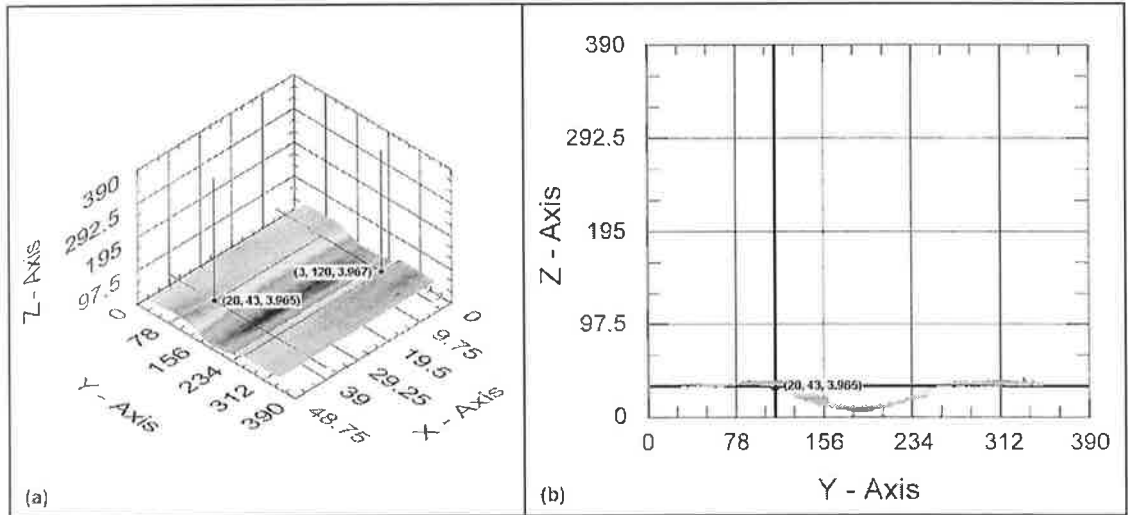


Figure 7: Channel 7, (a) isometric view and (b) front view

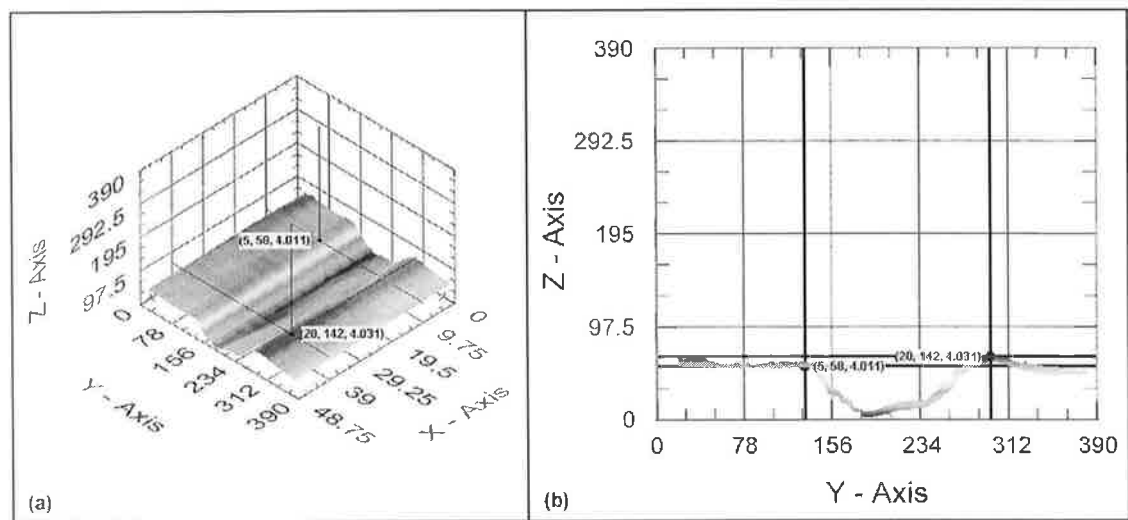


Figure 8: Channel 8, (a) isometric view and (b) front view

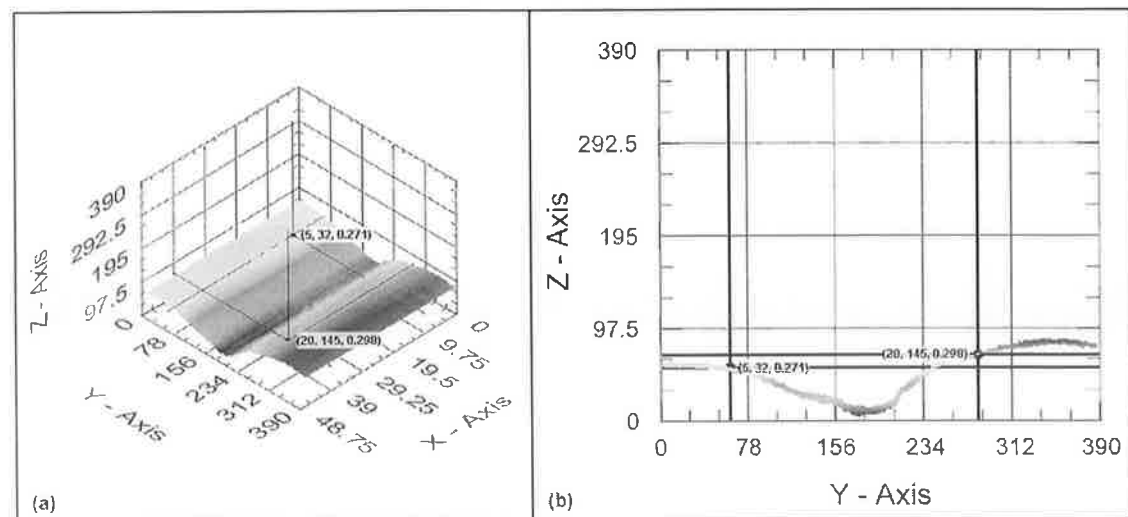


Figure 9: Channel 9, (a) isometric view and (b) front view

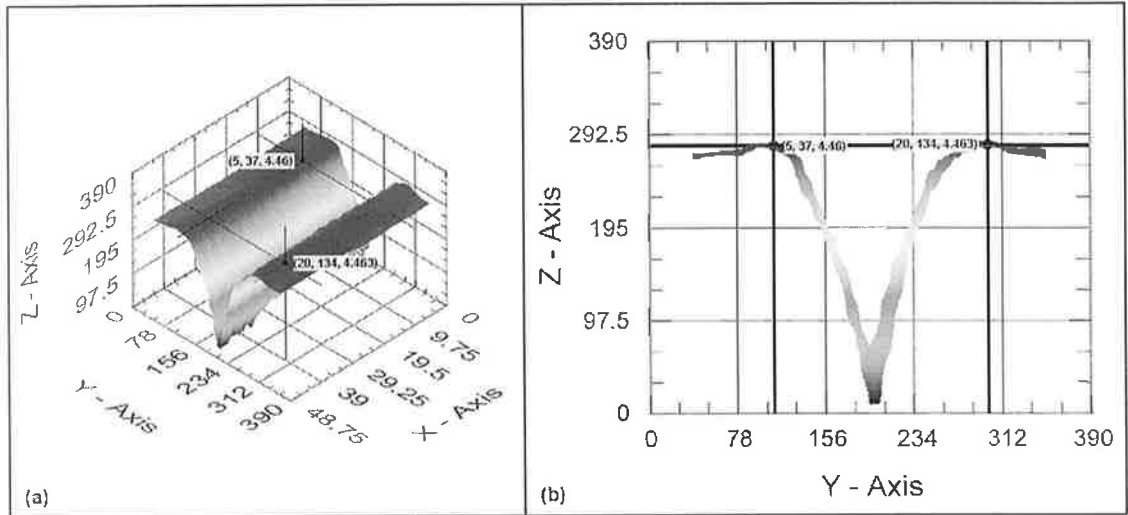


Figure 10: Channel 10, (a) isometric view and (b) front view

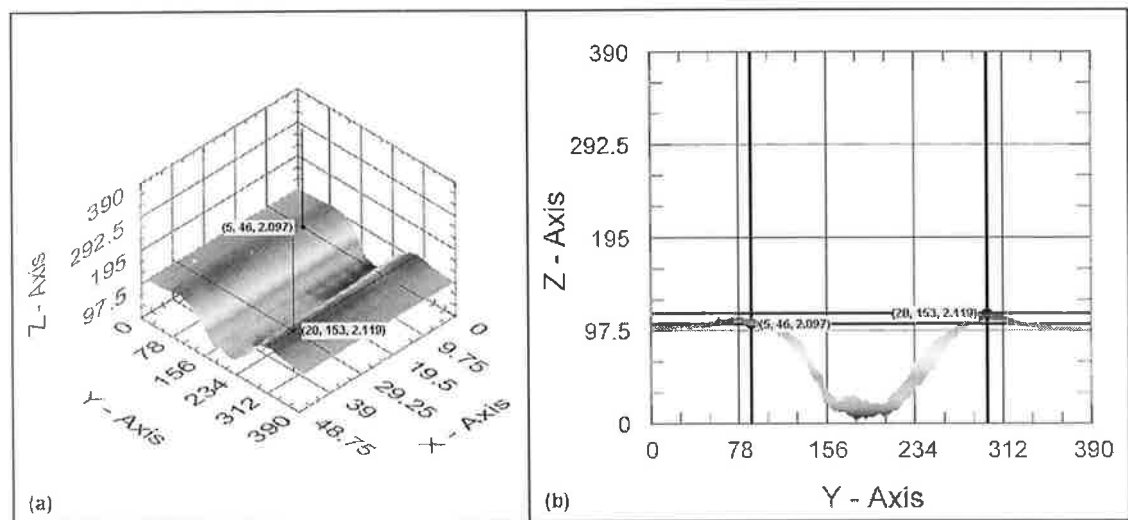


Figure 11: Channel 11, (a) isometric view and (b) front view

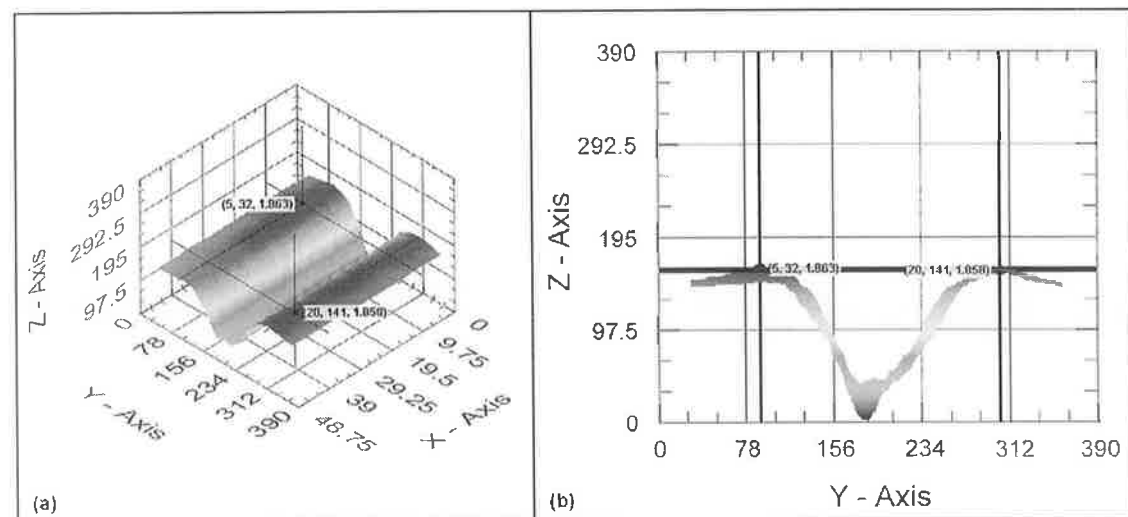


Figure 12: Channel 12, (a) isometric view and (b) front view

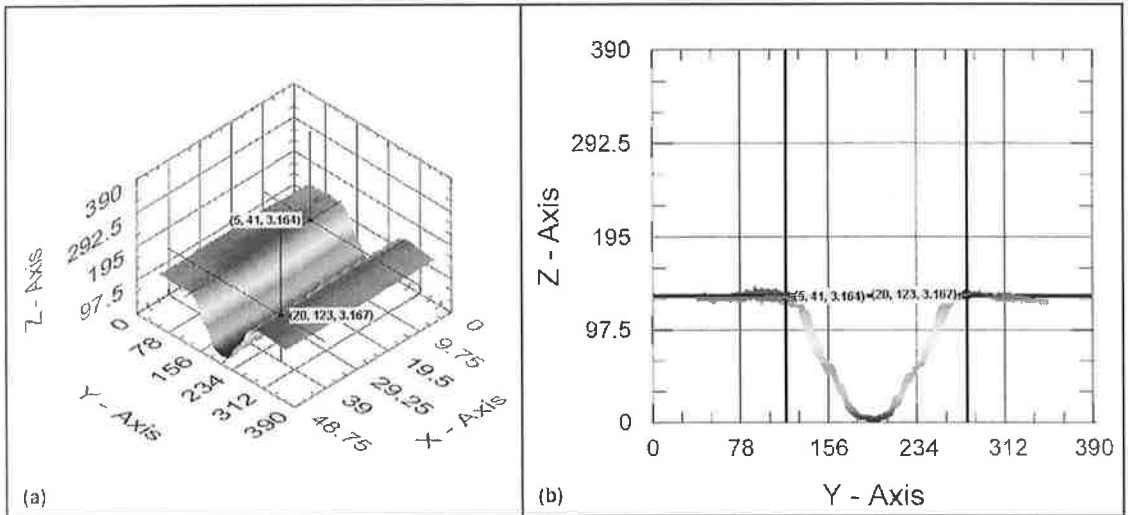


Figure 13: Channel 13, (a) isometric view and (b) front view

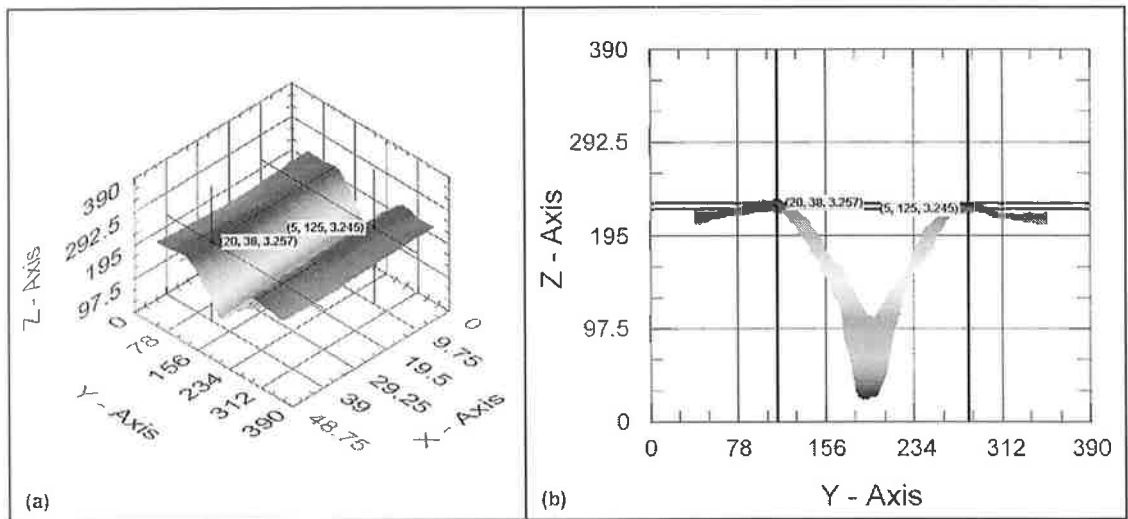


Figure 14: Channel 14, (a) isometric view and (b) front view

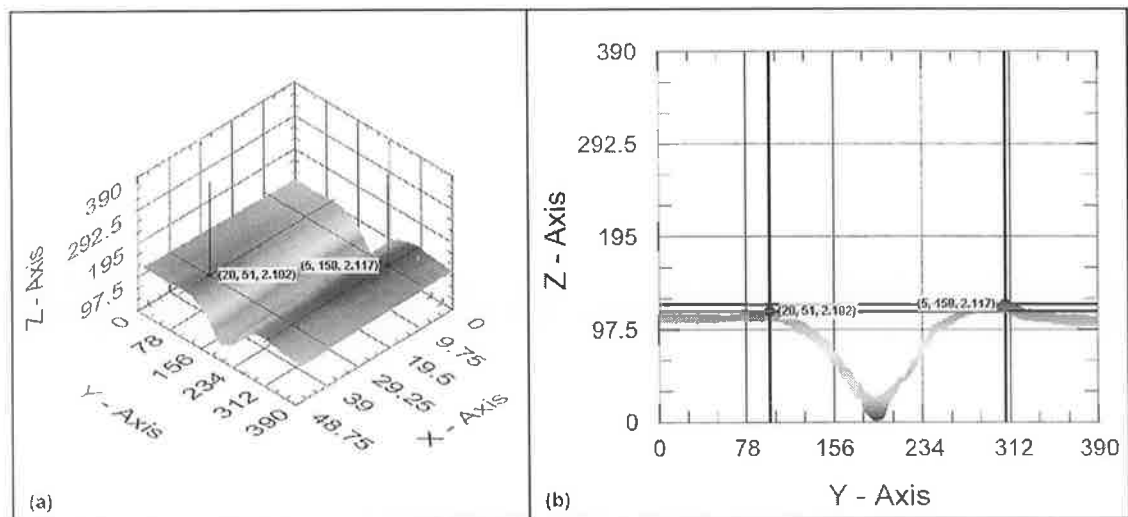


Figure 15: Channel 15, (a) isometric view and (b) front view

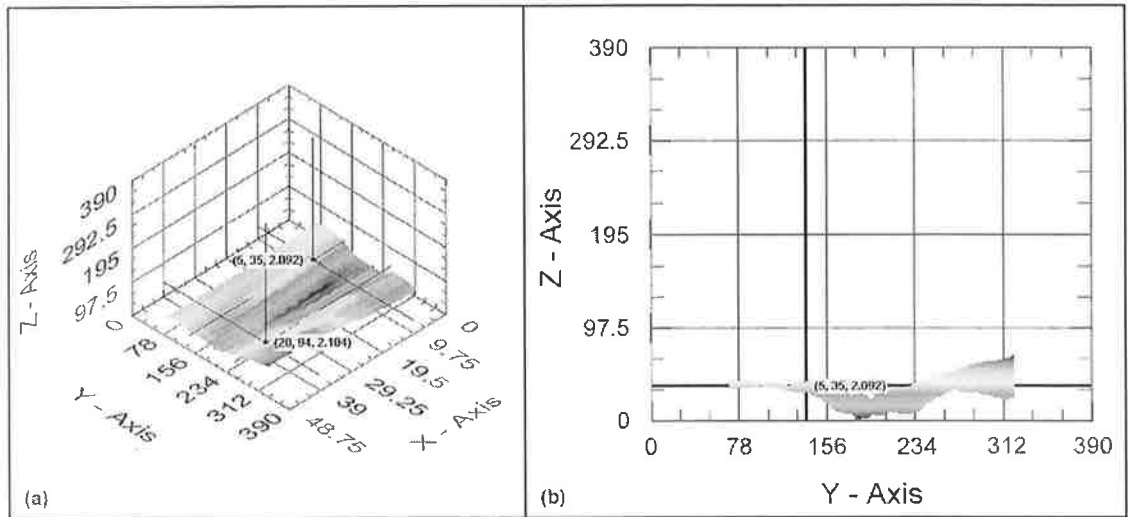


Figure 16: Channel 16, (a) isometric view and (b) front view

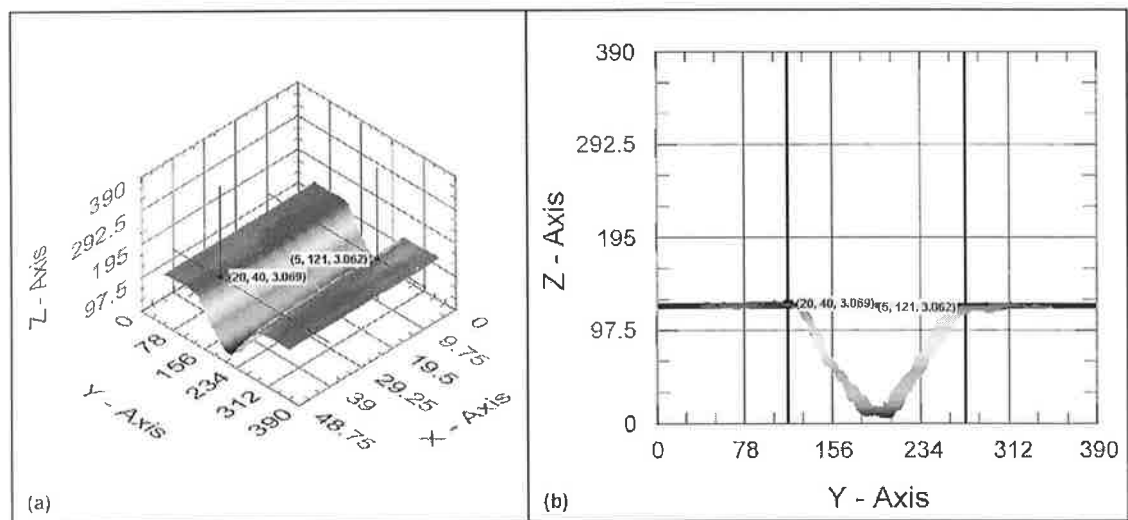


Figure 17: Channel 17, (a) isometric view and (b) front view

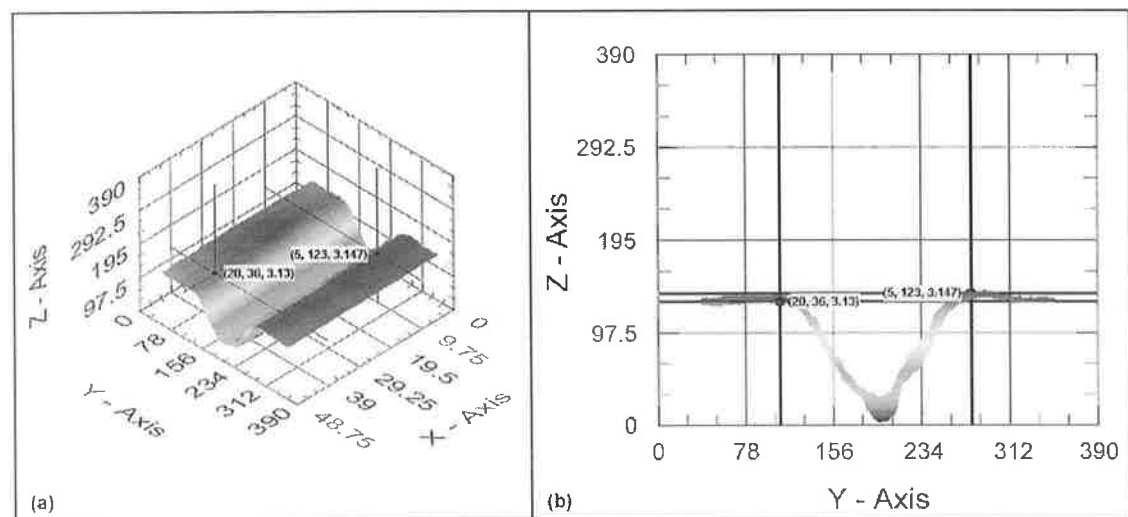


Figure 18: Channel 18, (a) isometric view and (b) front view

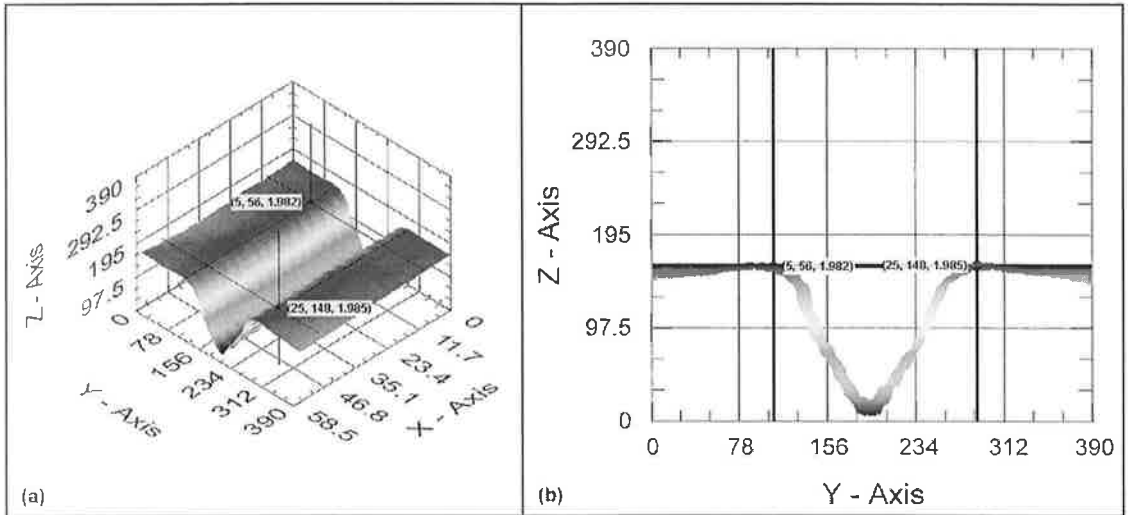


Figure 19: Channel 19, (a) isometric view and (b) front view

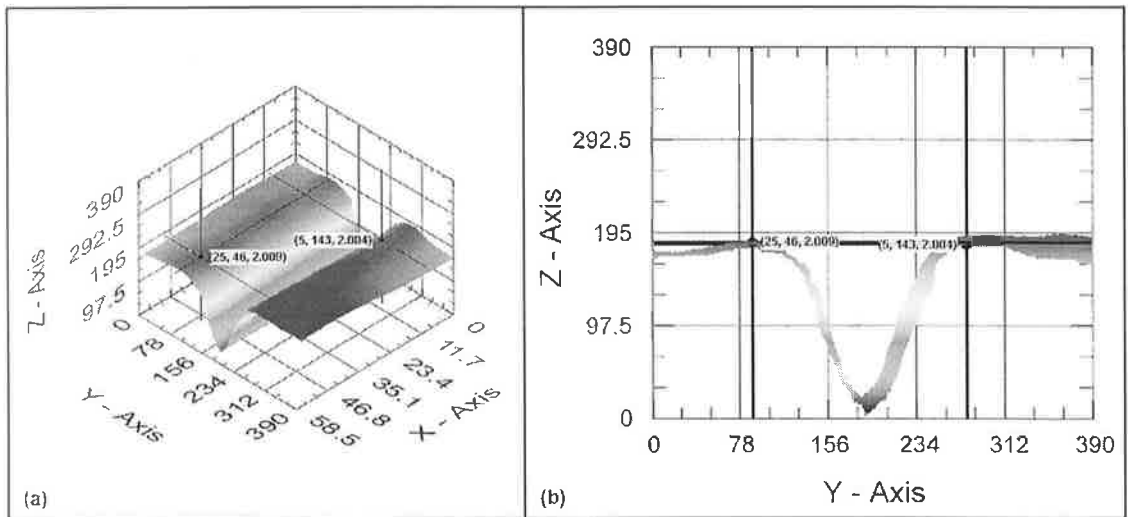


Figure 20: Channel 20, (a) isometric view and (b) front view

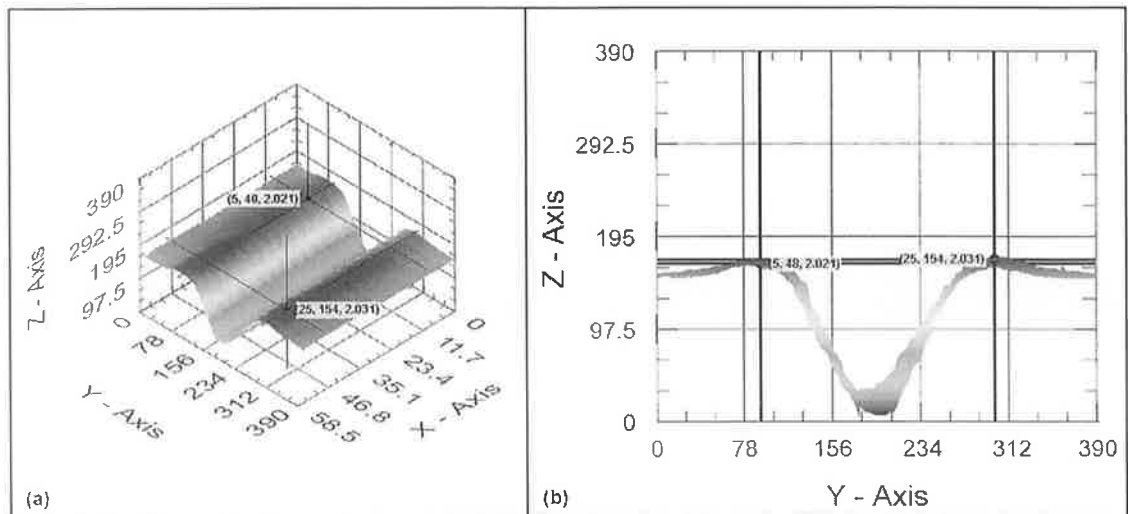


Figure 21: Channel 21, (a) isometric view and (b) front view

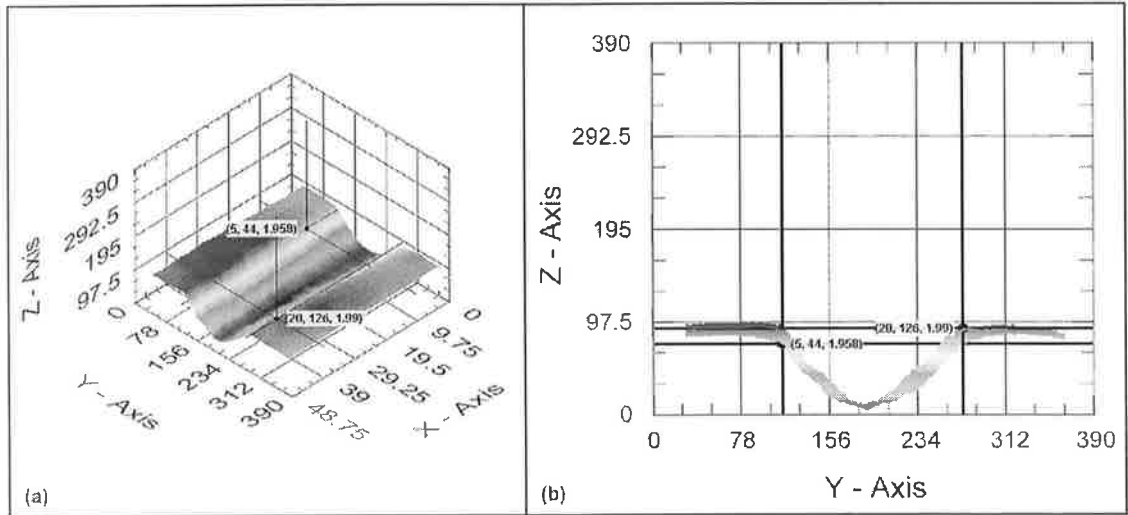


Figure 22: Channel 22, (a) isometric view and (b) front view

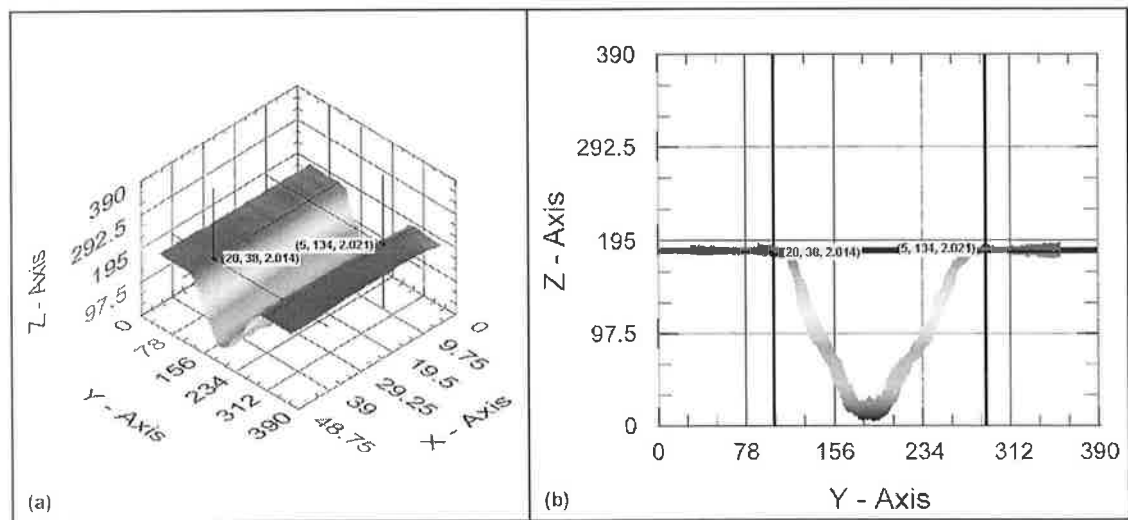


Figure 23: Channel 23, (a) isometric view and (b) front view

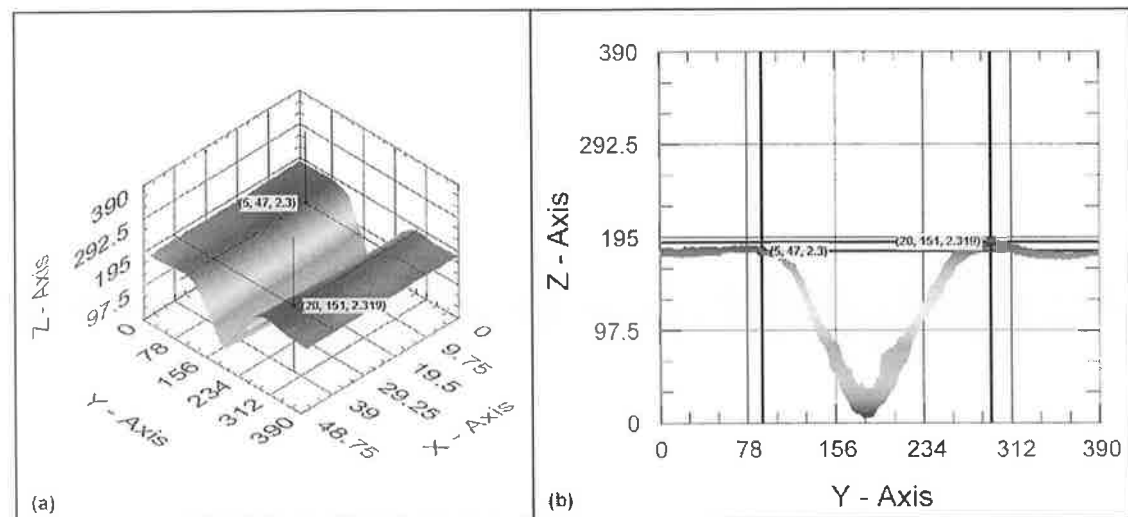


Figure 24: Channel 24, (a) isometric view and (b) front view

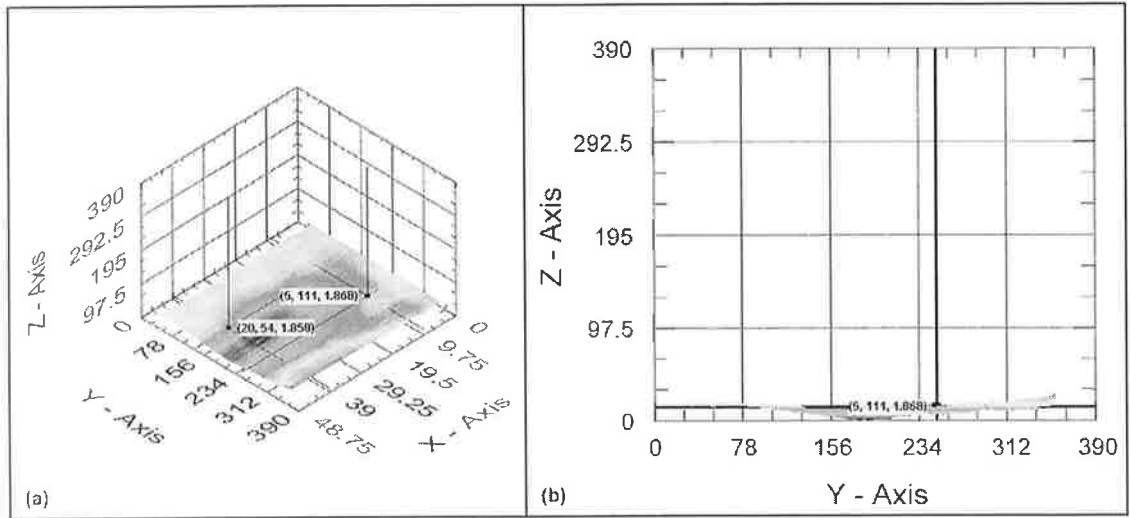


Figure 25: Channel 25, (a) isometric view and (b) front view

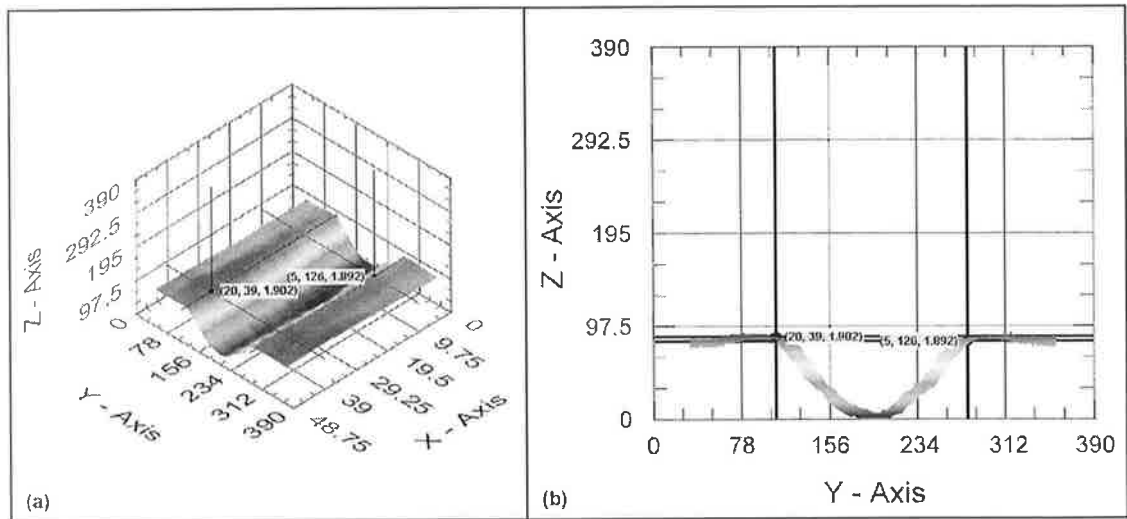


Figure 26: Channel 26, (a) isometric view and (b) front view

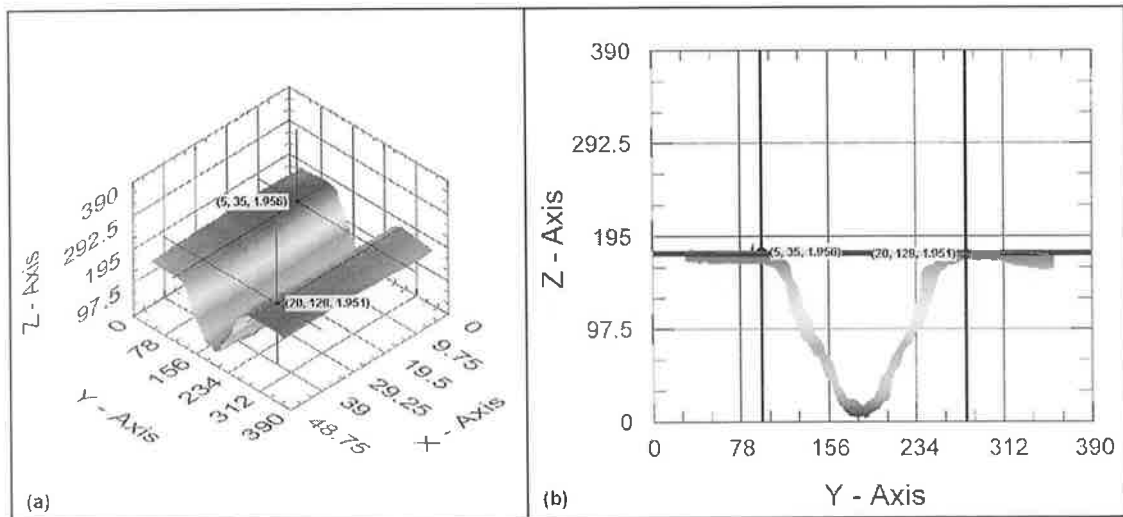


Figure 27: Channel 27, (a) isometric view and (b) front view

Table D.8: Width measurements of the channels fabricated at Df = -2 mm.

Scan ID	DoE ID	Conv. Unit	Left1	Right1	Width1	Left2	Right2	Width2	Left3	Right3	Width3	Average	Rnd Average
7	1	1.95	58	150	179.4	58	150	179.4	58	150	179.4	179.4	179
8	2	1.95	40	139	193.05	40	139	193.05	40	139	193.05	193.05	193
9	3	1.95	29	136	208.65	29	136	208.65	29	136	208.65	208.65	209
4	4	1.95	50	123	142.35	50	123	142.35	50	123	142.35	142.35	142
5	5	1.95	50	132	159.9	50	132	159.9	50	132	159.9	159.9	160
6	6	1.95	25	127	198.9	25	127	198.9	25	127	198.9	198.9	199
1	7	1.95	43	120	150.15	43	120	150.15	43	120	150.15	150.15	150
2	8	1.95	58	142	163.8	58	142	163.8	58	142	163.8	163.8	164
3	9	1.95	32	145	220.35	32	145	220.35	32	145	220.35	220.35	220
16	10	1.95	37	134	189.15	37	134	189.15	37	134	189.15	189.15	189
17	11	1.95	46	153	208.65	46	153	208.65	46	153	208.65	208.65	209
18	12	1.95	32	141	212.55	32	141	212.55	32	141	212.55	212.55	213
13	13	1.95	41	123	159.9	41	123	159.9	41	123	159.9	159.9	160
14	14	1.95	38	125	169.65	38	125	169.65	38	125	169.65	169.65	170
15	15	1.95	51	158	208.65	51	158	208.65	51	158	208.65	208.65	209
10	16	1.95	35	94	115.05	35	94	115.05	35	94	115.05	115.05	115
11	17	1.95	40	121	157.95	40	121	157.95	40	121	157.95	157.95	158
12	18	1.95	36	123	169.65	36	123	169.65	36	123	169.65	169.65	170
25	19	1.95	56	148	179.4	56	148	179.4	56	148	179.4	179.4	179
26	20	1.95	46	143	189.15	46	143	189.15	46	143	189.15	189.15	189
27	21	1.95	48	154	206.7	48	154	206.7	48	154	206.7	206.7	207
22	22	1.95	44	126	159.9	44	126	159.9	44	126	159.9	159.9	160
23	23	1.95	38	134	187.2	38	134	187.2	38	134	187.2	187.2	187
24	24	1.95	47	151	202.8	47	151	202.8	47	151	202.8	202.8	203
19	25	1.95	54	111	111.15	54	111	111.15	54	111	111.15	111.15	111
20	26	1.95	39	126	169.65	39	126	169.65	39	126	169.65	169.65	170
21	27	1.95	35	128	181.35	35	128	181.35	35	128	181.35	181.35	181

Table D.9: Depth measurements of the channels fabricated at Df = -2 mm.

Scan ID	DoE ID	Conv. Unit	Upper1	Lower1	Depth1	Upper2	Lower2	Depth2	Upper3	Lower3	Depth3	Average	Rnd Average
7	1	500	2.041	1.794	123.5	2.041	1.855	93	2.041	1.829	106	107.5	108
8	2	500	3.308	2.615	346.5	3.308	2.622	343	3.308	2.615	346.5	345.33	345
9	3	500	3.345	2.961	192	3.345	2.949	198	3.345	2.937	204	198	198
4	4	500	3.213	3.037	88	3.213	2.993	110	3.213	2.976	118.5	105.5	106
5	5	500	3.225	3.079	73	3.225	3.088	68.5	3.225	3.091	67	69.5	70
6	6	500	3.501	3.02	240.5	3.501	3.005	248	3.501	2.986	257.5	248.67	249
1	7	500	3.965	3.918	23.5	3.965	3.911	27	3.965	3.921	22	24.167	24
2	8	500	4.011	3.911	50	4.011	3.916	47.5	4.011	3.926	42.5	46.67	47
3	9	500	0.271	0.181	45	0.271	0.186	42.5	0.271	0.171	50	45.83	46
16	10	500	4.46	4.038	211	4.46	4.011	224.5	4.46	3.979	240.5	225.33	225
17	11	500	2.097	1.902	97.5	2.097	1.926	85.5	2.097	1.938	79.5	87.5	88
18	12	500	1.846	1.558	144	1.846	1.582	132	1.846	1.619	113.5	129.83	130
13	13	500	3.164	2.9	132	3.164	2.913	125.5	3.164	2.9	132	129.83	130
14	14	500	3.257	2.869	194	3.257	2.854	201.5	3.257	3.018	119.5	171.67	172
15	15	500	2.095	1.899	98	2.095	1.885	105	2.095	1.926	84.5	95.83	96
10	16	500	2.092	2.041	25.5	2.092	2.034	29	2.092	2.068	12	22.17	22
11	17	500	3.069	2.839	115	3.069	2.854	107.5	3.069	2.834	117.5	113.33	113
12	18	500	3.13	2.893	118.5	3.13	2.91	110	3.13	2.878	126	118.17	118
25	19	500	1.98	1.68	150	1.98	1.707	136.5	1.98	1.677	151.5	146	146
26	20	500	2.004	1.663	170.5	2.004	1.675	164.5	2.004	1.68	162	165.67	166
27	21	500	2.014	1.709	152.5	2.014	1.731	141.5	2.014	1.758	128	140.67	141
22	22	500	1.987	1.829	79	1.987	1.824	81.5	1.987	1.836	75.5	78.67	79
23	23	500	2.014	1.667	173.5	2.014	1.672	171	2.014	1.694	160	168.17	168
24	24	500	2.3	1.951	174.5	2.3	1.985	157.5	2.3	2.007	146.5	159.5	160
19	25	500	1.868	1.853	7.5	1.868	1.843	12.5	1.868	1.846	11	10.33	10
20	26	500	1.892	1.736	78	1.892	1.741	75.5	1.892	1.743	74.5	76	76
21	27	500	1.948	1.633	157.5	1.948	1.611	168.5	1.948	1.636	156	160.67	161

Table D.10: Ra measurements of the channels fabricated at Df = -2 mm.

Scan ID	DoE ID	Left	Center	Right	Average Ra	Rounded Ra
7	1	5.316	14.29	7.016	8.874	9
8	2	42.9	1.902	36.47	27.09066667	27
9	3	7.272	7.62	79.35	31.414	31
4	4	7.528	20.69	9.236	12.48466667	12
5	5	5.65	3.109	2.052	3.603666667	4
6	6	60.82	9.885	62.61	44.43833333	44
1	7	3.207	1.622	1.341	2.056666667	2
2	8	2.972	2.845	4.729	3.515333333	4
3	9	2.734	2.106	3.566	2.802	3
16	10	4.15	15.92	12.38	10.81666667	11
17	11	1.467	7.868	8.696	6.010333333	6
18	12	3.296	18.95	3.863	8.703	9
13	13	3.948	1.934	3.479	3.120333333	3
14	14	11.08	34.24	5.994	17.10466667	17
15	15	5.279	12.97	3.553	7.267333333	7
10	16	4.646	7.309	7.2	6.385	6
11	17	1.973	3.19	6.198	3.787	4
12	18	3.628	12.11	9.369	8.369	8
25	19	6.561	6.009	7.945	6.838333333	7
26	20	7.625	3.71	16.67	9.335	9
27	21	6.145	10.79	9.555	8.83	9
22	22	3.699	1.882	7.686	4.422333333	4
23	23	9.845	8.574	9.686	9.368333333	9
24	24	9.205	11.94	3.597	8.247333333	8
19	25	3.718	4.565	3.702	3.995	4
20	26	4.876	2.239	5.488	4.201	4
21	27	8.284	5.079	6.268	6.543666667	7

Table D.11: Rq measurements of the channels fabricated at Df = -2 mm.

Scan ID	DoE ID	Left	Center	Right	Average Rq	Rounded Rq
7	1	6.011	17.34	8.623	10.658	11
8	2	78.96	2.186	46.39	42.512	43
9	3	8.873	8.465	101.2	39.512667	40
4	4	8.57	22.89	10.4	13.953333	14
5	5	6.054	3.43	2.424	3.9693333	4
6	6	71.84	11.06	85.1	56	56
1	7	4.346	2.308	1.617	2.757	3
2	8	3.117	3.533	5.149	3.933	4
3	9	2.919	2.396	3.876	3.0636667	3
16	10	7.418	21.42	14.8	14.546	15
17	11	1.992	8.331	10.71	7.011	7
18	12	3.878	20.98	4.586	9.8146667	10
13	13	5.974	2.273	4.621	4.2893333	4
14	14	13.29	39.77	8.688	20.582667	21
15	15	7.488	13.71	4.108	8.4353333	8
10	16	6.383	8.886	8.437	7.902	8
11	17	2.386	3.753	8.863	5.0006667	5
12	18	4.977	13.48	10.47	9.6423333	10
25	19	8.819	7.024	9.017	8.2866667	8
26	20	9.372	5.995	18.83	11.399	11
27	21	7.353	11.97	11.75	10.357667	10
22	22	4.77	2.279	8.557	5.202	5
23	23	12.02	9.862	11.52	11.134	11
24	24	11.21	13.3	4.693	9.7343333	10
19	25	4.586	5.528	4.437	4.8503333	5
20	26	5.752	2.564	6.57	4.962	5
21	27	9.023	5.836	6.503	7.1206667	7

Table D.12: Rku measurements of the channels fabricated at Df = -2 mm.

Scan ID	DoE ID	Left	Center	Right	Average Rku	Rounded Rku
7	1	2.025	1.813	2.257	2.03166667	2
8	2	11.42	1.894	2.55	5.288	5
9	3	2.632	1.665	1.801	2.03266667	2
4	4	1.77	1.788	1.835	1.79766667	2
5	5	1.58	1.541	2.117	1.746	2
6	6	2.518	1.59	4.359	2.82233333	3
1	7	2.958	5.65	2.631	3.74633333	4
2	8	1.309	2.412	1.524	1.74833333	2
3	9	1.536	1.998	1.698	1.744	2
16	10	14.67	5.174	2.905	7.583	8
17	11	7.589	1.38	2.425	3.798	4
18	12	2.103	1.427	2.747	2.09233333	2
13	13	6.461	2.161	3.808	4.14333333	4
14	14	2.273	2.234	5.121	3.20933333	3
15	15	4.636	1.256	2.004	2.632	3
10	16	3.206	2.993	2.231	2.81	3
11	17	2.239	1.687	4.053	2.65966667	3
12	18	3.953	1.583	1.777	2.43766667	2
25	19	3.804	2.092	2.028	2.64133333	3
26	20	2.187	8.859	1.884	4.31	4
27	21	2.094	1.512	2.129	1.91166667	2
22	22	3.375	2.955	1.729	2.68633333	3
23	23	3.201	2.002	1.956	2.38633333	2
24	24	1.907	1.545	2.737	2.063	2
19	25	2.23	2.455	2.271	2.31866667	2
20	26	2.056	1.89	2.058	2.00133333	2
21	27	1.595	1.984	1.263	1.614	2

Table D.13: Rsk measurements of the channels fabricated at Df = -2 mm.

Scan ID	DoE ID	Left	Center	Right	Average Rsk	Rounded Rsk
7	1	-0.6878	0.3125	-0.6165	-0.3306	0
8	2	-3.165	0.4644	0.2027	-0.8326333	-1
9	3	-1.004	-0.4239	-0.1244	-0.5174333	-1
4	4	-0.1057	-0.5861	-0.7945	-0.4954333	0
5	5	0.7063	0.02708	0.7916	0.50832667	1
6	6	-1.148	-0.1971	0.03557	-0.43651	0
1	7	-0.6848	-1.337	0.5912	-0.4768667	0
2	8	-0.1235	-0.4212	-0.301	-0.2819	0
3	9	0.1564	0.588	0.2172	0.32053333	0
16	10	3.269	1.617	-0.4821	1.46796667	1
17	11	-1.875	0.4077	-0.8349	-0.7674	-1
18	12	-0.232	-0.1702	0.9261	0.17463333	0
13	13	1.955	0.02854	1.518	1.16718	1
14	14	0.6899	2.234	1.732	1.55196667	2
15	15	-1.651	0.03403	-0.7614	-0.79279	-1
10	16	0.3583	-1.093	-0.8191	-0.5179333	-1
11	17	-0.0549	-0.0808	-0.3866	-0.1741067	0
12	18	1.625	0.2167	-0.336	0.5019	1
25	19	1.606	0.5646	-0.9476	0.40766667	0
26	20	0.07619	2.408	-0.0682	0.80534667	1
27	21	0.5903	0.1708	-0.5035	0.08586667	0
22	22	0.6022	0.9536	0.274	0.60993333	1
23	23	-1.142	-0.739	-0.0883	-0.65643	-1
24	24	0.2916	0.0603	0.0345	0.1288	0
19	25	-0.4317	-0.8478	-0.6721	-0.6505333	-1
20	26	0.4477	0.449	-0.6974	0.06643333	0
21	27	0.3151	-0.5338	0.03872	-0.0599933	0

Table D.14: General quality factors of the produced channels at Df = -2 mm.

Scan ID	DoE ID	Average Width	Average Depth	Aspect Ratio	Quality of Ratio	Average Ra	Quality of Ra	Channel Shape	Quality of Shape
61	1	179	108	0.60		9			
62	2	193	345	1.79		27			
63	3	209	198	0.95		31			
58	4	142	106	0.74		12			
59	5	160	70	0.43		4			
60	6	199	249	1.25		44			
55	7	150	24	0.16		2			
56	8	164	47	0.28		4			
57	9	220	46	0.21		3			
70	10	189	225	1.19		11			
71	11	209	88	0.42		6			
72	12	213	130	0.61		9			
67	13	160	130	0.81		3			
68	14	170	172	1.01		17			
69	15	209	96	0.46		7			
64	16	115	22	0.19		6			
65	17	158	113	0.72		4			
66	18	170	118	0.70		8			
79	19	179	146	0.81		7			
80	20	189	166	0.88		9			
81	21	207	141	0.68		9			
76	22	160	79	0.49		4			
77	23	187	168	0.90		9			
78	24	203	160	0.79		8			
73	25	111	10	0.09		4			
74	26	170	76	0.45		4			
75	27	181	161	0.89		7			

D.8.2 Df = +2 mm channels' 3D scans

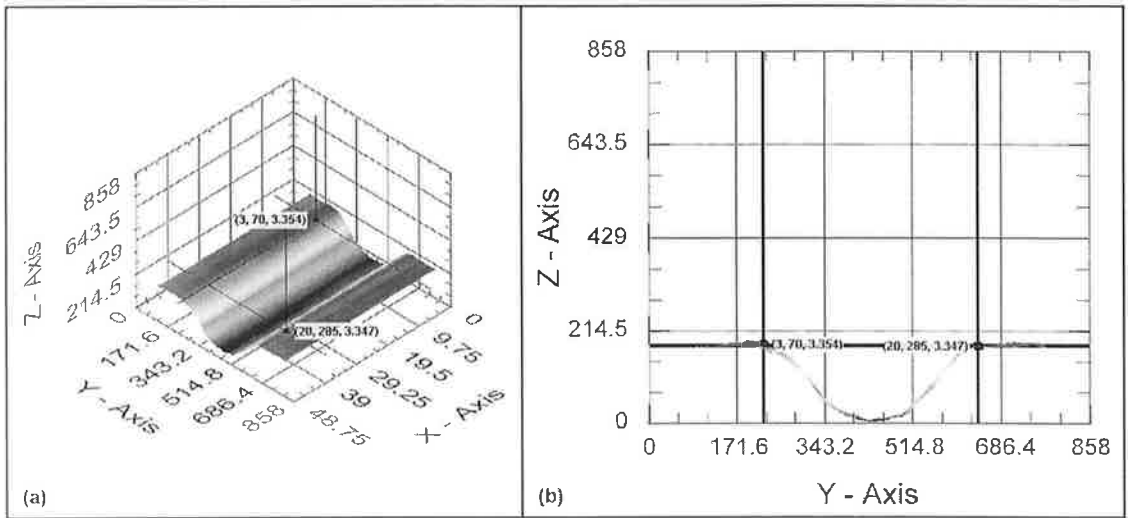


Figure 1: Channel 1, (a) isometric view and (b) front view

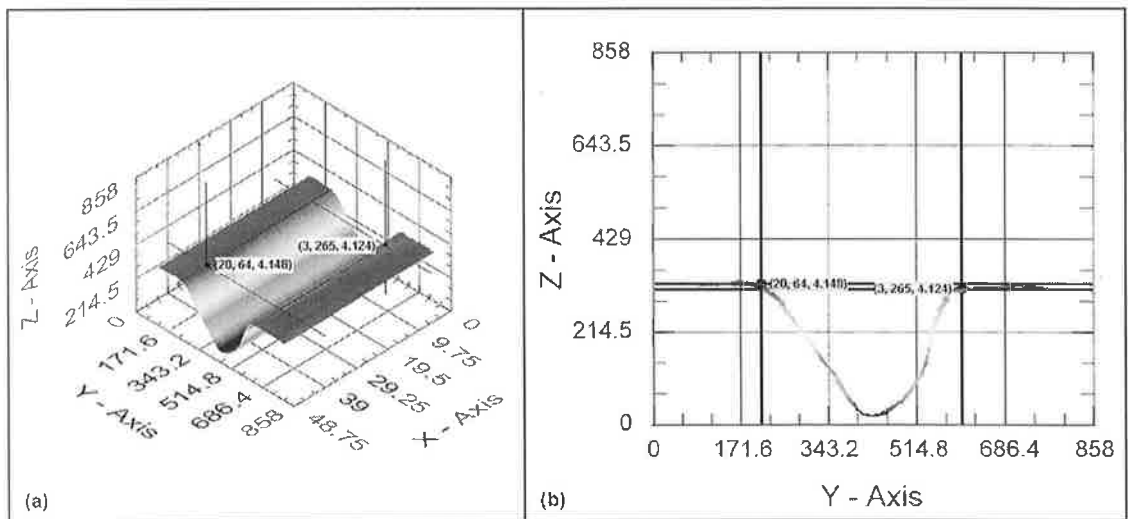


Figure 2: Channel 2, (a) isometric view and (b) front view

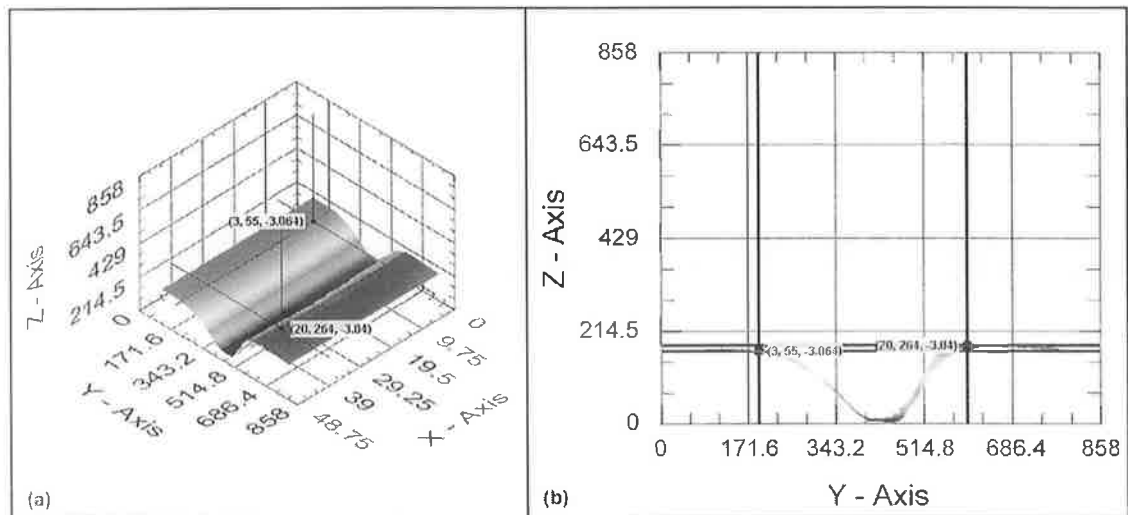


Figure 3: Channel 3, (a) isometric view and (b) front view

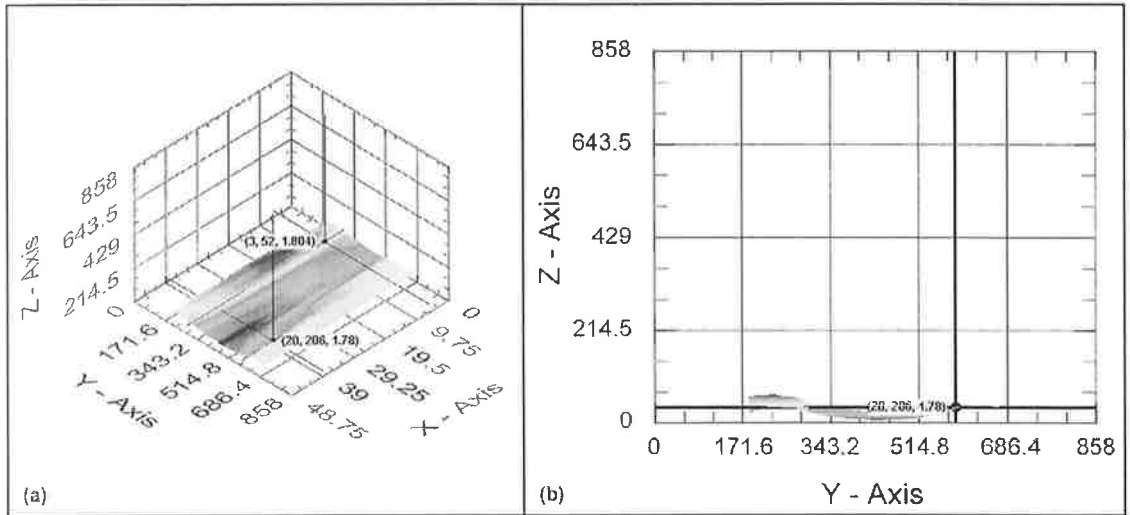


Figure 4: Channel 4, (a) isometric view and (b) front view

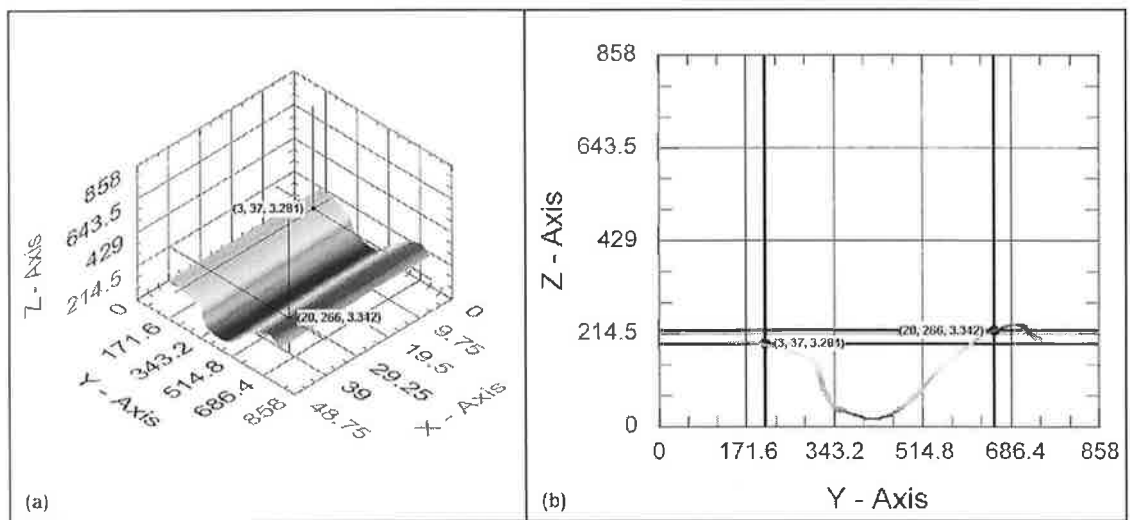


Figure 5: Channel 5, (a) isometric view and (b) front view

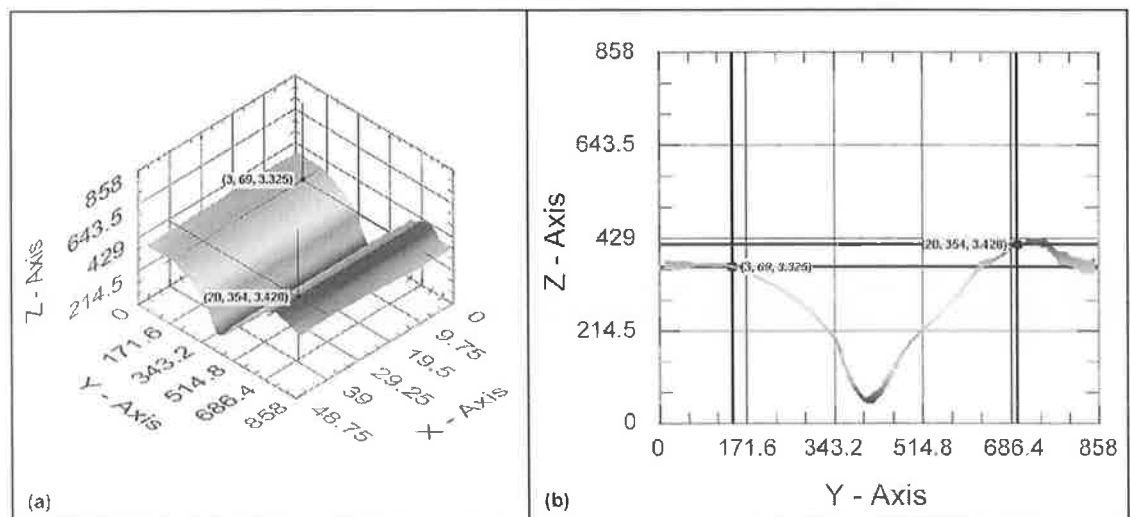


Figure 6: Channel 6, (a) isometric view and (b) front view

Figure 7: Channel 7, **not fabricated**

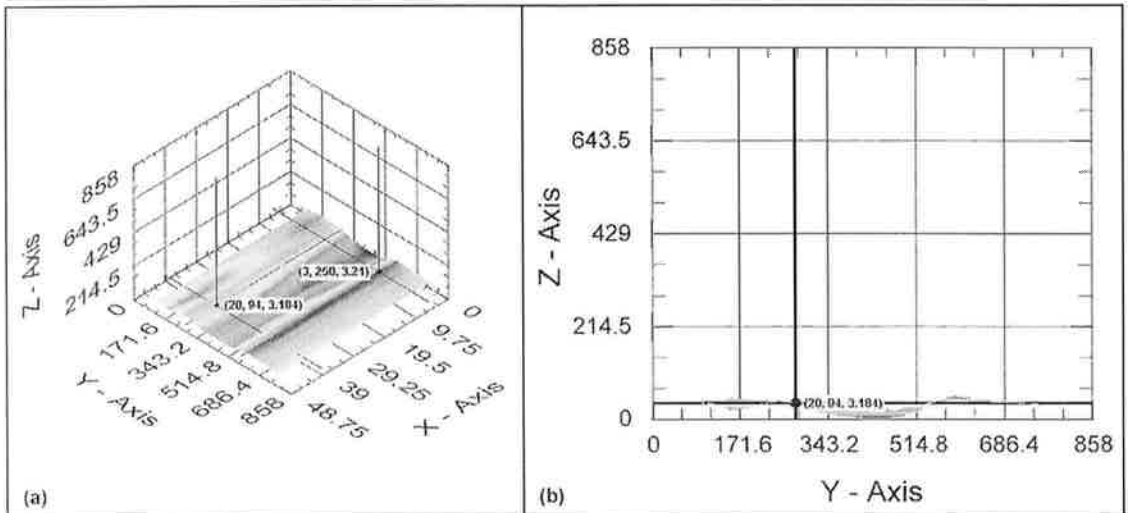


Figure 8: Channel 8, (a) isometric view and (b) front view

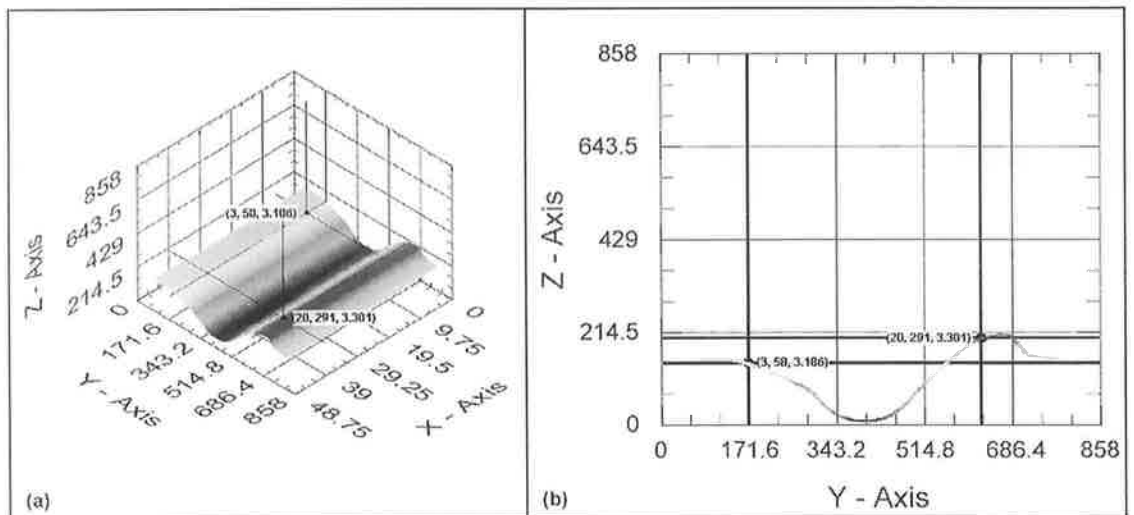


Figure 9: Channel 9, (a) isometric view and (b) front view

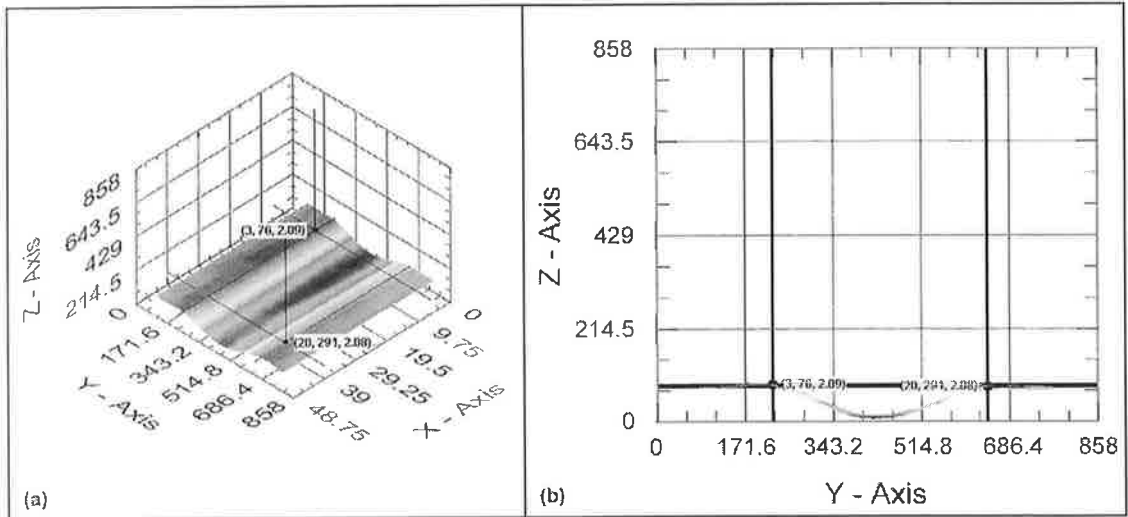


Figure 10: Channel 10, (a) isometric view and (b) front view

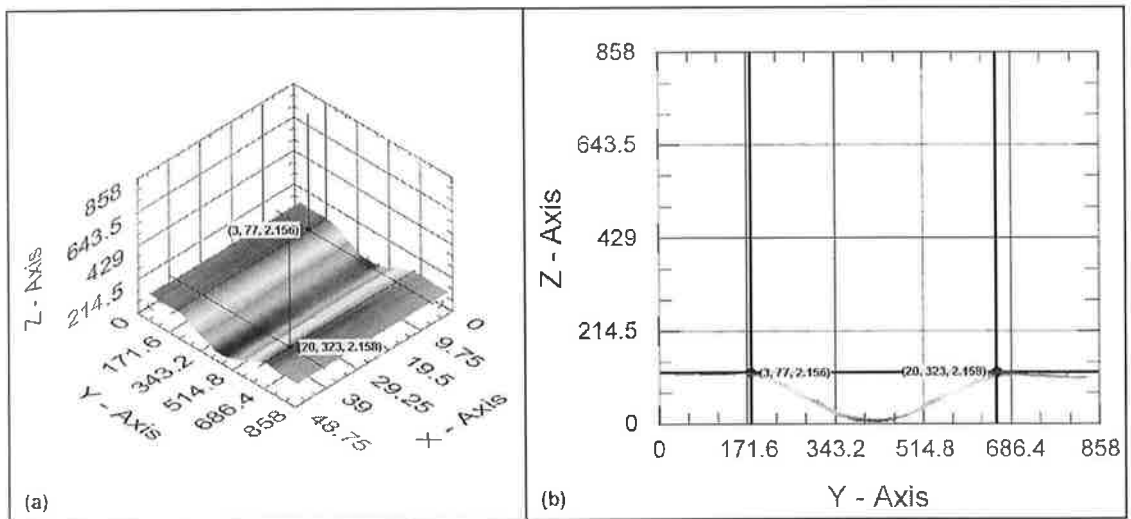


Figure 11: Channel 11, (a) isometric view and (b) front view

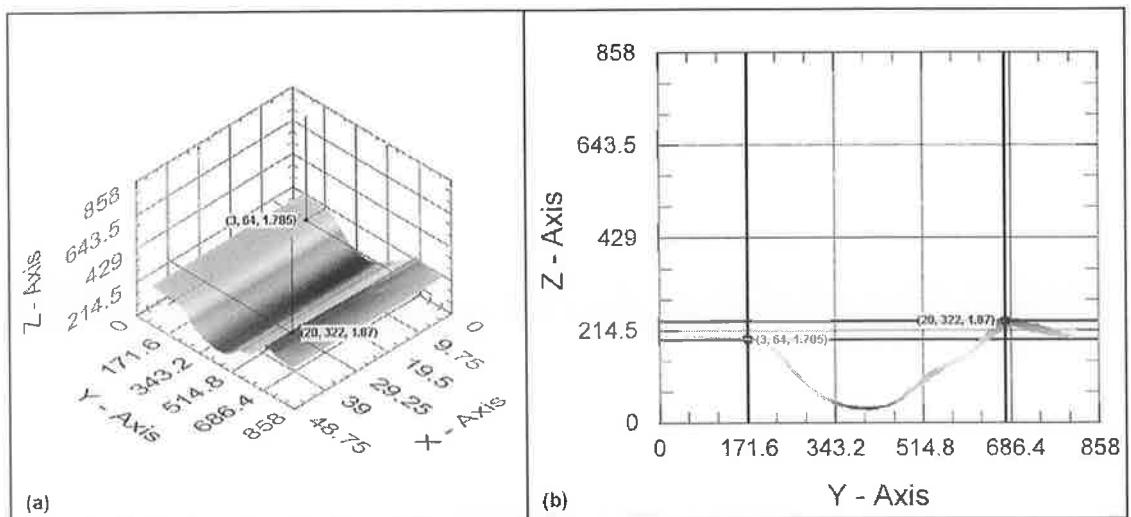


Figure 12: Channel 12, (a) isometric view and (b) front view

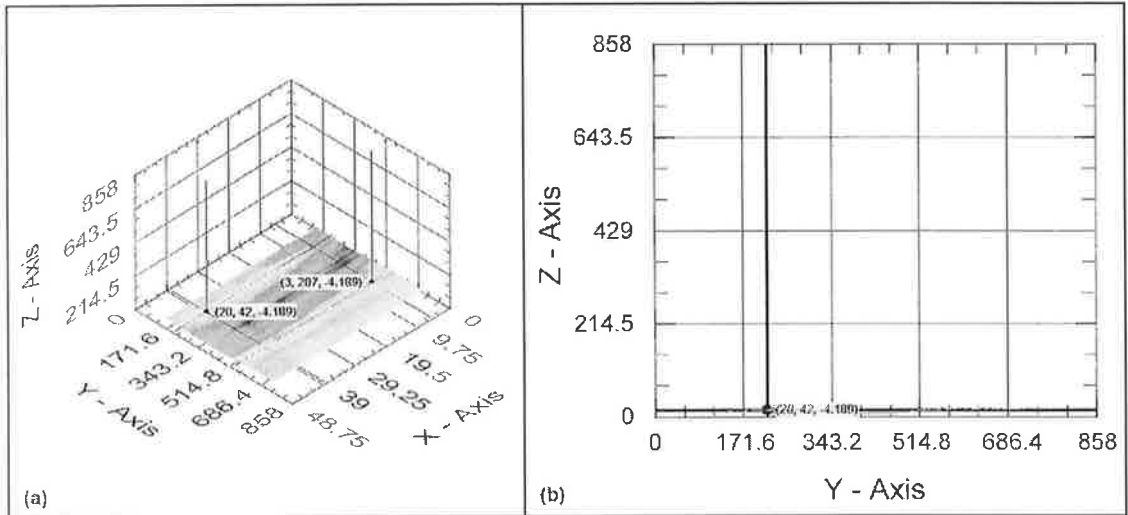


Figure 13: Channel 13, (a) isometric view and (b) front view

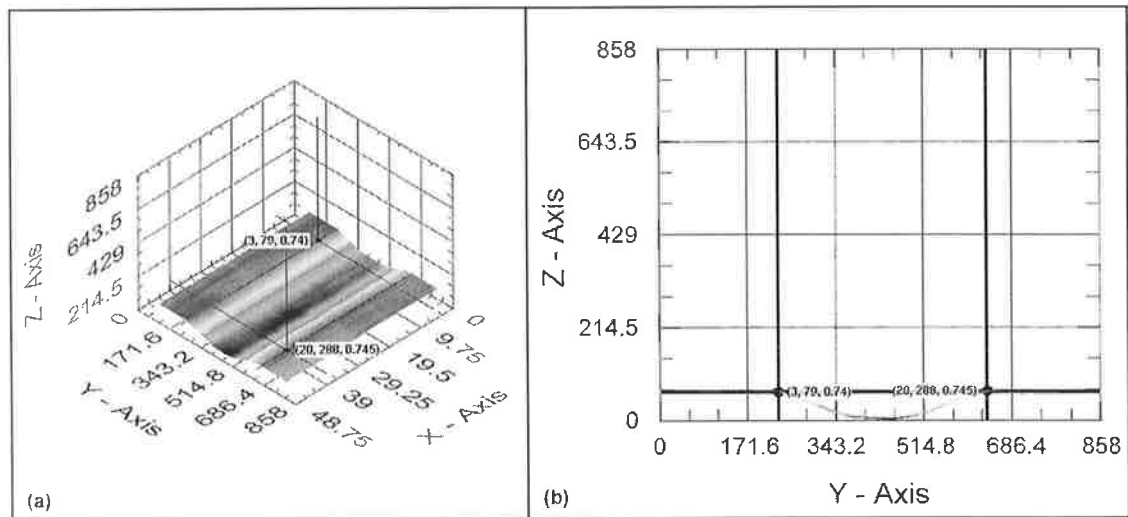


Figure 14: Channel 14, (a) isometric view and (b) front view

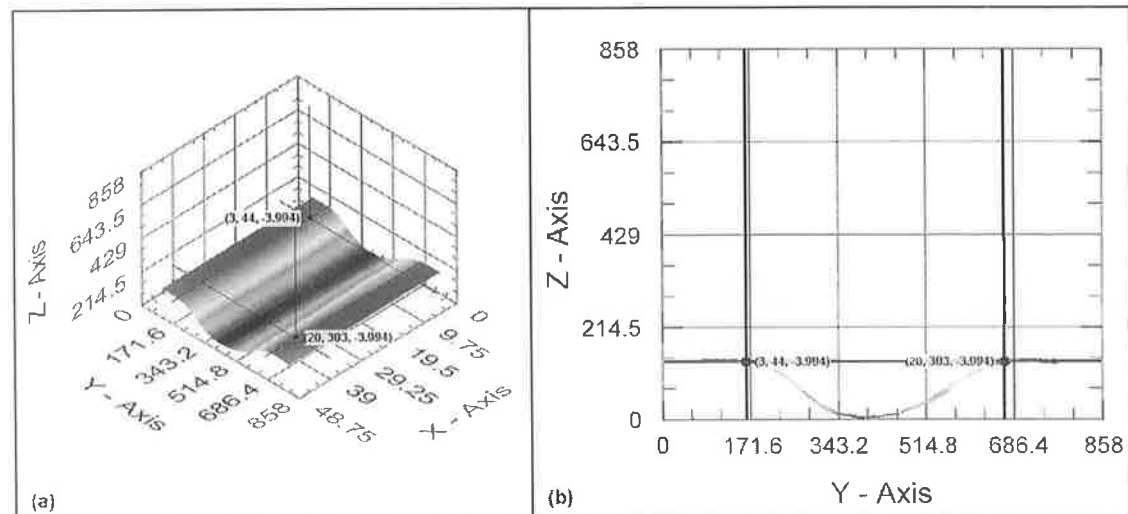


Figure 15: Channel 15, (a) isometric view and (b) front view

Figure 16: Channel 16, **not fabricated**

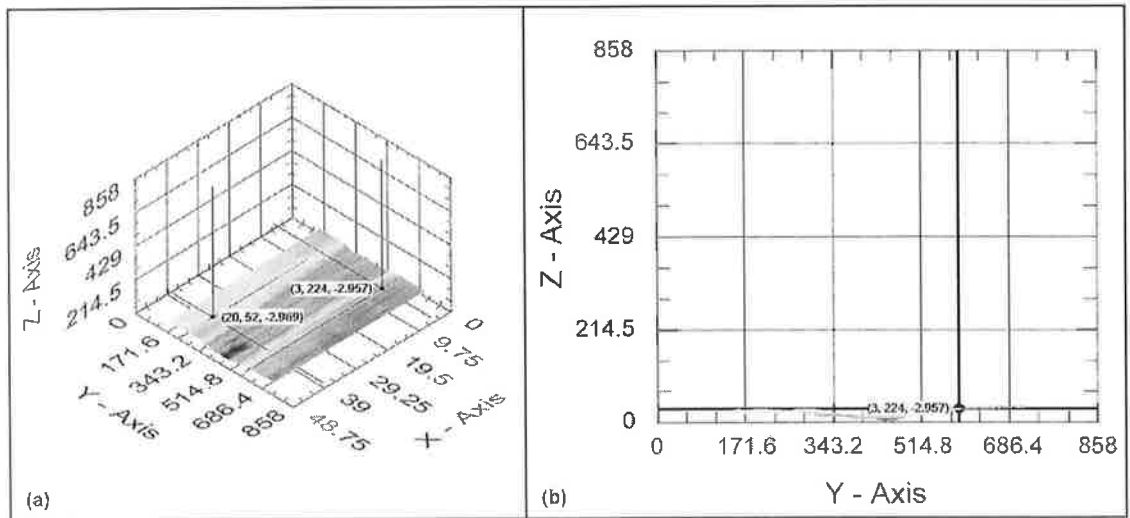


Figure 17: Channel 17, (a) isometric view and (b) front view

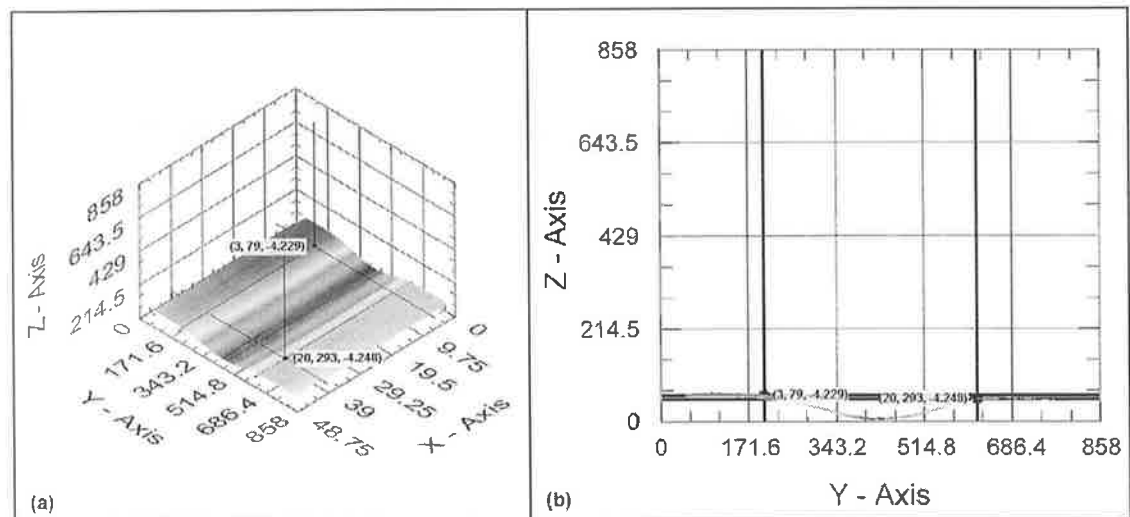


Figure 18: Channel 18, (a) isometric view and (b) front view

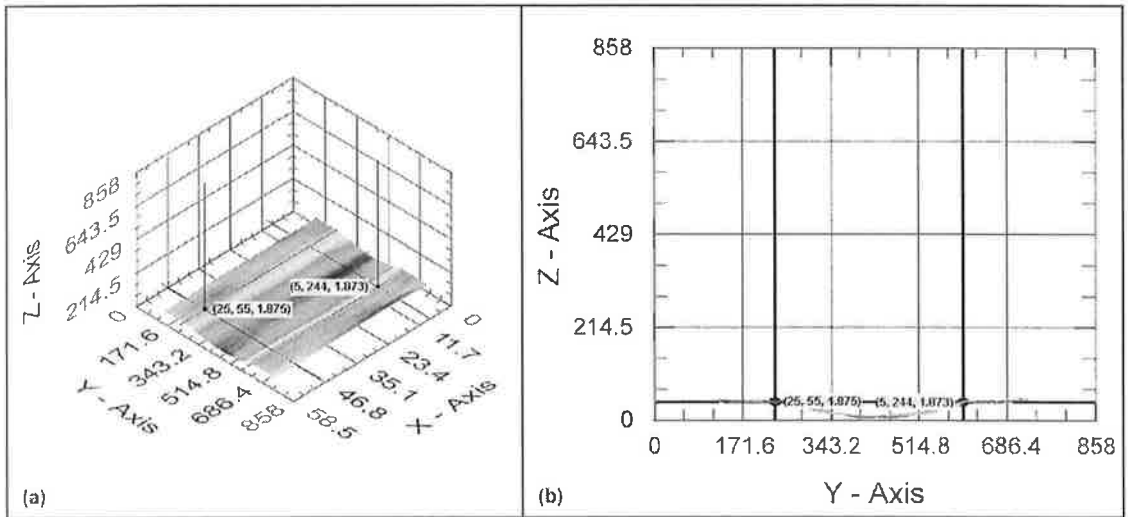


Figure 19: Channel 19, (a) isometric view and (b) front view

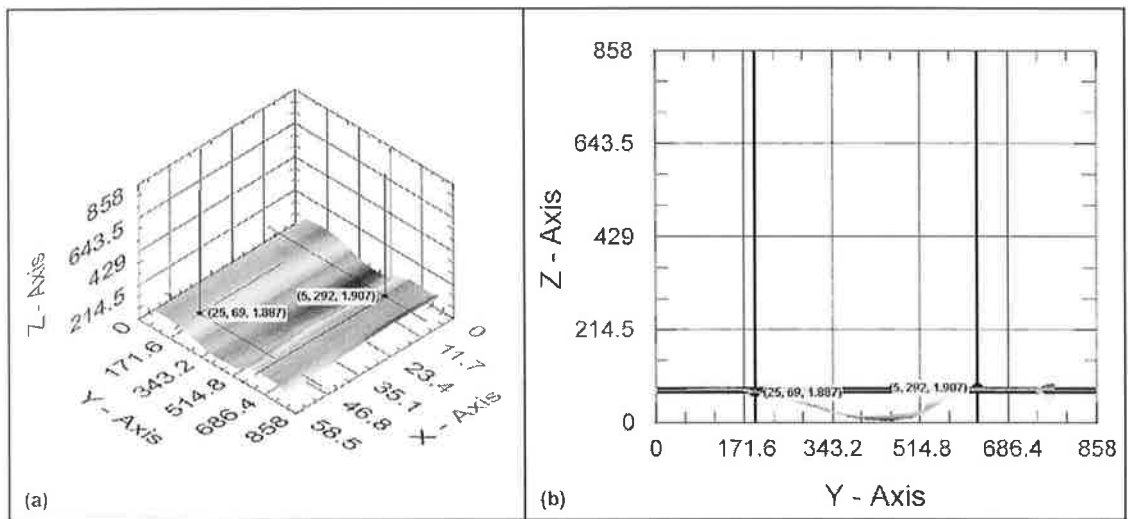


Figure 20: Channel 20, (a) isometric view and (b) front view

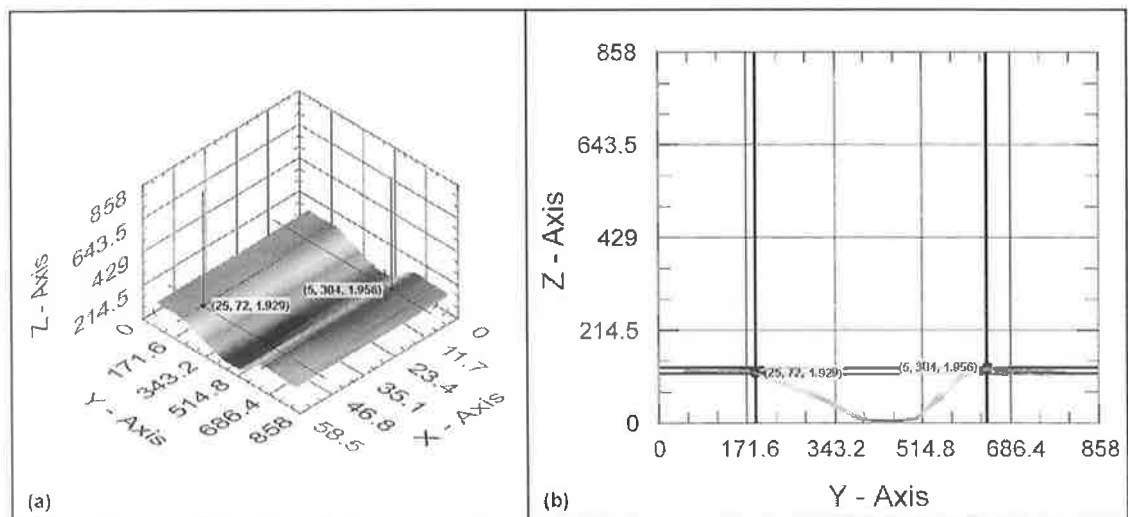


Figure 21: Channel 21, (a) isometric view and (b) front view

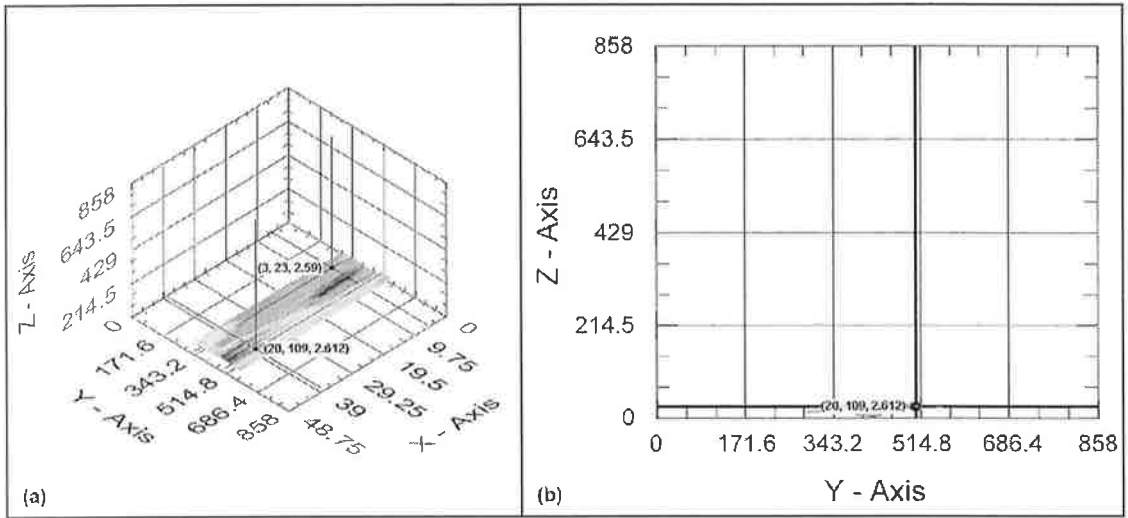


Figure 22: Channel 22, (a) isometric view and (b) front view

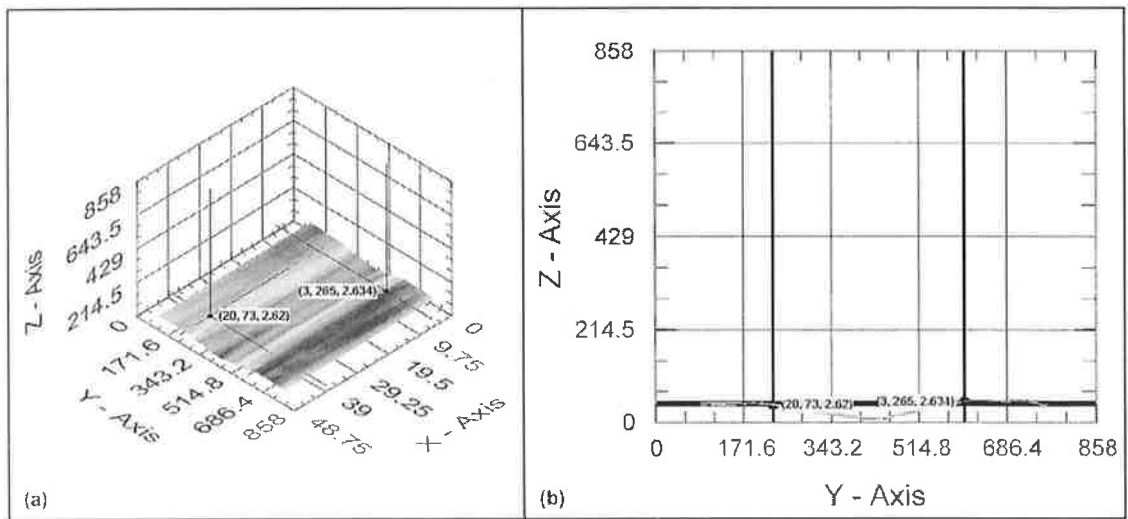


Figure 23: Channel 23, (a) isometric view and (b) front view

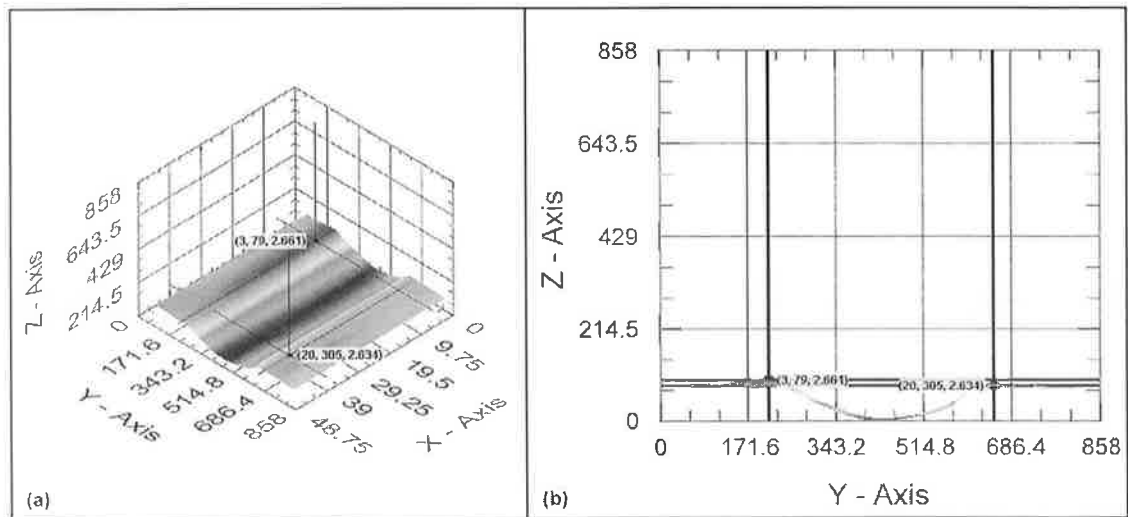


Figure 24: Channel 24, (a) isometric view and (b) front view

Figure 25: Channel 25, **not fabricated**

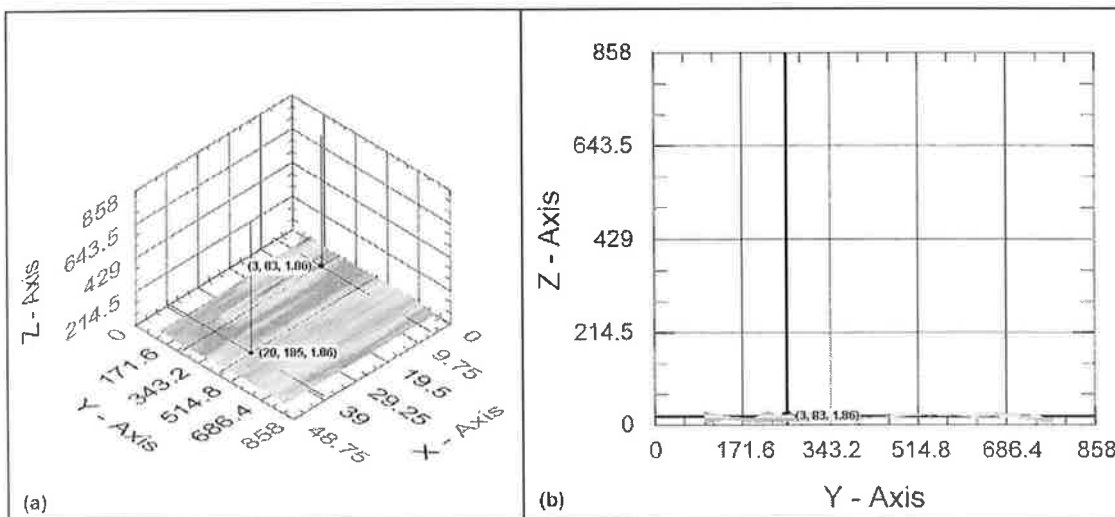


Figure 26: Channel 26, (a) isometric view and (b) front view

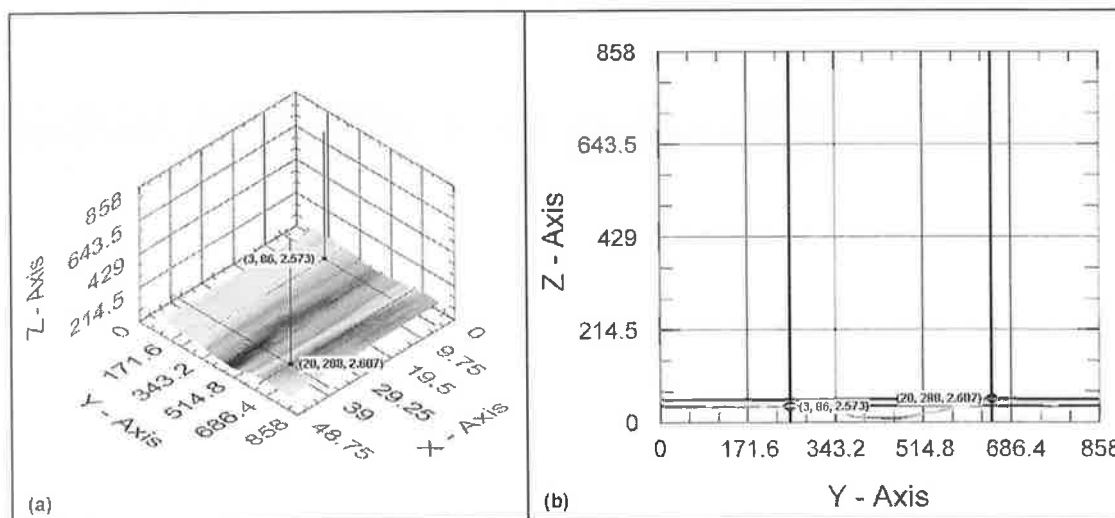


Figure 27: Channel 27, (a) isometric view and (b) front view

Table D.15: Width measurements of the channels fabricated at Df = +2 mm.

Scan ID	DoE ID	Conv. Unit	Left1	Right1	Width1	Left2	Right2	Width2	Left3	Right3	Width3	Average	Rnd Average
61	1	1.95	70	285	419.25	70	285	419.25	70	285	419.25	419.25	419
62	2	1.95	64	265	391.95	64	265	391.95	64	265	391.95	391.95	392
63	3	1.95	55	264	407.55	55	264	407.55	55	264	407.55	407.55	408
58	4	1.95	52	206	300.3	52	206	300.3	52	206	300.3	300.3	300
59	5	1.95	37	266	446.55	37	266	446.55	37	266	446.55	446.55	447
60	6	1.95	69	354	555.75	69	354	555.75	69	354	555.75	555.75	556
55	7	1.95	not fabricated										
56	8	1.95	94	250	304.2	94	248	300.3	94	249	302.25	302.25	302
57	9	1.95	58	291	454.35	58	291	454.35	58	291	454.35	454.35	454
70	10	1.95	76	291	419.25	76	291	419.25	76	291	419.25	419.25	419
71	11	1.95	77	323	479.7	77	323	479.7	77	323	479.7	479.7	480
72	12	1.95	64	322	503.1	64	322	503.1	64	322	503.1	503.1	503
67	13	1.95	42	207	321.75	42	207	321.75	42	207	321.75	321.75	322
68	14	1.95	79	288	407.55	79	288	407.55	79	288	407.55	407.55	408
69	15	1.95	44	303	505.05	44	303	505.05	44	303	505.05	505.05	505
64	16	1.95	not fabricated										
65	17	1.95	52	224	335.4	52	224	335.4	52	224	335.4	335.4	335
66	18	1.95	79	293	417.3	79	293	417.3	79	293	417.3	417.3	417
79	19	1.95	55	244	368.55	55	244	368.55	55	244	368.55	368.55	369
80	20	1.95	69	292	434.85	69	292	434.85	69	292	434.85	434.85	435
81	21	1.95	72	304	452.4	72	304	452.4	72	304	452.4	452.4	452
76	22	1.95	23	109	167.7	23	109	167.7	23	109	167.7	167.7	168
77	23	1.95	73	265	374.4	73	265	374.4	73	265	374.4	374.4	374
78	24	1.95	79	305	440.7	79	305	440.7	79	305	440.7	440.7	441
73	25	1.95	not fabricated										
74	26	1.95	83	185	198.9	83	185	198.9	83	185	198.9	198.9	199
75	27	1.95	86	288	393.9	86	288	393.9	86	288	393.9	393.9	394

Table D.16: Depth measurements of the channels fabricated at Df = +2 mm.

Scan ID	DoE ID	Conv. Unit	Upper1	Lower1	Depth1	Upper2	Lower2	Depth2	Upper3	Lower3	Depth3	Average	Rnd Average
61	1	500	3.354	3	177	3.354	3.003	175.5	3.354	2.996	179	177.17	177
62	2	500	4.148	3.546	301	4.148	3.54	304	4.148	3.537	305.5	303.5	304
63	3	500	-3.064	-3.376	156	-3.064	-3.381	158.5	-3.064	-3.389	162.5	159	159
58	4	500	1.804	1.76	22	1.804	1.736	34	1.804	1.724	40	32	32
59	5	500	3.281	2.939	171	3.281	2.932	174.5	3.281	2.935	173	172.83	173
60	6	500	3.325	2.708	308.5	3.325	2.7	312.5	3.325	2.739	293	304.67	305
55	7	500	not fabricated										
56	8	500	3.191	3.115	38	3.191	3.123	34	3.191	3.142	24.5	32.17	32
57	9	500	3.193	2.922	135.5	3.193	2.915	139	3.193	2.917	138	137.5	138
70	10	500	2.09	1.936	77	2.09	1.938	76	2.09	1.943	73.5	75.5	75
71	11	500	2.156	1.931	112.5	2.156	1.941	107.5	2.156	1.926	115	111.67	112
72	12	500	1.785	1.458	163.5	1.785	1.465	160	1.785	1.467	159	160.83	161
67	13	500	-4.189	-4.214	12.5	-4.189	-4.211	11	-4.189	-4.207	9	10.83	11
68	14	500	0.745	0.623	61	0.745	0.618	63.5	0.745	0.613	66	63.5	64
69	15	500	-3.994	-4.253	129.5	-3.994	-4.248	127	-3.994	-4.255	130.5	129	129
64	16	500	not fabricated										
65	17	500	-2.957	-3	21.5	-2.957	-3.005	24	-2.957	-3.001	22	22.5	23
66	18	500	-4.248	-4.343	47.5	-4.248	-4.338	45	-4.248	-4.336	44	45.5	45
79	19	500	1.875	1.802	36.5	1.875	1.807	34	1.875	1.804	35.5	35.33	35
80	20	500	1.887	1.76	63.5	1.887	1.77	58.5	1.887	1.78	53.5	58.5	59
81	21	500	1.929	1.709	110	1.929	1.711	109	1.929	1.707	111	110	110
76	22	500	2.59	2.573	8.5	2.59	2.581	4.5	2.59	2.583	3.5	5.5	5
77	23	500	2.62	2.559	30.5	2.62	2.561	29.5	2.62	2.551	34.5	31.5	32
78	24	500	2.634	2.476	79	2.634	2.478	78	2.634	2.473	80.5	79.17	79
73	25	500	not fabricated										
74	26	500	1.86	1.843	8.5	1.86	1.853	3.5	1.86	1.848	6	6	6
75	27	500	2.573	2.52	26.5	2.573	2.517	28	2.573	2.51	31.5	28.67	29

Table D.17: Ra measurements of the channels fabricated at Df = +2 mm.

Scan ID	DoE ID	Left	Center	Right	Average Ra	Rounded Ra	
61	1	1.309	1.65	3.09	2.01633333	2	
62	2	2.499	1.972	3.577	2.68266667	3	
63	3	2.521	2.938	4.295	3.25133333	3	
58	4	4.149	7.648	8.276	6.691	7	
59	5	5.301	1.176	3.248	3.24166667	3	
60	6	4.792	5.093	1.821	3.902	4	
55	7	not fabricated					
56	8	6.199	5.557	2.157	4.63766667	5	
57	9	2.545	1.322	2.785	2.21733333	2	
70	10	1.579	2.743	1.735	2.019	2	
71	11	1.864	3.441	3.185	2.83	3	
72	12	2.982	2.977	3.013	2.99066667	3	
67	13	1.922	1.035	2.519	1.82533333	2	
68	14	0.685	2.001	1.951	1.5457	2	
69	15	1.113	2.026	3.576	2.23833333	2	
64	16	not fabricated					
65	17	1.666	3.257	1.487	2.13666667	2	
66	18	2.713	1.05	1.435	1.73266667	2	
79	19	0.999	1.933	2.217	1.71633333	2	
80	20	2.093	4.741	4.097	3.64366667	4	
81	21	4.904	2.35	4.295	3.84966667	4	
76	22	2.481	6.198	9.171	5.95	6	
77	23	3.331	1.354	1.899	2.19466667	2	
78	24	3.071	0.6564	2.951	2.22613333	2	
73	25	not fabricated					
74	26	1.503	1.995	1.149	1.549	2	
75	27	3.448	1.719	2.008	2.39166667	2	

Table D.18: Rq measurements of the channels fabricated at Df = +2 mm.

Scan ID	DoE ID	Left	Center	Right	Average Rq	Rounded Rq	
61	1	1.949	2.001	4.208	2.7193333	3	
62	2	2.711	2.395	4.255	3.1203333	3	
63	3	2.902	3.252	5.998	4.0506667	4	
58	4	5.17	8.704	9.339	7.7376667	8	
59	5	6.688	1.355	3.834	3.959	4	
60	6	5.82	6.088	2.253	4.7203333	5	
55	7	not fabricated					
56	8	6.817	5.961	2.573	5.117	5	
57	9	2.953	1.583	3.112	2.5493333	3	
70	10	2.121	3.067	2.247	2.4783333	2	
71	11	2.323	3.848	3.837	3.336	3	
72	12	3.728	3.231	3.861	3.6066667	4	
67	13	2.406	1.451	3.152	2.3363333	2	
68	14	1.374	2.35	2.441	2.055	2	
69	15	1.889	2.446	4.188	2.841	3	
64	16	not fabricated					
65	17	1.791	4.054	2.034	2.6263333	3	
66	18	2.963	1.3	1.884	2.049	2	
79	19	1.301	2.222	2.658	2.0603333	2	
80	20	2.806	5.053	5.525	4.4613333	4	
81	21	5.353	2.631	5.288	4.424	4	
76	22	3.306	7.691	10.11	7.0356667	7	
77	23	3.866	1.704	2.97	2.8466667	3	
78	24	3.256	0.735	3.166	2.3857667	2	
73	25	not fabricated					
74	26	1.598	2.618	1.392	1.8693333	2	
75	27	3.984	2.304	2.31	2.866	3	

Table D.19: Rku measurements of the channels fabricated at Df = +2 mm.

Scan ID	DoE ID	Left	Center	Right	Average Rku	Rounded Rku	
61	1	6.649	2.341	6.366	5.11866667	5	
62	2	1.54	2.323	2.253	2.03866667	2	
63	3	2.554	1.864	6.658	3.692	4	
58	4	2.242	1.75	1.798	1.93	2	
59	5	2.196	1.71	2.581	2.16233333	2	
60	6	2.103	2.277	2.82	2.4	2	
55	7	not fabricated					
56	8	1.569	1.32	2.819	1.90266667	2	
57	9	1.72	2.212	1.703	1.87833333	2	
70	10	3.777	1.509	2.888	2.72466667	3	
71	11	2.789	1.64	2.741	2.39	2	
72	12	2.941	1.397	4.207	2.84833333	3	
67	13	2.95	3.034	3.142	3.042	3	
68	14	10.68	1.741	2.882	5.101	5	
69	15	15.59	1.868	2.036	6.498	6	
64	16	not fabricated					
65	17	1.592	2.329	3.346	2.42233333	2	
66	18	1.574	2.552	3.438	2.52133333	3	
79	19	4.615	1.955	2.298	2.956	3	
80	20	2.87	1.376	2.623	2.28966667	2	
81	21	1.514	1.627	2.905	2.01533333	2	
76	22	3.207	2.542	1.488	2.41233333	2	
77	23	2.208	3.944	4.381	3.511	4	
78	24	1.537	2.419	1.444	1.8	2	
73	25	not fabricated					
74	26	1.411	3.707	2.603	2.57366667	3	
75	27	1.738	3.237	1.682	2.219	2	

Table D.20: Rsk measurements of the channels fabricated at Df = +2 mm.

Scan ID	DoE ID	Left	Center	Right	Average Rsk	Rounded Rsk	
61	1	1.724	-0.1163	-1.317	0.0969	0	
62	2	-0.1273	-0.6183	-0.1379	-0.2945	0	
63	3	0.4009	-0.1744	-1.718	-0.4971667	0	
58	4	0.1693	-0.1119	0.348	0.13513333	0	
59	5	-0.2712	0.414	1.001	0.38126667	0	
60	6	-0.6741	-0.3558	0.4514	-0.1928333	0	
55	7	not fabricated					
56	8	0.2239	-0.2088	0.8248	0.27996667	0	
57	9	-0.0373	-0.1518	0.1106	-0.0261667	0	
70	10	0.9196	-0.271	-0.0254	0.20773	0	
71	11	1.011	0.2442	0.8684	0.70786667	1	
72	12	0.9514	0.18	1.129	0.75346667	1	
67	13	1.132	0.4622	-1.042	0.18406667	0	
68	14	1.945	-0.2298	-0.9389	0.25876667	0	
69	15	3.528	0.4735	0.4684	1.48996667	1	
64	16	not fabricated					
65	17	0.2513	-0.3709	1.275	0.38513333	0	
66	18	0.3494	0.2115	-0.6017	-0.0136	0	
79	19	-1.395	0.4658	-0.1052	-0.3448	0	
80	20	0.8681	-0.0401	0.1043	0.31075333	0	
81	21	-0.3192	-0.2942	-1.16	-0.5911333	-1	
76	22	-0.4622	-0.8399	-0.0339	-0.44534	0	
77	23	0.6653	1.226	0.8335	0.90826667	1	
78	24	0.5457	-0.1433	-0.0613	0.1137	0	
73	25	not fabricated					
74	26	0.03978	-1.267	0.1277	-0.3665067	0	
75	27	-0.1392	-0.7911	0.05689	-0.2911367	0	

Table D.21: General quality factors of the produced channels at Df = +2 mm.

Scan ID	DoE ID	Average Width	Average Depth	Aspect Ratio	Quality of Ratio	Average Ra	Quality of Ra	Channel Shape	Quality of Shape	
7	1	419	177	0.42		2				
8	2	392	304	0.77		3				
9	3	408	159	0.39		3				
4	4	300	32	0.11		7				
5	5	447	173	0.39		3				
6	6	556	305	0.55		4				
1	7	not fabricated								
2	8	302	32	0.11		5				
3	9	454	138	0.30		2				
16	10	419	75	0.18		2				
17	11	480	112	0.23		3				
18	12	503	161	0.32		3				
13	13	322	11	0.03		2				
14	14	408	64	0.16		2				
15	15	505	129	0.26		2				
10	16	not fabricated								
11	17	335	23	0.07		2				
12	18	417	45	0.11		2				
25	19	369	35	0.10		2				
26	20	435	59	0.13		4				
27	21	452	110	0.24		4				
22	22	168	5	0.03		6				
23	23	374	32	0.08		2				
24	24	441	79	0.18		2				
19	25	not fabricated								
20	26	199	6	0.03		2				
21	27	394	29	0.07		2				

D.9 RSM definitions

Statistical analysis of the experimental results was performed. Response surface methodology (RSM) is a graphical and numerical representation of a model that expresses experimental data. Such a model can be used to predict responses or outputs from different combinations of process control parameters [167].

The following is a summary of the statistical terms' definitions used in the ANOVA results in chapter 4.

1- **The degree of freedom** of each term used in the model is listed in the "df" column. The degree of freedom for the model is the number of model terms minus one. As for the each model term, the degree of freedom is the number of levels of the term minus one [172].

2- **The model/term mean square** is an estimate of the term's variance, calculated from the term's sum of squares divided by term's degrees of freedom [172].

3- **The F value** is calculated by term mean square divided by residual mean square [172].

4- **The p-value** shows whether the model/term is significant or not. The p-value is the probability of getting an F Value of this size if the model/term did not have an effect on the response. In general, a term that has a probability value less than 0.05, which is the significance threshold that sets the risk level in significance/non-significance detection, would be considered a significant effect [172].

5- **The R-Squared** is a measure of the amount of variation around the mean explained by the model [172].

6- **The Adj R-Squared** is a measure of the amount of variation around the mean explained by the model, adjusted for the number of terms in the model. The adjusted R-squared decreases as the number of terms in the model increases if those additional terms do not add value to the model [172].

7- **The Pred R-Squared** is a measure of the amount of variation in new data explained by the model [172].

8- **The Adequate Precision** is a signal to noise ratio. It compares the range of the predicted values at the design points to the average prediction error [172].

Appendix E – Extra Results from Chapter 5

E.1: E-Mail consultancies with Prof. Dowden.

First E-mail:

Dear Prof. Dowden,

I am using your book (The mathematics of thermal modeling) as a reference in my PhD study at Dublin City University. I would be very glad if you would advise me on two issues:

1- I am thermally modeling the process of micro-channel making on the surface of glass sheets using a pulsed CO₂ laser. I found the equations in section 4.3 quite useful. Do you recommend using these equations for estimating the ablated regions (since they do not account for phase changes)? Such an approximation was recommended by (W. W. Duley, Laser processing and analysis of materials, 1983, pp. 119).

2- During writing up, when I tried to re-calculate equation (4.17) to find the value of (a_n) in the Fourier series, I found a difficulty in getting the same answer provided. My calculation as per the attached document (equation.jpg) shows a difference in the magnitude ($2P_0/n\pi$). I found it to be equal to ($2P_0\tau/n\pi\tau_0$). Could you please advise if a different value of $P(t)$ in the integration range was used?

Thanks in advance for your precious time.

Respectfully yours,

Ahmed Issa.

Mechanical Engineering Department,
Dublin City University.
Phone: 00353 1700 7674
Fax: 00353 1700 5345
Mobile: 00353 863 987 212

The attached <equation.jpg>

$$\begin{aligned} a_n &= \frac{2}{t_0} \int_{-\tau/2}^{\tau/2} \frac{P_0 t_0}{\tau} \cdot \cos \frac{2\pi n}{t_0} t \cdot dt \\ &= \frac{2 P_0 t_0}{t_0 \tau} \int_{-\tau/2}^{\tau/2} \cos \frac{2\pi n}{t_0} t \cdot dt \\ &= \frac{2 P_0}{\tau} \cdot \frac{t_0}{2\pi n} \cdot \sin \frac{2\pi n}{t_0} t \Bigg|_{-\tau/2}^{\tau/2} \\ &= \frac{P_0 t_0}{\pi n \tau} \left(\sin \frac{2\pi n \tau}{2 t_0} - \sin -\frac{2\pi n \tau}{2 t_0} \right) \\ &= \frac{2 P_0 t_0}{\pi n \tau} \cdot \sin \left(\frac{\pi n \tau}{t_0} \right). \end{aligned}$$

Reply to the first e-mail:

Dear Ahmed,

I've put my replies in your text:

-----Original Message-----

From: ahmed.issa2@mail.dcu.ie [mailto:ahmed.issa2@mail.dcu.ie]

Sent: 31 May 2006 01:37

To: Dowden, John M

Subject: Query on pp. 125 of The mathematics of thermal modeling

Dear Prof. Dowden,

I am using your book (The mathematics of thermal modeling) as a reference in my PhD study at Dublin City University. I would be very glad if you would advise me on two issues:

1- I am thermally modeling the process of micro-channel making on the surface of glass sheets using a pulsed CO2 laser. I found the equations in section 4.3 quite useful. Do

you recommend using these equations for estimating the ablated regions (since they do not account for phase changes)? Such an approximation was recommended by (W. W. Duley, Laser processing and analysis of materials, 1983, pp. 119).

>This seems a reasonable thing to do. Of course, to cover yourself in a PhD thesis, you will need to point out that the equations do not account for phase change. If you can give some indication of the error then so much the better. If you can actually give a solution that would be better still, though I think that it is probably not worth the effort. To do it analytically is likely to be hard.

2- During writing up, when I tried to re-calculate equation (4.17) to find the value of (a_n) in the Fourier series, I found a difficulty in getting the same answer provided. My calculation as per the attached document (equation.jpg) shows a difference in the magnitude ($2P_0/n\pi$). I found it to be equal to ($2P_0 t_0/n\pi \tau$). Could you please advise if a different value of $P(t)$ in the integration range was used?

>Very wise of you to check. I seem to have changed my mind while writing out this example, as to how I wanted to define P_0 , and then not made all the changes necessary. (Almost certainly, I began by not including the ratio t_0/τ in 4.16). It shows how dangerous it is to change your mind half way!

I am glad you also noticed that n was missing next to t three times (the rhs of 4.17 and in the integral form of a_n)

This means that t_0/τ needs to be inserted:

-in the final form for a_n following 4.17

-before the two sums in 4.18

-before this sum in 4.19 - although in the last case if I had noticed it at the time I would have written it as $1+1/m$ at this point.

I don't think there are any further changes to the text but presumably figures 4.7-4.10 would look a bit different.

Thanks for pointing it out.

All good wishes - and good luck with the PhD.

John Dowden

Prof. J.M. Dowden

Department of Mathematical Sciences,

University of Essex, Colchester CO4 3SQ, UK.

email: dowdj (non-Essex users should add @essex.ac.uk)

Tel: +44 (0)1206 872958 Fax: +44 (0)1206 873043

Second E-mail:

Dear Prof. Dowden,

Thank you very much for your constructive reply. I have modified equation 4.17 according to your advice. However, I noticed that the results deviate from the initial assumption that ($T \Rightarrow +\infty$ as $r \Rightarrow 0$), i.e. as we move closer to the point source.

I have compared the results in the attached 2 pages file (comparison.doc). I would highly appreciate it if you could have a look at it and advise on the possible reasons of that.

Kind regards,

Ahmed Issa.

Mechanical Engineering Department,
Dublin City University.
Phone: 00353 1700 7674
Fax: 00353 1700 5345
Mobile: 00353 863 987 212

Contents of the attachment <comparison.doc>

Input Parameters:

Material	Lime-soda glass.
P_o	4.8 W
T_o	22 °C
Ux	5×10^{-3} m/s
t_o	4.386×10^{-3} s
τ	1.535×10^{-3} s
κ	8.401×10^{-7} m ² /s
λ	1.37 W/m.°C
Fourier series terms, n	20

The point heat source is in the surface of the sample. Three pulses isotherms were plotted for each case, the original and the modified equation.

1- The original equation:

$$T(x, y, z, t) = T_o + \frac{P_o}{2\pi k r} \exp\left[\frac{U}{2\alpha}(x-r)\right] + \frac{P_o}{\pi^2 k r} \sum_{n=1}^{\infty} \frac{1}{n} \sin \frac{n\pi\tau}{t_o} \exp\left[\frac{U}{2\alpha}(x-r \text{ Sn})\right] \times \cos\left(\frac{2n\pi t}{t_o} - \frac{U r n \text{ Si}}{4 \alpha \text{ Sn}}\right)$$

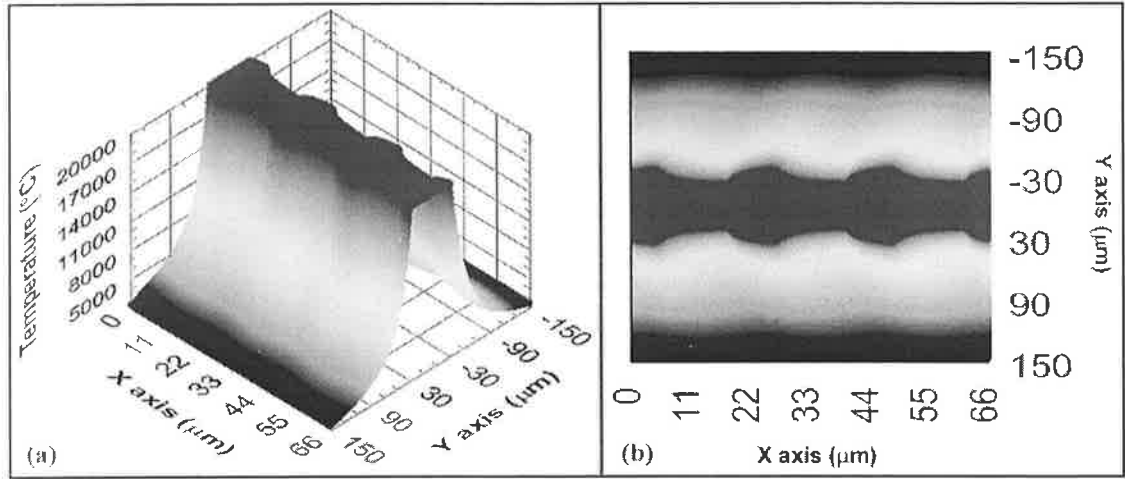


Figure 1: Original equation form. Isotherms of three pulses at $z = 0$
 (a) 3D temperature profile, (b) top view.

NOTES:

The temperatures here, needed to be truncated at 20,000 °C because $T \rightarrow +\infty$ as $y \rightarrow 0$.

The solution here satisfies the condition that temperatures will become infinite as we move closer to the point heat source.

2- The modified equation:

The term (t_0/τ) was added to the left of the series sum.

$$T(x, y, z, t) = T_o + \frac{P_o}{2\pi k r} \exp\left[\frac{U}{2\alpha}(x-r)\right] +$$

$$+ \frac{P_o \cdot t_o}{\pi^2 k r \cdot \tau} \sum_{n=1}^{\infty} \frac{1}{n} \sin \frac{n\pi\tau}{t_o} \exp\left[\frac{U}{2\alpha}(x-r \text{ Sn})\right] \times$$

$$\times \cos\left(\frac{2n\pi t}{t_o} - \frac{U r n \text{ Si}}{4 \alpha \text{ Sn}}\right)$$

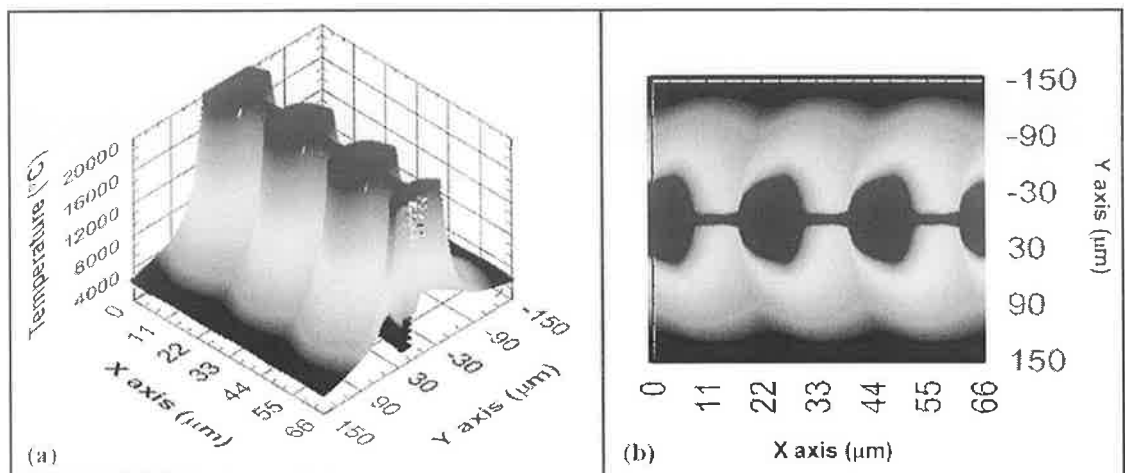


Figure 2: Modified equation form. Isotherms of three pulses at $z = 0$
 (a) 3D temperature profile, (b) top view.

NOTES:

The magnitudes of the temperatures isotherms are, approximately, the same as in figure (1) with a difference in their geometry. However, the temperatures here, needed to be truncated at 0 and 20,000 °C because $T \rightarrow \pm \infty$ as $y \rightarrow 0$.

It is noticed that the term (t_0/τ) has increased the magnitude of the series sum (which was negative for exactly 50% of the calculated temperatures). A small value of (r) in the denominator to the right of the series sum (imposed by $y \rightarrow 0$) caused a big drop in the temperature at certain points in time. This can be seen in the middle of the 3D view (figure 2).

According to the initial conditions and assumptions, the temperature should tend to $+\infty$ as y tends to 0.

Reply to the second e-mail:

Dear Ahmed,

I see that you are attempting to sum the series as $y \rightarrow 0$ with $z=0$ identically. I only did it for $z=0.1$. (Much safer!!) When $x < 0$, the series is absolutely convergent and the solution does not tend to infinity as $y \rightarrow 0$. Indeed I would not expect it to. There is however a problem in what you are doing. The series converges because of the exponential term; the exponent behaves roughly like a negative multiple of n for sufficiently large n . Unfortunately, this does not come into play until the value of n is really rather large in these circumstances. I would guess that your programme not only does not take enough terms but is probably also not capable of working to a sufficient number of decimal places to detect the effect. Don't forget the dangers of rounding errors. The problem gets bigger and bigger the closer you are to $x=0$.

[Compare with the formally quite different but qualitatively similar example of $1 - 1/2 + 1/3 - 1/4 \dots$ which sums to $\ln(2)$. Formally this is quite different because it is not absolutely convergent, but if you try to sum it numerically you will have great difficulty getting an answer plausibly near $\ln(2)$, and there is a qualitative similarity with what you are attempting.] In our example the early terms can be quite large but tend to cancel each other out without giving any clear indication of the ultimate value of the limit. It's a situation which easily leads to error.

The presence or otherwise of the factor t_0/τ makes no difference to these qualitative remarks.

(Your figure 1 looks rather like my fig 4.7 but it is of course a completely different situation. In your case the picture should taper gradually to the right. It's not apparent, but that is probably because you haven't calculated any further downstream.)

Good wishes,

John Dowden

Third e-mail:

Dear Prof. Dowden,

Thank you for the explanations, I think that the model now works as expected. I was calculating the temperatures by changing (y) and keeping a fixed value of (x). But now the calculation starts at $(x = a)$ and then $(x = U*t + a)$ which means that (r) changes with time. This seems to make the solution converge even at $z=0$.

I would like to know if you used the same method for fig 4.7 and 4.8, or $(x' = 0)$ was fixed throughout the calculation?

Kind regards,

Ahmed Issa.

Mechanical Engineering Department,
Dublin City University.
Phone: 00353 1700 7674
Fax: 00353 1700 5345
Mobile: 00353 863 987 212

Reply to third e-mail:

My figures are both for a fixed zero value of x, but I was trying to demonstrate something rather different from what I think interests you.

Good wishes,

John Dowden.

E.2: Modelling of the point heat source

The heat conduction equation for the problem is

$$\frac{\partial T}{\partial t} + U \frac{\partial T}{\partial x} = \alpha \left(\frac{\partial^2 T}{\partial x^2} + \frac{\partial^2 T}{\partial y^2} + \frac{\partial^2 T}{\partial z^2} \right) \quad (1)$$

where, α (m^2/s) is the thermal diffusivity of the material $= k/\rho \cdot c_p$, ρ (kg/m^3), c_p ($\text{J}/\text{kg}\cdot^\circ\text{C}$), k ($\text{W}/\text{m}\cdot^\circ\text{C}$) are the density, heat capacity and thermal conductivity of the material respectively.

If the power source can be expressed in terms of a Fourier series then the solution of equation (1) takes the form [179]

$$\text{Re} \left\{ \exp \left(i\omega t + \frac{Ux}{2\alpha} \right) S(r) \right\} \quad (2)$$

where $r = \sqrt{x^2 + y^2 + z^2}$. Substitution of (2) into the (1) and using the chain rule shows that S must satisfy

$$\left(i\omega + \frac{U^2}{4\alpha} \right) S = \frac{\alpha}{r} \frac{d^2}{dr^2} (rS)$$

The appropriate solution that tends to zero as r tends to infinity in all directions is

$$\frac{A}{r} \exp \left\{ i\omega t - \frac{Ur}{2\alpha} \sqrt{1 + \frac{4\alpha\omega i}{U^2}} \right\} \quad (3)$$

The square root must be the one with the real positive part. The previous steps are used in [179] to prove the form similarity between the steady state (time-independent) and transient (time-dependent) solutions. The multiple A is dependant on the heat source. The following calculations are depicted from the point heat source calculations for a time-independent temperature model [179]. However, the conclusions are the same for the transient model we are after here. The form of the time-independent solution for temperature model is similar to equation (3) except for the exponent terms

$$\frac{A}{r} \exp \left\{ \frac{Ur}{2\alpha} (x - r) \right\} \quad (\text{form of time-independent solution used in calculations of } A)$$

A point heat source inside the sample and at the origin as shown in figure 1 is considered (in our case it is on the surface, this will be treated later). The source is resembled by a small sphere Σ of radius a centered at the origin. The calculation of the heat flux output should be modelled then. The energy flow into the sphere boundaries is equal to the energy flowing out. The only contribution to the flux is then the portion due to Fourier's law.

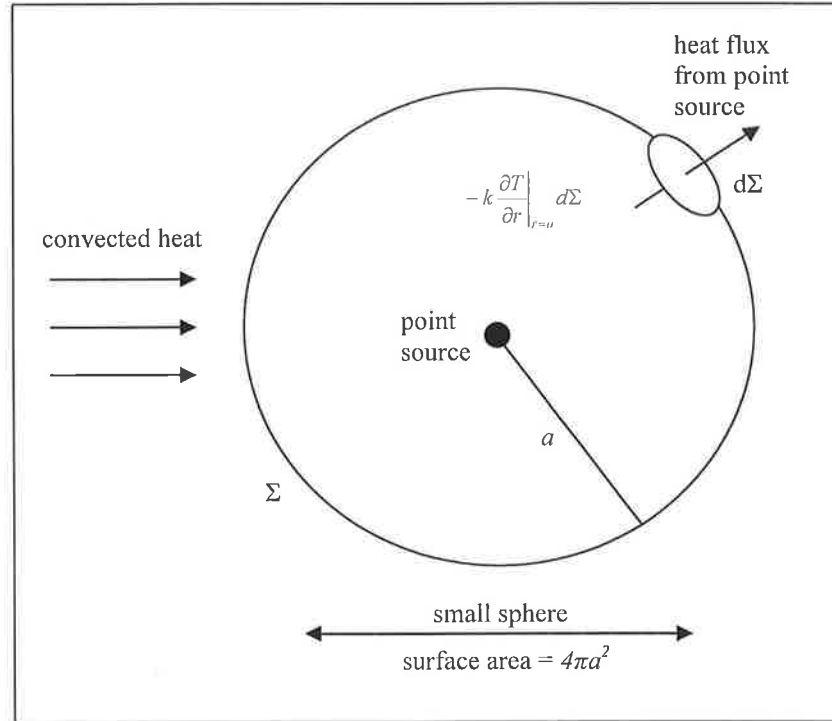


Figure 1: Flux of heat from a sphere representing a point heat source.

The Fourier portions have to be summed over the surface of the sphere, which will give the total power flowing across the surface from

$$P = \frac{1}{2} \int_{\Sigma} \left(-k \frac{\partial T}{\partial r} \right) d\Sigma = -\frac{1}{2} kA \int_{\Sigma} \frac{\partial}{\partial r} \left\{ \frac{1}{r} \exp \left[\frac{U}{2\alpha} (x-r) \right] \right\} d\Sigma$$

The $\frac{1}{2}$ multiplier is because only half of the sphere is needed if the point heat source is on the surface (suitable for this case). If the polar coordinate substitution $x = r \cos \theta$ is used then

$$P = \frac{1}{2} \int_{\Sigma} \left(-k \frac{\partial T}{\partial r} \right) d\Sigma = -\frac{1}{2} kA \int_{\Sigma} \frac{\partial}{\partial r} \left\{ \frac{1}{r} \exp \left[\frac{Ur}{2\alpha} (\cos \theta - 1) \right] \right\} d\Sigma$$

After differentiation, r can be set equal to a and the equation becomes

$$P = \frac{1}{2} kA \int_{\Sigma} \left\{ \frac{1}{a^2} \exp \left[\frac{Ua}{2\alpha} (\cos \theta - 1) \right] + O \left(\frac{1}{a} \right) \right\} d\Sigma$$

The notation $O(1/a)$ means that these terms are only as big as $1/a$ if a is small and hence can be neglected. Also the exponent term in the equation progressively approaches zero as a becomes smaller and smaller. The integral becomes

$$P = \frac{1}{2} kA \int_{\Sigma} \frac{1}{a^2} d\Sigma$$

$1/a^2$ is a constant on the surface of the half sphere. So the value of the integral is simply the surface area of the sphere, $4\pi a^2$ and the equation becomes

$$P = \frac{1}{2} kA \frac{1}{a^2} 4\pi a^2 = 2\pi kA$$

giving, $A = \frac{P}{2\pi k}$

So the solution for the equation takes this form

$$\frac{P}{2\pi k r} \exp \left\{ i\omega t - \frac{U}{2\alpha} \left(x - r \sqrt{1 + \frac{4\alpha\omega i}{U^2}} \right) \right\} \quad (4)$$

where $\omega = 2\pi/t_0$ is the radial frequency of the laser pulses. Now it is just a matter of taking the real parts of the exponent with the initial conditions of temperature $T = T_0$ at $t = 0$ and it is also the case as t tends to infinity after the heat source is terminated. It should also be noted that $T = T_0$ as well when r increases to infinity in all directions. These conditions were explained in the thesis (page 178). Equation (4) with the initial and boundary conditions gives

$$T(x, y, z, t) = T_0 + \frac{P(t)}{2\pi k r} \exp \left[i\omega t + \frac{U}{2\alpha} \left(x - r \sqrt{1 + \frac{4\alpha\omega i}{U^2}} \right) \right] \quad (5)$$

Which is the same as equation (5.3) in the thermal mathematical model chapter.

E.3 3D simulated channel profiles

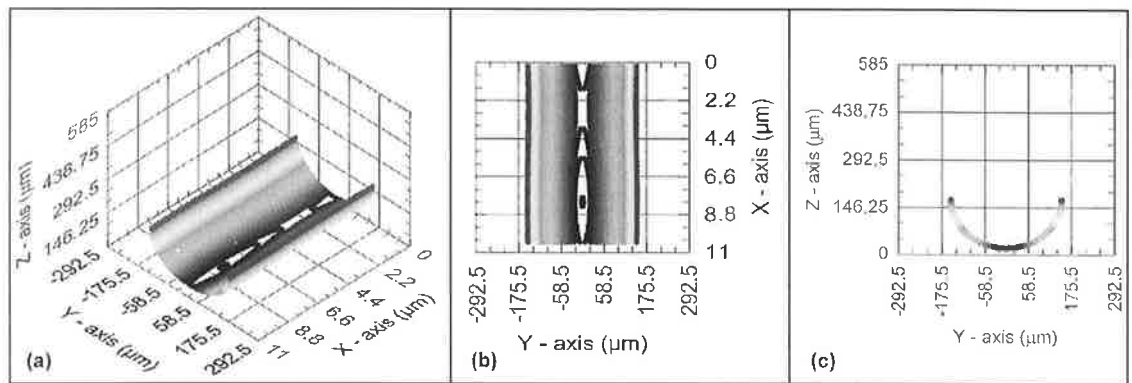


Figure 1: simulation of channel 1, (a) isometric, (b) top and (c) from views.

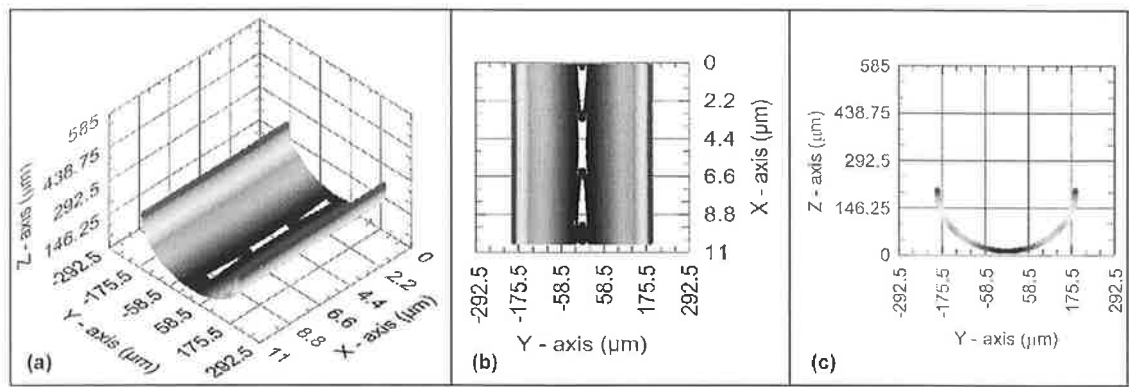


Figure 2: simulation of channel 2, (a) isometric, (b) top and (c) from views.

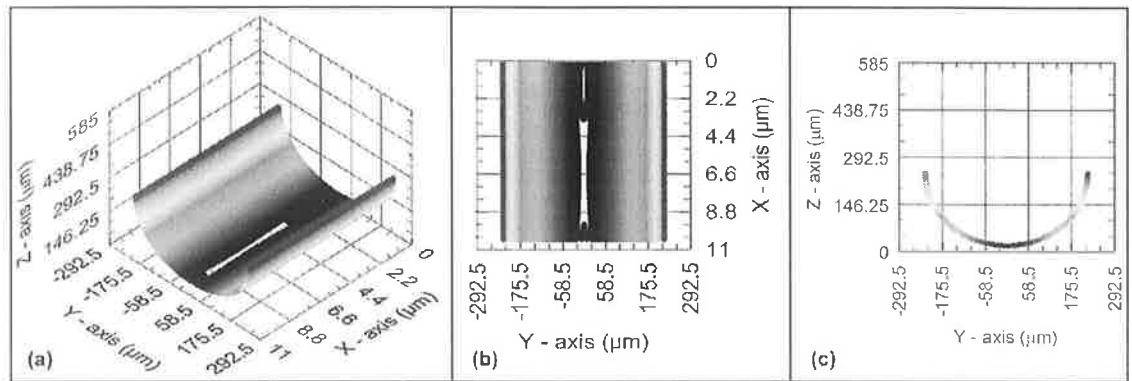


Figure 3: simulation of channel 3, (a) isometric, (b) top and (c) from views.

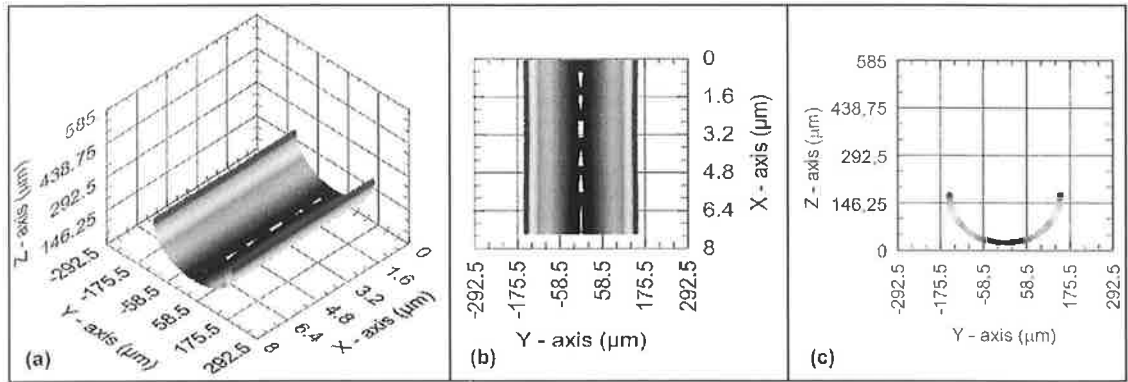


Figure 4: simulation of channel 4, (a) isometric, (b) top and (c) from views.

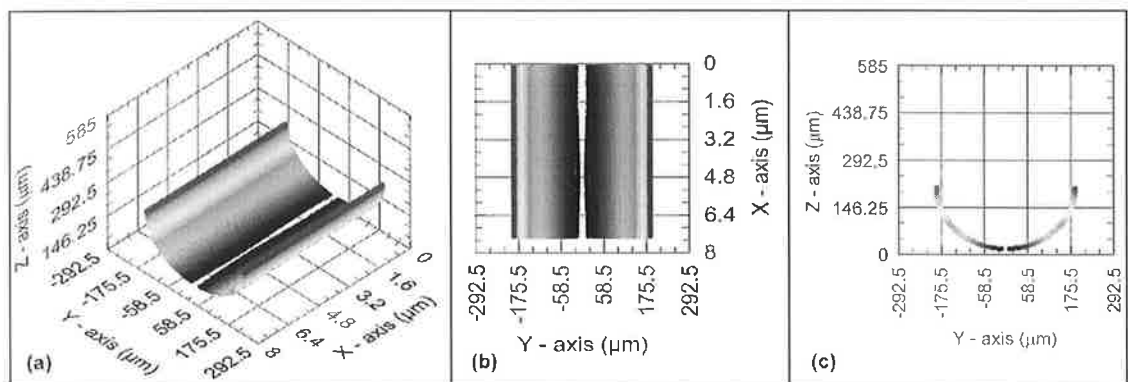


Figure 5: simulation of channel 5, (a) isometric, (b) top and (c) from views.

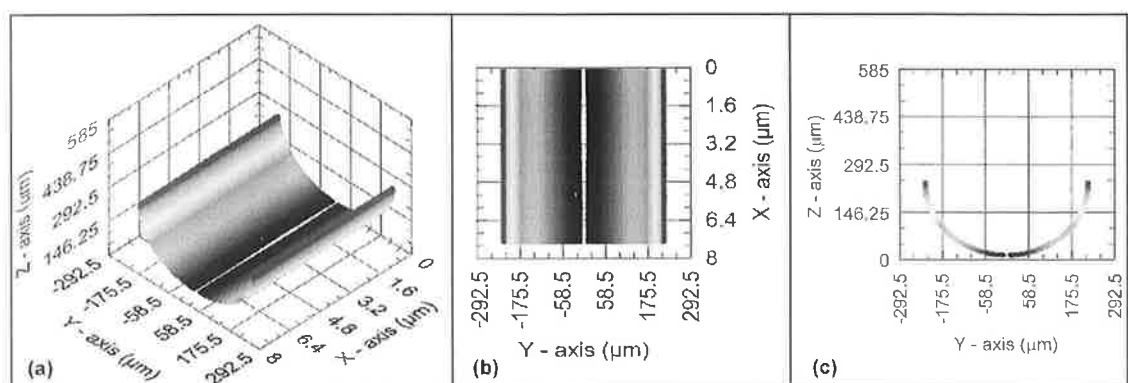


Figure 6: simulation of channel 6, (a) isometric, (b) top and (c) from views.

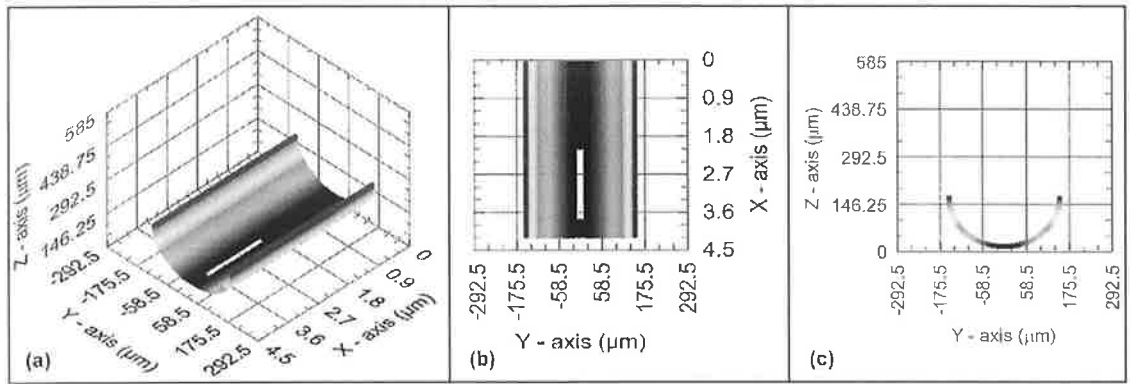


Figure 7: simulation of channel 7, (a) isometric, (b) top and (c) from views.

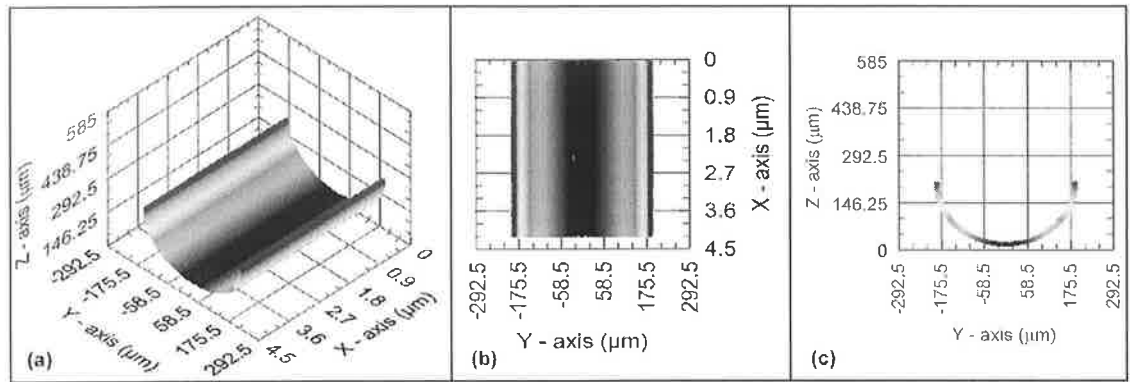


Figure 8: simulation of channel 8, (a) isometric, (b) top and (c) from views.

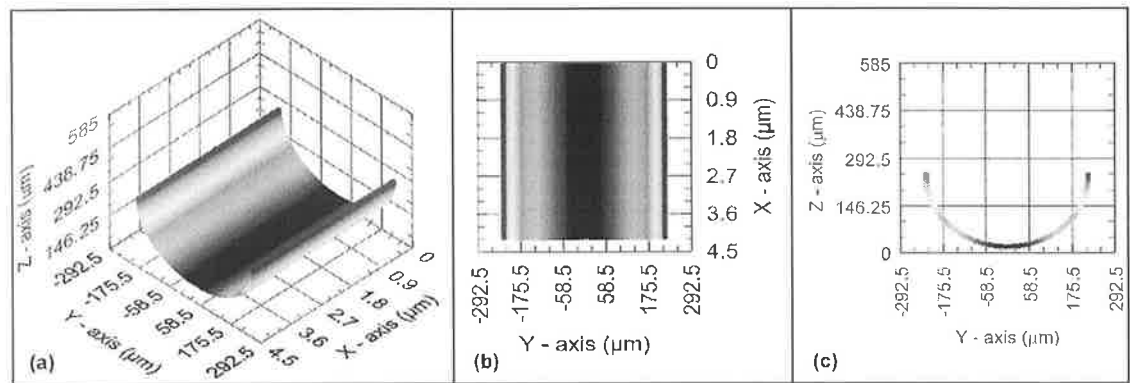


Figure 9: simulation of channel 9, (a) isometric, (b) top and (c) from views.

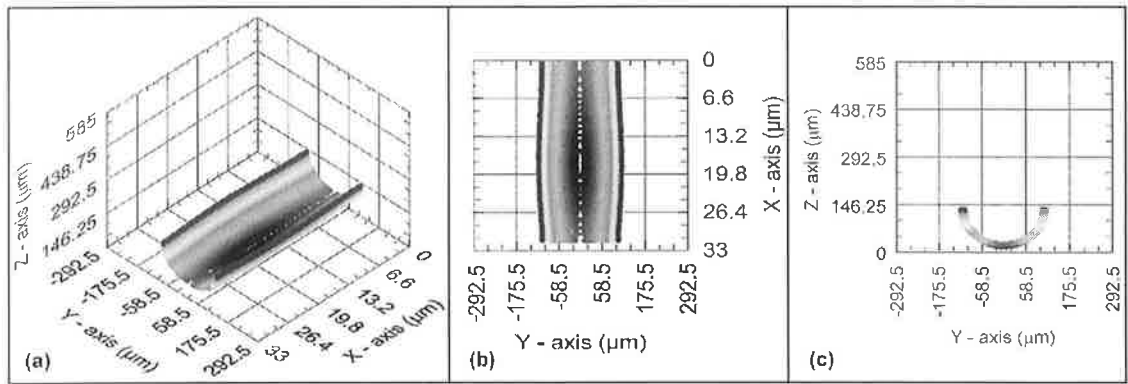


Figure 10: simulation of channel 10, (a) isometric, (b) top and (c) from views.

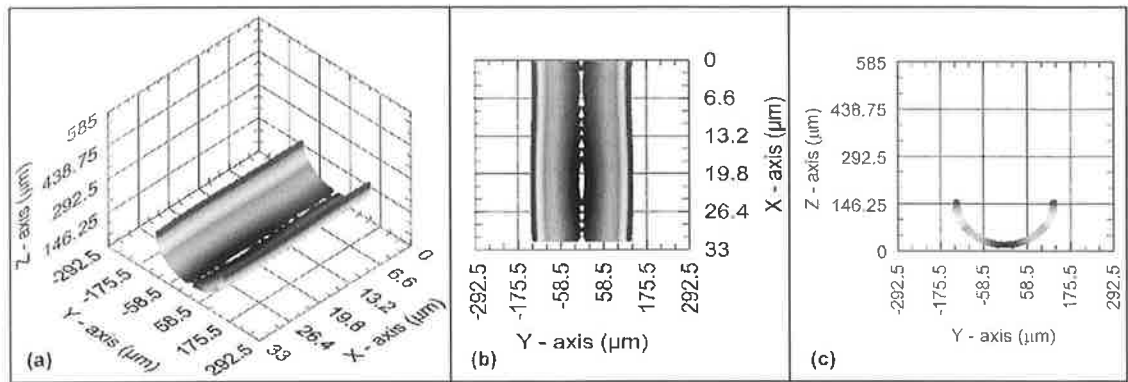


Figure 11: simulation of channel 11, (a) isometric, (b) top and (c) from views.

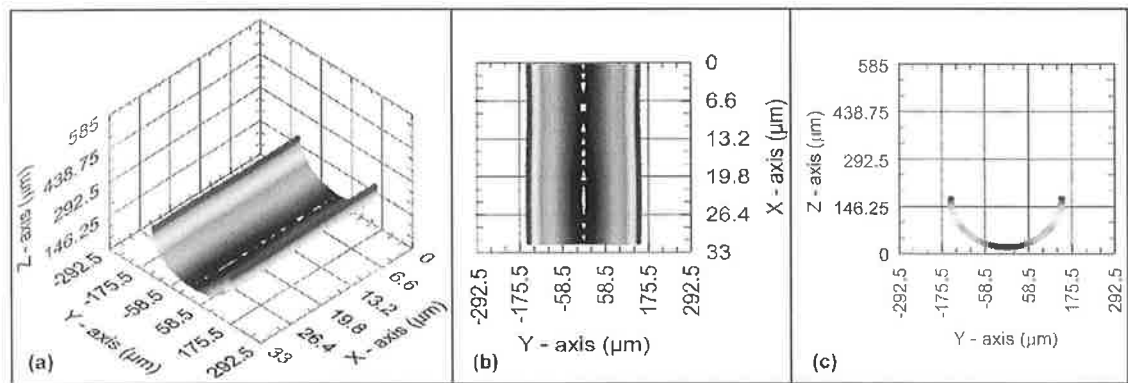


Figure 12: simulation of channel 12, (a) isometric, (b) top and (c) from views.

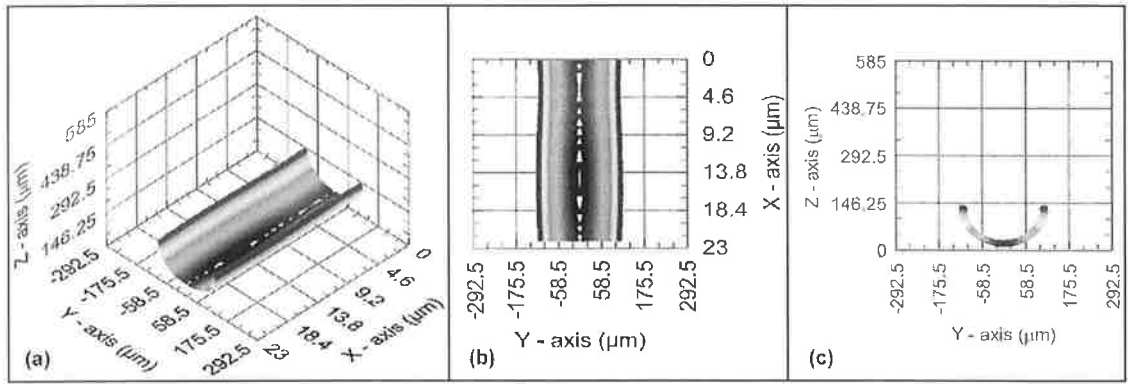


Figure 13: simulation of channel 13, (a) isometric, (b) top and (c) from views.

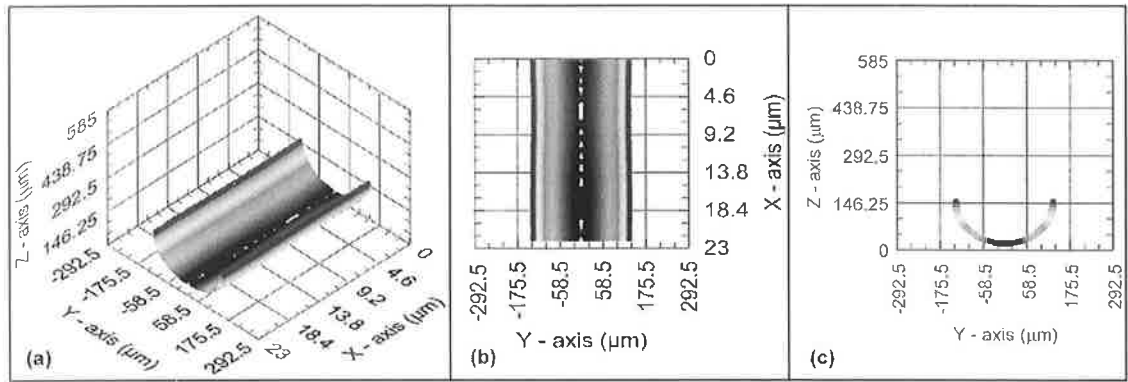


Figure 14: simulation of channel 14, (a) isometric, (b) top and (c) from views.

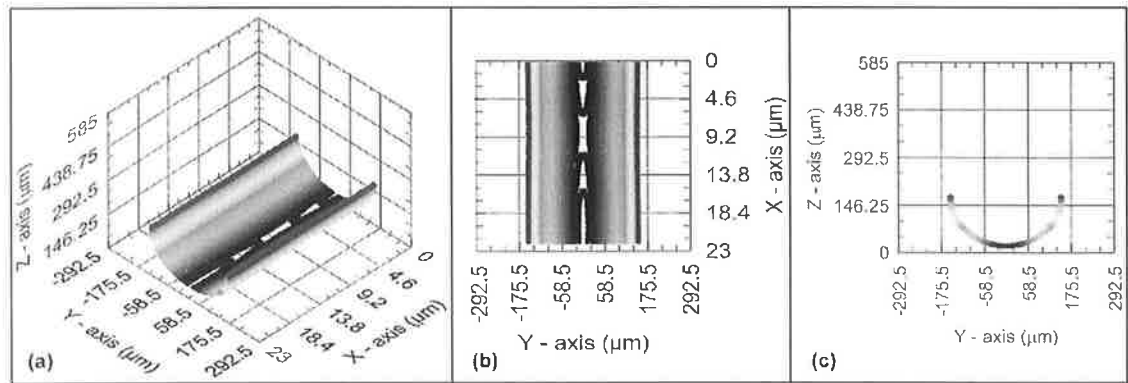


Figure 15: simulation of channel 15, (a) isometric, (b) top and (c) from views.

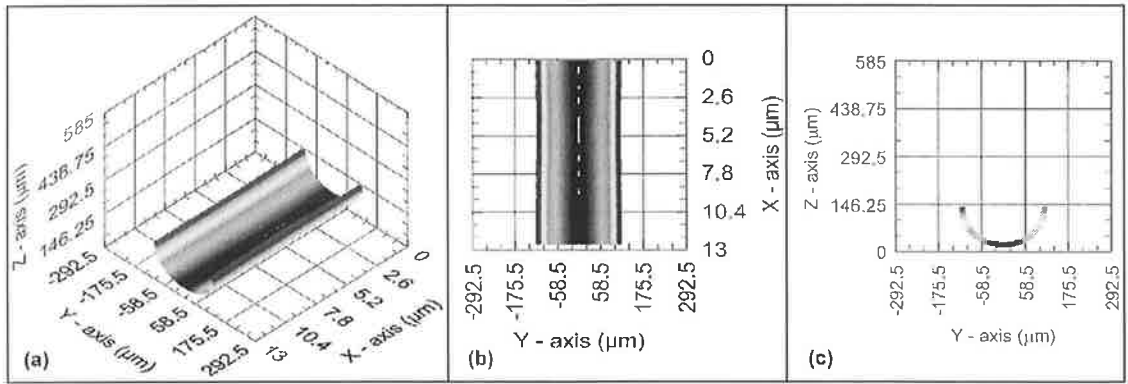


Figure 16: simulation of channel 16, (a) isometric, (b) top and (c) from views.

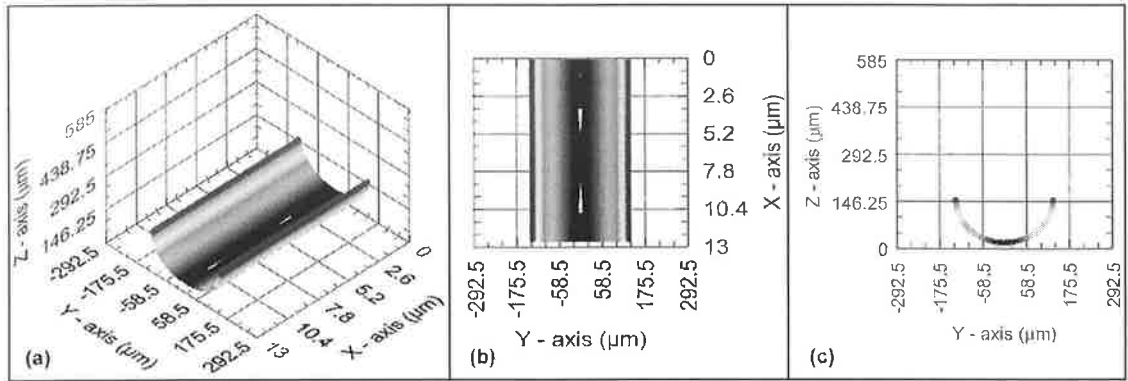


Figure 17: simulation of channel 17, (a) isometric, (b) top and (c) from views.

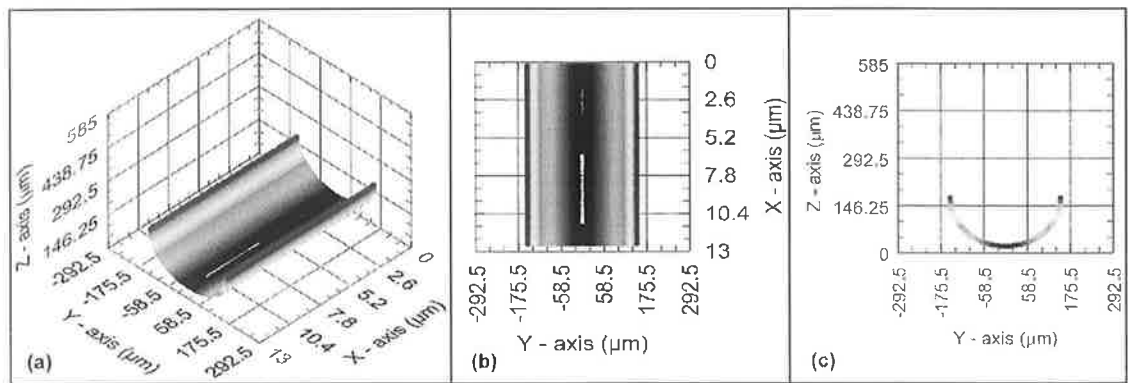


Figure 18: simulation of channel 18, (a) isometric, (b) top and (c) from views.

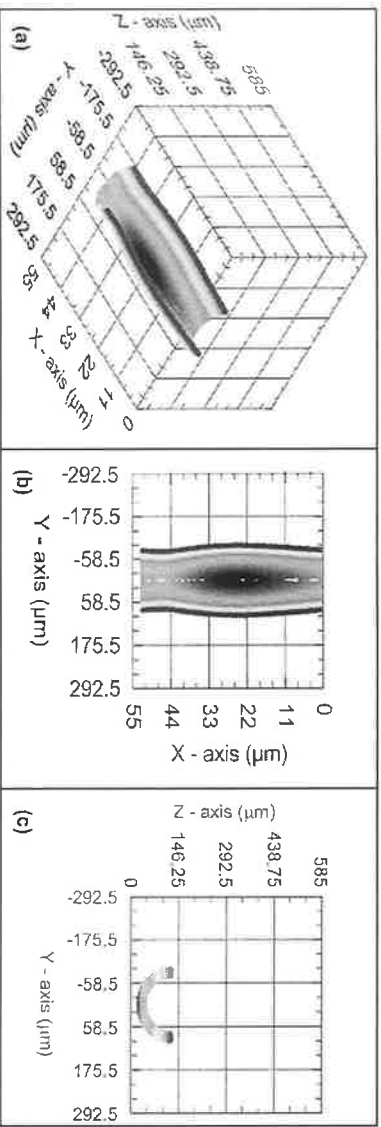


Figure 19: simulation of channel 19, (a) isometric, (b) top and (c) from views.

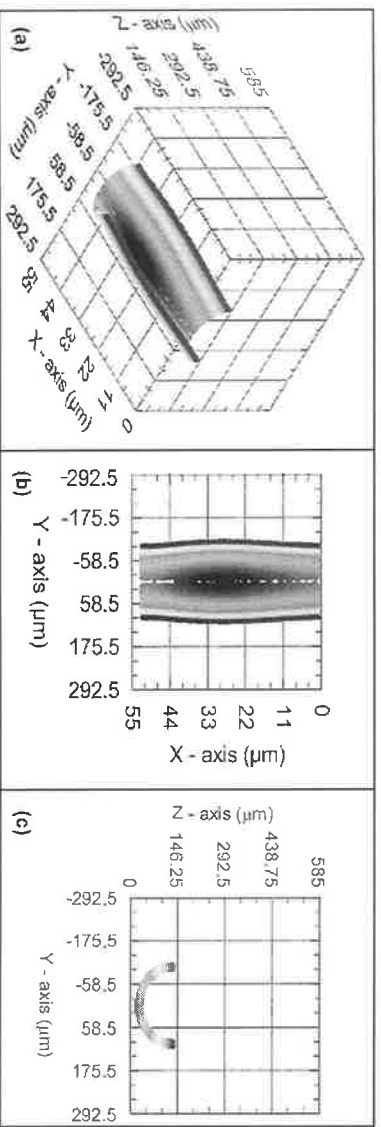


Figure 20: simulation of channel 20, (a) isometric, (b) top and (c) from views.

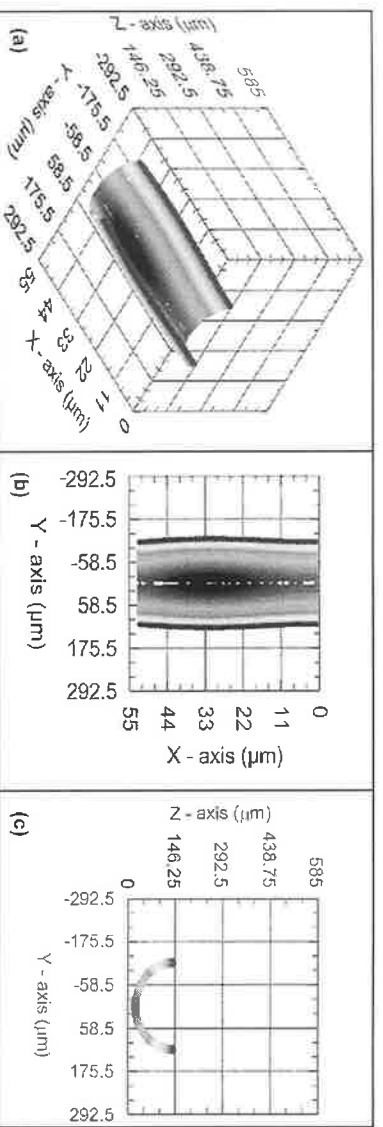


Figure 21: simulation of channel 21, (a) isometric, (b) top and (c) from views.

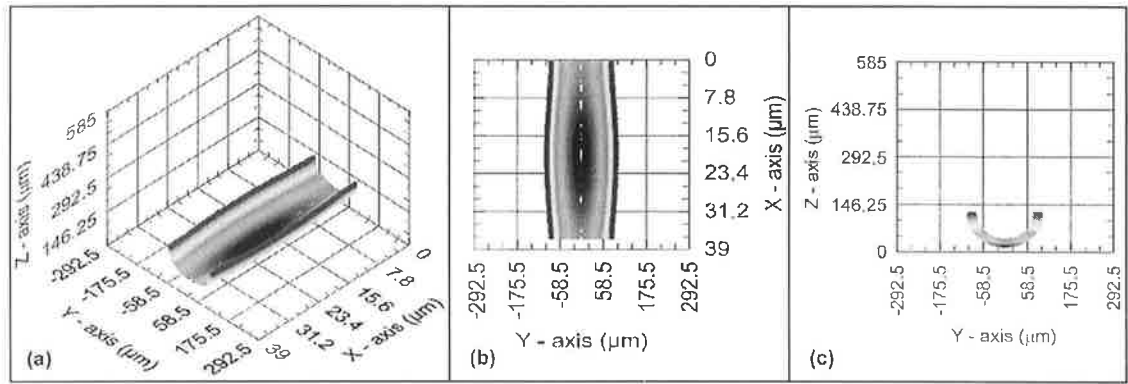


Figure 22: simulation of channel 22, (a) isometric, (b) top and (c) from views.

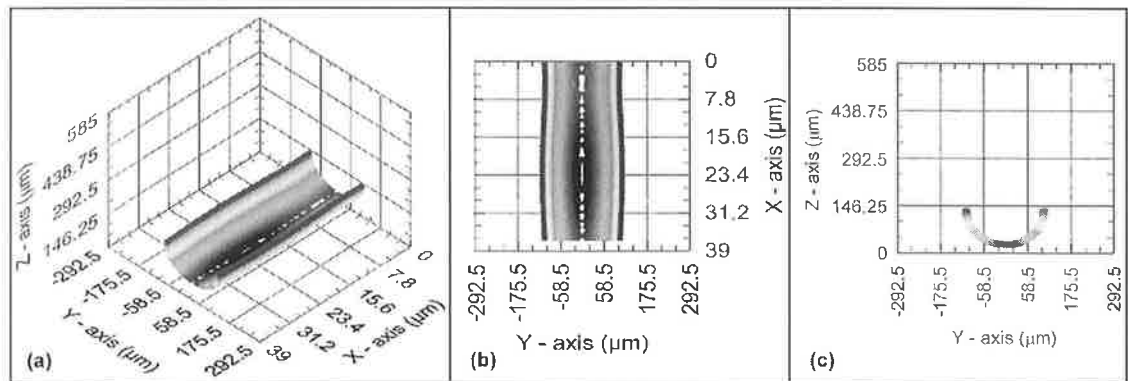


Figure 23: simulation of channel 23, (a) isometric, (b) top and (c) from views.

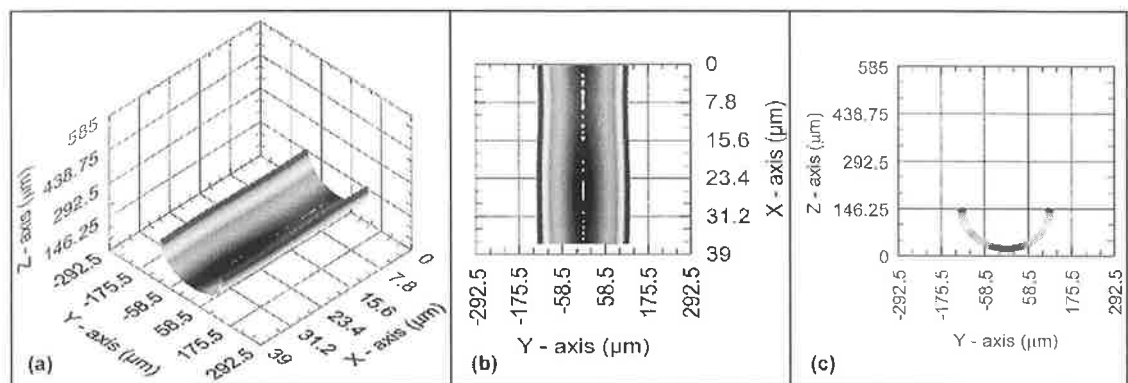


Figure 24: simulation of channel 24, (a) isometric, (b) top and (c) from views.

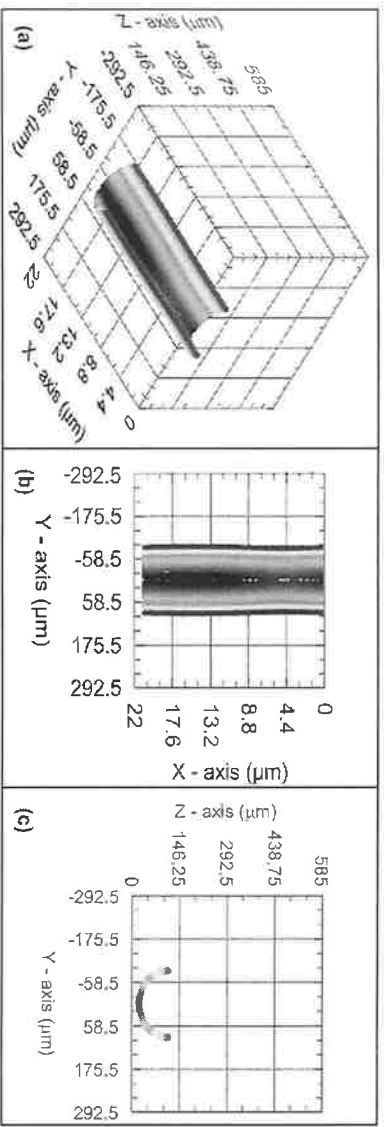


Figure 25: simulation of channel 25, (a) isometric, (b) top and (c) from views.

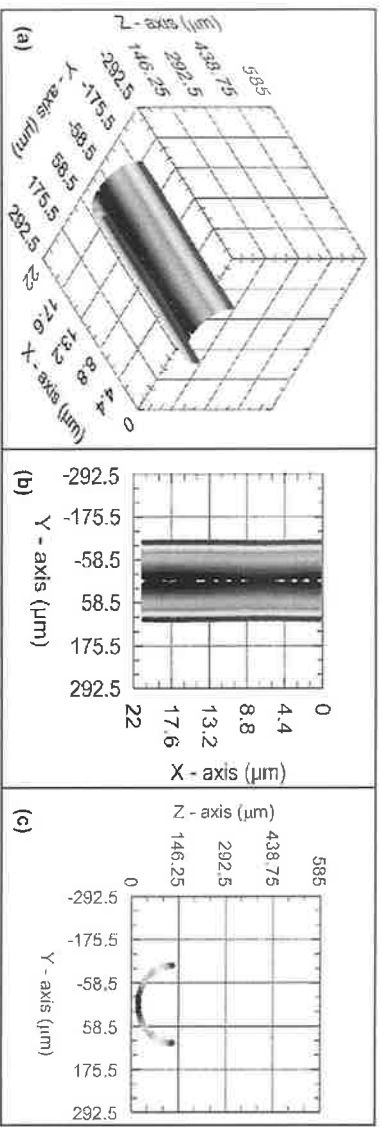


Figure 26: simulation of channel 26, (a) isometric, (b) top and (c) from views.

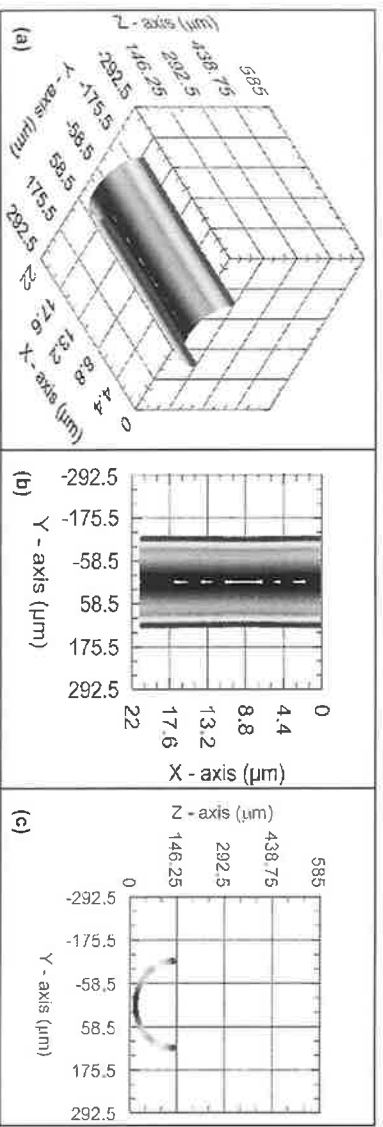


Figure 27: simulation of channel 27, (a) isometric, (b) top and (c) from views.

E.4 Numerical results from simulations

Table E.1: Dimensional parameters of simulated channels.

CH No.	P (W)	PRF (Hz)	U (mm/min)	Width (μm)	Depth (μm)
1	18	160	100	303.02	151.7
2	24	160	100	375.72	187.44
3	30	160	100	442.42	221.68
4	18	228	100	299.02	150.7
5	24	228	100	375.56	187.44
6	30	228	100	441.72	221.3
7	18	400	100	299	150.2
8	24	400	100	373.72	187.78
9	30	400	100	441.72	221.58
10	18	160	300	227.72	113.78
11	24	160	300	265.12	132.78
12	30	160	300	299.12	151.3
13	18	228	300	224.56	111.48
14	24	228	300	265.9	132.98
15	30	228	300	301.02	150.3
16	18	400	300	221.72	110.8
17	24	400	300	263.9	131.88
18	30	400	300	299.12	144.48
19	18	160	500	192.1	96.2
20	24	160	500	220.06	108.5
21	30	160	500	242.82	121.2
22	18	228	500	188.06	94
23	24	228	500	217.1	108.38
24	30	228	500	236.56	118.5
25	18	400	500	180.52	89.48
26	24	400	500	210.42	105.5
27	30	400	500	236.82	118.5

Table E.2: Ra values calculated from the simulated channels.

CH No.	Ra sides	Ra centre	Ra (μm)	Rq sides	Rq centre	Rq (μm)	Rku sides	Rku centre	Rku (μm)	Rsk sides	Rsk centre	Rsk (μm)
1	1.036	1.473	1.18	1.205	1.716	1.38	2.133	2.124	2.13	-0.099	-0.120	-0.11
2	0.661	0.645	0.66	0.874	0.849	0.87	2.493	2.470	2.49	0.103	0.075	0.09
3	0.676	0.500	0.62	0.690	0.510	0.63	1.120	1.120	1.12	0.310	0.310	0.31
4	1.194	0.761	1.05	1.373	0.874	1.21	1.883	1.919	1.90	-0.153	-0.193	-0.17
5	0.000	0.000	0.00	0.000	0.000	0.00	0.000	0.000	0.00	0.000	0.000	0.00
6	0.000	0.000	0.00	0.000	0.000	0.00	0.000	0.000	0.00	0.000	0.000	0.00
7	0.671	0.604	0.65	0.685	0.616	0.66	1.159	1.159	1.16	-0.366	-0.366	-0.37
8	0.000	0.000	0.00	0.000	0.000	0.00	0.000	0.000	0.00	0.000	0.000	0.00
9	0.000	0.000	0.00	0.000	0.000	0.00	0.000	0.000	0.00	0.000	0.000	0.00
10	5.348	4.204	4.97	5.983	4.706	5.56	1.564	1.603	1.58	-0.121	-0.209	-0.15
11	2.958	2.626	2.85	3.280	2.917	3.16	1.458	1.464	1.46	-0.097	-0.132	-0.11
12	2.578	1.705	2.29	2.875	1.907	2.55	1.511	1.524	1.52	-0.001	-0.048	-0.02
13	2.746	2.825	2.77	3.051	3.142	3.08	1.552	1.564	1.56	-0.177	-0.209	-0.19
14	2.500	1.465	2.16	2.851	1.674	2.46	1.655	1.682	1.66	-0.096	-0.163	-0.12
15	0.888	0.981	0.92	1.044	1.157	1.08	1.838	1.853	1.84	-0.308	-0.322	-0.31
16	1.815	0.846	1.49	2.033	0.951	1.67	1.639	1.677	1.65	-0.222	-0.276	-0.24
17	0.668	0.387	0.57	0.686	0.398	0.59	1.169	1.169	1.17	0.379	0.379	0.38
18	0.662	0.318	0.55	0.680	0.326	0.56	1.216	1.216	1.22	-0.437	-0.437	-0.44
19	11.060	7.229	9.78	12.540	8.229	11.10	1.645	1.736	1.68	-0.074	-0.339	-0.16
20	8.420	5.311	7.38	9.486	5.968	8.31	1.604	1.620	1.61	-0.020	-0.236	-0.09
21	7.776	4.076	6.54	8.714	4.543	7.32	1.575	1.556	1.57	0.074	-0.161	0.00
22	7.931	5.228	7.03	8.910	5.911	7.91	1.602	1.708	1.64	-0.207	-0.366	-0.26
23	3.550	3.570	3.56	3.978	4.004	3.99	1.593	1.618	1.60	-0.240	-0.285	-0.26
24	4.704	2.564	3.99	5.172	2.826	4.39	1.496	1.544	1.51	-0.163	-0.257	-0.19
25	4.298	1.994	3.53	4.776	2.224	3.93	1.592	1.661	1.62	-0.181	-0.303	-0.22
26	1.956	1.034	1.65	2.193	1.162	1.85	1.487	1.493	1.49	-0.072	-0.114	-0.09
27	1.355	0.732	1.15	1.533	0.827	1.30	1.710	1.720	1.71	-0.126	-0.167	-0.14

Table E.3: Comparison between simulation and experimental results

Simulation / Process parameters					Simulation dimensional results				Experimental dimensional results				% difference		
CH No.	P (W)	PRF (Hz)	U (mm/min)		Width (μm)	Depth (μm)	Ra (μm)		Width (μm)	Depth (μm)	Ra (μm)		% Width	% Depth	% Ra
1	18	160	100		303	152	1		315	213	7		-4.036	-40.41	-515.21
2	24	160	100		376	187	1		320	279	6		14.88	-48.67	-743.6
3	30	160	100		442	222	1		365	379	13		17.58	-71.12	-2018.18
4	18	228	100		299	151	1		248	120	5		17.18	20.15	-378.88
5	24	228	100		376	187	0		271	225	2		27.83	-19.86	NA
6	30	228	100		442	221	0		332	320	12		24.95	-44.44	NA
7	18	400	100		299	150	1		163	26	11		45.65	82.47	-1606.27
8	24	400	100		374	188	0		213	120	3		43.13	36.27	NA
9	30	400	100		442	222	0		327	256	6		25.98	-15.46	NA
10	18	160	300		228	114	5		308	135	2		-35.30	-18.21	55.99
11	24	160	300		265	133	3		324	202	5		-22.10	-51.76	-84.00
12	30	160	300		299	151	2		351	296	5		-17.34	-95.86	-115.45
13	18	228	300		225	111	3		231	45	4		-2.76	59.78	-53.43
14	24	228	300		266	133	2		267	148	4		-0.47	-11.17	-108.6
15	30	228	300		301	150	1		316	248	3		-4.94	-65.26	-183.85
16	18	400	300		222	111	1		118	13	7		46.78	88.27	-398.24
17	24	400	300		264	132	1		209	48	3		20.69	63.73	-418.14
18	30	400	300		299	144	1		308	142	4		-3.00	2.06	-541.95
19	18	160	500		192	96	10		302	74	3		-57.34	23.25	67.69
20	24	160	500		220	109	7		314	130	3		-42.67	-19.97	54.72
21	30	160	500		243	121	7		345	227	5		-42.14	-87.43	30.58
22	18	228	500		188	94	7		222	21	2		-18.21	78.01	66.50
23	24	228	500		217	108	4		267	89	4		-23.05	17.62	-7.29
24	30	228	500		237	119	4		310	166	6		-31.07	-39.66	-51.20
25	18	400	500		181	89	4		81	3	11		55.13	96.65	-225.69
26	24	400	500		210	106	2		187	30	2		11.04	71.41	-18.10
27	30	400	500		237	119	1		300	88	4		-26.53	25.46	-279.56

Appendix F – Extra Results from Chapter 6

F.1 Ablation rates results and their relation to the process parameters

Table F.1: Direct process control parameters and measured dimensional responses.

Scan ID	DoE ID	P (W)	PRF (Hz)	U (mm/min)	W_T , Average Width (μm)	d , Average Depth (μm)	Average Ra (μm)	W_B , Bottom Width (μm)
34	1	18	160	100	315	213	7.27	25
35	2	24	160	100	320	279	5.53	14
36	3	30	160	100	365	379	13.08	22
31	4	18	228	100	248	120	5.03	62
32	5	24	228	100	271	225	2.12	20
33	6	30	228	100	332	320	12.31	27
28	7	18	400	100	163	26	11.07	0
29	8	24	400	100	213	120	2.84	39
30	9	30	400	100	327	256	6.16	12
43	10	18	160	300	308	135	2.19	39
44	11	24	160	300	324	202	5.24	53
45	12	30	160	300	351	296	4.93	27
40	13	18	228	300	231	45	4.25	43
41	14	24	228	300	267	148	4.50	27
42	15	30	228	300	316	248	2.61	37
37	16	18	400	300	118	13	7.43	0
38	17	24	400	300	209	48	2.98	39
39	18	30	400	300	308	142	3.51	51
52	19	18	160	500	302	74	3.16	45
53	20	24	160	500	314	130	3.34	61
54	21	30	160	500	345	227	4.54	82
49	22	18	228	500	222	21	2.36	45
50	23	24	228	500	267	89	3.82	41
51	24	30	228	500	310	166	6.03	59
46	25	18	400	500	81	3	11.50	0
47	26	24	400	500	187	30	1.95	35
48	27	30	400	500	300	88	4.35	43
82	28	24	228	300	265	138	5.50	29
83	29	24	228	300	263	147	4.92	25
84	30	24	228	300	263	151	6.01	31
85	31	24	228	300	269	141	6.81	39
87	32	24	228	300	270	151	5.14	43

Table F.2: Indirect process control parameters and calculated dimensional responses.

Scan ID	DoE ID	I , Intensity (kW/cm ²)	E_p , Pulse Energy (mJ)	F , Fluence/pulse (kJ/cm ²)	F_{th} , Pulse Fluence/m (J/cm)	ρ , Density (g/ μ m ³)	l , Length (μ m)	N , No. of pulses	A , side area (μ m ²)
34	1	282.94	112.50	1.77	108	2.5E-12	15000	1440	3.62E+04
35	2	377.26	150.00	2.36	144	2.5E-12	15000	1440	4.65E+04
36	3	471.57	187.50	2.95	180	2.5E-12	15000	1440	7.33E+04
31	4	282.94	78.95	1.24	108	2.5E-12	15000	2052	1.86E+04
32	5	377.26	105.26	1.65	144	2.5E-12	15000	2052	3.27E+04
33	6	471.57	131.58	2.07	180	2.5E-12	15000	2052	5.73E+04
28	7	282.94	45.00	0.71	108	2.5E-12	15000	3600	2.14E+03
29	8	377.26	60.00	0.94	144	2.5E-12	15000	3600	1.51E+04
30	9	471.57	75.00	1.18	180	2.5E-12	15000	3600	4.34E+04
43	10	282.94	112.50	1.77	36	2.5E-12	15000	480	2.33E+04
44	11	377.26	150.00	2.36	48	2.5E-12	15000	480	3.80E+04
45	12	471.57	187.50	2.95	60	2.5E-12	15000	480	5.60E+04
40	13	282.94	78.95	1.24	36	2.5E-12	15000	684	6.14E+03
41	14	377.26	105.26	1.65	48	2.5E-12	15000	684	2.17E+04
42	15	471.57	131.58	2.07	60	2.5E-12	15000	684	4.38E+04
37	16	282.94	45.00	0.71	36	2.5E-12	15000	1200	7.67E+02
38	17	377.26	60.00	0.94	48	2.5E-12	15000	1200	5.94E+03
39	18	471.57	75.00	1.18	60	2.5E-12	15000	1200	2.54E+04
52	19	282.94	112.50	1.77	21.6	2.5E-12	15000	288	1.28E+04
53	20	377.26	150.00	2.36	28.8	2.5E-12	15000	288	2.44E+04
54	21	471.57	187.50	2.95	36	2.5E-12	15000	288	4.85E+04
49	22	282.94	78.95	1.24	21.6	2.5E-12	15000	410.4	2.76E+03
50	23	377.26	105.26	1.65	28.8	2.5E-12	15000	410.4	1.38E+04
51	24	471.57	131.58	2.07	36	2.5E-12	15000	410.4	3.05E+04
46	25	282.94	45.00	0.71	21.6	2.5E-12	15000	720	1.22E+02
47	26	377.26	60.00	0.94	28.8	2.5E-12	15000	720	3.35E+03
48	27	471.57	75.00	1.18	36	2.5E-12	15000	720	1.51E+04
82	28	377.26	105.26	1.65	48	2.5E-12	15000	684	2.02E+04
83	29	377.26	105.26	1.65	48	2.5E-12	15000	684	2.11E+04
84	30	377.26	105.26	1.65	48	2.5E-12	15000	684	2.23E+04
85	31	377.26	105.26	1.65	48	2.5E-12	15000	684	2.18E+04
87	32	377.26	105.26	1.65	48	2.5E-12	15000	684	2.37E+04

Table F.3: Volume and mass ablation rates.

Scan ID	DoE ID	V, Volume (μm^3)	V_p ($\mu\text{m}^3/\text{pulse}$)	V_s ($\mu\text{m}^3/\text{s}$)	V_J ($\mu\text{m}^3/\text{J}$)	M, Mass (g)	M_p (g/pulse)	M_s (g/s)	M_J (g/J)	E_T , Total energy (J)
34	1	5.44E+08	3.77E+05	6.04E+07	3.36E+06	1.36E-03	9.44E-07	1.51E-04	8.39E-06	162.00
35	2	6.98E+08	4.84E+05	7.75E+07	3.23E+06	1.74E-03	1.21E-06	1.94E-04	8.07E-06	216.00
36	3	1.10E+09	7.64E+05	1.22E+08	4.07E+06	2.75E-03	1.91E-06	3.06E-04	1.02E-05	270.00
31	4	2.79E+08	1.36E+05	3.11E+07	1.73E+06	6.99E-04	3.40E-07	7.76E-05	4.31E-06	162.00
32	5	4.90E+08	2.39E+05	5.45E+07	2.27E+06	1.23E-03	5.97E-07	1.36E-04	5.68E-06	216.00
33	6	8.59E+08	4.19E+05	9.55E+07	3.18E+06	2.15E-03	1.05E-06	2.39E-04	7.96E-06	270.00
28	7	3.21E+07	8.91E+03	3.57E+06	1.98E+05	8.02E-05	2.23E-08	8.91E-06	4.95E-07	162.00
29	8	2.26E+08	6.27E+04	2.51E+07	1.05E+06	5.64E-04	1.57E-07	6.27E-05	2.61E-06	216.00
30	9	6.50E+08	1.81E+05	7.23E+07	2.41E+06	1.63E-03	4.52E-07	1.81E-04	6.02E-06	270.00
43	10	3.50E+08	7.29E+05	1.17E+08	6.48E+06	8.75E-04	1.82E-06	2.92E-04	1.62E-05	54.00
44	11	5.69E+08	1.19E+06	1.90E+08	7.91E+06	1.42E-03	2.97E-06	4.74E-04	1.98E-05	72.00
45	12	8.40E+08	1.75E+06	2.80E+08	9.33E+06	2.10E-03	4.38E-06	7.00E-04	2.33E-05	90.00
40	13	9.20E+07	1.35E+05	3.07E+07	1.70E+06	2.30E-04	3.36E-07	7.67E-05	4.26E-06	54.00
41	14	3.26E+08	4.77E+05	1.09E+08	4.53E+06	8.15E-04	1.19E-06	2.72E-04	1.13E-05	72.00
42	15	6.57E+08	9.61E+05	2.19E+08	7.30E+06	1.64E-03	2.40E-06	5.48E-04	1.83E-05	90.00
37	16	1.15E+07	9.59E+03	3.84E+06	2.13E+05	2.88E-05	2.40E-08	9.59E-06	5.33E-07	54.00
38	17	8.91E+07	7.42E+04	2.97E+07	1.24E+06	2.23E-04	1.86E-07	7.42E-05	3.09E-06	72.00
39	18	3.81E+08	3.18E+05	1.27E+08	4.23E+06	9.53E-04	7.94E-07	3.18E-04	1.06E-05	90.00
52	19	1.92E+08	6.68E+05	1.07E+08	5.93E+06	4.81E-04	1.67E-06	2.67E-04	1.48E-05	32.40
53	20	3.66E+08	1.27E+06	2.03E+08	8.47E+06	9.15E-04	3.18E-06	5.08E-04	2.12E-05	43.20
54	21	7.28E+08	2.53E+06	4.04E+08	1.35E+07	1.82E-03	6.32E-06	1.01E-03	3.37E-05	54.00
49	22	4.14E+07	1.01E+05	2.30E+07	1.28E+06	1.04E-04	2.52E-07	5.75E-05	3.20E-06	32.40
50	23	2.06E+08	5.03E+05	1.15E+08	4.78E+06	5.16E-04	1.26E-06	2.87E-04	1.19E-05	43.20
51	24	4.58E+08	1.12E+06	2.54E+08	8.48E+06	1.15E-03	2.79E-06	6.36E-04	2.12E-05	54.00
46	25	1.82E+06	2.53E+03	1.01E+06	5.63E+04	4.56E-06	6.33E-09	2.53E-06	1.41E-07	32.40
47	26	5.03E+07	6.98E+04	2.79E+07	1.16E+06	1.26E-04	1.75E-07	6.98E-05	2.91E-06	43.20
48	27	2.27E+08	3.15E+05	1.26E+08	4.20E+06	5.68E-04	7.88E-07	3.15E-04	1.05E-05	54.00
82	28	3.03E+08	4.43E+05	1.01E+08	4.21E+06	7.58E-04	1.11E-06	2.53E-04	1.05E-05	72.00
83	29	3.17E+08	4.64E+05	1.06E+08	4.40E+06	7.93E-04	1.16E-06	2.64E-04	1.10E-05	72.00
84	30	3.34E+08	4.88E+05	1.11E+08	4.64E+06	8.35E-04	1.22E-06	2.78E-04	1.16E-05	72.00
85	31	3.27E+08	4.77E+05	1.09E+08	4.54E+06	8.16E-04	1.19E-06	2.72E-04	1.13E-05	72.00
87	32	3.55E+08	5.19E+05	1.18E+08	4.93E+06	8.87E-04	1.30E-06	2.96E-04	1.23E-05	72.00

F.2 Extra results from simulated parameters effects

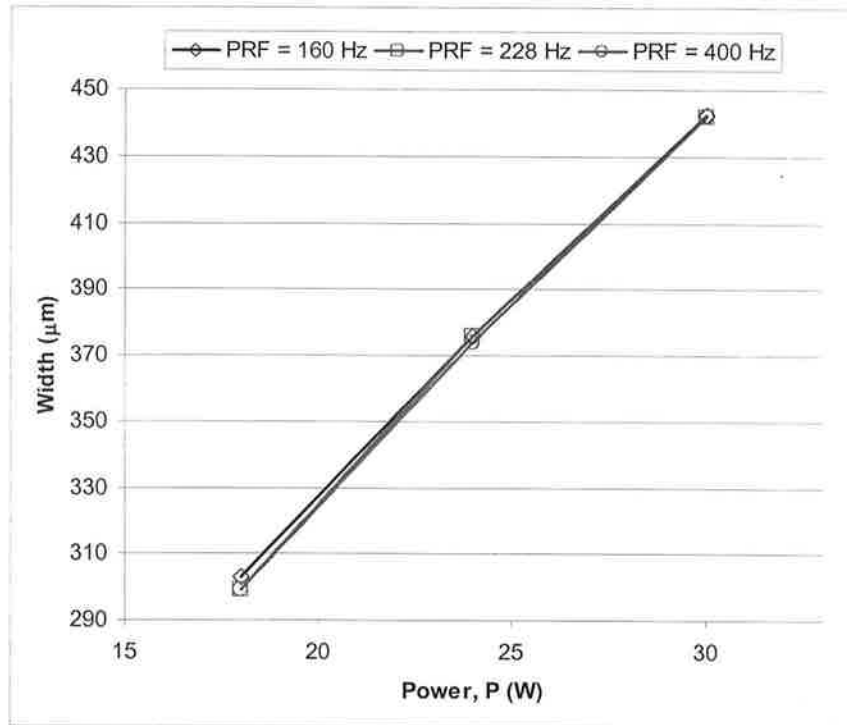


Figure F.1: PRF and P effects on channel width at $U = 100$ mm/min.

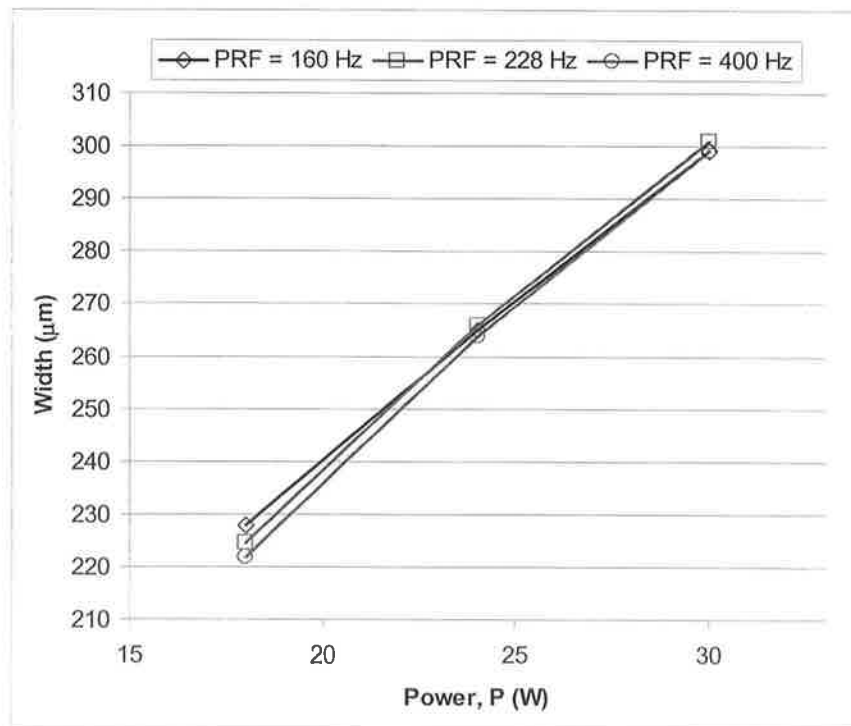


Figure F.2: PRF and P effects on channel width at $U = 300$ mm/min.

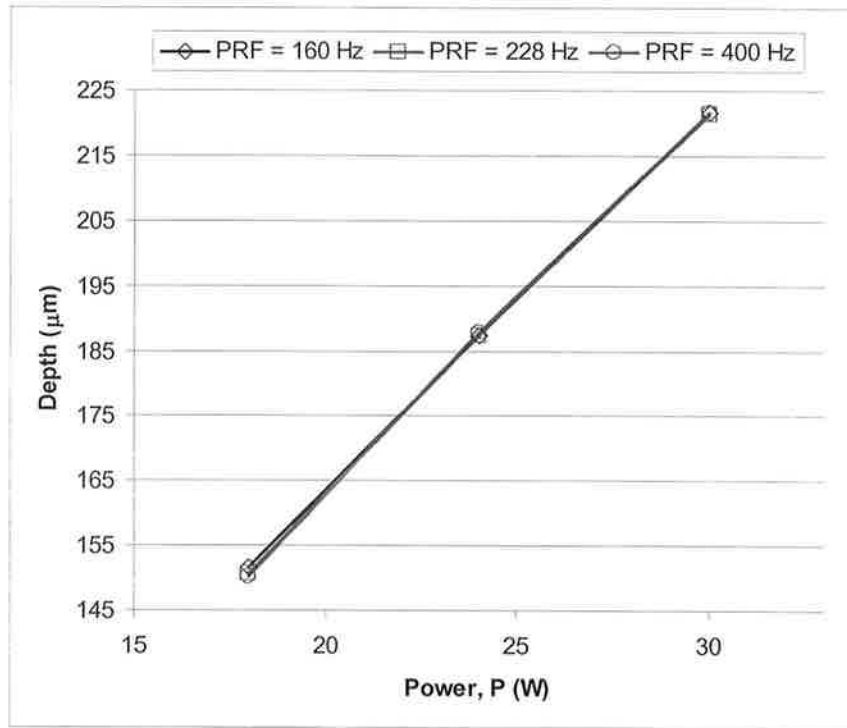


Figure F.3: PRF and P effects on channel depth at $U = 100$ mm/min.

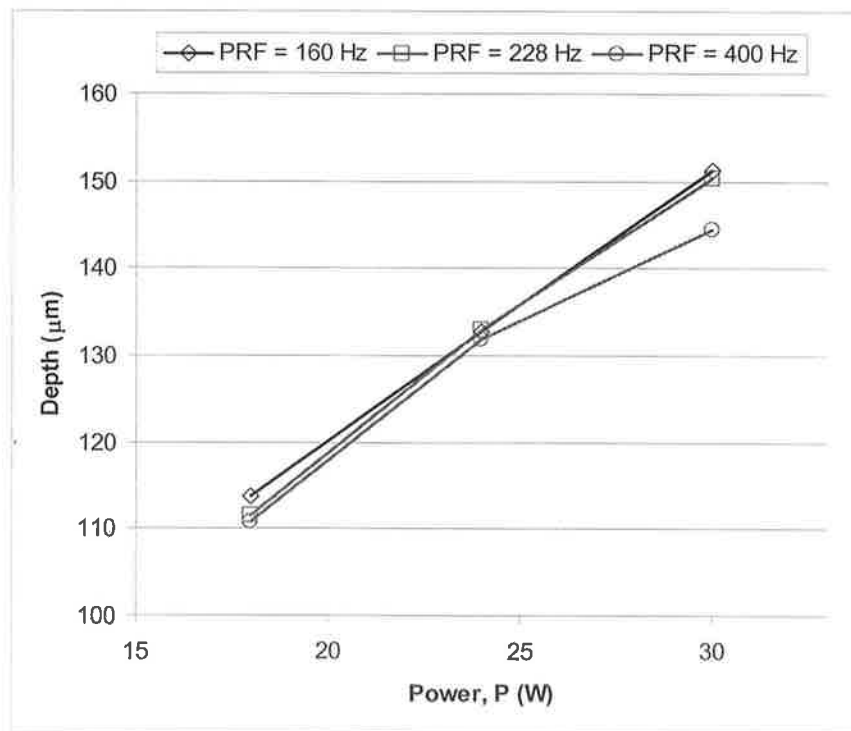


Figure F.4: PRF and P effects on channel depth at $U = 300$ mm/min.